CRANFIELD UNIVERSITY

A. BEEVERS

TRANSITION MODELLING FOR AXIAL COMPRESSOR FLOWS

SCHOOL OF ENGINEERING

EngD THESIS

This page has been left intentionally blank.

CRANFIELD UNIVERSITY

SCHOOL OF ENGINEERING

EngD THESIS

Academic Year: 2007/08

A. BEEVERS

Transition Modelling for Axial Compressor Flows

Academic Supervisor: Dr. João Amaral-Teixeira

Industrial Supervisor: Mr. Roger Wells, Siemens Industrial Turbomachinery Ltd

Management Supervisor: Dr. Palie Smart

3^{rd} November 2008

This thesis is submitted in partial fulfillment of the requirements for the degree of Engineering Doctorate.

This page has been left intentionally blank.

Abstract

The application of Menter's transition model (Menter et al. (2004a), hereafter known as the $\gamma - \theta$ model) available in the CFX CFD code, for use within an axial compressor design group was studied. Simulations of a range of turbomachinery applicable test cases were undertaken, including a range of transitional flat plates and a 2D compressor cascade. Results were compared to experimental data and the results of simulations performed with standard turbulence models.

The $\gamma - \theta$ model significantly improved the prediction of the boundary layer development, compared to the turbulence models. Comparisons with experimental data were also good. Features such as mid-chord transitional separation bubbles were predicted with the $\gamma - \theta$ model, but not with the turbulence models. The $\gamma - \theta$ model offered no consistent improved accuracy over the $k - \omega$ SST turbulence model when predicting leading edge separation bubbles. The more accurate simulation of the boundary layer enables a closer prediction of viscous losses.

2D and 3D unsteady simulations of a low-speed axial compressor stator blade boundary layer, subject to impinging rotor wakes, were conducted. The purpose was to determine the performance of the $\gamma - \theta$ model in this environment,

as there is no available literature for this. For both simulations, the model gave a good qualitative agreement to experimental data in the prediction of passing rotor wake effects on the suction surface. The effects on the pressure surface transition region due to wake passing were poorly predicted.

All models were simulated on low and high-speed axial compressor stages. Results showed no improvement over the turbulence models of the $\gamma - \theta$ model to predict blade exit parameters. The $\gamma - \theta$ model does not present a significant enough improvement in the prediction of the flow to warrant its regular use in the design of axial compressor blading. However, it presents a useful tool in the development of high lift compressor blading.

Acknowledgements

While the contents of this thesis is my own work, there are many whom require my grateful thanks because of their assistance along the way. Firstly, my original supervisor Paul Ivey, who made the project possible and provided me with valuable direction within the first year of the project. My gratitude must also go to the man who took over the reigns, Joao Teixeira, who regularly instructed me to advect myself downstairs and let gravity take its course. Joao will always be remembered as the champion of 'wonky little cases'.

Financial assistance for the project was provided by both EPSRC, and by Roger Wells, at Siemens Industrial Turbomachinery. His industrial knowledge and experience provided many a learning opportunity for myself.

My appreciation extends to Chris Freeman, the omniscient encyclopedia of all things related to turbomachinery, and for his direction in the battle against the enemy. My campaign has ended. I return from the field of battle with my colours waving in the breeze.

I would like to thank Mark Savill and Greg Walker for their providing the unsteady experimental data and their input to the unsteady transition simu-

lations work. Without them, Chapters 6 and 7 would not have been possible. Also to Kath Tipping who often seems to do a sterling job behind the scenes of coordinating the entire EngD course at Cranfield.

My office colleagues, especially Robin and Kevin, often made the office a much brighter place to be, probably to the detriment and annoyance of everyone else along the corridor. Also, without whom, nicknames such as "The Hound", "The Ferret", "The Cat", "Duncan", "The Shire Horse", "The Dungeonmaster", "The Patsy", "Valentino Rossi" and "Vaguely Unhelpful Ray" would never be known. Robin and I shared many of the very long, dark, hard hours in the office together in the final six months of our respective projects. We learned the value of consuming microwavable meals in order to rationalise our efforts.

Finally, I wish to thank my family, who never faltered in giving me kind words of encouragement and support when it seemed as if the end had no end. My parents have always set a good example of the value of hard work and the need to better one's abilities. Especially so for my father for his wise words of counsel throughout the four years.

Contents

List of Figures

List of Tables

Nomenclature

Abbreviations

DES Detached Eddy Simulation

DNS Direct Numerical Simulation

EVM Eddy Viscosity Model

HPC High Pressure Compressor

HSRC High Speed Research Compressor

IMechE Institute of Mechanical Engineers

LES Large Eddy Simulation

LSRC Low Speed Research Compressor

PEST Political, Economic, Social, Technological

PS Pressure Surface

RANS Reynolds Averaged Navier Stokes

RSM Reynolds Stress Model

SS Suction Surface

SST Shear Stress Transport

SWOT Strengths, Weaknesses, Opportunities, Threats

TKE Turbulent Kinetic Energy

TS Tollmein-Schlicting

URANS Unsteady Reynolds Averaged Navier Stokes

Greek Letters

α Inlet flow angle

δ^* Displacement thickness

δ_{ij} Reynolds stress model identity matrix

ϵ Eddy dissipation rate

γ Turbulence intermittency

λ Turbulent length scale

λ_θ Local pressure gradient

μ Dynamic viscosity

μ_t Eddy viscosity

ν_t Limited form of eddy viscosity

ω Specific dissipation rate

ϕ Flow coefficient

Π_{ij} Reynolds stress model pressure-strain correlation

ρ Density

τ Shear stress, Turbulence weight factor

τ_{ij} Reynolds stress tensor

θ Momentum thickness

Roman Letters

a Circumferential offset of stator blade leading edge from the centre of the IGV wake avenue

C Absolute velocity

c_f Local skin friction coefficient

c_p Local pressure coefficient

D_k Turbulent kinetic energy destruction term

$F1$ Blending function for $k-\omega$ SST model

$F2$ Blending function for $k-\omega$ SST model

H Shape factor

H_m Average shape factor from the neutral stability point to transition

i Flow incidence angle

K Acceleration parameter

k Turbulent kinetic energy

K_{crit} Critical acceleration parameter

K_L Laminar kinetic energy term

K_T Turbulent kinetic energy term

L Characteristic length

l Length scale

L_ϵ Eddy length scale

$n\hat{\sigma}$ Spot propagation parameter

p Pressure

P_{ij} Reynolds stress model exact production term

P_k Turbulent kinetic energy production term

P_{kb} Buoyancy production term

P_t Total pressure

$P_{\theta t}$ Production term for $\gamma - \theta$ model

R Leading edge radius

Re Reynolds number

Re_c Reynolds number based upon blade chord length

Re_L Reynolds number based upon length of transition region

Re_T Turbulent Reynolds number

Re_v Vorticity Reynolds number

Re_X Reynolds number based on distance from leading edge

Re_{XE} Reynolds number based on distance from leading edge at the end of transition

Re_{θ} Momentum thickness Reynolds number

$Re_{\theta i}$ Momentum thickness Reynolds number at the point of neutral stability

Re_{θ_m} Mean value of momentum thickness Reynolds number from the neutral stability point to transition

$Re_{\theta t}$ Momentum thickness transition Reynolds number

$Re_{\theta_{tc}}$ Critical momentum thickness transition Reynolds number

S Invariant strain rate, Blade pitch

$\dot{s}$ Entropy generation rate

s^* Non-dimensionalised distance along the blade surface

S_{ij} Mean strain rate tensor

t^* Non-dimensionalised time based on rotor passing period

t_{se} Transition length

Tu Turbulence intensity

$\widetilde{Tu}$ Periodic turbulence intensity

Tu_D Total disturbance level

U Tangential blade velocity

u Velocity in streamwise direction

$< u >$ Ensemble averaged velocity

$\bar{u}$ Time averaged velocity

$U_{i,j,k}$ Velocity in tensor notation

u_{in} Inlet velocity

U_{mb} Tangential blade speed at mid-span

u'_{rms} RMS time-mean velocity

u_s Pitchwise averaged velocity

U_∞ Freestream velocity

$-\overline{u'v'}$ Reynolds stresses

v Velocity perpendicular to streamwise axial direction

$Variable_s$ Start of transition

$Variable_{ref}$ Reference variable

$Variable_{t_e}$ Transition end point

$Variable_{t_s}$ Transition start point

W Relative velocity

w/S Circumferential distance non-dimensionalised by stator pitch

x, y, z Cartesian coordinates

x_{ijk} Position vector in tensor notation

x_{sep} Streamwise distance of boundary layer separation point

x_{st} Distance between boundary layer separation and the start of transition

Y Total pressure loss coefficient

Y_p Profile loss coefficient

y_{step} Step height

y^+ Non dimensional wall distance

This page has been left intentionally blank.

Chapter 1

Introduction

The importance of 3D CFD as a tool within the design process for an axial compressor cannot be understated. Since the 1980s, its use has become almost ubiquitous amongst the gas turbine community. Design cycle time and costs have been reduced through its use (Brilliant et al., 2004). The requirement for more costly and sometimes less informationally rich physical testing has lessened. The main advantage of CFD is that in a matter of hours, it allows the user to see and understand the flow within a compressor blade passage, and to estimate the associated losses. From this, blade designs can be fine tuned to reduce losses induced by viscous effects such as separation and corner stall. This can be repeated within a few hours with a new blade design.

As the flow conditions change significantly from the design flow conditions, those viscous flow features become more prominent and dominate the flow. Large regions of separated flow and corner stall can combine to cause the blade passage to stall or the compressor to surge. Thus the simulation of these features increases in significance. The accurate prediction of off-design flows through an axial compressor is essential to the efficient running and

longevity of the compressor and gas turbine engine, as machine configurations can be fine tuned to reduce the effects of these phenomena. Poor prediction can lead to an extended and costly design cycle, and a compressor which does not meet its design intent. This in turn affects the efficiency and fuel burn of the engine. Before one can accurately simulate the flow away from the design point, the flow and its viscous effects at the design point must be understood and predicted with large degree of confidence.

One of the critical components of the 3D CFD simulation process is the turbulence model. A turbulence model attempts to describe the effect of turbulence upon the flow by closing out the Reynolds Stress equations created by Reynolds Averaging the Navier-Stokes equations. Whilst most modern turbulence models have been shown to give suitable predictions for even multi-stage simulations (Belamri et al., 2005), the accuracy of the turbulence model degrades when simulating those viscous effects at off-design flows, as shown by Woollatt et al. (2005). Indeed, Halstead et al. (1997a) showed effects such as aerodynamic loss, boundary layer transition, unsteadiness due to impinging wakes and flow separation, all require improvement on their prediction using turbulence models.

With the current trend of rising fuel prices, legislation for lower emissions and increasing global competition, the gas turbine manufacturer is seeking to increase both the efficiency and power output of the engine across its range of operation whilst reducing costs. This can be achieved in part through a fine tuning of the current blade design, or a reduction in blade count with a significant blade redesign.

The role of transition prediction is starting to become more important in the prediction of both design and off-design performance. Menter et al. (2005) showed that using a transition model significantly improved the prediction of the loss coefficient. The location of transition onset and its length can have a considerable influence on the blade design process, as it not only affects the point of and amount of separation (both separation bubble and terminal separation), which leads to blockage and a reduction in stage loading, but also determines the amount of laminar flow and the growth of the boundary layer along the blade. As the loss is proportional to the momentum thickness of the boundary layer at the trailing edge, studies by Halstead et al. (1997c), Walker et al. (1999) and Wheeler et al. (2007a) show the impact of unsteady effects on the transition region and subsequent momentum thickness at the trailing edge to be significant. Thus, the simulation of transition in compressors gives a more accurate representation of the losses at design, but also assists in the improvement of the off-design performance. Indeed Praisner et al. (2007) found that incorporating a transition model into the design process enlarged the design envelope available from which to design a low pressure turbine aerofoil.

The effects of wake-induced transition upon the transient boundary layer were studied by Howell (1999) and Ottavy et al. (2004). They concluded that the simulation of wake-induced transition is essential for future compressor designs. As modern compressors have reached efficiency levels which are difficult to improve upon, weight reduction and a decrease in production costs can be achieved through reducing the number of blades. Howell (1999) demonstrated through an unsteady analysis of a low pressure turbine blade row, the unsteadiness of passing wakes of upstream blade rows can produce

higher lift blades without increasing profile loss. It was shown that the process of wake-induced transition was a key factor of this discovery. Wake impingement and subsequent laminar calmed regions reduced the establishment of a separation bubble on the suction surface and reduced loss. This counter-balanced any increase in loss due to wake-induced turbulence. Wake effects generally increase the profile loss of a blade (Wheeler et al., 2007a). Shobeiri (2005) stated that an accurate prediction of the unsteady boundary layer transition behaviour is a prerequisite for a reliable calculation of the blade profile losses, heat transfer characteristics and, thus, the efficiency of the turbine or compressor stages.

There is not a considerable amount of literature reviewing the use of transition models in axial compressors, as the focus has been on using transition modelling for predicting heat transfer in turbines. Currently, there is little literature available detailing an unsteady simulation of wake-induced transition in an axial compressor. The work in this thesis attempts to demonstrate the current capabilities of a commercial code to simulate the unsteady transitional boundary layer affected by impinging wakes. The thesis also attempts to show the benefits of transition prediction for axial compressors and discusses appropriate methods and best practise.

1.1 Thesis Description

Chapter 2 discusses the implications of managing the use of CFD in the design process. A treatise detailing past, present and future methods of integrating CFD into the design process alongside experimental methods, the

current research taking place in numerical simulation, and a suggestion of a strategy of developing the CFD capabilities in a small turbomachinery group is included.

A review of the literature on turbulence and transition modelling is contained within Chapter 3. An overview of some current main simulation techniques and available models is given. Supporting arguments for the use of and development of transition modelling are set forth. A review of best practice in the use of turbulence models concludes the chapter.

Chapter 4 presents the results of initial simulations designed to highlight the capabilities and limitations of current turbulence models available in a commercial code through a series of test cases. These test cases include a backward facing step, transitional flat plates and a compressor cascade. The details of the models used are included.

Once the case for using a transition model has been highlighted, the transition process within an axial compressor is reviewed in Chapter 5. The material will familiarise the reader with processes and terms used in further chapters.

Simulations of unsteady wake-induced transition in a 2D and 3D environment are shown in Chapters 6 and 7 respectively. The effectiveness of the methodologies and transition model used is assessed. The methodology and results of simulations of both a low speed and high speed axial compressor are given in Chapter 8. This chapter aims to verify the performance of the models used in Chapter 4 in an actual turbomachinery environment. It also

aims to show any benefits of using a transition model to evaluate some key stage performance variables. Finally, Chapter 9 draws the thesis to a close with an overview of the findings of the work as a whole, and contains recommendations for future work.

Chapter 2

Industrial Relevance of Research - Implications for the Design Process

2.1 Introduction

The design process undertaken for an axial compressor is a complex one, involving many iterations and requiring extensive analysis to ensure the resulting design performs to its design intention when installed in the engine. To ensure the compressor performs as designed, a series of physical tests are performed. These tests confirm the degree to which the theoretical performance of the compressor matches the installed performance. These physical tests range from a simple, single passage cascade test to a full engine test. The type of test required is dependent upon the stage of progression through the design process.

Since the introduction of numerical simulation methods, such as 3D CFD,

into the design process, the degree to which physical testing is required to validate a design before market entry is lessening. Especially with the advent of 3D CFD, the length of the design process and its associated costs have been reduced. There is a careful balance to be struck between the absolute reliance on CFD results and an aggressive reduction in physical testing. Both numerical and experimental methods have their associated risks which require managing in such a way as to reduce the overall design process length and costs. However, this process must be conducted such as to minimise the risk of the finished engine not meeting its design intent.

Both numerical and experimental methods can be viewed essentially as data gathering exercises, by which the gathered data is compared against the expected values calculated in the design process. The extent to which 3D CFD is used at the expense of reducing the experimental testing is decided by the project manager. To be able to make this decision, the project manager should know and understand the strengths and weaknesses of each method of data gathering. A summary of these can be found in Table 2.1.

The main purpose behind undertaking physical testing can be summarised in a roundabout manner by one time US Defence Secretary, Donald Rumsfeld, who when giving a news briefing is quoted as saying "... as we know, there are known knowns; there are things we know we know. We also know there are known unknowns; that is to say we know there are some things we do not know. But there are also unknown unknowns - the ones we don't know we don't know." (Rumsfeld, 2002). Expressed more plainly, physical testing is required to verify the correct application of well understood physics models, to validate models based upon incomplete physical understanding, and to

	Physical Testing	**CFD**
Strengths	Highest level of accuracy	Relatively quick to obtain results
	Captures all physical effects	Complete flow information
	Easily measure complete compressor / machine	Relatively low up front capital and running cost
	Includes all geometry details	Can run many concurrent simulations
	Rapid data acquisition over range of conditions	Easily simulate new configurations
	Can capture unsteady effects	Can simulate experimental procedures
	Can quantify performance and losses	Always available & easily repeatable
	Only way to measure turbulence	Do not have to deal with scaling issues
Weaknesses	High up front investment and running costs	Cannot accurately account for all physical phenomena
	Data available only at instrumentation location	Limited by computational resources
	High cost and time to set up new configurations	Not easy to simulate multi-stage
	Equipment intrusiveness can affect results	Performance degrades away from design point
	May require non realistic set-up	Results are user and code dependent
	Significant cost and risk to obtain high quality results	Time consuming to obtain range of flow conditions
	Scale effects need to be accounted for	Unsteady effects difficult to model
	Limitations due to instrumentation used and subsequent failures	Least effective at predicting losses
	Difficult to repeat	Feasibility requires simplified geometry

Table 2.1: Comparison of strengths and weaknesses of physical testing and CFD

discover if there are any phenomena which have not been accounted for and which may affect the performance of the compressor. Physical testing will always be required to some degree to discover these, the unknown unknowns.

Physical testing is considered by industry to give the highest level of accuracy of results, as it has the capability to capture all of the physical effects found in a gas turbine. It can capture in service real time unsteady data rapidly over a range of operating conditions for a particular machine with a particular geometry arrangement. It is limited to the type of test undertaken, i.e. full machine or single stage etc, and can be costly in both time and money to change the geometry undergoing testing. The richness of the data, or the amount of information, contained within the data, and also its spacial density is reduced compared to the amount gained using CFD. The instrumentation used can sometimes alter the accuracy of the data gathered (such as the disturbance of hot wire probes acquiring boundary layer data close to the blade surface), and unreliable instrumentation can compromise parts of the data. Though physical testing is always costly and provides a limited amount of information by comparison to numerical methods (assuming that the test facilities already exist, a complete high-speed compressor test program may cost up to several £M), the idiosyncratic nature of the computational alternative carries too great a risk to be solely relied upon.

3D CFD gives the opportunity for the designer to understand and more clearly attempt to control the three dimensional nature of the flow. It gives greater richness and spatial density of flow information when compared with physical testing. The capabilities of the software and the modelling of the physics give 3D CFD its ascendancy in the simulation hierarchy for most

aerodynamic simulations conducted in the design process. Geometrical and machine arrangement changes can be made and re-run relatively easily, although variations in operating conditions require re-runs which may take hours, days or possibly weeks depending upon the complexity of the model and the computational grid used. A physical test run may only take an hour or two. However, given enough computational resources, CFD simulations may be ran concurrently and during non-working hours, reducing the overall time required.

Experimental set-ups can be simulated using CFD to understand the if the instrumentation has a significant adverse effect on the part of the flow being studied or whether a simplified set-up is representative of the more complex geometry. CFD does not have to account for any scaling effects, as the simulation can compute the full size geometry and the simulations are repeatable as the boundary conditions remain constant if not altered by the user. Perhaps most importantly, it is relatively inexpensive to run and maintain compared to a physical test facility. The capital required to acquire facilities to run a CFD code can range from a couple of £k for a good PC workstation to more than £1M for a powerful supercomputer facility[1].

All industrially relevant numerical methods have their limitations, which primarily stem from insufficient computing power to use methods which fully resolve the smallest scales of turbulence (see Section 3.3.1). Using turbulence models necessitates that not all physical effects are accounted for. However not all physical effects are accounted for due to the limitation of knowledge

[1]Cranfield University's new Astral cluster, an HP DL140 G3 cluster with 800 processors and 12 GFlops cost £0.8M

of certain physical processes, such as transition. Unsteady and multi-stage effects are also difficult to model, whilst codes are widely reported to degrade in accuracy the further the operating condition is from the design point. The accuracy of the results are heavily dependent upon the capabilities of the code and the skill of the user. The geometry used in the simulations is often simplified to reduce computational cost, and may cause the so called "unknown unknowns" to be neglected in the simulation, only to be discovered during physical testing. These factors contribute to the limited accuracy of loss prediction using numerical simulations. Accurate loss prediction is vital as it determines the pressure rise throughout the compressor. The compressor is then matched to the turbine based upon its stage distribution. Failure to match the turbine and compressor will result in an inefficient engine.

As loss prediction is crucial to the design process, CFD is used to predict the losses generated by a range of incremental blade designs and varying flow conditions. CFD is used as a data enrichment tool alongside physical testing programs, once it has been validated against known appropriate experimental data (Hooker et al., 2006). It is almost universally accepted that empirical comparisons of CFD data with experimental data will always be necessary, due to the complex nature of multi-stage machines, even if it is due to the difference between simulated and actual geometry (Smith Jr, 2002). Giles (1998) states that the main reason this happens is to reduce the risk of so called 'design surprises' in the design process, equivalent to 'unknown unknowns'.

With rising prices for the earth's natural resources, such as gas and oil, and the increasing competition in a global marketplace, to remain competitive,

engine development costs, running costs and environmental impact must be realised. Customer drivers as given by Charles Soothill, Vice President at Alstom Power Turbo-Systems include, time to market and product quality. These are vital if the engine manufacturer is to avoid incurring penalties from the customer and / or regulator. He reflects the attitude across the whole of the gas turbine industry when he mentions that validation is important and Alstom constantly aims to reduce the time between specification launch and product delivery. He argues that "by taking time out of a process and being more consistent in the technology applied, the business risk is reduced" (Hanna, 2006). Engine manufacturers are constantly searching for ways to reduce design cycle time and costs, whilst improving the efficiency and power output of its engines. With a full compressor test and other test schedules costing anywhere up to several £M per schedule, 3D CFD and other simulations are used to reduce the amount of testing required, the number of required design cycles, engine development time and hence cost. However, as Herring (2006) explains, since the development of 3D CFD, and hence the greater use of sweep and lean etc to increase efficiency, blades have become more 3D, and less applicable to traditional 2D blade families. This means that increased testing of 3D blades is now required, which is more costly. Testing now takes place more commonly on cheaper low speed test facilities and the results can be transformed into high-speed blades (Lyes, 1999).

As the number of design cycles are reduced, the application of the phrase 'getting it right first time' becomes more prevalent, as engineering mistakes or reworks can be costly as shall be shown shortly. An engine manufacturers ability to reduce its time to market, whilst still producing an engine which matches its design intent, ultimately depends upon how it utilises its com-

putational, experimental, knowledge and labour resources. This chapter will attempt to show how new models and techniques may be used to more easily explore the design envelope, and develop more advanced blading through a greater return of information from computational simulations. It will describe how investment in more advanced 3D CFD techniques will increase the accuracy and quality of the CFD results. In conjunction with the work detailed within this thesis, the benefits of using these more advanced CFD techniques wisely will become apparent.

Firstly, the example of the Pratt & Whitney PW6000 engine provides a useful examination of some of the issues involved in such a complex process. This example was abbreviated from Bowen (2006).

2.1.1 Example - Pratt and Whitney PW6000 Engine

The Pratt & Whitney PW6000 engine was developed for installation on the new Airbus A318, intended to be launched at the end of 2002 after a year long certification programme. The A318 is a 100 seat, short haul aircraft developed to complement the A320 family and rival Boeing's 737. The Pratt engine was developed specifically for the A318, offering a weight and cost reduction and fuel burn efficiency saving over other suitable, more powerful and heavier engines such as CFM56 and IAE V2500 (of which Pratt & Whitney was a partner). The first A318 prototype flew its maiden voyage on Jan. 15, 2002, but the milestone flight served to highlight mistakes made in the design of the Pratt engines. The airplane burned some 6% more fuel than projected, a discovery that forced Airbus to extensively amend its certification schedule to accommodate the approval first of a version powered by CFM56-5s. After

completing 100 hours of testing in the first prototype with the PW6000s, Airbus fitted the airplane with the CFMs, allowing it to resume flight testing on Aug. 29, 2002, in time to meet its new certification and first-delivery targets.

The source of the fuel-efficiency problem in the Pratt & Whitney-powered A318 stemmed from an ambition to lighten and simplify the engine by minimising the number of stages in the high-pressure compressor (HPC). The engine was designed with four fewer stages, and life-limited parts in the compressor and turbine were designed to be replaced at the same time. The PW6000's five-stage HPC design placed an unobtainable pressure rise demand on each stage, creating a condition in which fuel burn reached a point of diminishing returns. To rectify this, Pratt & Whitney adopted a six-stage compressor design from German engine builder MTU at considerable extra cost. The change resulted in a three-year delay in the engine's certification and service entry, from late 2002 to 2006. The forced delay of the launch of the A318 caused Airbus to lose major customers including, British Airways, Egyptair, Air China and American Airlines. Another knock on effect for the Airbus A318 was that it was forced to use the heavier CFM56 engine exclusively early on, which reduced the expected fuel efficiency. This caused customers to either buy the slightly larger A319, or cancel their orders. By the time Pratt & Whitney brought the PW6000 engine into service, Airbus had lost a large proportion of its market for the A318. Despite being redesigned over fuel burn rates, the PW6000 still uses more fuel than the CFM56. With high oil prices, airlines may still choose CFM56 engines, but Pratt & Whitney insists that reduced maintenance costs make the PW6000 a more affordable choice. The PW6000 engine has already lost millions of dollars on its projected profits. This example is not simply one of a poor

design, but a catalogue of changes made to the way Pratt & Whitney used CFD in their design process, brought upon by several factors, which adversely affected their product.

During the 1980s Pratt & Whitney, a resource rich organisation, had a leadership in technology development in its engines. In the 1980s the organisation was geographically divided so that most of the military and space activities were located in Florida, with the civil engine activities located in Connecticut. Even though it had world class analytical skills, it could also afford to use a "build them and bust them" philosophy. Activities were also checked and double checked and so on as the task delivery went up the organisation. In the early 1990s Pratt & Whitney adopted new computational simulation techniques to develop a cheaper, faster analysis process than the old "build them and bust them" method. Also their new Integrated Product Deployment (IPD) managed product development process bypassed much of the engineer's influence through the programs office working directly with markets and customers to develop engine specifications and costs. In the mid 1990s, Pratt & Whitney chose an aggressive strategy to reduce new engine development costs from $1 billion to $300 million and reduce development times from 45 months to 30 months. Engineering was placed with manufacturing in module centres to reduce the possibility of designing non manufacturable components. Engineers now had to report to module centre general management, further reducing their authority in the product development process.

During the mid to late 1990s, Pratt & Whitney closed their highly successful Florida military development plant and relocated to Connecticut to reduce fixed costs. Well over half of the Florida senior engineers, known as the

"oak trees", at Pratt & Whitney, chose to leave rather than relocate. This coupled with Pratt & Whitney's intensive use of computational methods (including CFD) over "build them and bust them" physical testing techniques, contributed the PW6000 problems. It is widely acknowledged by the gas turbine industry and engineers working at Pratt & Whitney at the time that the problems with the PW6000 HPC resulted in the management selling a product that the engineers could not actually create. This was due to a lack of authority of the engineers and the overuse of CFD over testing. This left Pratt & Whitney in a precarious position of needing a virtually flawless product development program to be able to compete in the future.

This example shows how external influences such as poor strategy choices and increased market competition, can lead to a change in the design process that builds in inherent problems which can lead to a non-delivery of an acceptable engine. In this case, the effects reached not only Pratt & Whitney, but also Airbus in the loss of orders and expected market share, to which it has never recovered for the A318, but also Airbus' customers who had to change their orders and make changes to their strategic plans. In the power generation market, the non-delivery of an engine with agreed performance specifications would affect the company through increased fuel costs, which the manufacturer would have to pass on to the end customer through either electricity prices (if selling to the market) or an increase in product prices (if manufacturing products). Manufacturers may be fined by the customer if the engine cannot meet the required specifications. Engine customers may also be fined if found in breach of environmental laws and regulations, or if the performance leads to a deviation from predicted maintenance schedules, then this would also increase the cost of running the engine as compared to

the business case it was purchased on.

Through this example it has been shown that the increased use of CFD in the design process must be carefully managed. Pratt & Whitney over-relied on the use of CFD at the expense of reducing physical testing. At the same time, they reduced the longstanding knowledge base through their relocation program. Without this knowledge, problems in the design process went unacknowledged by younger engineers until it was too late. The changes to the reporting system which reduced the authority of the engineers also contributed to the failure of the initial PW6000 engine. Engineers were no longer allowed to have full control over decisions to use CFD and or physical test data for the design.

This chapter will now turn its attention to describing the design process, and how CFD may be typically utilised by a conventional axial compressor design team.

2.2 CFD in the Design Process

The design process for an axial compressor is a complex one with many factors to consider. The aerodynamic aspects, whilst important are only one of a number of considerations, including structural integrity and acoustic performance. Indeed, the importance of avoiding blade failure or ring failure is far greater than increasing aerodynamic efficiency. A schematic representation of a typical design process is shown in Figure 2.1. From initial specifications such as required pressure rise, mass flow, etc, 1D meanline and 2D through-

flow calculations are conducted which enable a more detailed specification for blade design and annulus shape. From the resulting blade shape, 3D CFD simulations are then used to optimise the blade shape to reduce aerodynamic loss and increase pressure rise. When the 3D blade shape has been consolidated, mechanical integrity analyses such as finite element stress analysis, vibration and flutter analysis are undertaken to ensure the blade operates without mechanical failure. This process may take many iterations to converge upon an appropriate design. Once an appropriate solution has been found, certain components or groups of components may undergo a physical testing schedule dependent upon the change from previous tested designs. This may confirm the validity of the simulations, or highlight areas where further refinement of the design is advisable.

Since its inception, the use of CFD in the design process has evolved and increased over the years. This section will compare the design process from the early days of CFD to the present. It will also indicate, to the extent it is possible to fathom to an outside observer, the role it plays within the design process of the Compressor Group at Siemens Industrial Turbomachinery Ltd, Lincoln, UK.

2.2.1 Past use of CFD

CFD has been used in companies such as Alstom since 1970s (Hanna, 2006) when they developed their own codes for turbomachinery applications. For many years though, 2D highly empirical codes were used to predict such parameters as deviation, pressure rise, wall blockage, tip clearance and secondary flows. 2D blade profiles created from well documented blade families

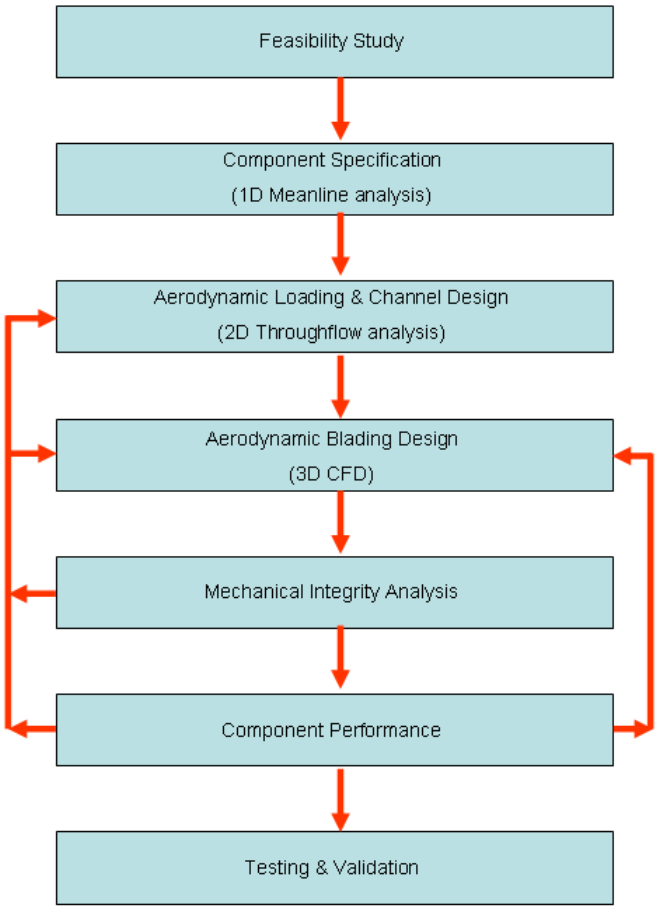

Figure 2.1: Generic Design Process for an Axial Compressor.

were used. Large test programs were still required to validate the numerical results and adjust subsequent empirical correlations. As these codes are highly empirical, when the simulated flow starts to significantly depart from the design flow, or if the blading significantly deviates from the blading upon which the empiricism is based, the empiricism becomes less relevant, thus reducing the accuracy of the codes. For the 2D codes to be of good accuracy, the viscous flow effects must be included in the code, either directly, or

indirectly through empiricism.

Before the more widespread application of 3D CFD at the start of the 1980s, blade-to-blade (S1) and through-flow (S2) calculations were the main numerical methods used to develop blade and annulus profiles. These S1/S2 methods calculated the inlet and outlet conditions for the 3D CFD code. At this time, the CFD code was unable to provide multi-row simulations due to a lack of available computational power. As Denton and Dawes (1999) explain, only until the late 1980s was 3D CFD able to be used as a routine design tool. Advances in computational power now allowed grids of sufficient density, which returned lower errors than the S1/S2 codes to be used. However, the inability to simulate unsteady blade row interaction limited its use in the design process. CFD methods at this stage also could not accurately predict absolute loss levels, as compared to other methods. The S1/S2 calculations continued to play an important part in the initial phases of the design process.

Since the practical inception of 3D CFD in the 1980s and its more common use in 1990s, the type of model used has evolved. Due to the increase in computing power, more comprehensive physics are now included. Initially, RANS based codes included simple mixing length models, and later, one-equation models. Two-equation models such as the k-ϵ and k-ω models became popular during the 1990s and remain so to this day. Reynolds Stress models were introduced in the late 1990s. Reynolds Stress models attempt to calculate the Reynolds Stresses rather than modelling them as with earlier algebraic, one and two equation models. At this time, low Reynolds number transition models also came to the fore. With increased computing power, one could integrate to the wall without the use of wall functions.

A general aerodynamic design process as used in Rolls-Royce during the late 80s - early 90s is given by Scrivener et al. (1991);

1. Through-flow model is established with appropriate loss and deviation profiles. 3D CFD inputs are taken, and a turbulent boundary layer is added from previous 3D solution to an upstream or similar blade row.

2. Blade profiles are designed to match the 3D solution using a 2D blade-to-blade design program.

3. 3D solutions are compared to the design intent.

4. Blade rows are modified until the design exit flow is achieved in the 3D solution. Modifications which preserve the 2D design intent and minimise 3D effects are chosen.

This generalised design process still holds true today as will now be discussed.

2.2.2 Present use of CFD

The generic steps of the design process have altered little with the increased development of 3D CFD, but the way in which CFD is used due to its increased capabilities, has changed. An example given by Pratt & Whitney (Brilliant et al., 2004) is used to describe a typical design process used today;

A 1D mean-line steady state code assuming ideal gas and compressible flow analysis is ran to define the flowpath shape and length, the number of blades and stage pressure ratios. It incorporates viscous effects via empirical loss models, which have been calibrated by past experience and results. This

enables the user to achieve reliable results quickly, but also prevents the new machine being radically different from previous machines. This also returns a first estimate of expectant weight and cost of the compressor.

From this, the 2D streamline code is used to define the blade radial profiles, velocity triangles and loading on 2D planes from hub to casing. It requires inputs from the 1D meanline code, previous 3D CFD simulations and past experience. It accounts for the boundary layer, secondary flows and wakes via historical data from cascades and test rigs. The results are compared to 1D meanline analysis and iterations may be required until a suitable solution is achieved. This may take approximately 2 months to work through.

Blade shapes are produced via a 2D potential flow solver, with the use of loss buckets to calculate the required surge margin. Again, this is iterated with the 2D streamline code to optimise the 2D blade profiles. Once this has been achieved, 3D CFD is ran for more than one speedline to confirm the previous analyses and to fine tune the blade design. Tweaks are made typically to prevent separation and corner stall. If significant 3D alterations are made to the blade, then it may require further 1D and 2D analysis to approve the 3D changes. The design is then analysed for mechanical loading, flutter and acoustic analysis.

3D CFD analysis has proved to be an invaluable tool within the design process because of the increased information it gives to the blade designer. 3D blade designs have become almost ubiquitous as the designer seeks to benefit from the use of lean, sweep, twist and bow. 3D blade designs can reduce the amount of separation and increase the stage pressure ratio. These designs

are possible by using more recent models such as Menter's $k-\omega$ SST model (Menter, 1994). Separation prediction through $k-\omega$ models, is now greatly improved; corner separation can now be predicted with some certainty, allowing the designer to fully utilise the advantages of 3D blade design.

More recently, transition models are being used. Transition models have been shown to give a more accurate description of aerodynamic loss (Menter et al., 2005) than a fully turbulent turbulence model. Howell (1999) and Ottavy et al. (2004) also showed that the use of a transition model could reduce blade count for high lift aerofoils. As they are still in their relative infancy, further work is required to increase their accuracy and a real degree of confidence for use for an industrial application.

3D swirling flows such as large corner stall regions are now more ably predicted using modern Reynolds Stress models, enabling a greater understanding of vortices that are found in a compressor. Mixing planes containing improved mathematics allow multistage machines to be simulated. Stall and surge still cannot be fully simulated with any degree of confidence, although moderately off-design flows are within the capabilities of modern turbulence models. Optimisation is starting to gain momentum, especially in R&D projects, where a large amount of blade designs are assessed both aerodynamically and mechanically. However, due to the very large demand on computational resources to gain reasonable results, it is seldom used in commercial activities.

Even with all these capabilities, Horlock and Denton (2005) warn that 3D CFD methods used in conjunction with traditional analytical methods such

as 1D mean-line design and 2D through-flow calculations are only of benefit after those traditional methods are refined and corrected. Even today, loss predictions are still not accurate. Considerable experience and good judgement are required to interpret loss predictions. Indeed Bruna et al. (2006) state that the use of reduced order modelling tools (1-D, 2-D, through-flow) is still the most effective way to explore the design space of a new configuration.

Pratt & Whitney found that using 3D CFD for their PW6000 LP compressor increased the time taken for its design, but more importantly, reduced the risk of a redesign. They stated that 30% of the total design process was spent using 3D CFD. Most likely this is because the solving time and post processing time is much greater for 3D CFD than for 1D and 2D code. A greater solving time is due to the increased complexity of the code, and the greater post processing time is due to the greater richness of information, because of the increased capabilities of the code, of which the designer must scrutinise.

Traditionally, companies have been reticent to commit large portions of time waiting for the CFD to converge to a solution for actual commercial projects. 2-3 CFD solutions per day when developing a speed line characteristic may be common. The level of detail and turbulence model used depends upon the level of computing power available to the user. Historically proved and trusted turbulence models and codes are used. The limitations of the turbulence model and code, along with the historical discrepancy between computational and experimental results are known by the project manager. The discrepancy is used for new designs, typically small evolutions of previous designs, to calculate the actual performance from the CFD analysis. A new turbulence or transition model, or CFD code will not be accepted for de-

tailed design analysis, until it has a proven historical record of a consistent and predictable level of accuracy. Companies with a large amount of available computing power may use more complex or new models or codes to explore new blade designs, or design processes such as multi-disciplinary optimisation techniques. However, these practices tend to be kept to R&D activities, rather than commercial projects.

2.2.3 CFD in Siemens Compressor Design Process

In general, the use of CFD within the design process at Siemens Industrial Turbomachinery, Lincoln, UK is similar to that which has been described. However, the finer points of how CFD is used by Siemens should be discussed. All of the aerodynamicists can use the CFD for general simulations, but each has his or her own speciality. During the early stages of the design / redesign process, all of the aerodynamicists can run the various design tools, such as CFD, forced response and basic stress simulations but as the process progresses through to the fine detail stages, their speciality is called upon at resolving certain problems, such as flutter etc. The mechanical stress analysis is passed to an finite element analysis specialist during the more detailed stages of the design process.

Siemens use MULTALL as their 3D CFD software rather than a newer commercial code, as they are familiar with the software's simulation characteristics, such as the delta between experiment and its predictions. The critical aspect of the CFD package is that they can predict the delta between CFD and experiment, so that it can be repeatable on the same grid using the same criteria, whilst the size of the delta is of secondary importance. Siemens use

the same grid criteria and setup for all their cases so they can attribute the variation in the results to the change in geometry, or flow conditions. A downside to using MULTALL is that although it is already set up for turbomachinery, due to the gridding structure, it is limited to using a certain range of blades shapes. Grids for blades with high stagger often result in a large proportion of highly skewed elements. Another advantage is that the user can run an approximately 500k nodes per stage run which solves 5-6 times quicker than CFX. This is essential as the compressor group does not have a large amount of computing resources available to them. The advantages and disadvantages of using in-house or commercial software can be seen in Table 2.2.

The issue of trust in the CFD code is the most important issue for Siemens. Any developments in the current code, or any new code which is acquired, must be benchmarked against a large quantity of experimental test cases, specific to Siemens. The group will only trust a new CFD code or development through developing a history of repeatable and predictable results. In other words, the code must produce the same results given the same inputs, and the code must calculate the same general trends as with their current codes. They also need to know how they can quantify the deficiencies in the code to understand where and why the inaccuracies between computation and experiment exist.

Finite element analysis is trusted almost implicitly to produce correct results, whereas CFD can at best come to within $\pm 3\%$ of profile loss and total pressure rise from experimental data. They also trust the in-house 2D throughflow code more than 3D CFD. Because of this, they use 2D through-

	In-House	Commercial
Advantages	Familiarity with users	Includes latest capabilities
	Optimised for company designs	Wider range of applications available
	Often solves quicker than commercial code	Very good technical support
	Results output optimised	Less empirical by nature
	General historical knowledge available	Superior post processing capabilities
	Autonomy over direction of future developments	Support available from user forums
Weaknesses	Requires in-house support	Uncertainty in mechanics of code
	Code developer support can be slow to respond	Results output not always optimised
	Legacy compatibility can be poor	Limited by licenses
	Documentation can be poor and outdated	Often computationally more expensive

Table 2.2: Comparison of advantages and disadvantages of using in-house vs commercial codes

flow calculations more than 3D CFD simulations and still require a certain level of physical testing to confirm 2D and 3D computational data. Physical testing is reduced if incremental changes are being made, rather than a new blade design. The level of testing required is decided through experience rather than a specific formula or rule.

Nonetheless, 3D CFD is used more than previously. The main constraint Siemens face with running 3D CFD is the time taken to run a simulation

with their computational resources. As stated previously, the group limits the size of most simulations to 500k nodes to enable them to run 3 cases per day. They would like to run multi-stage, unsteady simulations but require more computing power to feasibly do so. If they require a very large simulation or programme of simulations, such as unsteady multi-stage, then they may either use a university to carry out the program, or commission a program of physical testing. It may take less time to conduct a physical test program with their own resources than to wait for a third party to conduct 3D simulations.

A summary of the use of 3D CFD in Siemens can be given as; 3D CFD is used as a design tool, rather than design validation. Design validation is given through physical testing. 3D CFD is used to explore new designs before being taken through the full design process. The way in which CFD is used depends very much upon the resources available. The generic resources available at Siemens will now be discussed, and used to implement a suggestion for a strategy to enhance their CFD capability.

2.3 Resource Based View of Siemens

Barney (1986) concludes that for a firm to make an above normal profit on acquiring strategic resources in the marketplace, it is best to look at its own unique skills and capabilities, rather than an environmental analysis before acquiring those resources. Thus a resource based view of the firm has been taken to analyse the strategy for Siemens' design process. The resources available to Siemens Industrial Turbomachinery at Lincoln have been split

into the following;

- Hardware
- Software
- Financial
- Labour

This section will describe these resources and link them to the strategy suggested further in this chapter.

2.3.1 Hardware

Each aerodynamicist in the compressor group has their own dual processor workstation from which they carry out their CFD simulations. Workstation specifications for employees depend upon their work requirements, so the aerodynamicists have the latest specification available when purchased. They are updated every couple of years. The group has access to a central computing cluster, but rarely use it, only for large simulations. Most of their CFD simulations only take approximately 4 hours to complete.

The group has access to many physical testing facilities, which include a full compressor, single blade row cascades, stress and safety testing facilities. The group can choose whether they use complete engine tests, module tests (i.e. compressor), sub-module tests (i.e. transonic stages only) or cascade tests. These facilities tend to only give general machine and blade performance data. The amount of physical testing done depends upon the budget given from a higher management level, which the compressor group leader must bid for. The compressor group always sponsors a doctoral student, who in turn

may have access to physical testing facilities, or high performance computing facilities. Additional budget will generally be required to use the former.

2.3.2 Software

The group has full access to their own in-house 2D and 3D codes. These codes have been developed specifically in-house and in collaboration with universities. They also have access to the 3D commercial CFX code, but the licenses are centrally purchased. They rarely use this code, only for comparison with their code, as it takes 2-3 times longer to complete a simulation compared to their own in house codes. If the licenses were not held centrally, they would not buy any of their own. Conversely, Siemens Germany only use CFX, and as a result, have a good working relationship with them.

2.3.3 Financial

The group does not have an excessively large cash flow compared to other gas turbine groups or companies. They are always given the required financial support for operational work (i.e. re-blading, customer problem solving etc). Typically, the operational tasks consume 60% of the resources, and R&D 40%. R&D takes whatever is left over in terms of budget and time, but Siemens recognize a minimum amount if R&D is required, so it is never reduced to 0% for large periods of time. The compressor group leader must submit proposals to higher management and the Department for Trade and Industry for funding for R&D.

2.3.4 Labour

The compressor group in Lincoln has 4 aerodynamicists, with a further 4 in Fingspong, Sweden. Regular collaborations occur between the groups. Collaboration also takes place with USA and Germany (large $>$ 100 MW engines). Although it is sometimes a difficult exercise due to company bureaucracy, there are many interesting ideas and examples that may be applied to the smaller engines at Lincoln. They have specialists in 3D separation, flutter and CFD. It is not clear if they are also specialists in physical testing, but they are required to lead the physical testing teams. All aerodynamicists are given sufficient training by either the group, or by the software vendor to ensure correct use of the computational codes used by the group. New aerodynamicists are also allowed to complete additional courses such as MSc's, and are encouraged to become accredited with IMechE to enhance their professional development.

After Siemens bought Alstom in Lincoln, the aerodynamicists, who were originally located together in the same office, were removed from their current office and located with specific project groups around the site in an effort to more efficiently utilise resources available. To aid natural interaction between engineers, most offices are open plan.

Now that the resources currently available to Siemens have been discussed, the new and future advances in CFD will be explored, from both the technical work in this thesis and work conducted within the field of turbomachinery. A strategy of development and changes to Siemens' design process will be given. This will be compared with the strategy from another company with differing resources. The comparison between effective use of resources will

be given.

2.4 Implications of Current Research on Design Process

Understanding the current and medium term topics of research is an important task for industrial groups, as these topics will filter through to become industry standard in the medium term future. A search of past ASME conferences, relevant journals, university and other research establishment websites, reveals 4 main areas of research currently taking place. They are; Unsteady transition modelling using RANS codes, large eddy simulations (LES), developing Reynolds Stress models and developing reliable optimisation methods. Direct numerical simulation is increasingly being used to understand the fundamental physics of turbulence and transition, but computational demands mean that it will not be a viable design tool for some time to come, and hence will not be mentioned further in this chapter.

The most common topic for current research appears to be modelling unsteady transitional flows using unsteady RANS codes (URANS). Cranfield University, Cambridge University and DLR in Germany along with other smaller groups are undertaking studies in this area. It is more common to model turbine blading, because of heat transfer requirements, but the modelling of compressor blading is becoming a more frequent occurrence. There is much work to be undertaken on understanding the physics required in correlations and models used. How the model is connected to the correct transport equations also requires some work. Modelling both the transition

process and unsteady flows requires a greater time to solve, or a greater computational resource for the same solver time. Grid resolution needs to be much finer than when used in steady state simulations to capture the unsteady processes. This may double the node count of a steady state grid thought to be 'fine'. In addition, up to 400 transient results files may be required per unsteady simulation, all which require storing and post processing in order to achieve the benefits of running the unsteady simulation.

As a greater resources are required to store and post process the results, many simulations of this nature are currently defined as a 2D slice at mid-span. Post processing many files requires the post processing to be set-up in batch mode, and may require to run overnight. For 3D unsteady simulations, these problems are magnified. New post processing routines will also be needed to take into account the time varying nature of the results. These results will assist the aerodynamicist to further understand the unsteady development of the boundary layer, the development of separation and separation bubbles. It will benefit the understanding of how the boundary layer is affected by unsteady phenomena such as wake impingement and potential effects, and how they contribute to entropy generation and loss. Nevertheless, for some time to come, URANS models will not account for wake mixing and other anisotropic events that affect transition, as the models are based upon the Bousinesque assumption which is not valid for these phenomena.

To validate these new models and simulations, more experimental data is required. This includes hot film data from the blade surface, and possible use of laser techniques such as Particle Image Velocimetry or Laser Doppler Velocimetry, all of which are expensive techniques to use compared to more tra-

ditional hot wire experimental set-ups. Unless this data is acquired, URANS transition modelling will not become a mainstream design tool. Further to this, transition modelling on the rotor will continue to be uncertain as the physics remain unclear due to the problems involved with gathering data on the rotor blade surface.

The largest benefit for designers may be to use URANS transition to increase lift and reduce blade count as explained by Howell (1999) and Ottavy et al. (2004). Exploring these benefits will account for more time during the design process due to the combination of blade count and blade profiles required. It may be best suited to be used during an R&D exercise, and perhaps with an optimiser.

The use of LES for turbomachinery applications is currently being developed at institutions such as Manchester University, Imperial College, Stanford University and Aachen University. LES must be run transiently, requiring longer run times, computational power and storage facilities similar to that previously discussed for URANS transition modelling. For LES though, as a more refined grid is used than for URANS, these issues become greater. The same is also true for post processing as there is not only a greater amount of nodes to post process, but LES delivers the user a larger amount of information per node, giving a richer view of the flow.

LES gives the designer all of the benefits of URANS transition and the added advantage of more accurate accounting of anisotropic effects found in transition, wake mixing, vortices and separated regions. As blading and compressor design become even more refined, interactions from secondary gas path flows

with the primary gas path will be scrutinised using techniques such as LES. Designers will fine tune the compressor design due to information gained from these simulations. As mentioned when discussing URANS transition, the lack of trust in relying upon new techniques and a lack of appropriate experimental data of which to compare with will be the limiting factor in the industrial use of LES. To gain this data, a greater variety of test facilities are required to be developed. A step change in computational methods requires a step change in experimental methods.

Research on Reynolds Stress models (RSM) is not as common, but is taking place at Manchester University and in other research groups around the world. RSM's are often seen as halfway houses between RANS and LES, as they are not based on the Bousinesque assumption, so have the ability to predict swirling flows, but also suffer from the limitations of using RANS equations. They have the capacity to predict anisotropic flows, but due to their complexity, the development progress is often slow, and the computational requirement is much larger than a two-equation turbulence model. It is the authors opinion that due to the rate of increasing computing power, and the slow development of RSM's, LES will become a design tool sooner than RSM's.

The final major area of research to be discussed is optimisation, both single objective and multi objective optimisation capable of optimising aerodynamically, mechanically and acoustically. Currently, major institutions such as Cranfield University, Rolls-Royce, Cambridge University and ANSYS are researching this topic. Optimisation is far from the panacea as thought by some; the selection of appropriate objective functions and their relative im-

portance in relation to one another is a crucial decision made by the user. Design envelopes are constrained somewhat by the experience of blade designs already collated. Large portions of R&D time may be required to cycle through differing objective function settings and relative weightings.

Some expect optimisation to be used initially to explore how current performance specifications may be achieved using new designs, rather than exploring more demanding design specifications (Harvey et al. (2003b), Jarrett et al. (2007)). Blade sections, or stage modules can be modified and explored individually rather than necessarily looking to optimise the whole compressor or engine. The design space can in theory be developed locally for a blade section and also globally for the stage, module or compressor.

For relatively few initial basic simulations, some optimisers can give the user an educated view of the design space to show the interaction of the objective functions. From there, users can narrow the field of study around a central point from where they can test a small amount of more refined cases. After the design process has been asserted upon these cases, the most suitable design may be manufactured and tested. Exploring the design space can result in a non-incremental design change, which may produce encouraging computational results, but will require extensive testing as the historical experience may not cover the new blade design. Trust in the design will need to be acquired during the testing process. Indeed, optimisation encourages conservatism as the designer should understand how he/she arrived at the end result, and where the discontinuities in the design parameters lie. It is this reason why industrial optimisation for some time to come will be constrained to the current design envelope.

As many cases may be simulated to effectively cover the design space, many licences and computing nodes are required to run the necessary cases concurrently. It is not feasible to run optimisation software on a single workstation. The results created will use a large amount of storage capacity.

Discussions on the setup and defining of the initial objective functions will encourage the engineers to work together more effectively as constraints are agreed at the start of the design process. As a multi-objective software will utilise different software packages for the various disciplines, consensus and compatibility amongst the packages used needs to be achieved. If all disciplines are available in the same package, a global optimum for the entire object may be found (including engineering, manufacturing, cost and reliability constraints), rather than finding a local optimum for aerodynamics or vibration etc. For these possibilities to be realised, new software may need to be developed in house, or purchased from a commercial vendor, to allow the appropriate information to be passed from software package to software package.

Kipouros et al. (2008) developed a multi-objective optimiser, using the Tabu approach, which does not place a weighting system as such onto the different objectives to obtain a single optimum blade. Instead it uses *Pareto equivalenvcy* to find a range of alternative designs, each giving an optimal design, but with varying trade-offs from which the designer can choose from. This way, some of the bias from the designer in the form of optimisation inputs is reduced. Kipouros et al. (2008) showed this method to reduce both the blockage and entropy generation from an axial compressor stator blade to a

greater degree than the same problem posed by Harvey et al. (2003a) using a single-objective approach.

Jarrett et al. (2007) summarise two main ways in which optimisation can reduce the total design time; Firstly, if all packages are used in the same umbrella package, then time is saved in data handling and crossover between packages. Secondly, the design space can be understood much quicker than previously. Through optimisation, the design process can become leaner, yet more informative than it is at present. This was highlighted by Harvey et al. (2003a), who used a single objective optimisation software to design a compressor stator blade in one week, which gave comparable results to a manually-derived solution which took man months to design. Through this exercise, the authors also discovered an unusual use of lean and sweep to reduce secondary flow blockage.

In more general terms, as computing power continues to increase at a greater rate than the increased complexity of turbulence models, engineers will be able to simulate more complex geometry and secondary flows such as leakage, cooling and cavity flows. Increased research with more complex models due to a larger computational resource will ultimately cause these models to become more feasible and reliable. This will also cause an increase in testing to validate these models (Horlock and Denton, 2005).

As well as more complex geometry, a greater volume of unsteady simulations will be undertaken, giving a more accurate indication of the flow through the machine, the losses incurred and the assessment of the mechanical limitations of the blading. The use of LES and DNS for research on both blade design

and for understanding of physics associated with turbulence and transition modelling will take place on a more frequent event. It is unlikely that DNS will become the method of choice in ones current working lifetime due to its huge computational requirement. However LES will become more commonplace, especially in steady state simulations with no multi-disciplinary optimisation involvement.

All of this increased computing power and more accurate simulation techniques will not spell the end for the use of empiricism in CFD. Many, including Smith Jr (2002) believe that empirical comparisons with experimental data will always be necessary, due to the complex nature of multi-stage machines, even if it is due to the geometry not being exactly what the analyser assumes it to be.

2.5 Looking Ahead - Siemens' Strategy

A discussion of the main issues of the use of CFD in the design process, the current CFD tools available, and the immediate and intermediate future of CFD development has taken place. An appreciation of the current resources available at Siemens have also been noted. This section will now present a suitable strategy for Siemens in their use and development of their CFD capabilities.

To understand the business environment within Siemens, which affects the compressor group, a PEST analysis was undertaken. Its main findings can be seen in Table 2.3. A PEST analysis is a tool which helps create an un-

derstanding of the macro-environment of the firm, or in this case, the compressor group. It enables the user to understand what the external political, economic, social and technological influences which may impact upon the strategy of the firm, for good or for bad. The PEST analysis was conducted with an internal view within Siemens. The main questions are concerned with the level of funding available for labour required to develop the CFD code, and if the code becomes more computationally expensive relative to the general increase in standard computing power, is there funding to increase the groups computing power? Perhaps the most important issue is the strategic choice of whether or not a step change in the compressor design occurs. If so, then a step change in the capabilities if the CFD code is required, along with the validation programme required to gain the trust in the code.

In an attempt to understand the advantages and disadvantages of the current CFD tools used by Siemens, a SWOT analysis was undertaken. Table 2.4 shows the main findings of this analysis. A SWOT analysis scans the external environment in which the firm operates, and compares any opportunities and threats presented to the firm by outside influences to the firm's internal strengths and weaknesses. A strategy can be developed which seeks to either maximise its strengths, reduced any threats, develop its weaknesses or pursue opportunities. The SWOT analysis considers both the internal and advantages and disadvantages of the current CFD practices used by Siemens. Its main advantage comes from an in depth knowledge of the current code and a run time of only a few hours per case. Results can be gained and processed in a matter of hours. However, the blade shape is limited to the structured

Political	**Economic**
Funding available for workstation upgrade? Funding available for in-house CFD code developer Time set aside for team to develop code? Step change in design to take place?	Funding available for code licences? Funding available for computing cluster? Funding for in-house CFD code developer & support?
Social	**Technological**
Does the team have sufficient code writing skills?	Computing power available Current work limited by code capabilities

Table 2.3: PEST analysis for Siemens compressor group

nature of the gridding process, and any changes to the code or models must be made by the engineers within the group. Due to time constraints, new modelling techniques may not be able to be developed and included into the code.

Conversely, as the code is in-house, Siemens have full control over its development, and can therefore direct its development for their specific requirements and product strategy. They have the opportunity to insert any new method or model they deem fit for their needs. The problems may occur in the medium term future if new methods from outside sources such as optimisation or LES require new grid or file structures which cannot be given by the

Strengths	**Weaknesses**
Quick turnaround	Only structured grids can be used
Good understanding of current code	Limited number of grid points used
No licence required	Models are limited
	No outside support given
Opportunities	**Threats**
New models available for testing	Require unstructured grids for some new designs?
New models can increase accuracy	Future optimisation packages may require new file structures

Table 2.4: SWOT analysis for Siemens compressor group

current software. The in-house software may require alteration to fit with these new methods.

Given these findings and the previous discussions within this chapter, a suitable strategy for Siemens would be one which maximises its current strengths of using the current code, with developing opportunities to keep abreast of current developments and integrate them into their code. This kind of a strategy would reduce the likelihood of a large scale change to the code. The recommendations are given in two main categories; First, what techniques should be developed, and secondly, how should they be developed and integrated.

From the research conducted, it is clear that the pace of development of current turbulence models, such as Spallart-Almaras, k-ϵ and k-ω is slowing down. New developments with these models mostly offer little performance

over a well tuned model at design conditions. Only when off-design is approached can any new development give a significant improvement. For this reason, the focus of turbulence modelling is very much on transition modelling and LES. At off-design, transition prediction becomes more important, and LES has a greater ability to capture the behaviour of the flow over the models using the Bousinesque assumption.

As the unsteady behaviour of the flow around a blade is becoming more important to understand, further work into the mixing plane is necessary to enable important information about the upstream wake passing through the plane and impinging onto the downstream blade. Both upstream and downstream pressure fluctuations are required to be accounted for. Also if conducting unsteady simulations, the wake mixing process accounted for by the code is in need of improvement. These process will be shown to be important in the correct prediction of the unsteady boundary layer.

Finally, methods of optimisation will start to become an essential tool for the blading design process. Although not to become part of the mainstream design process, its study of and use of an optimisation tool will provide the aerodynamicist with many new avenues of thought regarding blade design.

Given the resources available to Siemens, it is felt that an appropriate way of developing these capabilities is through working closely with universities and other research groups within the larger Siemens group. It is recommended that Siemens create strong research links with one or two high quality research establishments, who would then work with Siemens on developing their CFD code. Universities are ideal for this. The university should have

a strong record of code development, and have their own in-house code employing a similar solver and models to enable a closer like for like comparison of the work. It is thought to be unfeasible that Siemens allow the universities to work directly with their code. However, an aerodynamicist at Siemens, responsible for code development should work closely with the universities in the development and implementation of the capabilities of the code. This enables the aerodynamicist to keep abreast of new developments without having to spend precious resources in developing them him/herself. Regular visits and short internships at Siemens will enable the student to assist the aerodynamicist in the implementation of the new code developments.

Similarly, the compressor group at Siemens could develop a closer working link to both the turbine group and other groups within Siemens such as Westinghouse and Siemens Germany. A standardisation of in-house codes throughout the company would create a synergy of knowledge. Regular in-company workshops could facilitate the development of the codes used. This may depend heavily on the state of internal company politics.

Universities are best placed to assist in the development of the code due to their experimental facilities. As mentioned, new methods require new experimental data by which to develop and validate them. Funding should be made available for experimental programmes to take place. Doctoral students working in tandem could undertake both an experimental and computational study of the physics in question. Universities may also be able to grant a greater amount of time on the experimental programme to that which could be undertaken within the company. The time allotted would also be less sensitive to the immediate commercial requirements of the company.

Universities also have access to large computing facilities which are ideal for trialing new unsteady, transition or LES methods. Such studies require many processors for an extended period of time up to one or two months. This is not currently feasible for companies with limited computing resources.

It is recommended that within approximately 5 years, a programme for developing LES capabilities is started. Consultation with the combustion group would prove invaluable as using LES is now standard practice amongst combustion groups. Lessons learned from their experience would be fed into any programme of work undertaken. Working with the universities, programmes to both investigate the implementation of LES within the group and the investigation of important physical phenomena through LES and experiments are suggested. Once complete, the group may wish to lobby for an increase of current computing power on-site if the current facility is not sufficient to cope with the increase use from the compressor group.

Perhaps, the most important decisions which will take place, are not which resources are developed and maintained through the suggestions just mentioned, but how the resources are managed and used. For this, it is suggested that one with a greater experience of the industry and the design process develop a suitable strategy for the efficient use of resources within a group such as Siemens.

2.6 Chapter Closure

It has been shown that the use of CFD within the design process of an axial compressor is essential. The advantages of the correct use of CFD cannot be overstated. However, as in the Pratt & Whitney case study, the improper use of or over-reliance upon CFD can bring disastrous financial consequences. What may seem like an isolated case of over-reliance upon CFD was actually part of a systematic process in reaction to environmental decisions.

Both CFD and physical testing have an integral part within the design process. Each has their own advantages and limitations. Physical testing is limited by the number of data points and richness of the data it can produce. However, it can give valuable data from actual in-service machine conditions. Conversely, CFD is limited by the in-service geometry and flow conditions it can simulate, but gives the user a much richer picture of the entire flow simulated.

Since the introduction of 3D CFD into the design process in the 1980s, its importance has steadily increased, in-line with the advances in its capabilities and trustworthiness. Current methods used are now reliable and repeatable. The user can determine the characteristics of the codes and models used and define an appropriate error to in-service conditions. Limitations in the off-design prediction capabilities and the unsteady flow conditions are some of the limitations which require a solution to. Only extended experimental and computational programmes of work will allow these limitations to be reduced. A new code or model will require substantial testing to gain the necessary understanding of its behaviour before it is sufficiently trusted to be integrated into the design process.

An appreciation of the advantages and disadvantages of using both in-house and commercial CFD codes was given. In-house codes can be developed specifically for a particular geometry or flow conditions and can produce a solution in a shorter space of time than commercial codes, but require a greater use of human resources to maintain. On the other hand, commercial codes can be used well for a variety of geometrical arrangements and flow conditions, and contain the latest developments in modelling techniques, but they may tie the user down to using their commercial meshing and post-processing tools and may solve at a slower rate than an in-house code.

The resources available to Siemens were assessed, and a strategic overview of future CFD capability development. This was based upon the resources available and the current research topics undertaken by the worldwide CFD community. Important areas of research which are suggested to be developed further include unsteady modelling of the flow, transition modelling, LES and optimisation. With the resources available to Siemens, it is suggested that they develop strategic relationships with one or two universities to develop these capabilities. The universities should have a strong background in both developing CFD codes and models, and undertaking experimental projects. The compressor group is encouraged to strengthen relationships between other groups within Siemens Industrial Turbomachinery, such as combustion and turbines, and also within other Siemens divisions such as Westinghouse and Siemens Germany.

Chapter 3

Literature Review

3.1 Introduction

This chapter will highlight the main issues surrounding turbulence modelling, the current models available and the best practice recommended to successfully use them. It will also give a discussion on main areas of research being currently undertaken within the field of turbulence modelling.

3.2 Axial Compressor Flow

Although the reader should be familiar with the flow within an axial compressor, a short review is included to highlight some issues surrounding turbulence modelling later in the chapter. Flow in an axial compressor can be complex, as shown by Figure 3.1. In a blade row, flow enters the passage and is turned by the blades. The boundary layer on the blade surfaces may often experience a transition from a laminar to a turbulent state, normally between the leading edge and mid-chord, dependent upon the flow conditions. The flow on the suction surface may experience terminal or temporary separa-

tion. Towards the hub, secondary flows form due to blade, hub and casing curvature. The pressure gradient between the suction and pressure sides of adjacent blades causes twin vortices to form in the passage. Flow past the blade suction surface and hub interacts and causes local separation, known as corner stall. Horseshoe vortices can form towards the hub on the pressure surface due to the difference in the velocities of the local hub and blade flows. The acceleration of the fluid at the blade surface further from the annulus is larger than at closer to the annulus, creating a pressure difference and a resulting vortex. Toward the casing, flow passes through between the tip and casing from the pressure side to the suction side due to the pressure difference experienced by the suction and pressure surfaces. The endwall effects and tip leakage flow strongly influence the promotion and reduction of the boundary layer towards the blade tip. A scraping vortex also results from the reaction of the endwall region boundary layer to the tip leakage flow, but only at high speeds (> 6000 rpm). Spanwise secondary flow occurs due to momentum and pressure differences between hub and casing. Finally, incoming wakes from upstream blade rows bring transient high disturbance environments which interact with the above events. When running the compressor at flows away from design conditions, these features, all of which may be difficult to predict computationally, become more severe.

3.3 Turbulence Modelling

The chapter now switches its attention to computational matters. Turbulence modelling is the name derived from the method of closing out the Reynolds averaged Navier-Stokes (RANS) equations. The method of closure determines the effectiveness and characteristics of the model. Two main

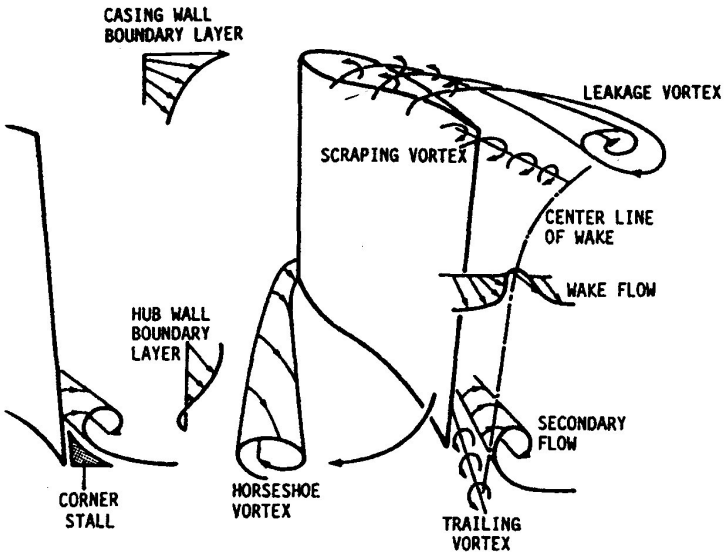

Figure 3.1: Flow through an axial compressor. Taken from Cumpsty (1989)

types of RANS based models exist; those that use the eddy viscosity hypothesis to develop a set of equations to describe unknown quantities in the Reynolds Stress equations, and those that attempt to close the RANS equations by solving the Reynolds Stress equations directly. The latter are known as Reynolds Stress Models (RSM). There are many variations of the turbulence models described above, and indeed other classifications of solving the RANS equations. These can be classified as below;

- Eddy Viscosity Models
- Reynolds Stress Models
- Linear Stability Models
- Large Eddy Simulation / Detached Eddy Simulation
- Direct Numerical Simulation

Direct numerical simulation is not classed as a turbulence model, as its base equations fully describe the flow and require no closure. The above methods will now be critiqued to highlight some of their advantages and disadvantages.

3.3.1 Direct Numerical Simulation

Direct numerical simulation (DNS) is a method that solves the full Navier-Stokes equations rather than the Reynolds averaged version. It requires a grid with a node spacing less than or equal to the smallest scale of turbulence. It has been referred to by many, including Jacobs and Durbin (2001), as experimental data, as it is fully able to describe the flow. However, the size of grid required has kept simulations to low Reynolds numbers and small problems, such as simulations around the leading edge of the compressor blade. It will be many years until the technique and the computing power will be advanced enough for it to be commonplace in industrial applications. For this reason, nothing more will be mentioned on direct numerical simulation.

3.3.2 Large Eddy Simulation

Large eddy simulation (LES) solves filtered Navier-Stokes equations for the largest scales of turbulence. According to Kolmogorov (1941), the largest sales of turbulence contain the energy and cascade it through to the smaller scales where it is dissipated. LES solves the largest scales and uses a subgrid model to model the smallest scales. The subgrid model introduces eddy viscosity into the governing equations, but the model has not been classed here as an eddy viscosity model as it does not use RANS equations.

LES provides transient results to the user, and is especially useful for predicting transition and separated regions (Nichols and Nelson, 2003). Singer (1993) stated that early standard Smagorinsky subgrid models were overly diffusive during the boundary layer transition region, but later dynamic versions proved to reduce this which enabled them obtain a greater degree of accuracy.

LES is becoming more practical with greater computing power now available, but is limited to institutions with large supercomputers. A less computationally expensive method which combines elements of both LES and RANS is called detached eddy simulation (DES). As the scale of turbulence within the boundary layer is relatively small, a RANS method is employed within the attached boundary layer, and an LES method is employed in the separated regions where the scales of turbulence are larger. This can prove problematic, as the switching from one method to another can sometimes be abrupt, causing a nonphysical solution (Nichols and Nelson, 2003). As with DNS, these methods are not considered for use in the project, but will be referred to later in this chapter.

3.3.3 Linear Stability Models

Linear stability models, based upon the Orr-Sommerfeld equation (linearised unsteady Navier-Stokes equations) for hydrodynamic stability, are used to determine whether a laminar base flow is receptive to infinitesimal perturbations and whether a fluctuation imposed on that base flow will grow into turbulence. The growth of these fluctuations develop into Tollmein-Schlichting waves, which start the natural transition process from a laminar boundary

layer to a turbulent boundary layer. Johnson (1994) observed that as the method is based upon linearised theory, it is only applicable to low freestream turbulence flows in which natural transition occurs. Higher freestream turbulence flows result in bypass transition, which is a non-linear process. Therefore linear stability theory cannot predict this process (Reed et al., 1996). This was demonstrated by Solomon et al. (1999) when the well known linear stability model, the e^N method, failed to accurately predict the transition region of an incoming rotor wake on a stator surface, when it performed well in between the wakes, which was deemed to be subject to natural transition. However, progress is being made in using parabolised stability equations that have a limited capability in predicting non-linear processes (Saric et al., 1998). This method is still not suitable for turbomachinery applications.

3.3.4 Eddy Viscosity Models

Eddy viscosity models (EVM) are based upon the Boussinesq assumption which assumes the principal axes of the Reynolds stress tensor, τ_{ij}, are coincident with those of the mean strain-rate tensor, S_{ij} at all points within the turbulent flow Wilcox (1993b). A coefficient called the Eddy Viscosity (μ_T) is used to relate τ_{ij} and S_{ij}. There are three common types of EVM;

1. Algebraic (zero equation) models
2. One equation models
3. Two equation models

Algebraic Models

Algebraic, or zero-equation models are also known as mixing length models. They use a correlation to define a mixing length, which in turn determines the eddy viscosity of the flow. The most well known algebraic model may be that of Baldwin and Lomax (1978), which correlates the boundary layer profile to the eddy viscosity. Wilcox (1993b) explains that as no length scale for turbulence is calculated, it is only appropriate for very simple flows, where the boundary layer is attached and there is little pressure gradient, or quick and easy calculations where detailed physics is not required at that stage. These models are not suitable for modern day turbomachinery applications.

One Equation Models

One equation models calculate the eddy viscosity using the turbulence energy equation and an algebraic formulation for the length scale. Until the Spalart-Allmaras model (Spalart and Allmaras, 1992), these models did not give sufficient improvement over algebraic models to justify the additional computational cost and complexity. The Spalart-Allmaras model relies on local variables as opposed to integral variables used in zero equation models. Gatski and Rumsey (2002) showed that these models do still have excessive diffusion in 3D vortical flow (such as secondary flow vortices), making them unsuitable for off-design turbomachinery cases where separation is expected. Edwards et al. (2001) used a modified transition function within the model to predict flows over a flat plate and supercritical aerofoil, of which only the flat plate returned accurate results. This was because the aerofoil case gave turbulence intensity limits outside of the model's calibrated parameters.

Two Equation Models

Of the two equation, eddy viscosity hypothesis based turbulence models, the k-ϵ and k-ω models are the most popular. The k-ϵ model is currently the most commonly used turbulence model in the aerospace industry, mainly due to its numerical robustness, and well established predictive performance. It uses k and ϵ to denote the kinetic energy and length scale of turbulence. The exact equation for ϵ is derived by taking moments of the Navier-Stokes equations, to yield an equation describing ϵ as a function of production, dissipation, molecular diffusion and turbulence transport. The k-ω models use k and the turbulence frequency (or specific dissipation rate), ω, to describe the turbulence. They have the advantage over k-ϵ models in that the use of ω allows for more appropriate modelling of the boundary layer, as ω can be calculated throughout the boundary layer, whereas ϵ requires a damping strategy for it to be valid throughout the boundary layer.

3.3.5 Reynolds Stress Models

RSM models attempt to fully close the turbulence problem by solving the individual stress components of the Reynolds stresses, rather than model them. They attempt to include the effects of curvature and rotation on the turbulence structure. Something which eddy viscosity models fail to do. They have the ability to simulate the additional anisotropy of the Reynolds stresses due to the Coriolis forces appearing in the rotating frame of reference. They are not based upon the eddy viscosity hypothesis and assume that the flow is fully three dimensional, making the eddy viscosity no longer scalar, as assumed by k-ϵ and k-ω, but tensor. This, and the fact that they utilise an

exact production term means that the RSM models should accurately predict swirling or secondary flows, although this is not always the case (Neel et al., 2003). The main difference between eddy viscosity and RSM models is that RSM models account for the transport of the principal turbulent shear stress $\tau = -\rho\overline{u'v'}$. The drawback with the model is that the dissipation, pressure-strain and turbulent diffusion terms cannot be computed exactly, and must be modelled, creating extra complexity and a tendency for numerical instability. Since the dissipation equation used can be from the standard k-ϵ model, when they are used within the RSM, these equations become even stiffer. This requires a finer grid within the boundary layer which causes the solution to converge even more slowly, whilst using a greater computational resource.

This section has given a brief overview of available techniques to model turbulence within the boundary layer. The work contained in this thesis will only deal with turbulence and transition modelling using either eddy viscosity models or Reynolds Stress models as they are the only viable options available in the CFX code. Some of the issues related to using these models will now be detailed.

3.4 Modelling Issues

There are a number of issues with the above models that prevent them from giving a 100% accurate solution. Some of these include the grid setup, discretisation scheme, boundary conditions, and post-processing dependent errors. The major problem in solving actual turbulence is that very small

scales are required (i.e. Re = 1), which requires a substantial amount of computational effort. Therefore, actual turbulence solving (i.e. DNS, LES) is limited to low-Reynolds number flows for most computing facilities. This is primarily a hardware issue, and shall not be discussed further in this thesis. The modelling issues discussed in this section are those to do with the assumptions and approximations to the physics used to close out or calculate the Reynolds stresses.

Most importantly, the Boussinesq assumption is not valid for all flows. As Wilcox (1993b) explains, it assumes that the principal axes of the Reynolds stress tensor, τ_{ij}, are coincident with those of the mean strain-rate tensor, S_{ij} at all points within the turbulent flow. The coefficient of proportionality between τ_{ij} and S_{ij} is the eddy viscosity, μ_T, which depends upon the flow history, freestream turbulence intensity etc, and is hence not a property of the flow. The Boussinesq assumption brings certain principle deficiencies into the turbulence models, such as the lack of ability to cope with sudden changes in mean strain rate (i.e. turbulence) and extra rates of strain such as flow over curves surfaces or additional body forces i.e. buoyancy. In these instances, the principal axes of τ_{ij} are not necessarily coincident with S_{ij}. The Reynolds stresses depend upon mean flow and turbulence scales, and therefore the assumptions used in two-equation models can be inaccurate for non-equilibrium flows. Flows with boundary layer separation, high streamline curvature, secondary motion and three dimensionality all invalidate the Boussinesq assumption. Eddy viscosity models therefore rely solely upon limited physically valid assumptions to predict the flow. Since the RSM models inherently calculate the Reynolds Stresses directly, they overcome this problem to some degree, but their complex nature brings other deficiencies as

previously discussed.

For two-equation EVM models, the choices for k, ϵ and ω and their relationships with the length scale were found from dimensional analysis completed in the 40s and 50s. However useful this has been, it does not reveal the underlying physics involved, and like the low-Re models, could be down to chance or generality that the relationships seem appropriate. Wilcox (1993a) stated that there was no fundamental reason that μ_T should depend only upon turbulence parameters such as k, l, ϵ or ω.

Menter (2002), while discussing the requirements of turbulence models for turbomachinery, agreed with that set out in Chapter 1, that the accurate prediction of the boundary layer is of great importance. He states that the three most important issues in the modelling of the boundary layer for turbomachinery flows are;

1. Separation prediction - location and amount
2. Near wall treatment
3. Transition prediction - location, then length

These three items will now be addressed in turn. This thesis makes no attempt to directly address other important issues in turbomachinery modelling, such as the mixing plane and solver architecture etc, as they do not directly affect the development of the boundary layer.

3.4.1 Separation Prediction

Menter (1994) states that the basic inadequacy of two-equation RANS mod-

els is their failure to correctly predict the onset and amount of separation in adverse pressure gradient flows. The level of the eddy viscosity within the wake region of the boundary layer ultimately determines the ability of an eddy viscosity model to predict strong adverse pressure gradient flows. This is most apparent for k-ϵ models, and to some degree the k-ω and RSM models. The eddy diffusion hypothesis is not valid within the wake region in adverse pressure gradient flows, as the distance between the energy-containing eddies and dissipating eddies is reduced due to the smallness of Re_T and the local isotropy assumption must be abandoned. Non-isotropic effects must be incorporated artificially, such as in low-Re k-ϵ models. Furthermore, Bradshaw observed that the principal turbulent shear stress is proportional to the turbulent kinetic energy in the wake region of an equilibrium boundary layer (Menter, 1992), but in a non-equilibrium flow (i.e. free shear flow), Driver (1991) showed that this is not true. In other words, the dissipation length scale used in the ϵ equation becomes non-linear. In most k-ϵ models, ϵ is linear. Hence k-ϵ models, and to some degree, standard k-ω models, over-predict the amount of turbulent shear stress in the wake region that causes them to predict separation much later than in reality, and therefore the amount of separation is reduced. As RSM models account for the transport of the principal turbulent shear stress, they do not suffer from this problem as will be shown. Menter (1994) developed the Shear Stress Transport addition to the k-ω model to prevent the build up of the principal shear stress in the wake region, whilst attempting to keep the Boussinesq assumption valid for adverse pressure gradient flows. The Shear Stress Transport model also conforms to Driver's observations by limiting itself to wall bounded flows.

3.4.2 Near Wall Modelling

"The goal of developing a quantitative theory of near-wall turbulence, based on the dynamical interaction of a small number of structures has not been attained, and is likely unattainable." (Pope, 2000). In his presentation in Lucerne, Menter (2002) proposed that wall function boundary conditions are the single most limiting factor in industrial CFD computations regarding accuracy. This is true as one looks at the role of wall functions. The uncertainty in the scalable wall function formulation is the reliance in the derivation of the existence of a logarithmic layer outside the sublayer, which is not guaranteed for complex flows. Also, no consistent grid refinement can be performed using standard wall functions because the integration point falls into the sublayer region, where the assumptions used in the derivation are no longer correct (Grotjans and Menter, 1998). However, Wilcox (1988a) demonstrated that the model's wall functions' errors only play a minor role in the discrepancy between experiment and prediction. The model's main source of error within the boundary layer comes from their ill-fitting description of the boundary layer itself (Wilcox, 1993a). Therefore, a model, *ceterus paribus*, not using wall functions, but rather resolving the boundary layer, should give a more accurate estimation.

3.4.3 Transition Prediction

Borello et al. (2005) echoed Menter's comments when they too stated that the prediction of the evolution of turbulence and the location of transition incipience are major problems for current modelling methods. Turbulence models become less accurate at off-design conditions, when transition is in-

volved in separation (Hourmouziadis, 1989). Menter et al. (2004b) suggest that fully turbulent turbulence models often over predict wall shear stress and heat transfer distributions, and will not predict blockage and loss correctly, leading to incorrect engine performance estimates. Halstead et al. (1997b) found that an aerofoil profile loss can be over-predicted as much as 35% due to the incorrect placement of the start of transition (or if the flow is presumed turbulent from the leading edge).

Two main problems are prevalent for RANS based models when attempting to model the transition region. First, the RANS equations conceal via the averaging process, the instantaneous instabilities leading to turbulent spot formation and propagation that are the source of laminar to turbulent transition. Roberts and Yaras (2005b) argue that because the process of bypass transition is influenced by the propagation of pressure fluctuations from the freestream into the boundary layer (Section 5.2), and also seems preferentially sensitive to wall-normal turbulence fluctuations, relative to other components, it has been put forth that any model accounting for the diffusive transport of turbulence from the freestream into the boundary layer will in essence have the ability to capture the essential phenomenological features of transition. Therefore it remains possible to capture somewhat the transition process through RANS based models.

Secondly, not enough is known about the transition process to fully capture it without resorting to DNS. DNS has already been shown to be prohibitive for use with most computing facilities, especially for industrial applications. On the whole, for simple cases, as will be shown, the transition process can be described to a satisfactory level, but not for industrial turbomachinery

applications.

Apart from DNS and LES, the three most common methods to predict transition are linear stability theory (the e^N method being most common), eddy viscosity, two equation models, namely those utilising low-Re formulations, and those based upon correlations. Section 3.3.3 has already documented some of the shortcomings of linear stability theory methods, namely that they cannot predict bypass transition ($Tu > 1\%$) as they cannot account for non-linear processes involved in bypass transition.

Two equation Low-Re EVM models (typically k-ϵ) use a turbulent Reynolds number, Re_T, and damping functions in the near wall region to calculate the transition region. Whilst they may work successfully for certain cases, they do not have the consistency across a range of flow conditions or geometry (see Savill (1993a), Savill (1993b), Borello and Rispoli (2003) for examples). Indeed, Roberts and Yaras (2005b) believe there are no fundamental grounds for the use of low-Re models in the prediction of transition, as their formulation do not have any fundamental grounds to capture the correct physics of the transition process, as they have been tailored to predict the near wall region of fully turbulent boundary layers. The use of Re_T seems somehow to capture the transition process because it is a general number representing the ratio of k to ϵ, which mimics the relationship of k to ϵ found in the transition region. Barakos et al. (1998) explains that one reason that low-Re models are limited to only working well for certain flow conditions is that they are still not able to capture the important effects arising from normal stress anisotropy during the transition process, but because they can predict pressure fluctuations, Roberts and Yaras (2005b) felt there is still hope in

capturing the transition process through conventional statistical closures in low-Re models. Zheng et al. (1998) summarised some of the issues with using low-Re models - namely that they predict transition too early for attached flows and too late for separated flows. If transition is to be modelled without resorting to empirical correlations (i.e. through using low-Re models etc), it is necessary to correctly reproduce the laminar flow characteristics upstream of its final onset (Boiko et al., 2002). As they are based upon the RANS equations, it is not possible for low-Re models to obtain sufficient information about the pre-transitional laminar boundary layer.

Correlation based RANS models do not model the physics of the transition process, unlike current turbulence models and turbulence, but correlate the effects of transition from experimental data into the CFD model. The physics of the transition process has been taken into account during the development of the correlations. In this way, the formulation is not specific to one transition process, but can be used for all processes provided the appropriate correlations are available. Correlations are based upon typical values found in the free-stream, such as turbulence intensity or pressure gradient outside the boundary layer. This information is diffused into the boundary layer by a standard diffusion term. In this way, free-stream influences and variations can be taken into account. The correlations are only as accurate as the data they were developed from and the suitability of the turbulence model for that application. The correlation will normally define the start of the transition region, and dependent upon whether the transition region is modelled as point like or not, an intermittency function will be used to modify the eddy viscosity from laminar to turbulent according to the intermittency ranging from 0 to 1.

Models that utilise a point-like transition region fail to accurately predict natural transition and all but high Tu ($Tu > 7\%$) regimes. Vicedo et al. (2004) showed that transition models using an intermittency distribution method predicted the transition region with greater accuracy than the same model using a point-like intermittency function. Further, for turbomachine blade flows, Walker (1989) stated that a point transition model becomes inadequate due to the length of the transition region, especially when laminar separation bubbles are present.

The method the code uses to obtain the required data for the correlation also affects the accuracy of the transition model. Correlations reliant upon non-local information such as momentum thickness are not suited to parallelized codes and unstructured grids, as it is difficult for the search algorithms to detect the boundary layer parameters, as the boundary layer may be distributed among many processors. This makes the task of creating a line perpendicular to the surface difficult, in addition to the task of defining the boundary layer edge, and uses considerable computational resource. Further, the accuracy of the model using non-local variables will depend upon the accuracy of the search algorithm employed linking the correlation to the variables. Menter et al. (2004a) suggest using a correlation based upon local variables overcomes these problems.

Correlations must account for the important effects for the flow conditions they are to be used with. The relevant flow physics must be contained within the correlation and the relevant flow and geometry actors for the transition process (such as Tu and pressure gradient parameter) must interact with

Author	**Correlation**
Abu-Ghannam and Shaw (1980)	$Re_{\theta t} = 163 + exp\{F(\lambda_\theta - \frac{F(\lambda_\theta)}{6.91}\tau\}$
Mayle and Dullenkopf (1991)	$Re_{\theta t} = 400Tu^{-\frac{5}{8}}$
Johnson (1994)	$Re_{\theta t} = 46(Tu + 10^4 Tu^4)^{-1/2}$

Table 3.1: Common correlations for transition in turbomachinery

the code and correlation to correctly calculate the transition region for that analysis. This is highlighted by examples of correlations given in Table 3.1. Abu-Ghannam & Shaw's correlation was one of the first to gain significant popularity, and is often the baseline correlation to which other correlations are compared. Although the Abu-Ghannam & Shaw correlation shows good agreement with experimental data for flows with zero and adverse pressure gradients, Suzen and Huang (2002) argue that it is not very sensitive to flows subject to strong favorable pressure gradients, in which one would expect the transition to be delayed as a result of flow acceleration. Koyabu et al. (2005) showed that Mayle's correlation based solely upon Tu was inappropriate for pressure gradient flows. Howell (1999) also felt that Mayle's correlation was not suitable for turbomachinery flows. However, he felt that using inlet wake Tu was more appropriate than background Tu. Similar results were found by the author for Johnson's correlation. So it is seen that there are other important physical actors that should be accounted for when using a correlation to define the transition region.

The main limitation of using correlations is that the correlation data and its interaction with the code is limited by the physics that one is able to collect from experimental data with current techniques and hardware. In a

commercial sense it is also limited by the cost at which that data is obtained. The lack of physical understanding of the transition process has meant some important effects are not properly accounted for. This problem may be reduced in time with increased use of DNS.

Some correlations, such as Mayle's, specifically account for either natural or bypass transition (Mayle's accounts for bypass only), and therefore do not accurately predict the type of transition region not accounted for. Separated transition has been challenging, and still not fully accounted for. Early work by Mayle (1991) showed that there was no current way of predicting the length of a separation bubble, which affects exit flow angles and performance. Current studies have shown that this deficiency has been overcome to an extent (Menter et al., 2004b). Hatman and Wang (1999) developed a correlation for separated transition, which depended upon knowing the length of the bubble *a priori* and the maximum bubble elevation. This worked well for flat plate, but they were cautious about recommending it for other cases such as aerofoils. Menter et al. (2004a) had to allow the local intermittency to unphysically rise above 1 in the model formulation to achieve an accurate solution using the correlation for attached boundary layers. The model formulated by Vicedo et al. (2004) (Section 3.5) showed promising results in the prediction of separation bubbles. According to Solomon et al. (1996), models using a constant pressure gradient parameter to predict transition length in a rapidly changing pressure gradient region (i.e. blade leading edge) cannot accurately predict the length of transition. This again highlights the need for the correlation to include such important physics, and the code to use local variables to calculate these parameters in the correlation.

Geometric considerations such as streamline curvature have not been accounted for so far in correlations made public. Indeed Menter et al. (2005) concede that streamline curvature and also crossflow instability have not been accounted for in their correlations. Most importantly, unsteady flow phenomena such as transition due to wakes, the induced calming effect behind the wakes, the subsequent suppression of any separation bubble and the negative jet effect have yet to be modelled accurately. There are to date no papers available on RANS based correlation models attempting to account for and model these phenomena. Previous simulations by Halstead et al. (1997b) and Solomon et al. (1999) both showed that the effects of the upstream wake on the transition region were not fully replicated in their simulations. Also, most correlations tend to depend upon 2D data, and are not thought to be appropriate for use in predicting end-wall boundary layers or leakage flows.

It has been found that even in bypass transition, there is still evidence of laminar boundary layer instabilities as found in natural transition (Hughes and Walker, 2001). Therefore, transition models that entrain turbulence and instabilities from the freestream cannot attempt to fundamentally model the transition process correctly, regardless of whether they are of the correlation type or not.

Most of the work of predicting transition using RANS models has been through using eddy viscosity models. However, Borello et al. (2005) argue that it is requisite to predict two effects. Firstly, the true viscosity effect (i.e. low-Re), which has a scalar character. Secondly, the non-viscous, wall-orientation-biased wall-blocking effects. This second effect primarily suppresses the turbulent fluctuations normal to the wall, which has a strong

effect on the turbulence anisotropy close to the wall, and is not predictable from eddy-viscosity models. Thus they argue that Reynolds Stress models have a better chance at predicting the stress anisotropy, streamline curvature and rotation, which are essential for the prediction of transition. It is probably due to their complexity and sometimes unexpected behaviour that they are not utilised in earnest for the purpose of transition prediction.

3.5 Review of Some Transition Models

A short review of some of the reported transition models will fill the remainder of this literature review in order to familiarise the reader with some concepts that will be used when giving precis' of the transition modelling used in later sections. A more comprehensive review of transition models and modelling strategies can be found in Savill (1996), Savill (2002a) and Savill (2002b).

$\gamma - \theta$ Model, Menter et al. (2004a)

The $\gamma - \theta$ model uses two separate correlations to calculate the start of the transition region (θ correlation) and the intermittency distribution within the transition region (γ correlation). When used in the CFX code, the $\gamma - \theta$ model uses Menter's $k - \omega$ SST model (Menter, 1994) as a base turbulent model. The turbulent viscosity production in the $k - \omega$ SST model is switched on and altered by the intermittency distribution correlation. The θ correlation calculates the Reynolds number based on momentum thickness, $Re_{\theta t}$ which is the minimum expected value which allows transition to take place at that particular point in space and time. The momentum thickness is correlated to the

Reynolds Vorticity number, Re_v. When the momentum thickness Reynolds number at the boundary layer edge, $Re_\theta >= Re_{\theta t}$ then the intermittency function is switched on. The intermittency and $Re_{\theta t}$ are both transported into the boundary layer, whilst incorporating a lag function. For separated flows the intermittency is allowed to artificially rise above 1 to account for the undamped rapid transition region. Results for a variety of cases from flat plates to cascades and steady state 3D turbomachinery and aerospace cases have shown it to have a good degree of accuracy. Its main failure is sometimes the failure to accurately predict the rapid transition of attached boundary layers in high turbulence, adverse pressure gradient flows. Results can be found in Menter et al. (2004b), Menter et al. (2005) and Menter et al. (2006).

$k - \epsilon - \gamma$ Model, Vicedo et al. (2004)

Developed specifically for separated transition, this model attempts to account for the transport of intermittency through the transition region. The transport of intermittency is very important, especially in the prediction of separation bubbles, as it affects the entrainment effect and subsequent reattachment point of the bubble. The authors believe that the improvement of their transition model for the prediction of separation bubbles is due to the modelling of the entrainment process. Utilising the k-ϵ model of Yang and Shih (1993) as its baseline turbulent model, it uses a differential equation rather than a correlation to model the intermittency. This allows the modelling of intermittent free shear flows, as found in separation bubbles, and can be extended into 3D by using additional derivatives, rather than being restricted by 2D correlations. The start of transition is determined by the following, given by Mayle (1991);

$$x_{st} \approx x_{sep} A Re_{\theta_s}^{0.7} \frac{\theta_s}{Re_{\theta_s}} \tag{3.1}$$

Where A is a constant.

Intermittency is modelled by 4 main terms; production, transport, dissipation and entrainment, instead of a singular term. The authors claim that among the model's strengths are; its allowance for diffusion and convection of kinetic energy from the freestream flow to the boundary layer, and the varying normal distribution across it. They also claim that streamwise development of intermittency is accounted for. They feel that these claims are important to accurately model the wake - boundary layer interaction phenomena.

The results do show an improvement over previous non-predictive intermittency transition models, where transition intermittency is modelled as point like. At higher freestream turbulence levels, the model is not as accurate, due to the inability to predict sufficient upstream displacement of transition onset, but does show an improvement over previous models. It was only tested on steady state flat plate test cases (ERCOTFAC T3LB, T3LC, T3LD).

Prescribed Unsteady Intermittency Method, Vilmin et al. (2003)
Based on the k-ϵ model of Yang and Shih (1993), the Prescribed Unsteady Intermittency Method (PUIM) aims to simulate the creation and propagation of turbulent spots through the transition region. Transition onset is calculated using Mayle's correlation for both attached and separated flow. These correlations have previously been shown in this chapter. The intermittency factor through the transition region is calculated using either Narasimha's

(Narasimha, 1957) concentrated breakdown concept, or a continuous breakdown concept to account for the calmed region. Spot production rate is taken from either Mayle (1991) or Gostelow et al. (1992). Both methods are dependent on the pressure gradient and turbulence intensity at the boundary layer edge. For turbulence levels less than 1%, it uses the e^N method demonstrated by Solomon et al. (1999).

The Prescribed Unsteady Intermittency Method models the steady boundary layer well for the low speed compressor of Walker et al. (1999) (as used in Chapters 6 and 7), showing the separation bubble at mid-chord on the suction side. The modelling of the unsteady wake affected boundary layer is less clear due to the poor quality of the figures given in the paper.

Turbulence Weight Factor τ Model, Steelant (1999)

This model uses a turbulent weight factor τ to account for the effects of both the freestream and boundary layer instabilities via a transport equation. The transport equation used for τ includes convective, diffusive, production and sink terms. $\tau = \gamma + \omega$ measures the diffusion of freestream turbulent eddies (ω) into the boundary layer and the growth of turbulent spots during transition (γ). τ is 0% at the wall and 100% in the freestream.

It returned reasonable results for the ERCOFTAC T3A and T3C1 flat plate test cases. It predicted slightly early transition for the T3C1 case, but returned a good shape factor form. The results for the sonic turbine guide vane gave a reasonable form, but highlighted the need to account for compressibility effects into the model.

Low-Re k_T Model, Walters and Leylek (2004)

Based upon a low-Re model, the k_T model aims to model the effects of streamwise fluctuations within the pre-transitional boundary layer via the term 'laminar kinetic energy' (K_L). The laminar kinetic energy accounts for the energy fluctuations within the pre-transitional laminar boundary layer which cause the streamwise velocity fluctuations. The model calculates the transfer of energy from K_L to K_T (i.e. laminar to turbulent kinetic energy) based on the effective length scale and fluid viscosity. This determines the start of transition. The transitional part of the boundary layer is calculated via the production term governing the energy transfer between streamwise fluctuations and turbulent energy. This depends on mean flow and K_L.

The k_T model gives good results for channel flow, and flat plate cases (Tu = 0.2-6.2%, $Re = 2 \times 10^6$), where it determined when natural, mixed and by-pass transition occurred. The poorest agreement came for low (Tu = 0.6%) and then high (Tu = 19.5%) for a highly loaded turbine blade on the suction surface. The k_T model gave the general form, but not at the correct streamwise position (late transition for low Tu, early transition for high Tu).

Dynamic Intermittency Model, Lodefier and Dick (2005)

Lodefier and Dick (2005) developed a model based upon the turbulent weight factor model of Steelant (1999), and implemented it into Menter's k-ω SST model. It has two dynamic equations for intermittency: one for near-wall intermittency, and one for freestream intermittency. The sum of the two is the total intermittency factor, which multiplies the turbulent viscosity computed by the turbulence model. Lodefier and Dick think that in theory, a set of conditionally averaged turbulent and non-turbulent mass, momentum and

energy equations are required to fully capture the interaction between turbulent and non-turbulent regions during the transition process, but since that involves doubling the amount of equations, in practice, the concept of intermittency is used in a combination of turbulent equations only. As transition occurs in the free shear layer, they use the freestream velocity as the velocity scale. They are able to define the edge of the boundary layer as having a level of rotation equal to 1% of the maximum level along a perpendicular profile to the wall. At the boundary layer edge, the turbulence intensity is stored with the streamwise coordinate. This makes the turbulence intensity known throughout the entire boundary layer.

Tested against the T106a turbine, it produced good results at low Tu, showing a suppression of the separation bubble between wake passings. However, post wake effects, it predicts the separation bubbles lasting until the trailing edge, as transition was not detected in the model. This is not the case in reality, as natural transition takes place to cause early reattachment, but the model is not able to predict natural transition. At high Tu the model predicts a transition start point further upstream than experiment in between wakes, and also no separation occurs as it does in experimental data. Transition takes place along the whole of the wake period.

Quasi-Laminar Pre-Transitional Model, Praisner and Clark (2007)
The model tries to account for the effect of freestream turbulence on the pre-transitional laminar boundary layer. Instead of setting $\mu_T = 0$ they minimise the production of both k and ω, which allows for the convection and diffusion of freestream turbulence into what they refer to as the 'quasi-laminar' boundary layer. Transition onset in attached flows was given by the

following equation;

$$Re_\theta = A(Tu\frac{\theta}{\lambda})^B \tag{3.2}$$

Where A and B are constants, and λ is the turbulent length scale. The onset of separated flow transition was given by an in-house database attached to the code. Transition was expected to occur in bypass mode and therefore was modelled as point-like. The base turbulence model was the Wilcox $k-\omega$ model (Wilcox, 1993b).

When tested on a low pressure turbine it predicted transition at the correct position on the pressure surface, but as it used a trip, or point-like method, it did not account for the very high acceleration taking place just after the start of transition, drawing out the transition region. Hence it greatly over predicted the heat transfer on the pressure surface. On the suction surface, the model predicted transition to take place where the shock / boundary layer interaction occurred, instead of approximately 40% chord further upstream as shown by experimental results. However, the experimental data showed that a large increase in heat transfer took place at the shock / boundary layer interaction region, showing that the boundary layer greatly increased its turbulence in this region, probably through a greater concentration in turbulent spots. Overall, the model did provide a significant improvement in the prediction of profile losses over the use of either purely laminar or turbulent models when tested on both cascade and multi-stage low pressure turbines.

They found that since their model was grounded in attached flow bypass transition, it performed poorly when predicting separated flow transition.

They recommended that more work be done into separated flow transition prediction. This confirms the author's thoughts that there should be a separate process to predict attached and separated flow transition. They also recommend future work to include the effect of surface roughness. Their model improved the accuracy of efficiency predictions at midspan for individual low pressure turbines, but failed to reduce the error found between the different engine designs tested. They felt research should be undertaken into the interaction of secondary flows and cavity / main gas path interactions and the transition process.

3.6 Best Practice

After reviewing the literature, it was apparent that a code of best practice must be followed. The list below highlights some of the best practice mentioned, which will be followed for the simulations contained in this thesis;

- For turbomachinery applications, an O-grid must be used for the boundary layer.
- All boundary layers must be resolved by a minimum of 10 grid nodes.
- Leading and trailing edges are to have a greater amount of nodes to ensure proper resolution of the stagnation points.
- Minimum grid element angle of 20° to be used.
- for ω based models, a maximum of $y^+ = 2$ to be used for first grid node spacing from surface.

3.7 Chapter Closure

This literature review has shown that for most industrial applications, RANS based models give the best balance of accuracy vs computational cost, and their behaviour has been well documented, enabling the user to have a degree of confidence in their use. The $k-\omega$ SST model has shown to be the RANS model of choice. Predicting unsteady transition is becoming the key area of current research as transition can have a significant effect on the downstream boundary layer and losses. Current transition correlations, such as Menter et al. (2004a), built into RANS based turbulence models can give a good prediction in steady and some unsteady turbomachinery flows. More work must be done to develop these correlations in order to fully predict the unsteady transition region due to effects from incoming wakes etc.

This page has been left intentionally blank.

Chapter 4

Initial Test Cases Simulations

Some of the deficiencies of current turbulence models have been outlined in Chapter 3. Such deficiencies are particularly found in flows with separation, pressure gradients, transition, shear flows and geometry curvature. To highlight these deficiencies, and understand more fully how the turbulence models available in the CFX code behave over a variety of flow regimes, a number of initial CFD simulations were performed with previous versions of the code, releases 5.7 and 10. The cases included a fully turbulent flat plate described by Wieghardt (1969), a backward facing step (Driver and Seegmiller, 1985), a series of transitional flat plates from the ERCOFTAC T3A,Am,B,C and L series, a flat plate subject to shear flow (Palikaras et al., 2002) and a 2D compressor cascade (Deutsch and Zierke, 1987).

The results from the simulations will show that for most applications, the $k-\omega$ SST model is the model of choice over the $k-\epsilon$ and Reynolds Stress models, and that the $\gamma-\theta$ transition model is a useful extension of the $k-\omega$ SST model.

4.1 CFX 5.7 - 11 Codes and Turbulence Models

The CFX code used was upgraded from version 5.7 to version 10, then to version 11 during the project. This did not affect the main solver or the turbulence and transition models. The solver uses an element based finite volume method with a second order discretisation scheme. It is a coupled solver, in which all the hydrodynamic equations are solved as a single system. The turbulence models used in the project were the two equation $k-\epsilon$ and $k-\omega$ SST models and the ω-based Reynolds Stress model. The transition model available was the $\gamma-\theta$ model described in Section 3.5. These models did not alter between the versions of the code. A brief description of them follows.

4.1.1 k-ϵ Model

One of the most prominent turbulence models, the $k-\epsilon$ model, has been implemented in most general purpose CFD codes and is considered the industry standard model. It has proven to be stable and numerically robust and has a well established envelope of predictive capability. For general purpose simulations, the $k-\epsilon$ model offers a good compromise in terms of accuracy and robustness. The transport equations used for k and ϵ are;

Turbulent kinetic energy

$$\frac{\partial(\rho k)}{\partial t}+\nabla\bullet(\rho uk)=\nabla\bullet[(\mu+\frac{\mu_t}{\sigma_k})\nabla k]+P_k-\rho\epsilon \tag{4.1}$$

Dissipation rate

$$\frac{\partial(\rho\epsilon)}{\partial t} + \nabla \bullet (\rho u\epsilon) = \nabla \bullet [(\mu + \frac{\mu_t}{\sigma_\epsilon})\nabla\epsilon] + \frac{\epsilon}{k}(C_{\epsilon 1}P_k - C_{\epsilon 2}\rho\epsilon) \tag{4.2}$$

and the turbulent viscosity is given by;

$$\mu_t = \rho\frac{C_\mu k^2}{\epsilon} \tag{4.3}$$

where $C_{\epsilon 1}$, $C_{\epsilon 2}$, C_μ, σ_k and σ_ϵ are empirically derived constants. P_k is the turbulence production due to viscous and buoyancy forces and is given by;

$$P_k = \mu_t \nabla U \bullet (\nabla u + \nabla u^T) - \frac{2}{3}\nabla \bullet u(3\mu_t \nabla \bullet u + \rho k) + P_{kb} \tag{4.4}$$

Within CFX, the $k - \epsilon$ model uses the scalable wall-function approach to improve robustness and accuracy when the near-wall mesh is very fine ($y^+ <$ 11.06). The $k-\epsilon$ model equations become extremely stiff through the viscous sub-layer. To avoid the problems associated with stiffness, the model uses scalable wall functions to integrate to the wall. The wall functions operate by relating the near wall tangential velocity to wall shear stress, with the relative velocity being related to the turbulent kinetic energy. This relationship is used within the viscous sub-layer of the boundary layer for the scalable wall function to ensure that the minimum distance the grid surface is to the wall coincides with the edge of the viscous sub-layer, given as $y^+ = 11.06$. This ensures all grid points are outside the viscous sub-layer. However, this can create discrepancies in the calculation of mass and momentum balance, as the viscous sub-layer portion is neglected. In flows at lower Reynolds numbers ($R_e \leq 10^5$), it may cause an error in the displacement thickness of up to 25%. However, it allows a solution to be found without using superfine grids to calculate the flow equations within the viscous sub-layer.

4.1.2 kω SST Model

The k-ω SST model (Menter, 1994) solves the transport equations for turbulent kinetic energy k, and the specific dissipation rate of k, ω, in a similar fashion to the k-ϵ models. To avoid the sensitivity to the inlet value of ω suffered by the original Wilcox (1988b) model, the transport equations are based upon ω-converted k-ϵ transport equations, and include a blending function to switch from using ϵ in the freestream to ω in the boundary layer. The transport equations are;

Turbulent kinetic energy

$$\frac{\partial(\rho k)}{\partial t} + \nabla \bullet (\rho u k) = \nabla \bullet [(\mu + \frac{\mu_t}{\sigma_{k2}})\nabla k] + P_k - \beta' \rho k \omega \tag{4.5}$$

Specific dissipation rate

$$\frac{\partial(\rho\omega)}{\partial t} + \nabla \bullet (\rho u \omega) = \nabla \bullet [(\mu + \frac{\mu_y}{\sigma_{\omega 3}})\nabla \omega] + (1 - F_1) 2\rho \frac{1}{\sigma_{\omega 2}\omega} \nabla k \nabla \omega + \alpha_3 \frac{\omega}{k} P_k - \beta_3 \rho \omega^2 \tag{4.6}$$

Where $\beta', \alpha_1, \beta_1, \sigma_{k1}, \sigma_{\omega 1}, \alpha_2, \beta_2, \sigma_{k2}$ and $\sigma_{\omega 2}$ are constants, with F_1 being the blending function. F_1 is 1 at the surface, and switches to 0 in the boundary layer, so that at the boundary layer edge, the k-ϵ equation is used. The turbulent viscosity is calculated by;

$$\mu_t = \rho \frac{k}{\omega} \tag{4.7}$$

The eddy viscosity production function also includes a limiter (Equation 4.8), which prevents the build up of turbulent kinetic energy in stagnation areas and adverse pressure gradient flows, allowing the model to capture the transport of turbulent shear stress. The build up of turbulent kinetic energy

causes an over prediction of eddy viscosity, resulting in an early separation point. The limiter operates by using a blending function F2 in a similar way to blending function F1 (Equation 4.6), both based upon the flow variables and the distance to the nearest surface. This restriction only affects the solution within the boundary layer, as the underlying assumptions are not correct for free shear flows.

$$\nu_t = \frac{a_1 k}{max(a_1\omega, SF_2)} = \mu_t/\rho \tag{4.8}$$

As the model can be used in the viscous sub-layer, it provides a low-Reynolds solution, only automatically switching to a wall function formulation if the grid refinement is not suitably high. It overcomes the problems with scalable wall functions used by k-ϵ models for lower Reynolds number flows (Re$< 10^5$). As the grid is refined, this changeover point is moved virtually down towards the wall until all of the sub-layer is modelled in the low-Re mode. The k-ω SST model provides a more accurate solution to the flow inside the boundary layer and more accurately predicts separation under adverse pressure gradients, one of the failings of k-ϵ models. CFX recommend using a wall distance $y^+ \approx 2$ for adequate sub-layer resolution.

4.1.3 Omega-Reynolds Stress Model

CFX recommends the use of their BSL Reynolds Stress model for wall bounded flows (ANSYS-CFX, 2005). The baseline (BSL) RSM model utilises the same automatic ω near wall treatment applied to the k-ω SST model. As it also

suffers from the sensitivity of ω in the freestream, the model is based upon the same ω formulation used by the k-ω SST model and is blended between the freestream and boundary layer in the same manner. The modelled equations for the Reynolds stresses are;

$$\frac{\partial(\rho\tau_{ij})}{\partial t} + \frac{\partial(U_k\rho\tau_{ij})}{\partial x_k} = -\rho P_{ij} + \frac{2}{3}\beta'\rho\omega k\delta_{ij} \\ -\rho\Pi_{ij} + \frac{\partial}{\partial x_k}\left[\left(\mu + \frac{\mu_t}{\sigma^*}\right)\frac{\partial\tau_{ij}}{\partial x_k}\right] \tag{4.9}$$

where σ^*, σ, β are coefficients and Π is the pressure strain correlation. The transport equation for the specific dissipation rate (ω) is;

$$\frac{\partial(\rho\omega)}{\partial t} + \partial(U_k\rho\omega) = \alpha_3\frac{\omega}{k}P_k - \beta_3\rho\omega^2 \\ +\frac{\partial}{\partial x_k}\left[\left(\mu + \frac{\mu_t}{\sigma_{\omega 3}}\right)\frac{\partial\omega}{\partial x_k}\right] + (1-F_1)2\rho\frac{1}{\sigma_2\omega}\frac{\partial k}{\partial x_k}\frac{\partial\omega}{\partial x_k} \tag{4.10}$$

where $\alpha_3, \beta_3, \sigma_{\omega 3}, \sigma_2$ are coefficients, who's values are dependent upon if the model is operating in the boundary layer (ω regime) or the freestream (ϵ regime). F_1 is the blending function between the ω based equation and the ϵ based equation, the same as in the k-ω SST model. The turbulent viscosity μ_t is also calculated as given in Equation 4.7.

4.1.4 $\gamma - \theta$ Transition Model

The $\gamma - \theta$ transition model available in CFX has already been reviewed in Section 3.5. The $\gamma - \theta$ model uses two separate correlations to calculate

the start of the transition region and the intermittency distribution within the transition region. The k-ω SST model is used as a baseline turbulent model from which the turbulent viscosity is switched on and altered by the intermittency distribution. The θ correlation calculates the Reynolds number based on momentum thickness, $Re_{\theta t}$ that transition is expected to start. It is given by;

$$Re_{\theta t} = 803.73[Tu + 0.6067]^{-1.027} F(\lambda_\theta, K) \tag{4.11}$$

$$F(\lambda_\theta, K) = 1 - \left[-10.32\lambda_\theta - 89.47\lambda_\theta^2 - 265.51\lambda_\theta^3\right] e^{\left[\frac{-Tu}{3.0}\right]}, \lambda_\theta \leq 0 \tag{4.12}$$

$$F(\lambda_\theta, K) = 1 + [0.0962[K \cdot 10^6] + 0.148[K \cdot 10^6]^2 + 0.0141[K \cdot 10^6]^3] \left(1 - e^{\left[\frac{-Tu}{1.5}\right]}\right) + 0.556\left[1 - e^{[-23.9\lambda_\theta]}\right] e^{\left[\frac{-Tu}{1.5}\right]}, \lambda_\theta \geq 0 \tag{4.13}$$

In order to only use local variables, the momentum thickness is correlated to the Reynolds Vorticity number, Re_v. When the momentum thickness Reynolds number at the boundary layer edge, $Re_\theta >= Re_{\theta t}$ the intermittency function is switched on. The correlation for the intermittency is proprietary and is hence not available here. The values of intermittency and $Re_{\theta t}$ are both transported into the boundary layer via Equations 4.14 and 4.15 respectively, which incorporate a lag function. For separated flows the intermittency is allowed to artificially rise above 1 to account for the undamped rapid transition region.

$$\frac{\partial(\rho\gamma)}{\partial t} + \frac{\partial(\rho U_j \gamma)}{\partial x_j} = P_{\gamma 1} - E_{\gamma 1} + P_{\gamma 2} - E_{\gamma 2} + \frac{\partial}{\partial x_j}\left[\left(\mu + \frac{\mu_t}{\sigma_f}\right)\frac{\partial \gamma}{\partial x_j}\right] \tag{4.14}$$

where $P_{\gamma 1}$, $E_{\gamma 1}$, $P_{\gamma 2}$ and E_{γ} are transition sources.

$$\frac{\partial(\rho\tilde{R}e_{\theta t})}{\partial t} + \frac{\partial(\rho U_j\tilde{R}e_{\theta t})}{\partial x_j} = P_{\theta t} + \frac{\partial}{\partial x_j}\left[\sigma_{\theta t}(\mu+\mu_t)\frac{\partial\tilde{R}e_{\theta t}}{\partial x_j}\right] \tag{4.15}$$

The transition model is coupled to the k-ω SST turbulence model using via the following equations;

Turbulent kinetic energy

$$\frac{\partial}{\partial t}(\rho k) + \frac{\partial}{\partial x_j}(\rho u_j k) = \tilde{P}_k - \tilde{D}_k + \frac{\partial}{\partial x_j}\left((\mu+\sigma_k\mu_t)\frac{\partial k}{\partial x_j}\right) \tag{4.16}$$

Specific dissipation rate

$$\frac{\partial}{\partial t}(\rho\omega) + \frac{\partial}{\partial x_j}(\rho u_j\omega) = \alpha\frac{P_k}{V_t} - D_\omega + Cd_\omega + \frac{\partial}{\partial x_j}\left((\mu+\sigma_k\mu_t)\frac{\partial\omega}{\partial x_j}\right) \tag{4.17}$$

4.2 Turbulent Flat Plate

A turbulent flat plate was used as an initial study to show any differences in results during grid refinement, and differences between turbulence models. The case originated from the study by Wieghardt (1969). It consists of an incompressible flow over a flat plate, 5m long with an inlet velocity of M = 0.1. 3 grids were used to examine grid independency. The domain contained 100 streamwise nodes with an average y^+ value of 30 (coarse), 10 (medium) and 1 (fine) respectively. All simulations converged with residuals $\geq 10^{-6}$. As this is a fully turbulent test case, the $\gamma - \theta$ model was not used.

All turbulence models returned a close agreement with the experimental data. Of all the models, the RSM model on the coarse grid and k-ω on the fine grid gave the closest result. A plot of local skin friction coefficient (cf) against the distance from the leading edge (Figure 4.1) highlights this. The k-ϵ model on

the fine grid returned the closest result of all the k-ϵ models. The difference between turbulence models on the different grids was small, proving grid independence. For the k-ω SST and k-ϵ models, the medium grid returned the poorest results. The only discernable difference is that the k-ϵ model exhibits slightly greater velocity in the lower part of the boundary layer, (Figure 4.2) and a slightly lower velocity in the upper part of the boundary layer as compared to the ω based models.

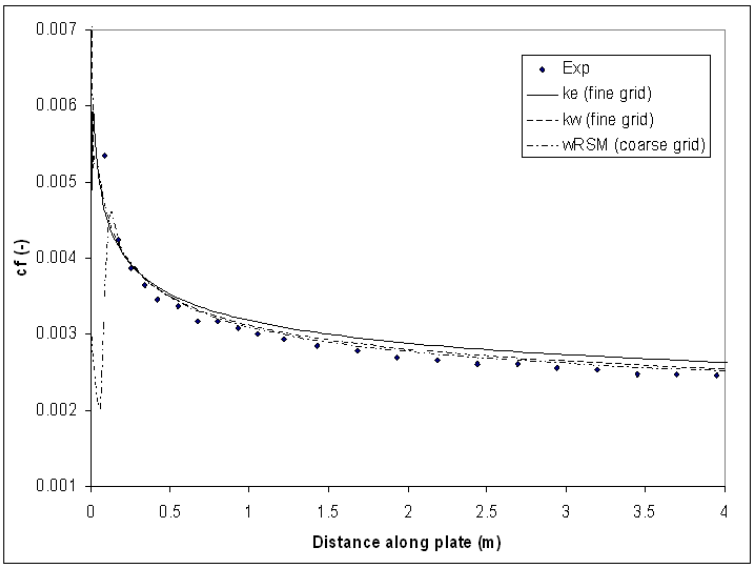

Figure 4.1: Comparison of local skin friction coefficient for turbulent flat plate for the closest results per turbulence model

Section Closure

All of the turbulence models tested showed they were accurate and repeatable when being used on a fully turbulent flat plate. The ω based models gave more accurate results than the ϵ based models as they do not use wall functions. However, differences are negligible and it is not surprising that all the models gave a good agreement as the constants used by the models are

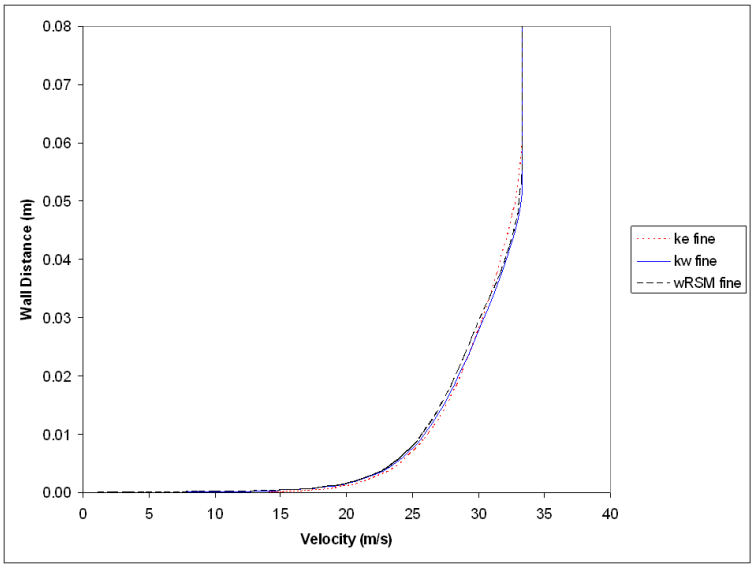

Figure 4.2: Comparison of boundary layer profile for turbulent flat plate using fine grid

optimised on turbulent flat plates.

4.3 Backward Facing Step

The backward facing step flow is a popular test case for the application of turbulence models on separated flows as the geometry is simple and covers many important flow phenomena, such as separation, recirculation, reattachment, shear-layer mixing and the development of the boundary layer downstream of the reattachment point. The experimental case reported by Driver and Seegmiller (1985) was chosen as it had previously served as a test case for ANSYS CFX. The models used for comparison were the k-ϵ, k-ω SST and RSM models. Again, the $\gamma - \theta$ model was not used as this case is fully turbulent from the inlet.

The dimensions for the computational domain are shown in Figure 4.3. The domain was 150mm wide, allowing for any 3D aspects of the flow. Any 3D effects were found to be negligible, especially at the centreline of the domain from which the results were taken. A coarse grid ($y^+ \approx 11$) and a refined grid ($y^+ \approx 1$) were used. A turbulent velocity profile with a maximum value of 40ms^{-1}, Tu = 0.24% and eddy length scale, $L_\epsilon = 0.12$m was used as inlet conditions. The outlet was specified as an average static pressure of 94.4Pa.

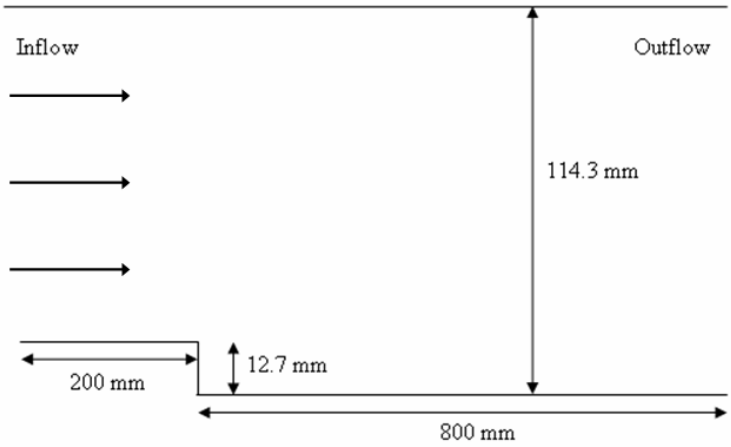

Figure 4.3: Computational domain for flow over backward facing step

Figures 4.4 to 4.8 show the comparisons between simulated and experimental data for c_f, c_p and normalised velocity profiles for all simulations. The k-ω SST model predicts well the reattachment point and the behavior of c_f and local pressure coefficient, c_p (Figures 4.4 and 4.5 respectively). It slightly over-predicts the extent of the separated region. It does not capture the full extent of the pressure recovery after reattachment, suggesting it over-estimates the losses during separation. The RSM model under-predicts the length of the separated region, and the extent of the recirculation of the flow within this region, as shown by the lower negative skin friction. This is a

little surprising as it was developed specifically for this type of flow. The k-ϵ model under-predicts the length of the separated region, but shows a more accurate pressure recovery (Figure 4.5) than the two ω based models. This may be due to the increased levels of eddy viscosity and turbulent kinetic energy over the ω based models within the separated region as shown in Figures 4.6 and 4.7. This also explains why the skin friction has a greater value than the ω based models.

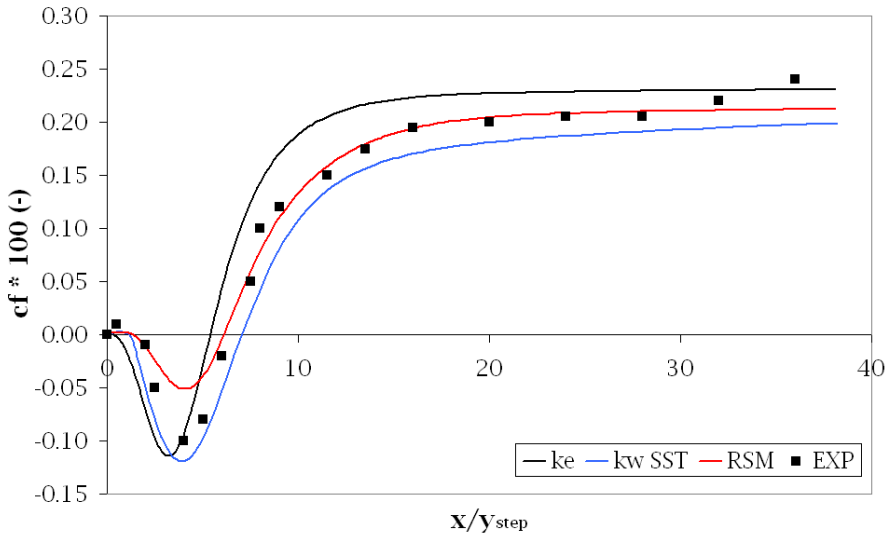

Figure 4.4: Local skin friction coefficient for all models

The normalised velocity profiles (Figure 4.8) show that the non of the models capture the full retardation of the flow during the separation region, and that the k-ϵ model recovers to experimental values at approximately $y/y_{step} = 6.5$, where y_{step} is the step height. This may be due in some part to the wall functions used in the k-ϵ model forcing the velocity distribution to return to flat plate values. Both the ω based models do not fully recover to experimental values until approximately $y/y_{step} = 32$ (406.4mm past step). The models

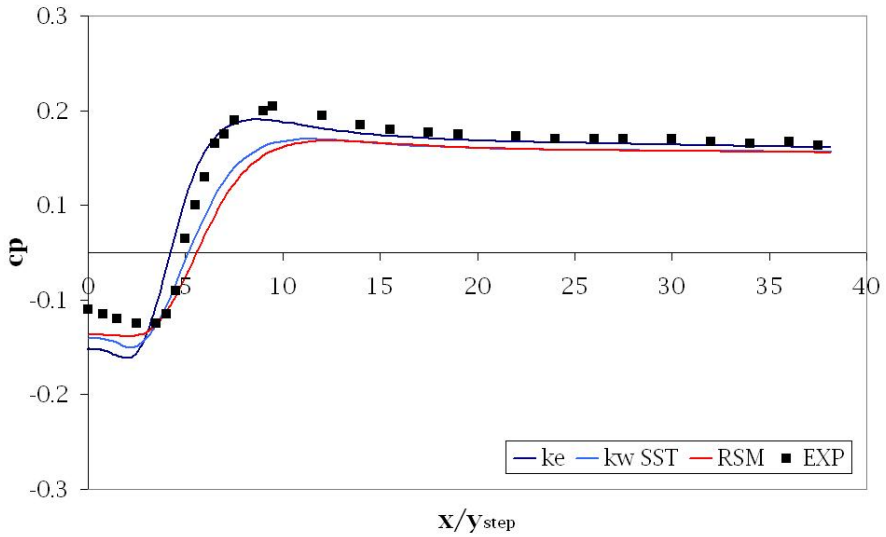

Figure 4.5: Local pressure coefficient for all models

do not fully capture the shear layer / freestream edge of the separated region as shown by the inflection point at or just below $y/y_{step} \lessapprox 1$ at $y/y_{step} = 2$ & 4, where y is the normal distance from the wall.

Section Closure

The ω based models have shown their superiority in predicting the extent of the separated region, with the k-ω SST model giving the most accurate solution. The k-ϵ model's better prediction of pressure coefficient is due to the prediction of a smaller separated region and hence a reduction in loss. It should not be confused with a more accurate prediction of the separated region. The RSM model should, in theory, have returned a more accurate solution than the other models, but it did not. Although returning the correct form, the velocity profiles showed that all of the models can improve on their prediction of the boundary layer during and post separation.

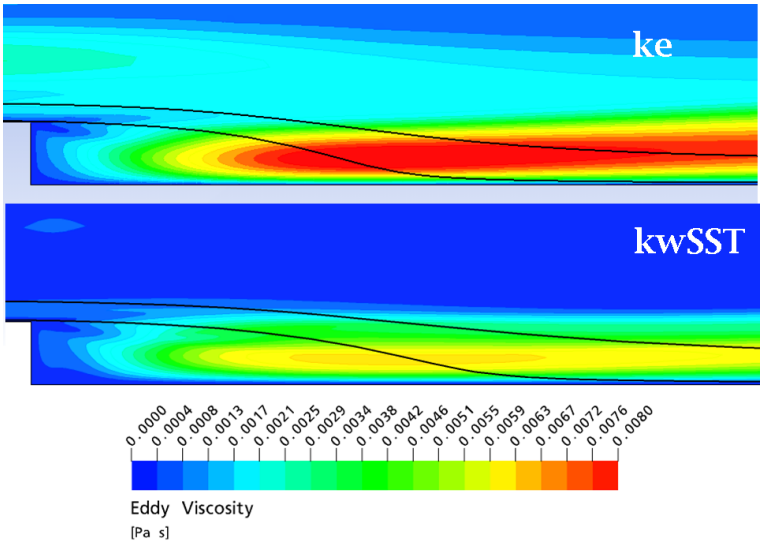

Figure 4.6: Comparison of eddy viscosity levels and streamlines for k-ϵ (above) and k-ω SST (below)

4.4 Transitional Flat Plate

The T3 flat plate test case series has been used extensively by the ERCOFTAC (European Research Community on Flow, Turbulence and Combustion) transition special interest group project. Developed in the early 1990s by Rolls-Royce, it has become the standard test case series against which almost all transition models are verified and validated on. The T3ABC share the same plate geometry with the C series having an additional tunnel wall contour to simulate a favourable to adverse pressure gradient similar to that of an aft-loaded turbine blade (Figure 4.9). A schematic of the experimental set-up for the T3ABC series is shown in Figure 4.10. The test plate is 1700mm long, 20mm thick, 710mm wide and has a small leading edge radius of 0.75mm with a 5° chamfer inclining from the leading edge to the lower surface. Circulation about it is controlled by a combination of a trailing edge

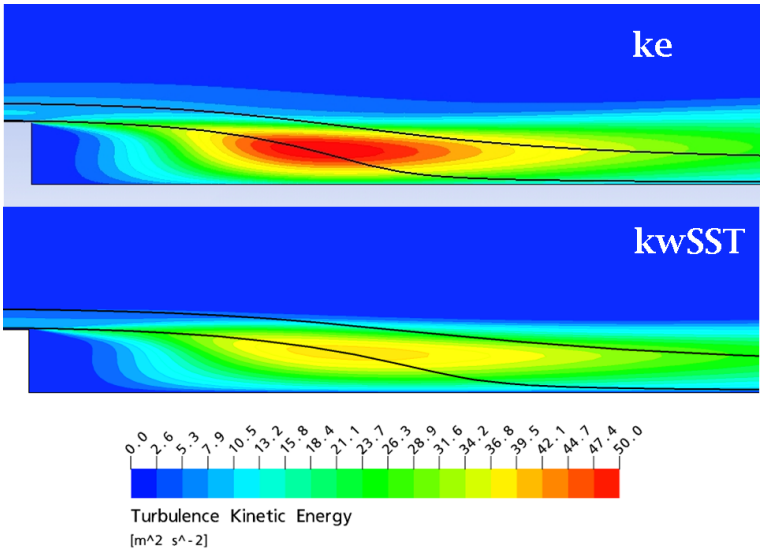

Figure 4.7: Comparison of turbulent kinetic energy levels and streamlines for k-ϵ (above) and k-ω SST (below)

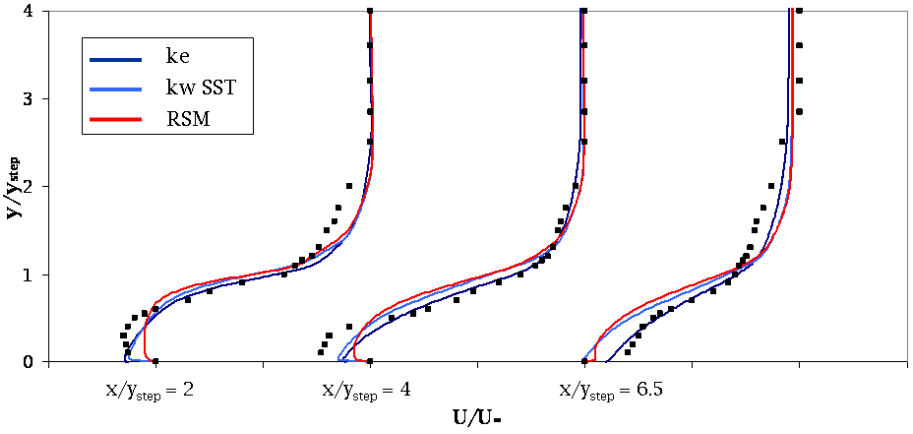

Figure 4.8: Normalised velocity profiles for all models

flap and adjusting the pressure drop across the working section exit plane (by means of gauzes). The test plate is inclined at 0.5° to the main flow vector which, together with the circulation control measures, ensures attached, steady leading edge flow with the stagnation streamline located on the test

surface. The T3L series plate has a 10mm thickness and a 10mm diameter semi-circular leading edge, which causes a transitional separation bubble to form just past the leading edge. The plate has zero incidence to the flow. Both velocity and freestream turbulence intensity are varied. A schematic of the experimental set-up for the T3L series is shown in Figure 4.11. As the inlet $Tu \gtrapprox 1\%$, the mode of transition is expected to be bypass. Details of the cases simulated are shown in Table 4.1.

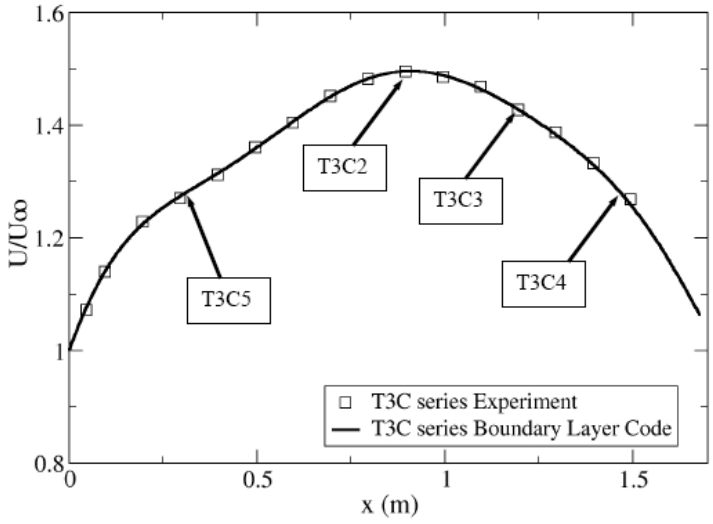

Figure 4.9: Normalised velocity distribution for T3C cases vs distance from leading edge, with transition onset location shown. Reproduced from Langtry (2006)

There is discussion in the early papers (Savill (1993a), Savill (1993b)) about which setup and inlet conditions are best for use on the T3ABC test cases as it is not feasible for the computational methods to simulate the flow control methods used in the experimental setup. The papers concluded that no one setup was definitively correct. In past computational studies (Savill

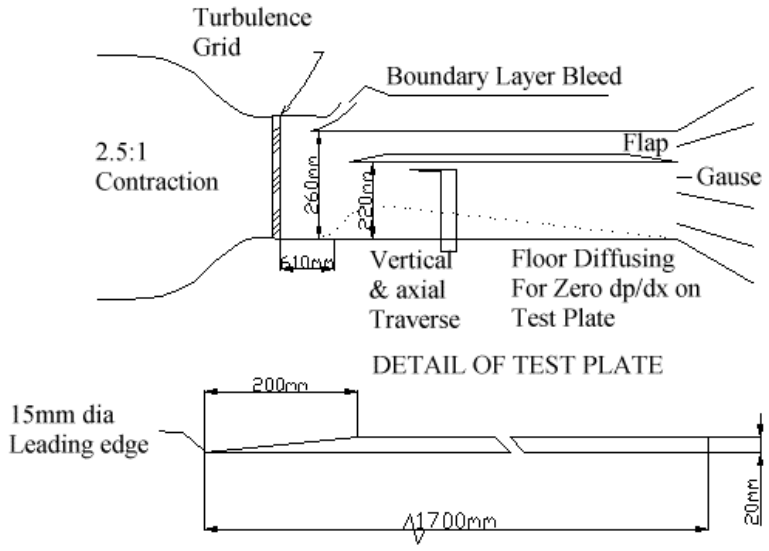

Figure 4.10: Schematic showing the experimental set-up for the ERCOFTAC T3ABC test cases

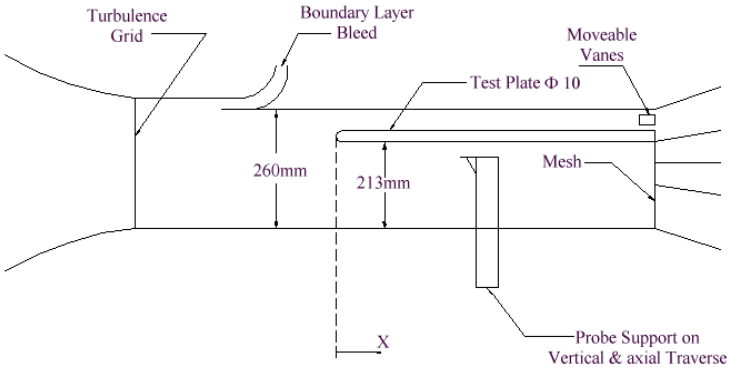

Figure 4.11: Schematic showing the experimental set-up for the ERCOFTAC T3ABC test cases

(1993a), Savill (1993b)), models have successfully qualitatively simulated the flow pattern for T3A&B series, but have not all successfully simulated the flows for T3C series where an adverse pressure gradient is present. Savill (1993b) states that the transition region in the T3ABC series is difficult to

Table 4.1: T3 Flat plate series case conditions.

Case	Re_l (10^5)	Inlet Tu (%)	Pressure Gradient
T3A	5.98	3	
T3Am	21.9	0.9	
T3B	10.4	6	
T3C1	6.53	6.6	✓
T3C2	5.54	3	✓
T3C3	4.1	3	✓
T3C4	1.33	3	✓
T3C5	9.3	3	✓
T3L1	1.3	0.2	
T3L2	1.3	0.65	
T3L3	1.3	2.3	
T3L4	1.3	5.5	
T3L5	0.65	2.3	
T3L6	2.61	2.3	

simulate due the simulation being overly sensitive to inlet conditions.

As there was no separation bubble at the leading edge, and the reassurance from the papers that early transition did not take place, a Blasius boundary layer profile for the plate and tunnel wall was used at the domain inlet at a position of 25mm downstream of the leading edge. Free stream turbulence intensity was either extrapolated back from experimental data downstream of the domain inlet position, or gained from experimental measurements at that position. Early results using this method revealed significant irregularities

in the pre-transitional boundary layer development. Instead, the inlet was changed to 50mm upstream of the leading edge, with symmetry applied at the centre of the leading edge, so that only half the plate was modelled. Uniform velocity, turbulence intensity and turbulent viscosity ratio were specified at the inlet. Turbulence intensity and viscosity ratio were calculated using Equation 4.18 (where β, β^* are constants) and compared to experimental data to ensure correct decay of turbulence intensity. The grid used ensured that the $y^+ \leq 1$ at all times.

$$Tu = \left(Tu_{inlet}^2 \left[1 + \frac{3\rho U_\infty x \beta Tu_{inlet}^2}{2\mu(\mu_t/\mu)} \right]^{-\frac{\beta*}{\beta}} \right)^{0.5} \tag{4.18}$$

The T3L series test cases were modelled in a similar manner, but without the use of symmetry through the centreline of the plate. This didn't appear to affect the results as the stagnation point was directly on the centre point of the leading edge. The computational domain started 25mm upstream of the leading edge. The freestream turbulence intensity and viscosity ratio were again specified using Equation 4.18 and comparing with experiential data available. The essentially 2D grids used gave a $y^+ = 1$ as a maximum value for each flow condition. To enable the models to simulate the separation bubble at the leading edge, a much greater density of streamwise elements were placed at the leading edge.

The results for the T3A test case are shown in Figures 4.12 to 4.14. As expected, Figure 4.12 shows the $\gamma - \theta$ model to be the most accurate, as it is the only model to predict transition. The transition start and length, with

the associated overshoot are all well predicted. There is no real appreciable difference in the skin friction results for the turbulent models. They do not predict the skin friction overshoot due to the transition process. The $\gamma - \theta$ model also returns a suitable value of momentum thickness (Figure 4.13) through the transition region, although it does not predict the correct rate of growth of the post transitional boundary layer. The turbulent models over predict the momentum thickness along the plate, but this is because they do not take into account the thinner laminar and transitional boundary layer. Post transition, similar to the $\gamma - \theta$ model, they under predict the growth rate of the boundary layer, but at the similar rate to the $\gamma - \theta$ model. Using a turbulent model in this situation would lead to an over prediction of loss as the boundary layer is thicker than in reality. Whilst giving a good prediction though the transition boundary layer, the $\gamma - \theta$ model under, then over predicts the shape factor in the pre and post transitional boundary layer (Figure 4.14). This is due to the over, then under prediction of the displacement thickness. The ω based turbulent models return a closer shape factor for the turbulent boundary layer, whilst the k-ϵ model gives a poor result. It can only be assumed that this is purely due to its use of wall functions.

Results for T3Am, T3B and T3C series follow a similar pattern as described for the T3A results. For the T3Am case, the results for local skin friction in Figure 4.15 show a major deficiency for the $\gamma - \theta$ model; namely that it does not function well for low freestream turbulence flows, i.e. flows which cause natural transition. The results given are comparable to those reported by Menter et al. (2004a) and Misaka and Obayashi (2006). Menter states that the correlation has not taken into account the effect of the freestream turbulence on the length scale. As expected, the momentum thickness and

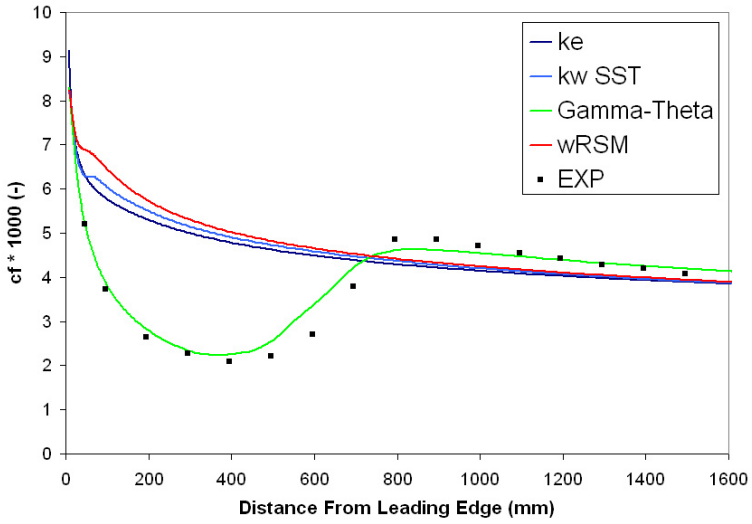

Figure 4.12: T3A c_f results.

shape factor (Figure 4.16) were both incorrectly predicted. The momentum thickness followed a similar pattern to the T3A results, but the shape factor, although having a similar form to the experimental data, starts to reduce much earlier (at 500mm) than one would expect (approximately 1000mm), from inspecting the skin friction results. Again, the k-ϵ model returns a much lower value for shape factor then the ω based turbulent models.

As with the T3Am case, the results of the T3B simulations compared favorably to past simulations conducted by Menter et al. (2004a) and Misaka and Obayashi (2006). Although the end of transition and the subsequent turbulent boundary layer were well predicted by the $\gamma - \theta$ model, the start of transition occurred too early, terminating the development of the laminar boundary layer, as shown by the increased level of skin friction during the transition region (Figure 4.17). Previous studies by the author revealed that

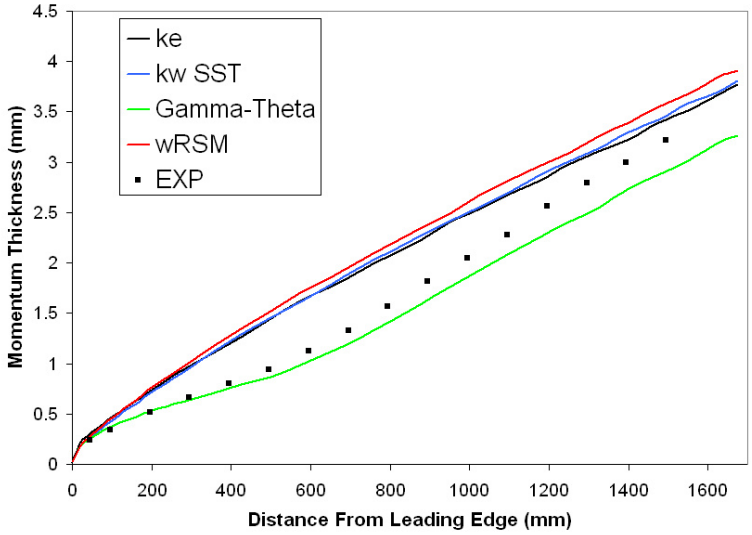

Figure 4.13: T3A momentum thickness results.

arbitrarily reducing the length scale gave a more accurate prediction. Figure 4.17 also shows good agreement with the ω based turbulent models for the post transitional boundary layer. All models return a similar over prediction of the rate of growth of momentum thickness (not shown), and as transition occurs close to the leading edge, all ω based models give a good agreement to the shape factor. Again, as with T3A and T3Am, the k-ϵ model does not give good agreement with the experimental shape factor. All ω based models were seen to produce a greater level of eddy viscosity than the k-ϵ model toward the leading edge. As eddy viscosity is essentially $f(k/l)$, the length scale given by ω is reduced, compared to ϵ, allowing the ω based models to give a superior performance in the prediction of the boundary layer properties such as shape factor. Only the ω based models returned values of shape factor close to 2 at the leading edge, to capture somewhat the boundary layer close to separation, as discussed in the documentation surrounding

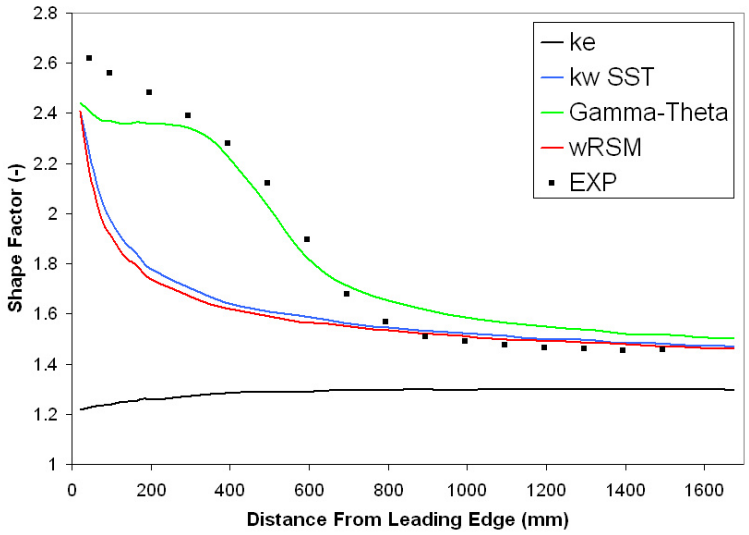

Figure 4.14: T3A shape factor results.

the experimental results.

The T3C series skin friction results are shown in Figures 4.18 to 4.22. As shown in Figure 4.9, the transition point varies from regions of accelerating flow to regions of decelerating flow. The results will be discussed in the order according to increasing distance from the leading edge of the location of the transition region. The literature to date has only reported on T3A,Am,B,C4 cases from the T3ABC series. Therefore, there is no comparison for which the author to judge the performance of the models against for the remaining cases. During the simulation period, a variation of inlet conditions was used to find a more suitable combination for those cases in which the models did not perform well for in the hope of a more favourable comparison with the experimental data. Through this, the optimum combination of inlet conditions were used to give the best performance for the case simulated.

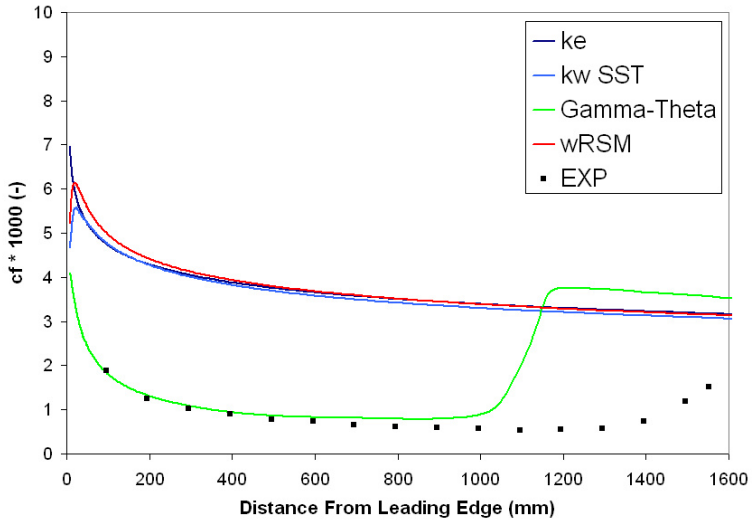

Figure 4.15: T3Am c_f results.

The T3C1 case is the original T3C case, and the transition start point is located only approximately 190mm from the leading edge, in the region of greatest acceleration of the flow. Figure 4.18 shows that non of the models correctly predict the level of skin friction and hence momentum thickness in the accelerating flow. In particular, the $\gamma - \theta$ model gives a poor prediction of the laminar and transitional state of the boundary layer. The transition region appears to be very short, shown by the kink in the curve. During the accelerating region, the freestream turbulence is somewhat damped, which causes a later transition than in reality. Equation 4.18 is only truly valid for zero pressure gradient flows, presenting the user with a difficulty of knowing what level of freestream turbulence should be specified at the inlet, and the appropriate associated decay. The problem of a short transition region is similar to the T3B case (Figure 4.17), both having freestream turbulence

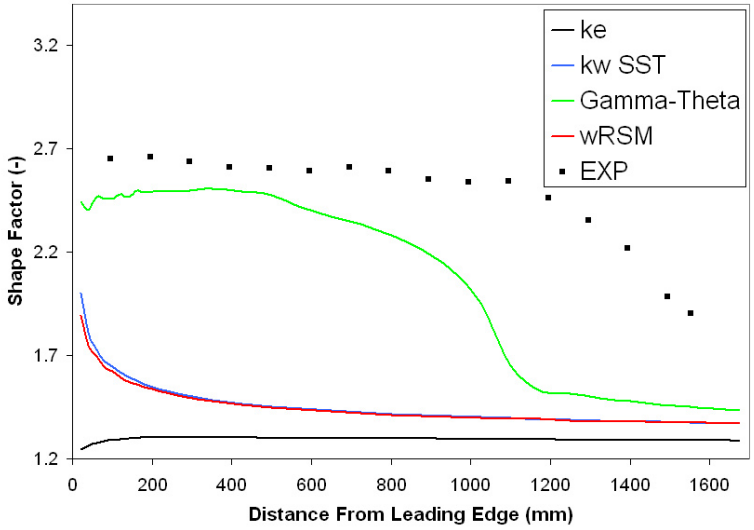

Figure 4.16: T3Am shape factor results.

levels >6%. All models return a lower value of skin friction than the experimental value, indicating that the combination of inlet turbulence intensity and viscosity ratio are not correct to allow the models to correctly simulate the flow phenomena. However, altering the inlet conditions did not prove useful in obtaining a more accurate result.

The T3C5 case is also located in the acceleration region of the flow, but the acceleration is not as great as for the T3C1 case. Freestream turbulence levels are half that of T3C1 case. Both of these factors combine to allow the $\gamma - \theta$ model to predict a more favourable comparison with experimental data than for the T3C1 case (Figure 4.19). All models under predict the level of skin friction in the turbulent boundary layer.

The start of transition for the T3C2 case is located at the point of no ac-

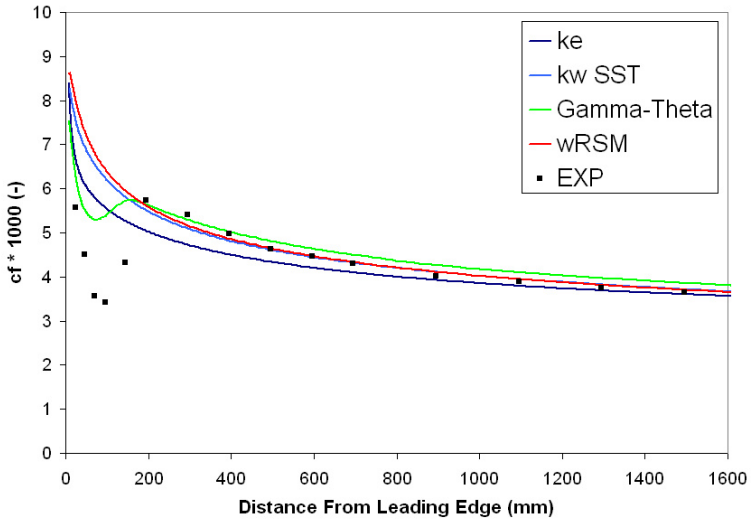

Figure 4.17: T3B c_f results

celeration. Figure 4.20 shows that the $\gamma - \theta$ model predicts well the level of skin friction in the laminar boundary layer, but fails to accurately simulate the correct transition start point and length and the level of turbulent skin friction. It does still prove superior to the turbulent models used however. As with most of the T3C series, there is no real appreciable difference between the ω based turbulent models. It is thought that the difference between simulated and experimental results is due to the reduction of freestream turbulence through the acceleration region, requiring a greater $Re_{\theta t}$ to trigger transition. Due to the low viscosity ratio used to fit the data from Equation 4.18 to the experimental data, the freestream turbulence is more susceptible to being reduced due to the acceleration of the flow.

The inlet conditions in the T3C3 case cause transition to occur just past the start of the deceleration of the flow. The $\gamma - \theta$ model gives a very good

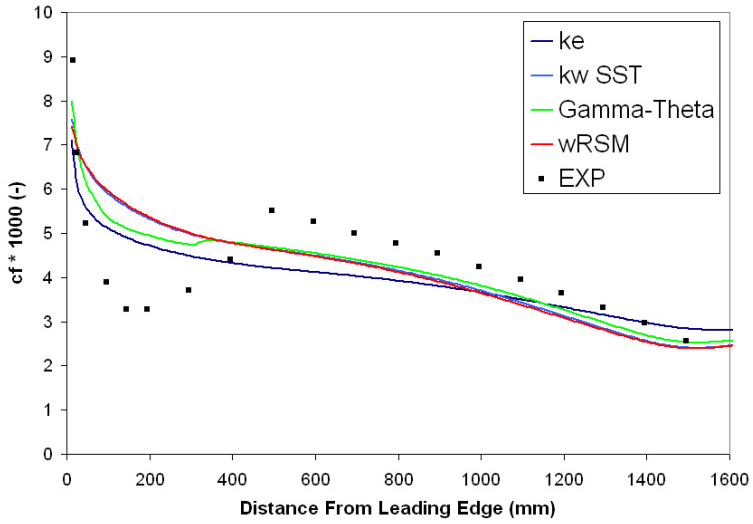

Figure 4.18: T3C1 c_f results.

agreement with the experimental data as shown in Figure 4.21. This may be due to the increase in local freestream turbulence resulting from the deceleration of the flow. The laminar boundary layer and transition start point are well predicted, however the length of the transition region is too short, and the $\gamma - \theta$ model predicts the end of transition to occur before the end of the plate, whereas the experimental data shows that the transition process is not completed before the end of the plate. None of the turbulent models used were able to simulate the correct level of skin friction. However, comparisons are limited in this case as there is no experimental data for a fully turbulent boundary layer.

Finally, the T3C4 case transition start point is situated in the region of greatest deceleration, toward the end of the plate. The low Reynolds number makes it susceptible to separation during deceleration. Figure 4.22 shows

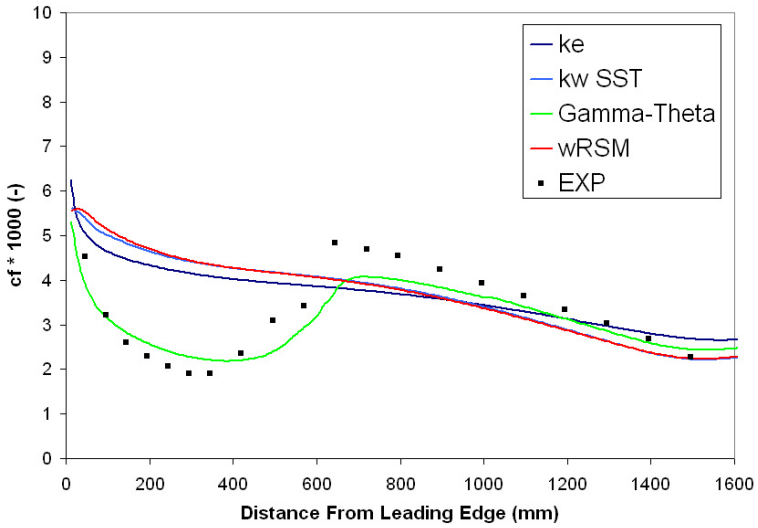

Figure 4.19: T3C5 c_f results.

the $\gamma - \theta$ model to compare well to experimental skin friction data, and even predict the separation bubble occurring just before the end of the plate. The results are comparable to literature previously mentioned in this section. The recovery of the boundary layer from the separation bubble is not complete, as shown by both the experimental and CFD data. Importantly, the turbulent models do not predict the separation bubble, as the predicted turbulent boundary layer is able to resist the adverse pressure gradient without separating. This case shows the greatest variation in results from the turbulent models, with skin friction calculated by the ω based models to give the more appropriate form.

The T3L series can be split into two main groupings; increasing freestream turbulence at constant inlet velocity, and increasing velocity at constant freestream turbulence. Both groupings cause the separation bubble to shorten

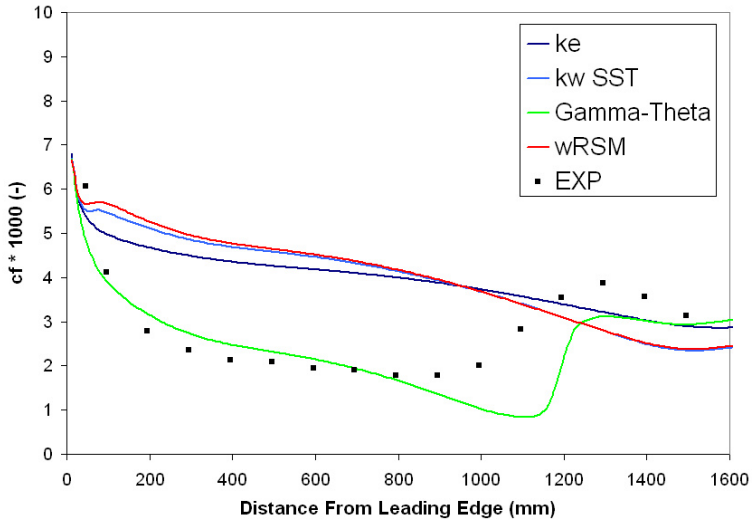

Figure 4.20: T3C2 c_f results.

as either the freestream turbulence or velocity increase. The results for the T3L series will be discussed per grouping.

The results of local skin friction and displacement thickness for increasing freestream turbulence at constant inlet velocity are shown in Figures 4.23 and 4.24. Overall, all the ω based models predicted the bubble length well. They all show a reduction in bubble length with increase in Tu. Only the k-ϵ model fails to predict the separation bubble. Figure 4.23 does not show any particular model giving a superior prediction of bubble length for all cases. The $\gamma - \theta$ model and RSM model do not show any particular pattern relative to the bubble length throughout the cases, indicating that they are sensitive to the inlet conditions. Conversely, the k-ω SST model appears to constantly predict a shorter separation bubble than the experimental data. The RSM model has a tendency to predict a higher skin friction as the tur-

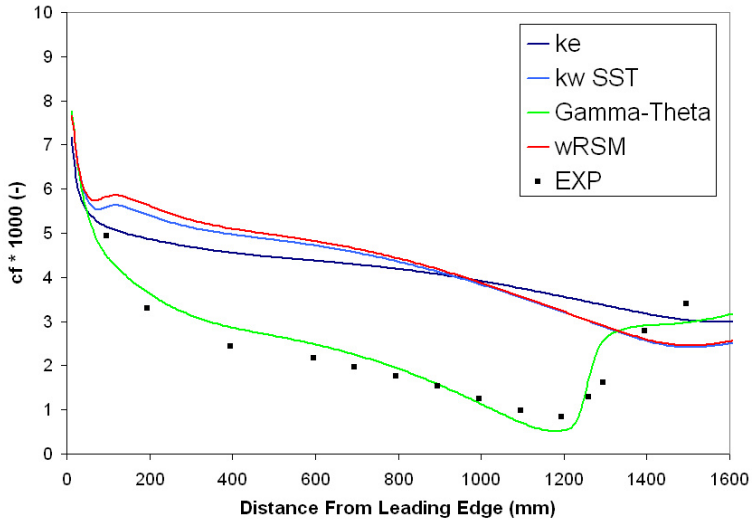

Figure 4.21: T3C3 c_f results.

bulent boundary layer becomes fully attached to the plate as compared to the other ω based models.

The effect of predicting separated transition can bee seen by comparing the k-ω SST and $\gamma - \theta$ models. Figure 4.23 shows that the maximum negative skin friction correlates to the maximum displacement of the bubble shown in Figure 4.24. The $\gamma - \theta$ model predicts a later maximum displacement than the k-ω SST model as one would expect from a detached laminar boundary layer, compared to a turbulent separated boundary layer. It also shows a greater negative skin friction than any of the models. This indicates that the models correctly predict entrainment from the separated shear layer to start at a later distance for a transitional shear layer than for a fully turbulent shear layer. This can be seen by the later increase in turbulent kinetic energy for the $\gamma - \theta$ model compared to the k-ω SST model as depicted in

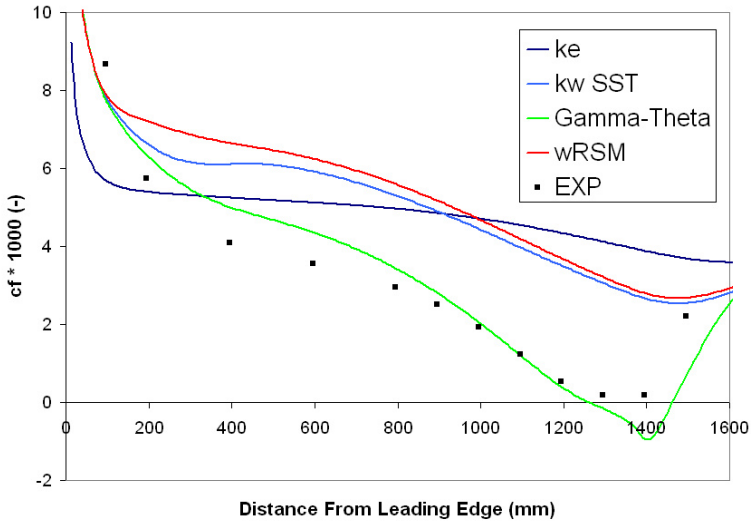

Figure 4.22: T3C4 c_f results.

Figure 4.25. Figures 4.25 and 4.26 show that the greater negative skin friction is due to the $\gamma - \theta$ model predicting a greater turbulent kinetic energy and a larger negative reverse flow velocity than the k-ω SST model. The $\gamma - \theta$ model artificially allows the intermittency to increase above 1, causing a greater local turbulent kinetic energy distribution during the transition region of the separated shear layer. Figure 4.27 shows the $\gamma - \theta$ model artificially allows intermittency to increase above one, and its effect as the bubble length changes. The RSM model has the lowest negative skin friction as it has the smallest amount of turbulent kinetic energy and reverse flow velocity.

The qualitative prediction of displacement thickness agrees well with the experimental data for all ω based models as shown in Figure 4.24. The k-ω SST model tends to give the better prediction of the models as it generally predicts the shortest and smallest separation bubble. In all but the lowest

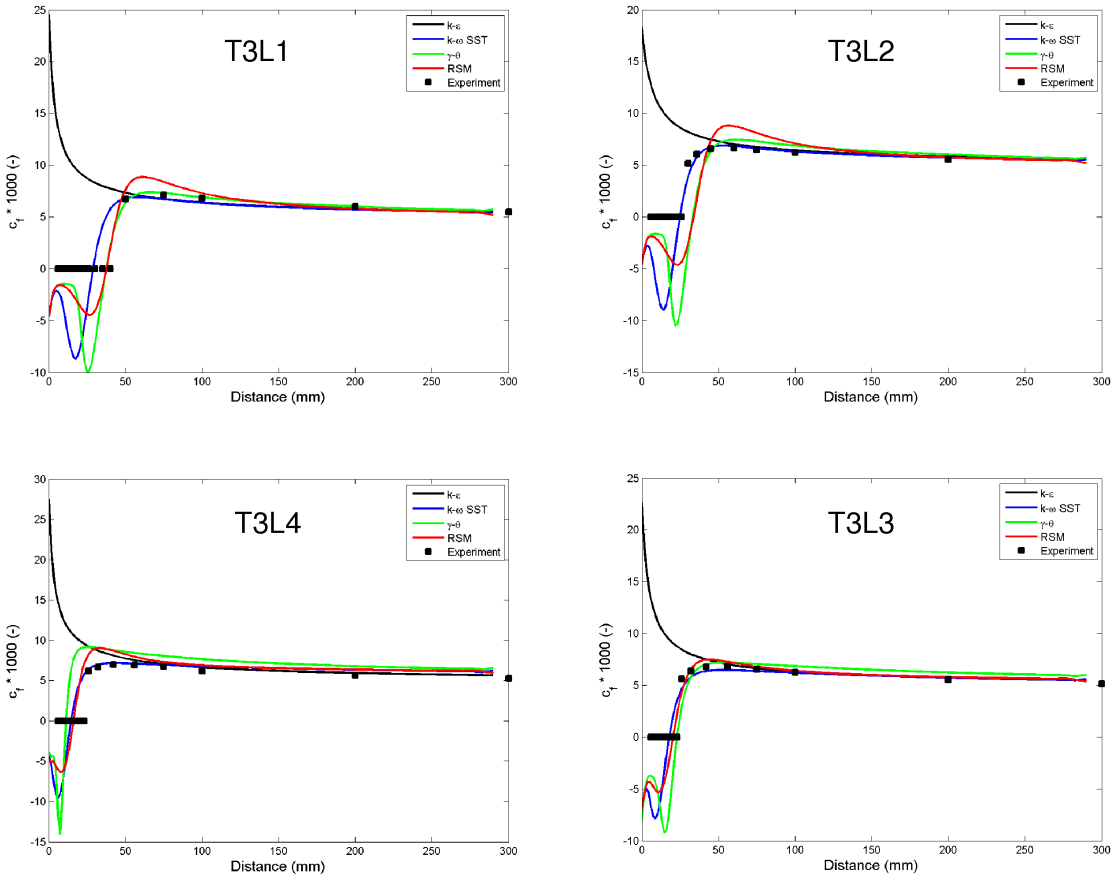

Figure 4.23: Local skin friction for T3L1234 cases, increasing Tu in clockwise direction starting from top left, constant inlet velocity.

freestream turbulence case (T3L1) the ω based models return a favourable comparison with post bubble displacement thickness. Momentum predictions (not shown) compare very well with experiment for all cases except T3L1, showing that the models are able to correctly estimate the loss for this series of cases. Even the k-ϵ model gives a good comparison for momentum thickness, although not through the bubble. The k-ϵ model, although not able to predict separation, does return favourable results post reattachment. Over-

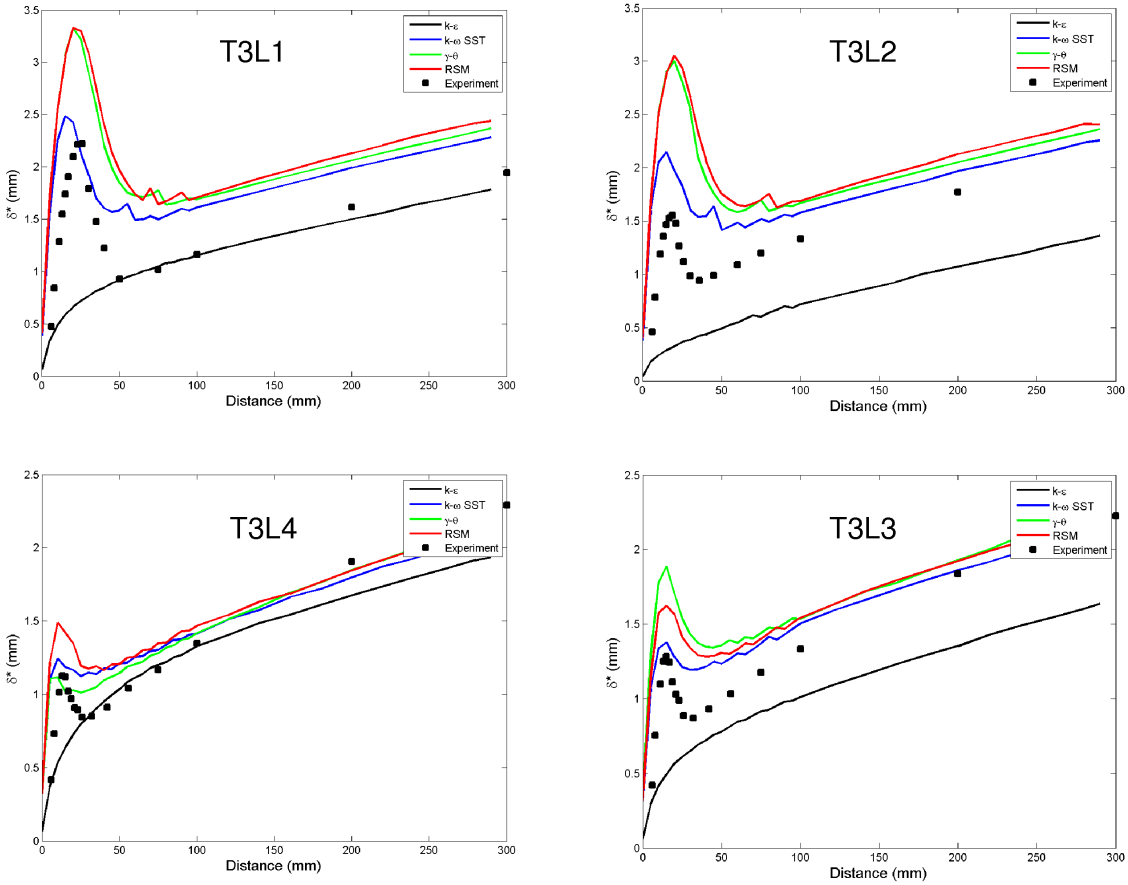

Figure 4.24: Displacement thickness for T3L1234 cases, increasing Tu in clockwise direction starting from top left, constant inlet velocity.

all, it is difficult to see an emerging pattern of behaviour of the models with increasing freestream turbulence for the test cases, apart from the superior performance of the ω based models compared to the k-ϵ model.

The results of local skin friction and momentum thickness for increasing velocity at constant freestream turbulence are shown in Figures 4.28 and 4.29. As with the previous set of results for increasing freestream turbulence, there

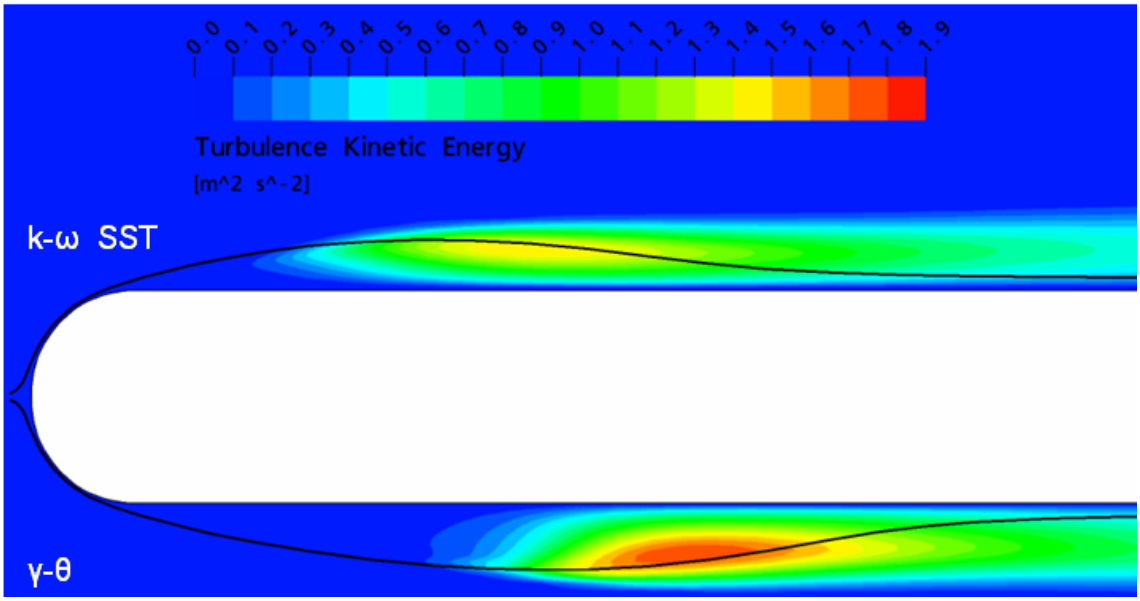

Figure 4.25: Comparison of turbulent kinetic energy in the separation bubble for the T3L1 case. Top - k-ω SST, bottom - $\gamma - \theta$

is no relative pattern to the results, apart from that the models successfully predict a shortening of the separation bubble with increasing velocity. Again, the k-ω SST model constantly predicts a shorter bubble then experiment and its behaviour is more predictable than the other ω based models. The $\gamma - \theta$ model exhibits a larger turbulent kinetic energy and increased reverse flow velocity as compared to the other models. All models tend to return a more accurate prediction of momentum thickness at the higher velocities (Figure 4.29, T3L3 & T3L6).

Although all models show a reduction in the size of the displacement thickness in line with the trend shown by experimental results (not shown), their relative accuracy does not improve, and the models still predict the displace-

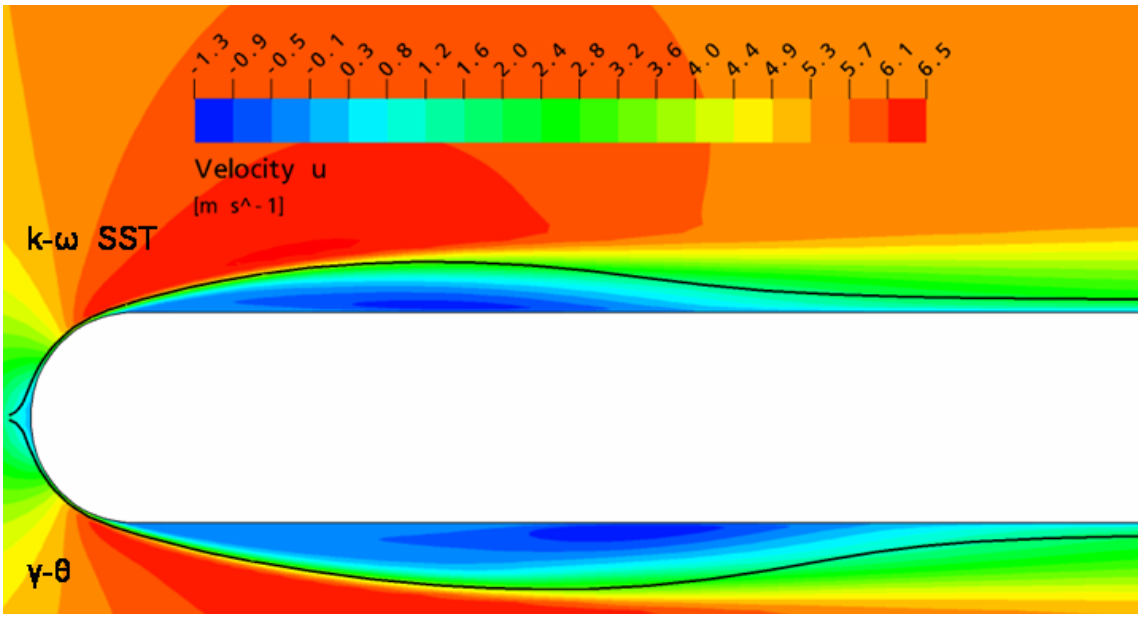

Figure 4.26: Comparison of velocity in the separation bubble in the T3L1 case. Top - k-ω SST, bottom - $\gamma - \theta$

ment thickness to up to twice the height of the experimental data. Although not in all cases, this discrepancy can translate into increased momentum thickness along the length of the plate, hence an overestimate in loss. Overall, the simulations compared well with others such as Borello et al. (2005). Displacement and momentum thickness were similar, however, only the T3C1 case was presented in their results.

Section Closure

The ERCOFTAC T3 series has shown through a series of transitional test cases where it may be necessary to predict transition. For cases where transition is close to the leading edge (T3B, T3L), a fully turbulent model may be used, as the boundary layer development will not have significantly devi-

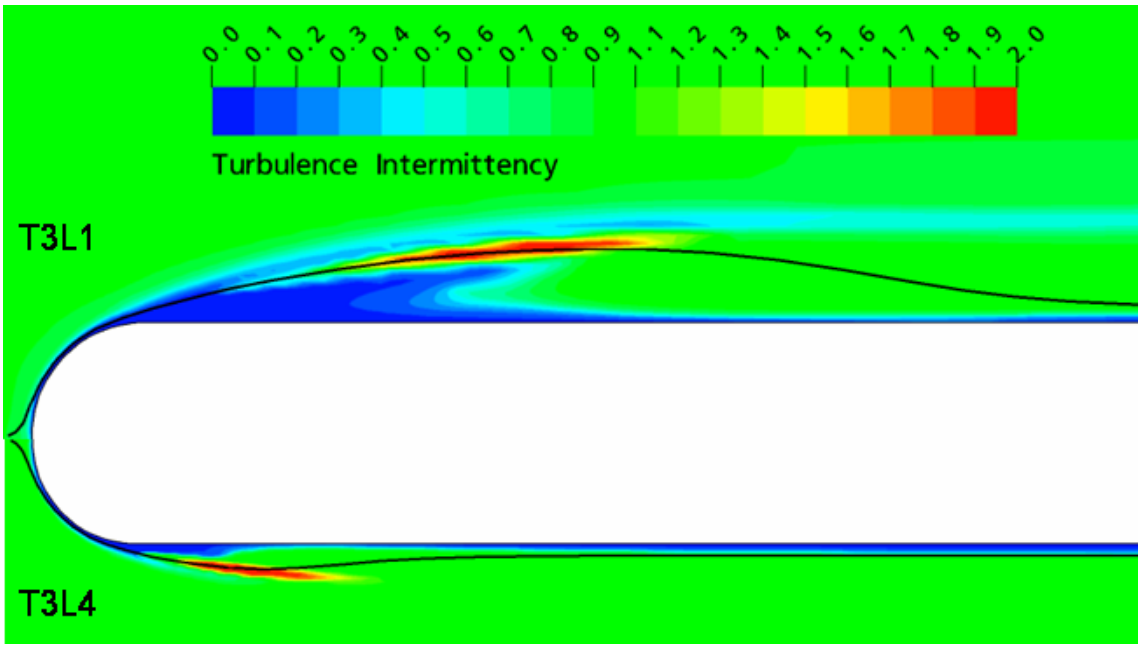

Figure 4.27: Comparison of turbulent intermittency in the separation bubble for the $\gamma - \theta$ model. Top - T3L1, bottom - T3L4

ated from a fully turbulent boundary layer. For other cases where transition occurs a significant distance from the leading edge, a transition model is required to present more accurate estimates of boundary layer development and loss.

The k-ϵ model has shown, that it can be used if transition is at or near the leading edge, or if the separation bubble at the leading edge is short. The T3L346 cases showed that non-prediction of the short separation bubble did not adversely affect the boundary layer prediction to a great degree. The k-ω SST model provided the most predictable performance over the range of test cases, especially the T3L series. Using the RSM model did not appear to give superior results, especially for the adverse pressure gradient and

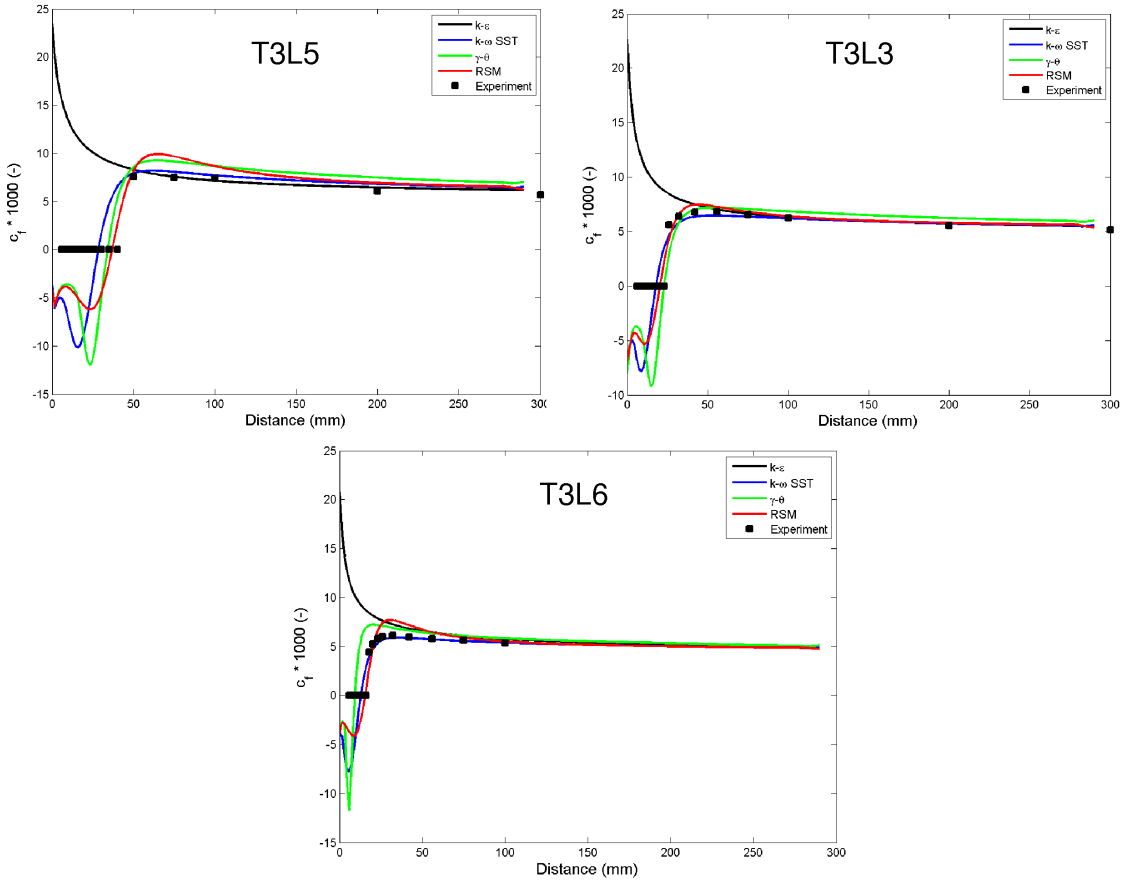

Figure 4.28: Local skin friction for T3L356 cases, increasing inlet velocity in clockwise direction starting from top left, constant Tu.

separated flows. Along with the $\gamma - \theta$ model, it is seems more sensitive to inlet conditions than the k-ϵ or k-ω SST models. The $\gamma - \theta$ model has the capability to provide very good comparisons in flows with medium freestream turbulence (≈2-4%) with either no or an adverse pressure gradient. On the whole, it did not provide as good a comparison with experimental results for low or high freestream turbulence, or favourable pressure gradients. It gave a variable performance when predicting the separation bubbles in the

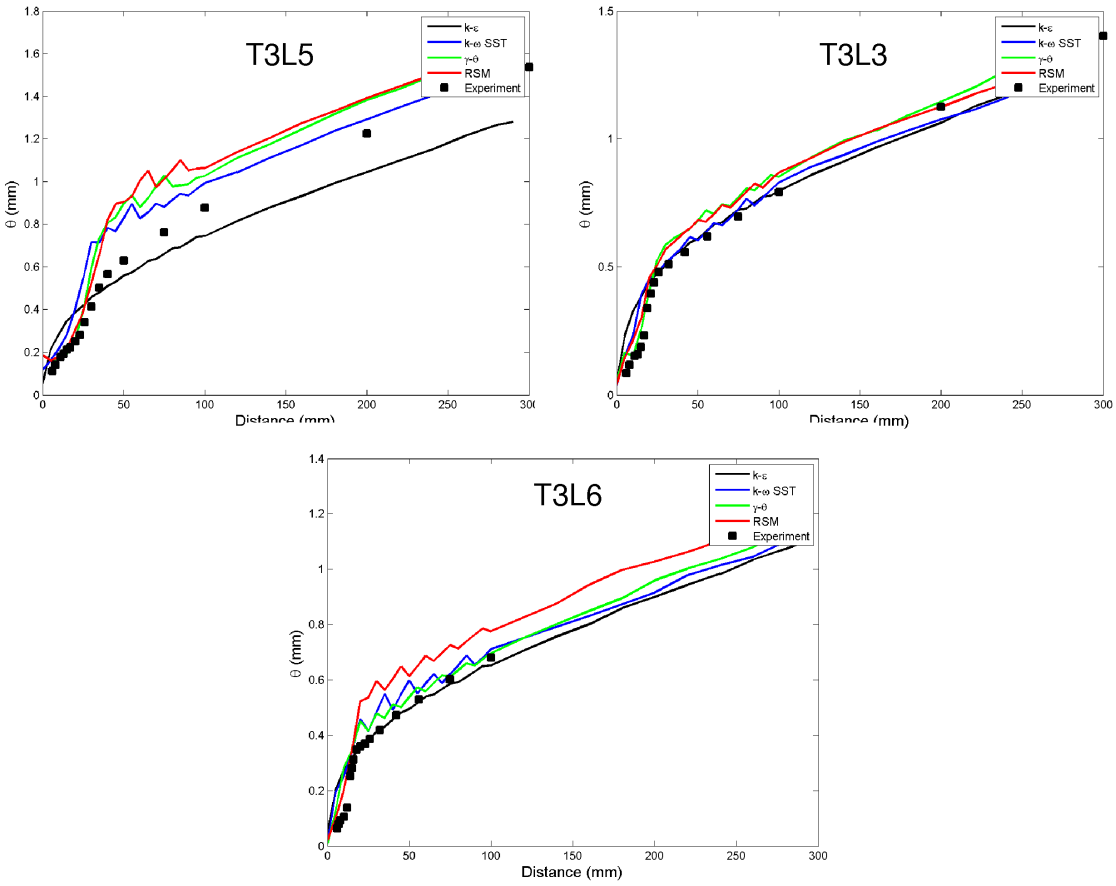

Figure 4.29: Momentum thickness for T3L356 cases, increasing inlet velocity in clockwise direction starting from top left, constant Tu.

T3L series. As the model does not always return consistent a transition start point or length, relative to the experimental data, as shown here, it is not recommended to be used if there is no transition data available *a priori*.

4.5 Transitional Flat Plate Subject to Shear Flow

A group of test cases from Aristotle University of Thessaloniki, similar to the ERCOFTAC T3L4 test case, were developed to understand the effects of anisotropic freestream turbulence and shear flow on the transition process of a separation bubble on a flat plate. Uniform and positive shear flow are reported in Palikaras et al. (2002), whilst the negative shear flow is reported in Palikaras et al. (2003). The test cases share the same geometry as the ERCOFTAC T3L series cases. A schematic of the set-up is shown in Figure 4.30. Inlet conditions consist of a freestream turbulence of 7%, and a velocity on the stagnation streamline of $5ms^{-1}$. The velocity profile for each case is summarised in Figure 4.31. Experimental and CFD results were obtained from the upper surface of the plate.

The grid consisted of 193 streamwise nodes along the surface of the plate, of which 370mm was modelled. The O-grid surrounding the plate had a maximum value of $y^+ = 0.55$, and consisted of 41 nodes orthogonal to the plate. The region from the inlet to the leading edge was also very densely meshed in an attempt to fully capture the effects of the shear in the freestream flow as shown in Figure 4.32. Total node count for the grid was approximately 260,000 with 3 nodes across the width of the plate. All of the ω based model simulations and mesh creation were undertaken by a summer exchange student, Antoine Fernbach (Fernbach, 2007). The k-ϵ simulations, results presentation and conclusions were conducted by the author.

Figure 4.33 shows the effect of shear at the inlet on the length of the separa-

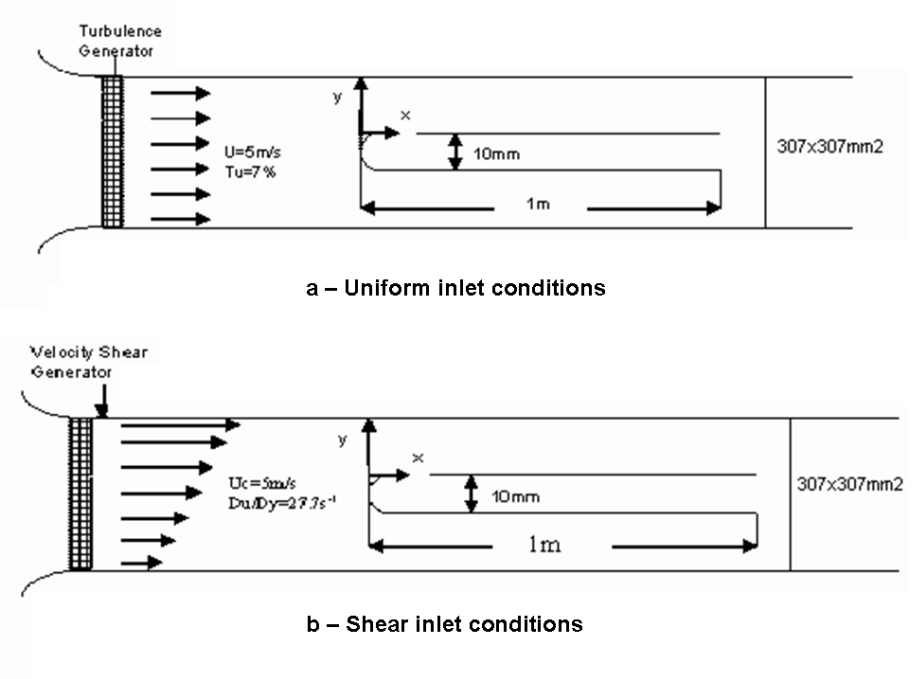

Figure 4.30: Schematic showing the experimental set-up for the University of Thessaloniki test cases

tion bubble for the ω based models. The length of the separation bubble is non-dimensionalised with the radius of the leading edge (R). The k-ϵ model is not shown as it again, similar to the T3L cases, predicted no separation. For uniform inlet velocity, all ω based models give a good prediction of the separation bubble. When shear was applied at the inlet, the models either under predicted (positive shear) or under predicted (negative shear) the length of the separation bubble by values up to 1.5 x/R. This correlates to values of up to 7.5mm. If compared to the T3L4 case, which consisted of a 5 ms^{-1} uniform inlet velocity and a freestream turbulence of 5.5 %, the results for the uniform and negative shear are comparable in terms of accuracy, but the positive shear results show a greater discrepancy. A comparison of error for each of the ω based models for both the uniform case and T3L4 case are

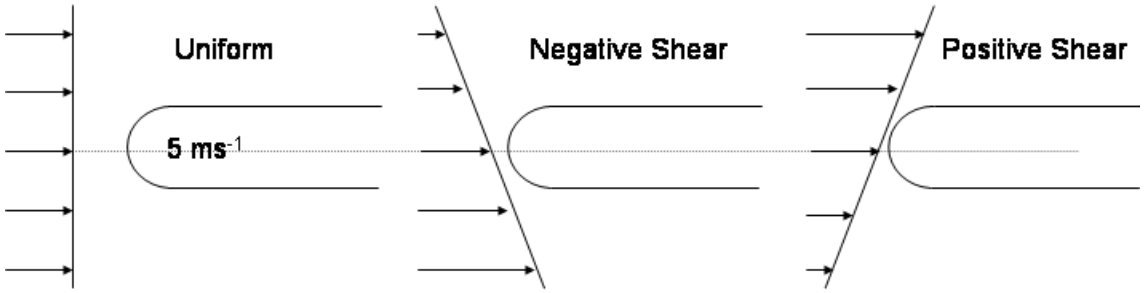

Figure 4.31: Summary of inlet velocity conditions for shear and uniform flat plate cases.

Model	Uniform	T3L4
k-ω SST	13%	40%
$\gamma - \theta$	9%	51%
RSM	13%	30%

Table 4.2: Estimation of percentage error of ω based turbulence models on the length of the separation bubble for current uniform and T3L4 test case

shown in Table 4.2. Compared to the original CFD results given in Palikaras et al. (2003), these results are poor. Their results showed a near perfect agreement for uniform and positive shear, and only a 5% error for the negative shear case. They used both a low-Re k-ϵ and a low-Re k-ϵ based RSM model. However, their simulations were only converged to residuals of 10^{-4}.

Figure 4.33 shows that the $\gamma - \theta$ model is the most sensitive model to velocity shear. Both the k-ω SST and RSM models gave an almost constant straight line relationship when comparing bubble length with shear. This shows that in particular, the RSM model has a predictable influence to shear

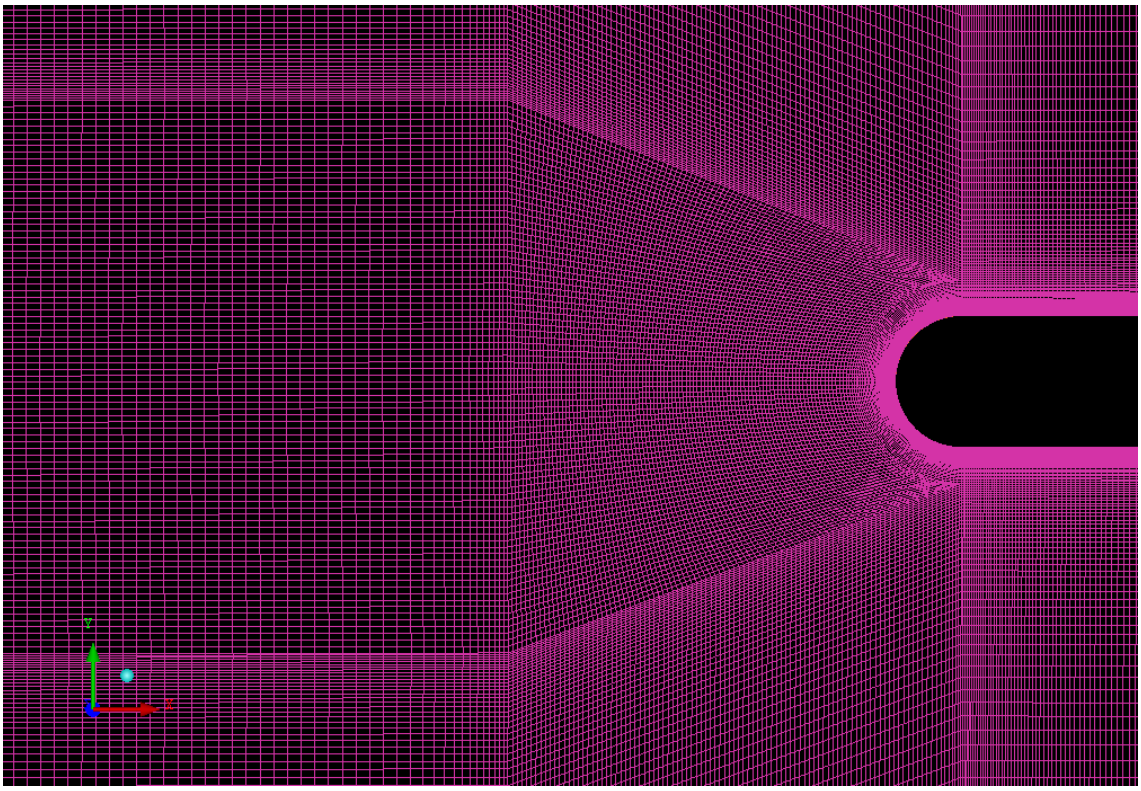

Figure 4.32: View of mesh used for transitional flat plate subject to shear flow.

and anisotropic turbulence for this particular case. This is good news as the RSM model was developed to account for such phenomena. Conversely to the results reported by Palikaras et al. (2003), the CFX RSM model proved to be the least accurate. They reported that the Wilcox k-ω model (Wilcox, 1998) gave the poorest agreement, with a thicker and longer separation bubble than the ϵ based models.

There is some uncertainty in the accuracy of the estimation of the length of the separation bubble. As Palikaras et al. (2003) used a single hot wire, they

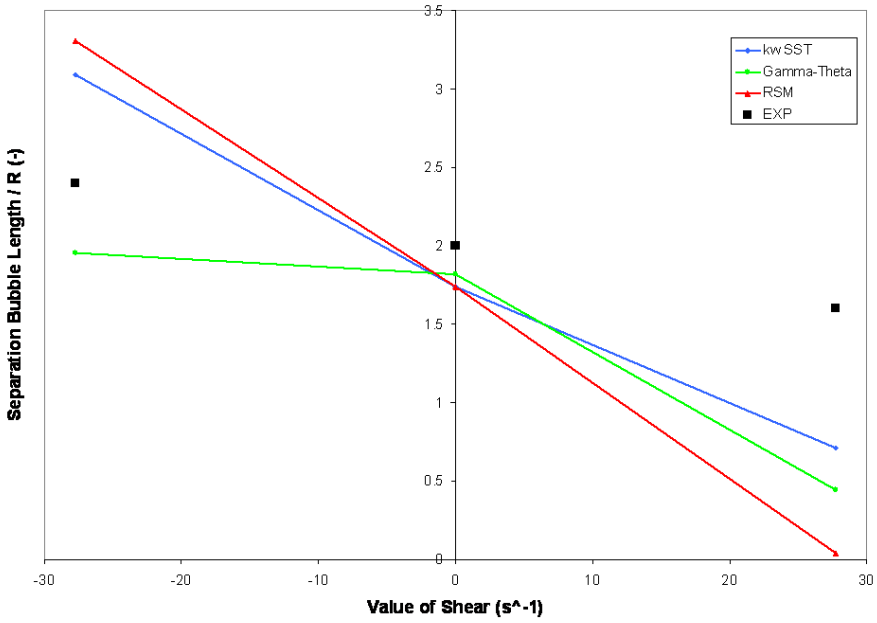

Figure 4.33: Length of separation bubble for both shear and uniform inlet conditions.

were unable to show the recirculation region of the separated boundary layer. The closest data point to the wall was at y = 0.3mm (y^+=5). To determine if the boundary layer was separated, a polynomial curve was introduced to create data points between the wall and y = 0.3mm for the velocity profile using the gradient of velocity between y = 0.3 & 0.4mm. They do not give the polynomial, the error occurring through using the polynomial, nor do they show which velocity profiles they have determined that show separated flow. Therefore, there remains some doubt over the trustworthiness of the results for separation length. However, the good agreement found between their CFD and experimental results would lead one to expect that no gross errors were included.

Their report showed that the greatest effect of shear on the length of the separation bubble was the movement of the stagnation region around the leading edge. Momentum losses and losses due to friction and curvature are greater for the negative shear, which lead to a larger recirculation region. A comparison for the RSM model is shown in Figure 4.34. The movement of the location of the stagnation point in Figure 4.34 is in agreement with the reported CFD results. The extent of the movement is greater, but is not the main factor in bubble length as the other models were found to have the same stagnation point location. Bubble length is primarily controlled by the stagnation location at the leading edge, then the model properties. The experimental longitudal Reynolds stress for all cases was shown to be approximately the same, indicating that it is not the variation of Reynolds stresses which causes the difference in length of separation bubble.

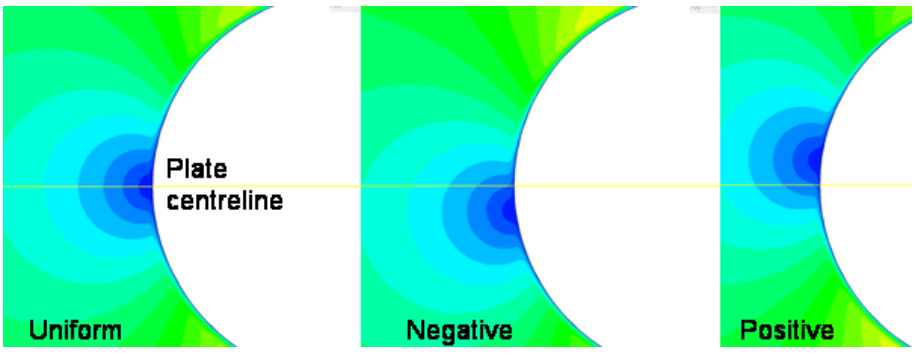

Figure 4.34: Comparison of position of the stagnation point with changing shear for RSM model.

The altering of the position of the stagnation point also explains the increased sensitivity exhibited by the $\gamma - \theta$ model shown in Figure 4.33. As

the shear changes from positive to uniform to negative, the thickness of the separation bubble increases. Figure 4.35 shows that for the positive shear and uniform inlet conditions, the bubble thickness is such that the transition is damped by the viscous effects at the wall. The bubble found in the positive shear case remains laminar, whilst for the uniform velocity case, transition occurs, as indicated by the arrowhead-like indentation of turbulent flow into the laminar flow at the streamline shown in the Figure 4.35. The separation bubble found in the negative shear case is much thicker than the other cases, and the model allows the intermittency to rise artificially above 1 to enable rapid transition, undamped by near-wall viscous effects. Transition occurs rapidly enough to be completed before reattachment. The laminar / fully turbulent separation bubble is much shorter than a fully laminar bubble under the same flow conditions. It is this factor which shortens the length of the separation bubble in negative shear conditions to a similar length to the bubble in the uniform velocity inlet case. As the other models used do not simulate transition, they are not affected by the stagnation location in this way. The inaccuracies in bubble length come from the model formulation and constants used.

Section Closure

All models exhibited a tendency to magnify the effects of shear on the flow and the subsequent location of the stagnation region. This manifested itself in the error of the size of the separation bubble. The RSM model surprisingly gave the poorest correlation of bubble size, even though it was developed for anisotropic flows. The $\gamma - \theta$ model was found to be sensitive to bubble height. If large enough, the distance of the shear layer from the wall may be sufficient enough to allow undamped rapid transition, reducing the length

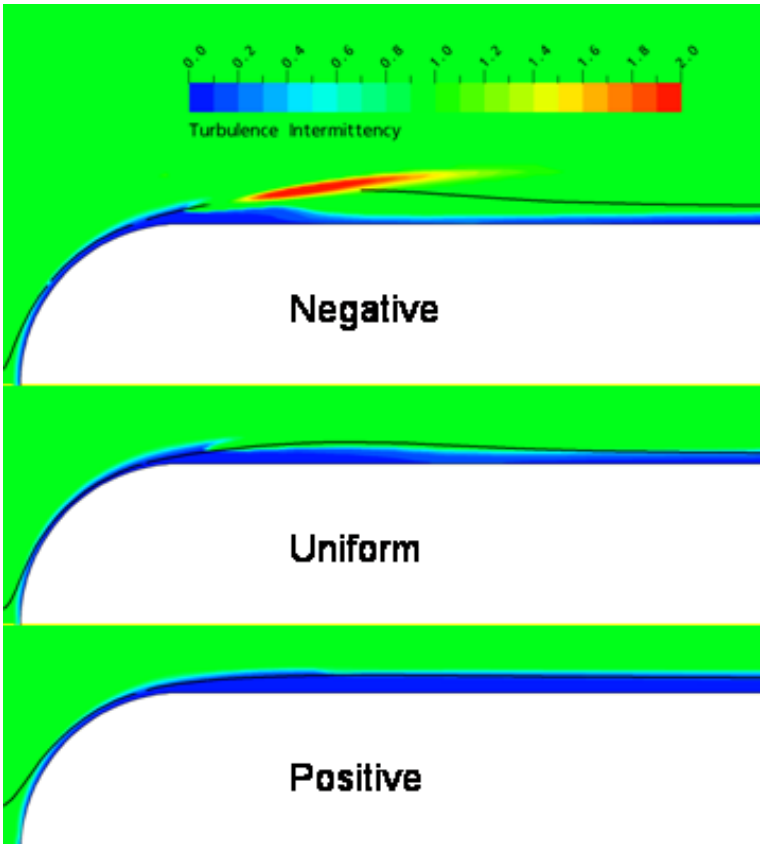

Figure 4.35: Comparison of turbulence intermittency in the separation bubble with changing shear for $\gamma - \theta$ model.

of the separation as compared to a damped transitional separation bubble of the same characteristics up to the start of transition. This may return unexpected or inaccurate results.

4.6 Zierke & Deutsch 2D Cascade

The Zierke & Deutsch 2D cascade as used by ERCOFTAC groups consists of highly loaded DCA blading. The schematic of the cascade facility used for the experiments is shown in Figure 4.36. Two incidence angles were simulated, 5° (Deutsch and Zierke, 1987) and -8.5° (Zierke and Deutsch, 1990). Re_c was approximately 5×10^5 for both incidences and experimental data confirmed a free stream turbulence intensity of 0.18%. Experimental data for pressure distribution around the blade, and wakes just past the trailing edge and further downstream are available for comparison. A quasi-2D single passage grid was used, having a maximum $y^+ = 0.8$. The total node count for the grid was ≈ 157,000, with 161 nodes chordwise along each blade surface, and 6 nodes in the spanwise direction. Nodes were more densely populated toward the leading edge to capture the effects of separation bubble on the suction surface (5° incidence) and on the pressure surface (-8.5° incidence) found at the leading edge. Inlet boundary conditions consisted of a velocity specification at set angle to give the experimental velocity and incidence angle. An average static pressure boundary condition was applied to the outlet according to experimental results.

Figure 4.37 shows the local pressure coefficient distribution, c_p, for the 5° incidence. All the models gave a good prediction of the pressure around the blade. The blade gives a mildly adverse pressure gradient up to approximately 60% chord, before experiencing a favourable then zero pressure gradient after 80% chord. The ω based models all show the separation bubble just after the leading edge on the suction surface, and the separated region starting at approximately 60% chord. This can also be demonstrated by observing the local skin friction coefficient in Figure 4.38. The lack of sep-

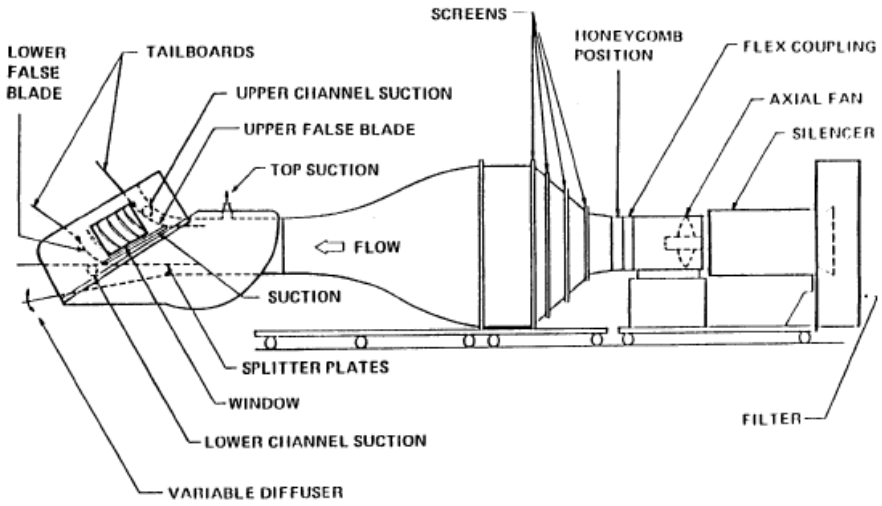

Figure 4.36: Schematic showing the experimental set-up for the Zierke and Deutsch test cases

aration in the form of a bubble, or terminal separation is clearly visible for the k-ϵ model.

The ω based models all predict a longer bubble length than experiment. The k-ω SST and $\gamma - \theta$ models return similar reattachment points of 3.9% and 3.4% chord respectively, whilst the RSM model, as with the T3L series, gives the latest reattachment point of 5.3% chord. This is over twice the size observed in experiment, however, this may be easily accounted for. The experimental radius of the semi-circular leading edge is $9.14\mu m$, whereas the computational geometry had a radius of 0.865mm as the geometry and meshing tool (ICEM) had difficulties creating surfaces around the leading edge as it was a much smaller feature in comparison to the main geometry size. The $\gamma - \theta$ model correctly showed that transition on the suction surface took place in the separation bubble.

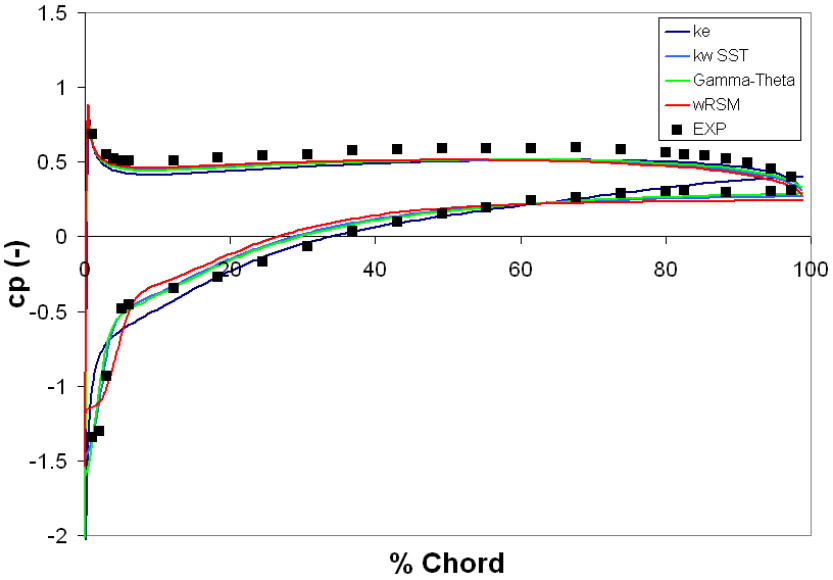

Figure 4.37: c_p distribution for i = 5°.

Separation on the suction surface was shown to be intermittent from 63.2% chord and terminal at 65.6% chord. The ω based models all give good comparative results of terminal separation points of 59%, 62% and 60% chord for the k-ω SST, $\gamma - \theta$ and RSM models respectively. Although not shown, as it does not give negative results for separated regions, the ω based models give the correct form and values for c_f along the suction surface. As with the T3L series, the $\gamma - \theta$ model gives the greatest negative value of c_f through the separation bubble, followed by the k-ω SST and RSM models. As can be seen in Figure 4.38, the RSM model shows the least amount of separation, but as will be shown later, this only means it has the lowest amount of backflow within its separated region. The RSM model has proved throughout this section to consistently predict the greatest amount of separation, but with the least amount of backflow. The prediction of not only the point of,

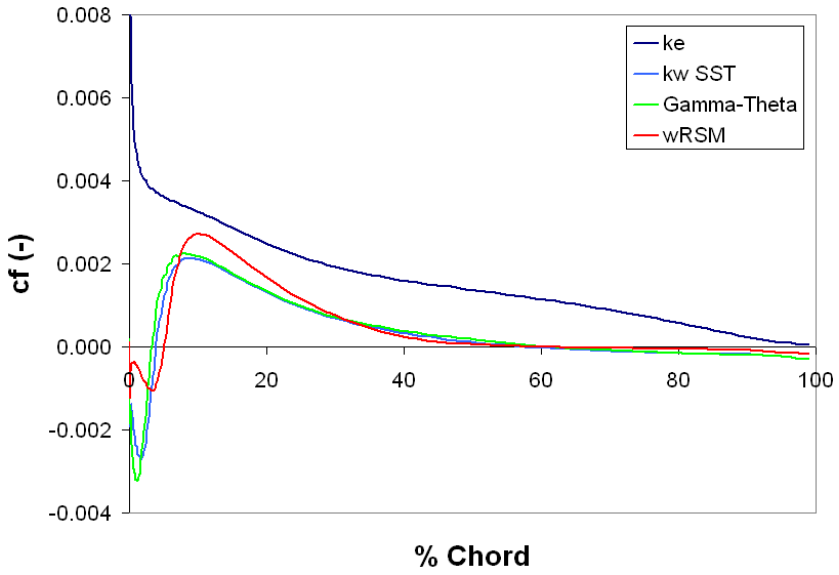

Figure 4.38: c_f distribution on the suction surface for i = 5°.

but also the amount of separation is important as it affects the size of the trailing wake as will be shown.

The $\gamma - \theta$ model predicts that transition on the pressure surface starts at approximately 42% chord and finishes at approximately 70% chord (Figure 4.39). This is too early in comparison to experimental data. Deutsch and Zierke (1988) show from velocity profiles that the transition region starts at approximately 64% chord and does not completely finish due to the acceleration of the flow past 80% chord. The $\gamma - \theta$ model shows that it finishes the transition process at approximately 70% chord, but then may start to relaminarise, characterised by a reduction of c_f compared to the k-ω SST model.

The prediction of the near wakes can be seen in Figures 4.40 and 4.41. The

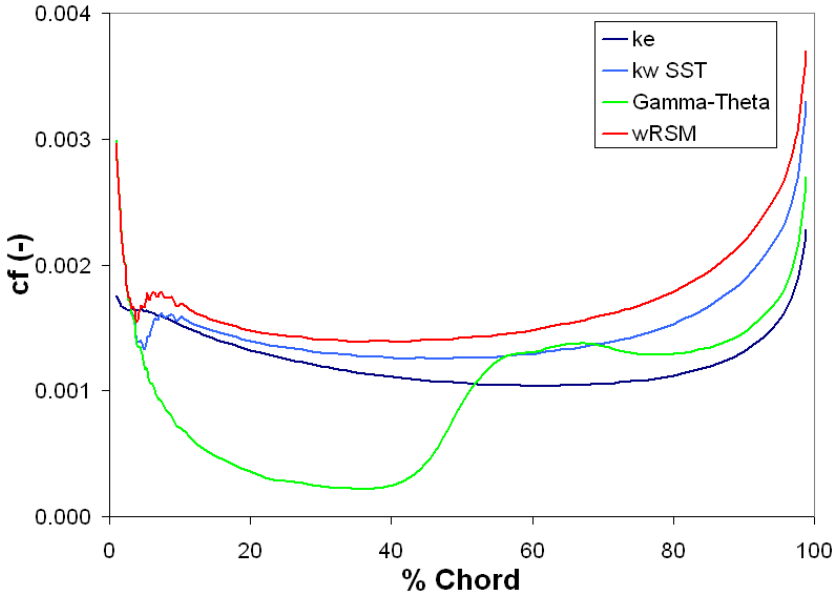

Figure 4.39: c_f distribution on the pressure surface for i = 5°.

distance y is the distance measured from the arc of a virtually extended pressure surface. The ω based models all give a good prediction of the wake width and velocity defect for the near wake at 105.4% chord, whereas the k-ϵ model does not fully predict the extent of loss within the wake, nor the wake width. The freestream velocity is also shown to be approximately 5ms^{-1} less for the ω based models than shown by experiment. For the wake further downstream at 152.6% chord, although the models show the same pattern in wake defect and width prediction, they have not given the correct deviation. The ω based models show a consistent pattern that the model which gives the least separation in terms of length and amount of, returns the higher freestream velocity. In the values of the wake at 105.4% chord, the effect of the amount of separation can clearly be seen to widen the defect region of the suction surface side (bottom side) of the wake. This is not so clear at

152.6% chord as the wake has had more time to mix with the freestream and decay.

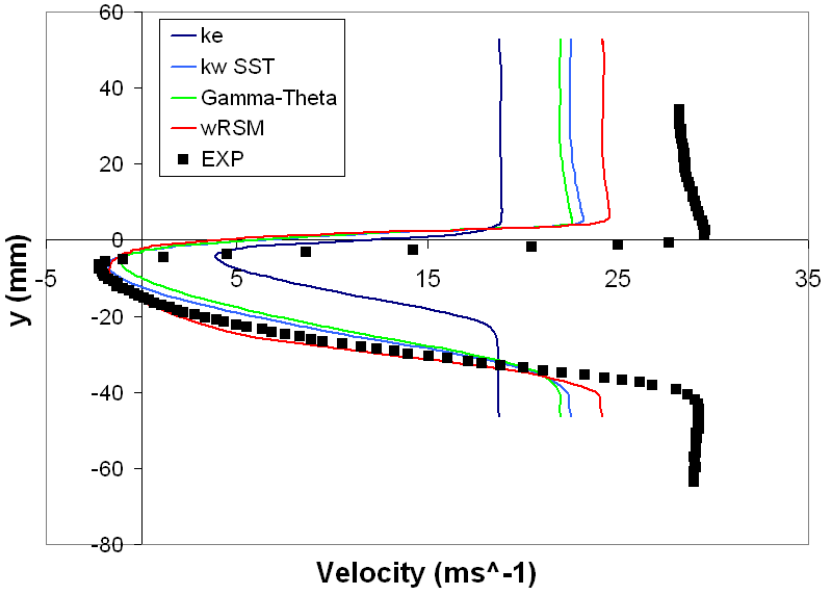

Figure 4.40: Trailing wake at 105.4% chord, i = 5°.

From Figures 4.40 and 4.41, it is difficult to appropriate a level of loss due to transition alone, because of the large region of separation on the suction surface. As transition occurs towards the leading edge within the separation bubble on the suction surface, the friction loss will be similar for both the k-ω SST and $\gamma - \theta$ models. On the pressure surface, friction loss is much lower than on the suction surface, because of the lower flow velocity. Any difference in loss due to transition occurring around mid-chord is likely to be small. Therefore, the difference in the resulting wakes for the k-ω SST and $\gamma - \theta$ models is likely to be due to the amount of separation on the suction surface experienced by each model.

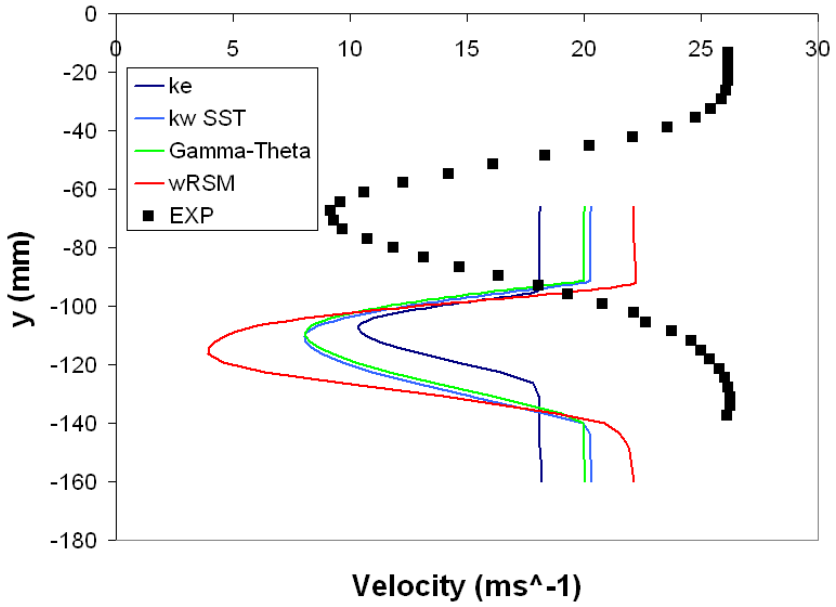

Figure 4.41: Trailing wake at 152.6% chord, i = 5°.

As with the 5° incidence, all of the models gave a favourable agreement for the pressure distribution around the blade for the -8.5° incidence, as observed in Figure 4.42. Again, whilst all of the ω based models predicted well the pressure surface separation bubble at the leading edge, the k-ϵ model did not. The same relationship between level of backflow, bubble length and turbulence model exists for this case. Zierke and Deutsch (1990) did not divulge the length of the bubble, but from data presented, it reattaches before 9.7% chord. At least it can be seen that the models have not over predicted the length of the bubble to a very large extent. All models seem to agree with experiment that the maximum blade loading is situated at approximately 21% chord.

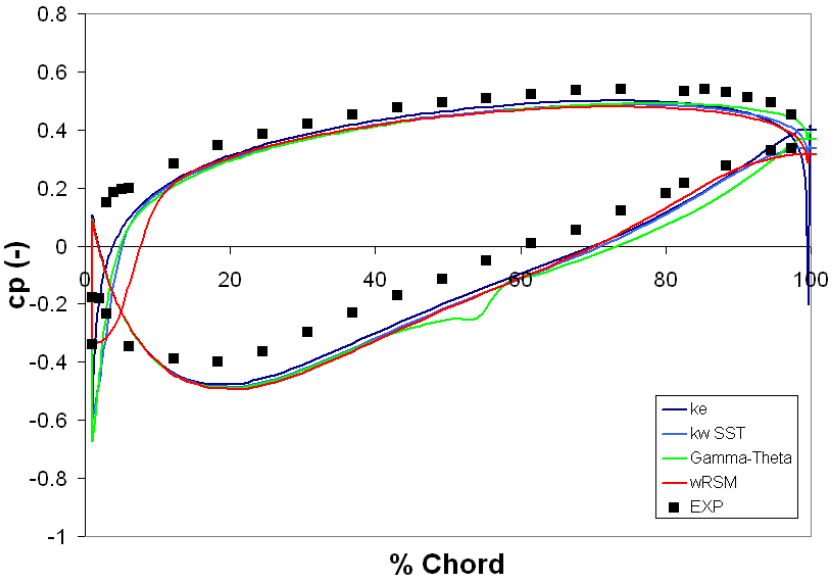

Figure 4.42: c_p distribution for i = -8.5°.

The experiments proved that transition on the pressure surface takes place within the separation bubble at the leading edge and just beyond, with full recovery into a turbulent boundary layer taking place before 9.7% chord. The $\gamma - \theta$ model showed transition to rapidly occur in a very short distance towards the start of the separation bubble, and returned a fully turbulent boundary layer upon reattachment.

The $\gamma - \theta$ model correctly shows the experimentally observed laminar / turbulent separation bubble at approximately mid-chord on the suction surface as shown in Figure 4.43. The experimental c_p distribution does not show the separation bubble, but both oil and chemical surface flow visualisation tests showed the bubble to start at 35%, begin to undergo transition at 56% and reattach at 60% chord. The transition process was deemed to be complete

at 70.6% chord. As the other models all predict turbulent boundary layers throughout, they were unable to show the separation bubble, as it would only occur for a laminar boundary layer. The $\gamma - \theta$ model predicted separation at 42%, transition starting at 52.7%, and reattachment at 57.6%. The sudden spike of negative c_f in Figure 4.43 is the point at which the transition process starts. Although the $\gamma - \theta$ model gave a favourable comparison to experiment for both length and placement on the suction surface, it may have been more accurate if there were a greater density of streamwise grid nodes in this region. There were 12 streamwise nodes along the length of the bubble. Transition occurred abruptly, but not totally point like, as it seems that transition was fully completed around 77% chord, however the main transition process occurred within the bubble itself at the point where the turbulence generation was invoked. This initial process may have taken place over a slightly longer region if more streamwise grid nodes were present. This may also explain why the $\gamma - \theta$ model would only converge to 10^{-5} rather than 10^{-6} for the turbulent models.

The prediction of the laminar / turbulent separation bubble by the $\gamma - \theta$ model alters the behaviour of the flow somewhat toward the trailing edge. Separation was experimentally identified to occur at 97.6% chord on the suction surface. Both the k-ω SST and RSM model predict separation to occur at 95.7% and 94% chord respectively. As the $\gamma - \theta$ model's turbulent boundary layer contains new turbulence, it is able to resist the tendency to detach from the surface, whereas the old turbulence in the k-ω SST and RSM models boundary layers is not able to prevent separation. Evidently, the $\gamma - \theta$ either under predicted the loss on the boundary layer, or over predicted the turbulence production (as may be shown from a greater value of c_f in Figure 4.43).

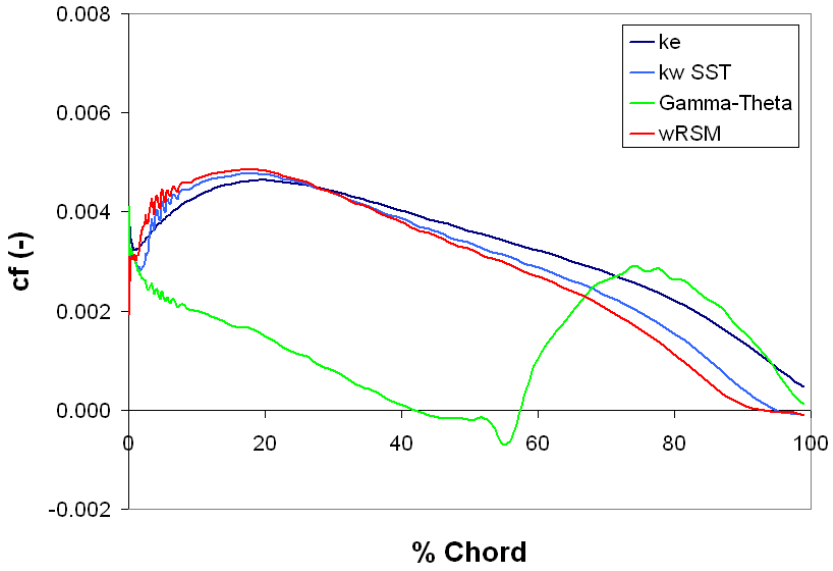

Figure 4.43: c_f distribution on the suction surface for i = -8.5°.

A similar scenario of wake prediction exists for both i = 5° and i = -8.5°, where little change from experimental deviation exists for the near wake (106% chord), but difference in deviation increases for the far wake (131.9% chord). Both experimental and computational showed near symmetric wakes as there is very little separation (Figure 4.44), although the RSM model shows a small additional loss region in the pressure surface side (top side in Figure 4.44) of the wake. It is unclear why this may occur. It is mixed out at 131.9% chord.

The effects of transition on the trailing edge is evident from Figure 4.44. Here one can observe the difference between the k-ω SST and $\gamma - \theta$ models. As transition occurs at approximately mid-chord and there is no appreciable separation on either surface, any difference in the wake is due to the state

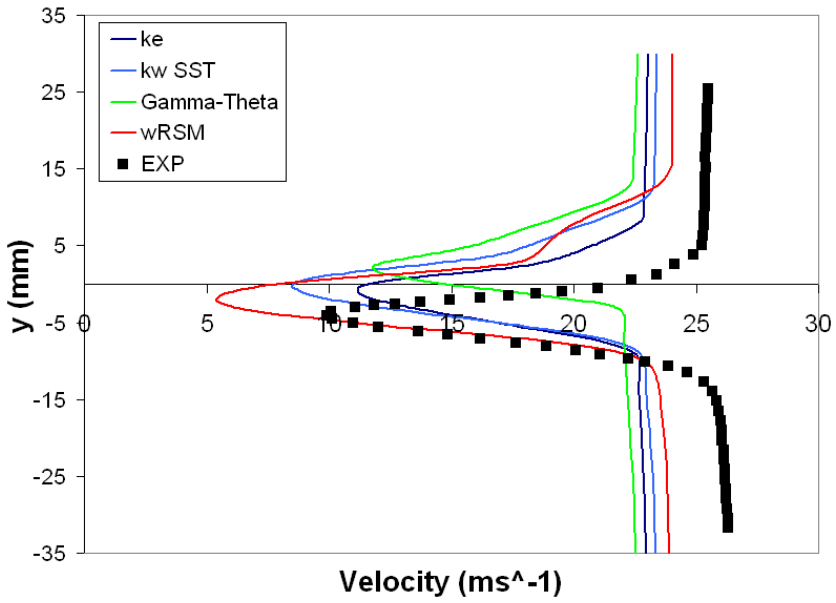

Figure 4.44: Trailing wake at 106% chord, i = -8.5°.

of the boundary layer at the trailing edge. A closer observation of the c_p distribution at the trailing edge (Figure 4.42) and the c_f distribution on the suction surface towards the trailing edge (Figure 4.43) shows k-ω SST model to have a greater amount of separation than the $\gamma - \theta$ model. This is due to the $\gamma - \theta$ model having a greater amount of turbulent kinetic energy in the boundary layer as turbulence occurs at mid-chord, meaning that loss will be lower in the front portion of the surface, and that fresh turbulence further downstream will enable the boundary layer to resist separation for a greater surface distance. Hence the velocity deficit in the $\gamma - \theta$ model's wake is smaller, and the wake is not as wide.

Section Closure

These cases have shown that the k-ϵ model is not suitable for use where sepa-

ration prediction is required. The prediction of wake loss is highly dependent upon separation prediction. The ω based models gave a good prediction of separation at both the leading and trailing edges, even though the bubble length at the leading edge was greater than experimental values. As discussed, this is probably due to the larger leading edge radius enforced by the meshing limitations of ICEM. The $\gamma - \theta$ model provided good agreement of transition location and to a lesser degree, transition length for both separated and attached transition, especially as the automatic features of the model were used, rather than specifying them as with the T3 series test cases. The grid density used may affect the start point and length of the simulated transition process, so it is important for the user to understand where this occurs *a priori* and refine the grid accordingly.

4.7 Chapter Closure

This chapter has shown that the k-ω SST model is the model of choice for most flow types. It gave a fairly consistent performance for predicting separation, both bubble and terminal, and performed admirably at predicting the development of the turbulent boundary layer. The k-ϵ model offered in the CFX code should not be used for flows which include separation or large adverse pressure gradients. It may be used for flows with a small transitional separation bubble at the leading edge only as the subsequent development of the turbulent boundary layer does not deviate sufficiently from the fully attached turbulent boundary layer. If this feature is unknown beforehand, then the k-ω SST model should be used.

The $\gamma - \theta$ performed reasonably well over the range of test cases, and can be of benefit if transition occurs at an appreciable distance downstream of the leading edge. If transition occurs at or near the leading edge, in either attached or separated flow, then the overall characteristics of the flow and boundary layer can be suitable simulated using a turbulent model, rather than a transition model. Therefore, when conducting a compressor analysis, it may not be beneficial to model any stages from the middle of the intermediate compressor onwards, as transition is thought to occur close to the leading edge. If transition occurs downstream of the leading edge, then the work in this chapter has shown that transition prediction can provide the user with an increased understanding and accuracy of the development of the boundary layer and subsequent loss prediction. It has been shown that using the $\gamma - \theta$ model can give a more accurate value of loss in a compressor. Menter et al. (2005) simulated the RGW cascade of Shultz and Gallus (1988), using the $\gamma - \theta$ model, and predicted the loss coefficient to be 0.11, as compared to 0.19 using the k-ω SST model, and the experimental value of 0.097. However, to use the $\gamma - \theta$ model responsibly, one must have an understanding of the flow conditions and development of the boundary layer *a priori* to fine tune the initial conditions to achieve appropriate results. It appears that it would be most appropriate to use it on low to intermediate pressure compressor stators, as transition is likely not to take place at the leading edge, and boundary layer data is more likely to be available for the stators, rather than rotors.

Overall, the RSM, whilst having the capability to, did not perform as well as either the k-ω SST or the $\gamma - \theta$ models. It consistently predicted larger regions of separation and overestimated the resultant loss. It was the most

inaccurate model at predicting the effects of anisotropic flow in the form of a shear inlet. It is not recommended to be used for more standard compressor CFD applications. It may offer superior performance for 3D wake wake interaction, but this is beyond the remit of this thesis. All of the models gave appreciable discrepancies of the velocity profiles in their prediction of separation. This is the main problem as to why they cannot consistently correctly predict the length of a separation bubble or the point of terminal separation toward the trailing edge.

In general, one of the main difficulties was the inlet specifications required for flows experiencing changing pressure gradients (i.e. T3C series). In particular, it is unclear what value of freestream turbulence and length scale to specify at the inlet. The $\gamma - \theta$ model was the model primarily sensitive to changes in the inlet conditions. The T3C cases and Zierke & Deutsch cases showed that the model gave a better prediction of the transition region when it occurred in adverse pressure gradient conditions. In fact, it was encouraging to see the model perform well in the cascade cases using the automatically prescribed inlet conditions for length scale and viscosity ratio.

Chapter 5

Transition in Axial Compressors

As shown in Chapter 4, one of the least well predicted aspects of compressor flow modelling is the modelling of the transition region. The theory of flow transitioning from laminar to turbulent flow was first described by O. Reynolds in the 1880s. It took approximately 100 years before this phenomena could begin to be computed, with credible models starting to be proposed in the 1980s. Theoretical and experimental work started in earnest in the 1950s with work being carried out by people such as Maekawa and Atsumi (1952), Schubauer and Klebanoff (1956) and Narasimha (1957). The importance of the prediction of the transition process has come more to the fore since the introduction of controlled diffusion blades (CDA) which assume transition starts at a prescribed point on the suction surface, and afterwards, turbulent flow theory can be used to predict its performance. Additionally, as compressor efficiency increases and loss is reduced, engineers need to look for non-traditional ways to increase performance. Transition, whilst not having a large effect on efficiency can play an important role.

For a long time, the transition region of the boundary layer was underestimated in its importance, being considered as a sudden event (Singh, 1974). Abu-Ghannam and Shaw (1980) argued that the transition region can be lengthy, relative to the size of the body under consideration and should not be ignored. Indeed Walker (1989) showed the transition region can extend to approximately 10% - 20% of the chord length. Studies by Abu-Ghannam and Shaw (1980), Mayle (1991) and Roberts and Yaras (2005a) etc, show the transition region to depend on factors such as surface roughness, pressure gradients, freestream turbulence, Reynolds number and flow history. Lee and Kang (2000) argue that freestream turbulence and pressure gradient have the greatest effect on boundary layer transition. This is reflected by others such as Abu-Ghannam and Shaw (1980) and Mayle (1991) who include these parameters as primary variables in their correlations (see Section 3.4.3). More recent studies such as Wheeler et al. (2007b) have shown for compressors that the leading edge geometry plays an important role in the effect of transition upon the suction surface.

Literature suggests transition occurs through 4 main modes, which are dependent upon freestream conditions, as shown by Mayle (1991), (Figure 5.1). They are;

1. Natural (low freestream turbulence)
2. Bypass (high freestream turbulence)
3. Separated flow
4. Reverse

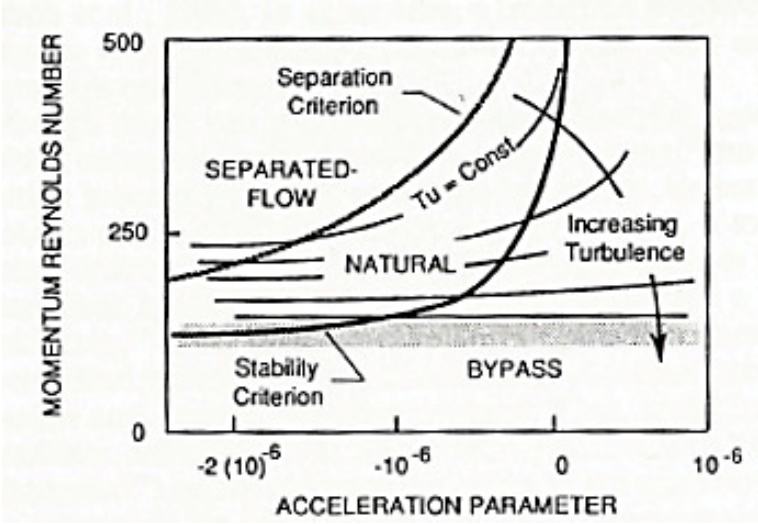

Figure 5.1: Modes of transition according to freestream conditions. Taken from Mayle (1991)

Transitional flow on a typical compressor is shown in Figure 5.2. On the suction surface, small laminar separation bubbles may be formed near the leading edge due to the large variations in pressure distribution and a possible lack of smoothness in the blade profile due to the manufacturing process. As the flow accelerates then decelerates around the leading edge, both boundary layer shape factor and momentum thickness increase and the boundary layer becomes receptive to both Tollmein-Schlicting waves and streaky structures which later form turbulent spots and transition. Henderson et al. (2006) found these instabilities to convect along the boundary layer between 0.5-0.7U_∞. Transition occurs due to this combination of Tollmein-Schlicting waves and streaky structures, normally beginning near the point of minimum pressure and continuing into the adverse pressure region. The leading edge is the principle receptivity site for the transition process on the suction surface (Henderson et al. (2006), Wheeler et al. (2007a)). A good blade design will

ensure that transition is completed before the boundary layer experiences a strong adverse pressure gradient towards the trailing edge. Most transition in axial compressors takes place in the bypass mode (Mayle, 1991), although Solomon et al. (1999) have shown there is a degree of overlap between natural and bypass modes. Generally, bypass or separation transition will occur depending upon the critical acceleration parameter, K_{crit}, and the level of freestream turbulence (see Figure 5.1). However, for some low speed axial fans, natural transition may take place instead.

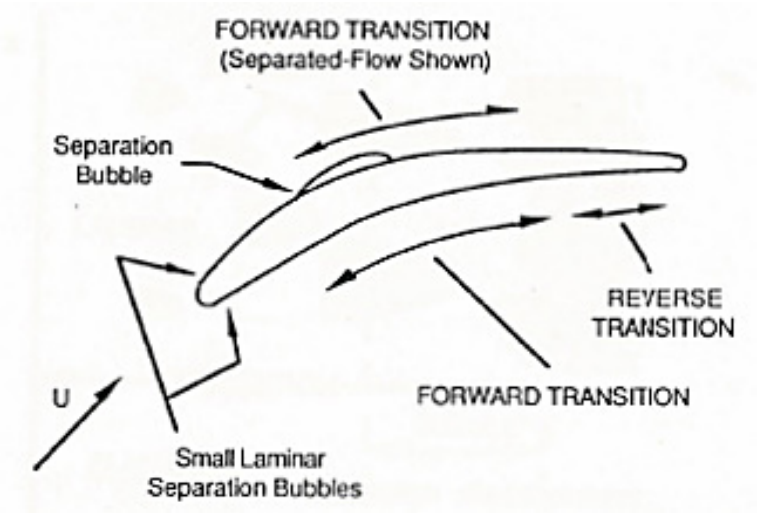

Figure 5.2: Transition on a typical blade at design conditions. Taken from Mayle (1991)

On the pressure surface, transition begins before the point of maximum pressure. Toward the trailing edge, the flow stretches and accelerates, removing the root causes of transition. Since there is no fresh turbulence production, the flow may once again become laminar. This process is known as reverse transition.

Separated flow transition is the least known (Lou and Hourmouziadis, 2000), although studies such as Howell (1999) have shed some light on the process in turbomachinery conditions. In turbomachinery flows, wake-induced and shock induced transition can occur (Mayle, 1991). Wake-induced transition is traditionally classed as bypass transition, but studies such as Henderson et al. (2006) have shown it to be of both natural and bypass for a compressor, depending upon which surface is being considered. Shock induced transition will not be considered in this work, as this research deals with subsonic axial compressors only. Halstead et al. (1997a) and Iseler et al. (2006) showed that several modes of transition can take place on the same aerofoil at the same location at different times due to changing freestream conditions. Thus it is essential to understand how the different modes of transition occur. These are covered in this chapter as well as how the mechanics of transition are affected by the freestream conditions and machine geometry.

5.1 Natural

Schubauer and Klebanoff (1956) were some of the first to report on the phenomena of natural transition. It is called natural as it is thought that the process is instigated from instabilities produced only in and by the laminar boundary layer. The process of natural transition is schematically shown in Figure 5.3a. Linear instabilities in the laminar boundary layer amplify and develop into non-linear, Tollmein-Schlicting (TS) waves (I), which typically travel at a speed of 0.3 - 0.35 U_∞. The TS waves develop into periodic concentrations of spanwise 3D Λ-shaped structures (II) which further develop into

regular non-linear streamwise vortical structures or loops (III). These loops were found by Diorio et al. (2007) to produce turbulent kinetic energy at their peripheries and dissipate energy in their cores. The vortical structures cause the formation of strong shear layers (IV). At the head of the loops or streamwise vortical structures, turbulent spots burst forth (V) and develop by merging into one another (VI), forming fully turbulent flow. After each turbulent spot comes a region of calm during which transition will not occur, as it prohibits a fresh breakdown behind it. As turbulence always convects downstream, it can only maintain itself by fresh breakdowns in the following upstream laminar flow. Schubauer and Klebanoff (1956) found that the transition point could not be made stationary. According to Mayle (1991), natural transition is thought to occur at Reynolds numbers $Re_{xt_s} \cong 350,000$ and freestream $Tu < 1\%$.

Surface roughness plays a role in transition. At high Reynolds numbers ($Re > 500,000$), the boundary layer becomes very sensitive to instabilities. Interaction of roughness induced instabilities inside the boundary layer with disturbances of sufficient strength already present initiate breakdowns in the laminar boundary layer. The breakdown is point like rather than simultaneous along a line, creating a wedge which includes intermittent and fully turbulent flow (Figure 5.4).

The length of transitional flow is governed by the turbulent spot inception rate. Emmons (1951) first proposed how turbulent spots develop and grow (Figure 5.5a). He proposed that turbulent spots formed randomly in both space and time during the laminar boundary layer to eventually form a transition region. Narasimha (1957) later modified this to say that the turbulent

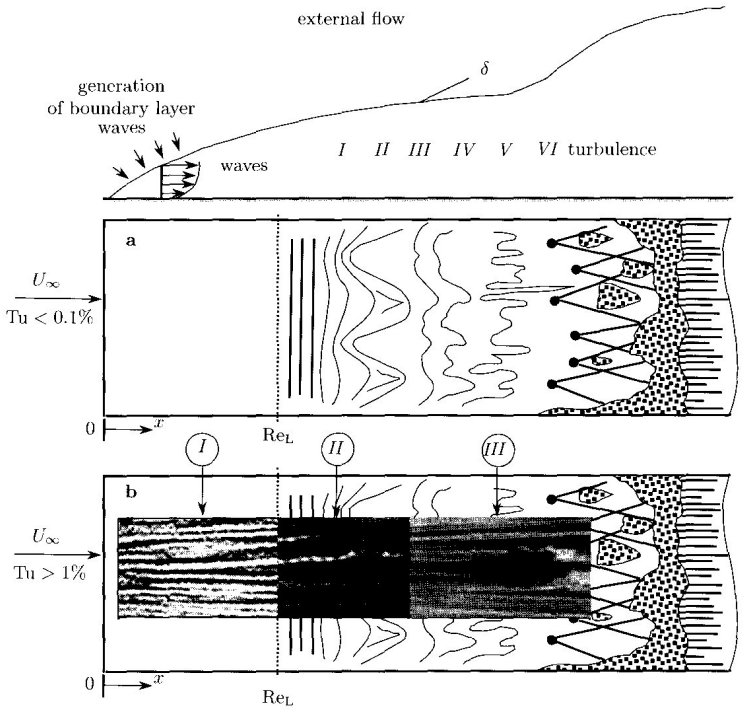

Figure 5.3: a - Natural and b - bypass transition process. Taken from Boiko et al. (2002)

spots form randomly in time and cross stream position at a preferred streamwise location (Figure 5.5b), rather than at intermittent distributions. Spot propagation is linked to variations in the stability of the laminar boundary layer, and variations occuring in the spreading angle of the spots (wedge) and the longitudinal length of propagation. Solomon et al. (1996) found that spot propagation characteristics varied significantly from predicted values for an adverse pressure gradient ($\lambda_\theta < 0$), dispelling the previous theory by Chen and Thyson (1971) and Mayle (1992), that they should not vary significantly with pressure gradient within the transition zone.

Natural transition is not normally found to be the main transition process

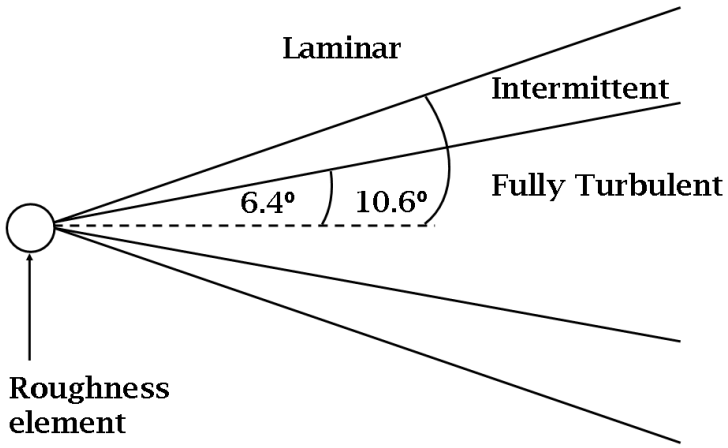

Figure 5.4: Turbulence wedge produced by surface roughness

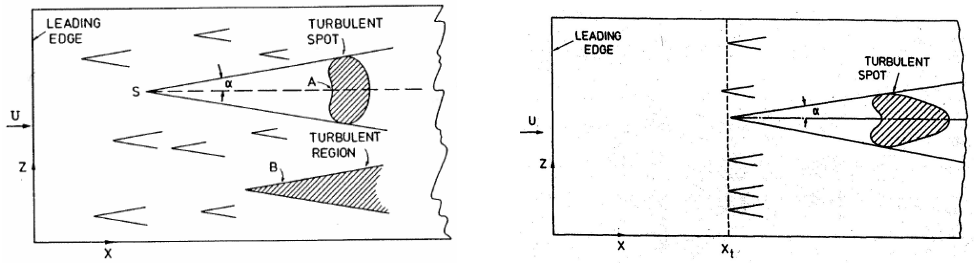

Figure 5.5: a - Emmons turbulent spot, b - Narsimha turbulent spot

on compressor blading due to the high turbulence (Tu typically $> 3\%$) and higher Reynolds numbers. Bypass transition is the generally accepted most common mode of transition, and will be the focus of this part of the literature review.

5.2 Bypass

Natural and bypass transition, have similar underlying processes. Bypass transition is primarily induced from forced disturbances of sufficient amplitude outside the boundary layer. These forced disturbances can come from freestream turbulence and surface roughness. Stages I to III of natural transition (Figure 5.3a) are bypassed (Schreiber and Steinert, 2002). Transition occurs through freestream localised vortical disturbances developing into streaks (I)(Figure 5.3b). These streaky structures contain high and low streamwise velocities, which modulate in the boundary layer in a spanwise direction. Streak generation develops into streamwise waviness and is accompanied by the generation of high frequency wave packets and incipient turbulent spots due to different non-linear mechanisms including the interaction with TS waves and secondary instabilities (II). Turbulent spots develop and merge into one another (III), forming fully turbulent flow.

Bypass transition occurs in a shorter distance than natural transition as stages I-III are bypassed, shortening the length of the unstable laminar flow. The process does not follow bypass transition *per se*, according to Hughes and Walker (2001), but has interaction with effects found in natural transition such as TS waves. They discovered that instabilities were found in wake-induced bypass transition regions on a 1.5 stage compressor. However, at high freestream turbulence levels or unsteadiness, Cumpsty (1989) notes that transition by amplification of TS waves in the attached boundary layer can be ignored. This was confirmed by Hughes and Walker (2001) in their study of a low speed axial compressor at low Re (Re $\approx 1.17 \times 10^5$). They discovered that instabilities do not always occur prior to transition when the loading is low ($V_a/U_{mb} = 0.84$) and separation bubbles form close to the

leading edge (pressure surface), or when loading was high ($V_a/U_{mb} = 0.6$) and wake induced transition starts very close to the leading edge (suction surface).

The propagation of turbulent spots is much greater in a bypass transition region than in a natural transition region. Halstead et al. (1997a) showed that turbulent spots are triangular in shape and spread laterally at an angle of about 22 degrees, and have convection velocities of the leading and trailing edges of $0.88U_\infty$ and $0.5U_\infty$ respectively, as shown in Figure 5.6.

As shown in Figure 5.6c, after the turbulent spot has passed, a region of laminar-like flow occurs. It still has an elevated wall shear stress, compared to laminar flow, and suppresses new turbulent breakdowns due to the spot trailing edge having a higher propagation velocity ($0.5U_\infty$) than that of a TS wave ($0.3U_\infty$). It also has an essentially laminar boundary layer profile. Iseler et al. (2006) differentiates a calmed area from a laminar region by stating that the calmed area had high shear stress and low shape factor as compared with a laminar region. The boundary layer at this point is more stable in this region, due to its relaxing from turbulent to laminar flow, further helping to suppress instabilities. Thus Halstead et al. (1997a) claim that this calmed region can only be terminated by the merging of neighbouring turbulent spots or by strong bypass events. They also claim that calmed regions are more resistant to separation in adverse pressure gradients due to their elevated levels of shear stress and low shape factors.

Fransson et al. (2005) showed that the initial disturbance energy in the boundary layer which then undergoes bypass transition, is proportional to

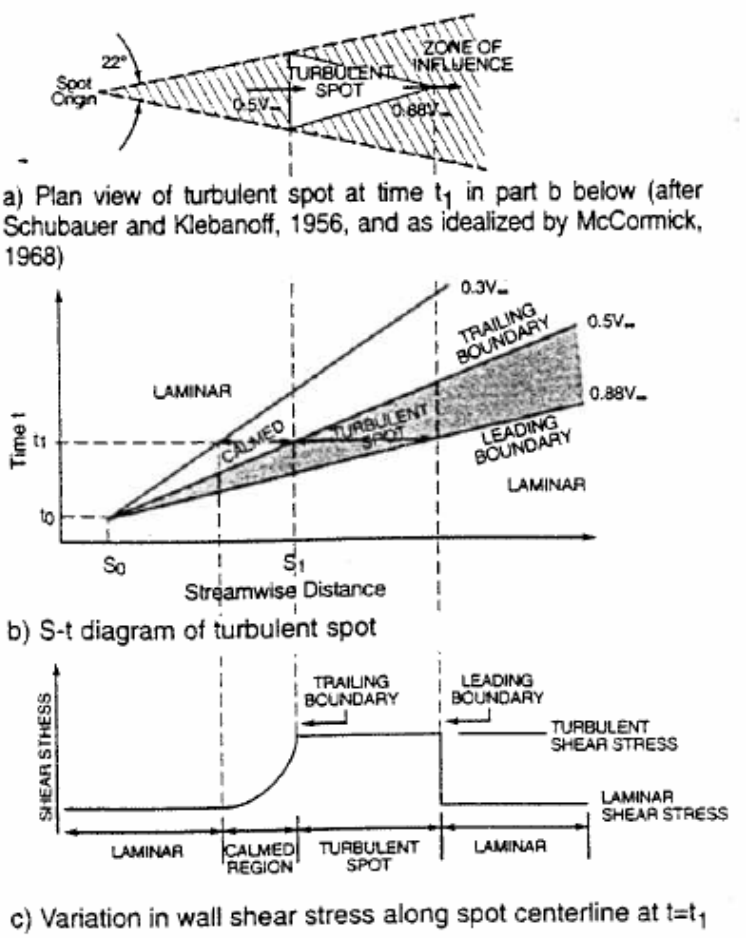

Figure 5.6: Characteristics of a turbulent spot. Taken from Halstead et al. (1997a)

Tu^2. Their experiments showed that the energy grows in a linear proportion to the Reynolds number based on streamwise distance. The transitional Reynolds number was shown to be inversely proportional to $Tu^2 Re_x$ for the range of $1.4\% \leq Tu \leq 6.7\%$. If scaled with the length of the transition zone, then the intermittency function has a universal shape shown in Figure 5.7. The Reynolds number based on this transition zone length was found to increase linearly with the transition Reynolds number. They also discovered

that there is a minimum length of the transition zone at high Tu.

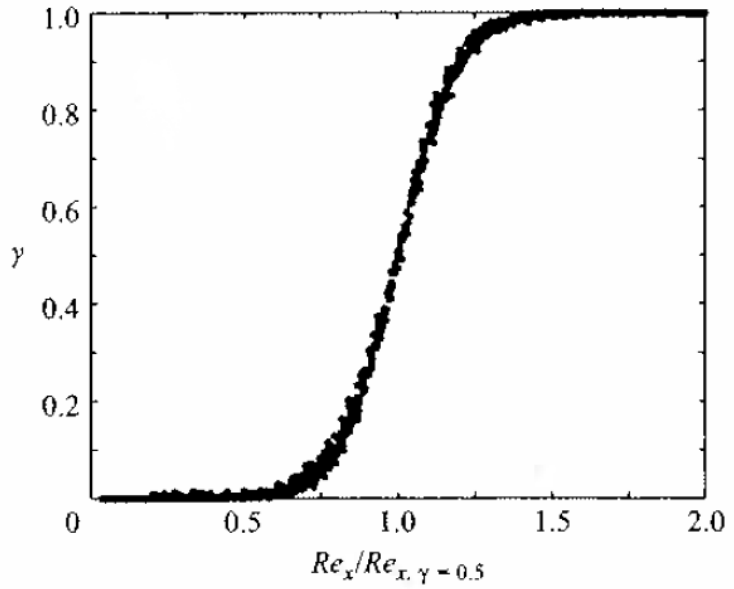

Figure 5.7: Universal intermittency function. Taken from Fransson et al. (2005)

They showed this through the prediction the propagation rate of turbulent spots on a flat plate. Turbulence is essentially the constant development and merging of turbulent spots. They concluded that Equation 5.1 accurately described the propagation rate of turbulent spots for a flat plate over a range of higher (6.7%) and lower (1.4%) turbulence intensities.

$$n\hat{\sigma} = \frac{1.52}{\Delta Re^2_{tr,min}}(1 + \frac{kC}{\Delta Re_{tr,min}} Tu^{-2})^{-2} \tag{5.1}$$

where $n\hat{\sigma}$ is the spot propagation rate, and k, C and $Re_{tr.min}$ are constants.

High values of Tu give a constant value of n$\hat{\sigma}$ in Equation 5.1. This can be seen as a result of a minimum Re for the transition, i.e. for high Tu, a

further increase does not lower Re_{tr} and hence $\mathrm{n}\hat{\sigma}$ appears to stay constant. However, this is only valid for $Tu > 1\%$.

As mentioned previously, the transitional boundary layer has a greater degree of turbulence anisotropy. In the measurements obtained by Ubaldi et al. (1996) for a turbine, it was shown that during the transition region, the boundary layer profiles showed a great increase in Reynolds stress ($-\overline{u'v'}$) at approximately $10 < y^+ < 100$ as compared to the laminar and turbulent boundary layer profiles, showing that the turbulence anisotropy in the transition region is much larger than in a turbulent one.

This bypass transition is the key transition process in the both separated and wake-induced transition. The interaction of those transition factors is very important, and shall be discussed further.

5.3 Separated

Separated flow transition has been described as possibly the least well understood transition phenomena (Howell, 1999). From what is known of separated flow transition, the laminar boundary layer separates and experiences a rapid period of transition. Dependent upon flow conditions, the now turbulent boundary layer will reattach due to entrainment effects, creating a separation bubble. According to Cumpsty (1989), the chordwise length of the separation bubble can typically be up to approximately 10%. Separation bubbles are often found during areas of high freestream turbulence or adverse pressure gradient.

Lou and Hourmouziadis (2000) and Howell (1999) give good descriptions of the transition process via a separation bubble;

- As the boundary layer experiences the same static pressure, when the lower momentum fluid closest to the surface stagnates under the adverse pressure gradient, it creates a blockage that forces the flow to separate from the blade surface, creating a shear layer.

- Instabilities in the now unstable free shear layer originate at the maximum vorticity point of the velocity profile and energy is transferred from the shear flow to the instability waves.

- In a relatively short distance, the instability waves are amplified downstream and trigger transition.

- Due to the turbulent fluctuation, the momentum transfer across the shear layer is increased. The turbulent shear layer entrains higher momentum flow from the freestream which mix together and transports momentum from the outer layer to the inner layer. This causes the shear layer to reattach to the blade surface, resulting in a separation bubble.

- As the free shear layer has considerably less damping capability than the attached boundary layer, transition takes place rapidly over an extremely short transition length. Iseler et al. (2006) found that this is due to a higher production of turbulent kinetic energy; its length is much shorter than attached bypass transition at the same flow conditions.

The general bubble configuration is therefore: a separated shear layer, a stagnant fluid region and the area of rms velocity maximum. The separation point remains almost constant, and the flow fluctuations originate on the line of inflection points gained from the velocity profiles (Figure 5.8). The maximum displacement locations, reattachment points, and maximum rms velocity locations vary considerably. This occurs naturally as the process is inherently unsteady, but also occurs due to other effects such as wake impingement from upstream blades. Halstead et al. (1997c) also found that modulation of the separation bubble on a stator blade can occur from the upstream stator blade wakes impinging on the upstream rotor blade. The rotor blade boundary layer is affected and these changes are transported along the blade surface into the rotor wake. The alteration of the rotor wake is then convected downstream onto the stator blade. The length of the bubble is also affected by freestream turbulence. Walraevens and Cumpsty (1993) showed that the length of the transitional separation bubble decreased with increasing freestream turbulence.

Roberts and Yaras (2005a) noted that separation bubbles can be affected by either the natural or bypass instability modes. For separation bubbles with either shear layers close to the surface, or a large thickness of the shear layer, transition is preceded by Tollmien-Schlichting instabilities, due to the significant levels of wall damping. For large separation bubbles, or those with the shear layer relatively far from the wall and free from wall damping effects, bypass transition mode takes place due to the inviscid Kelvin-Helmholtz instability. Once separated, transition is primarily controlled by the momentum thickness Reynolds number at separation.

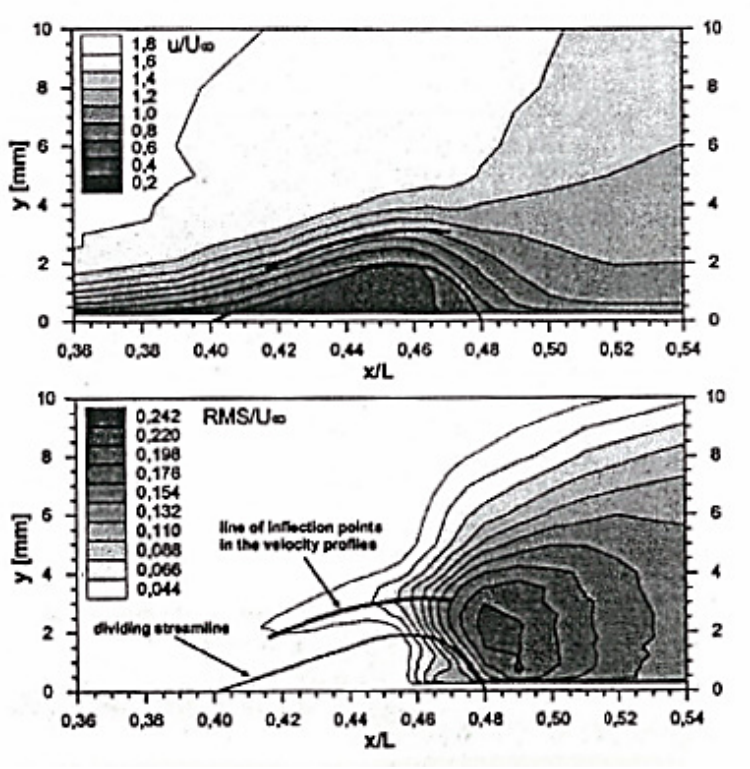

Figure 5.8: Velocity field around a separation bubble. Taken from Lou and Hourmouziadis (2000)

Hodson (1991) points out that failure to achieve accurate prediction of the development of the separation bubble (i.e. transition point and length) can affect the compressor efficiency by several percent and the life of components by more than an order of magnitude. Therefore it is important to predict separated flow transition, as it alters the length of the separation bubble. The prediction of the length of the separation bubble is critical in predicting exit flow angles, deviations and the pressure distribution over the local blade surface, as indicted by Howell (1999). The change in pressure distribution due to separation bubbles was studied by Roberts (1980). The effect on pressure distribution by a separation bubble can be seen in Figure 5.9. Long bubbles

produce large deviations, and should be avoided, whereas short bubbles can be an effective way to force turbulent flow and continued attachment of the boundary layer (Mayle, 1991).

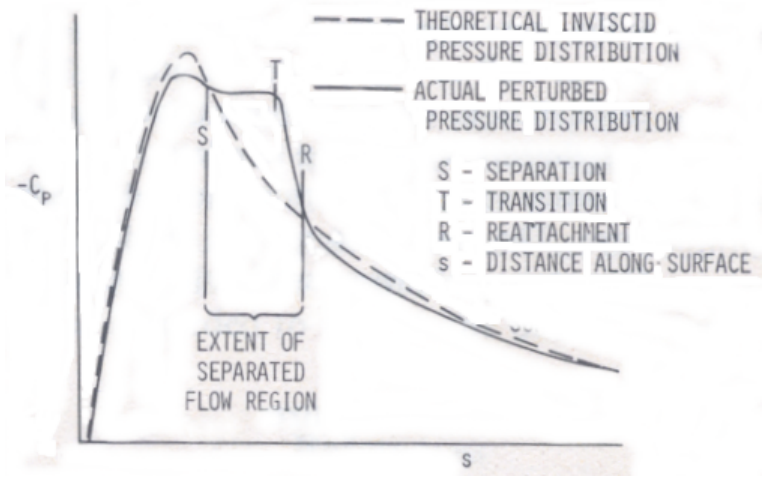

Figure 5.9: Comparison of pressure distribution between prediction and non-prediction of a separation bubble. Taken from Roberts (1980)

5.3.1 Wake-Induced

An overview of wake-induced transition is shown in Figure 5.10. In turbomachinery, periodic wakes from upstream rotor and stator blades pass through the machine and impinge on downstream blades. Wakes contain increased turbulence compared to the freestream. Wake impingement often causes the laminar boundary layer to locally undergo transition in bypass mode, creating what is termed as a wake-induced transitional strip. Mayle and Dullenkopf (1991) showed that the wake-induced transition strip propagates downstream at less than the wake-passing velocity. After wake impingement

passes downstream of that point on the blade, the boundary layer returns to its laminar state. This change creates a region in which no turbulence is allowed to occur for a period of time, depending on the strength of the wake. For example, Halstead et al. (1997c) found that as Reynolds number and loading are lowered, wake-induced transitional strips are lowered and eliminated along with its associated calming effect. The transition between wake passings is the transition process which would normally take place if there were no wake impingements. Therefore, it is possible for both natural and bypass transition to co-exist on the same unsteady boundary layer.

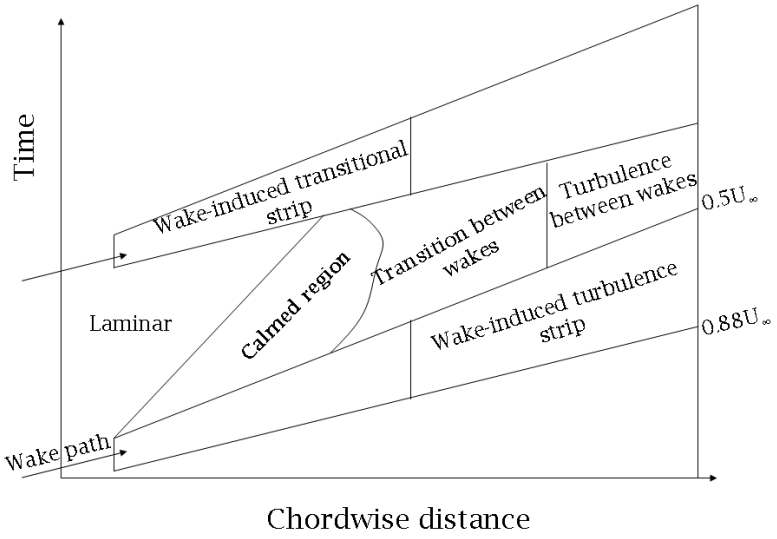

Figure 5.10: Wake-induced transition on the surface of a blade

The classically accepted process by which wakes cause transition in the laminar boundary layer can be explained as thus; A wake with its vortical core, high turbulence intensity and an intermittency of approximately unity, im-

pinges on the blade surface boundary layer. Its turbulent fluctuations undergo a strong damping by the shear layer and wall shear stress forces. Only fluctuations parallel to the surface are allowed to pass through the shear layer into the boundary layer. This effect has been described by Durbin and Wu (2007) and is known as shear sheltering. The fluctuations entering the boundary layer cause strong negative jet-like fluctuations, roughly parallel to the surface, which lift up the boundary layer fluid into a more tangential jet. Breakdown occurs at the boundary layer edge due to instabilities caused by these tangential jets. The wake does not actually cause transition to occur as it does not penetrate the boundary layer, but its influence creates the conditions necessary for transition.

Shobeiri (2005) conducted experiments of wake impingement on a curved plate. He found there was a phase lag of the propagation of the wake into the boundary layer, believed to be caused by the effect of molecular viscosity in the boundary layer. Velocity measurements from the freestream, through the boundary layer showed a velocity defect in the wake in the freestream and wake region, reducing to no defect and then a velocity excess in the boundary layer. This effect was due to the vortical structure of the wake transporting higher turbulent kinetic energy into the boundary layer, which in turn energised the boundary layer. The lag between Tu and intermittency was confirmed in the s-t diagrams included in the work. To cause transition, the wake impingement must create the condition within the boundary layer that the local turbulence level is very high, $\geq 23\%$ was recorded by Johnson and Dris (2000). This is in part why there is a lag between wake impingement and transition as it requires a finite amount of time for the turbulent kinetic energy to increase to 23% in the boundary layer.

More recently, studies by Henderson et al. (2006), Wheeler et al. (2007a) and Wheeler et al. (2007b) have shown that impinging wakes affect the transition process on the suction surface of a compressor blade differently than on the pressure surface, or in a turbine blade boundary layer. As described previously, Henderson et al. (2006) showed that on the compressor blade suction surface, transition starts due to instabilities at the leading edge and convects along the boundary layer between 0.5-0.7U_∞. Wheeler et al. (2007a) detailed how a spike in the pressure coefficient is present at the leading edge due to the acceleration and deceleration of the flow as it passes around the leading edge. This pressure spike increases as the wake passes over, due to a change of incidence caused by the wake. The increase in incidence also increases the local turbulent kinetic energy as described by Hobson et al. (1999). In the leading edge region, both shape factor and momentum thickness increase during wake passing. $Re_\theta \geq Re_{\theta_c}$ indicating the development of turbulent spots from either natural or bypass forms of transition modes. The thickened boundary layer created by the wake passing at the leading edge convects downstream between 0.6-0.7U_∞. This thicker section of the boundary layer undergoes transition earlier than the position of pre-wake boundary layer. The calmed region follows the wake-induced transitional region as usual between 0.35-0.5U_∞. The leading edge remains the main region of receptivity for wake-induced transition, whereas for the pressure surface, receptivity for wake-induced transition remains local.

Wheeler et al. (2007b) found that if a suction surface laminar leading edge separation bubble is present, the wake causes transition to occur before reattachment. The early turbulence in the now turbulent and thickened reat-

tached boundary layer convects downstream at a speed of 0.7-U_∞, whilst the same transition mechanism described above continues to convect at a speed of 0.6-0.7U_∞. A by-product of the wake passing, according to Wheeler et al. (2007b), was that the reattached inter-wake laminar boundary layer was more susceptible to early transition.

The effect of a periodically impinging wakes on the boundary layer accounts for more than just the transition location. Documented by many, including Cumpsty et al. (1995), Halstead et al. (1997c), Howell (1999) and Thomas and Gostelow (2005), impinging wakes suppress separation bubbles downstream of the leading edge region during the wake passing and extending into the calmed region. Cumpsty et al. (1995), showed a compressor blade boundary layer and the effect a passing wake had upon it. The wake suppressed the separation bubble at mid chord and severely changed the boundary layer profile in the local area. They discovered the boundary layer velocity profile in the calmed region to be linear to almost the freestream, whilst the skin friction was comparable to a turbulent boundary layer. It was thought that the velocity profile resembled the viscous sub-layer of a turbulent boundary layer, but extrapolated out to the freestream. Howell (1999) showed this to be true also in a separation bubble experiencing the calming effect of a passing wake. He also showed that the gradient of the velocity profile increased as the boundary layer thickened. This calmed area also resisted adverse pressure gradients that would otherwise cause the laminar boundary layer to separate. As the incoming wakes distort the velocity profile, they alter the momentum thickness and shape factor. Howell (1999) showed the momentum thickness to peak during the wake passing, then fall slightly and plateau through the calmed region, before reducing to pre-wake levels.

Thomas and Gostelow (2005) showed the suppression time of the separation bubble to be related to wake impingement frequency. If the wake frequency is high enough, then separation is suppressed completely. This phenomena has caused Howell (1999) to ponder upon the ability of wakes to be utilised to suppress secondary flows and reduce the associated losses. Once fully formed, he showed that it took 45% of a spot passing period for the effect of the calmed region to disappear. For a wake passing, further downstream, this time was increased to 60%. He attributed this to a greater number of spots and hence calmed regions present in that region. Thomas and Gostelow (2005) showed the calmed region to extend beyond the trailing edge of the turbulent strip for a time interval equivalent to the turbulent strip.

The calmed region has a significant effect on suppressing transition, turbulence and separation in the boundary layer. Part of this is due to the velocity of the trailing edge of a turbulent spot being approximately $0.5U_\infty$, which is greater than the propagation velocity of T-S waves ($\approx 0.3U_\infty$). Therefore, no natural transition can take place in the calmed region. Thomas and Gostelow (2005) showed that even with increased wake frequency, which caused following wakes to impinge in the calmed region of the previous wake, wake turbulence levels were reduced up to 40%. This proves that the calmed region always operates on the boundary layer, regardless of new events taking place in it. The calmed region can be shown by its combination of high shape factor for a turbulent boundary layer and as shown in Figure 5.6, a decreasing, but still elevated wall shear stress behind the turbulent strip. If a CFD code cannot predict the wall shear and shape factor effects of the calmed region, it should show that transition is delayed for the appropriate

time after the wake has passed.

Computational work by Wu and Durbin (2000) gave similar results to Shobeiri (2005), in that from both RANS and DNS simulations, the boundary layer beneath the wake was seen to thicken. Wu and Durbin (2000) concluded that this thickening was due to the forced response of the buffeted boundary layer to the passing wake. It is also due to the negative jet effect that often accompanies passing wakes.

The negative jet effect is caused by the wake defect. Some have referred to this as a slip velocity (Mallach et al., 2007). In Figure 5.11, the absolute velocity (C) of the stator wake is reduced within the wake. As the tangential velocity (U) remains unaffected by the wake, the relative velocity (W) also decreases and is now at a different angle to flow outside the wake. As the wake travels through the freestream the flow experiences a change in relative velocity, the difference being called the negative jet, or slip velocity. The same is true for a reduction in relative velocity causing a similar change in absolute velocity in rotor wakes. Although tangential velocity in a rotor wake is reduced slightly, the negative jet still occurs.

The negative jet removes fluid from one surface and transports it to the other surface due to the velocity defect, although Howell (1999) argues that no fluid actually reaches the other surface as the wake will have convected through the passage before one surface fluid has time to travel to the other surface. Upon impingement onto the blade suction surface, the suction side of the wake causes an acceleration of the flow into the wake, whilst a deceleration of the flow into the wake can be observed on the pressure side of the wake.

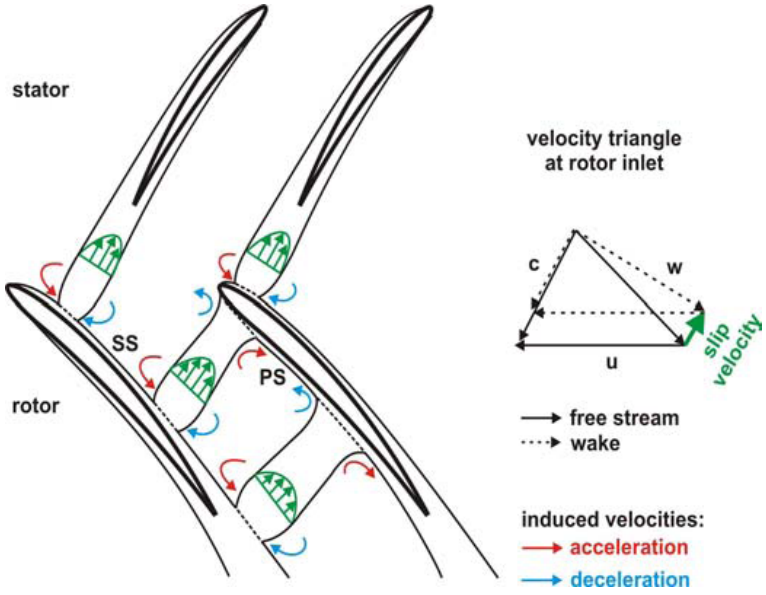

Figure 5.11: The negative jet effect on a compressor rotor blade. Taken from Mallach et al. (2007).

This is reversed for impingement on the pressure surface. The effects of local velocity and pressure can be found in Figure 5.12.

Koyabu et al. (2005) studied the effect of the negative jet on a flat plate subject to both favourable and adverse pressure gradients. Using rotating bars to create the wakes, they conducted their experiments by rotating the bars in both normal and reversed directions to simulate wake impingement on both the suction surface and pressure surface of a blade respectively. The negative jet had a greater effect on the suction surface than on the pressure surface, inducing turbulent spots from x/L = 0.1, as compared to x/L = 0.45 for the reversed direction (where x is the distance from the plate leading edge, and L is the length of the plate).

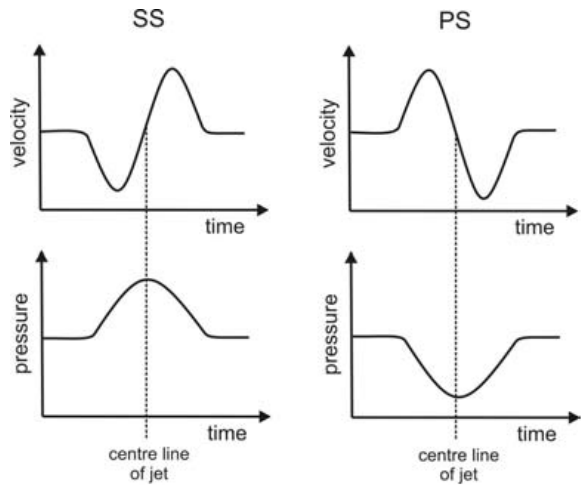

Figure 5.12: Local velocity and pressure effects due to the negative jet on a compressor blade. Taken from Mallach et al. (2007).

Varying the width of the rotating bars, they found that for the thinner and lower Tu wake (3mm diameter bar, 5% Tu), the calmed region lasted longer than for the wider and higher Tu wake (5mm diameter bar, 8% Tu) for the aft loaded turbine-like case. Initially, one would think that this opposes the statements previously given that a thicker and higher Tu wake produces a longer sustaining calmed region. However, the 3mm bar wake experienced delayed transition by approximately 20x/L over the 5mm bar wake. It was not strong enough to initially overcome the stabilising effects of the favourable pressure gradient present for most of the plate length. It was thought that the turbulence in the 3mm bar wake was newer than the 5mm bar wake, and so was able to maintain the calmed region for longer. Koyabu et al. (2003) concluded that the more noticeable effects of bypass transition due to passing wakes occur in the adverse pressure gradient region. They determined that

it was due to the pressure gradient magnifying any effects caused by the wake.

They also found the normal rotation wakes to produce a greater momentum thickness than for the reverse rotation wakes, which they attributed to the negative jet effect. In an earlier study, Koyabu et al. (2003) discovered that the normal rotation direction produced a thicker wake than the reverse rotation wake, which they again think is due to the negative jet effect. Hence they also found the calmed area is extended for the thicker wakes. The negative jet is also affected by the loading, thickness and camber of the blades as mentioned by Howell (1999).

As loading is increased, wakes become wider and more turbulent. Walker et al. (1999), Halstead et al. (1997c) and Koyabu et al. (2003) have shown this, and demonstrated the start of transition to move towards the leading edge of the blade in both the wake and non-wake regions, and the calming effect to have an extended region over lower loading calmed regions.

Wakes and wake-induced transition have an important part to play in reducing the loss generation in the compressor blade boundary layer. Loss generation in the boundary layer can be assessed by calculating the momentum thickness at the trailing edge of the blade as shown by Howell (1999). He also showed that when wakes were present, they reduced the loss in the boundary layer further than just when turbulence spots were present. Therefore, it is important to be able to understand and model the effects of wake-induced transition.

5.4 Relaminarisation

Relaminarisation or reverse transition occurs when the momentum thickness Reynolds number is not sufficiently high to support self sustaining turbulence production. Laminar flow then occurs. It normally happens during strong or sustained acceleration after transition has already taken place. However, this is most often found on the pressure surface of turbine blades.

This chapter has so far described the various modes of transition typically found in an axial compressor. There are certain factors which affect all modes of transition. Rather than explaining the effects of those factors in each transition mode section, these factors will now be explored.

5.5 Factors Affecting Transition

As already shown to some degree, the transition processes that take place in an axial compressor are affected by a wide range of freestream, geometrical and machine arrangement factors. Some of these factors have already become apparent through the discussions so far in this chapter. It is these factors which are preferentially included in the correlations used by transition models. A selection of correlations were reviewed in Section 3.5. This section will detail some of the main factors currently known to affect the transition process, some of which are included in current correlations, some of which are not.

5.5.1 Reynolds Number

The effect of Reynolds number is inextricably linked to changes in the freestream turbulence. Changes in Re affect loading, boundary layer separation, corner stall, wake size and strength, and incidence angle. All of these affect the level of general unsteadiness in the freestream downstream of their occurrence.

For a given machine arrangement, as the Reynolds number decreases, transition moves downstream. This is partly due to the decrease in the intensity of the any wake-induced transitional strips and a general decrease in Tu associated with Re. The calmed regions also weaken and transition is more likely to occur via laminar separation. The wakes tend to only have a modulating effect on any separation bubble or bypass transition length that may be present. As Re increases, transition moves upstream toward the leading edge, and the transition length becomes shorter. The strengthening of any wake-induced transition and its associated calmed region reduces the likelihood of transition via laminar separation between wake passings. Towards near stall, Halstead et al. (1997c) found that the boundary layer may go through separated flow transition with turbulent reattachment.

5.5.2 Freestream Turbulence

As freestream turbulence increases, the transition region moves upstream towards the leading edge and reduces in length. Transition increasingly occurs in bypass mode as Tu is too high for natural transition to take place, and separation bubbles tend to reduce in size or become fully suppressed for a given Reynolds number. Decreasing the Tu moves the transition point down-

stream and will tend to occur in separation mode, as it will be increasingly likely that a laminar separation bubble will be present.

For a given machine at a given operating point, freestream turbulence is the prime factor in the transition region starting point and length. In their experiments previously mentioned, Koyabu et al. (2003) found that artificially raising the background freestream turbulence via a turbulence grid had a greater effect than the wake turbulence. They concluded that the boundary layer is more susceptible to increases in Tu whilst at lower freestream Tu values than at higher freestream Tu values. This is confirmed by Abu-Ghannam and Shaw's (Abu-Ghannam and Shaw, 1980) experiments in which they discovered that increasing freestream turbulence above 7% did not have an appreciable effect on the transition start point or length on a flat plate, as the correlation is asymptotic to $\mathrm{Re}_{\theta_{ts}}$=163 at this level of Tu. This value is also the Tollmien-Schlichting limit of instability.

Similarly, Abu-Ghannam and Shaw (1980) discovered that with increasing Tu, changes in pressure gradient had a reduced effect on the length of the transition region. For Tu values causing the Reynolds number based upon the length of the transition region, $\mathrm{Re}_L \leqslant 1.5 \times 10^5$, the pressure gradient has no effect on the length of transition, as Re_{xe} (Reynolds number based upon the distance from the leading edge at the end of the transition region) was found to be at its asymptotic limit at this point when plotted against Tu. Therefore Tu is the prime factor in determining the transition region length at high values of Tu.

5.5.3 Local Pressure Gradient

Abu-Ghannam and Shaw (1980) found that favourable pressure gradients tend to delay the onset of transition, whilst adverse pressure gradients tend to advance the onset of transition, although both have a negligible effect when a high level of free stream turbulence is present. They also found that the past history of pressure gradient tends to affect transition to a greater degree than the local value at transition. They felt that rather than an average past history of pressure gradient affecting the transition region, it was the extreme value of the pressure gradient in the flow history. However, most correlations seem to use the local value of pressure gradient, rather than the past history of pressure gradient. This is due to the difficulties of using non-local variables in the correlation as explained in Section 3.4.3.

Walker (1968) developed a correlation for transition length on an axial compressor blade, dependent upon Reynolds number and local pressure gradient;

$$(Re_{\theta_t} - Re_{\theta_i})/Re_{\theta_m} = 1.70 - 0.32H_m \tag{5.2}$$

Where Re_{θ_t} is the momentum thickness Reynolds number at the transition point, Re_{θ_i} is the momentum thickness Reynolds number at the point of neutral stability in the boundary layer, Re_{θ_m} is mean value of momentum thickness Reynolds number from the neutral stability point to transition, and H_m is the shape factor over the same region.

Lower values of $Re_{\theta m}$ reduce the instability length. Hence, when the neutral stability point is near the leading edge due to a peak in pressure distribution, transition will also take place close to the leading edge as the change in Re_θ over the transition region will be small. However, as transition moves

downstream, the transition length increases due to an increase in Re_{θ_i}.

The pressure gradient is also closely linked with the acceleration of the flow. The flow acceleration is measured by the acceleration parameter, K. When the flow is accelerating (positive K), the start of transition is delayed and the length extended according to Mayle (1991). Mayle (1991) also defined a critical acceleration for transition, $K_{crit} = -5.13 \times 10^{-7} Tu^{5/4}$. When K>$K_{crit}$, transition occurs before laminar boundary layer separation, while for K<K_{crit}, separation precedes transition. If K> 3×10^6, then transition cannot occur. The closer K is to K_{crit}, the longer the transition region becomes, as demonstrated by both Mayle (1991) and Ubaldi et al. (1996).

Koyabu et al. (2005) reported that transitional streaks were seen between wake passings only when the flow started to decelerate, showing that the acceleration had previously prevented the laminar boundary layer experiencing transition up until maximum velocity.

5.5.4 Wake Frequency

An increase in wake passing frequency results in the moving upstream of the transition start point between wakes, as described by Shobeiri (2005). He presented two mechanisms by which transition is affected by wake frequency. The first is an earlier mixing of the wakes due to the reduction of their spacing, which leads to a higher freestream turbulence that inherently affects the onset of transition by moving it upstream. The second mechanism is the increased impinging frequency of the primary wake strips, which introduce an excessive turbulent kinetic energy transport into the boundary layer, causing

a shift of transition start toward the leading edge. It is conceivable that the combination of these two mechanisms would make additional contributions to the shift of the transition start point.

Halstead et al. (1997c) discovered that when increasing the wake frequency to the point that the calmed region did not have enough time to decay in between wakes, bypass transition dominated between wakes. When wake passing frequency was reduced to allow calming to cease, separated transition dominated between wakes. When wakes begin to impinge in the calmed region, it is primarily the wake frequency which determines the start of transition. Conversely, when wake frequency does not increase to the point where there is not enough time for the calmed region to decay between wakes, Obremski and Fejer (1967) found that it is the disturbance amplitude, not frequency which determined the transition Reynolds number at onset.

5.5.5 Surface Roughness

Roberts and Yaras (2005a) found from their experiments that the start of the transition region moved upstream with increased roughness height, increased space between roughness elements and increased proportion of roughness elements being depressions. If the roughness height is sufficiently large, it may trip the laminar boundary layer into bypass transition mode. Roughness strips are a classic method used in experiments to trip the boundary layer to ensure a turbulent boundary layer is present. As the project is only considering smooth surfaces, nothing more shall be said on the matter.

5.5.6 Surface Curvature in Blade Geometry

The effects of surface curvature on the transition process are rarely studied and discussed, as for most turbomachinery applications, its effect is minor compared to freestream turbulence, pressure gradients and wake impingement.

Longitudinal curvature due to blade curvature either suppresses (concave curvature) or amplifies (convex curvature) turbulent fluctuations (Kozulovic and Rober, 2006). If a fluid element is moved due to turbulent motion from one streamline to another, and the difference in the centrifugal forces of that streamline is directed in the same direction as the movement direction of the fluid element (convex curvature), then the turbulent fluctuation will be amplified. If the direction of the movement is different to the direction of the centrifugal force (concave curvature) then the fluctuation is suppressed. This is revelent to transitional flows as the instabilities in the boundary layer are likely to be affected by camber. *Ceteris paribus*, the higher the camber, the further downstream the start of the transitional region.

5.5.7 Cross-flow Instability

Compressor rotor blades are often subject to radial migration of the flow around the blade. This flow is essentially a cross-flow which can cause both stationary instabilities around the leading edge and traveling vortices in the flow. These vortices are excited by the cross-flow according to Singer (1993) and can cause significant distortion of the time-averaged flow quantities in the laminar boundary layer. Similar to Görtler instabilities caused by streamline

curvature, these instabilities have the possibility of altering the physics of the transition process.

5.5.8 Effect of Varying The Transition Parameters

Much has been mentioned about the effect of certain factors on the transition region and the development of the boundary layer as a whole. The effect of varying these factors can, in a simplistic manner, be demonstrated through the varying of the transitional Reynolds number used by a correlation type transition model.

To show the effect of varying the aforementioned parameters, the Menter $\gamma - \theta$ model was used to simulate the transition region found on the ERCOFTAC T3A test case (see Section 4.4). The model was used in the one equation mode, where the transition onset momentum thickness Reynolds number (Re_{θ_t}) is specified by the user and is treated as constant. This circumvents the use of the Re_θ transport equation given by the correlation, hence no local effects such as Tu or pressure gradient are accounted for. Intermittency distribution is calculated by the model. Re_{θ_t} was varied between 100 and 350, with $\mathrm{Re}_{\theta_t} = 260$ being specified as the actual experimental value (Menter et al., 2002). The results are shown below (Figures 5.13 to 5.15).

Figures 5.13 & 5.15 clearly show the transition region moving downstream with increasing Re_θ specified. As the transition region moves downstream, the boundary layer thickness (Figure 5.14) at the rear end of the plate reduces, reducing the blockage factor.

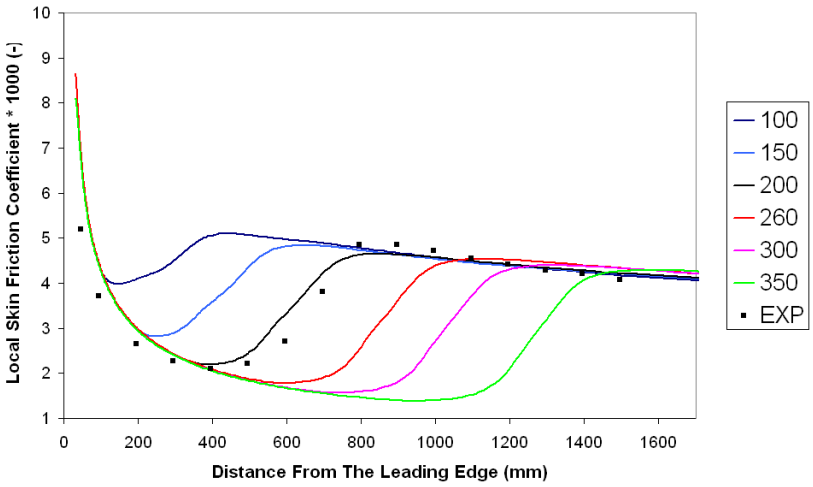

Figure 5.13: Variation of local skin friction with Re_θ for T3A

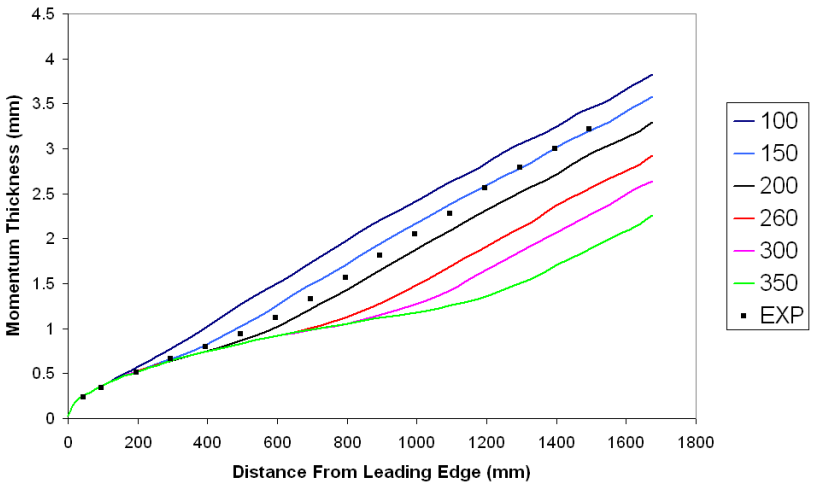

Figure 5.14: Variation of momentum thickness with Re_θ for T3A

5.6 The Effect of Transition on Loss

The profile loss in an axial compressor blade row can be greatly affected by the unsteady influence of wake-induced transition. Contribution towards the

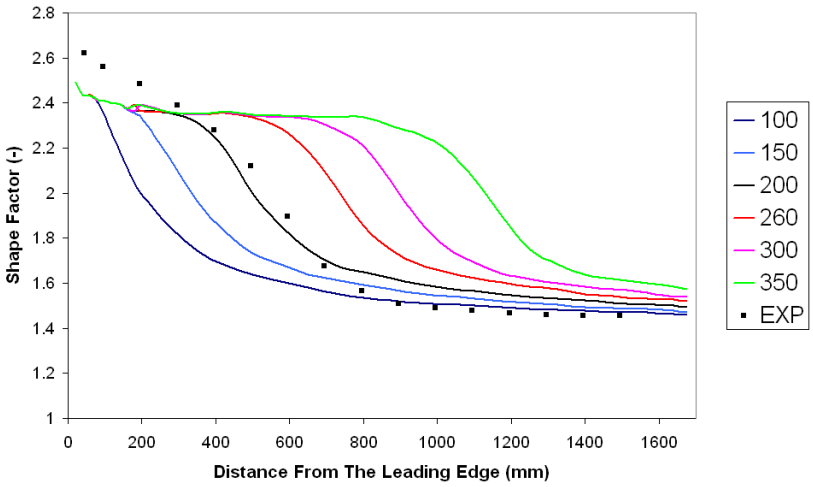

Figure 5.15: Variation of shape factor with Re_θ for T3A

loss created by the profile of a blade can classified into entropy generation within the boundary layer and trailing edge loss. Denton (1993) showed that the loss generated via entropy production rate is proportional to U_∞^3. For the range of Reynolds Numbers of a typical axial compressor, a turbulent boundary layer creates a greater loss than a laminar one at the same point on the blade surface, having a dissipation coefficient of $C_D = 0.0056 Re_\theta^{-1/6}$, compared to laminar coefficient $C_D = 0.173 Re_\theta^{-1}$. In a typical Re_θ range, i.e. $300 < Re_\theta < 1000$, the dissipation coefficient of a laminar boundary layer is between 2 and 5 times smaller than that of a turbulent boundary layer. The suction surface losses are much greater than the pressure surface losses due to the greater velocities experienced there. Further, Coull et al. (2008) showed that losses from separation bubbles and the associated turbulent reattachment process dominated over normal attached boundary layer losses. This shows the importance of correctly predicting the point and length of transition.

The effect of impinging wakes upon the boundary layer was shown by Wheeler et al. (2007a), Wheeler et al. (2007b) and Coull et al. (2008) to have a very significant effect upon loss generation. Coull et al. (2008) found that for a boundary layer in a low speed turbine-like pressure distribution on a flat plate subject to impinging wakes, wake impingement, and the subsequent shifting upstream of the transition region generated a greater loss than under steady state, no-wake conditions. Only when a large separation bubble, present under no-wake steady state conditions was present, did the wakes reduce the profile loss. As separation bubbles generate a greater loss than a turbulent boundary layer, the periodic suppression of the separation bubble reduced the time averaged loss. Wheeler et al. (2007a) hypothesised that the additional turbulent wetted patch on the compressor blade due to early wake-induced transition, and its subsequent increased momentum thickness at the trailing edge, increased the loss generated. They found that the additional turbulent wetted patch was greater than the associated additional calmed region. However, an increase in wake frequency is likely to increase the loss generation in this situation where no large separation bubble is present.

Wheeler et al. (2007b) discovered that a compressor blade with a circular leading edge, producing a small laminar separation bubble at the leading edge which reattached turbulent under wake influence, experienced a lower variation in loss due to wake impingement, than the same blade with an elliptical leading edge, upon which a small leading edge separation bubble remained laminar during wake impingement. They discussed that the relatively small fluctuation in loss for the circular leading edge blade could be due to the post-wake reattached laminar boundary layer, downstream of the

separation bubble, being more susceptible to transition when perturbed by a wake. The total profile loss was 32% greater for the circular leading edge blade than for the elliptical leading edge blade.

Therefore, as the loss generated is greatly affected by the point of transition, the prediction of wake-induced transition can be significantly important to the overall profile loss prediction of a compressor blade.

5.7 Chapter Closure

This chapter has detailed and discussed the modes of transition typically found on an axial compressor blade. Multi-modes of transition can be found on a blade at any given time, and the interaction of the different transition mechanisms is complex. One can see that not all of the physics of the transition process can be fully represented with current RANS codes. The physics discussed must needs be somehow captured within correlations and other relationships within the code for a transition model to hope to be successful in accurately predicting the unsteady boundary layer.

Chapter 6

2D Wake-Induced Transition Simulations

6.1 Introduction

The general application of turbulence and transition modelling to turbomachinery flows and has been explored in Chapters 4 and 8. The phenomena of transition and its effects on the boundary layer, within the context of turbomachinery applications, has been discussed in Chapter 5. Attention is now turned to the unsteady simulation of transition in an axial compressor. Experimental data has been obtained for a low speed 1.5 stage axial compressor for three loading conditions. 2D steady state and unsteady simulations using the $\gamma - \theta$ model in CFX will highlight some of the issues regarding the required simulation set-up to model wake-induced transition and show the applicability of the model to successfully simulate this phenomena.

This chapter contains the methodology, results and analysis for the 2D simulations undertaken. Steady state 2D simulations were conducted first to

ensure the simplification of the geometry and inlet conditions used were appropriate. The steady state results were then used to initialise the unsteady simulations. Chapter 7 will attempt to show the advantages and disadvantages of using a transition model in a 3D simulation in comparison to using a 2D simulation.

6.2 Low Speed Axial Compressor

The University of Tasmania research compressor, in Hobart, Australia, is a 1.5 stage low speed axial compressor with a rotational speed of approximately 500rpm. Traditionally it has been used to investigate the unsteady effects on the development of the flow on the stator blade at mid-span. Past studies have been used to understand the effect of clocking (Walker et al., 1999), Reynolds number & blade loading (Solomon and Walker, 2000), freestream turbulence (Henderson et al., 2005) and axial spacing between rotor and stator (Henderson et al., 2006) on the development of the flow on the stator at mid-span.

The compressor consists of 38 IGV blades, 37 rotor blades and 38 stator blades, all of British C4 design. The blades have a constant chord length of 76.2mm and an aspect ratio of 3. The layout is shown in Figure 6.1. Further details, along with the data used for this work, can be found in Walker et al. (1999). Hot film data was provided at mid-span on the stator, and hot wire data 42.5mm upstream of the stator leading edge. Blade pressure tappings at stator mid-span provided pressure information around the stator blade. Data at mid-span only can be used as the radial flow component has been

shown to be negligible.

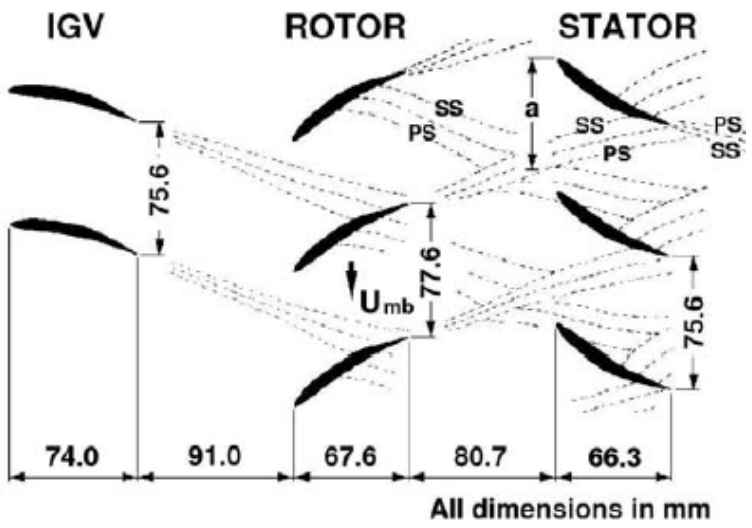

Figure 6.1: A cross section of the University of Tasmania's low speed compressor at mid-span (Reproduced from Henderson et al. (2006))

The data obtained was originally used to understand the effect of clocking on wake-induced transition for three loading conditions. The set-up and experimental data used for comparison was for the a/S = 0 clocking case (see Figure 6.1) where the IGV wake impinges on the leading edge of the stator blade. S is defined as the blade pitch, and a is the circumferential offset of stator blade leading edge from the centre of the IGV wake avenue. The machine operating conditions at mid-span for the stator are shown in Table 6.1. The benefits of using this particular compressor data was that the hot film data gives a time dependent picture of wake-induced transition, including the calming effect post wake transition, and as it involves relatively low Reynolds numbers, the node count for the grid is reduced, decreasing the solving and post processing time. A reduced storage requirement is needed

Loading	ϕ (u/U_{mb})	i (°)	Re_c	Tu (%)
High	0.600	4.1	110000	3.15
Medium	0.675	1.2	117000	2.27
Low	0.840	-6.1	130000	2.03

Table 6.1: Experimental data upstream of the stator

as compared to a high speed compressor.

6.3 2D Steady State: Numerical Procedure

A quasi-2D slice at mid-span was used to approximate the compressor geometry in the stator passage. It was thought appropriate to do so as the radial component of the flow is negligible (Walker et al., 1999). The 2D geometry was created using ANSYS ICEM. The location of the inlet was placed 42.5mm upstream of the stator leading edge, the same streamwise point at which the hot wire data was acquired. The outlet was located 1.85 of the chord length downstream of the trailing edge to reduce convergence problems due to wake impingement on the outlet. An O-grid was placed around the blade to maximise orthogonality of the elements in the boundary layer. The O-grid contained 70 nodes perpendicular to the blade surface with a maximum $y^+ < 1$, and 512 nodes distributed around the blade surface. The maximum streamwise elemental length was 0.6mm. The spanwise thickness of the domain was 2.5mm. The number of nodes in the spanwise direction was 3. 170 nodes were placed in the circumferential direction to provide a very fine resolution of the incoming wake used in the unsteady simulations.

The total size of the grid contained 232,200 nodes of which a relatively large proportion of this amount was contained from the inlet to approximately mid chord in order to maximise the resolution of the wake.

A constant velocity calculated from the specified Reynolds number was applied at the correct angle for the required incidence at the inlet, along with a constant turbulence intensity. Both sets of values match the experimental values given in Table 6.1. Past studies of this data set include the study of Solomon et al. (1999) which used the e^N model within the MISES code. In this study, to account for uncertainties in the experimental data and computational modelling, the incidence angles were altered until a better agreement was found. A sensitivity study of inlet angles was undertaken in the current study to discover if this was also the case. Velocities were recalculated, using Equation 6.1, to take into account of the change of inlet angle. The study found the experimental inlet angles and velocities that give the optimum result for the CFX code. The inlet viscosity ratio was left at the default value of 10 as there was no data available to match the decay of turbulence through the domain.

$$u_{in} = \frac{U_{mb}\phi}{cos(\alpha)} \tag{6.1}$$

As no data was available for the pressure difference upstream and downstream of the stator, the outlet was set to an average of atmospheric pressure, with any required change in pressure needing to be made by the code at the inlet. The boundaries perpendicular to the spanwise direction were parallel to each other. A requirement of the use of symmetry boundary conditions is that

two boundaries must be parallel. Therefore the streamtube contraction due to the boundary layer which would be present on the hub and casing was not modelled. This did not appear to have any significant effect upon the results as will be shown. The boundaries parallel to the blade surface were modelled as periodic 1:1 connections. The simulations were run until the rms values of the residuals were approximately 1×10^{-6}. The $\gamma - \theta$ model was used for all the simulations.

6.4 2D Steady State: Results

The blade surface velocities at mid-span normalised by the blade speed (U_{mb}) at mid-span, are shown for all three loading conditions in Figure 6.2. The low and medium loading results offer a more favourable comparison than the high loading. The discontinuity and subsequent reduction in velocity on the suction surface is indicative of transition occurring in the separation bubble at that point. This is confirmed by analysing the local skin friction coefficient for the suction surface (Figure 6.3). The high loading case shows the greatest discrepancy of surface velocity on the suction surface, which is caused by the transition separation bubble moving further upstream than in experiment. The leading edge velocity distribution for the low loading case shows a relatively greater loading on the pressure surface, and subsequently reduces loading on the suction surface. The flow recovers to experimental values by 30% chord.

Solomon et al. (1999) discussed the observation of suction surface separation bubbles in their results and in previous similar experimental data. They ob-

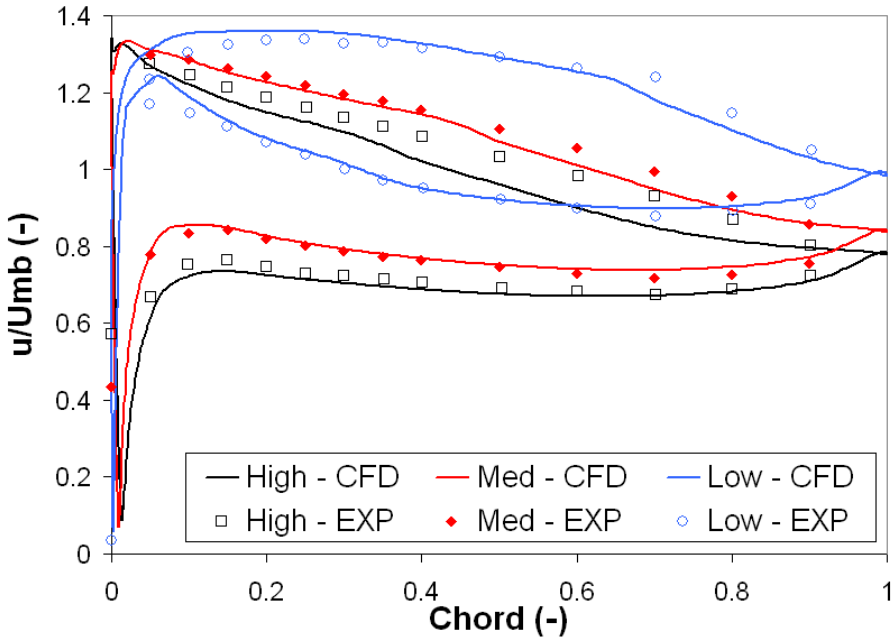

Figure 6.2: Comparison of CFD and experimental blade surface velocity distributions

served separation bubbles for both the low and medium loading, but not for the high loading case. The comparison between the current bubble lengths and those of (Solomon et al., 1999) are given in Table 6.2. Although no experimental data for bubble length is available, the previous simulations by (Solomon et al., 1999) were shown to be be located in the correct region of the suction surface. The current results show that the bubble occurs too early along the suction surface for the low and medium loading cases, whilst the bubble present in the high loading case results should not be present. This discrepancy may well be caused by the omission of accounting for the contraction of the streamtube, which was measured by Walker (1972) to be 2.2%. Including this would reduce the adverse pressure gradient, causing the bubble to either move downstream or disappear.

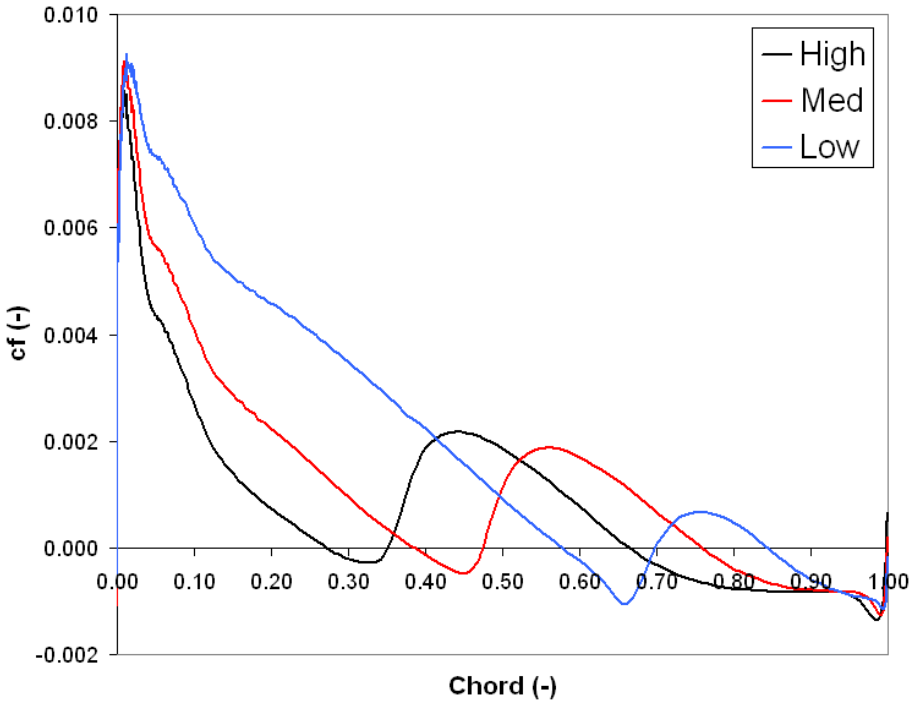

Figure 6.3: Comparison of c_f on the suction surface for all loadings

The transition process on the suction surface initiates just before the start of the bubble on the suction surface and concludes just before reattachment. Transition occurs in damped mode (intermittency does not rise above 1), as the bubbles are thin and the viscosity at the wall damps the transition taking place within the bubble. If streamtube contraction effects were to be accounted for, the terminal separation shown to take place towards the trailing edge would also move downstream. It is thought that the terminal separation point is too far forward, but there is no comparable experimental evidence to show this is actually the case. There is less commonality between the three loading conditions of the transition process taking place on the pressure surface. Both the high and medium loading show no transition

	Current			Solomon et al. (1999)		
Loading	Separation s*	Reattachment s*	Length s*	Separation s*	Reattachment s*	Length s*
High	0.269	0.348	0.079	-	-	-
Med	0.387	0.466	0.079	0.54	0.57	0.03
Low	0.58	0.697	0.117	0.65	0.78	0.13

Table 6.2: Comparison between current 2D steady state simulations and previous simulation of Solomon et al. (1999) for separation bubble parameters on the suction surface.

taking place, whilst the low loading case predicts transition to occur between approximately 30% - 50% chord. In the low loading case, the flow is close to separation in this region, but remains attached.

The CFD results can be compared to the experimental results for the transition region found on both surfaces (Figure 6.4). It can be seen that in general, the $\gamma - \theta$ model has predicted transition to occur too far forward on the suction surface and not at all for the pressure surface in medium and high loading conditions. Whilst the transition and separation bubble location have not been predicted as well as in past simulations, the velocity distribution around the blade for the incidence angles and Reynolds numbers were the closest match out of the steady state simulations undertaken. It was felt that this was the most important aspect to consider, as incidence angles and inlet Reynolds numbers will vary with time in the unsteady simulations. Additionally, the incidence angles and Reynolds numbers given in Walker et al. (1999) were time averaged from unsteady data, so take into account

the variation due to the passing of the rotor wake and its effect on the IGV wake.

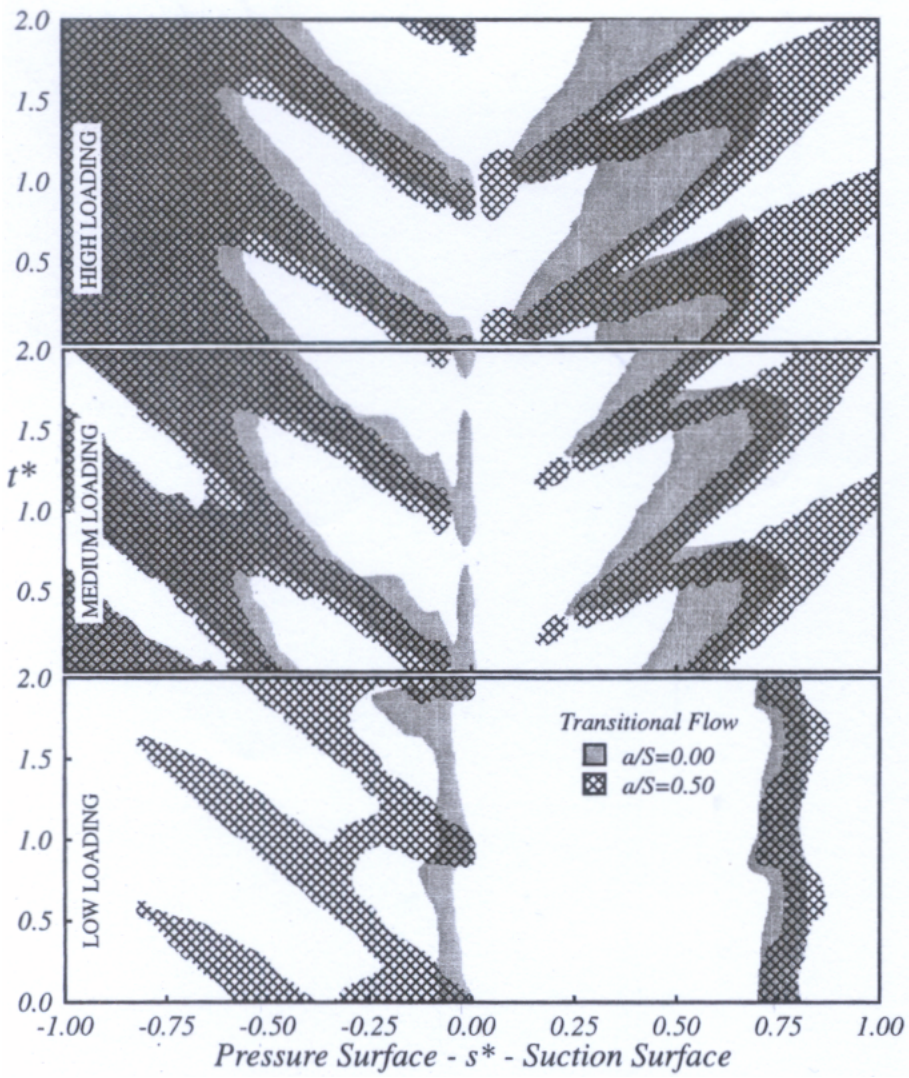

Figure 6.4: Time dependent comparison of the experimental transition region on both surfaces for all loadings. Taken from Walker et al. (1999)

6.5 2D Unsteady State: Numerical Procedure - Medium Loading

The rationale driving the 2D unsteady modelling work was to attempt to discover what the optimum set-up for a 2D simulation would be, given the available experimental data and the characteristics of the $\gamma - \theta$ model. Variations of inlet conditions were simulated and the results compared against each other and experimental data to determine which features are important in modelling unsteady wake induced transition and its subsequent effects on the boundary layer. For this, the medium loading condition was used as it contained noticeable effects from both background turbulence and wake effects from the passing rotor, including the suppression of the transitional separation bubble. The optimum set-up was then used for the low and high loading conditions.

Features of the incoming wakes which were either known to be essential for, or may have a significant effect on simulating wake induced transition were identified. Some of them were discussed in Chapter 5. These effects included; the negative jet effect in the rotor and IGV wake, increased turbulence within both wakes, the resultant effects of the IGV and rotor wakes interacting, which include turbulence, velocity and wake movement effects, the appropriate wake strength throughout the domain and its impingement on the stator suction surface, and finally the complexity of the wake structure was sought to be modelled.

The initial simulation included few of these features. Each subsequent simulation built upon its predecessor by including additional features, until the

most complex inlet conditions were replicated. Additional simulations were conducted to discover the sensitivity of relevant parameters such as wake turbulence intensity. A summary of the simulations and the features included is given in Table 6.3. The theory behind each feature, and how they were implemented in the simulation will now be explained.

The same grid used for the steady state cases was also used for the unsteady simulations. Identical boundary conditions for the outlet, symmetry and periodic boundaries were used for the unsteady cases. Only the inlet conditions were altered from the steady state case. The experimental hot wire data at 55.7% chord upstream of the stator leading edge for the medium loading case is shown in Figure 6.5. The shaded / contour chart represents the time-varying data (where t* is the time normalised by the rotor passing time) against stator pitch (where w/S is the circumferential distance normalised by stator pitch). The data on the left of the figure represents the hot wire measurement at t* for the normalised velocity $\bar{u}/u_s$, random disturbance level (Tu) and the total disturbance level (Tu_D).

Walker et al. (1997), when analysing the hot wire measurements at varying axial distances between the rotor and stator used in the medium loading case, showed that the turbulence measured by the hot wire probe is as a result of two main category of flow phenomena; stationary and random background disturbances, and periodic disturbances. By the same reasoning, the total velocity measured by the hot wire probe will also be the sum of velocity components associated with either the stationary and random flow phenomena, or the periodic flow phenomena. Consequently it was decided to model both a stationary (IGV wake & background effects) and periodic (Rotor wake)

	IGV Wake				Rotor Wake				
Case #	Tu	Vel	Neg Jet	Motion	Tu	Vel	Neg Jet	Motion	Comments
1	Exp	Simple	X	X	Simple 4.3%	Simple	X	✓	Tu effects only
2	Exp	Simple	X	X	Simple 4.3%	Simple	✓	✓	Neg jet in rotor wake added
3	Exp	Simple	✓	X	Simple 4.3%	Simple	✓	✓	Neg jet in IGV added
4	Exp	Exp	✓	X	Exp 4.3%	Exp	✓	✓	Experimental values used for both wakes
5	Exp	Simple	✓	X	Simple 30%	Simple	✓	✓	↑ Rotor Tu over Case 3
6	Exp	Simple	✓	X	Simple 4.3%	Simple	✓	✓	↑ Visc ratio (70) over case 3
7	↑ Exp	Simple	✓	✓	Simple 30%	Simple	✓	✓	IGV wake movement simulated over case 5. ↑ IGV Tu over case 5

Table 6.3: Summary of inlet wake features used in unsteady simulations for medium loading

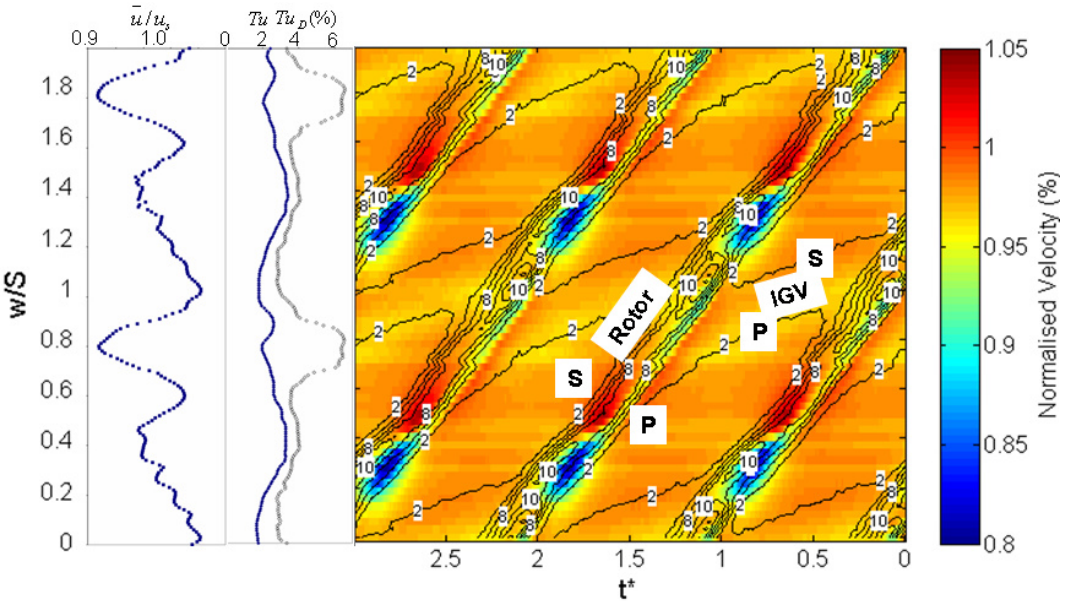

Figure 6.5: Normalised inflow velocity and turbulence at 55.7% chord axial distance upstream of stator leading edge. Shaded regions represent normalised velocity. Line contours represent turbulence intensity (%)

phenomenon at the inlet.

Stationary and periodic effects were represented at the inlet by two separate inputs; one for the velocity and one for the level of turbulence, making four separate inputs for both phenomena. Figure 6.6 shows that between the IGV wake (Tu), the disturbance level in the rotor wake ($\widetilde{Tu}$) is nearly equal to the total disturbance level (Tu_D). The background disturbance appears to have little bearing on the total disturbance level. Between the rotor wakes, the total disturbance level suggests it can be approximated by the superposition of both the stationary and periodic disturbances, with the stationary (IGV) disturbance level being the more dominant of the two. The shaded contour plot in Figure 6.5 highlights some of the effects arising from wake-

wake interaction. During the time when the IGV and rotor wakes interact, the turbulence level can be seen to rise to approximately 10%. This first seems to occur as the centre of the rotor wake passes through the suction surface side of the IGV wake. It has a greater concentration in the low velocity region, indicated by the blue shading. The phenomena creating the low velocity region will be discussed shortly. This region has the effect of increasing the disturbance level, as it is defined by the following relationship to the local velocity;

$$Tu_D = u'_{rms}/U \tag{6.2}$$

where u'_{rms} is the rms time-mean velocity and U, the local velocity.

Therefore, when the IGV and rotor wakes interact, the resultant total disturbance level rises and remains at that level for a period of time after the main interaction has ceased. From this analysis, it was decided to calculate the periodic (rotor) turbulence level from the hot wire data given in Figure 6.5. The stationary turbulence was subtracted from the total disturbance to give the periodic disturbance. This data, covering two stator pitches, was converted into a Fourier series using a Matlab script. The number of coefficients required to adequately describe the experimental data was determined through trial and error, comparing the resultant Fourier series against the experimental data. The Fourier series reduced the random component found in the data, so as to represent only the main features. This was more prevalent in the periodic input, hence the use of 'Exp' to describe the stationary (IGV) turbulence input and the use of 'Simple' to describe the periodic (ro-

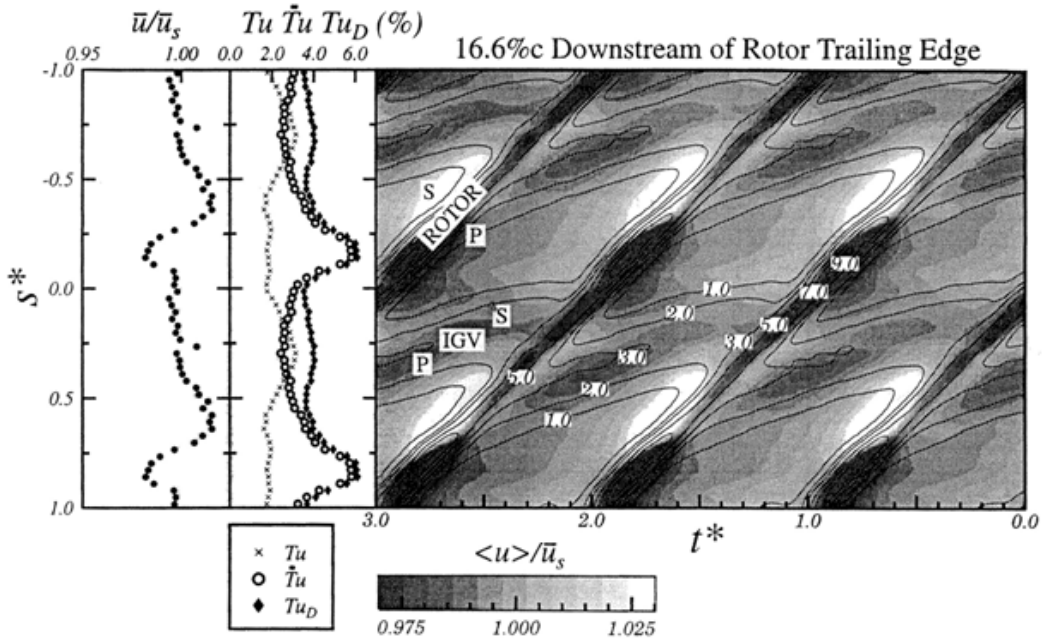

Figure 6.6: Normalised inflow velocity and turbulence from 16.6% chord axial distance downstream of rotor trailing edge. Shaded regions represent normalised velocity. Line contours represent turbulence intensity (%). Taken from Walker et al. (1997)

tor) turbulence input.

The resultant Fourier series was entered into CFX as an expression. Periodicity of the Fourier series input was ensured by using a non-dimensional distance along the inlet in the Fourier series, which repeated with every rotor passing. Using this non-dimensional distance and a repeating, non-dimensional time, the periodic input was caused to translate along the inlet from one periodic boundary to the other and repeat with every rotor passing. The stationary turbulence Fourier series input again used the non-dimensional distance created for the periodic input, but remained in the same

position at the inlet. The stationary input was positioned such that the IGV wake impinged upon the stator leading edge as given in the experimental data. The total turbulence level experienced at the inlet was given by superimposing the stationary and periodic turbulence levels. This way, the input data managed to give a good representation of the experimental data. This method was also endorsed by Walker[1].

For the first case (Run 1, Table 6.3) only the change in turbulence level within the rotor wake was simulated. This was accomplished by the method just described. The maximum disturbance level in the rotor wake was approximately 4.3%, which resulted in a total disturbance level of 6.5% between the IGV wake and 8.6% when interacting with the IGV wake. A comparison of the turbulence inputs at the inlet are shown in Figure 6.7. The undulating part of the periodic profile is due to the nature of the Fourier conversion of a straight line. The value of turbulence is below 0.5% and therefore has no significant influence on the flow conditions. The decay rate of the inlet turbulence was determined by Equation 4.18. The turbulence level of the rotor wake when impinging on the stator blade was was calculated to be approximately 4.2%, using a viscosity ratio of 25. A greater viscosity ratio would decrease the decay rate of turbulence, but CFX (ANSYS-CFX, 2005) recommend the use of a viscosity ratio as low as is feasible as high viscosity ratios close to 100 have not been fully investigated as to their effects on the $\gamma - \theta$ model. It is thought that the high viscosity values may significantly cause the skin friction to deviate from the laminar value.

A constant velocity with incidence 1.2° was applied at the inlet. This was

[1]Personal communication

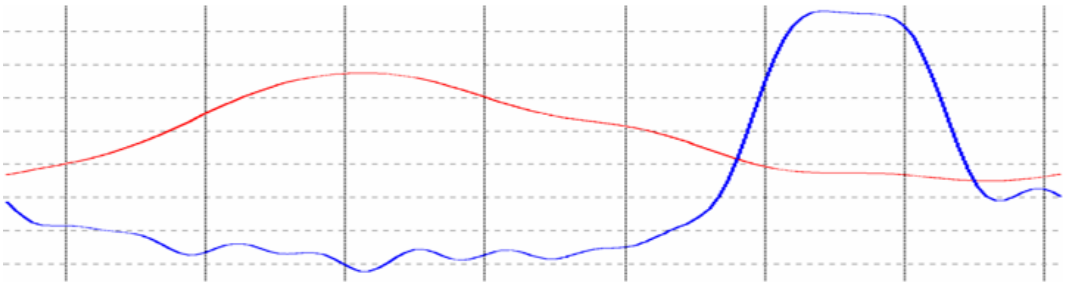

Figure 6.7: Form of the stationary (red) and periodic (blue) disturbance level inputs at the inlet for Runs 1,2,3 & 6

the same as in the steady state medium loading case. Therefore the velocity defect and its associated negative jet was not modelled. The purpose of Run 1 was to understand the impact of only a periodic disturbance on the transition behaviour and boundary development on the stator blade.

Run 2 investigates the impact of the negative jet effect caused by the velocity defect in the rotor wake. The turbulence inlet conditions remained the same as for Run 1. For this run, a velocity input Fourier series, based on the same non-dimensional distance as the turbulence Fourier series, was created to describe the rotor wake defect. To create the periodic rotor input, the hot-wire velocity data shown at the far left of Figure 6.5 was compared to both the stationary, total and periodic hot-wire turbulence data so that the periodicity was aligned. The defect (identified as a value of $\overline{u}/u_s < 1$), aligned with the periodic rise in turbulence associated with the rotor wake was used to create a Fourier series which has a value of unity apart from at the point at which the velocity defect exists. The average velocity used in Run 1 was multiplied by this input to give the velocity specified at the inlet. The components of the velocity were specified via a polynomial equation. A

constant whirl velocity was assumed, and the subsequent absolute flow angles and velocities were calculated for a range of axial velocities. The flow angles were plotted against the absolute velocity, and a polynomial curve fitted. The curve was fitted so that the incidence at the average velocity for the medium loading case gave the correct incidence of 1.2°. During the velocity defect in the rotor wake, the flow angle changed to create the negative jet effect shown in Figure 5.11.

Run 3 included the additional effect of the negative jet in the IGV wake impinging on the stator leading edge. The same principles used in the construction of the periodic velocity Fourier series were used for this task. The resulting inputs for both turbulence and velocity are shown in Figure 6.8.

The interaction of the wakes and its effect on velocity can be shown somewhat in Figure 6.5. The rotor wake is seen to widen upon interaction with the IGV wake. Two periodic regions of low energy fluid are found in the centre of the IGV and rotor wake interaction and on the suction side of the IGV wake. The latter is low energy fluid from the rotor wake. They are dependent upon the upstream characteristics of the wake, and are shown to increase in size with the increase in loading. These upstream characteristics include fluctuations of rotor lift and unsteady vortex shedding according to Walker et al. (1997). The interaction of the wakes restricts the relative motion of the fluid in the rotor wake towards the rotor trailing edge, which produces this low energy fluid. The restriction, along with turbulent wake mixing, causes an increase in time mean velocity found on the pressure side of the IGV wake just after rotor wake passing event.

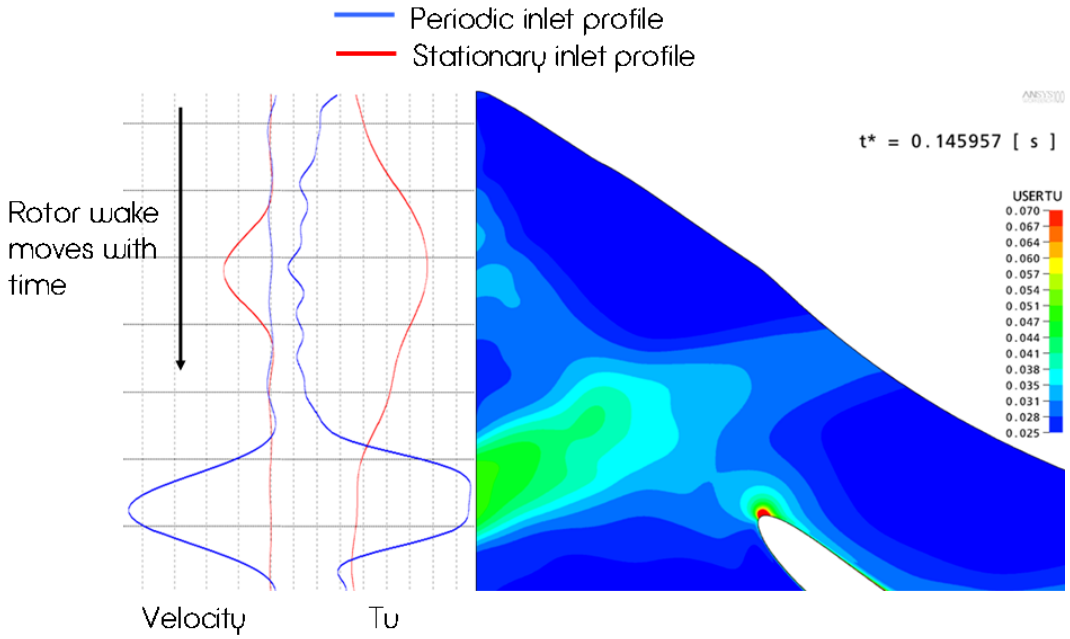

Figure 6.8: Form of stationary (red) and periodic (blue) inputs at the inlet for Runs 3 & 6. Also shown is the turbulence intensity throughout up to the stator leading edge

Observations conducted by Oro et al. (2007) on a similar low-speed axial fan showed the stationary wakes (IGV/Stator) to have the same tangential velocity as the main flow field and a reduced axial velocity. They proved that it is the axial velocity which is most affected by wake-wake interaction. A significant turbulent region was found to be transported from the separation found on the stationary blade. It is transported axially downstream and interacted with the rotor wake. As the stationary wake is chopped by the rotor blade, the two sections are transported downstream at different rates, causing a discontinuity of the wake at the rotor trailing edge. This effect was also found to have some influence over the high and low energy regions either side of the rotor wake found in the current data.

The conclusions from these studies is that wake-wake interaction is a highly complex, 3D viscous process. As such it is inherently impossible to model in 2D without a high degree of simplification. The main features to be recognised from the above work and Figure 6.5 are the low energy fluid regions, and that they occur in the region of the IGV and rotor wake interaction. In order to simulate this, it was decided to multiply the value of the stationary velocity input by the periodic velocity input and the average velocity used in the steady state simulations. This would have the effect of creating a low velocity region during the time when the periodic defect reaches the stationary defect at the inlet. Therefore only one periodic low velocity region was created with a minimum velocity at the centre of the two wakes. A high velocity region was not created. With the lack of understanding behind these processes and the 2D nature of the simulation, it was felt that this method represented a good estimation of the main velocity effect.

The literature reviewed does not attempt to comment on the relative direction of the velocity within the wakes and the high and low energy fluid regions. It is thought that in the regions, the flow may have a much greater vorticity. Due to the incomplete information available, it was decided to use the current polynomial equation for the velocity direction for this and subsequent cases.

Run 4 investigated whether it is necessary to simulate more detailed velocity and turbulence profiles at the inlet. It was thought that more detailed profiles may assist in the simulation of wake interaction and may also contain valuable instabilities which would be transported to the boundary layer on

the stator. These instabilities would then account for some of the features of wake induced transition observed in the experimental data. The Fourier series used for the turbulence and velocity inputs had the lowest amount of smoothing possible. Again, the flow angle was specified by the polynomial equation used in the previous runs.

Run 5 investigated whether the decay of the turbulence level in the wake was too great before impinging upon the stator blade. It was felt that during the earlier runs that the wake may not have been of sufficient strength upon impingement of the boundary layer to cause the boundary layer to undergo transition due to its increased turbulence. Using the same viscosity ratio, a new set of values for the periodic disturbance input were created. The rotor wake was kept at the same width, but the maximum turbulence intensity was increased to 30%. This would have the effect of increasing the rotor wake turbulence from 4% to approximately 5.3% at the stator leading edge. All other aspects of the simulation were the same as for Run 3.

Another way of increasing the level of turbulence impinging the stator blade from both the IGV and rotor wakes was to increase the viscosity ratio. Using the same conditions as in Run 3, the viscosity ratio in Run 6 was increased from 25 to 70. This had the effect of increasing the approximate level of turbulence in the rotor wake at the stator leading edge from 4% to 5.1%. To ascertain whether this value of viscosity ratio was too high, the laminar skin friction from both Run 3 and Run 6 was compared. The comparison is discussed in the results section of this chapter.

Run 7 attempted to artificially account for the shifting of the IGV wake dur-

ing its interaction with the rotor wake. Both Figure 6.5 and Oro et al. (2007) show the sudden shifting of the IGV wake due to the interaction with the rotor wake, and it progressively returning to its pre-shifted location. The rotation of the flow through the rotor passage causes the wake to progressively return to its pre-rotor-interaction position. The discontinuity occurs as the rotor wake passes from the pressure side to the suction side of the IGV wake.

A Fourier series was developed to account for the movement of the IGV wake, and was integrated into the non-dimensional, time dependent distance variable used to calculate the values of velocity and turbulence for the stationary phenomena. The timing of this was such to cause the IGV wake to suddenly shift circumferentially at the time the rotor wake is at the identical circumferential inlet position, and then slowly return to its former inlet position over the course of the periodic time period. Run 7 also included a general increase in the turbulence level of the stationary turbulence input. This was increased by a factor of 1.06, which brought the base level of turbulence (i.e. not included in the IGV) wake to 1.88% from 1.5% previously. The peak turbulence value in the IGV wake increased from 3.4% to 3.6%.

Each case was initialised from the steady state solution and run for a time period equal to six rotor passes. By this point the flow starting from the new unsteady boundary conditions had passed through the domain. Each iteration consisted of four coefficient loops, with the rms residuals converging to a value of 10^{-6}. The Courant number was always below 1.5. The case was restarted and ran for a further two rotor passes, in which transient results files were made at a rate of approximately 287 per rotor passing. The results of each of the runs will now be discussed.

6.6 2D Unsteady State: Results - Medium Loading

The results of the simulations will now be discussed in the order described in the previous section. Appendix A contains the results of the simulations. It contains inlet conditions, blade surface, boundary layer and passage data. Some figures detailing direct comparisons with experimental data or possessing a specific interest to only a particular run will be shown within this chapter.

The results for Run 1 are shown in Figures A.1 to A.10. Figure A.1a shows the normalised velocity and turbulence intensity provided by the inputs at the inlet to the computational domain. The figure only shows two rotor wake passings (t*) over one pitch (w/S) as compared to the three wake passings over two pitches in the experimental data. Only two wake passings over one pitch were simulated because of the limitation of data storage available to store the CFD results. The velocity was normalised against the constant inlet velocity specified for the steady state simulation. As no velocity defects were simulated, a constant velocity is present. The rotor wake is clearly visible as the band of contours travelling from the bottom left, diagonally towards the top-right of the figure. The IGV wake is represented by the horizontal pattern of turbulence at approximately w/S = 0.65. The maximum rotor wake turbulence occurs in the region of interaction with the IGV wake, and has a maximum value of approximately 7%. This is greater than the experimental value of approximately 5% at this point (shown in Figure 6.5). Figure A.1a

does not mimic the experimental low momentum, high turbulence fluid in the rotor wake on the suction side of the IGV wake. Here, the experimental turbulence reaches a value of approximately 9%. This was expected, as it is the low momentum fluid which has a magnifying effect on the level of turbulence as previously discussed. The turbulence level in the IGV wake is comparable with that in the experiment.

To assess the effects of wake interaction and diffusion simulated by the CFD code, a line parallel to the domain inlet (12% chord downstream) was created, and the velocity and turbulence level measured. This is shown in Figure A.1b, and is of the same format as Figure A.1a. The maximum turbulence level in the rotor wake has reduced to approximately 5% and the turbulence level in the IGV wake between rotor passings has reduced to approximately 2.5%. In general, the turbulence level has reduced asymptotically and has diffused to give a less erratic distribution across the flow field. The region of maximum turbulence within the rotor wake has stretched along the length of the wake due to diffusion and also the higher turbulence levels initially reduce at a greater rate than lower turbulence levels, reducing to a similar level of turbulence intensity to the initially specified lower turbulence levels by this position. The horizontal changes in velocity along the line are due to the downstream effects of the stagnation region at the stator leading edge. The flow at the bottom of Figure A.1b accelerates due to the flow passing the suction surface further downstream, and decelerates towards the middle of the figure as the flow stagnates at the leading edge.

The experimental hot film data showing the turbulence intermittency and the probability of relaxing flow for the medium loading case is shown in Fig-

ure 6.9. The probability of relaxing flow is a measure of the calming influence of the passing of turbulent spots in the flow. The greater the probability, the more likely the flow is being calmed. The figure shows the effect of the wakes on the development of the boundary layer on both the pressure (PS) and (SS) suction surfaces. The dark red regions represent a fully developed turbulent boundary layer and the dark blue, a purely laminar boundary layer.

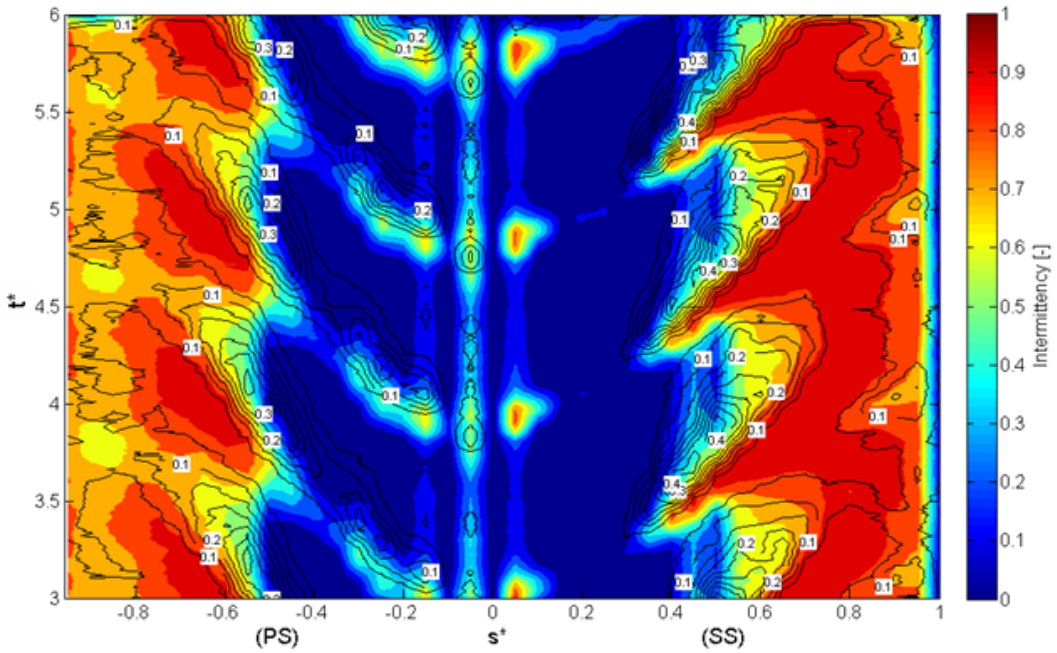

Figure 6.9: Experimental intermittency (shaded) and relaxing flow (contours) on blade surface for medium loading case

On both surfaces, the effects of the impinging wakes are clearly visible. On the suction surface, the wakes are shown to move the start of transition upstream to approximately s* = 0.25. The transition process is complete by approximately s* = 0.5. Between the wakes, the transition period is between approximately s* = 0.5 and s* = 0.75. The calmed region between the wakes

can be seen as the yellow and green shading with the relaxing flow contours overlayed. The shape of the transitional behaviour is comparable to Figure 5.10. The pattern of transition shown in Figure 6.9 indicates that the wake frequency may be such that wakes impinge at intervals roughly equal to the length of time which the calming effect has an influence on the boundary layer as the transition region between wakes does not significantly move upstream at any moment between wake passings. Transition commences just past the leading edge on both the suction and pressure surfaces, but is seen to relaminarise shortly afterwards, more quickly on the suction surface, before restarting further downstream. Walker et al. (1999) surmise that after the initial decay of transition, the intermittency remains at a low level until a critical situation is reached and sustained transition is allowed to occur. They suggest that this initial transitional region is due to the impingement of the rotor wake which will cause an increased amount of highly turbulent fluid to be deposited onto the thin boundary layer. Transition occurs, but is not sustainable. The reason why this is more pronounced on the pressure surface is that the negative jet in the rotor wake transports fluid towards the pressure surface and away from the suction surface. The pressure surface shows that transition is only fully completed in the wake path.

The blade surface data from Run 1 is shown in Figures A.1c to A.3. The normalised wall shear and turbulence intermittency for both surfaces are shown in Figures A.1c and A.1d respectively. The effect of the rotor wake can clearly been seen in both figures. The normalised wall shear is the absolute wall shear normalised by the time averaged absolute wall shear at that value of s*. The light blue regions at approximately s* = 0.65 correspond to the small separation bubble found between the wakes. This is corroborated

by examining Figure A.2a, which shows the contour lines of intermittency overlayed on a shaded plot of local skin friction. The light green region at approximately $s^* = 0.65$ on the suction surface represents the negative skin friction experienced by the surface during the separation bubble. At rotor passing time values of approximately $t^* = 0.1$ & 1.1, the bubble is suppressed by the impinging rotor wake. It is more apparent by studying Figure A.1c, where the attached wake affected boundary layer is shown by the red / yellow regions on the suction surface.

These regions are directly linked with the rotor wakes and their effect on the transition region. Figure A.1d is a plot of turbulence intermittency on a virtual surface, 0.2mm from the actual surface. It is the same data as shown in Figure A.2a. Unlike using hot films, intermittency data cannot be taken from the computational blade surface as it lies beneath the laminar sub-layer, which by definition, in CFD, has an intermittency of zero. From measurements taken in the CFD results, the edge of the laminar sub-layer in the fully developed turbulent boundary layer was located at a distance of approximately 0.2mm from the wall. Therefore, an intermittency value of one at this wall distance confirms a fully turbulent boundary layer. A small time lag between the start of transition in reality and the point at which intermittency > 0 is detected at this virtual surface as shown in Figure 6.10. Here, the intermittency in the boundary layer on the suction surface for Run 1 is shown along with the surface at 0.2mm from the wall (shown by light green line in the laminar region of the boundary layer). Transition starts at the left of the figure as indicated by the region of red jutting into the laminar (blue) boundary layer. The virtual surface at 0.2mm from the wall does not experience a change in intermittency for a short distance afterwards (off past

the right hand side of the figure). Therefore the intermittency results cannot be taken as read, but more as a qualitative inference of the behaviour of the transition region.

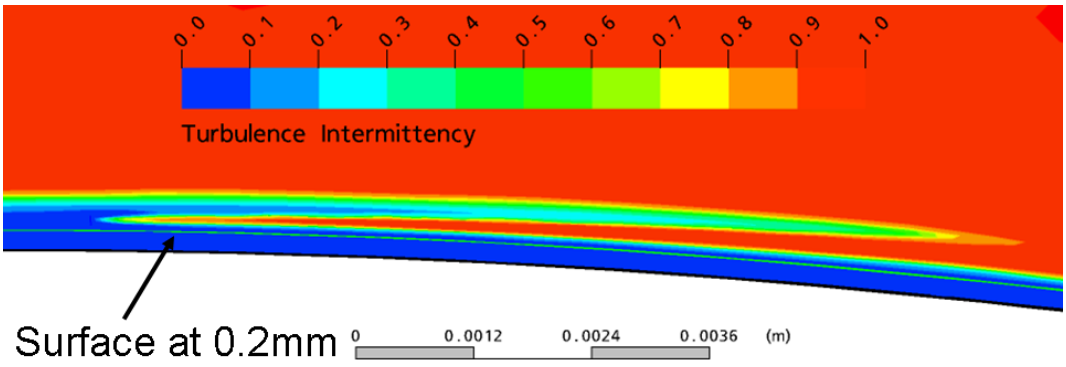

Figure 6.10: Intermittency in the boundary layer on the suction surface of Run 1 stator

The intermittency on the suction surface shows that in the rotor wake, the transition region moves upstream slightly and is elongated (shown by the regions of lighter blue shading), occurring between approximately s* = 0.5 and 0.85. This is because transition is now occurring in an attached boundary layer, rather than a separation bubble as in between the wakes. Transition occurs in damped mode. However, the effect on the transition region of using an increased turbulence level alone for the rotor wake is small. Similarly changes in the pressure surface boundary layer are small. A slight increase in both normalised wall shear and local skin friction in the wake path can be observed. This corresponds to a moving upstream of the transition region, although transition is still not complete by the trailing edge.

The rotor wake has the effect of slightly increasing momentum thickness and decreasing the boundary layer shape factor on both surfaces. This is confirmed by studying Figures A.3a-e. Integral parameters are plotted against rotor passing time at various distances along the suction and pressure surfaces. Only small variations are found in the parameters. The variation in momentum thickness is more pronounced at greater values of s*, as the boundary layer has grown at different rates due to the wake influence.

Figure A.4a-e shows the time variation of intermittency at the same values of s* as for Figure A.3. Plots a and d indicate that the wake has caused the start of transition to move upstream of those values of s* on the suction and pressure surface respectively. This is shown by the lack of a laminar (blue) region visible above the main laminar boundary layer. If compared with Figure 6.10, it is clear that the boundary layer at $0 < t^* < 0.6$ & $1 < t^* < 1.6$ in Figure A.4a, shows the approximate starting point of the transition region between wakes. From this, it is inferred that transition between wakes starts at approximately s* = 0.35 on the suction surface, and s* = 0.4 on the pressure surface, with the pressure surface transition starting later than the suction surface owing to the reduced gap between the laminar regions. This is similar to the results found for the steady state case. Figures A.5a & d confirm this by showing an increase in turbulence intensity in the regions where transition has taken place further upstream in the wake path. They also show the time lag experienced by a higher level of freestream turbulence being transported through the boundary layer. Plot c, at s* = 0.8 on the suction surface, shows two small regions close to the surface at t* = 0.8 & 1.8. At this point the boundary layer is at its separation point, allowing turbulence to directly impinge upon the blade surface.

Figure A.4c highlights an anomaly in the $\gamma - \theta$ model. A region of artificially high (i.e > 1) intermittency is found above distances of 1.4mm from the wall. This is caused by a rapid change in shear strain rate in this region. The model predicts that the boundary layer is separated. For separated boundary layers, transition is allowed to artificially increase above 1 as shown in Chapter 4, and the already fully turbulent boundary layer experiences a further quasi-transition process.

Figure A.6 shows tangential velocity plots at various positions along the blade surfaces. It confirms the time at which the wake affects the boundary layer, by showing a slight thickening of the boundary layer. Figures A.7 to A.10 show the effects of the wake in the passage at four different values of t* which correspond to the rotor wake impinging at the leading edge, at s* = 0.25, 0.5 and 0.75. Figure A.7 shows the turbulence of the wakes travelling through the domain. Two instances of geometry are shown for clarity and the maximum turbulence value in red is equal to 6.6%. The plots show the IGV wake impinging at the stator leading edge. The rotor wake travels through the domain and is rotated slightly as it travels through the passage between the blades. The rotor wake passing over the suction surface is stretched, whilst in the centre of the passage its thickness is slightly reduced. This is in accordance with other literature, such as Lodefier and Dick (2005), who observed a similar pattern. However, unlike this simulation, they observed the wake impinging on the pressure surface to decrease in thickness, rather than thicken as observed in Run 1. They simulated full wake effects within a turbine, within which the negative jet transports fluid from the pressure surface towards the suction surface. The negative jet works opposite in a

compressor, transporting fluid from the suction surface towards the pressure surface. The current pattern results are due to two effects. Firstly, the turbulence intensity naturally increases as the flow starts to decelerate below pre-blade passage freestream values just past the leading edge. Secondly, for a similar reason, there is a large area of higher turbulence intensity flow in the stagnation region, which is located on the pressure side of the leading edge. Some of this fluid is transported along the pressure surface. Similarly, the turbulence intensity along the suction side is reduced as the flow accelerates sharply before gradually reducing to pre-blade passage freestream values.

Figure A.7 also demonstrates that there is perhaps too much numerical diffusion of the IGV and rotor wakes. The edges of the wakes become blurred and are not akin to a clean cut cross shape as one would expect. The CFD code has started to mix the boundaries of the wakes so much so that it is sometimes difficult to distinguish between the wakes when they are in close proximity. The maximum turbulence in the rotor wake occurs when mixing with the IGV wake as expected.

The results for Run 2 can be seen in Figures A.11 to A.20. Run 2 differs only from Run 1 in that the rotor wake includes a velocity defect. Figures A.11a & b show a similar pattern for turbulence at the inlet and at 42.7% chord upstream of stator leading edge as for Run 1. The rotor wake velocity defect is clearly visible as the band of green shading extending towards the top right of the plots. Downstream of the inlet (Figure A.11b), the rotor wake defect and stagnation velocity defect interact to produce a non-uniform slight velocity defect of approximately 1% between rotor wakes. The combined velocity defects in both the rotor and stagnation region create a greater defect within

the rotor wake where it passes through the stagnation affected region. An additional 2% defect is experienced in this region, shown by the light blue shading in Figure A.11b. As expected, this does not fully represent the experimental data shown in Figure 6.5.

To investigate whether the rotor wake velocity defect is transported through the computational domain, a plane parallel to the blade span, mid-way through the domain was created. The velocity components at each node were time averaged. This data was then compared against the velocity components at a given time-step, and the relative velocity calculated. The rotor wake velocity defect was shown to exist throughout the domain. An example of this is shown in Figure 6.11. Fluid in the rotor wake is transported away from the suction surface and toward the pressure surface.

The velocity defect in the rotor wake has a much more marked effect on the development of the boundary layer than the increased turbulence intensity. Figure A.11b shows the normalised wall shear on both surfaces. The effect of the wake is to cause the transition start point to move further upstream, thus reducing the normalised wall shear (blue streak on suction surface), transition is complete by approximately s* = 0.6 (shown in Figure A.11c). The dark red region of high wall shear between s* = 0.5 & 0.7 indicates that a turbulent boundary layer is present. Indeed it is confirmed by the higher skin friction within the wake path shown in Figure A.12a. As transition occurs earlier in the wake path, the flow towards the trailing edge tends to separate further upstream, as shown by the deeper turquoise areas in the suction surface at s* > 0.8. The separation point of the boundary layer on the suction surface is also demonstrated by the dark blue shaded meandering

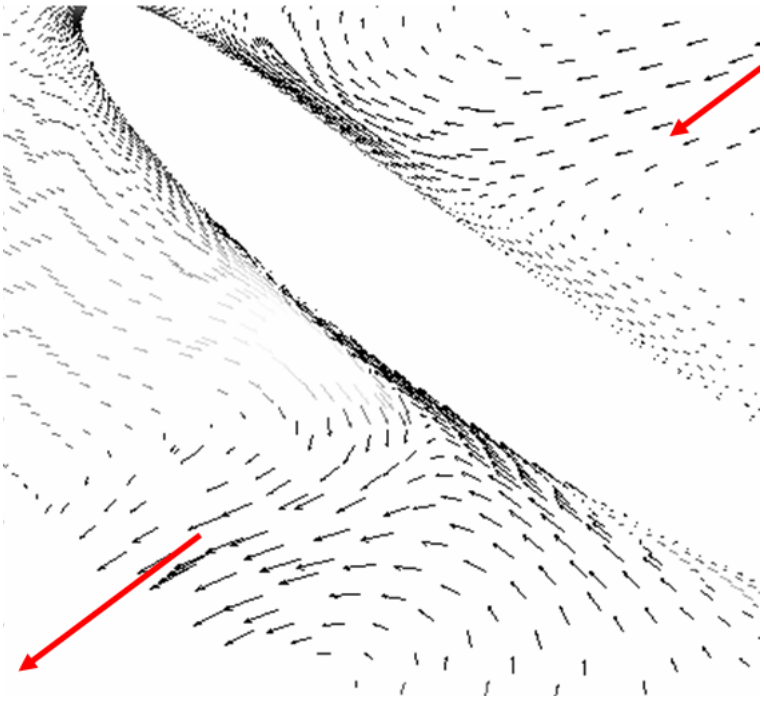

Figure 6.11: Relative velocity vectors showing rotor wake defect. Red arrows represent the position of the rotor wake

line between s* = 0.8 & 1 in Figure A.11c. Here, the normalised wall shear must be zero. Between the wakes, the separation occurs further downstream. However, the wake affects the boundary layer such that terminal separation only occurs a significant distance towards the trailing edge in comparison to separation in the wake path for at least t* = 0.2 after the wake has passed.

The CFD intermittency plot (Figure A.11d) gives a similar form to the experimental data (Figure 6.9). The exact form is not replicated as transition between the wakes is controlled by the small separation bubble which is now located approximately between s* = 0.55 - 0.65. The length of the bubble increases with time after the rotor wake passing. Although transition is

showed to start upstream of s* = 0.35, by inspection of Figure A.14a, it is not as clearly observed in Figure A.11d. This is because of the thickness of the laminar region of the boundary layer exceeding the distance from the surface at which the intermittency data was taken (see Figure A.14a). A small increase in intermittency can be seen by the arrow-like of lighter blue shading along the wake path.

Figures A.11c and A.11d show only a small effect on the point of transition on the pressure surface. Indeed in Figures A.11c and A.12a do not appear to give patterns consistent with the wake paths expected. A reduction in normalised wall shear occurs at approximately the same time along most of the pressure surface. The wake reduces wall shear, but Figure A.12a indicates by only an insignificant amount. In contrast, there is a significant indication of the wake path on the pressure surface if the momentum thickness and shape factor are studied (Figures A.12b & c respectively). The momentum thickness in the wake path can be seen as the diagonal light blue regions, and the shape factor, the diagonal dark blue regions. The same differing patterns of wall shear and integral parameters will be shown to be consistent throughout the remainder of the cases. Further study into this matter is required. The shape factor suggests the boundary layer in the wake path is fully turbulent, but a video showing the time dependent intermittency in the boundary layer around the blade suggested that transition starts at earliest s* = 0.4. The boundary layer takes an entire rotor passing period to return to its pre wake-affected level, as shown in Figures A.3d & e. This is not uncommon, as observed by Howell (1999).

Figures showing the momentum thickness and shape factor (Figures A.12b

& c respectively) for the suction surface highlight an interesting effect of the CFD code. The maximum momentum thickness and lowest shape factor are not aligned as one might expect. Figure 6.12 shows the position in time (t*) of the measured greatest momentum thickness and shape factor for the length of the suction surface. Momentum thickness keeps to the expected wake path, whereas there is a significant deviation of the position of maximum shape factor from the wake path. The deviation represents the region of the boundary layer affected by the wake. The wake affects the post wake boundary layer such that it remains less laminar for a period before returning to its post wake state. This may be viewed as a calmed region. This calming effect is diminished by s* = 0.7 when the point of maximum momentum thickness and maximum shape factor again correspond. The greatest region of calmed flow appears to be at s* = 0.3, which corresponds to the onset of transition in the wake path. A similar pattern of relaxing flow (calmed region) is shown in Figure 6.9, albeit it is approximately 0.1s* further downstream.

Figure A.14b & c suggest that transition is nearly complete both within and outside the wake affected boundary layer at s* = 0.55. Transition has been fully completed for the whole boundary layer at s* = 0.8. Plots d & e show that the rotor wake has not had a significant effect on the transition process on the pressure surface. More significant consequences can be seen in Figure A.13d. The wake passes s* = 0.4 at t* = 0.1 and 1.1. The boundary layer becomes turbulent before steadily returning to its pre-wake laminar state at t* = 0.6 and 1.6. Prior to wake passing, a sharp rise in shape factor and a reduction in momentum thickness and displacement thickness is observed, similar to that of Howell (1999) for a turbine suction surface. Figure A.14d

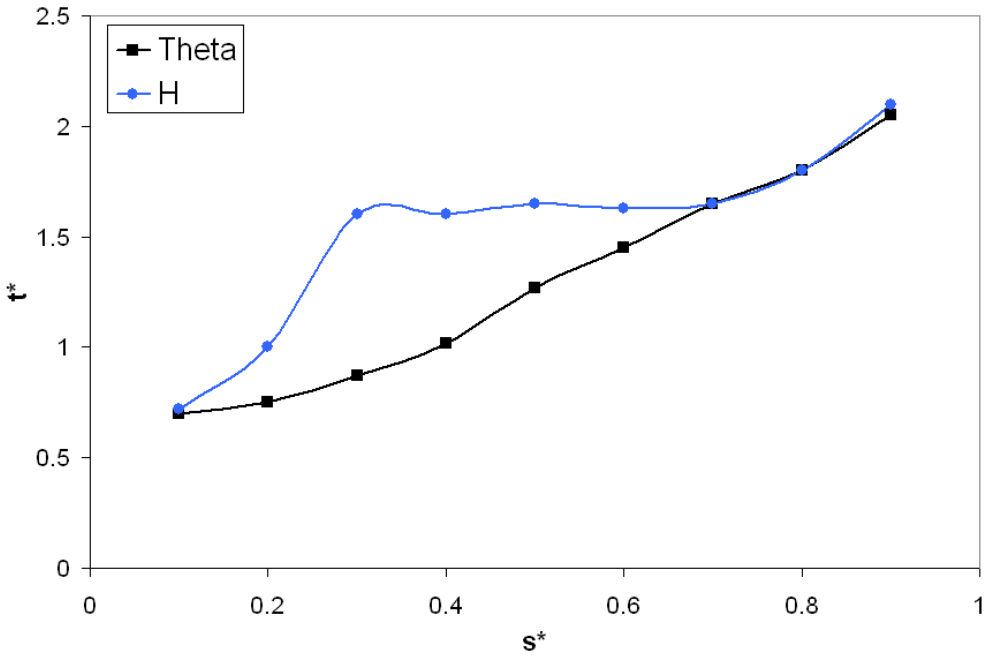

Figure 6.12: Position of highest momentum thickness and shape factor on the suction surface for Run 2

shows a roughly wedge shape introduction of high intermittency into the pre-wake boundary layer, starting at t* = 0.7. The wake does not pass this point on the pressure surface until t* = 1.2. The local acceleration of the fluid prior to wake passing (Figure 6.11) and subsequent local deceleration post wake may locally alter Re_{θ_t} to encourage, then discourage transition. The increase in shape factor (shown in Figure A.3d) suggests that the boundary layer is near to separation. This would conclude that the wake suppresses the tendency to separate. The timing of these undulations correspond to the higher normalised wall shear stress found along nearly the entire length of the pressure surface. The greatest normalised wall shear in the streak at t* = 0.1 and 1.1 is found at s* = 0.4. However, there is no consistent pattern linking these two figures.

The reason for the early downstream influence of the wake may also be due to the transport of turbulence from the stagnation region across the early part of the pressure surface. Figures A.15d and A.17 (top left plot) show that as the wake impinges on the leading edge (t* = 0.5), turbulence is transported across the pressure surface in advance of the wake. Lower velocity fluid is also transported as shown in Figure A.16d (see t* = 0.65).

The negative jet in the wake has a more visible affect on the profile of the boundary layer than increased turbulence alone. Figures A.15a and A.16a both show a more significant change in the boundary layer turbulence and velocity levels during wake passing than for Run 1. The greater instabilities and the change in velocity profile caused by the negative jet on the wake passing over the suction surface are transported into the boundary layer. Figure A.16a highlights the lag involved in the transportation of these effects. The wake positioned at t* = 0.7 does not affect the inner region of the boundary layer until t* = 1. Figure A.15a confirms this by showing that the initial instability is transported through the boundary layer starting at t* = 0.9.

The varying position of the start of transition for both surfaces with time is shown in Figure A.18. The start of transition moves upstream as the rotor wake impinges on the blade. The change is more visible on the suction surface than the pressure surface. The rotor wake maintains its correct profile through the domain (Figure A.17) more than for Run 1. The wake expands at the suction surface but also at the pressure surface. A large area of higher than freestream turbulence builds up towards the pressure surface. As the relative wake flow meets the pressure surface, a low velocity region develops

(see dark blue region in Figure A.20). Turbulence intensity naturally rises as the velocity decreases in this region, even though the turbulent kinetic energy decreases as the wake travels through the passage. Figure A.20 also shows the effect the rotor wake has on the suction surface velocity. Maximum velocity is reduced as the wake passes, and returns to pre-wake levels once the wake has passed.

The results for Run 3 can be viewed in Figures A.21 to A.30. Run 3 features a velocity defect in the IGV wake which was not included in Run 2. A comparison of Figures A.21a & b, and Figures A.11a & b reveals a similar pattern in the flow at the inlet and upstream of the leading edge. The IGV velocity defect is clearly visible as the band of horizontal orange shading in Figure A.21a and green shading in A.21b. The velocity deficit in Figure A.21b is reduced further when the IGV and rotor wakes meet. This region is more comparable in magnitude to the experimental values than for Runs 1 & 2. Within it, the maximum value of turbulence intensity rises to approximately 5.5% from 5% in Run 2. The region extends in the rotor wake past the suction side of the IGV wake, to replicate somewhat the behaviour of the experimental wakes. It remains for a short time period (0.15t*) within the IGV wake before it is mixed out. Similar to experimental results, there is a reduction in the magnitude of the velocity defect just after the pressure surface side of the IGV wake within the rotor wake. Fluctuations of higher velocity seen in Figure 6.5 are observed either side of the rotor wake found at $w/S = 0$.

A comparison of normalised wall shear between Run 2 and Run 3 finds similar patterns, albeit the features of high and low shear are intensified for Run 3. It is thought that due to the IGV wake defect, the flow angle is locally

altered within the wake. A comparison of flow angle to the axial direction for Runs 2 & 3 is shown in Figure 6.13. The flow in the region of the IGV wake path has a slightly higher flow angle for Run 3 than Run 2. This impinges on the stator LE, changing the receptivity of the boundary layer to incoming disturbances at the LE. These disturbances are propagated downstream through the boundary layer. The balance of turbulent flow passing each surface is also altered, with the flow preferring to go past the suction surface.

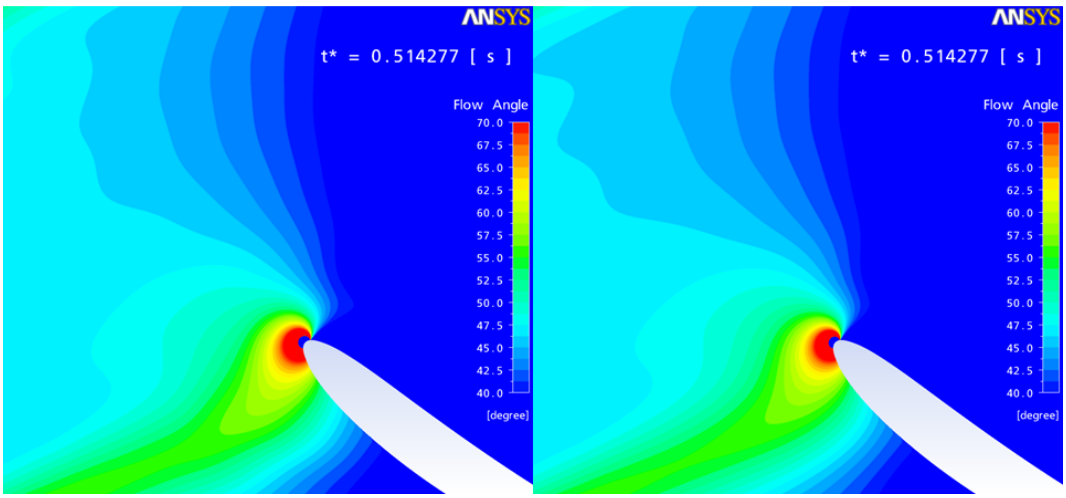

Figure 6.13: Comparison of flow angle near the leading edge for Run 3 (left) and Run 2 (right)

The suction surface shows some variation in the pattern of wall shear compared to that in Run 2. The region of high wall shear just after transition is complete (s* = 0.4 - 0.65) is elongated as compared to Run 2. The regions of potential separation shown by the blue shading at the same s* are also lengthened. The line of wall shear = 0, where terminal separation occurs is also brought forward by approximately 0.05s*. The regions of separation

are intensified as a larger separation region is present. Figure A.25c shows the separated shear layer at s* = 0.8 by the high level of turbulence intensity. This matches the upstream movement of the separation point shown in Figure A.21c. Separation occurs after s* = 0.8 where the region of high turbulence meets the t* axis (Figure A.25c).

The height of the laminar boundary layer on the pressure surface has been reduced by approximately 0.2mm as compared to Run 2, as shown in Figure A.24d. This is directly due to the increased flow angle brought about by the IGV wake deficit. The boundary layer develops at a faster rate. The influence of the transition process is observed at an earlier stage as can be seen in Figure A.21d. Here, the influence of the rotor wake can be seen as the parallel bands of lighter blue running from right to left on the pressure surface. Transition is still not complete at the trailing edge in contradiction to the experimental data.

Transition on the suction surface appears to be very similar to Run 2. Transition starts further upstream, as shown by comparing Figures A.24a and A.14a. Although the laminar boundary layer is shown to have the same thickness between wakes, the effects of the wedge-like start of transition (Figure 6.10) are not seen. In the rotor wake, the laminar part of the boundary layer is only 0.15mm thick, a reduction of approximately 0.05mm from Run 2. Consequently, the effects of transition are more evident within the wake path. The high intermittency within the wake is shown further upstream (Figure A.21d).

Local skin friction on the pressure surface is increased along with the mov-

ing upstream of the start of transition (Figure A.22a) due to a more rapid boundary layer development. As already noted for the normalised wall shear, the regions of higher skin friction found on the suction surface are brought upstream, and the suppression of separation increases at s* = 0.5 as shown by an increase in the level of positive skin friction between wakes. This is an indication of a stronger calming influence of the wakes. The figure also highlights the moving upstream of the terminal separation region by the larger regions of turquoise found toward the trailing edge.

The pattern of earlier development of a turbulent boundary layer on the pressure and suction surfaces is continued when viewing the momentum thickness and shape factor in Figures A.22b & c. The high momentum thickness region on the pressure surface in the wake has a greater effect on the post wake boundary layer. This is demonstrated by a lower shape factor in and between wakes, suggesting that an effect similar to a calmed region may be at work. The boundary layer recovers to laminar like values at 0.2t* before the next wake passes. Turbulent flow within the rotor wake path is further upstream than Run 2, and a subsequent reduction in the strength of the laminar flow post wake occurs, as shown by the reduction of the yellow shading between s* = 0.1 - 0.4 (Figure A.22b).

Figure A.26a demonstrates that the initial development of the boundary layer is affected to a greater extent in Run 3 than in Run 2. There is a larger difference in boundary layer thickness post wake passing (s* > 0.6) than for Run 2. The lag between wake passing and boundary layer thickness is more due to effects at the leading edge. Turbulence and velocity profile changes in the boundary layer at the leading edge are caused when the wake impinges

at the leading edge. They then travel through the boundary layer at a lower velocity than the wake. The velocity plots also show that the velocity is not constant between wake passings, creating further modulation in the boundary layer as shown with the local skin friction.

The rotor wake structure passing through the domain (Figure A.27) has a structure more conformed to past experimental observations than either Run 1 or Run 2. The wake retains its higher turbulence as it convects through the passage. An appropriate amount of rotation is achieved, and the wake spreads at the suction surface. The wake at the pressure surface also stretches and widens throughout the passage. As with the previous runs, there are no separate vortices to be found on the suction side of the rotor wake as normally found (Oro et al., 2007). These vortices are the result of the interaction of the IGV and rotor wakes. The lack of viscous mixing of the wakes is one of the greatest deficiencies of the code for this application.

Plots of velocity through the domain are shown in Figure A.30. They show a greater variation of velocity during the wake passing period than for Run 2. The regions of lower velocity on both the suction and pressure surface regions during wake passing are strengthened. This also is shown in Figure A.29 where a greater turbulence intensity is observed, particularly on the pressure surface, due to the lower velocity found in the wake regions.

A comparison between the experimental data, Run 3 results and the MISES results of Solomon et al. (1999) is contained in Figure 6.14. Contours of $\gamma = 0.1$ are plotted for both surfaces during two rotor passings. The MISES results plotted here are those from the standard code with both the Abu-

Ghannam and Shaw correlation and the e^N mode active. The MISES results were also time shifted along a line of $0.7U_\infty$. No such correction was made for the current results.

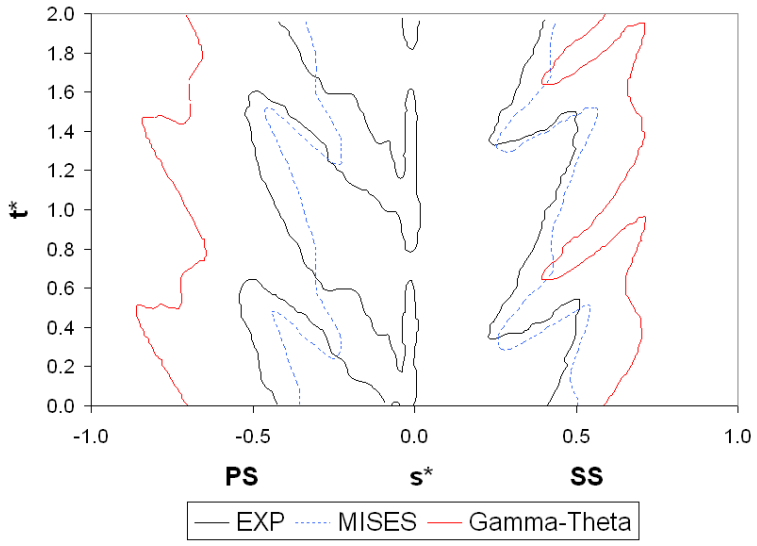

Figure 6.14: Comparison of $\gamma = 0.1$ contour lines, indicating the start of transition, for experimental results, MISES (Solomon et al., 1999) and $\gamma - \theta$ models.

The general agreement between the MISES results and experimental data is good, although transition within the pressure surface wake path does not occur far enough upstream to agree well with experiment. In contrast, the results for the $\gamma - \theta$ model present a poor comparison for the streamwise position of transition onset. However, the correct streamwise position of transition completion has already been shown to have been predicted through a comparison of Figures 6.9 and A.21d.

This poor comparison for the start of transition is due to the use of a virtual

surface at a fixed distance from the wall. As shown in Figure 6.10, a lag exists before the increase in intermittency reaches the virtual surface. The transition region as seen by a slice normal to the blade surface, is very thin. The value of intermittency registered on the virtual surface rapidly changes from laminar to turbulent due to small changes in the thickness of the laminar region of the boundary layer, when the transition region normal to the surface is close to the same distance from the wall as the virtual surface. This is observed by the closeness of the intermittency contours in Figure A.22a. The virtual surface experiences a rapid rise in intermittency during the regions where transition is nearly complete. Therefore, transition can start significantly upstream of the point at which the virtual surface detects an increase in intermittency. Further intermittency plots indicated that transition starts in the wake path on the suction surface between $0.25 < s^* < 0.3$ which is more comparable to experimental evidence. Whilst the method of using a virtual surface at a specified wall distance returns a good comparison of the end of transition, it is not appropriate to be used to determine the start of transition with the $\gamma - \theta$ model.

The stagnation pressure loss for Run 3 was compared with the profile loss given for the steady state simulation. The stagnation pressure loss coefficient (Y_p) is given by;

$$Y_p \approx \frac{2(\theta_{SS} + \theta_{PS})}{pcos\alpha_{exit}} \frac{u_{exit}^2}{u_{inlet}^2} \tag{6.3}$$

where θ_{SS} and θ_{PS} are the time-averaged momentum thicknesses at 95% suction surface and pressure surface distance respectively.

The unsteady pressure loss, Y_p=6.68% as compared to the steady state pres-

sure loss of Y_p=6.52%, gives only a 2.3% increase in loss for the unsteady calculations. This may appear only a small amount at first, but this can be explained when considering the point of suction surface terminal separation between the steady state case (Figure 6.3) and Run 3 (Figure A.21c). The steady state suction surface separation point is approximately s*=0.76, whereas for Run 3, the earliest separation occurs is approximately s*=0.8.

Figure 6.15 shows the momentum thickness of both the pressure and suction surfaces at s*=0.95 for Run 3 normalised by the steady state momentum thickness. Even though the separation occurs later, there is an increase in the momentum thickness towards the trailing edge of the suction surface. This is likely to be due to the earlier transition start point experienced by the wake passing effects, which increases the turbulent wetted area of the surface. As suction surface terminal separation already occurs well before the trailing edge in the steady state simulation, the rotor wakes are not able to suppress it sufficiently to reduce the pressure loss at the trailing edge.

The momentum thickness at s*=0.95 on the pressure surface is much smaller than that of the suction surface, as shown in FigureA.22b. Even though Figure 6.15 shows a much larger increase in the peak momentum thickness as compared to the steady state, it also shows regions where for almost a quarter of the rotor passing time, the momentum thickness is reduced below that of the steady state value, leading to a reduction of loss during this period. Perhaps more significantly, as the momentum thickness on the pressure surface is much less than that of the suction surface, any increase in time averaged momentum thickness has a much reduced effect on loss as compared to the suction surface.

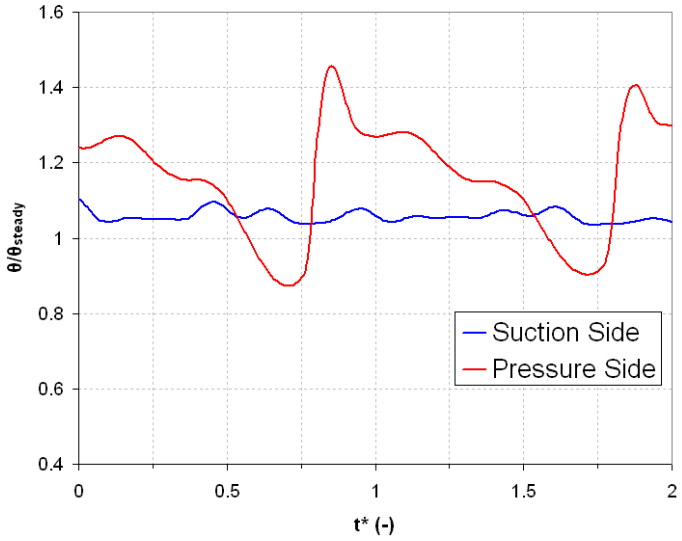

Figure 6.15: Run 3 normalised momentum thickness for both pressure and suction surfaces at s*=0.95. Momentum thickness normalised against steady state momentum thickness.

Experimental values with little smoothing were applied for the velocity and turbulence inputs for Run 4. Velocity defects were included in both wakes. Figures A.31 - A.40 show the CFD results from Run 4. In the main, the features discussed in Run 3 were all present in a similar form in Run 4. Differences between Run 3 and Run 4 results were small and were partially due to the greater variation about the general trends used for the inputs at the inlet.

The inlet velocity and turbulence intensity were more comparable to experimental data. A lower value of velocity in the IGV / rotor wake mixing region is present (Figure A.31a) but is not as low as the experimental value (see Figure 6.5). This decreases by the time the flow passes the point 42.7% upstream

of the stator leading edge (Figure A.31b,) but only reduces to $\frac{<u>}{u_s} = 0.87$. The experimental value is $\frac{<u>}{u_s} = 0.8$. These plots show two regions of higher turbulence within the rotor wake. These regions correspond to the low velocity regions. The higher velocity flow either side of the rotor wake is clearly visible in both plots along with the higher velocity regions bordering the pressure side of the IGV wake and both sides of the rotor wake. The pattern of velocity in Figure A.31b is more in common with the experimental values given further upstream. Some wake mixing has been achieved; The region of lower momentum fluid found during the IGV and rotor wake interaction is larger than for Run 3. In general, the velocity of the flow outside the wakes has increased by approximately 1% from that in Run 3.

The development of the unsteady boundary layer is very similar for Run 4 as for Run 3. The same features are found as for the previous run. The suction surface exhibits a slightly thinner wake influence as shown in both the normalised wall shear and the intermittency plots (Figures A.31c and d respectively). The normalised wall shear shows that while the intensity of the effect along the wake path has not been reduced, it has lengthened in the streamwise direction and shortened in its time duration. The intermittency plot shows that between wake passing, the transition region has a less consistent end point. Variations in both momentum thickness and shape factor (Figures A.32b and c respectively) allude to a secondary effect occurring just after the wake at the leading edge. It is thought that either the regions of higher velocity either side of the rotor wake on the pressure surface side of the IGV wake, or the additional low momentum region in the rotor wake cause a secondary acceleration in the transition process. These effects cause an early transition and suppress the separation bubble found between the

wakes. The yellow shaded regions at s* = 0.7 on the skin friction and intermittency figure (Figure A.32a) show the extent of the post wake calmed region.

On the pressure surface, the transition region has moved upstream, both in and between the wakes. It is thought that this is due to the general reduction in the IGV wake velocity. As the inlet flow angle is linked to absolute velocity via a polynomial, when the velocity decreases, the flow angle (incidence) increases. The start of the transition region has also moved upstream in Run 3 when the IGV wake deficit caused the flow angle to increase. As the flow angle has increased again, the transition region has moved yet further upstream. The momentum thickness is see to increase both in and between the wakes. Again, a similar double effect of increased momentum thickness approximately mid-way between wakes on the pressure surface is present. Highly laminar flow is only visible 0.2t* prior to wake passing, and transforms to turbulent flow by s* = 0.7.

The integral parameter comparison plots confirm that there are two influences in the boundary layer (see Figure A.33). The second effect, increases the momentum thickness just after wake passing. It travels at a slower rate through the boundary layer, so on the suction surface, by s* = 0.55, the time interval between the effects has grown. The pattern is similar for the pressure surface.

Intermittency (Figure A.34), turbulence (Figure A.35) and velocity (Figure A.36) boundary layer plots all show similar patterns to Run 3. The artificially high intermittency at s* = 0.55 on the suction surface is reduced as the

separation bubble on the suction surface has moved 0.05s* downstream. A sharp reduction of turbulence can be seen either side of the wake turbulence at $s^* = 0.35$ on the suction surface. The velocity plots on the suction surface show that there is a greater velocity in the flow between the wakes and that the flow between the wakes is not as uniform as it has been in previous runs (see Figure A.36a). This may be the cause of the secondary effect already described.

Figure A.38 shows a build up of artificially high intermittency in the stagnation region of the leading edge before the rotor wake reaches the leading edge. It is transported along the suction surface shear layer by the wake, until it is dissipated in the passage. The wake-induced and post wake-induced transition regions can also clearly be seen. They do not seem to indicate that this region of high intermittency affects the transition region. Plots of the turbulence intensity in the passage (Figure A.37) show a greater rotation of the wake as it travels through the passage.

The sensitivity of the $\gamma - \theta$ model to the level of turbulence in the rotor wake was examined in Run 5. Run 5 had the same inlet conditions as Run 3, except that the rotor wake turbulence level was 30%, rather than 4.3%. The results of Run 5 are contained within Figures A.41 to A.50. The larger turbulence within the rotor wake is apparent when viewing the turbulence and velocity at the inlet and 42.7% upstream of the stator leading edge (Figures A.41a & b respectively). The turbulence level between rotor wake passings and the velocity field remains the same as in Run 3. The IGV wake turbulence is thickened slightly between the rotor wake passing, due to the increased diffusion of turbulence from the rotor wake to the IGV wake. Figure A.41b shows

the pattern of turbulence and both the pattern and magnitude of velocity to be similar to Run 3.

Figures A.41c to A.50 indicate there is no additional significant effect upon the development of the boundary layer on both surfaces as compared to Run 3. As the rotor wake has a higher turbulence level, the diffusion process thickens the rotor wake compared to Run 3, as shown in Figure A.47. The rotor wake retains the same shape as it travels through the domain, as in Run 3, but contains a higher turbulence level. This difference brings about a small change within the boundary layer on both surfaces. On the pressure surface, the transition region within the wakes is thickened and moved upstream slightly (Figures A.41d & A.42a (see line of $\gamma = 0.1$)). This indicates that transition occurs at a faster rate than in Run 3. A reduction in shape factor on both surfaces (Figure A.42c) indicates a more turbulent boundary layer in the wake path.

In the wake path on the suction surface, the turbulent boundary layer also develops at a faster rate. The intermittency plot (Figure A.41d) shows the fully turbulent region of the boundary layer to move upstream by 0.05s*. The level of intermittency within the wake path continues to develop in Run 5 until a fully turbulent boundary layer is observed at s* = 0.55. This is opposite to Run 3, where the intermittency within the wake path decreases between s* = 0.45 - 0.5 (Figure A.21d). The shape factor in the wake region between s* = 0.35 - 0.65 decreases, confirming the above observations that the boundary layer is now more developed than in Run 3. Between rotor wake passing at $s* < 0.45$, shape factor is also reduced. This would confirm that the model has a type of calming influence over the post-wake boundary

layer. This may also be the reason for the slightly reduced artificially high intermittency regions at s* = 0.55 on the suction surface (Figure A.44b). Here the separation is suppressed for longer than Run 3, and has less time to fully re-establish itself, post calming region.

A comparison of Run 3 and Run 5 shows the velocity defect is more important than the level of turbulence. Run 6 examined the sensitivity of the $\gamma - \theta$ model to the viscosity ratio specified at the inlet. The viscosity ratio was previously used to determine the decay of turbulence and hence the position of the transition region along the flat plate in Chapter 4. The results for Run 6 can be seen in Figures A.51 to A.60. The results can be directly compared with Run 3, as the viscosity ratio at the inlet is the only difference between the two set-ups.

Figure A.51a shows there is no difference between Run 6 and Run 3 at the inlet, as the viscosity ratio will not have affected the flow at that point. At 42.7% upstream of the leading edge, the high level of turbulence in the rotor wake at the point of mixing with the IGV wake has thickened significantly. The higher viscosity ratio causes the turbulence to decay less rapidly than in Run 3. Therefore the turbulence remains at a higher level as it diffuses into the freestream. The turbulence level in the IGV wake between the rotor wake passing is also generally higher than in Run 3. The level is approximately 4% rather than 3%.

The main effect of increasing the viscosity ratio is that the start of transition within the rotor wake path moves upstream. Figures A.51c & d show the wake imprint on the pressure surface is widened, and the transition process

is more complete by the trailing edge. The average wall shear increases, and the normalised wall shear then shows a greater intensity with the high and low regions. On the suction surface, transition within the rotor wake path is also brought upstream. The normalised wall shear shows a stretching of the high wall shear region, indicative of a newly attached turbulent boundary layer. The intermittency plot (Figure A.51d) also shows the transition region with the wake path moving upstream compared to Run 3. Near to the leading edge, the boundary layer shows an almost uniform level of intermittency throughout for all t*. It is thought that this is due to the higher viscosity level suppressing the growth of the boundary layer in this region. The surface at which the intermittency data is taken from therefore remains in the freestream for a longer period of time.

The transition post wake is seen to be delayed slightly compared to Run 3. It may be that if the higher viscosity ratio has reduced the rate of boundary layer development, then naturally, transition occurs further downstream. Or indeed the calming effect may be stronger due to the increased viscosity ratio. It is not apparent as to how these questions may be answered. A stronger calming effect may be the answer as the local skin friction (Figure A.52a) post wake is greater than for Run 3. This high level of skin friction is indicative of a turbulent level of skin friction within a laminar boundary layer. After 0.1t*, the completion of transition has recovered back to values of s* seen in Run 3. This is also shown in Figure A.52a. The higher skin friction within the wake path extends to s* = 0.75 rather than s* = 0.7 in Run 3. Between rotor wake passings, the region of low or negative skin friction is increased, although the negative region is decreased, adding substance to the thought that the calming effect is greater in Run 6. It extends further

upstream just prior to wake passing.

The momentum thickness (Figure A.52b) shows no significant deviation from that found in Run 3. It mimics the pattern found in the intermittency plot. The shape factor on the pressure surface exhibits a slight increase within the wake path. Figure A.53d shows a slight decrease of momentum thickness within the wake path at $s^* = 0.4$ on the pressure surface. The displacement thickness is not observed to change at this point, causing a slight reduction in shape factor. On the suction surface, the shape factor between wake passings increases for $s^* < 0.4$. Therefore the flow is more likely to be laminar or close to separating. The region of low shape factor in the wake path, for $s^* > 0.4$, increases in size. This signals that the amount of turbulent flow increases within this region, and the boundary layer is either more fully developed, or is more resistant against separation.

The same pattern and levels exhibited in the integral parameter plots for Run 3 are replicated in Run 6 (See Figure A.53). The only difference between Run 3 and Run 6 is toward the trailing edge on the suction surface, where separation is shown to take place further downstream in Run 6 due to lower shape factor, displacement and momentum thicknesses. Figure A.54e shows that due to the wider region of higher turbulence within the rotor wake, and the moving upstream of the transition region, the increase in momentum thickness occurs approximately 0.1 t^* before Run 3.

The increase in viscosity ratio has the effect of increasing the thickness of the laminar boundary layer immediately post wake-passing. The thickness then decreases until the next wake passing event. This effect can be seen in

Figures A.54a & d. The boundary layer velocity plots in Figure A.56 show the effect of viscosity around the leading edge. Plot a shows the velocity between rotor wake passing to be more uniform than in Run 3.

The overall effect on increasing the viscosity ratio on wake structure and turbulence level is shown in Figure A.57. Here, it is easily visible that the width of high level turbulence associated with the rotor wakes increases. This is also confirmed in Figure A.59. Higher values of turbulence are found immediately around the blade for long periods before and after wake passing. The strength of the IGV wake is increased, and subsequently impinges at the leading edge with a higher level of turbulence. The wake structure remains similar. The region of high turbulence associated with the stagnation region significantly increases in size during rotor wake passing at the leading edge. The rotor wake is still seen to rotate as it travels through the passage. The regions of low turbulence within the domain are substantially decreased.

The final run explores the effect of increasing the turbulence level within the IGV wake and the artificially simulated movement of the IGV wake when interacting with the rotor wake. This is Run 7, and it is directly comparable to Run 5. Therefore all comparisons mentioned are for Run 7 are made against Run 5 unless stated otherwise. Figures A.61 - A.70 contain the results for Run 7. The inlet flow pattern is shown in Figure A.61a. Here the IGV wake is clearly seen to shift at the time the rotor wake passes, before gradually returning to its original position. The timing and amplitude of the oscillation is similar to that in experiment (See Figure 6.9). The IGV wake shifts when its centre is at the same position as the centre of the rotor wake. However, it is felt that the movement of the wake is too instantaneous as is shown by

the sudden change with w/S.

By the time the flow reaches 42.7% chord upstream of the leading edge, the movement of the IGV wake is not as sudden due to the diffusion process in the CFD as shown in Figure A.61b. The position of the low momentum fluid region has shifted towards the pressure side as compared to Run 5. This a direct effect of the movement of the IGV wake. The velocity defect in the IGV wake is similar to Run 5. Within the rotor wake, the secondary low momentum region is also shifted by a similar value of w/S as for the primary low momentum fluid region. This secondary region also increases its velocity deficit over that found in Run 5. As the IGV wake has a higher turbulence level than previous, the region of 4%Tu between rotor wakes, within the IGV wake is extended until the entire region within the IGV wake between the rotor wakes is at 4%Tu. The representation of wake movement and mixing is favourable with the experimental data. The turbulence levels and patterns are also similar, except the IGV wake is not as well defined as in Figure 6.9.

The two main features represented in Run 7 are that transition occurs further downstream than in Run 5 and there are now two separate phenomenological effects causing changes to the transition region. Figure A.61c highlights the first observation of transition occurring further downstream. The regions of high normalised wall shear, which represent a newly formed turbulent boundary layer, are thinner and occur further downstream. The wake path is more defined. The region of lower normalised wall shear between wakes has a higher value than for Run 5, as the boundary layer is not as well developed during this region. It will be shown that this is due to the variation of the stagnation region with time. The pressure surface shows a similar pattern as

for Run 5, but with a lower wall shear, suggesting that the boundary layer is also less well developed on this surface. Another difference between Run 7 and Run 5 is that the separation region has a more uniform streamwise position.

The intermittency plot in Figure A.61d shows more definitely that transition occurs further downstream in and between the rotor wake path on the suction surface. This is more apparent within the rotor wakes. The intermittency plots in Figure A.64 confirm that transition starts to occur further downstream between the wakes (plot a, $s^* = 35\%$), and that the transitional boundary layer within the wake is also thicker than in Run 5. On the pressure surface, Figure A.61d shows transition within the wake path is delayed as compared to Run 5, but the transition between wakes moves upstream. This suggests the wake has a smaller impact on transition and there is an additional phenomena which affects the flow between wakes.

The plot of local skin friction and intermittency in Figure A.62a shows a reduction in skin friction within the suction surface wake paths. Transition does not occur as early as in Run 5, and between the wakes, there is a larger region of flow close to or separating, but the amount of separation is reduced. This is shown by the lighter shade of green, which signifies a higher skin friction than a darker shade. It is thought that this effect is due to the effects at the leading edge, which alters the flow to a small degree around the blade. The rotor wake also is shown not to fully suppress the tendency of the boundary layer to separate at $s^* = 0.6$.

The additional phenomena occurring between rotor wake passings can be

more clearly seen in Figures A.62b & c. On the pressure surface, the rotor wake momentum thickness is clearly seen, but instead of a gradual decrease to pre-wake levels, it remains at an almost constant level until it reduces sharply just before wake passing. Downstream of s* = 0.6, the momentum thickness again rises. On the suction surface, again the wake path is clearly defined by the strip of higher momentum thickness starting from close to the leading edge. The initial impingement of the wake on the leading edge is shown by a block of higher momentum thickness at t* = 0.35. There is another similar block of higher momentum thickness at t* = 0.1. These blocks are also shown on the plot of shape factor. It appears to cause a small increase of momentum thickness and decrease in shape factor as it travels along a similar path to the wake path. It is thought that in previous runs, these two effects were caused at the same time at the leading edge, but the movement of the IGV has now caused that there is a time lag between them.

The wake paths on both the suction and pressure surfaces are shown to have a reduced thickness as compared to Run 5. A greater region of laminar flow is observed towards the leading edge on the pressure surface. The increased shape factor within the wake path shows the boundary layer to be less turbulent than in Run 5. Transition is delayed. The region of laminar flow prior to the wake passing event is in evidence for a longer time period. Similarly on the suction surface, the region of laminar flow between wakes is increased, and the boundary layer is found to be more highly laminar or closer to separation. The thinner wakes have a reduced effect on the boundary layer post-wake. The additional phenomena is thought to cause the second region of turbulent flow which is encroaches further upstream than the general turbulent flow between the wake paths.

The plots of integral parameters at various positions along both the suction and pressure surfaces show the secondary phenomenon. Figure A.63a shows two sudden increases in momentum thickness. One is associated with a sharp decrease in shape factor, and therefore is the rotor wake. The second just afterwards is associated with a rise in shape factor. As these phenomena travel along the suction surface (plots b & c), the wake effect on the integral parameters remains fairly constant, whereas the secondary effect appears to grow in magnitude and time. On the suction surface, the same pattern emerges, but there is a levelling off of momentum thickness and a shape factor of 1.8 signifying a more turbulent boundary layer, before momentum thickness reduces and shape factor rises as the boundary layer becomes laminar. The effect of the wake is much thinner than for previous runs.

Figure A.65 shows the thickness of the high turbulence levels to be reduced for all plots, showing that the boundary layer is not as well developed along both surfaces. This confirms that transition occurs later on both surfaces. This is also shown by the lack of high intermittency in Figure A.64b, as separation has moved downstream. Plot c shows that terminal separation has moved downstream as the increased intermittency is now shown on the plot as the separation streamline is now still close enough to the surface to be shown.

The velocity plots shown in Figure A.66 show the rotor wake to be thinner than previous, and between the wake, a more uniform freestream velocity at $s^* = 35\%$ on the suction surface. This indicates that the secondary phenomena seen in the previous plots are caused by an effect within the boundary layer itself, rather than from the freestream. The local change in flow angle

/ flow at the leading edge may only cause an alteration within the boundary layer, and not in the freestream outside the boundary layer to the extent that it can be detected. At s* = 55%, two lower velocity regions are visible. The have a similar time lag as shown in the shape and momentum thickness figures (Figures A.62b & c). Only the first low velocity region is associated with an increase in boundary layer thickness, hence this must be the rotor wake.

Although the wake pattern travelling through the domain (Figure A.67) remains identical to Run 5, the level of turbulence within the rotor wake has decreased. The region of high turbulence within the stagnation region is reduced and does not impinge upon the suction side of the leading edge to the same degree as in Run 5. This is made more apparent if Figure A.69 is viewed. The stagnation region itself has been reduced as shown in Figure A.70. The IGV wake causes it to impinge further towards the suction surface so that the rotor wake has a smaller effect on the flow around the suction surface as shown here.

6.7 2D Unsteady State: Results - Low Loading

The low loading case is characterised by a much reduced rotor wake influence upon the unsteady flow field. Transition occurs on both surfaces through laminar separation bubbles. The experimental hot-wire data for the inlet flow field is shown in Figure 6.16. The thickness of the rotor wakes has decreased from those of the medium loading case. The circumferential position of the

IGV wake has shifted to approximately w/S = 0.75 and consequently does not impinge directly upon the stator leading edge. The IGV wake is not displaced by as great a distance as in the medium loading case as the rotor wakes are substantially weaker. Low momentum regions of fluid still exist in the rotor wake on the suction side of the IGV wake. Here the velocity defect reaches 0.87 $\bar{u}/u_s$ and the local turbulence, 10%. The velocity defect within the IGV wake is more apparent. The hot wire data to the left of the figure shows no velocity defect (normalised velocity < 1) for the low loading case. From this it was decided not to model a velocity defect within the rotor wake. Simplistic velocity and turbulence distributions were chosen for the inlet inputs.

The CFD representation of the experimental hot wire data at the inlet is shown in Figure A.71a. Here the velocity defect of the IGV wake can clearly be seen running horizontally across the figure. The rotor wake is only discernable by the roughly diagonal bands of higher turbulence intensity. These bands are not as clearly visible as in the medium loading runs. The IGV wake and rotor wake have similar turbulence levels. Maximum turbulence levels found within the rotor wake, between the IGV wake, do not compare well to experimental values in the contour plot of Figure 6.16a suggesting another mechanism not captured by the hot wire data is present. The hot wire data alone does not warrant the high values of turbulence, such as 10%. The CFD inputs give a maximum turbulence level of 5.5% during the interaction of the wakes.

As the flow reaches 42.7% chord upstream of the leading edge (Figure 6.16b), the velocity defect in the IGV wake has decreased, similar to previous sim-

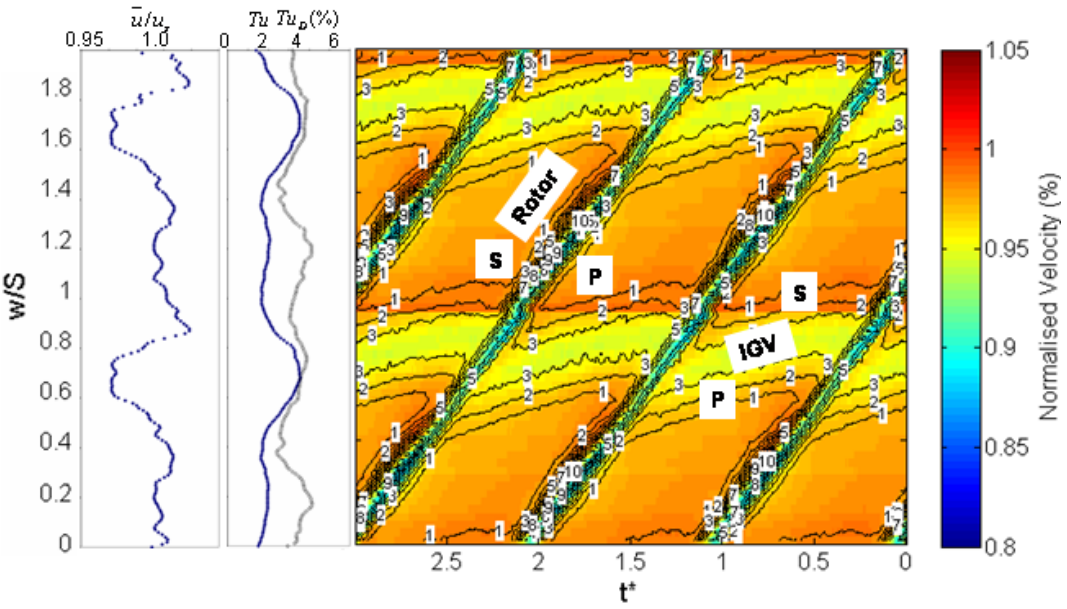

Figure 6.16: Normalised inflow velocity and turbulence at 55.7% chord axial distance upstream of stator leading edge for low loading case. Shaded regions represent normalised velocity. Line contours represent turbulence intensity (%)

ulations. A band of higher velocity flow on the pressure side of the IGV wake is present. The pattern of turbulence levels within the flow has not altered from that experienced at the inlet. Due to the already lower values of turbulence, the decay of turbulence from the inlet values is lower than that experienced for the medium loading case.

The hot film results showing intermittency and relaxing flow for the low loading case are shown in Figure 6.17. Transition occurs on the suction surface via a laminar separation bubble which detaches at mid-chord and reattaches at $s^* = 0.75$. The regions of relaxed flow represent the latter stages of the separation bubble after transition has occurred. The passing rotor wake briefly

suppresses the separation bubble, but not for the full wake passing period. Transition occurs on the pressure surface through a leading edge separation bubble which reattaches at s* = -0.1. Similarly, the separation bubble seems likely to be suppressed during wake passing and the transition start point moved upstream.

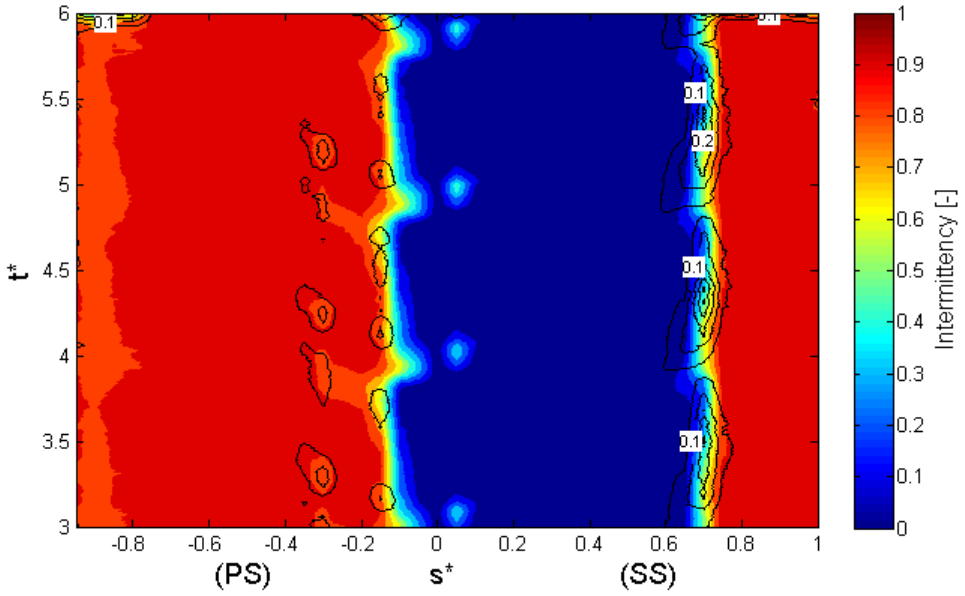

Figure 6.17: Experimental intermittency (shaded) and relaxing flow on blade surface for low loading case

The $\gamma - \theta$ model replicates the behaviour of the unsteady boundary layer to a large extent. On the suction surface, an intermittent separation bubble is present, with the dark blue ringed regions in Figure A.71c describing the extent of the bubble. The boundary layer separates at s* = 0.7 - 0.75 and reattaches at s* = 0.8. The bubble is shorter and further towards the trailing edge than experimental values indicate. The model is correct in predicting

that transition occurs within the bubble, and that the streamwise position of the transition region does not significantly alter during wake passing. Attached transition is indicated by the regions of high normalised wall shear (dark red regions at s* = 0.75). Terminal separation occurs at s* = 0.9 as opposed to s* = 0.85 determined by experiment. The region of high intermittency upstream of s* = 0.2 on the suction surface in Figure A.71d is due to the data collection surface being within the freestream in this region, as the laminar boundary layer is still extremely thin.

The separation bubble on the pressure surface is more clearly shown in Figure A.72a. Separation is indicated by the turquoise region towards the leading edge. The separation bubble almost uniformly starts at approximately s* = 0.17 and reattaches between s* = 0.35 and s* = 0.4. The influence of the rotor wake only modulates the reattachment point of the bubble by bringing it upstream by 0.1s*. Transition occurs within the bubble and progresses more rapidly within the wake path, as shown by comparing Figures A.71d and A.72a. As the wall shear is close to zero within this region, any increase or decrease due to the wake passing is augmented, as indicated by the alternating blue and red regions where the red regions represent the wake path. The local skin friction shows that the wall shear is always negative in this region. As transition occurs earlier, the wall shear is increased because the turbulent kinetic energy in the boundary layer increases. The wake has a greater effect upon the modulation of the transition region as compared to the experimental data. Transition occurs less rapidly and is complete by s* = 0.6 between wakes and s* = 0.4 within the wake path. This indicates in accordance to transition in the medium loading case, that transition occurs too rapidly. A revisit of the γ correlation may be required, especially as the

user cannot change this correlation within the CFX code.

This pattern of boundary layer development is confirmed in Figures A.72b & c. Upon separation, the suction surface inter-wake laminar boundary layer immediately undergoes transition, reducing the shape factor from 3.4 to 2.5. The reattached turbulent boundary layer remains close to separation until terminal separation occurs. The laminar boundary layer in the wake path does not undergo separation, as the maximum shape factor only reaches 2.8 for the laminar boundary layer before transition occurs at s* = 0.6. Transition occurs upstream of the separation bubble, at approximately the same position for the entire duration. Transition occurs in damped mode, but is accelerated through the bubble and is complete upon reattachment.

The shape factor results for the pressure surface confirm there is a separation bubble present on the pressure surface. Shape factor reaches a maximum value of 3.1 between wake passing and 2.9 within the wake path. Transition starts to occur at approximately the same position for the duration of the simulation, but the rapidity of transition increases during wake passing due to the increase in freestream turbulence within the wake passing to the boundary layer. Momentum thickness is seen to increase more rapidly during the wake path, indicating that transition occurs further upstream than between wakes.

In this loading case the changes to the velocity profile lag the start of transition. This is probably due to the wake causing the model to detect transition, which then alters the velocity profile. The rotor wake has no velocity defect, therefore cannot instantaneously or directly alter the velocity profile within

the boundary layer. This can be seen by comparing Figures A.72b, A.73b, A.74b and A.75b. At s* = 0.55, for $0.4 < t^* < 0.8$, the momentum thickness is seen to increase further upstream than at t* values greater or lower than those values just specified (Figure A.72b). Transition occurs upstream of s* = 0.55, as confirmed in Figure A.74b. Post wake, the transition region moves upstream, but only a small distance, just enough for the change to be registered in Figure A.74b. The increase in turbulence intensity within the boundary layer in Figure A.75b confirms that this is the wake path. The high intermittency shown in Figure A.74c is due to the terminal separation point moving upstream so that the start of the shear layer (which is still attached at this point) is upstream of s* = 0.8. At this point, the shape factor is close to 2.7, suggesting the flow is close to separation (see Figure A.73c).

Wake passing on the pressure surface is confirmed to occur at t* = 0.6. Displacement and momentum thickness are increased at this time (Figure A.73d), the orthogonal distance to the wall of the laminar part of the boundary layer is increased (Figure A.74d), and the local turbulence intensity within the region of the boundary layer also increases (Figure A.75d). The wake appears to have a gradual influence upon the boundary layer before its passing, and a much more abrupt relinquishing of its influence, post passing, as shown in Figure A.74d.

6.8 2D Unsteady State: Results - High Loading

The flow phenomena are more prominent at the inlet for the high loading case, increasing the definition of the flow phenomena found in the unsteady stator boundary layer. The inlet flow field for the high loading case is shown in Figure 6.18. The rotor wakes have widened and the low momentum regions of fluid have increased in size. Turbulence levels within the rotor wake have increased to 12% in the low momentum regions and 10% throughout the remainder of the wake. The IGV wake is shifted a greater distance during its interaction with the rotor wake. The turbulence level and velocity defect within the IGV wake remains similar to the low and medium loading cases.

The simulated inlet flow field and flow field at 42.7%c upstream of the stator leading edge are shown in Figures A.81a & b respectively. As with the low loading case, simplified velocity inputs were utilised which accounted for the wake velocity defects and turbulence levels only. The rotor wakes at the inlet are wider than in previous cases and the maximum turbulence level within the wake is 10%, which is comparable to experiment. The IGV wake has a greater velocity defect (0.95 $\bar{u}/u_s$) than the rotor wake (0.96 $\bar{u}/u_s$). The region of low momentum fluid during wake interaction is reduced in size because of this. Had the rotor had the greater velocity defect, the low momentum region would have been elongated either side of the IGV wake. Also, turbulence intensity between wakes remains high, at 5%, as opposed to experimental values of 1%.

Further downstream (Figure A.81b), the IGV wake has widened significantly

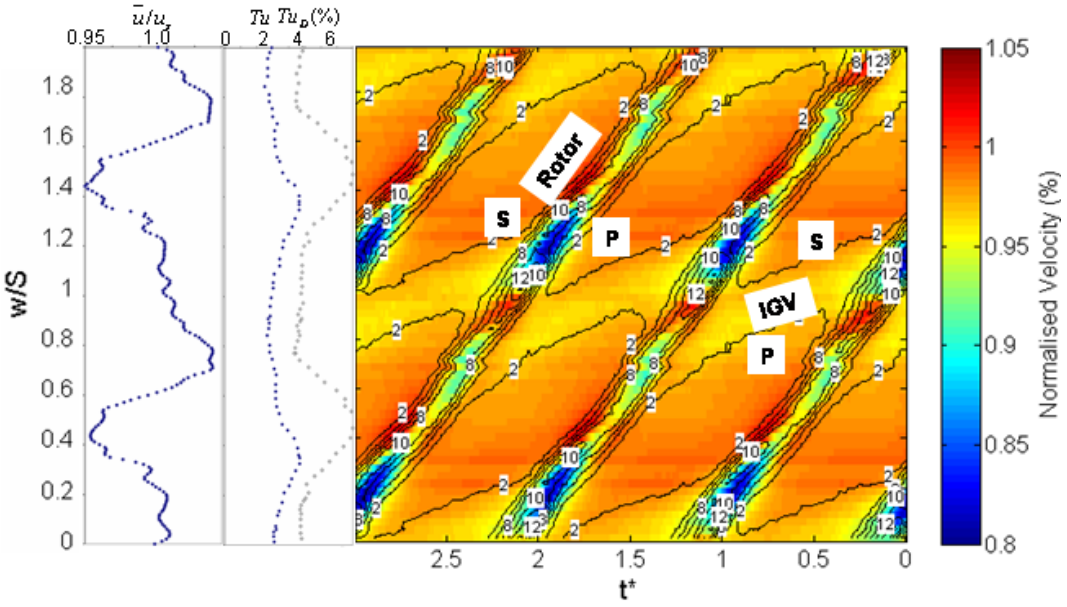

Figure 6.18: Normalised inflow velocity and turbulence at 55.7% chord axial distance upstream of stator leading edge for the high loading case. Shaded regions represent normalised velocity. Line contours represent turbulence intensity (%)

and its velocity defect increased. Large portions of the flow between the wakes have accelerated to normalised velocity levels above unity. The velocity defect within the rotor wake has reduced to higher values of 0.98 $\bar{u}/u_s$ directly because of the flow acceleration. Turbulence intensity within both wakes has remained high at values of approximately 7%.

The experimental intermittency and relaxing flow within the boundary layer on both surfaces for the high loading case is presented in Figure 6.19. The impinging rotor wakes have a greater effect upon the development of the boundary layer in this case than the previous loading cases covered. On the suction surface, transition occurs at the leading edge and is sustained

throughout the entire wake path. Between the wakes, the calmed region shown by the line contours achieves a maximum relaxation probability of 0.4 for a small region, which shows that only a weak calming effect is present. This calming effect continues for most of the post-wake passing time. Transition occurs between s* = 0.25 and s* = 0.65 between wake passings (Figure 6.4). Terminal separation towards the trailing edge modulates about s* = 0.8, occurring downstream of s* = 0.8 immediately post wake passing. On the pressure surface, only in the wake path is transition completed. Again a weak calming influence is experienced immediately post wake. Between wakes, transition is only half completed at the most. Transition within the wake path does not occur as rapidly as for that on the suction surface.

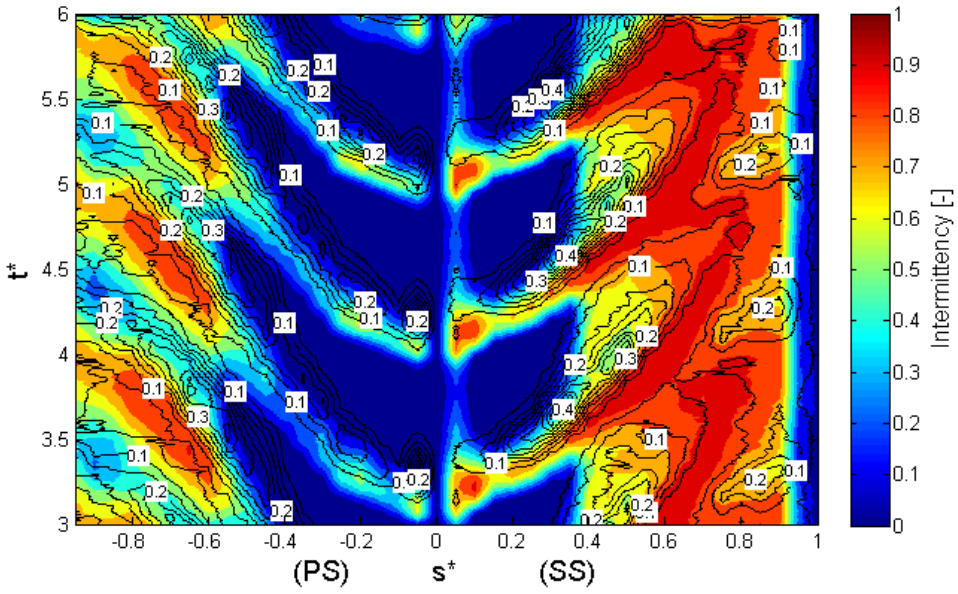

Figure 6.19: Experimental intermittency (shaded) and relaxing flow on blade surface for high loading case

The results of the CFD simulation for the high loading can be viewed in Figures A.81 to A.90. Figure A.81d shows that transition is never completed at any point in the pressure surface boundary layer. The wake passing has a similar effect on the wall shear (Figure A.81c) as it has with previous simulations, namely that it appears to affect a large portion of the blade surface at an instance. However, the effect of wake passing upon the integral parameters such as momentum thickness and shape factor are clearly defined (see Figures A.82b & c respectively). Momentum thickness increases within the wake path before a delay in returning to pre-wake levels. Similarly for the shape factor, the wake causes the boundary layer to assume a turbulent value of shape factor before returning to a laminar value just prior to the next wake passing. The boundary layer is shown to be mostly turbulent only within the wake path if shape factor is used as a guide, but the time dependent intermittency at both s* = 0.4 and s* = 0.7 (Figures A.84d & e) show no significant change in the state of the boundary layer. A comparison of these two figures show that the boundary layer has not started to become turbulent at any point. Comparisons of the integral parameters along the suction surface (Figures A.83d & e) confirm this. Similarly there is no increase in the level of turbulence within the boundary layer as shown in Figures A.85d & e.

These results seem to indicate that there is a disconnection between the integral parameters and turbulent development of the boundary layer. Even though within the wake path, the shape factor indicates a mostly turbulent boundary layer, the $\gamma - \theta$ model does not detect this. It is thought that even though the velocity profiles would indicate turbulent flow, as $Re_{\theta t} < Re_{\theta t_c}$ within the wake path, transition does not occur. This highlights one of the

deficiencies of the model, in that it is not directly the state of the boundary layer which determines whether it is transitional or not, it is the correlation with Re_v. If transition has found to be started upstream, it may be the γ correlation does not predict that conditions are such for further boundary layer development. Both the shape factor and momentum thickness plots show 2 separate events at the leading edge, similar to Run 7 for the medium loading case.

The effect of the wake on the transition process taking place in the suction surface boundary layer is more easily seen. Figure A.81d clearly shows the transition region occurring further upstream within the wake path. The calmed region characterised by an increase in wall shear is evident in Figure A.82a. A separation bubble is present toward the leading edge just after wake passing. This is shown by the region of zero normalised wall shear stress between s* = 0.05 and s* = 0.2 with a centre at t* = 0.9 and t* = 1.9 in Figure A.81c. A significant calmed region is shown as a reduction in intermittency between wakes (s* = 0.45 to s* = 0.6) in Figure A.81d. As transition moves upstream within the wake path, so does the terminal separation point towards the trailing edge. The earliest separation indicated by the normalised wall shear occurs at s* = 0.65 within the wake path. Between wakes, separation occurs at approximately s* = 0.8, with reattachment and further separation intermittency occurring. This takes place at s* = 0.9. Terminal separation occurs at a comparable streamwise distance with experiment between wakes, but 0.1s* upstream within the wake path.

The separation bubble towards the leading edge on the suction surface occurs prior to the large arrow-like region of fully turbulent flow toward the

beginning of the wake path. The momentum thickness within the wake path increases at a faster rate than between wakes, indicating a more rapid development of the boundary layer. Figure A.82c also gives an indication of separation at the leading and trailing edges. High values of shape factor are found in those regions already identified by the normalised wall shear as being separated. The shape factor also shows the influence of a turbulent like flow both during and post wake, indicative of the calmed region.

Figures A.84a & b show the time dependent intermittency within the boundary layer at s* = 0.35 and s* = 0.55 respectively. The separation streamline is clearly identified by the region of high intermittency at s* = 0.55. Even though the boundary layer has not separated, the shear layer is already visible. At s* = 0.35, remnants of the reattached shear layer are faintly visible.

6.9 Chapter Closure

The simulations undertaken in this chapter have shown that it is possible to model the basic effects of wake mixing and the unsteady effects of wake impingement on the boundary layer. The simulation of the development of an axial compressor stator blade unsteady boundary layer using two wake inputs and a transition model has never before been reported. This is also the first time an unsteady simulation using the $\gamma - \theta$ model within the CFX code has been reported for an axial compressor application. All three blade loading conditions simulated proved somewhat successful in replicating the experimental results.

The program of simulations conducted for the medium loading case showed it was essential to model the rotor wake velocity defect, whilst the increased turbulence within the wake did not have as significant an influence on the transition process. The velocity defect creates the negative jet effect which alters the velocity profile within the boundary layer. This creates the conditions which allows transition to occur in the boundary layer much further upstream of its pre-wake position. Run 1 showed that simulating only the increased turbulence in the rotor wake had only a minor effect on the position and length of the transition region, and therefore did not create a significant calmed region post wake passing. However, Run 1 demonstrated that weak separation can be suppressed by only simulating the increased level of turbulence in the wake. Subsequent simulations showed the importance of the velocity defect in both wakes.

The flow angle within the IGV wake impinging on the stator leading edge played an important role in the behaviour of the boundary layer on the suction surface and subsequently the transition region. As the flow angle was a function of the inlet velocity, the change in flow angle found within the IGV wake altered the flow field around the leading edge such that the boundary layer was more receptive to transition. It is uncertain if this is also a physical event, or if this is due to the code. Current CFD codes still cannot replicate the true effects associated with wakes within turbomachinery. Uzol et al. (2007) compared low speed axial fan PIV wake data to the results produced by the RNG k-ϵ and RSM unsteady RANS models available in FLUENT. They concluded that some critical flow features were not correctly predicted, such as the quick diffusion of the rotor wakes due to wake-wake interaction, and the location of the separation region on the suction surface of the rotor

and stator blades. The latter resulted in an over-prediction of the lateral velocity levels and flow angles. The comparison also highlighted the difficulties in accurately reproducing the correct rate of the diffusion of wakes in complex conditions.

The process by which unsteady wake-induced transition take place on the suction surface within the CFD code is thus; A region of high turbulent kinetic energy builds up at the leading edge. The rotor wake impinges upon and passes the leading edge. The velocity defect within the wake alters the velocity profile of the boundary layer. The turbulent kinetic energy at the leading edge travels along the suction surface of the blade at a slower velocity to the wake. It is thought that the velocity defect increases Re_θ, and whilst the boundary layer is recovering from the wake defect, the turbulent kinetic energy from the leading edge reaches this part of the boundary layer and reduces the Reynolds number at which transition can start, Re_{θ_t}. Transition now occurs. Hence the wake does not directly start the transition process, but creates the conditions within the boundary layer, such that the turbulence from the leading edge travelling behind the wake can start the transition process.

The $\gamma - \theta$ model implemented within the CFX code proved it could model the unsteady effects of wake-induced transition on the suction surface, including separation bubble suppression, the calmed region and the streamwise modulation of terminal separation toward the leading edge. Although the actual streamwise position of transition, the separation bubble and terminal separation could be improved upon in relation to the experimental data they were compared to, some of the errors were due to the set-up of the simulation,

namely the inlet boundary conditions.

The simulations showed the importance of obtaining accurate data from which to set the inlet conditions. To give a more accurate simulation, velocity, flow angle and turbulence level data for both wakes is required. The simulations were compromised somewhat by the lack of data detailing the flow angle of the two wakes, especially during the wake mixing process.

The stagnation pressure loss coefficient, based upon trailing edge momentum thickness, was compared for both the steady state and Run 3 calculations at the medium loading flow condition. The unsteady wake-affected simulation only predicted a 2.3% increase in loss over the steady state simulation. This was because the suction surface trailing edge momentum thickness did not vary significantly enough due to already high levels of separation at approximately s*=0.76 for the steady state case and s*=0.8 for Run 3. The effect of the wake passing was not able to suppress the separation enough to counteract the increase in momentum thickness due to early transition.

Another reason why the start point and length of the predicted (CFD) and measured (experiment) transition regions did not always agree was also due to the method used within the CFD results to determine the length of the transition region. The use of a surface at a constant distance from the blade surface to measure the turbulence intermittency could only give a qualitative estimate of the position of the transition region. The choice behind the distance of the surface from the blade surface was arbitrary, being approximate to the thickness of the viscous sub-layer. The method of coupling of the $\gamma - \theta$ model to the turbulence model caused the level of turbulence intermittency

to rapidly increase from 0 to 1 through the thickness of the boundary layer at a given streamwise distance. Hence, the region for intermittency levels between 0 and 1 is very small. This can be observed in Figure 6.10. In this way, the coupling of the models do not replicate the transition region as in reality. Any small change in boundary layer sub-layer thickness may indicate either a fully laminar or fully turbulent boundary layer depending if the surface from which the intermittency was taken was inside or outside the sub-layer. This makes it difficult to assess the position of the end of the transition region. For example, the virtual surface in Figure 6.10 does not detect the start of transition at all, within the boundary of the figure.

Data lines perpendicular to the blade surface, travelling through the boundary layer into the freestream were used to obtain the integral parameters, intermittency, turbulence intensity and velocity profiles shown in the results. Currently they are situated at every 5% surface distance. The intermittency data obtained from them can show the exact start of the transition region, but for this to occur a greater number of data lines are required, perhaps every 1% surface distance. Whilst this is possible, it is not practical due to the amount of data stored and the time taken to process the data. To enable a more precise comparison between experimental and CFD results it is suggested that the coupling of the model be altered to give a more gradual increase of intermittency throughout the transition region.

There is still more which can be improved in the $\gamma - \theta$ model. Firstly the transition criteria is assessed at the boundary layer edge, whilst it first occurs within the boundary layer (see Figure 6.10). Lodefier and Dick (2005) described how transition occurs due to both freestream turbulence (slow pro-

cess) and internal boundary layer instabilities (rapid process). Their dynamic intermittency model attempts to account for this. Initial results of the well known unsteady T106 turbine test case were promising (see also Lodefier et al. (2007)). The author suggests the consideration of implementing a boundary layer source for the start of transition and intermittency equations may reduce the slight lag seen in the results and is worthy of investigation.

Secondly, the model did not perform well for the prediction of transition on the pressure surface. For all results, transition did not occur as per the experiment. On the pressure surface, a positive jet impinges on the surface. This has the opposite characteristic of the negative jet on the suction surface. It was proved that transition was started, but did not develop significantly for Runs 1 and 7 (see Figures A.8 and A.68 respectively). Figures A.18, A.28, A.38, A.48, A.58 show that transition has not even begun for Runs 2 - 6. It is thought that as the positive jet retards the flow upon impingement on the pressure surface, Re_θ is reduced so that Re_{θ_t} is never reached, and the intermittency correlation is not activated. In Run 1, there is no rotor wake velocity defect, and in Run 7 the flow distribution has been altered by the shifting of the IGV wake. These may have been the factors which allowed transition to occur. Further simulations should be conducted as to whether the model itself is defective for this type of impingement, or whether some other factors were responsible.

Finally, it should be noted that the process of transition occurring within the CFD code and in reality are two different processes, and a direct like for like comparison on every physical process involved in the transition process is not possible. An example being that rapid undamped transition occurs via

an artificially high ($\gamma > 1$) in the $\gamma - \theta$ model, which is not physically possible.

Chapter 7

3D Wake-Induced Transition Simulations

7.1 Introduction

Attention is now turned to the 3D capabilities of the $\gamma-\theta$ model and the CFX code. The purpose of the work involved in this chapter is to compare it to the 2D results contained in Chapter 6. An assessment of the benefits gained and the disadvantages experienced by attempting to simulate wake-induced transition in a 3D environment will be made. Conclusions will be made as to whether an industrial organisation would benefit from using a 3D method, and if the method is able to enhance the simulation of wake-wake interaction.

7.2 Methodology

As there was little information about the overall flow parameters of the compressor, an appropriate mass flow was required to be found. A coarse grid

consisting of approximately 250k nodes per passage was created for the IGV, rotor and stator using CFX-Turbogrid. Using an atmospheric pressure constraint for the inlet, and varying a specified mass flow at the outlet, the flow coefficient was used to estimate an appropriate mass flow for each of the loading conditions. Overall stage total pressure coefficient and efficiency, along with passage total pressure coefficient and axial velocity coefficients were compared against Oliver (1961). The mass flow giving the best comparison per loading condition was identified.

A finer grid, consisting of approximately 1M nodes per passage was created. The y^+ value for the walls and blading was kept below 1. The mass flow for each of the loading conditions was run using first the k-ω SST model and the same parameters as previous, compared to the experimental data. The $\gamma - \theta$ model was then run and the characteristics of the transition region, along with the overall characteristics were then compared to experimental data.

Finally, an unsteady simulation was performed for the medium loading condition for the whole stage. The total grid size was approximately 15M nodes, with the IGV, rotor and stator grids, each containing 2.4M,4.8M and 8.4M nodes respectively. Further details on the grids used are given in Table 7.1. It was decided that in order to keep the node count to a manageable level to be able to have enough space to store the unsteady data, the rotor wake impinging on the stator blade would be the primary phenomena to model. Chapter 6 showed that the IGV wake itself did not have a significant impact upon the transition process. Therefore the majority of the nodes in the entire grid were concentrated between the trailing edge of the rotor and the stator trailing edge.

	IGV	Rotor	Stator
# of nodes	2,396,440	4,772,690	8,377,475
# Spanwise nodes	125	125	155
# Streamwise nodes	125	251	261
# Circumferential nodes	61	111	101
# O-Grid (perpendicular)	40	40	45
# O-Grid (around blade)	100	125	200
Blade y^+	0.8	0.8	0.8
Hub y^+	25	25	25
Shroud y^+	25	25	25

Table 7.1: Details of the grids used for 3D simulations

An atmospheric total pressure boundary with the flow being perpendicular to the boundary was specified at the inlet. A simulation of the bell-curve inlet used with the experimental machine, showed that there was no radial component of the flow at point at which the CFD inlet was created. The outlet boundary condition, two chord lengths downstream of the stator trailing edge was specified as the mass flow given by the initial steady state simulations. A rotating hub was specified for all domains, and tip gaps were modelled. A 1:1 periodic boundary condition was given to the passage sides, and the transient rotor-stator model was used for the frame change between the rotating and stationary domains. This option accounts for the interaction effects between the rotating and stationary blades. As the difference in blade count between the stationary and rotating blades is only one, only a single passage per blade row was required to be simulated. The pitch change between stationary and rotating blade row passages was 0.974 / 1.027, which

was deemed small enough not to require simulating multiple passages per blade row.

The same method for running the 2D unsteady simulations applied for running the 3D unsteady simulations. The simulation was initialised from a steady state case using the same grid. It was then ran for a total time equal to six rotor blade passings to allow the flow to transport through the stator passage and reach a quasi-steady state. The simulation was then run for a single rotor blade passing period, and transient data files outputted at a rate of 104 files per run, or every 0.0003 seconds. The rms Courant number was kept below 2.

7.3 Steady State Results: Medium Loading Condition

A comparison of the normalised velocity distribution around the stator blade at mid-span was used to determine the appropriate mass flow for the 3D case. A comparison between experimental, 2D and 3D CFD results for the normalised velocity distribution is shown in Figure 7.1. Whilst the 3D CFD velocity distribution is comparable to both the 2D CFD and experimental values, the velocity over the first half of the suction surface is approximately 0.05 u/U_{mb} below both 2D CFD and experimental values. Good agreement is achieved downstream of 0.5 chord and over the whole pressure surface. These values from the 3D CFD were deemed to be the most appropriate values from a comparison with other similar mass flows with the experimental data.

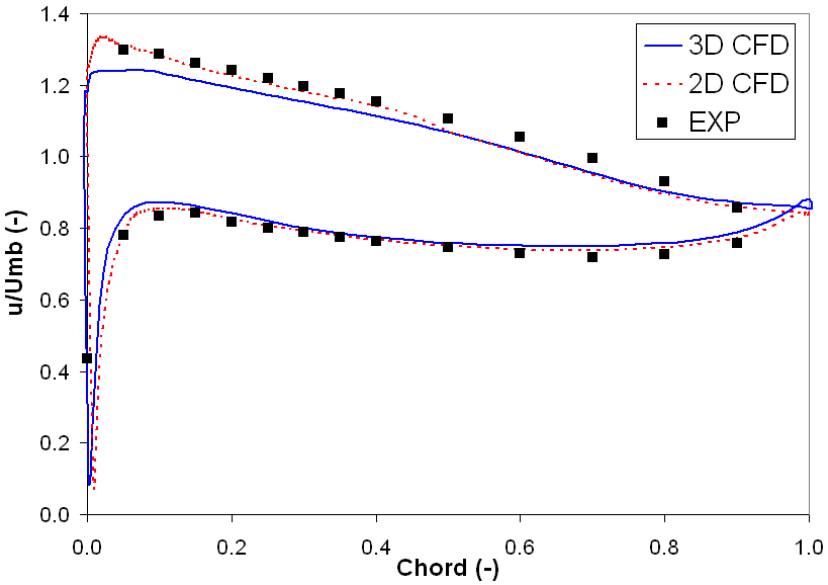

Figure 7.1: Comparison of experimental and CFD results for normalised velocity distribution around the stator blade at mid-span

The effect of reducing the velocity around the suction surface upstream of 0.5 chord is highlighted in Figure 7.2. The separation bubble found in both the 2D case and experiment is not present for the 3D case. The transition region of the boundary layer appears to be similar regardless of this. Transition still occurs between 0.4 and 0.55 chord. Terminal separation occurs a little later at 0.78 chord, rather than 0.76 chord for the 2D case. The main dissimilarity between the boundary layers in the two cases is that the transition within the boundary layer in the 3D case is not dependent upon the separation bubble, and so will have a greater propensity to shift in its streamwise position throughout the unsteady simulation.

Circumferentially averaged values of total pressure coefficient and axial veloc-

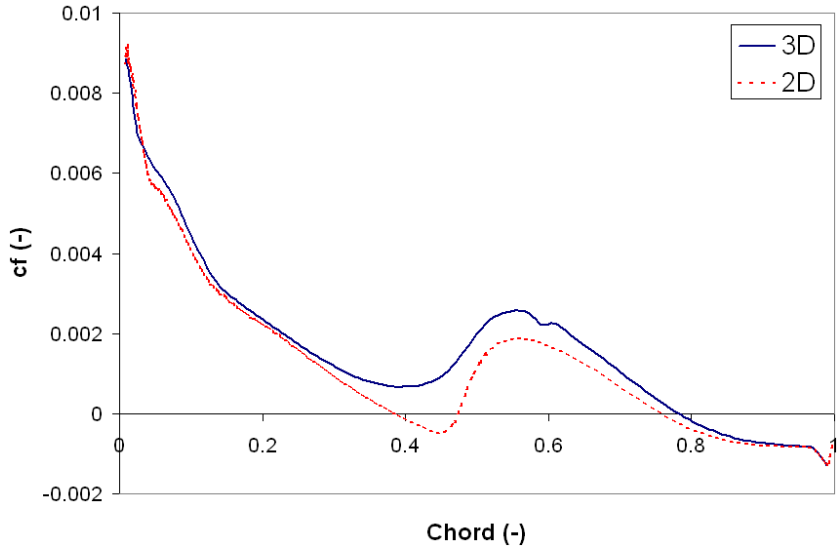

Figure 7.2: Comparison of 2D and 3D CFD results for local skin friction distribution at stator blade mid-span

ity coefficient were compared with 3D experimental data from Oliver (1961). The experimental data was taken as part of a program to compare the use of machined blades as opposed to the traditional sand cast blades. The same blading was used, but the rotor blades stagger was two degrees less than that in the current study. Investigatory CFD runs indicated the blading was fairly insensitive to a 2° stagger realignment. The rotational speed of the compressor was approximately 750 rpm as opposed to 500 rpm in the current study. An investigative CFD run using a rotational speed of 750 rpm revealed no significant difference between the results when normalised against the tangential blade speed at mid-span. Therefore it was considered appropriate to use the results from Oliver (1961) as a comparison to the results within this study. Oliver (1961) measured the flow at $\phi = 0.66$ rather than $\phi = 0.65$ as did Walker et al. (1999). The flow conditions used for the 3D medium loading case gave a value of $\phi = 0.654$. Therefore a comparison between

experimental results and CFD results is appropriate.

Comparisons between experimental and 3D CFD of total pressure coefficient and axial velocity coefficient at the stator exit are given in Figures 7.3 and 7.4. The total pressure coefficient is given by the total pressure rise normalised by the dynamic pressure based upon tangential rotor blade speed at mid-span. Similarly, the axial velocity coefficient is the axial velocity normalised by the same tangential rotor speed at mid-span. Whilst the experimental data shows an amount of scatter, perhaps due to the measuring techniques used at that time, the CFD data compares well. The total pressure rise predicted by the CFD is not as large as for experiment, but the velocity has a very good comparison. This being the case, the general trend is well predicted. The uncertainties with the scatter in the experimental data make a precise quantitative comparison unprofitable.

Further comparisons showing the rotor exit total pressure and axial velocity coefficients are shown in Figures B.1 and B.2 respectively (see Appendix B). They both give a similar level of comparison to that shown by the stator exit data. Overall the results from the steady state medium loading case show that the flow around the stator blade is similar to that simulated in the 2D case and exhibits a similar behaviour throughout the compressor to previous experimental data.

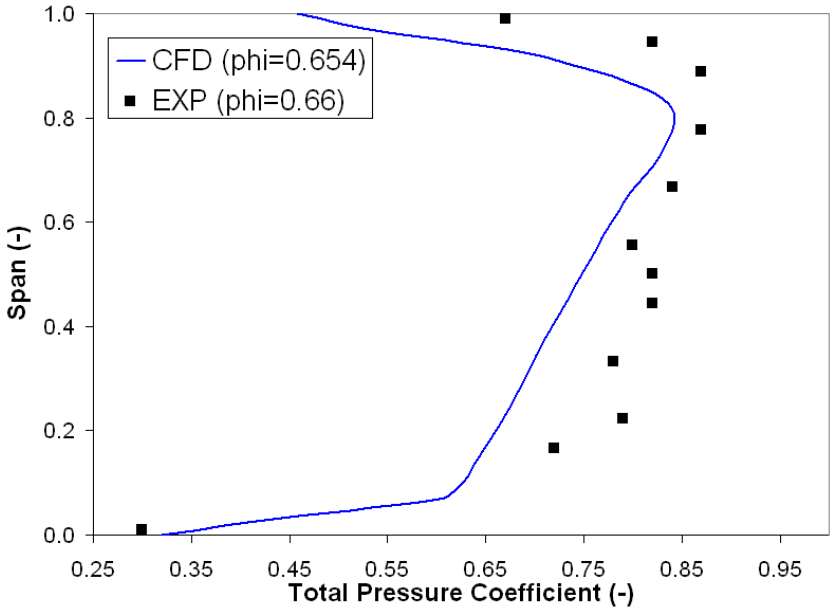

Figure 7.3: Comparison of 3D CFD and experimental values of pitch-wise averaged total pressure coefficient at stator exit

7.4 Unsteady Results: Medium Loading Condition

The normalised velocity and turbulence intensity at the stator inlet and 42.7% upstream of stator leading edge are shown in Figure 7.5. The streamwise position of the stator inlet is the same as for the 2D case, which corresponds to the point at which the experimental hot-wire data was gathered. Only one rotor passing is shown in the figures in this section, as results from only one rotor passing were obtained. Although most scales used in the figures remain the same to aid a direct comparison with the 2D cases, some have been adjusted to the values in these results.

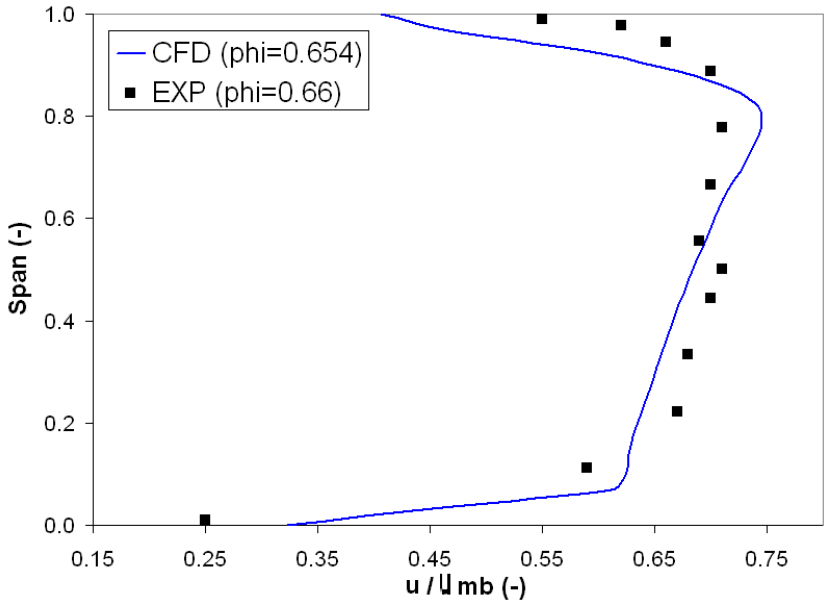

Figure 7.4: Comparison of 3D CFD and experimental values of pitch-wise averaged axial velocity coefficient at stator exit

As with the 2D case and experiential data, the rotor wake is clearly visible as the diagonal region of lower velocity flow. The rotor velocity defect is greater than the 2D case (approximately 0.88 $\bar{u}/u_s$ compared to 0.95 $\bar{u}/u_s$ for the 2D case) and also greater than the experimental values of approximately 0.95 $\bar{u}/u_s$. Turbulence intensity level within the rotor wake is comparable to the experimental data, being approximately 7%. Between rotor wake passings, the freestream turbulence level drops to approximately 1%, which is the value observed by Walker et al. (1999). The 2D case gives values of approximately 3% between rotor wake passings.

The IGV wake is also visible in Figure 7.5, having a velocity defect in its core of 0.98 $\bar{u}/u_s$, with a turbulence level of 2%. Experimental values give similar values for velocity defect, but a slightly higher turbulence level of

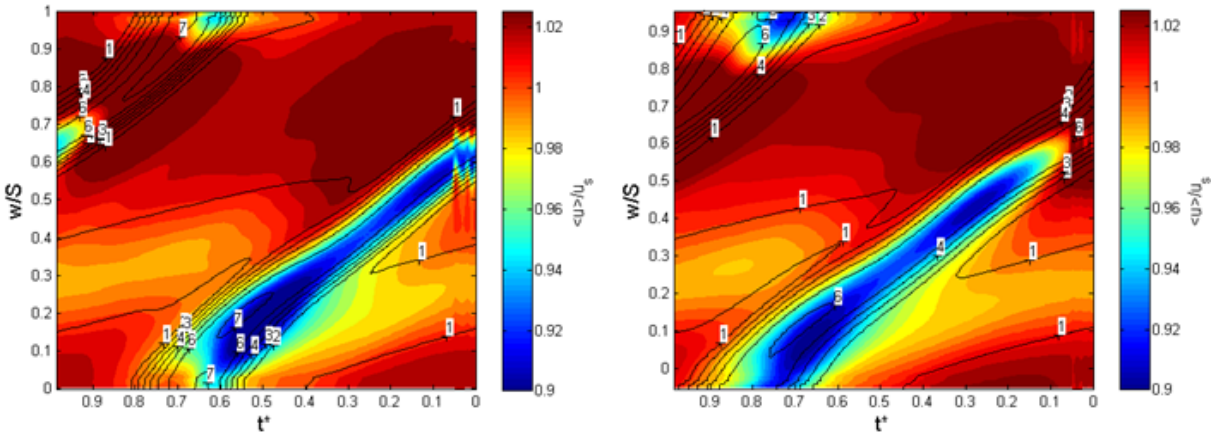

Figure 7.5: Normalised velocity (shaded) and turbulence intensity (contour) at mid-span for the stator inlet (left) and 42.7% upstream of stator leading edge (right)

approximately 3%. The sudden shifting of the IGV wake as it interacts with the rotor wake is captured. The IGV wake shifts from w/S = 0.3 to w/S = 0.1. The distance shifted is similar to experimental values. It was surprising to capture the IGV wake velocity defect so far downstream, given the grid that was used. It was thought the velocity defect would have been mixed out by this point. A region of lower momentum flow is observed within the IGV / rotor mixing region. As with the 2D case, no low momentum fluid regions are shown to be on the suction surface side of the IGV wake within the rotor wake. As the flow between the rotor wakes has a uniform trend, it should be clearer to ascribe changes in the boundary layer to the passing rotor wake.

The rotor wake is well represented as it travels through the domain, as shown in Figure B.3. The turbulence in the IGV wake is not observed past the rotor leading edge. However, Figure 7.5 shows a small increase within the IGV wake path. As the rotor wake convects through the stator passage it is

stretched in the suction surface region and is caused to rotate such that the wake near the suction surface convects at a faster rate than in the centre of the passage. Toward the pressure surface the rotor wake thickness increases due to the negative jet effect impinging on the pressure surface. The wake has a different pattern as it travels through the passage as to the 2D cases. The wake does not bow towards the centre of the passage, with the wake section at the centre of the passage being further downstream than the wake sections towards either blade surface. The relative velocity defect within the rotor wake is smaller in the pressure surface region than in the suction surface region, as the pressure surface region has a lower velocity. Therefore, the effect of the velocity defect should be reduced for the pressure surface.

The wake path along the surface of the stator blade is most discernable when observing the resultant shape factor. The shape factor for the 3D simulation is shown in Figure 7.6. Here the rotor wake starts at s* = 0.25 at t* = 0 on the suction surface, and starts at s* =0.1 at t* = 0 for the pressure surface. Values of shape factor upstream of 0.1s* were not possible for the 3D simulation. Figure 7.6 shows a laminar separation bubble on the suction surface at s* = 0.45 - 0.6.

The state of the boundary layer on the suction surface varies somewhat from that found in the 2D simulations. Two small separation bubbles adjacent to each other in the streamwise direction, are found at approximately mid-chord (s* = 0.45 - 0.6) prior to rotor wake passing. As the rotor wake passes, it does not fully suppress the separation bubbles, as shown by the shape factor in Figure B.4b. The first separation bubble remains in roughly the same streamwise position, whereas the second separation bubble follows the wake

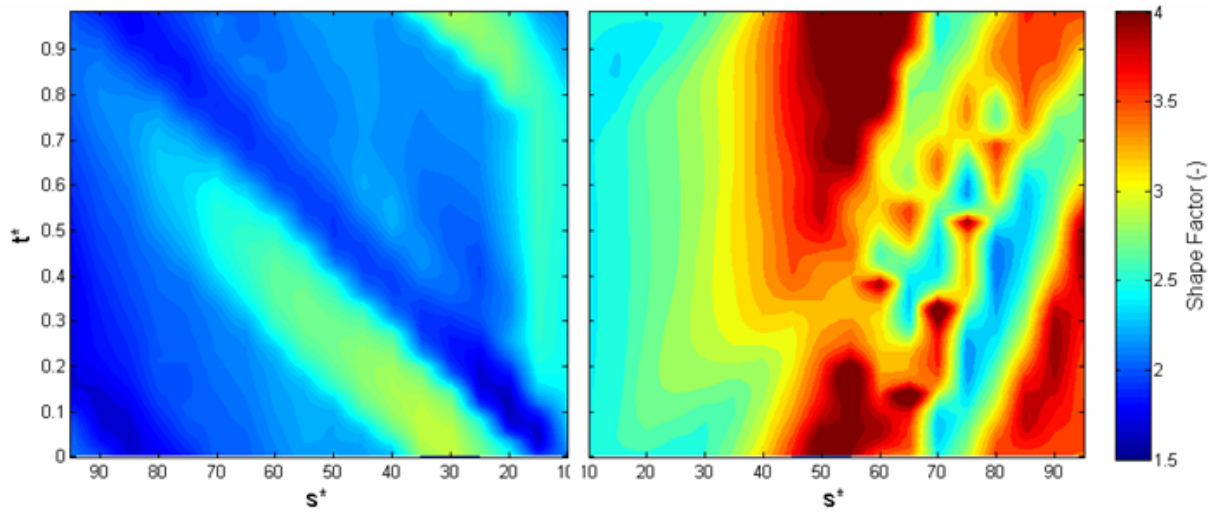

Figure 7.6: Shape factor on both surfaces for 3D simulation

along the suction surface, whilst maintaining its length. The shape factor during this period is still above 2.7, so the flow is still not fully turbulent. As the wake moves towards the trailing edge, the terminal separation is suppressed and the boundary layer reattaches. The second separation bubble continues to moves toward the trailing edge until it replaces the previous terminal separation. The momentum thickness is shown to increase within the wake path (Figure 7.7).

Figure B.5c shows the turbulence intermittency at s* = 0.8 on the suction surface. The artificially high regions of intermittency indicate the presence of the shear layer belonging to the separation bubble and terminal separation. At t* = 0, when the impinging wake is at approximately s* = 0.25, the flow is separated at s* = 0.8. This separation shifts toward the trailing edge as the wake travels along the blade surface. At t* = 0.2, the downstream effect of the upstream wake causes the terminal separation point to move down-

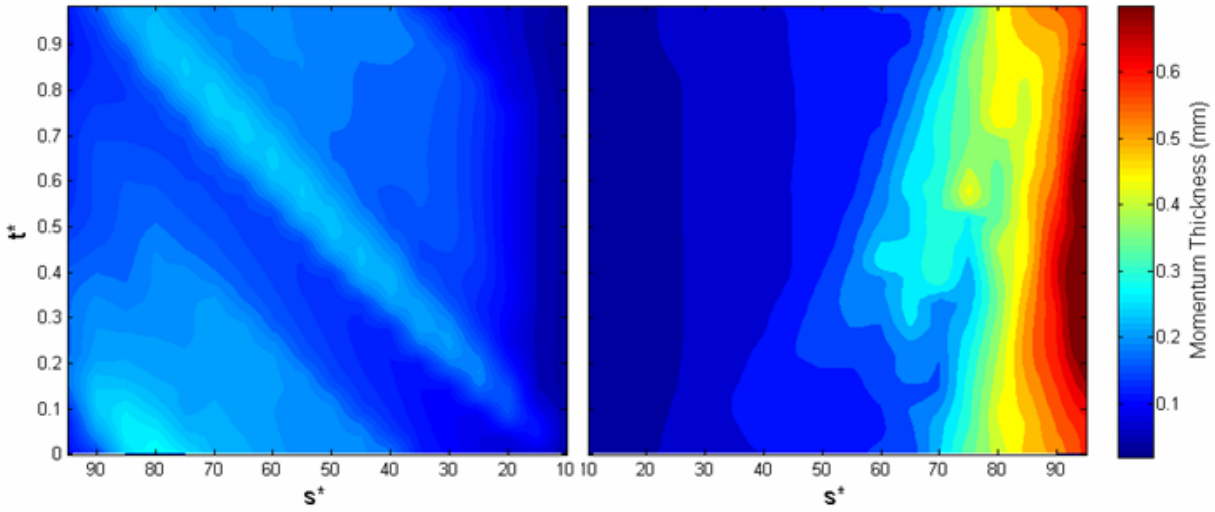

Figure 7.7: Momentum thickness on both surfaces for 3D simulation

stream of s* = 0.8. A transitional boundary layer appears to be present until the wake passes at t* = 0.55. The upstream separation bubble has travelled downstream at the trailing edge of the wake and reaches s* = 0.8 at t* = 0.6. Its shear layer passes briefly in 0.1t* before the terminal separation is re-established at t* = 0.7. This is also shown in Figure B.6c, where the dark red regions of high turbulence intensity occur during separation.

Figure 7.6 shows the reattached boundary layer is turbulent, and the flow remains attached until s* = 0.85. Within the wake path, the flow intermittently separates downstream of s* = 0.6, with terminal separation occurring at s* = 0.75. The plot of local skin friction (Figure 7.8) sheds light on the nature and exact position of the separated regions. Pre-wake passing, two small separation bubbles are present, shown by the diagonal dark blue regions.

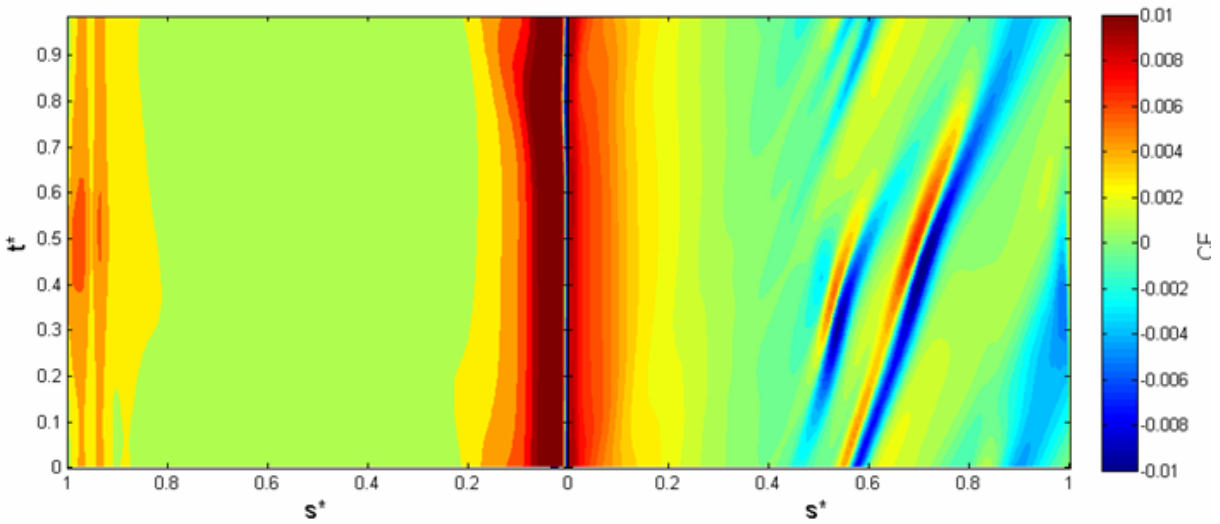

Figure 7.8: Local skin friction on both surfaces for 3D simulation

The effect of the rotor wake on the suction surface boundary layer is also clearly seen in Figures B.5a-c. The inter-wake boundary remains fully laminar until approximately s* = 0.55. At s* = 0.55 the turbulence production has just been activated as can be seen by the region of higher turbulence intermittency ($\gamma \approx 0.8$) within the laminar boundary layer between t* = 0.65 and t* = 0.9, at a wall distance of approximately 0.5mm. The wedge of turbulent flow is the now transitional separation bubble being shifted to this streamwise position by the wake passing. The laminar part of the wake affected boundary layer reduces to a thickness of approximately 0.2mm within the bubble. The wake has little other effect on the boundary layer at this point.

The flow on the pressure surface exhibits a remarkably similar behaviour as seen for the 2D case for Runs 3 and 4. Both the momentum thickness and shape factor plots (Figures 7.7 and 7.6 respectively), showing that during

wake passing the momentum thickness is clearly observed to increase, whilst the shape factor decreases. The boundary layer within the wake path does not undergo full transition, as shown by Figures B.4d and e. Even at s* = 0.7, the boundary layer within the wake path has a shape factor of approximately 1.83. As the boundary layer is not expected to be close to separation, the shape factor indicates that the boundary layer is still transitional.

The wake has a lag effect of reducing the thickness of the laminar region of the boundary layer post wake. A video of intermittency around the blade at mid-span showed the rotor wake to thicken the laminar region of the boundary layer immediately upstream of the wake, up until s* = 0.5. The intermittency plots through the boundary layer (Figures B.5d and e) on the pressure surface show a belated reduction in the thickness of the laminar region of the boundary layer before a sudden thickening of the laminar region pre wake. The wake passes at t* = 0.6. After this, the thickness of the laminar boundary layer remains almost constant before reducing at approximately 0.3t* before the next wake passing event. The position of the wake was determined by comparing the position of the increase in turbulence intensity and decrease in velocity in Figures B.4d and e, and B.7d and e respectively.

A slight calming effect is shown by the normalised wall shear stress in Figure 7.9. The elevated wall shear in evidence on the pressure surface is immediately post wake. The suction surface normalised wall shear shows the position of the separated regions at mid-span as indicated by the deep red regions. These regions are shown to shift towards the trailing edge with the passing wake.

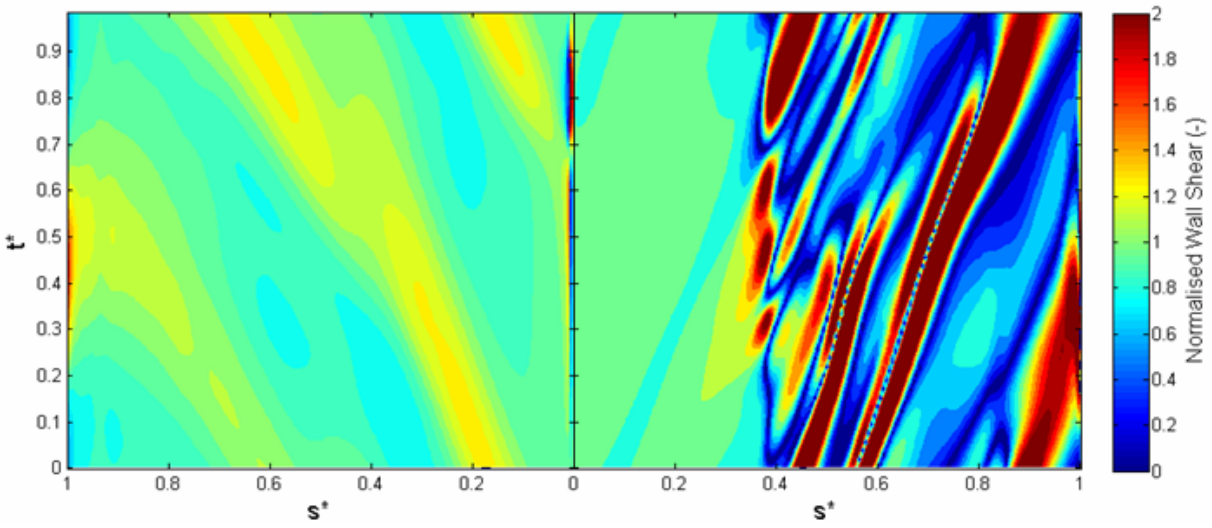

Figure 7.9: Normalised wall shear on both surfaces for the 3D simulation

7.5 Unsteady Results: Medium Loading Condition - Away From Mid-Span & Rotor Blade

Walker et al. (1999) suggest that the flow at mid-span is representative of the flow over the majority of the blade span. Figure 7.10 shows that whilst the separation of the boundary layer on the suction surface for the majority of the span occurs at a similar position, the start and end of the transition region is not uniform along the span. The transition region of the boundary layer is highly dependent upon the position of the separation bubble on the suction surface. Figure 7.10 shows transition to occur within the separated regions. The boundary layer at the hub experiences upstream transition

caused by the impinging wake, before the casing, as the wake reaches the surface toward the hub first. The position of the wake at mid-span is shown by the increased turbulent kinetic energy at the mid-span plane.

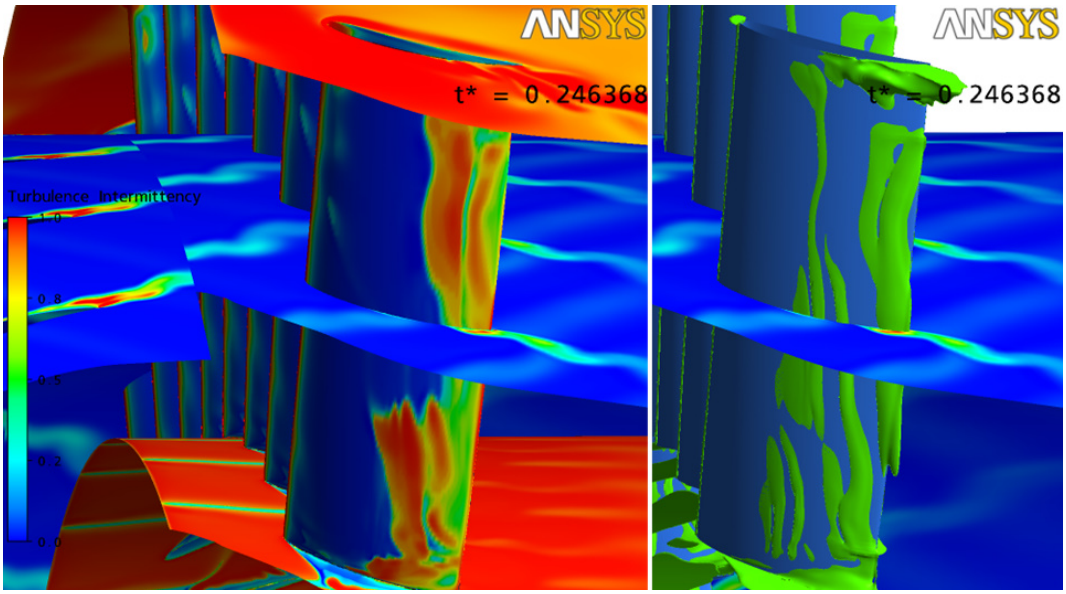

Figure 7.10: Turbulence intermittency (left) and separated regions (in green) (right) for the stator suction surface at t* = 0.246368. Turbulence kinetic energy at a plane at mid-span also shown.

The boundary layer towards the casing exhibits the earliest transition due to wake impingement. This is likely due to the greater velocity of the flow as the rotor blade tangential velocity is greater than at mid-span. At the hub the boundary layer experiences transition at a fairly constant streamwise position. This is due to the small region of corner stall found in this vicinity. This region of corner stall appears to span across the entire passage to the pressure surface.

The flow along the span of the pressure surface can be considered uniform. The impinging wake causes a brief reduction in the thickness of the laminar boundary layer at the leading edge, but this is temporary. The passing wake causes a region of earlier transitional flow near the hub and casing. The wake temporarily suppresses the weak corner stall at the hub. Post wake, the corner stall is re-established and the boundary layer experiences early transition because of it. A similar effect is observed toward the casing, but not to the same extent.

The boundary layer on the rotor pressure surface remains attached throughout the simulation time. Similar to the stator pressure surface, the impinging IGV wakes have little effect upon the boundary layer. The boundary layer remains laminar for the whole of the pressure surface throughout the simulation. On the rotor suction surface, a separation bubble occurs along the majority of the span between s* = 0.25 - 0.35. Transition occurs and is completed within this bubble. The bubble is only modulated by the passing IGV wake, but not fully suppressed. The boundary layer experiences terminal separation at approximately s* = 0.6 toward the hub, and s* = 0.7 toward the tip.

7.6 Chapter Closure

This section has shown that the 2D steady state case can be used as an approximation to the more computationally demanding 3D steady state case. The 2D case gave a closer approximation to the experimental data of the flow field around the blade than the 3D case, even though the streamtube

contraction was not accounted for. The 3D case did not account for the separation bubble present on the suction surface, but predicted transition to occur at the same point.

Even though the mass flow through the compressor was varied to achieve the most comparable solution to the experimental flow field data, it showed the 3D simulation could not achieve the required velocity of the flow upstream of 0.5 stator blade chord which created the separation bubble. Whilst the agreement of the position and length of the transition region between the 2D and 3D steady state simulations was good, the unsteady simulations showed a greater difference between them.

The 3D unsteady simulations gave a better agreement with inlet experimental hot-wire data than the 2D case. The wake structures, wake interaction, turbulence and velocity distributions were all well represented. The greatest difference between the 3D unsteady and steady state simulations was the appearance of intermittent separation on the suction surface starting at approximately mid chord. Even though all other conditions remained constant, the use of a transient simulation created conditions which allowed separation to occur in the suction surface, which weren't present in the steady state simulations. This shows that the time-averaging of the steady state process eliminates key unsteady effects from the simulation.

The greatest effects of wake-induced transition were found on the suction surface. Again, the negative jet effect was well simulated. Opposite to the 2D simulations, in the 3D case, transition was delayed due to the wake passing. It is thought that the wake did not fully suppress the intermittent separation.

As the separation bubbles were reduced in size and height only, rapid, undamped transition could not occur as it does in the bubble between wakes. Transition completion is delayed and the subsequent turbulent boundary layer remains attached until the trailing edge. For the suction surface at mid-span, the 2D unsteady simulation produced a more comparable result with experimental data. Also, as the momentum thickness at the trailing edge was reduced due to the flow being attached, the loss at the trailing edge is decreased. This is a benefit of using wake-induced transition to reduce separation and its resultant losses.

The pressure surface exhibited the least sensitivity to the impinging wake. Whilst the wake path was clear, both in terms of shape factor and momentum thickness, the effect of the wake upon the transition region was minimal. The behaviour of the pressure surface boundary layer was very similar to that displayed within the 2D case. Both simulations did not match the experimental observations in which the boundary layer became fully turbulent within the wake path, but transition was incomplete between wakes. As the relative flow within the wake impinging on the pressure surface was well simulated there must be another physical process which causes an early transition start point and reduced transition region.

It is not clear if a calming influence exists post wake on the suction surface, as the wake was not strong enough to suppress the separation on the suction surface. The normalised wall shear stress for the pressure surface, along with the integral parameter plots suggest a calming effect exists on the pressure surface.

The 3D simulation suggested that even as there was no significant radial component of the flow, the effect of the wake upon the boundary layer did vary significantly. On the suction surface, travelling from hub to casing, the boundary layer was seen to experience the start of transition at an earlier streamwise position. Intermittent separation occurred at approximately the same streamwise position for the entire span, but the blade toward the casing proved more receptive to earlier transition. On the pressure surface, the flow was proved to be uniform except for the regions within the corner stall region towards the hub.

The work conducted within this chapter has demonstrated that whilst the 3D simulation can simulate features of the time-dependent boundary layer, it is not accurate enough to be used as a design tool, given its very large computational cost. The use of one or more 2D simulations at various key blade heights is a more appropriate tool if no significant radial flow component is evident, as the input conditions to the blade in question can more closely be controlled than using a multi-passage 3D simulation. The 2D simulations gave a more accurate representation of the flow, and can feasibly be ran on an industrial work-station or small computing cluster if a special investigation into the effects of wake-induced transition is required.

This page has been left intentionally blank.

Chapter 8

Final Compressor Simulations

Chapter 4 investigated the predictive performance of the turbulence models available in ANSYS-CFX. It was shown that a more accurate prediction of the boundary layer, and hence loss could be gained from using a transition model. Chapters 6 and 7 showed that the $\gamma - \theta$ model as used in the CFX code could qualitatively predict the unsteady development of a wake-affected boundary layer. It is useful to understand how the use of a transition model may benefit the industrial user, to whom parameters such as stage pressure ratio, and exit flow angles are important. In this chapter, experimental stage exit data is compared to the CFD results from the $\gamma - \theta$ model and the other turbulence models already used in this work. Two test cases were chosen; Cranfield's low speed research compressor (LSRC) and Cranfield's high speed research compressor (HSRC). In both cases, only the first stage was simulated. Due to the limited amount of data for both cases, most comparisons are relative between turbulence models rather than purely with experimental data.

Corrected mass flow (Kg/s)	10.6
Stage pressure ratio	1.025
Rotor R_e	$2.95 * 10^5$
Corrected speed (r.p.m)	1045
Reaction	0.586
Flow Coefficient	0.6
Hub/Tip ratio	0.91

Table 8.1: LSRC Stage 1 parameters at design

8.1 Cranfield Low Speed Research Compressor

The Cranfield low speed research compressor as detailed by Lyes (1999), is a highly loaded repeating 4 stage axial compressor, designed to simulate loading and blade characteristics within a high speed machine, but with the advantage of low speed data acquisition abilities. It has a parallel annulus with a hub/tip ratio of 0.91. The blades are 2D controlled diffusion, with each stage having identical characteristics. The machine configuration for this data consisted of 37 IGV's, 101 rotor blades and 134 stator blades. Rotor and stator blades included 1.1% span and 1.12% span tip clearance and had aspect ratios of 0.91 and 1.04 respectively. For this study, only the IGV and 1st stage were modelled at design flow (Table 8.1).

8.1.1 Numerical Procedure - LSRC

Two sets of grids were used to ensure the final results were grid independent. Firstly, a coarse grid consisting of approximately 190,000 nodes per passage and y^+=25 on all surfaces was used for all models except the γ-θ model. At a y^+=25 the $\gamma - \theta$ model essentially behaves as the k-ω SST model giving a fully turbulent prediction (see (Langtry and Menter, 2004)). Therefore there was nothing to be gained from running the $\gamma - \theta$ model. The grids were developed in CFX Turbogrid, utilising an H block structure, with matching topology across the blade tip.

The same set of fine grids were used for all of the models regardless of whether the models used wall functions or not. The details of each grid are given in Table 8.2. The stator domain extended approximately 2.5 chord lengths downstream of the trailing edge to avoid convergence problems at the outlet. A general grid interface (GGI) and stage mixing plane were used to connect the separate domains. The inlet was set to atmospheric total pressure, whilst the mass flow at the outlet was altered until the desired results were achieved. The mass flow used was 0.0791kg/s per passage, which equates to an equivalent 10.5994kg/s for the whole machine. Tip gaps for all blades were modelled. All simulations were run in steady state until the rms residuals converged to 10^{-6}.

8.1.2 Numerical Results - LSRC

The total pressure ratio based on circumferential mass averaging for both the coarse grid and the fine grid were compared for both the rotor exit and

	IGV	Rotor	Stator
# of nodes	716,364	2,039,223	1,647,444
# Spanwise nodes	90	161	170
# Streamwise nodes	150	139	120
# Circumferential nodes	48	49	40
# O-Grid (perpendicular)	15	30	30
# O-Grid (around blade)	66	90	56
Blade y^+	8	1	2
Hub y^+	8	25	2
Casing y^+	8	25	2

Table 8.2: Details of grids used for LSRC simulations

stator exit. No significant differences between the results were discovered. The total pressure ratios calculated for all the models on the fine grid at rotor exit are shown in Figure 8.1. The experimental data shows a steady total pressure rise from 0.2 span to 0.8 span as the flow migrates towards the casing. Above 0.8 span the effect of the tip leakage and the casing boundary layer reduces the total pressure rise. Below 0.2 span, the total pressure ratio is seen to increase. This is not the case in reality. The cobra probe used, experiences a relatively higher dynamic pressure as the flow near the hub is entrained along with the motion of the hub. Added to the static pressure which does not deviate, this creates a total pressure rise. It was not reported in Lyes (1999) how this affected the total pressure ratio in the vicinity of 0.2 span.

All the models give a good representation of the total pressure rise at the rotor exit. As expected, they do not predict a total pressure rise toward the

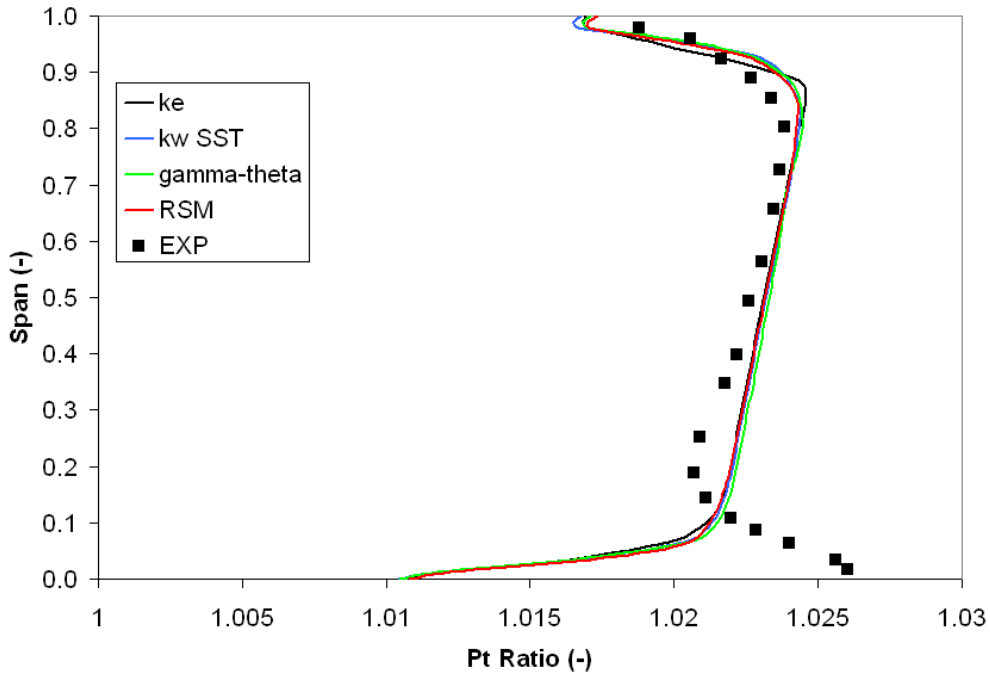

Figure 8.1: LSRC Rotor 1 exit Pitch-wise averaged pressure using fine grid

hub, as it is particular to the cobra probe. The three ω based models all returned almost identical values, with the $\gamma - \theta$ model giving a slight increase in pressure ratio below 0.6 span. The k-ϵ model gives a small increase in blockage toward the casing, with a less smooth transition to the mainstream flow at 0.9 span. The increase in total pressure ratio for all models occurs almost linearly from 0.1 to 0.8 span. The experimental data shows a similar pattern, but at a slightly more rapid rate of increase along the span. The main feature is that the models do not predict the same spanwise level of blockage in the rotor passage.

The flow angle at rotor exit confirmed that the k-ϵ model turned the flow on average 3° less than the ω based models. This is confirmed by observing both the c_p and c_f distributions about the rotor blade for all models. At 0.5

span, the k-ϵ model shows a greater region of negative work done on the flow towards the trailing edge (Figure 8.2). This is due to a thinner boundary layer on the suction surface, which increases c_p and a thicker boundary layer on the pressure surface, which reduces c_p. The results of local skin friction on both surfaces highlight this, as a lower c_f indicates a thicker boundary layer (when comparing two turbulent boundary layers) and a higher c_f indicates a thinner turbulent boundary layer. Local skin friction around the rotor blade at 0.5 span are shown in Figures 8.3 and 8.4.

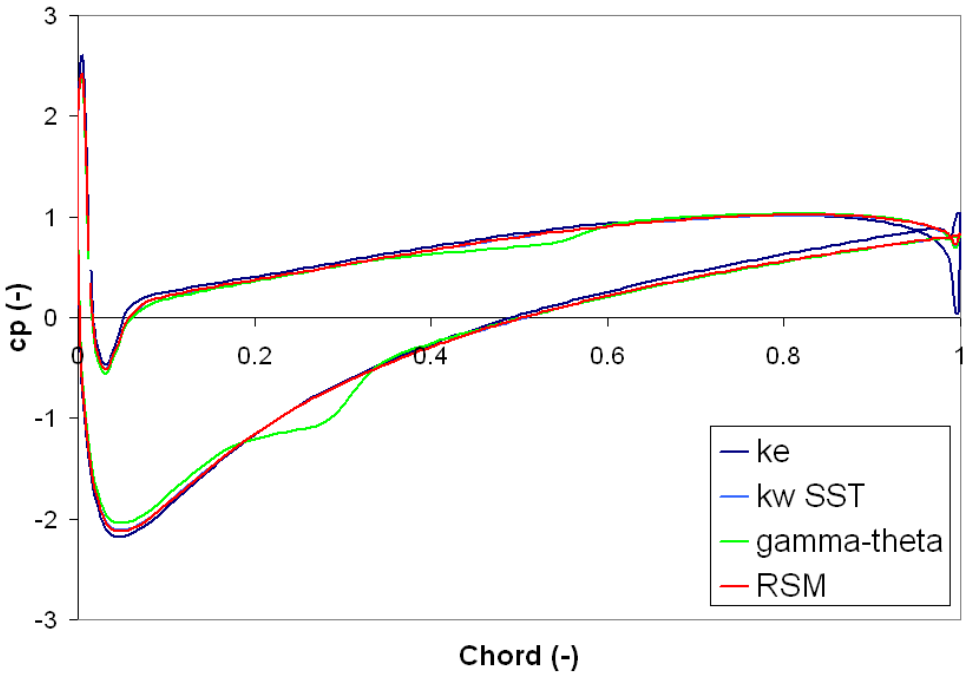

Figure 8.2: LSRC Rotor 1 blade local pressure coefficient

Figures 8.2 to 8.4 also show the $\gamma - \theta$ model to predict a transitional separation bubble on both surfaces. Whilst the suction surface bubble remains along the length of the span, the pressure surface bubble is not evident at either 0.15 or 0.85 span. However, all the results indicate that transition and

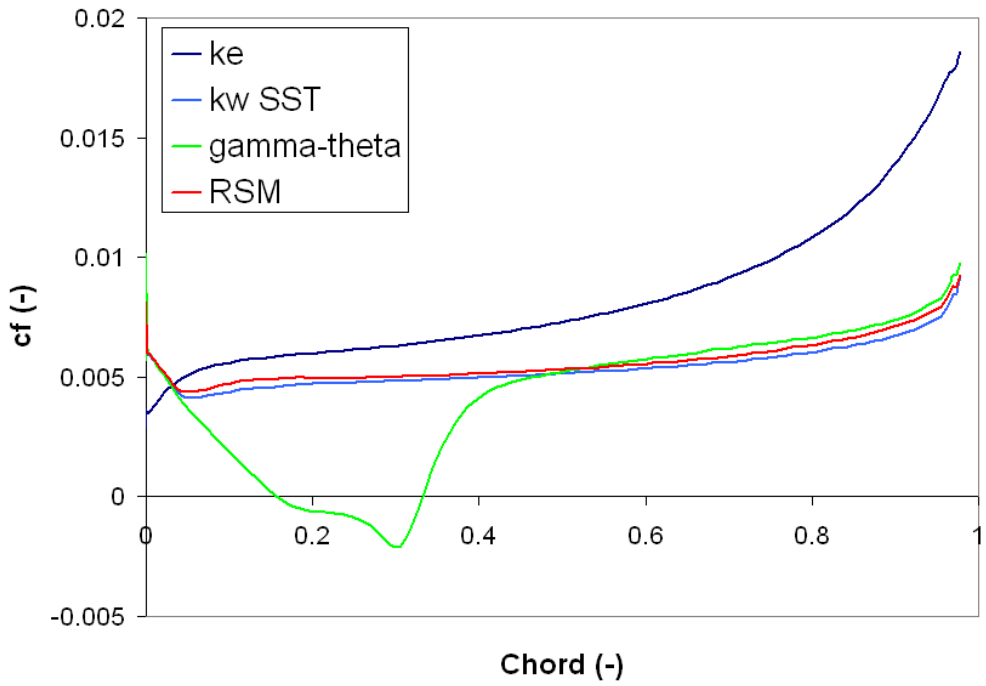

Figure 8.3: LSRC Rotor 1 blade local skin friction coefficient on the suction surface

separation bubbles predicted by the $\gamma - \theta$ model do not prevent the $\gamma - \theta$ model from predicting the same blade pressure rise as either the k-ω SST and RSM models.

The comparison of experimental and simulated total pressure ratio for the stator exit is shown in Figure 8.5. The total pressure ratio is reduced compared to the rotor exit as expected. The greater work done by the stator occurs at 0.7 span. A greater pressure loss towards the hub and casing are recorded. A greater discrepancy exists between experimental and numerical results than for the rotor exit. All models overestimate the loss toward the hub and casing, and do not predict the greater work done toward 0.7 span.

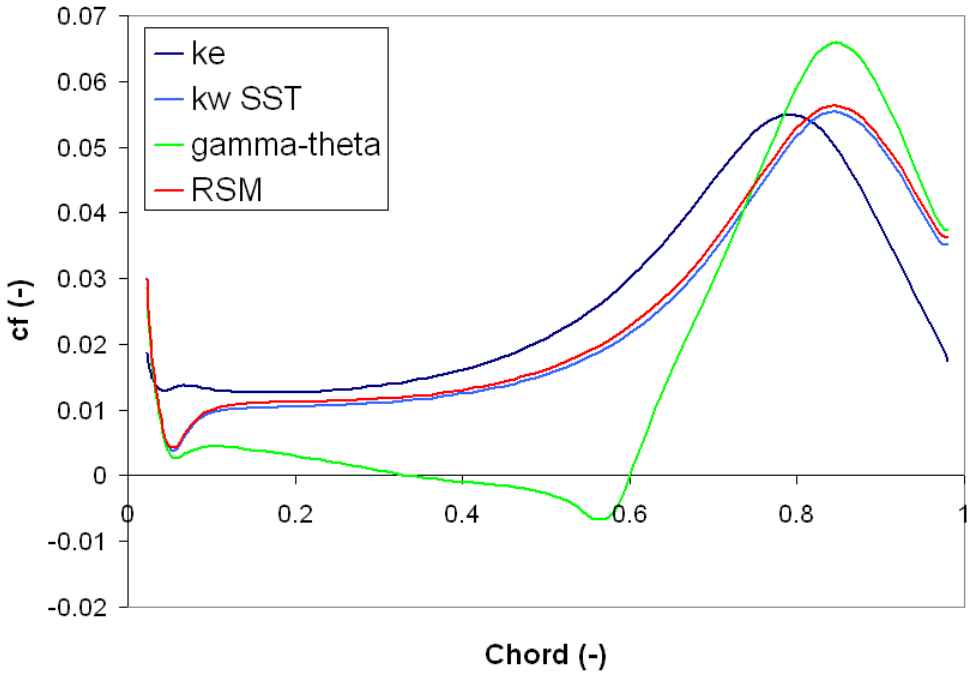

Figure 8.4: LSRC Rotor 1 blade local skin friction coefficient on the pressure surface

The k-ϵ model returns the greatest pressure loss through the stator passage, more so below 0.2 span. All ω based models give a similar total pressure ratio, with the $\gamma - \theta$ model showing the least total pressure loss, again more so at 0.2 span.

As the k-ϵ predicts less turning of the flow at rotor exit, the flow incidence angle on the downstream stator blade is decreased. This alters the pressure distribution around the blade as shown by both the resultant spanwise stator exit total pressure ratio (Figure 8.5) and c_p distribution at 0.5 span (Figure 8.6). The difference in incidence causes the boundary layer to develop at a different rate to the boundary layer predicted by the ω based models. This is shown by the k-ϵ model predicting a lower value of c_p than the ω based

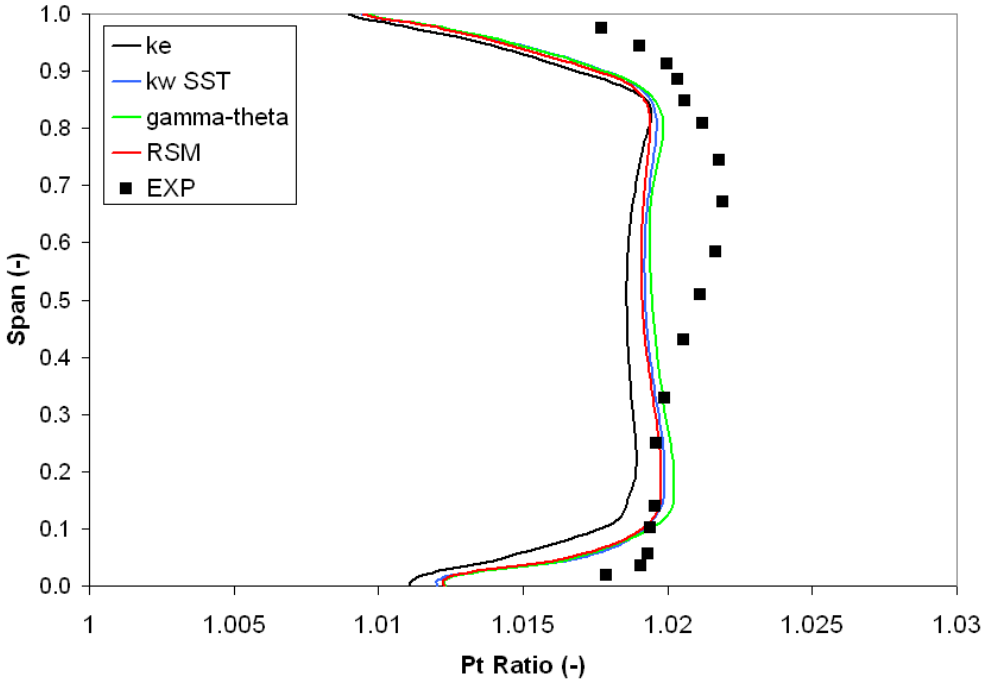

Figure 8.5: LSRC Stator 1 exit Pitch-wise averaged pressure using fine grid

models. As with the c_p distribution for the rotor blade, the ω based models all return similar values for the stator c_p distribution.

Figure 8.6 shows the $\gamma - \theta$ model to predict a small separation bubble between 27% and 32% chord on the suction surface. This does not occur along the entire blade span. Towards the hub at 0.15 span, the boundary layer is close to separation, but does not separate. Figure 8.7 shows that it is only the laminar boundary layer which separates. Transition is initiated in the resulting bubble and the reattached bubble is turbulent. The laminar boundary layer separates on the pressure surface at 0.15 span (see Figure 8.8), and the turbulent boundary layer is also close to separation. Only the k-ϵ model does not predict that the boundary layer is close to separation.

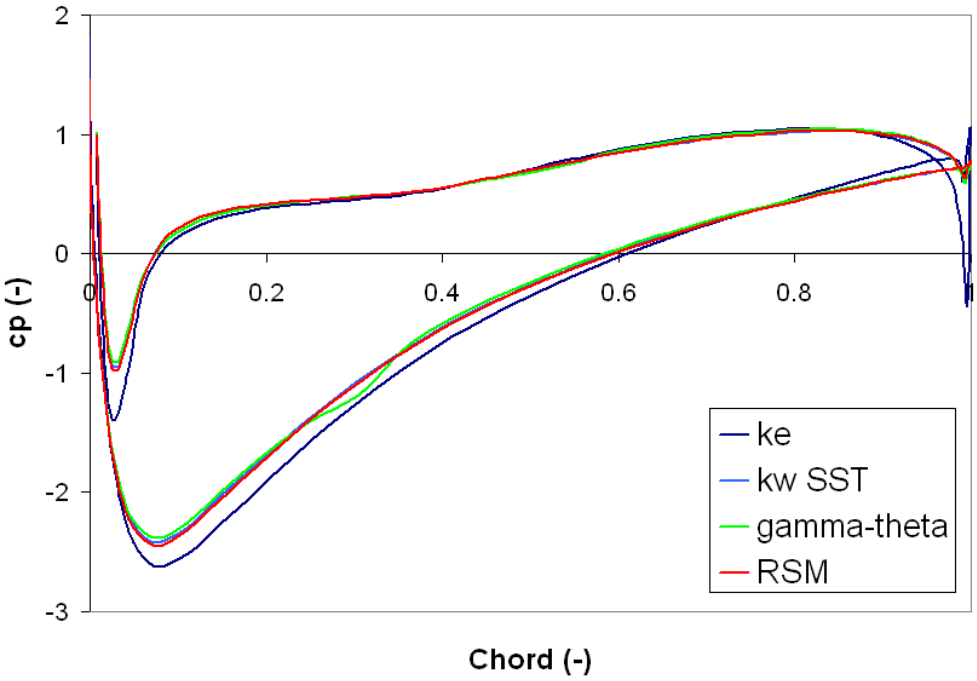

Figure 8.6: LSRC Stator 1 blade local pressure coefficient at 0.5 span

8.2 Cranfield High Speed Research Compressor Stage

The first Stage of the Cranfield University three stage high speed axial compressor was simulated to provide a comparison for the turbulence models within a high speed environment. The experimental data used was the datum data from the European AdComB project (Lippett et al., 2003). The blading consists of controlled diffusion type with a constant tip diameter and an exit hub/tip ratio of 0.91. The sections were conventionally stacked with no lean or sweep applied. The first stage consisted of 37 IGV's, 71 rotor

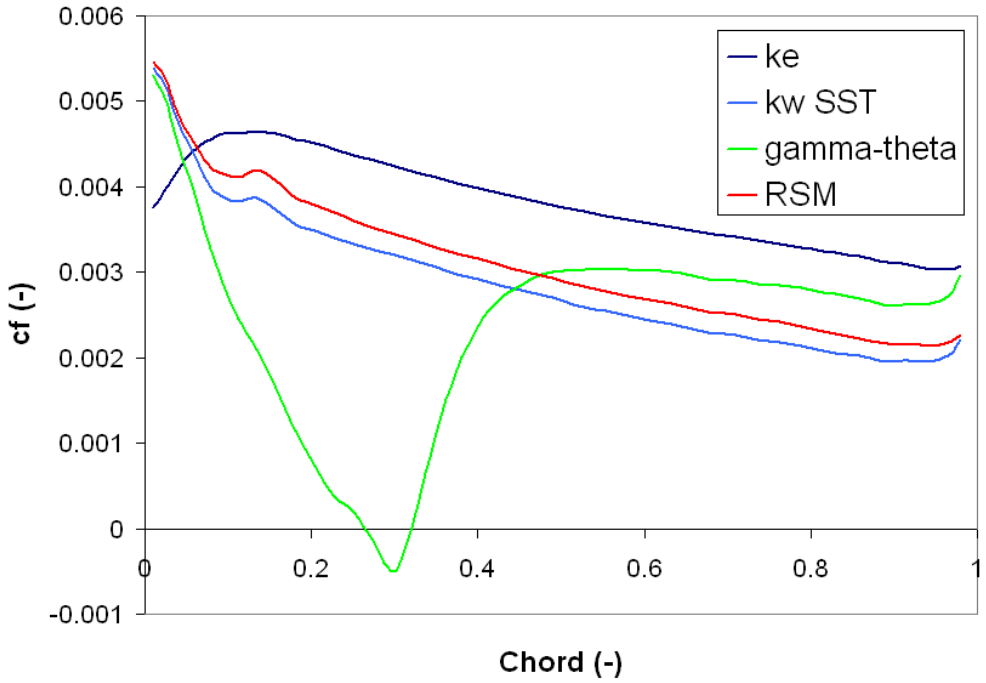

Figure 8.7: LSRC Stator 1 Blade local skin friction coefficient on the suction surface at mid-span

blades and 91 stator blades. Compressor and Stage 1 parameters for the design flow conditions are included in Table 8.3.

8.2.1 Numerical Procedure - HSRC

A similar methodology was used in the construction of the grids as was for the low speed case. A y^+ value of 8 was used on all surfaces to reduce the node count to a feasible level for the computational resources available at the time. The user manual (ANSYS-CFX, 2007) shows a $y^+ \leq 8$ does not significantly affect the relative position of the transition start point. The coarse grids contained approximately 230,000 nodes per passage, whilst the

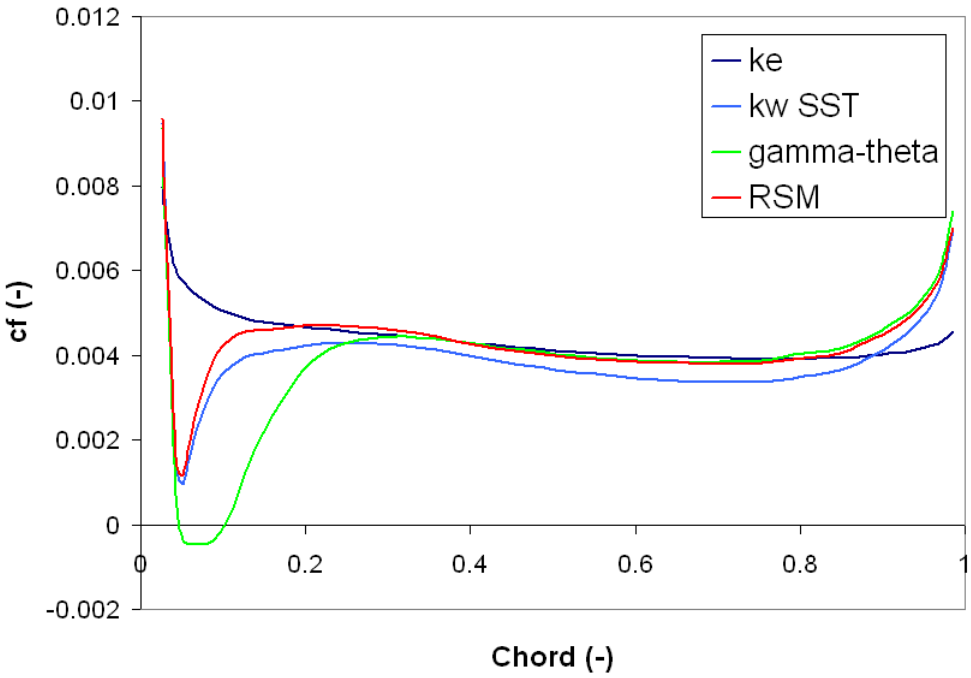

Figure 8.8: LSRC Stator 1 Blade local skin friction coefficient on the pressure surface at 0.15 span

fine grids contained approximately 1,200,000 nodes per passage. Details of node distribution and other parameters for the fine grids are given in Table 8.4.

8.2.2 Numerical Results - HSRC

Like the LSRC, both the coarse and fine grids gave similar results, proving grid independence. The results were comparable to Lippett (2003). Pitch-wise averaged total pressure ratio and yaw for the IGV exit are shown in Figures 8.9 and 8.10. Both show a good prediction from all of the turbulence models as compared to the experimental data. The blockage created by the

	Design
Corrected mass flow (kg/s)	10.6
Corrected speed (r.p.m)	9300
Flow coefficient	0.6997
Loading coefficient	0.5496
Reaction	0.5693
Rotor R_e.	5.82×10^5
Stator R_e.	4.78×10^5
Rotor max Mach. No.	0.8285
Stator max Mach. No	0.7418

Table 8.3: HSRC Stage 1 parameters at design point

	IGV	Rotor	Stator
# of nodes	1,191,610	1,276,821	1,138,428
# Spanwise nodes	75	83	79
# Streamwise nodes	157	169	157
# Circumferential nodes	85	73	73
# O-Grid (perpendicular)	18	18	18
# O-Grid (around blade)	84	84	84
Blade y^+	8	8	8
Hub y^+	8	8	8
Casing y^+	8	8	8

Table 8.4: Details of grids used for HSRC simulations

hub and casing boundary layers is predicted to be approximately 4% span less than experiment.

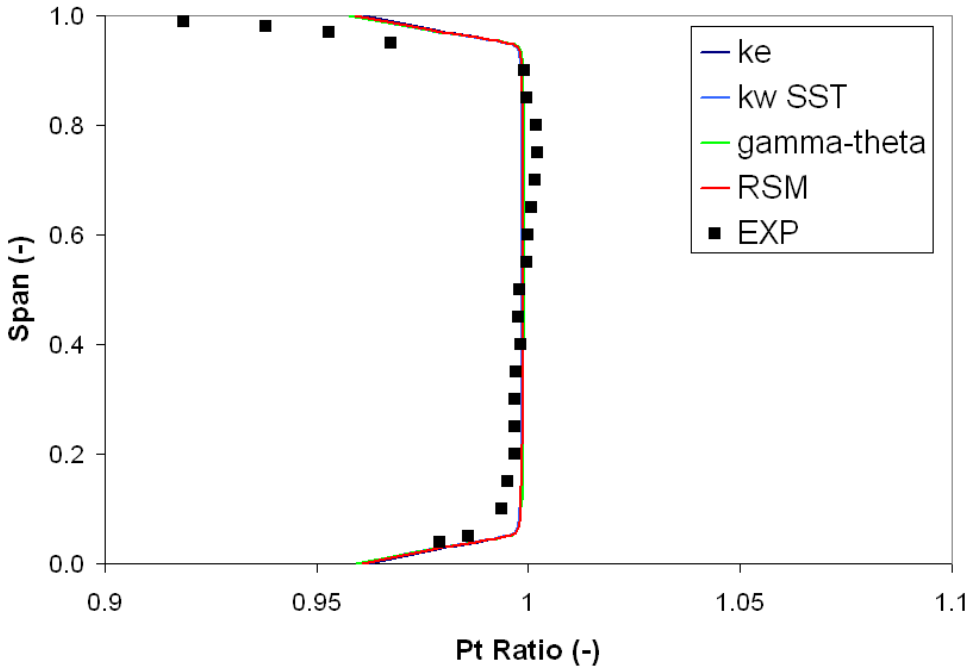

Figure 8.9: HSRC IGV Pitch-wise averaged pressure using fine grid

The CFD does not predict the slight increased loading above 0.5 span due to radial migration of the flow from the inlet. This may be due to the inlet conditions specified. The flow at the inlet was given to be parallel to the annulus, therefore, no radial migration is expected at this point in the compressor. All turbulence models predict the same levels of loss as shown by a near perfect matching of total pressure ratio at IGV exit.

Figure 8.10 shows that towards the casing region the CFD does not predict the same region of lower momentum flow which is characterised by the under-turning of the flow. Small regions of overturned flow toward the hub and casing at 0.1 and 0.85 span respectively are also not captured sufficiently. In the main, all of the ω based models give a good comparison of the yaw

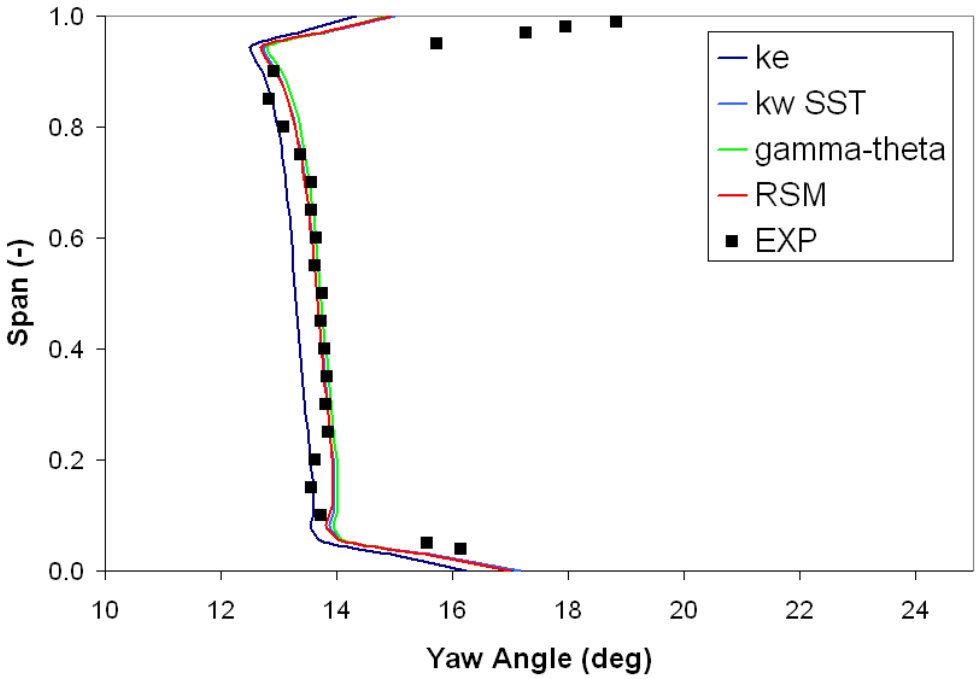

Figure 8.10: HSRC IGV Pitch-wise averaged yaw using fine grid

from hub to casing. The CFD is within a degree of the experimental values. The k-ϵ model however gives a significant deviation from the ω based models' results. It predicts an over-turning of the flow along the span of the IGV blade. The k-ϵ model is more sensitive to adverse pressure gradients and therefore will separate earlier at the trailing edge, which causes the deviation in yaw angle.

The pitch-wise averaged total pressure ratio at rotor exit (shown in Figure 8.11) is less well predicted. The characteristic of the CFD to not to predict a greater loading from above mid-span is again highlighted. All models again return similar values. The maximum difference between CFD and experimental values occurs at mid-span and is approximately 0.5. Towards the

hub, below 0.1 span, the k-ω model predicts a greater loss than the ω based models.

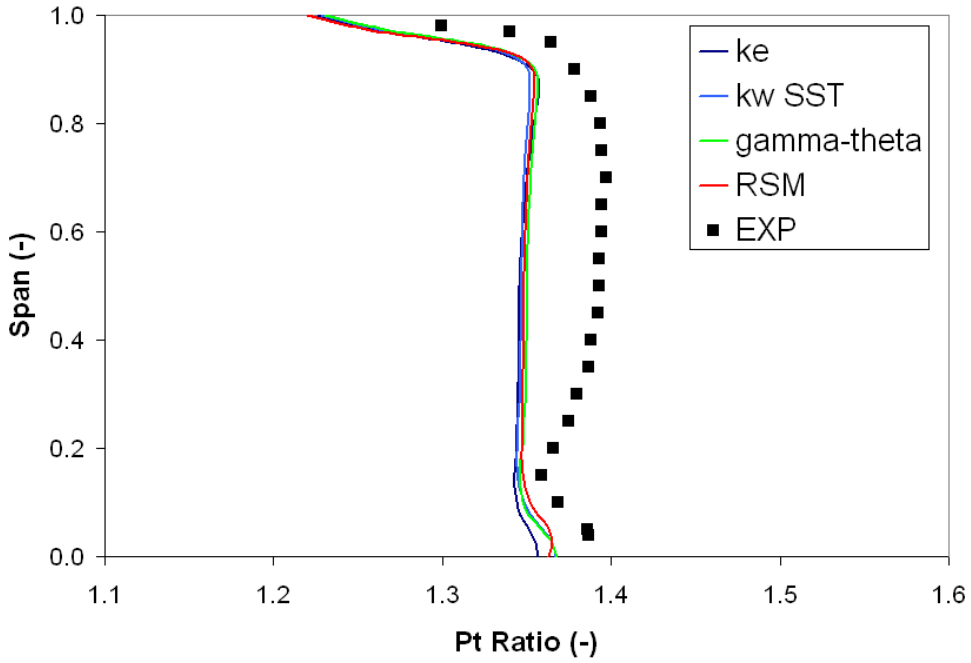

Figure 8.11: HSRC Rotor 1 Pitch-wise averaged pressure using fine grid

The pitch-wise averaged yaw from hub to casing is shown in Figure 8.12. The 3D nature of the rotor blade trailing edge creates an almost linear yaw from hub to casing outside of the boundary layer and tip regions. The CFD is within 3 degrees of the experimental values for most of the blade span. It also predicts well the tip region. However, towards the hub, the CFD is in opposite to the experimental data. All models predict a much larger under-turning of the flow from the secondary flow in this region than shown in the experiment. It is plausible that the CFD has over-predicted the vorticity of this region of flow.

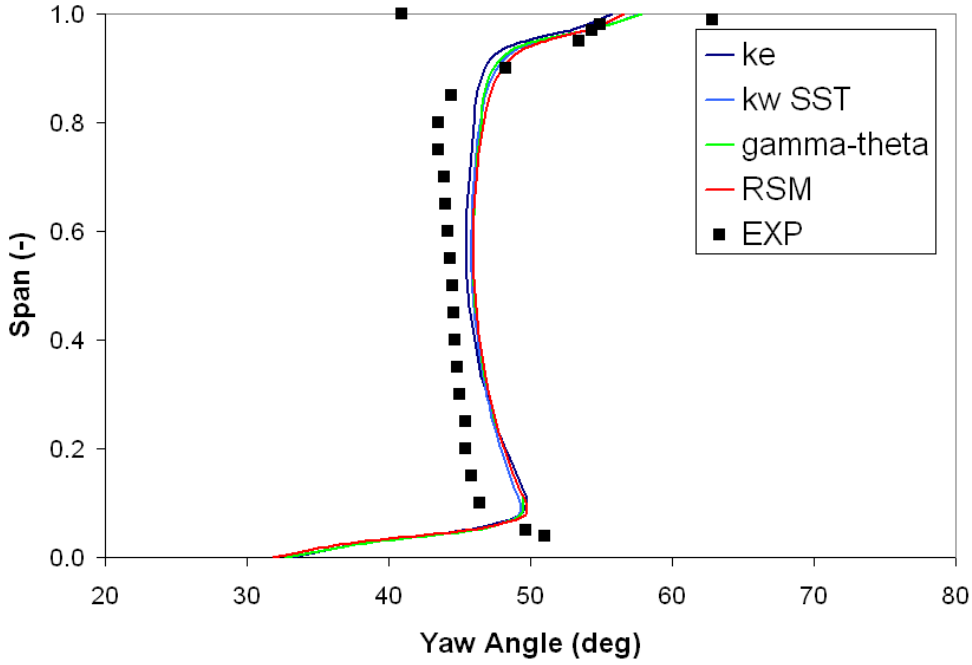

Figure 8.12: HSRC Rotor 1 Pitch-wise averaged yaw using fine grid

All of the models behave similarly. The $\gamma - \theta$ model predicts transition to occur at 0.5-0.6 chord on the suction surface, and 0.2-0.3 chord on the pressure surface. As shown by Figures 8.11 and 8.12, transition does not affect the pressure rise or direction of flow leaving the blade. This is mainly because there is no separation until the trailing edge. Predicting transition will have a greater effect on the boundary layer if separation occurs toward the trailing edge.

The comparison between experimental and CFD values for pitch-wise averaged total pressure ratio at stator exit (Figure 8.13) is similar to that of the rotor blade exit. This is not surprising as the stator exit is likely to give the same hub to casing pattern, but with a small total pressure loss. Again,

there is a negligible difference between the turbulence models used. The only difference between the models is towards the hub, with the ω near wall resolution based models identifying a smaller region of corner stall, than the k-ϵ model.

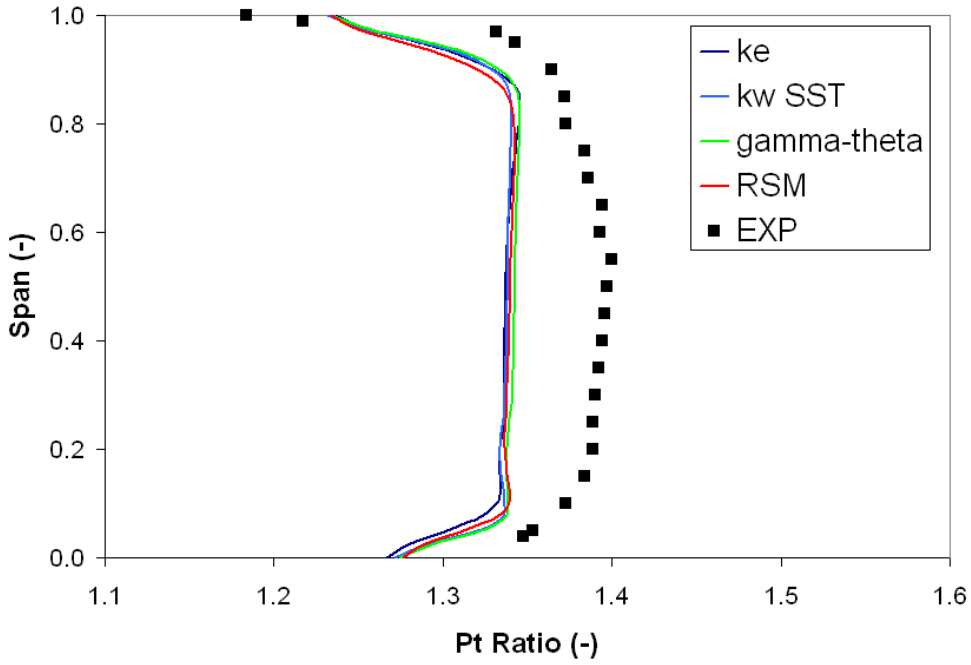

Figure 8.13: HSRC Stator 1 Pitch-wise averaged pressure using fine grid

The yaw is well predicted as for both the IGV and rotor. The pitch-wise averaged yaw from hub to casing at the stator exit is shown in Figure 8.14. All of the models predict a similar general trend, but starting from approximately 0.2 span, and extending to 0.9 span, the difference between CFD and experimental values grows to approximately 2 degrees. The RSM predicts an over-turning of the flow up to approximately 0.8 span. An examination of cp at 0.5 span (Figure 8.15) reveals that the RSM model predicts a lower

blade loading than the other models.

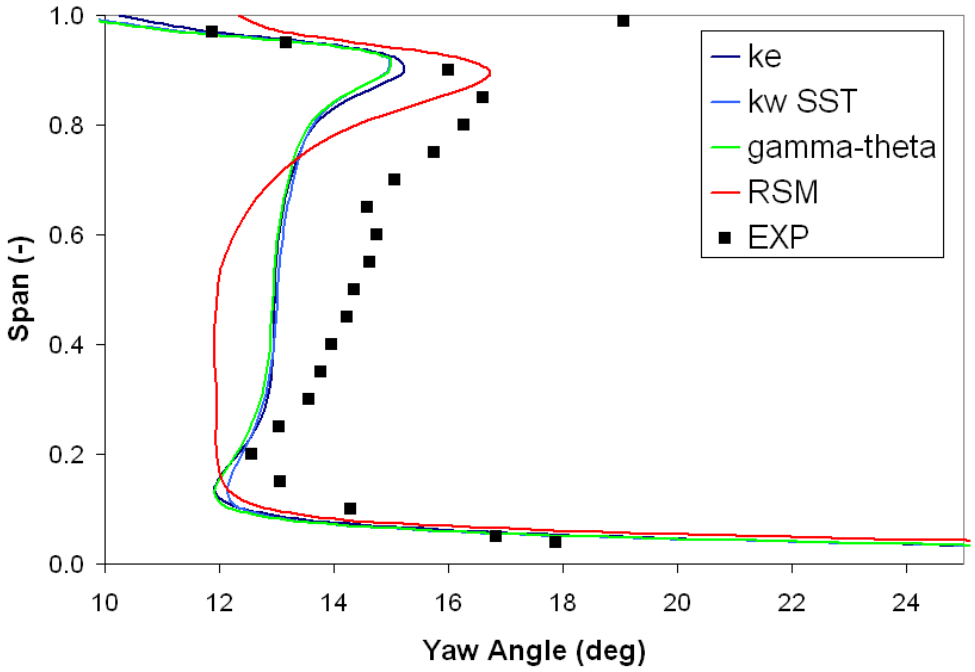

Figure 8.14: HSRC Stator 1 Pitch-wise averaged yaw using fine grid

The profile loss and total pressure loss were calculated for the stator blade to examine the difference between the fully turbulent k-ω SST model and the $\gamma - \theta$ transition model. This way, the effect of transition can be observed for both 2D and 3D loss quantities, as the $\gamma - \theta$ model uses the k-ω SST model as its baseline. The stagnation pressure loss was calculated by using Equation 6.3, and the trailing edge momentum thicknesses were computed at 97% surface distance at mid-span. The k-ω SST model predicted a Y_p=2.17% with the $\gamma - \theta$ model returning a value of Y_p=1.78%, giving an 18% reduction in the loss at mid-span. The total pressure loss for the full stator blade and passage was calculated to be Y=2.94% for the k-ω SST model and Y=2.7%

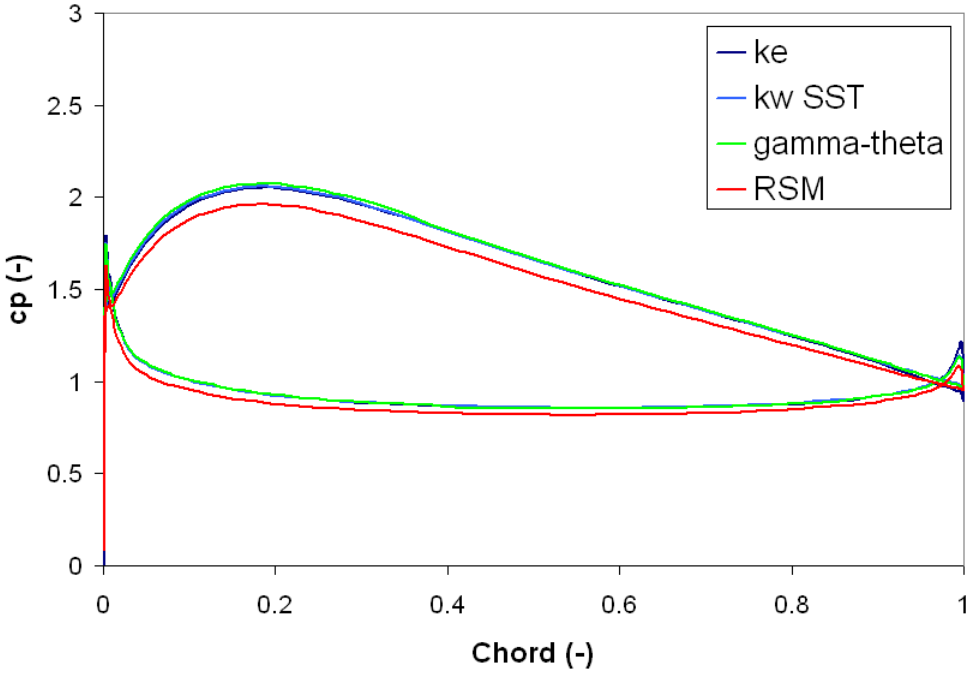

Figure 8.15: HSRC Stator 1 Local blade cp using fine grid

for the $\gamma - \theta$ model. This gives a reduction of loss by predicting transition of 8.2%.

Results of the local skin friction at mid-span (not shown) show that transition occurs on both surfaces between approximately 0.35-0.45 chord. This is post peak suction. This appears to be a plausible explanation to why the profile loss for the $\gamma - \theta$ model is 18% lower than that of the k-ω SST model. As the peak suction region creates the greatest entropy loss ($\dot{s} \propto U_{\infty}^{3}$), the turbulent boundary layer of the k-ω SST model will experience a much greater loss than the laminar boundary layer of the $\gamma - \theta$ model.

According to Denton (1993), in most machines, only approximately one third

of the total loss come from the profile loss. In general, the total loss for the blade row comes from the endwall loss, tip leakage loss and profile loss, all in approximately equal measure. As there is no tip gap for the stator blade, the total pressure loss is made up of only profile loss and endwall losses. A close examination of Figure 8.13 shows that both the k-ω SST model and the $\gamma - \theta$ model have an almost identical total pressure rise in the hub and casing endwall regions. The difference of total pressure rise develops between 0.10 and 0.80 span, where the dominant loss one would expect to find is boundary layer profile loss. Therefore it is hypothesised that the 8.2% decrease in total pressure loss, Y, is mainly due to the reduction in profile loss due to transition.

8.3 Chapter Closure

The case studies have shown that the prediction of transition may not necessarily result in the more accurate prediction of important stage variables such as flow angle or total pressure rise. On the whole, there was little difference between the models, with the exception of k-ϵ and RSM predictions of HSRC IGV and S1 exit flow angles respectively. The main differences between the models were observed for the local skin friction and coefficient of pressure distributions. These parameters are indicators of the state of the boundary layer. The loss calculations for the HSRC S1 showed the profile loss at S1 exit stage was affected the greatest, as compared to pressure ratios and flow angles. The calculations showed that a significant reduction, and hence a presumably more accurate value, in loss can be achieved by using a transition model rather than a fully turbulent model. It is interesting to

note that in this case, endwall loss did not appear to be affected by the use of a transition model. It is concluded that for non-loss calculations, it is a more efficient use of resources for the industrial user to use the $k-\omega$ SST model than any other of the models tested in this work.

For compressors, the prediction of separation is more important than that of transition, in comparison with gas turbines, although transition can have a significant effect on the position of separation. The use of the k-ϵ model must be kept to those flows where separation is known not to occur, as it cannot predict separation due to adverse pressure gradients or non-right angled geometry. Whilst the $\gamma-\theta$ model does offer a qualitative prediction of transition, it offers no improvement for flows where transition does not affect the separation point, as compared to the $k-\omega$ SST model, and requires a much finer grid to run on, which increases the computational cost. The advantage the $\gamma-\theta$ model has is the option for the users to use their own transition correlation, which would make the model more relevant for their particular machinery. Generally, k-ϵ models are not able to properly model the flow at the trailing edge when separation is present.

Mixing planes are not necessarily a source of inaccuracy for flows at design conditions. The computations showed that even though rotor passage behaviour is poorly predicted, the stator passage behaviour was found to be in good agreement with experimental data. There was no obvious sign or pattern of continuous degradation of passage results with each stage. Further it is suggested that if the user only requires passage data, rather than blade data, then they only require a coarse grid (y^+=25), rather than a fine grid (y^+=8).

Chapter 9

General Conclusions

The work contained in this thesis has concentrated on the current developments and capabilities in modelling both steady state and unsteady transition effects on axial compressor blading. After a review of current turbulence and transition models, a range of turbomachinery applicable test cases were used to highlight the performance of a range of turbulence and transition models available in the commercial ANSYS-CFX code. The turbulence models used were the k-ϵ, k-ω SST, ω-based BSL Reynolds Stress Model and the $\gamma - \theta$ transition model from Menter et al. (2004a).

The test cases increased in complexity and relative similarity from a simple flat plate, to a transitional flat plate, compressor cascade, a 2D then a 3D unsteady low speed axial compressor case, and finally a low speed and high speed steady state axial compressor stage. All four turbulence models mentioned above were used for all simulations except for the 2D and 3D unsteady simulations contained in Chapters 6 and 7 respectively.

Whilst a conclusions section was included at the end of each chapter, conclu-

sions for the work in a more overall context are included here. Recommendations for further study on the topic covered in this thesis are also included at the end of this chapter.

9.1 Steady State Simulations

The simulations conducted within the initial simulations showed that all models returned a good degree of agreement with the experimental data. Variable performance was experienced for cases with separation, both separation bubble and terminal separation, and for the flat plate with a shear velocity inlet case. The performance of the models was highly dependent upon the skill of the user to describe appropriate boundary conditions which gave a good representation of the flow. The inaccuracies inherent in the models themselves were secondary to the inaccuracies caused by inappropriate boundary conditions.

The test cases showed that the ω-based models returned results closer to experimental data than the k-ϵ model. This highlighted the fact that the more accurate prediction of the boundary layer given by the ω-based models was crucial to their accuracy. The greatest discrepancy occurred when the k-ϵ did not predict a separation bubble or the correct streamwise position of terminal separation toward the trailing edge. In practise, this means that simulations conducted with the k-ϵ model, should in general, predict a lower level of loss due to a decreased amount of separation, and a lower momentum thickness boundary layer at the trailing edge than if a separation bubble is present towards the leading edge. The ERCOFTAC T3L series showed the

rate of development of the boundary layer was affected by the prediction of the separation bubble toward the leading edge. The ωRSM model, even though attempting to account for the non-linear effects which occur due to separation, streamline curvature, flow shear etc, did not offer a consistent improvement in the accuracy of the results. Given the increased computational cost required to run this model, it does not offer enough additional benefits for it to be used. Therefore, it was concluded that for general purpose axial compressor CFD simulations, the k-ω SST model is the model of choice.

The literature review showed that a tremendous amount of research and development has gone into RANS based transition models. The $\gamma - \theta$ model performed well during the initial simulations and shows a great potential for its use in turbomachinery applications. It predicted well, features that only occured due to the presence of a laminar boundary layer. Examples were the separation bubble in the ERCOFTAC T3C4 flat plate test case, and the separation bubble found on the suction surface of the -8.5° incidence Zierke and Deutsch compressor cascade test case. Attached transition cases such as the ERCOFTAC T3A flat plate test case showed a more accurate development and thickening of the boundary layer. All of these factors assist the $\gamma - \theta$ model in predicting a more accurate level of loss at the trailing edge than a fully turbulent model.

Its greatest limitation was the accurate prediction of transition in a highly turbulent or accelerating flow. On the whole, the k-ω SST model gave a more accurate length of separation bubbles than the $\gamma - \theta$ model. The length of the transitional separation bubble depended upon the height of the bubble, as highlighted by the transitional flat plate subject to inlet shear flow. A

thin bubble causes slower, damped transition to occur, which is relatively longer than a higher bubble in which rapid, undamped transition occurs. The $\gamma - \theta$ was the model most sensitive to inlet conditions, as the point of transition depends upon the level of turbulence in the freestream, which in turn is also dependent upon the local velocity and the viscosity ratio specified at the inlet. Both the LSRC and HSRC showed the transition model does not provide the user with a more accurate pressure rise or flow angle information than any of the turbulence models used. However, the transition model does return a lower, and presumably more accurate level of loss within the compressor, and so is still a useful tool if a more accurate description of loss is required, particularly if the loss is linked to transition affected events, such as separation bubbles etc.

9.2 Unsteady Axial Compressor Simulation

Both the 2D and 3D simulations proved that the $\gamma-\theta$ model and the ANSYS-CFX code can simulate the main effects of unsteady wake-induced transition and its subsequent effects on the boundary layer. The model appeared to give a good qualitative comparison to the experimental data for the 2D high and medium loading cases, whilst still predicting the effects such as pressure surface transitional separation bubble for the 2D low loading case. A calmed region was present in the results which continued to suppress separation and transition for a period of wake passing. Again, the inlet conditions used to simulate the inlet and outlet conditions had a great effect on the accuracy of the simulation. The use of multiple Fourier series to describe the flow worked well. However, more detailed information on wake structure and wake mixing

behaviour is required. The negative jet created by the wake defect is essential in the prediction of wake-induced transition. The increase in turbulence found within the wake is of secondary importance. However, the correlations from Mayle and Abu-Ghannam and Shaw etc, describe the increase in freestream turbulence within the wake to have the greatest importance.

The process by which unsteady wake-induced transition took place on the suction surface within the CFD code was as follows; A region of high turbulent kinetic energy builds up at the leading edge. The rotor wake impinges upon and passes the leading edge. The velocity defect within the wake alters the velocity profile of the boundary layer. The turbulent kinetic energy at the leading edge travels along the suction surface of the blade at a slower velocity to the wake. It was thought that the velocity defect increases Re_θ, and whilst the boundary layer is recovering from the wake defect, the turbulent kinetic energy from the leading edge reaches this part of the boundary layer and reduces the Reynolds number at which transition can start, Re_{θ_t}. Transition now occurs. Hence the wake does not directly start the transition process, but creates the conditions within the boundary layer, such that the turbulence from the leading edge travelling behind the wake can start the transition process.

The superposition of the wake turbulence and velocity appeared to work well. However, a more accurate description of the relationship between total turbulence level, random and periodic turbulence is given by;

$$Tu_D^2 = \widetilde{Tu}^2 + Tu^2 \tag{9.1}$$

As given in Walker et al. (1999). Although this was not used, the difference

in using Equation 9.1 over the relationship used was not detrimental to the results. Using Equation 9.1 for the medium loading case would give a total disturbance value of approximately 7 - 8% for when the rotor wake and IGV wake interact. Run 5 of the 2D unsteady simulations showed that even an inlet turbulence intensity of 30% had only a small effect of the transition region. Therefore, the difference created by the use of Equation 9.1 would be minimal.

Whilst the $\gamma - \theta$ model gave a good prediction of the unsteady suction surface boundary layer, both the 2D and 3D simulations showed the streamwise position of the transition region on the pressure surface was poorly predicted. Experimental data shows that transition is complete within the wake path, and that $\gamma = 0.7$ toward the trailing edge between wakes. Both 2D and 3D CFD simulations showed transition to not be complete at any stage on the pressure surface, and only a small variation in the completion of the transition region within the wake path. It is thought that this is due to the model not fully accounting for the effects of the impinging positive jet process on pressure surface.

The 3D simulations also showed the impingement of the rotor wake on the suction surface did not have as great an effect as in the 2D case and the experimental data in suppressing the suction surface separation bubble. The unsteady boundary layer was inherently different to that of the steady state case due to fluctuations and instabilities captured in the unsteady simulation process. The non-suppression of the separation bubble also affected the strength of the subsequent calmed region. The calmed region post wake in the 2D simulations was more evident than in the 3D simulations. The 3D

simulation highlighted that although the position of the separation along the blade span was similar, the start of transition predicted by the model was not. Therefore it is not necessarily clear that the data used by Walker et al. (1999) at mid-span is representative of the whole span.

Due to both the computational cost involved and the uncertainty in some of the results, it is not expected that the use of unsteady transition modelling will become an integral design tool within the immediate future. The blade designer is currently able to obtain a similar amount of information on blade row exit conditions and loss estimations through the use of fully turbulent models such as the $k-\omega$ SST and S1 codes such as MISES.

The use of the transition model in a 3D simulation provides the blade designer with a valuable insight to the time dependent development of the boundary layer and any subsequent separation found on the blade. This becomes of a greater importance if the position of transition affects the terminal separation point on the blade surface. It also has the advantage of giving a greater amount of information about the boundary layer than is available by experiment. However, for special studies into the benefits of utilising wake effects to suppress separation and reduce losses for high lift or highly 3D blading, it is recommended that a set of 2D slices be simulated. They will give the blade designer a greater amount of information of the behaviour of the boundary layer, with a good degree of confidence in the qualitative accuracy of its results. These types of simulations will be of more use in long term projects, or on-going R&D work to assess the feasibility of new areas of research. As the frequency of the use of unsteady simulations increases, the use of a transition model becomes more important.

To allow for the correct use of a transition model, unsteady blade boundary layer data must be available. It is the authors belief that currently, an experimental study of unsteady wake-induced transition effects would yield a greater return of knowledge than by using current RANS based transition models. As there is no other documented simulation of unsteady axial compressor transitional boundary layer using the $\gamma-\theta$ model, this work is unique.

9.3 Further Work

Whilst the $\gamma - \theta$ model worked well in general, work must still be done to improve it for use in the design of axial compressor blading. Menter et al. (2004a) suggested some initial improvement to be investigated such as the inclusion of geometry curvature and freestream length scale. Freestream length scale is required as it can significantly alter within the wake, which affects the rate of transition within the wake-induced path. More investigations should be conducted to quantify the magnitude of these effects, and whether they should be included into the $\gamma - \theta$ model.

Piotrowski and Elsner (2007) described the use of the model within an axial turbine, with a variable freestream length scale correlation. It returned an improved accuracy over the current $\gamma - \theta$ model found in ANSYS-CFX. Wheeler et al. (2007a) showed the effect of pressure fluctuations within the wake-induced transition process. This is not currently included within the model. The γ correlation for the development of transition requires adjustment for the pressure surface and where transition takes place in a region of

flow acceleration and subject to a positive wake jet.

The way the wake jet interacts with the boundary layer does not currently seem to have been taken into account within the correlation or the code. It seems likely that both the correlations used and the model itself require some alterations to incorporate this effect. This may well improve the prediction of the calmed effect seen post wake, which was not always well predicted in the simulations, especially on the pressure surface. Schreiber and Steinert (2002) reason that the interaction of the surface particle induced instabilities with the disturbances coming from outside the boundary layer is a complex, but rather important mechanism that must be considered in future research work on transition onset. A comparison of the $\gamma - \theta$ model with the model of Lodefier and Dick (2005), which attempts to account for this interaction, may produce a useful learning exercise as to whether it is important for a CFD model to attempt to reproduce these interactions.

The use of the model within a transonic compressor is required to be studied, as this will be of greater use to a compressor design group than simpler low-speed axial compressors. The applicability of the transition model to a shock / laminar boundary layer interaction would be important for the design of high speed compressors. This is important as the shock can cause local separation of a laminar boundary layer, which increases the loss generation within the boundary layer. The interaction of transition with a shock wave, such as studied by Suder (1997) should be attempted to be understood and implemented.

Finally, this project has highlighted that to truly understand the workings

of the transition model, and indeed for any turbulence model, access to the source code and model variables is required. The author suggests that any further work conducted with the $\gamma - \theta$ mode be done within a code to which the user has full access to in order to conduct further investigations to the architecture of the model. This will be required to alter the model to make it more accurate at simulation axial compressor flows, and off-design flows.

References

Abu-Ghannam, B, J. and Shaw, R. (1980). Natural transition of boundary layers the effect of turbulence, pressure gradient, and flow history. *Journal of Mechanical Engineering Science, IMechE*, 22(5):213–228.

ANSYS-CFX (2005). *ANSYS CFX Release 10 User Manual*. ANSYS.

ANSYS-CFX (2007). *ANSYS CFX Release 11 User Manual*. ANSYS.

Baldwin, B. S. and Lomax, H. (1978). Thin layer approximation and algebraic model for separated turbulent flows. In *AIAA Conference*. AIAA Paper 78-257.

Barakos, G., Drikakis, D., and Leschziner, M. (1998). Numerical investigation of the dynamic stall phenomenon using non-linear eddy-viscosity models. In *16th AIAA Applied Aerodynamics Conference*, Albuquerque, New Mexico. AIAA-98-2740.

Barney, J. (1986). Strategic factor markets: Expectations, luck and business strategy. *Management Science*, 32(10):1231–1241.

Belamri, T., Galpin, P., Braune, A., and Cornelius, C. (2005). Cfd analysis of 15 stage axial compressor part ii: Results. In *Proceedings of GT2005, ASME Turbo Expo 2005: Power for Land, Sea and Air, Reno-Tahoe, Nevada, USA*, Reno, NV. ASME.

Boiko, A, V., Grek, G, R., Dovgal, A, V., and Kozlov, V, V. (2002). *The Origin of Turbulence in Near-Wall Flows*. Springer, Berlin.

Borello, D., Hanjalic, K., and Rispoli, F. (2005). Prediction of cascade flows with innovative second-moment closures. *Journal of Fluids Engineering*, 127:1059–1070.

Borello, D. and Rispoli, F. (2003). Improved non-equilibrium turbulence closure modelling for axial flow compressors simulation. In *Proceedings of ASME Turbo Expo 2003, Power for Land, Sea and Air*, Atlanta, Georgia, USA.

Bowen, H. K. (2006). Pratt & Whitney: Engineering standard work. Case Study 9-604-084, Harvard Business School.

Brilliant, L., Balamucki, S., Burger, G., Dong, Y., and Lejambre, C. (2004). Application of multistage cfd analysis to low pressure compressor design. In *GT2004-54263, Proceedings of ASME Turbo Expo 2004 Power for Land, Sea and Air, June 2004, Vienna, Austria*.

Bruna, D., Cravero, C., and Turner, M. (2006). The development of an aerodynamic performance prediction tool for modern axial flow compressor profiles. In *ASME Turbo Expo 2006: Power for Land, Sea and Air*, Barcelona, Spain. GT2006-90187.

Chen, K, K. and Thyson, N, A. (1971). Extension of emmons spot theory to flows on blunt bodies. *AIAA Journal*, 9(5):821–825. Cited in: Solomon, W,J., Walker, G,J., Gostelow, J,P., Transition Length Prediction for Flows With Rapidly Changing Pressure Gradients. ASME Journal of Turbomachinery, 118, 744-751.

Coull, J., Thomas, R., and Hodson, H. (2008). Velocity distributions for low pressure turbines. In *ASME Turbo Expo 2008: Power for Land, Sea and Air*, Berlin, Germany. ASME. GT2008-50589.

Cumpsty, N, A. (1989). *Compressor Aerodynamics*. Longman, Singapore.

Cumpsty, N., Dong, Y., and Li, Y. (1995). Compressor blade boundary layers in the presnce of wakes. In *ASME Turbo Expo*. 95-GT-443.

Denton, J. (1993). Loss mechanisms in turbomachines. *ASME Journal of Turbomachinery*, 115:621–656.

Denton, J. and Dawes, W. (1999). Computational fluid dynamics for turbomachinery. *Proceedings of Institute of Mechanical Engineers*, 213(Part C):107–124.

Deutsch, S. and Zierke, W, C. (1987). The measurements of boundary layers on a compressor blade in cascade: Part 1 a unique experimental facility. *ASME Journal of Turbomachinery*, 109:520–526.

Deutsch, S. and Zierke, W. (1988). The measurement of boundary layers on a comparison blade in cascade: Part 3 - pressure surface boundary layers and the near wake. *Journal of Turbomachinery*, 110:146–152.

Diorio, J., Kelley, D., and Wallace, J. (2007). The spatial relationships between dissipation and production rates and vortical structures in turbulent boundary and mixing layers. *Physics of Fluids*, pages 19–26.

Driver, D. (1991). Reynolds shear stress measurements in a separated boundary layer. AIAA Paper 91-1787.

Driver, D. and Seegmiller, H. (1985). Features of a reattaching turbulent shear layer in divergent channel flow. *AIAA Journal*, 23(2):163–171.

Durbin, P. and Wu, X. (2007). Transition beneath vortical disturbances. *Annual Review of Fluid Mechanics*, 39:107–128.

Edwards, J., Roy, C., Blottner, F., and Hassan, H. (2001). Development of a one-equation transition/turbulence model. *AIAA Journal*, 39(9):1691–1698.

Emmons, H. (1951). The laminar-turbulent transition in boundary layer - part i. *Journal of Aerospace Sciences*, 18:490–498.

Fernbach, A. (2007). Behaviour of transition models in cfx software. Report of Summer Exchange Project at Cranfield University (Unpublished).

Fransson, J., Matsubara, M., and Alfredsson, P. (2005). Transition induced by free-stream turbulence. *Journal of Fluid Mechanics*, 527:1–25.

Gatski, T. and Rumsey, C. (2002). *Closure Strategies for Turbulent and Transitional Flows*, chapter 1 - Linear and Nonlinear Eddy Viscosity Models, pages 9–46. Cambridge University Press.

Giles, M. (1998). Some thoughts on exploiting cfd for turbomachinery design. In *IMechE Symposium on Exploiting CFD for Turbomachinery Design*.

Gostelow, J., Blunden, A., and Walker, G. (1992). Effects of free-stream turbulence and adverse pressure gradients on boundary layer transition. *ASME Journal of Turbomachinery*, 116:392–404.

Grotjans, H. and Menter, F. (1998). Wall functions for general application cfd codes. In *ECCOMAS98 Proceedings of the Fourth European Computational Fluid Dynamics Conference*, pages 1112–1117, Athens, Greece.

Halstead, E, E., Wisler, D, C., Okiishi, T, H., Walker, G, J., Hodson, H, P., and Shin, H, W. (1997a). Boundary layer development in axial compressors and turbines: Part 1 of 4 composite picture. *ASME Journal of Turbomachinery*, 119:114–127.

Halstead, E, E., Wisler, D, C., Okiishi, T, H., Walker, G, J., Hodson, H, P., and Shin, H, W. (1997b). Boundary layer development in axial compressors and turbines: Part 4 of 4 computations and analyses. *ASME Journal of Turbomachinery*, 119:128–139.

Halstead, E, E., Wisler, D, C., Okiishi, T, H. a. W. G. J., Hodson, H, P., and Shin, H, W. (1997c). Boundary layer development in axial compressors and turbines: Part 2 of 4 compressors. *ASME Journal of Turbomachinery*, 119:426–444.

Hanna, K. (2006). Turbomachinery in the power generation industry. *Fluent News*, Fall:16–17.

Harvey, S., Dawes, W., and Bolger, J. (2003a). An automatic design optimisation system for axial compressors part ii: Experimental validation. In *Proceedings of ASME Turbo Expo 2003, Power for Land Sea and Air*, Atlanta, GA, USA. ASME. GT2003-38650.

Harvey, S., Dawes, W., and Gallimore, S. (2003b). An automatic design optimisation system for axial compressors part i: Software development. In *Proceedings of ASME Turbo Expo 2003, Power for Land Sea and Air*, Atlanta, GA, USA. ASME. GT2003-38115.

Hatman, A. and Wang, T. (1999). A prediction model for separated-flow transition. *Journal of Turbomachinery*, 121:594–602.

Henderson, A., Walker, G., and Hughes, J. (2005). The influence of turbulence on wake dispersion and blade row interaction in an axial compressor. In *ASME Turbo Expo 2005: Power for Land, Sea and Air*, Reno-Tahoe, Nevada, USA. ASME. GT2005-68432.

Henderson, A., Walker, G., and Hughes, J. (2006). Unsteady transition phenomena at a compressor blade leading edge. In *Proceedings of GT2006, ASME Turbo Expo 2006: Power for Land, Sea and Air, GT2006-90641*, Barcelona, Spain.

Herring, S, J. (2006). Exploiting the capabilities of experiment and numerical methods. In *GT2006-90208, Proceedings of GT2006, ASME Turbo Expo 2006: Power for Land, Sea and Air, May 8-11, Barcelona, Spain*, Barcelona, Spain.

Hobson, G., Wakefield, B., and Roberts, W. (1999). Turbulence amplification with incidence at the leading edge of a compressor cascade. *International Journal of Rotating Machinery*, 5(2):89–98.

Hodson, H, P. (1991). Aspect of unsteady blade-surface boundary layers and transition in axial turbomachines. In *VKI Lecture Series, Boundary Layers in Turbomachines*. Cited in: Lou, W., Hourmouziadis, J. (2000). Separation Bubbles Under Steady and Periodic-Unsteady Main Flow Conditions. ASME Journal of Turbomachinery, 122, 634-643.

Hooker, J., Hoyle, D., and Bevis, D. (2006). The application of cfd for the aerodynamic development of the c-5m galaxy. In *44th AIAA Aerospace Sciences Meeting and Exhibit, AIAA 2006-856*, Reno, Nevada.

Horlock, J. and Denton, J. (2005). A review of some early design practice

using computational fluid dynamics and a current perspective. *ASME Journal of Turbomachinery*, 127:5.

Hourmouziadis, J. (1989). Aerodynamic design of low pressure turbines. AGARD Lecture Series 167, Neuilly-Sur-Seine. Cited in: Lou, W., Hourmouziadis, J. (2000). Separation Bubbles Under Steady and Periodic-Unsteady Main Flow Conditions. ASME Journal of Turbomachinery, 122, 634-643.

Howell, R. (1999). *Wake - Separation Bubble Interactions in Low Reynolds Number Turbomachinery*. PhD thesis, Whittle Laboratory, Cambridge University Engineering Department.

Hughes, J, D. and Walker, G, J. (2001). Natural transition phenomena on an axial compressor blade. *ASME Journal of Turbomachinery*, 123:392–401.

Iseler, J., Hilgenfeld, L., and Pfitzner, M. (2006). Investigations of the boundary layer on a higher loaded compressor cascade with wake-induced transition. In *ASME Turbo Expo 2006: Power for Land, Sea and Air*, Barcelona, Spain. GT2006-90665.

Jacobs, R. and Durbin, P. (2001). Simulations of bypass transition. *Journal of Fluid Mechanics*, 428:185–212.

Jarrett, J., Dawes, W., and Clarkson, P. (2007). An approach to integrated multi-disciplinary turbomachinery design. *ASME Journal of Turbomachinery*, 129:488–494.

Johnson, M. (1994). A bypass transition model for boundary layers. *ASME Journal of Turbomachinery*, 116:759–764.

Johnson, M. and Dris, A. (2000). The origin of turbulent spots. *Journal of Turbomachinery*, 122(January):88–92.

Kipouros, T., Jaeggi, D., Dawes, W., Parks, G., Savill, A., and Clarkson, P. (2008). Biobjective design using optimisation for axial compressors using Tabu search. *AIAA Journal*, 46(3):710–711.

Kolmogorov, A. (1941). Dissipation of energy in a locally isotropic turbulence. *Doklady Akad. Nauk SSSR*, 32:141. English translation in: American Mathematical Society Translations 1958, Series 2, Vol 8, p. 87, Providence R.I.

Koyabu, E., Funazaki, K., and Kimura, M. (2005). Experimental studies on wake-induced bypass transition of flat-plate boundary layers under favourable and adverse pressure gradients. *Japan Society of Mechanical Engineers International Journal*, 48(3):579–588.

Koyabu, E., Funazaki, K.-i., and Kimura, M. (2003). Effects of periodic wake passing upon bypass transition of blade boundary layer and unsteady loss. In *Proceedings of the International Gas Turbine Congress 2003*, Tokyo. IGTC2003Tokyo TS-068.

Kozulovic, D. and Rober, T. (2006). Modelling the streamline curvature effects in turbomachinery flows. In *Proceedings of GT2006, ASME Turbo Expo 2006: Power for Land, Sea and Air, GT2006-90265*, Barcelona, Spain.

Langtry, R. (2006). *A Correlation-Based Transition Model using Local Variables for Unstructured Parallelized CFD Codes*. PhD thesis, Institut für Thermische Strömungsmaschinen und Maschinenlaboratorium, Universität Stuttgart.

Langtry, R. and Menter, F. (April 22, 2004). *User Manual - CFX 5.7 Transition Model*. ANSYS CFX, Staudenfeldweg 12, 83624 Otterfing, technical report ansys / tr-04-05 edition.

Lee, H. and Kang, S, H. (2000). Flow characteristics of transitional boundary layers on an airfoil in wakes. *ASME Journal of Turbomachinery*, 122:522 532.

Lippett, D. (2003). *The Acquisition of Three Dimensional Flow Measurements Through a Multi Stage High Speed Axial Flow Compressor*. PhD thesis, Cranfield University.

Lippett, D., Timmis, P., Ivey, P., Bailey, D., and Woollatt, G. (2003). Development of a new high-speed multi-stage compressor facility. In *International Gas Turbine Congress, Tokyo*.

Lodefier, K. and Dick, E. (2005). An unsteady rans transition model with dynamic description of intermittency. In *ASME Turbo Expo 2005: Power for Land, Sea and Air*, Reno-Tahoe, Nevada, USA. GT2005-68714.

Lodefier, K., Piotrowski, W., Kubacki, S., Elsner, W., and Dick, E. (2007). Validation of a dynamic intermittency model for the prediction of wake-induced bypass transition on turbine blades. In *Workshop on LES, Transition Modelling and Turbulent Combustion*, Het Pand, Ghent, Belgium.

Lou, W. and Hourmouziadis, J. (2000). Separation bubbles under steady and periodic-unsteady main flow conditions. *ASME Journal of Turbomachinery*, 122:634–643.

Lyes, P. A. (1999). *Low Speed Axial Compressor Design and Evaluation; High Speed Representation and Endwall Flow Control Studies*. PhD thesis, Cranfield University, Cranfield, UK.

Maekawa, T. and Atsumi, S. (1952). Transition caused by the laminar flow separation. Technical Memorandum 1352, National Advisory Committee for Aeronautics, Washington, USA.

Mallach, R., Lehman, I., and Vogeler, K. (2007). Periodical unsteady flow within a rotor blade row of an axial compressor - part i: Flow field at midspan. In *ASME Turbo Expo 2007: Power for Land, Sea and Air*, Montreal, Canada. GT2007-27210.

Mayle, R, E. (1991). The role of laminar-turbulent transition in gas turbine engines. *ASME Journal of Turbomachinery*, 113:509–537.

Mayle, R, E. (1992). Unsteady multimode transition in gas turbine engines. In *AGARD PEP 80*. AGARD. Cited in: Solomon, W,J., Walker, G,J., Gostelow, J,P., Transition Length Prediction for Flows With Rapidly Changing Pressure Gradients. ASME Journal of Turbomachinery, 118, 744-751.

Mayle, R. and Dullenkopf, K. (1991). More on the turbulent-strip theory for wake induced transition. *ASME Journal of Turbomachinery*, 113:428–432.

Menter, F. (1992). Performance of popular turbulence models for attached and separated adverse pressure gradient flows. *AIAA Journal*, 30(8):2066–2072.

Menter, F. (1994). Two equation eddy viscosity turbulence models for engineering applications. *AIAA Journal*, 32(8):1598–1605.

Menter, F. (2002). Turbulence modelling for turbomachinery applications, lucerne, switzerland. QFD (CFX) Presentation.

Menter, F., Esch, T., and Kubacki, S. (2002). Transition modelling based on local variables. In *5th International Symposium on Turbulence Modelling and Measurements*, pages 555–564, Mallorca, Spain.

Menter, F., Langtry, R., Likki, S, R., Suzen, Y, B., Huang, P, G., and Völker, S. (2004a). A correlation-based transition model using local variables part 1 model formulation. In *Proceedings of ASME Turbo Expo 2004, Power for Land Sea and Air*, Vienna, Austria. GT2004-53452.

Menter, F., Langtry, R., Likki, S., Suzen, Y., Huang, P., and Völker, S. (2004b). A correlation-based transition model using local variables part ii test cases and industrial applications. In *ASME TURBO EXPO 2004, Vienna, Austria*. GT2004-53454.

Menter, F., Langtry, R., and Volker, S. (2006). Transition modelling for general purpose cfd codes. *Flow Turbulence Combust*, 77:277–303.

Menter, F., Langtry, R., Volker, S., and Huang, P. (2005). Transition modelling for general purpose codes. In *ERCOFTAC International Symposium on Engineering Turbulence Modelling and Measurements - ETMM6*.

Misaka, T. and Obayashi, S. (2006). Application of local correlation-based transition model to flows around wings. In *44th AIAA Aerospace Sciences Meeting and Exhibit*, Reno, Nevada. AIAA 2006-918.

Narasimha, R. (1957). On the distribution of intermittency in the transition region of a boundary layer. *Journal of the Aeronautical Sciences*, 24:711–712. Cited in: Walker, G, J. (1989). Transitional flow on Axial Turbomachine Blading. AIAA Journal, 27(5): 595-602. Also cited in: Solomon, W, J., Walker, G, J., Gostelow, J, P., Transition Length Predic-

tion for Flows With Rapidly Changing Pressure Gradients. ASME Journal of Turbomachinery, 118: 744-751.

Neel, R, E., Godfrey, A, G., and Slack, D. (2003). Turbulence model validation in gasp version 4. In *33rd AIAA Fluid Dynamics Conference and Exhibit*, Orlando, Florida. AIAA 2003-3740.

Nichols, R. and Nelson, C. (2003). Application of hybrid rans/les turbulence models. In *41st Aerospaces Meeting and Exhibit*, Reno, Nevada. AIAA 2003-0083.

Obremski, H. and Fejer, A. (1967). Transition in oscillating boundary layer flows. *Journal of Fluid Mechanics*, 29:93–111.

Oliver, A. (1961). Comparison between sand cast and machined blades in the vortex wind tunnel. Report ME 103, Aeronautical Research Laboratories, Melbourne, Australia.

Oro, J., D'iaz, K., Morros, C., and Marigorto, E. (2007). Unsteady flow and wake transport in a low-speed axial fan with inlet guide vanes. *Journal of Fluids Engineering*, 129:1015–1027.

Ottavy, X., Vilmin, S., Hodson, H., and Gallimore, S. (2004). The effects of wake-passing unsteadiness over a highly loaded compressor-like flat plate. *ASME Journal of Turbomachinery*, 126(1):13–23.

Palikaras, A., Yakinthos, K., and Goulas, A. (2002). Transition on a flat plate with a semi-circular leading edge under uniform and positive shear free-stream flow. *International Journal of Heat and Fluid Flow*, 23:455–470.

Palikaras, A., Yakinthos, K., and Goulas, A. (2003). The effect of negative shear on the transitional separated flow around a semi-circular leading edge. *International Journal of Heat and Fluid Flow*, 24:421–430.

Piotrowski, W. and Elsner, W. (2007). Modelling of laminar-turbulent transition with the use of intermittency transport equation. In *Workshop on LES, Transition Modelling and Turbulent Combustion*, Het Pand, Ghent, Belgium.

Pope, S, B. (2000). *Turbulent Flows*. Cambridge University Press, Cambridge.

Praisner, T. and Clark, J. (2007). Predicting transition in turbomachinery - part i: A review and new model development. *ASME Journal of Turbomachinery*, 129:1–13.

Praisner, T., Grover, E., Rice, M., and Clark, J. (2007). Predicting transition in turbomachinery - part ii: Model validation and benchmarking. *ASME Journal of Turbomachinery*, 129:14–22.

Reed, H., Saric, W., and Arnal, D. (1996). Linear stability theory applied to boundary layers. *Annual Review of Fluid Mechanics*, 28:389–428.

Roberts, S. and Yaras, M. (2005a). Effects of surface-roughness geometry on separation-bubble transition. In *Proceedings of GT2005, ASME Turbo Expo 2005: Power for Land, Sea and Air*, Reno-Tahoe, Nevada, USA. ASME.

Roberts, S, T. and Yaras, M, I. (2005b). Modeling transition in separated and attached boundary layers. *ASME Journal of Turbomachinery*, 127:402–411.

Roberts, W. (1980). Calculation of laminar separation bubbles and their effect on airfoil performance. *AIAA Journal*, 18(1):25–31.

Rumsfeld, D. (2002). Department of defense news briefing. http://news.bbc.co.uk/1/hi/world/americas/3254852.stm.

Saric, W., Carrillo Jr, R., and Reibert, M. (1998). Nonlinear stability and transition in 3-d boundary layers. *Meccanica*, 33(5):469487.

Savill, A. (1996). *Turbulence and Transition Modeling*, chapter 6: One-point closures applied to transition, pages 233–268. Kluwer Academic Publishing.

Savill, A. (2002a). *Closure Strategies for Turbulent and Transitional Flows*, chapter Chapter 17: By-Pass Transition Using Conventional Closures, pages 464–492. Cambridge University Press.

Savill, A. (2002b). *Closure Strategies for Turbulent and Transitional Flows*, chapter Chapter 18: New Strategies in Modeling By-Pass Transition, pages 493–521. Cambridge University Press.

Savill, A, M. (1993a). *Engineering Turbulence Modelling And Experiments 2*, chapter Further Progress In The Turbulence Modelling Of By-pass Transition, pages 583–592. Rodi, W., and Martinelli, F., Elsevier, New York.

Savill, A, M. (1993b). *Near Wall Turbulent Flows*, chapter Some Recent Progress In The Turbulence Modelling Of By-pass Transition, pages 829–848. Elsevier, New York.

Schreiber, H.-A. and Steinert, W., a. K. B. (2002). Effects of reynolds number and free-stream turbulence on boundary layer transition in a compressor cascade. *ASME Journal of Turbomachinery*, 124:1–9.

Schubauer, G, B. and Klebanoff, P, S. (1956). Contributions on the mechanics of boundary-layer transition. Technical Report TN 1289, NACA.

Scrivener, C., Connolly, C., Cox, J., and Dailey, G. (1991). Use of cfd in the design of a modern multistage aero engine lp turbine design. In *Turbomachinery: Latest Development in a Changing Scene. Proceedings of the IME European Conference*, number C423/056 in IME/C-423/056. IMechE, London, UK.

Shobeiri, M. (2005). Intermittency based unsteady boundary layer transition modelling, implementation into navier-stokes equations. In *ASME Turbo Expo 2005: Power for Land, Sea and Air*, Reno-Tahoe, Nevada, USA. GT2005-68375.

Shultz, H. and Gallus, H. (1988). Experimental investigation of the three-dimensional flow in an annular compressor cascade. *Journal of Turbomachinery*, 110.

Singer, B. (1993). Modeling the transition region. Contractor Report 4492, NASA. High Technology Corporation.

Singh, U, K. (1974). *The Effect of viscosity on the flow past aerofoils in cascade*. PhD thesis, Liverpool University. Cited in: Abu-Ghannam, B,J, and Shaw, R. (1980). Natural Transition of Boundary Layers The Effect of Turbulence, Pressure Gradient, and Flow History. Journal of Mechanical Engineering Science, IMechE, 22(5), 213-228.

Smith Jr, L. (2002). Axial compressor aerodesign evolution at General Electric. *ASME Journal of Turbomachinery*, 124:321–330.

Solomon, W, J., Walker, G, J., and Gostelow, J, P. (1996). Transition

length prediction for flows with rapidly changing pressure gradients. *ASME Journal of Turbomachinery*, 118:744–751.

Solomon, W, J., Walker, G, J., and Hughes, J, D. (1999). Periodic transition on an axial compressor stator: Incident and clocking effects: Part ii transition onset predictions. *ASME Journal of Turbomachinery*, 121:408–415.

Solomon, W. and Walker, G. (2000). Incidence effects on wake-induced transition on an axial compressor blade. *Journal of Propulsion and Power*, 16(3):397–405.

Spalart, P. and Allmaras, S. (1992). A one equation turbulence model for aerodynamic flows. In *AIAA Conference*. AIAA Paper 92-0439.

Steelant, J. (1999). Modelling of laminar-turbulent transition for high free-stream turbulence. In *30th AIAA Fluid Dynamics Conference*, Norfolk, VA. AIAA. AIAA 99-3790.

Suder, K. (1997). Blockage development in a transonic, axial compressor rotor. Technical Memorandum 113115, NASA, Lewis Research Center, Cleveland, Ohio. Prepared for ASME Turbo Expo, 1997.

Suzen, Y. B., X. G. and Huang, P. G. (2002). Predictions of transitional flows in low-pressure turbines using an intermittency transport equation. *AIAA Journal*, 40(2):254266.

Thomas, R. and Gostelow, J. (2005). The pervasive effect of the calmed region. In *ASME Turbo Expo 2005: Power for Land, Sea and Air*, Reno-Tahoe, Nevada, USA. ASME. GT2005-69125.

Ubaldi, M., Zunino, P., Campora, U., and Ghiglione, A. (1996). Detailed velocity and turbulence measurements of the profile boundary layer in a large scale turbine cascade. In *International Gas Turbine and Aeroengine Congress & Exhibition*, Birmingham, UK. ASME. 96-GT-42.

Uzol, O., Brzozowski, D., Chow, Y.-C., Katz, J., and Meneveau, C. (2007). A database of piv measurements within a turbomachinery stage and sample comparisons with unsteady rans. *Journal of Turbulence*, 8:1–20.

Vicedo, J., Vilmin, S., Dawes, W., and Savill, A. (2004). Intermittency transport modelling of separated flow transition. *ASME Journal of Turbomchinery*, 126:424–431.

Vilmin, S., Hodson, H., Savill, A., and Dawes, W. (2003). Predicting wake-passing transition in turbomachinery using an intermittency-conditioned modelling approach. In *33rd AIAA Fluid Dynamics Conference and Exhibit*, Orlando, Florida.

Walker, G. (1972). *An Investigation of the Boundary Layer Behaviour on the Blading of a Single-Stage Axial-Flow Compressor*. PhD thesis, University of Tasmania.

Walker, G., Hughes, J., and Solomon, W. (1999). Periodic transition on an axial compressor stator: Incidence and clocking effects: Part 1 - experimental data. *ASME Journal of Turbomachinery*, 121:398–407.

Walker, G., Hughes, J., Solomon, W., and Kohler, I. (1997). Wake mixing and blade clocking effects in an axial compressor. In Billig, F., editor, *13th International Symposium on Air Breathing Engines*, volume 2, pages 1397–1406. International Society for Air Breathing Engines. ISABE 97-7188.

Walker, G, J. (1968). The prediction of boundary layer development on axial flow turbomachine blades. In *Conference on Hydraulics and Fluid Mechanics*. The Institution of Engineers, Australia.

Walker, G, J. (1989). Transitional flow on axial turbomachine blading. *AIAA Journal*, 27(5):595–602.

Walraevens, R. and Cumpsty, N. (1993). Leading edge separation bubble on turbomachinery blades. In *ASME Turbo Expo*. 93-GT-91.

Walters, D. and Leylek, J. (2004). A new model for boundary layer transition using a single-point rans approach. *ASME Journal of Turbomachinery*, 126:193–202.

Wheeler, A., Miller, R., and Hodson, H. (2007a). The effect of wake induced structures on compressor boundary-layers. *Journal of Turbomachinery*, 129:705–712.

Wheeler, A., Sofia, A., and Miller, R. (2007b). The effect of leading-edge geometry on wake interactions in compressors. In *Proceedings of ASME Turbo Expo 2007, Power for Land Sea and Air*, Montreal, Canada. ASME. GT2007-27802.

Wieghardt, K. (1969). Computation of turbulent boundary layers. In Coles, D. and Hirst, E., editors, *1968 AFOSR-IFP-Stanford Conference*, volume 2, Stanford University, CA.

Wilcox, D, C. (1988a). Reassessment of the scale determining equation for advanced turbulence models. *AIAA Journal*, 26(11):1299–1310.

Wilcox, D, C. (1993a). Comparison of two equation turbulence models for boundary layers with pressure gradient. *AIAA Journal*, 31(8):1414–1421.

Wilcox, D. (1988b). Multiscale model for turbulent flows. *AIAA Journal*, 26(11):1311–1320.

Wilcox, D. (1993b). *Turbulence Modeling for CFD*. DCW Industries.

Wilcox, D. (1998). *Turbulence Modelling for CFD*. DCW Industries, Palm Drive, La Canada, California, USA, 2 edition.

Woollatt, G., Lippet, D., Ivey, P., Timmis, P., and Charnley, B. (2005). The design, development and evaluation of 3d aerofiols for high speed axial compressors, part 2: Simulation and comparison with experiment. In *Proceedings of GT2005, ASME Turbo Expo 2005: Power for Land, Sea and Air, Reno-Tahoe, Nevada, USA*. ASME, ASME.

Wu, X. and Durbin, P. (2000). Boundary layer transition induced by periodic wakes. *ASME Journal of Turbomachinery*, 122:442–449.

Yang, Z. and Shih, T. (1993). New time scale based k-ϵ model for near-wall turbulence. *AIAA Journal*, 31(7):1191–1197.

Zheng, X., Liu, C., Liu, F., and Yang, C.-I. (1998). Turbulent transition simulation using the k-ω model. *International Journal for Numerical Methods in Engineering*, 42:907–926.

Zierke, W. and Deutsch, S. (1990). The measurement of boundary layers on a compressor blade in cascade: Part 4 flow fields for incidence angles of -1.5 and -8.5 degrees. *AMSE Journal of Turbomachinery*, 112:241–255.

This page has been left intentionally blank.

Appendix A

2D Unsteady Results Figures

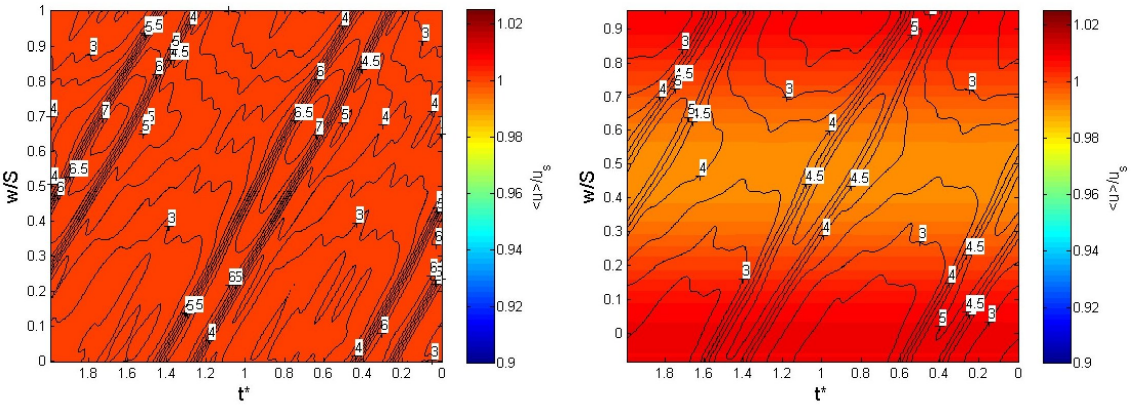

a) Normalised velocity (shading) & Tu (line) at Inlet

b) Normalised velocity (shading) & Tu (line) at 42.7%c upstream of stator leading edge

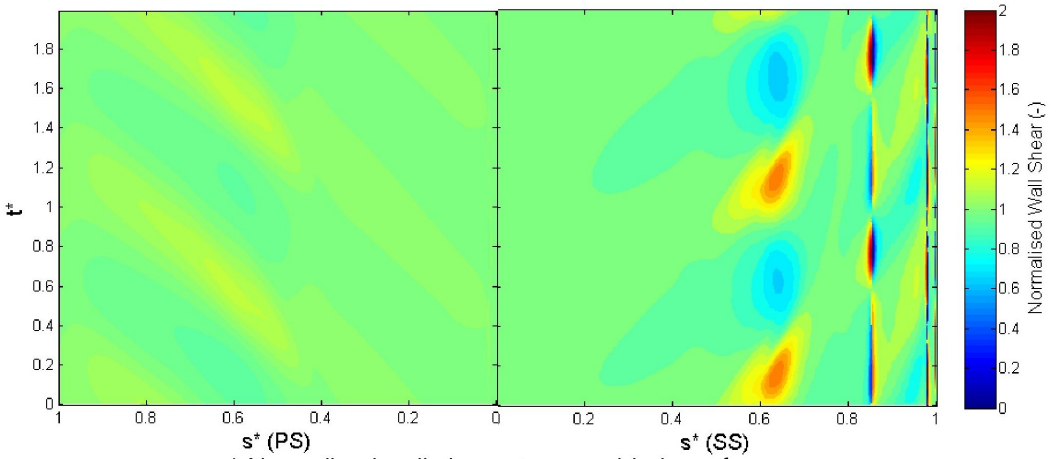

c) Normalised wall shear stress on blade surface

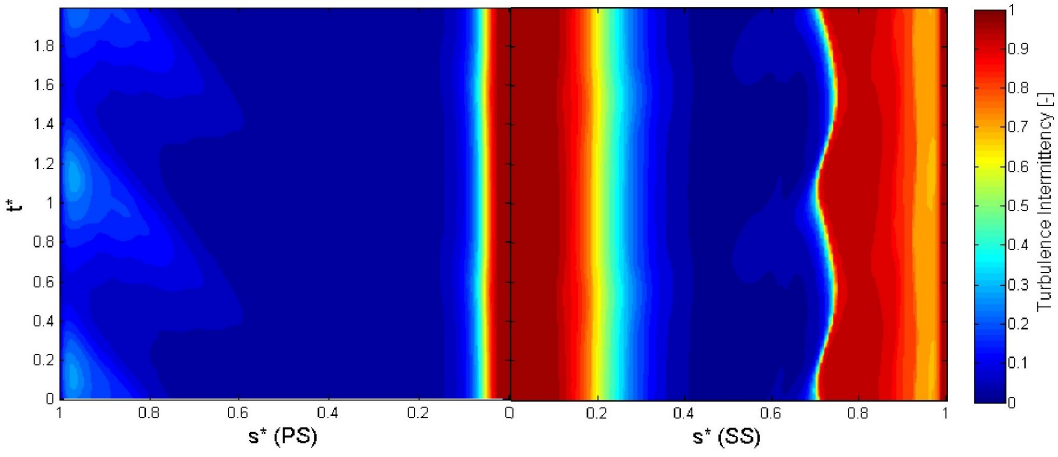

d) Turbulence intermittency at 0.2 mm from blade surface

Figure A.1: CFD results for Run 1

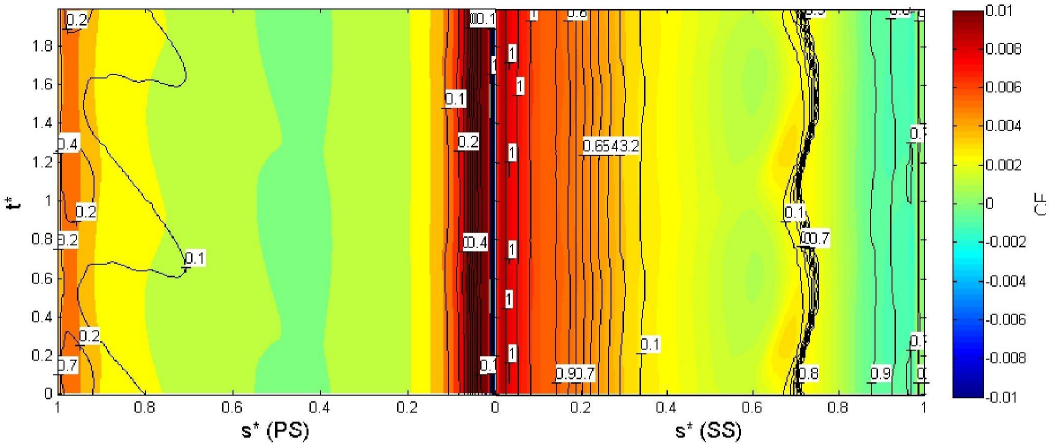

a) Local skin friction (shading) and turbulence intermittency (line) on blade surface

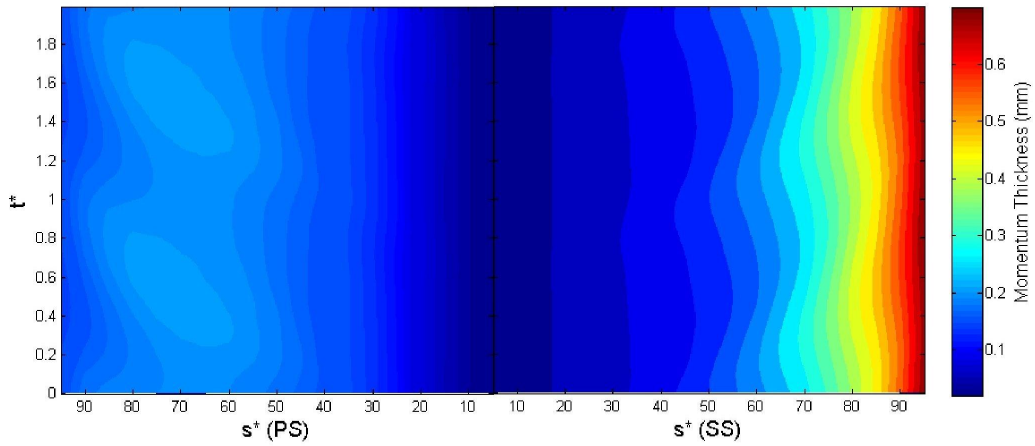

b) Momentum thickness on blade surface

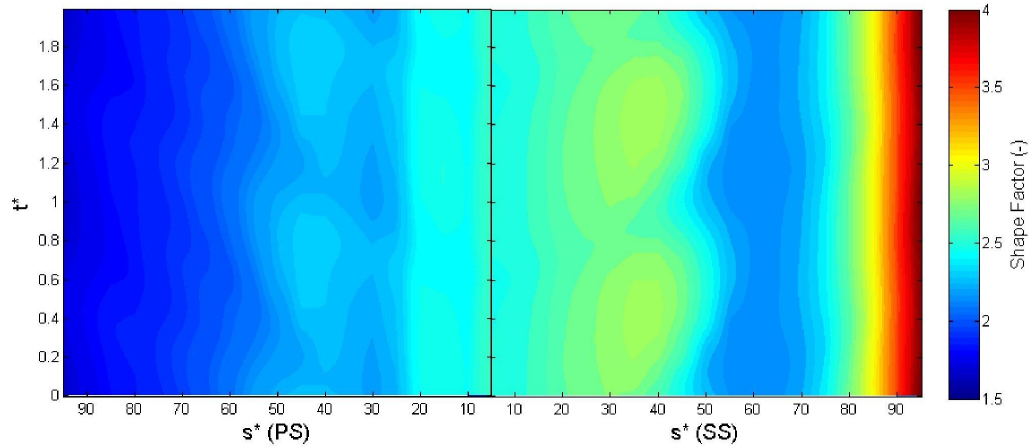

c) Shape factor on blade surface

Figure A.2: CFD results for Run 1

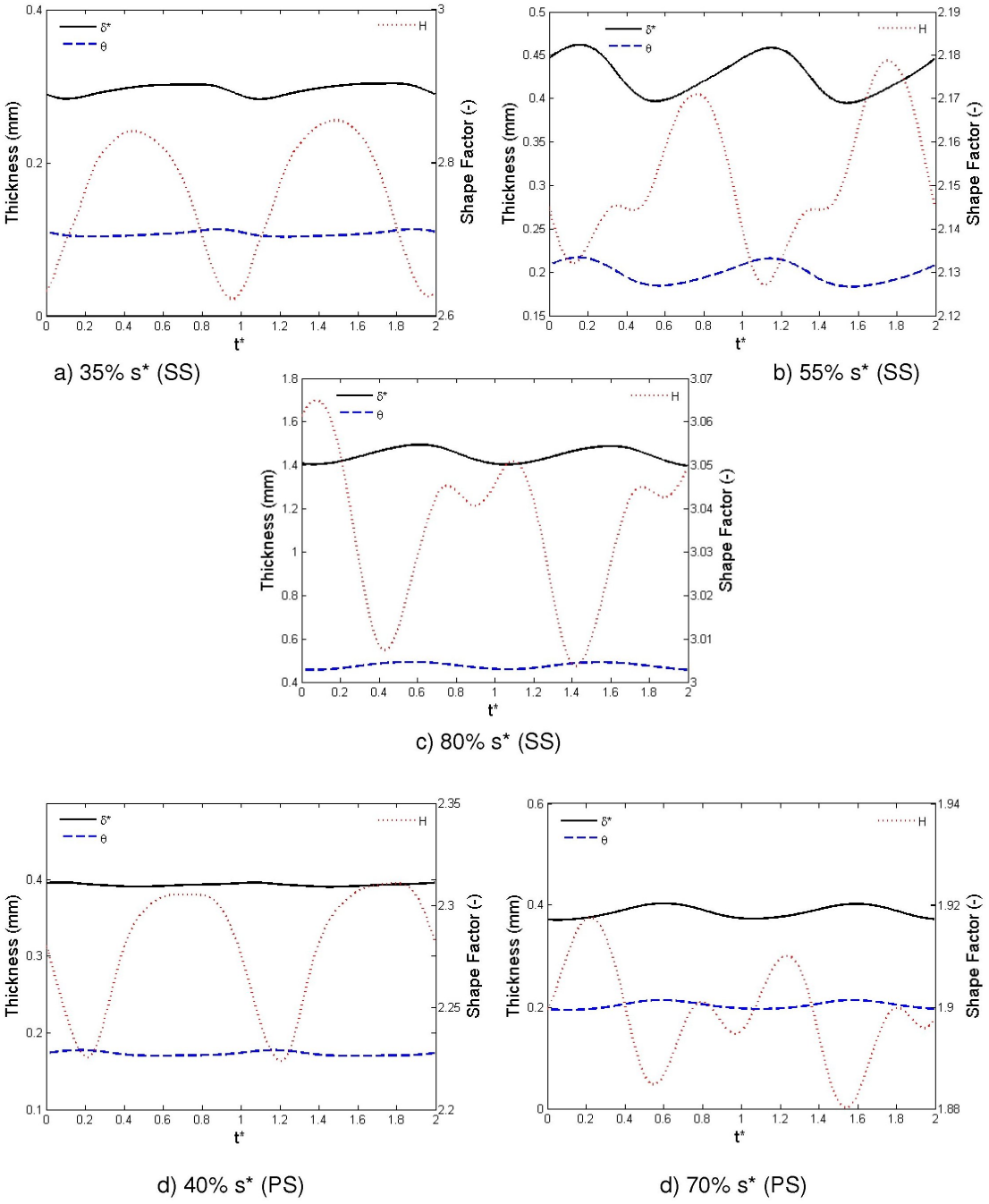

Figure A.3: CFD results for Run 1 - Integral parameters at various distances along suction (SS) and pressure (PS) surfaces

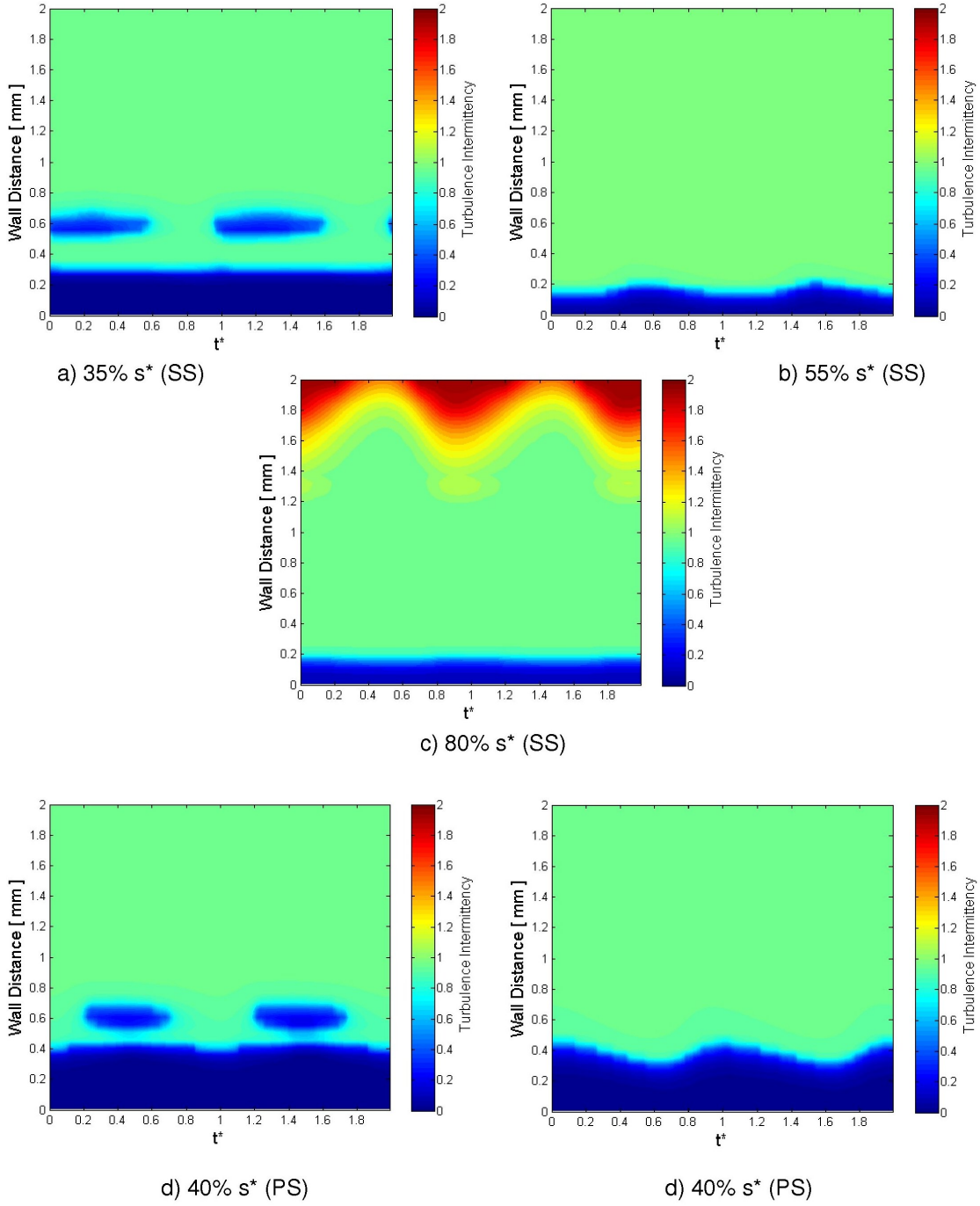

Figure A.4: CFD results for Run 1 - Intermittency at various distances along suction (SS) and pressure (PS) surfaces

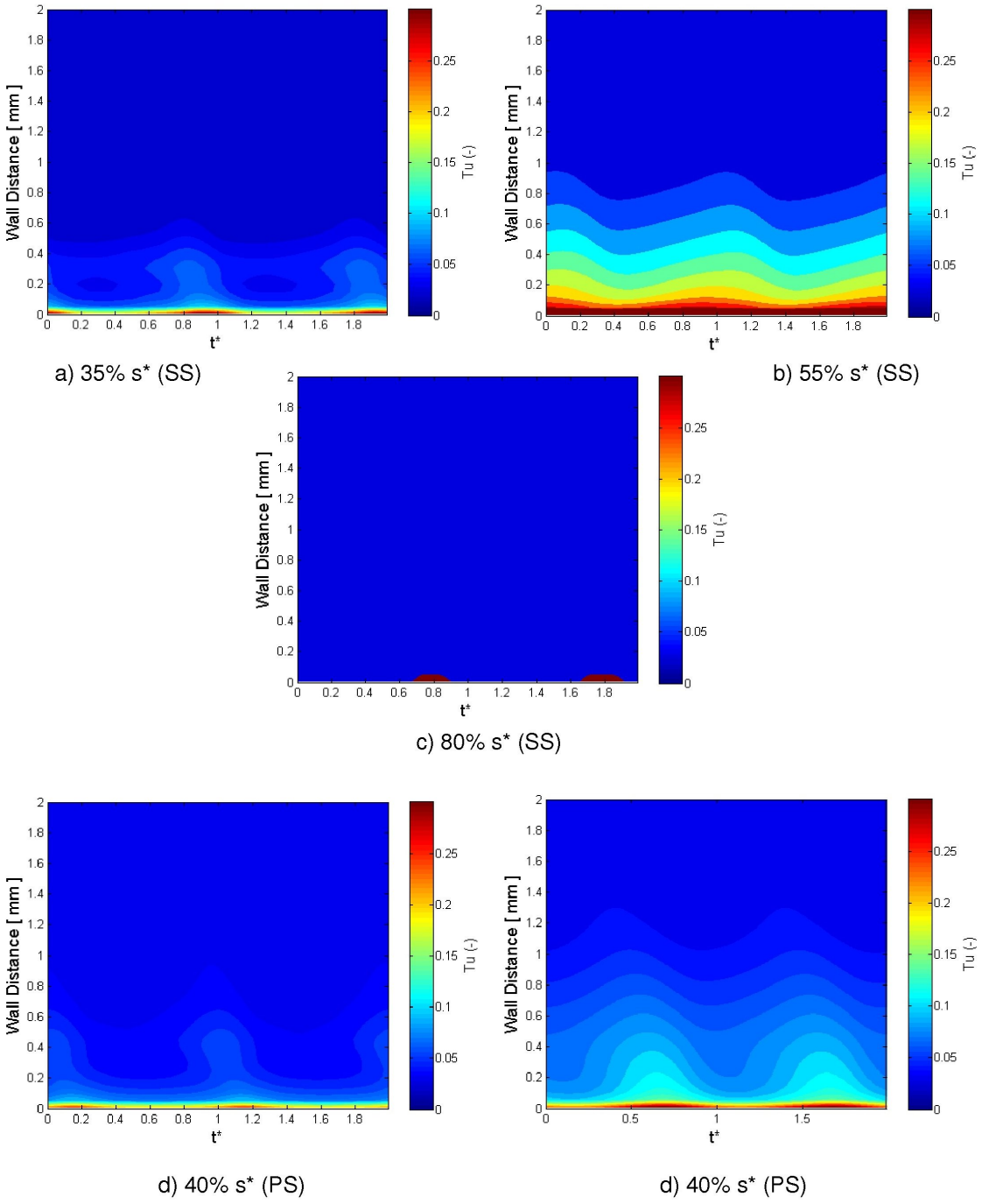

Figure A.5: CFD results for Run 1 - Turbulence intensity at various distances along suction (SS) and pressure (PS) surfaces

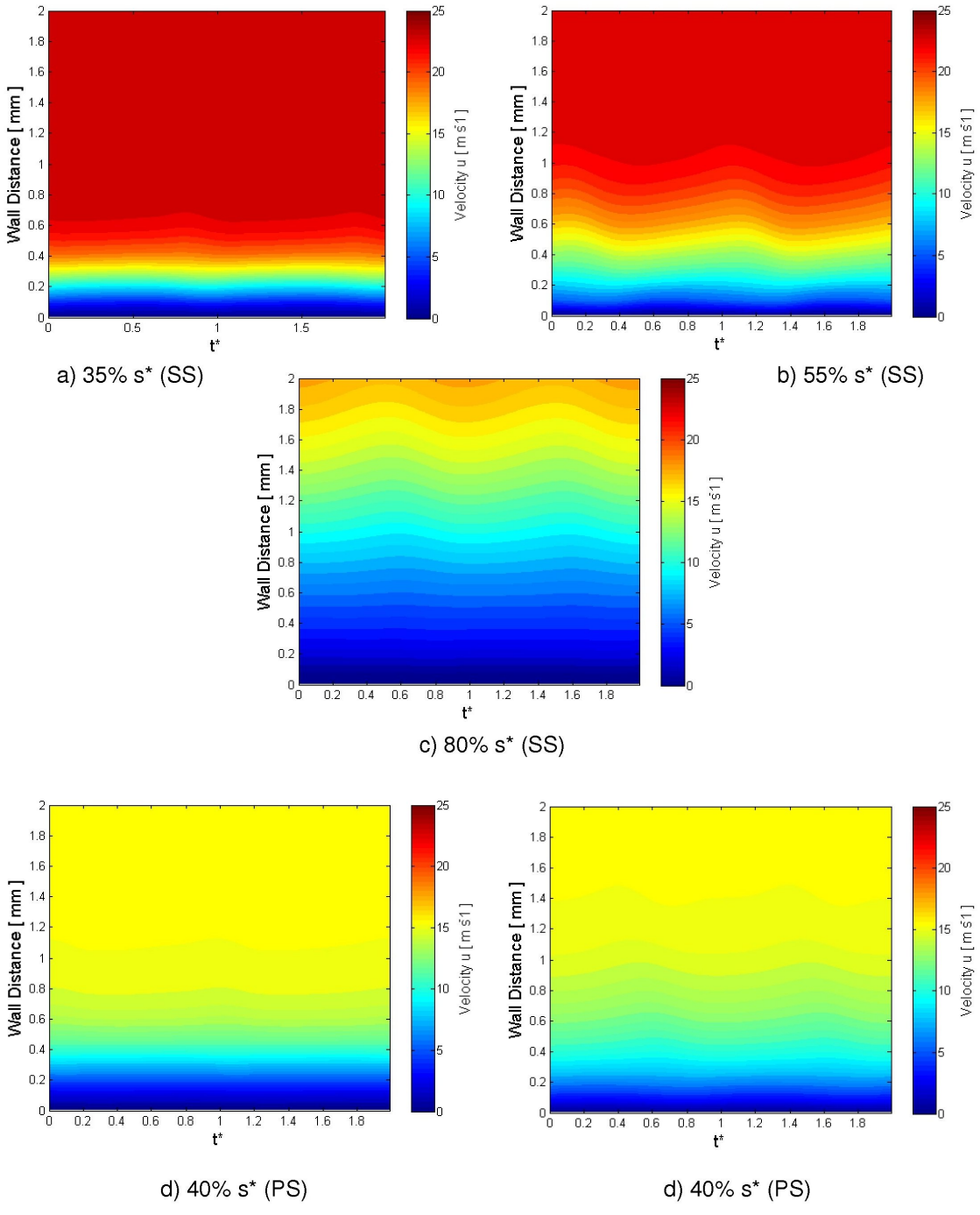

Figure A.6: CFD results for Run 1 - Tangential velocity at various distances along suction (SS) and pressure (PS) surfaces

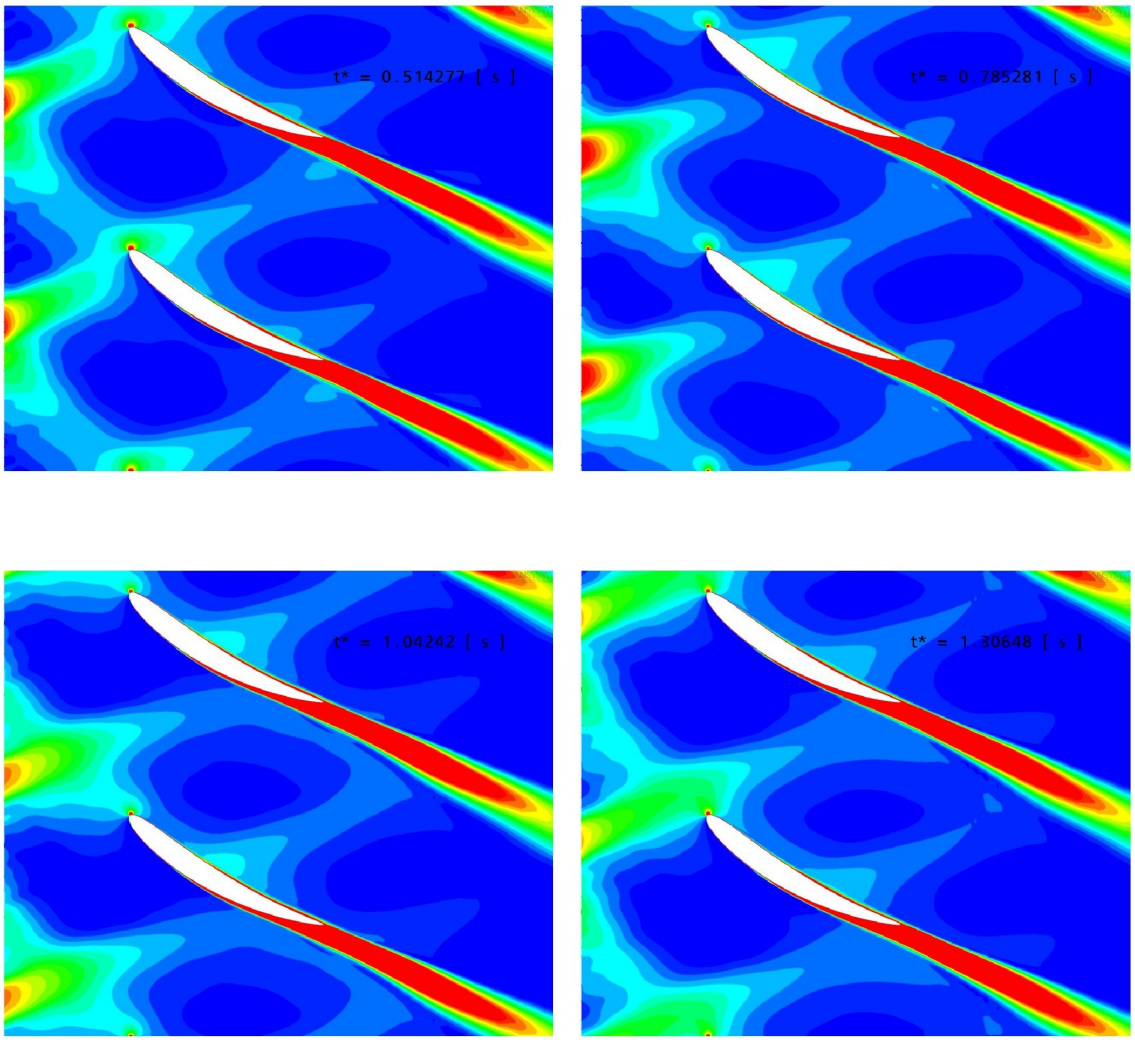

Figure A.7: CFD results for Run 1 - Wake turbulence transport through the domain at varying rotor passing time

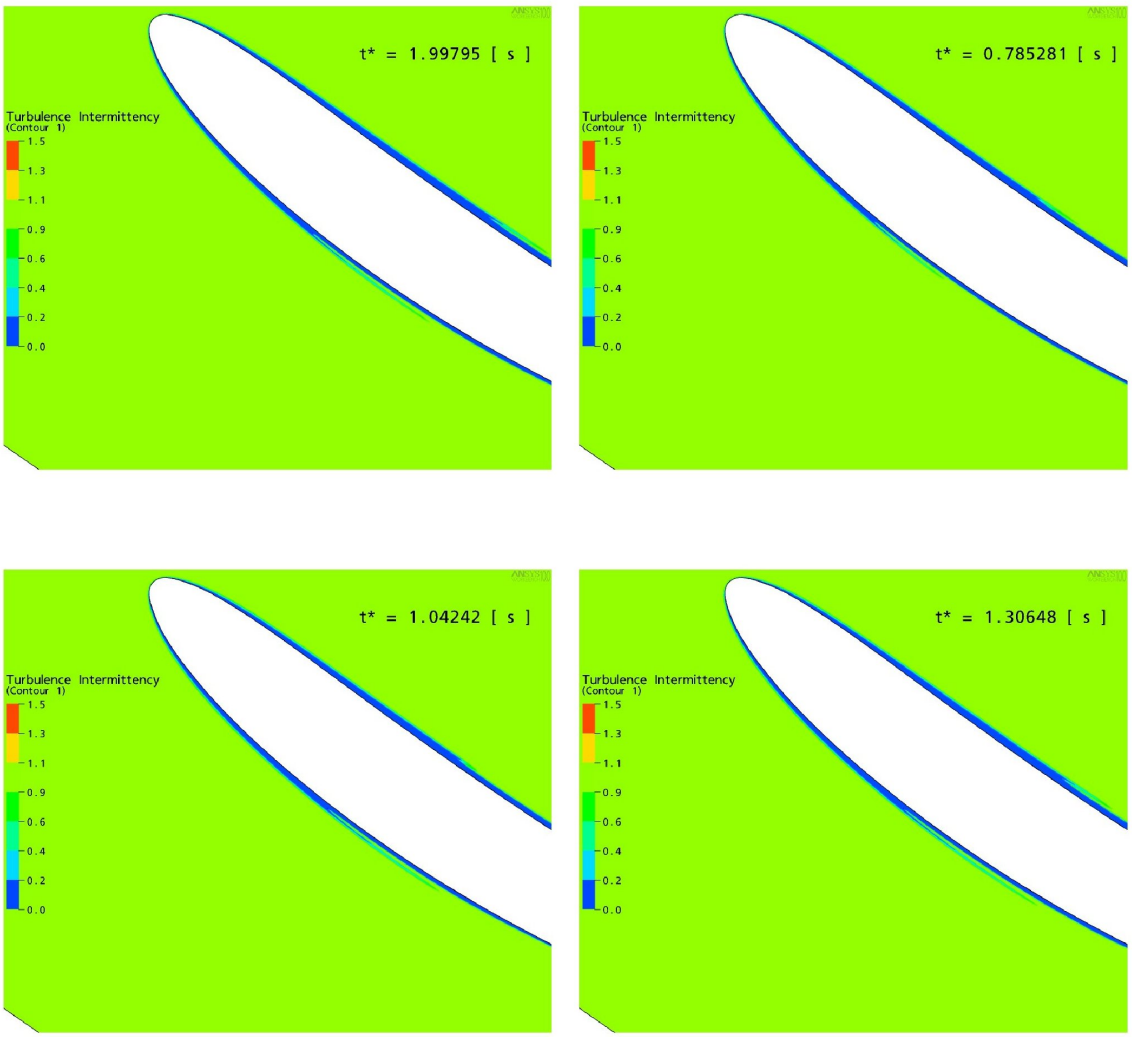

Figure A.8: CFD results for Run 1 - Intermittency in the boundary layer at varying rotor passing time

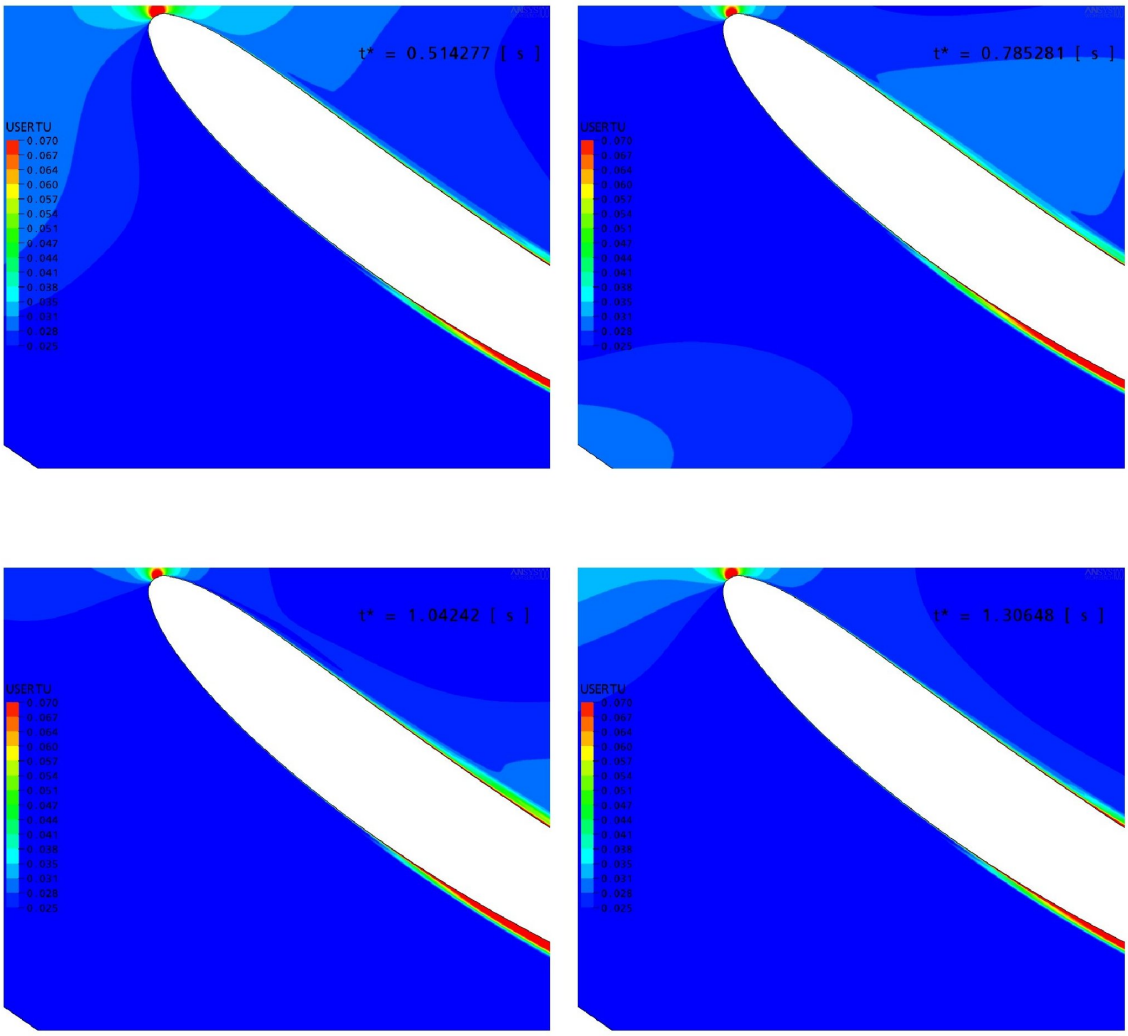

Figure A.9: CFD results for Run 1 - Wake turbulence transport effects on the stator boundary layer at varying rotor passing time

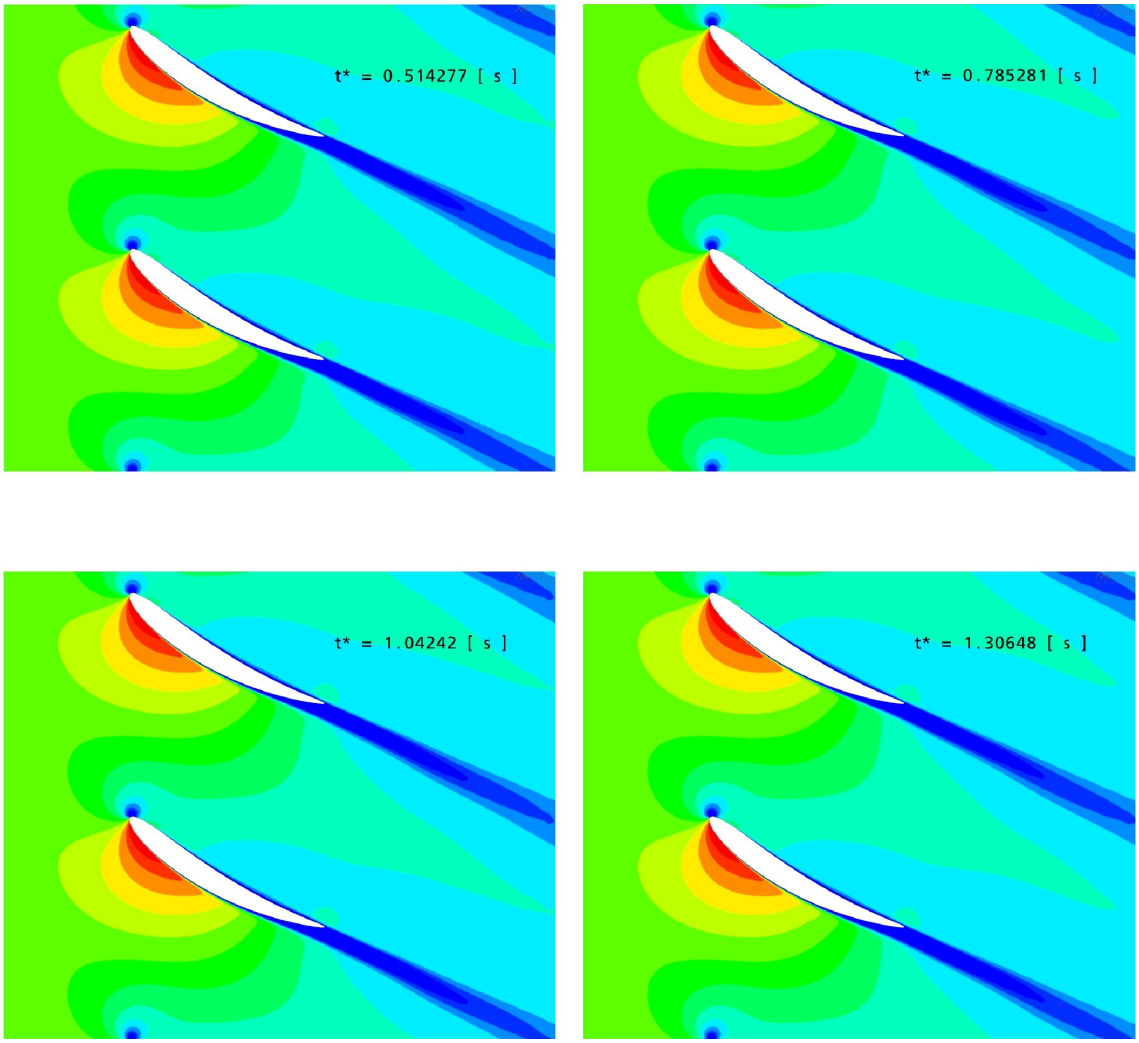

Figure A.10: CFD results for Run 1 - Velocity through passage at varying rotor passing time

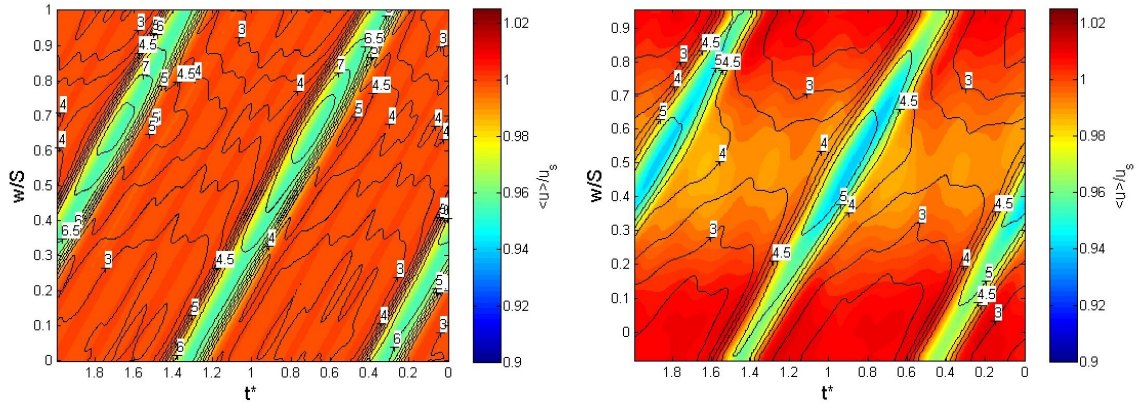

a) Normalised velocity (shading) & Tu (line) at Inlet

b) Normalised velocity (shading) & Tu (line) at 42.7%c upstream of stator leading edge

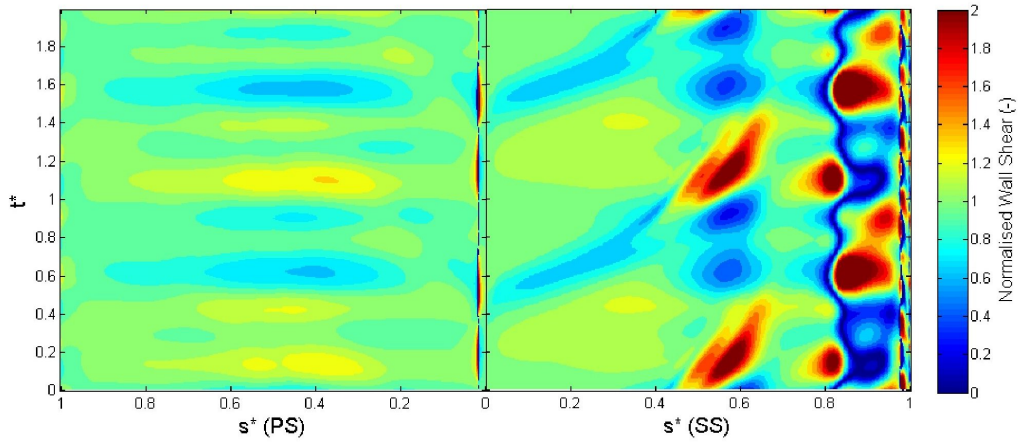

c) Normalised wall shear stress on blade surface

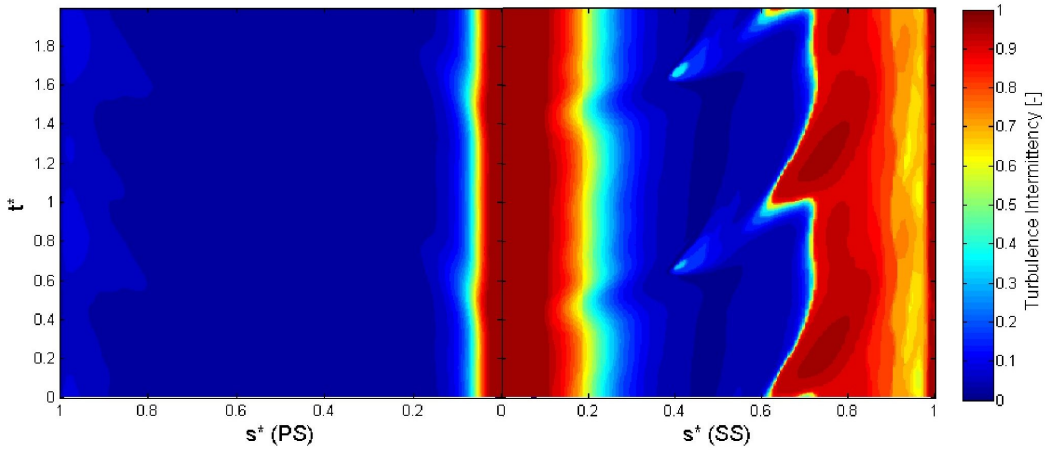

d) Turbulence intermittency at 0.2 mm from blade surface

Figure A.11: CFD results for Run 2

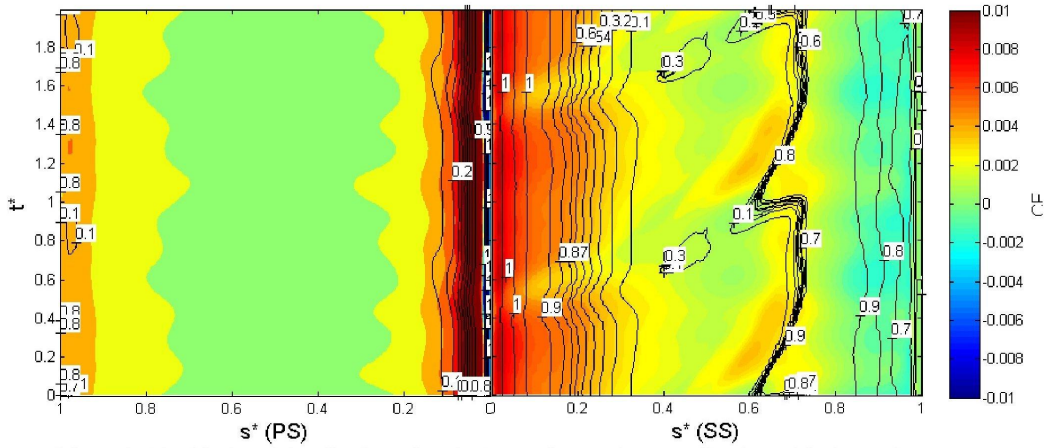

a) Local skin friction (shading) and turbulence intermittency (line) on blade surface

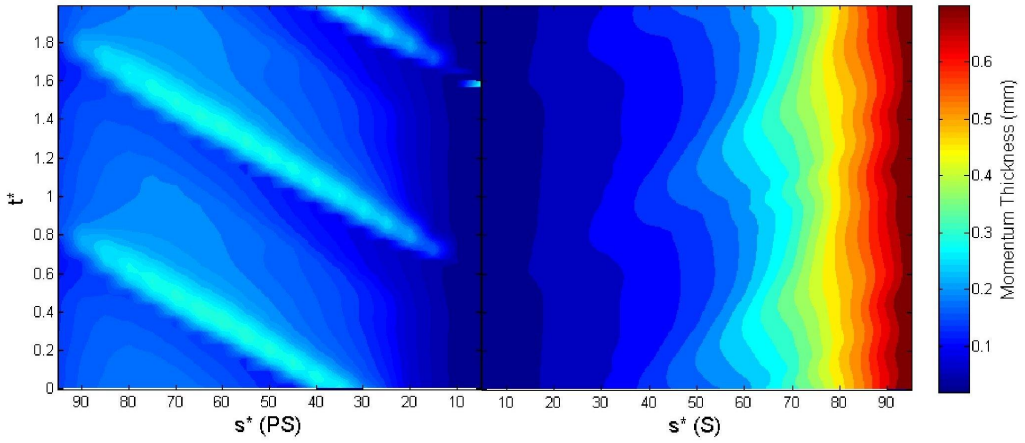

b) Momentum thickness on blade surface

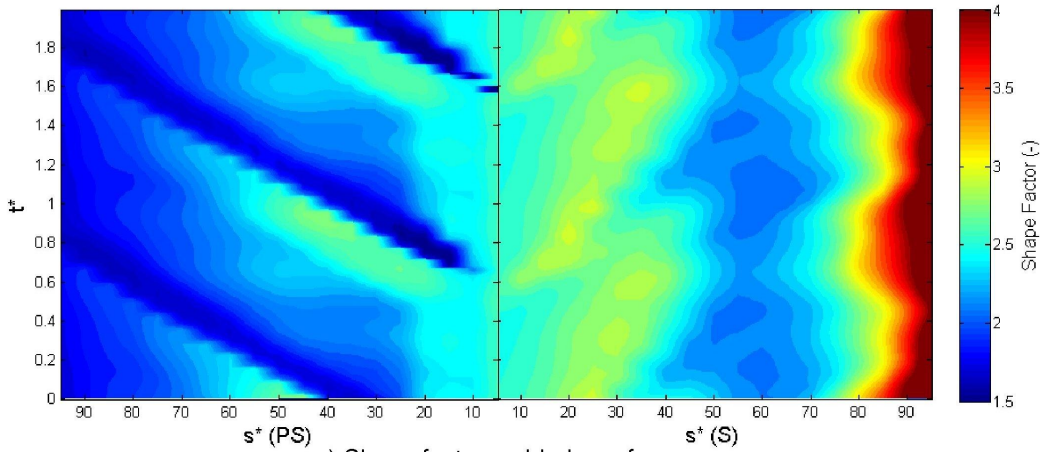

c) Shape factor on blade surface

Figure A.12: CFD results for Run 2

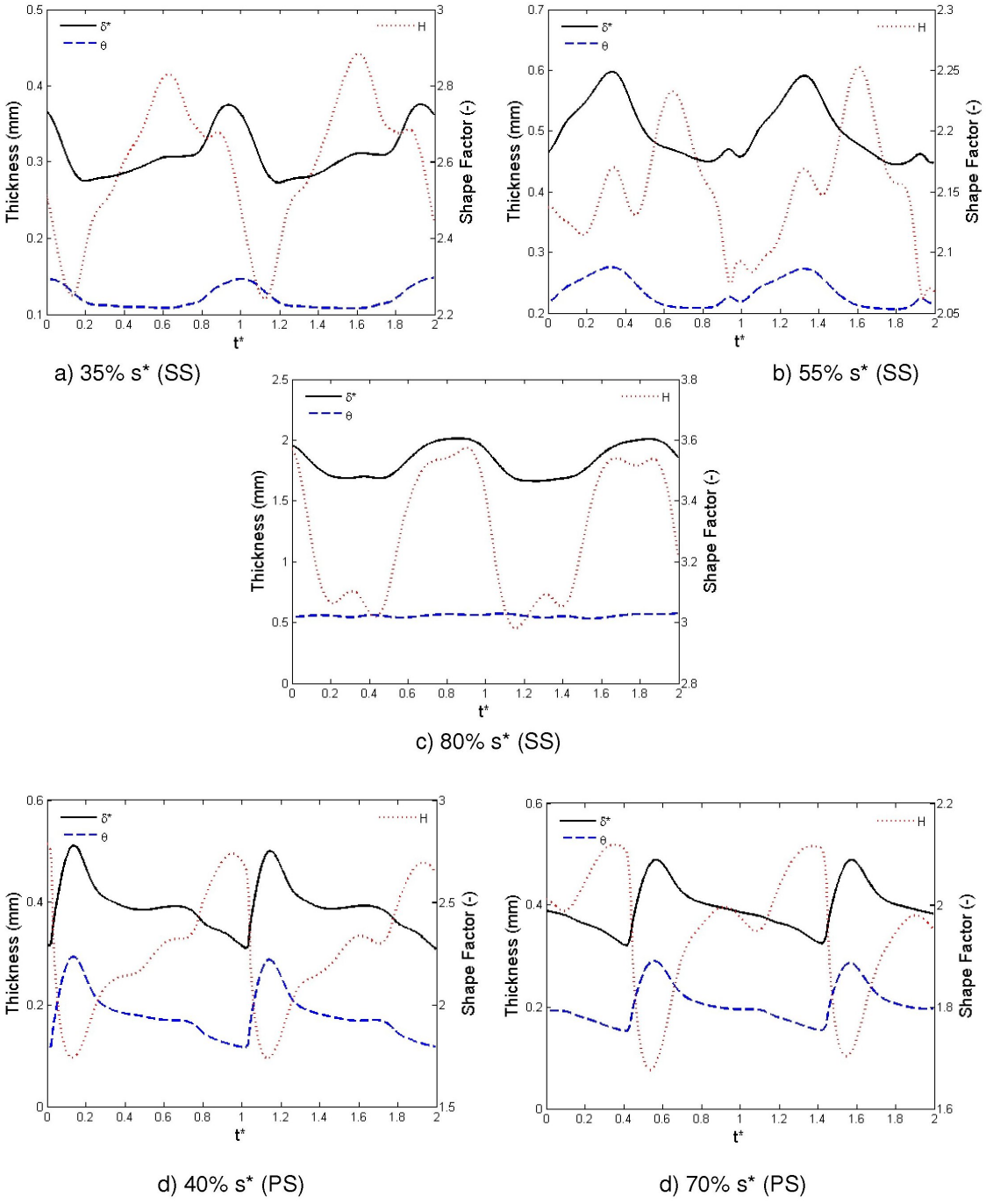

Figure A.13: CFD results for Run 2 - Integral parameters at various distances along suction (SS) and pressure (PS) surfaces

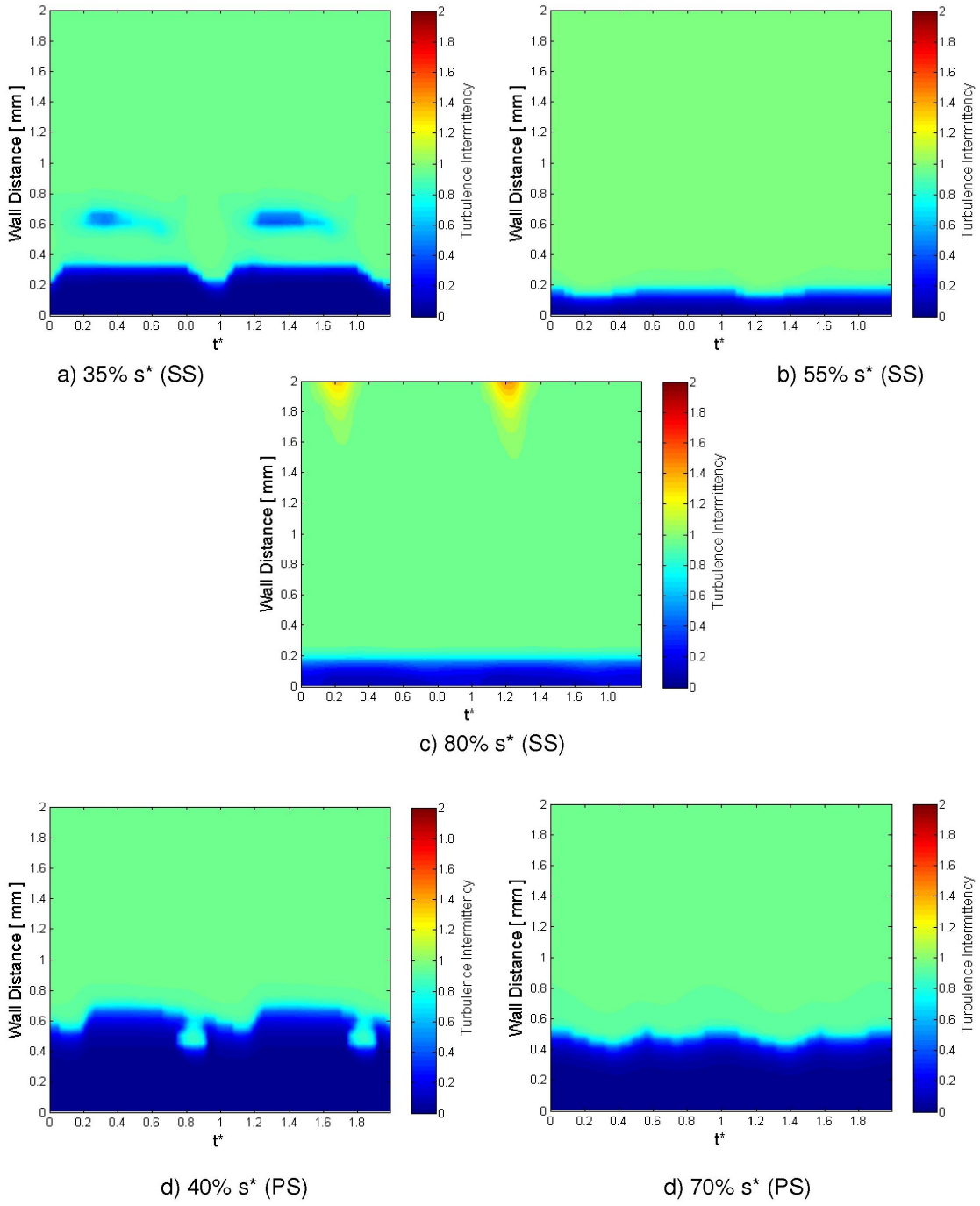

Figure A.14: CFD results for Run 2 - Intermittency at various distances along suction (SS) and pressure (PS) surfaces

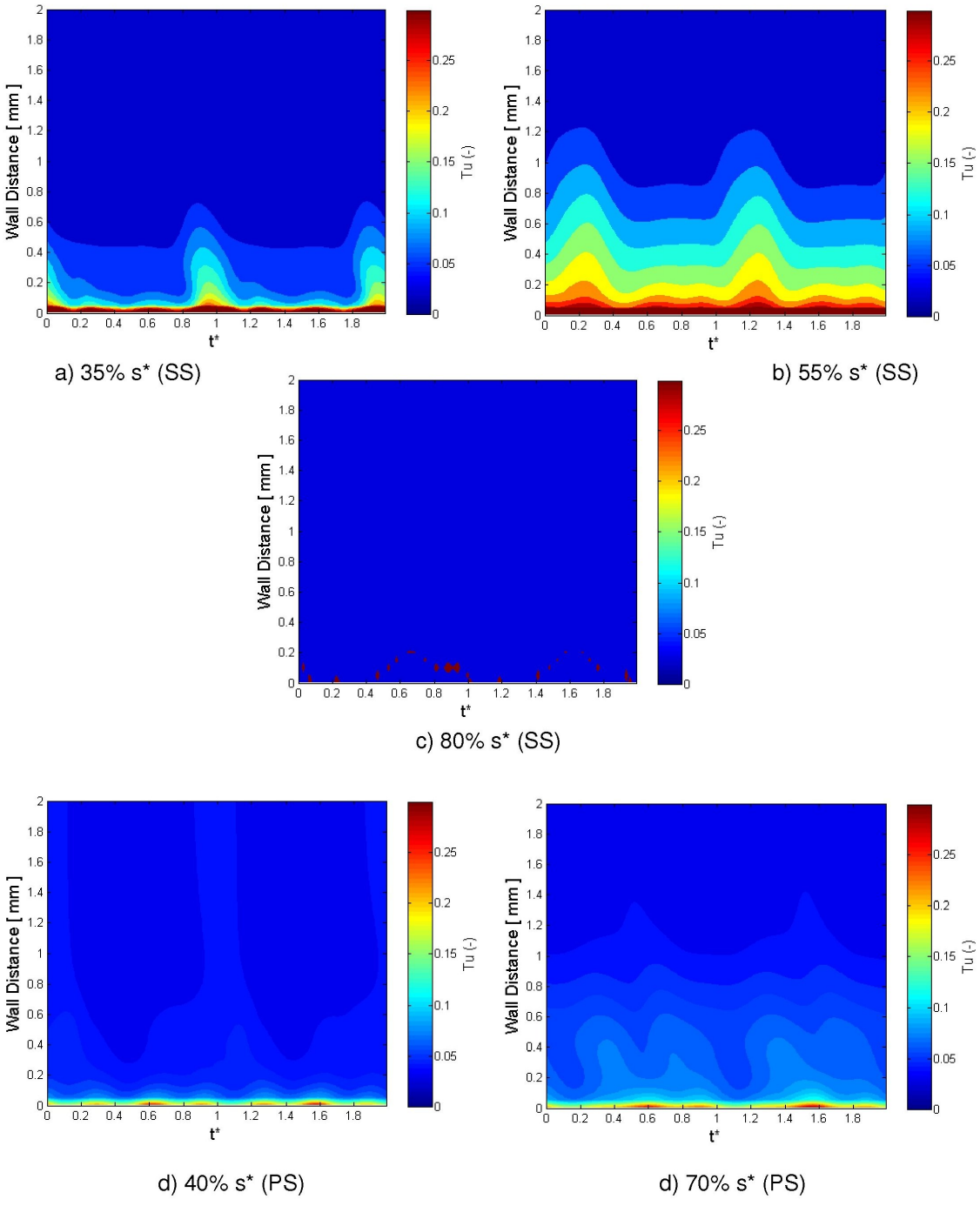

Figure A.15: CFD results for Run 2 - Turbulence intensity at various distances along suction (SS) and pressure (PS) surfaces

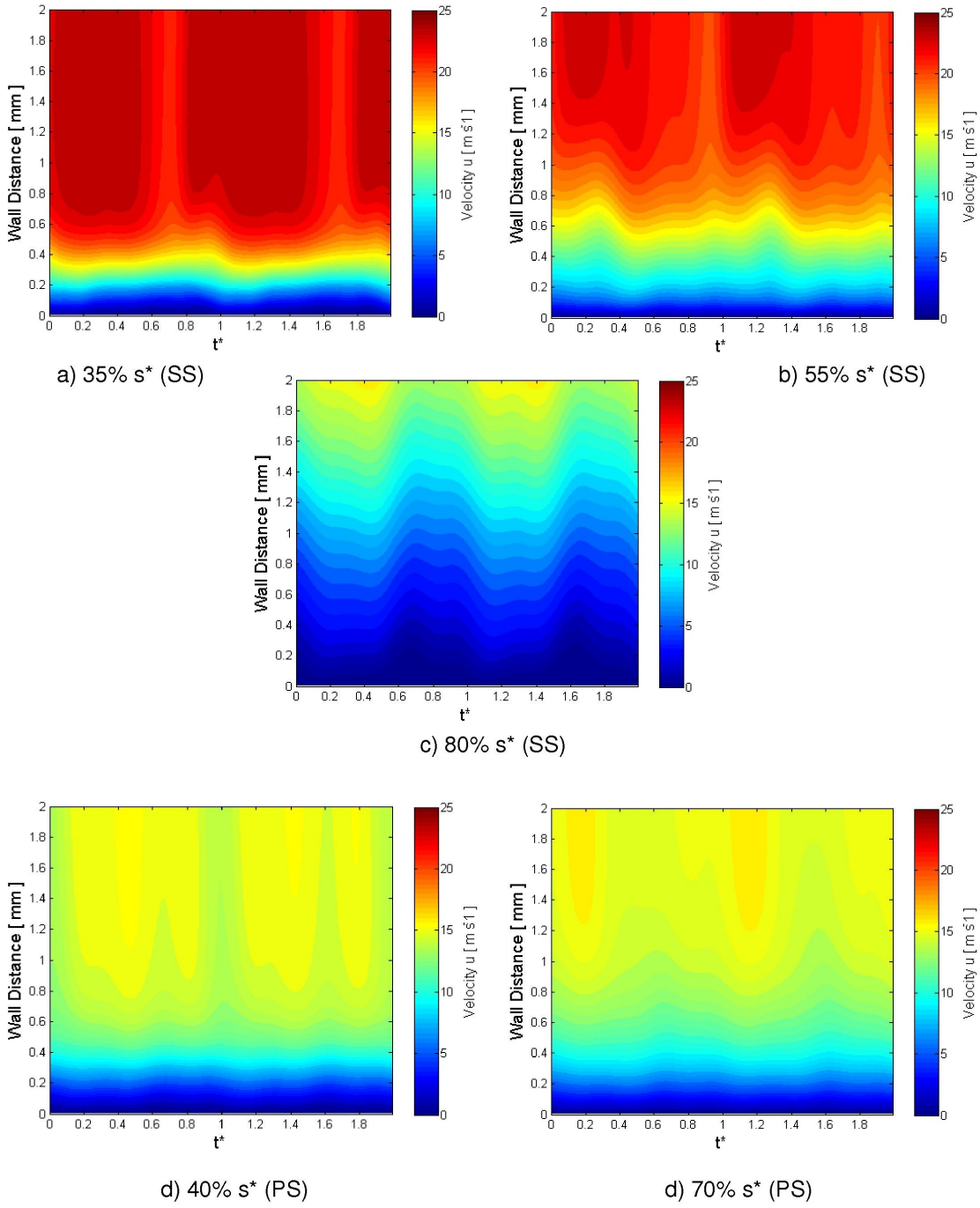

Figure A.16: CFD results for Run 2 - Tangential velocity at various distances along suction (SS) and pressure (PS) surfaces

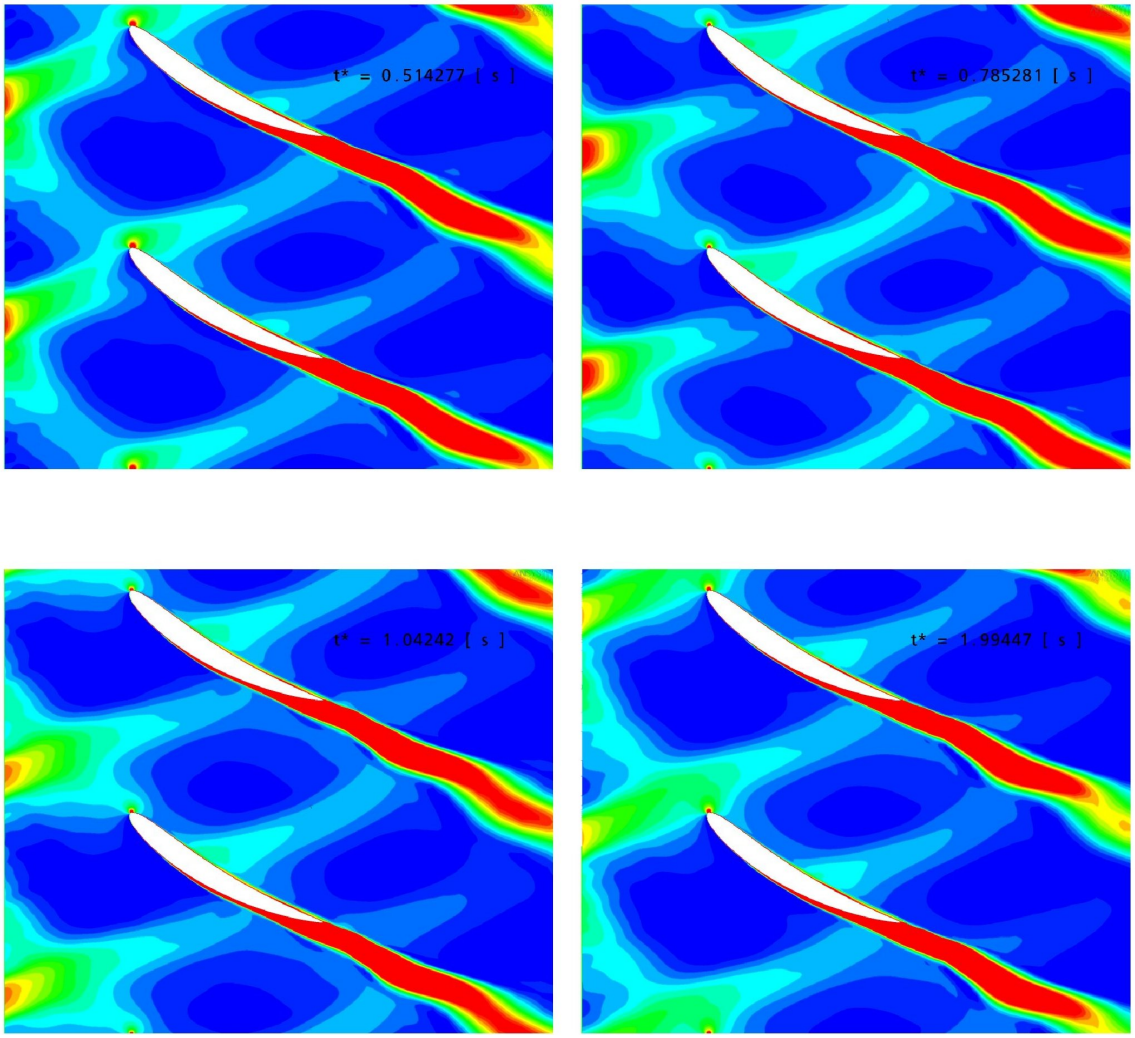

Figure A.17: CFD results for Run 2 - Wake turbulence transport through the domain at varying rotor passing time

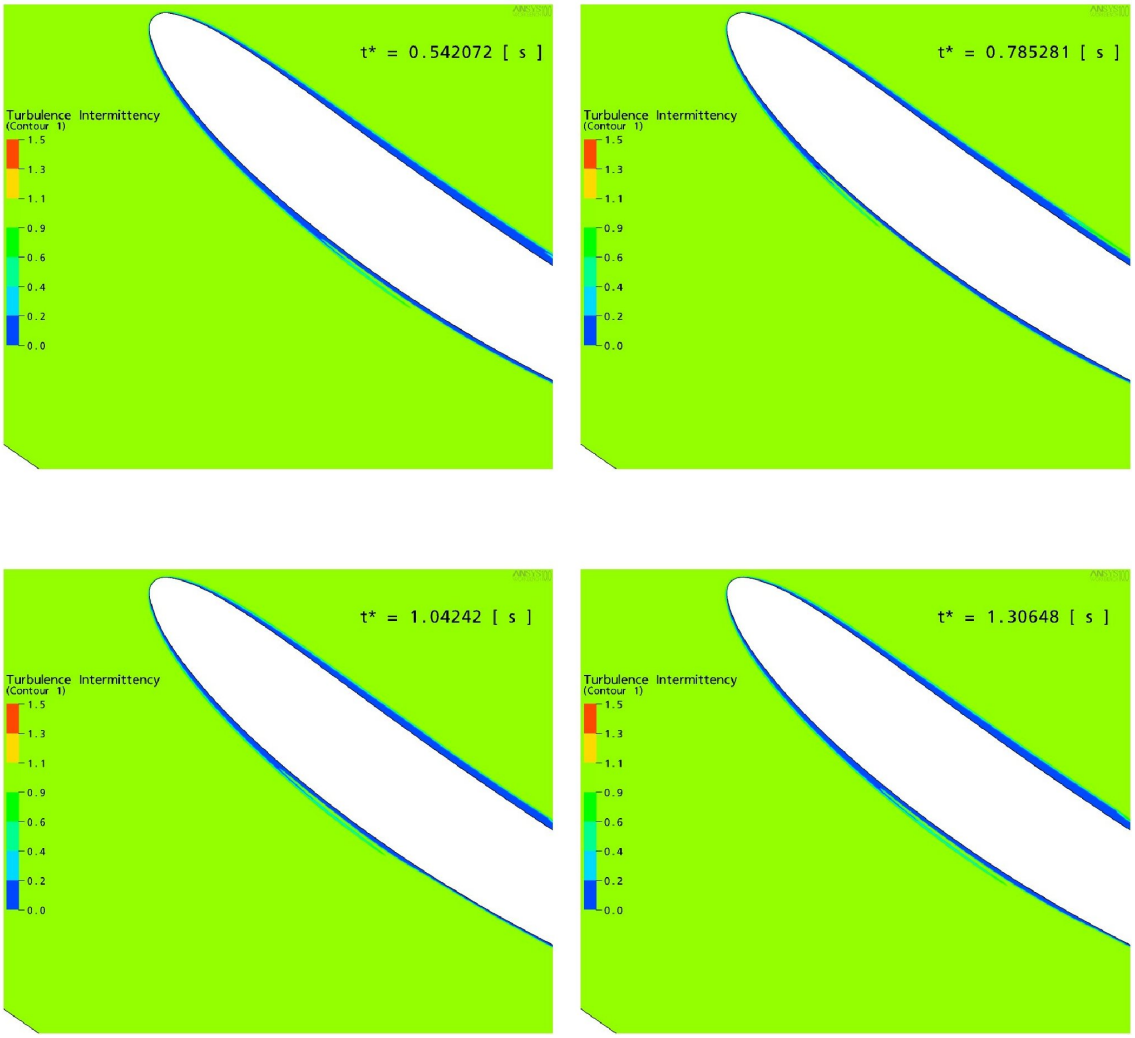

Figure A.18: CFD results for Run 2 - Intermittency in the boundary layer at varying rotor passing time

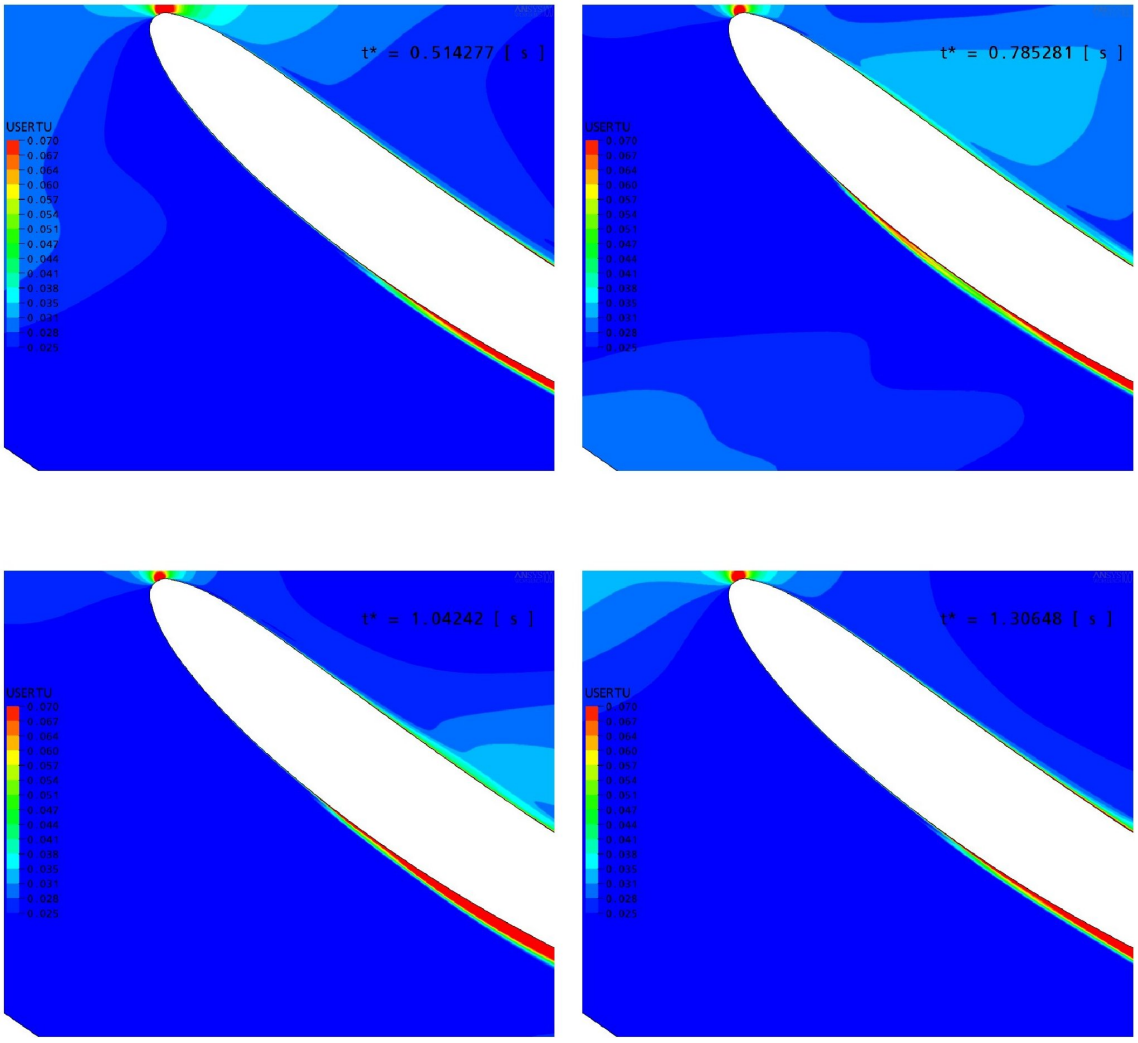

Figure A.19: CFD results for Run 2 - Wake turbulence transport effects on the stator boundary layer at varying rotor passing time

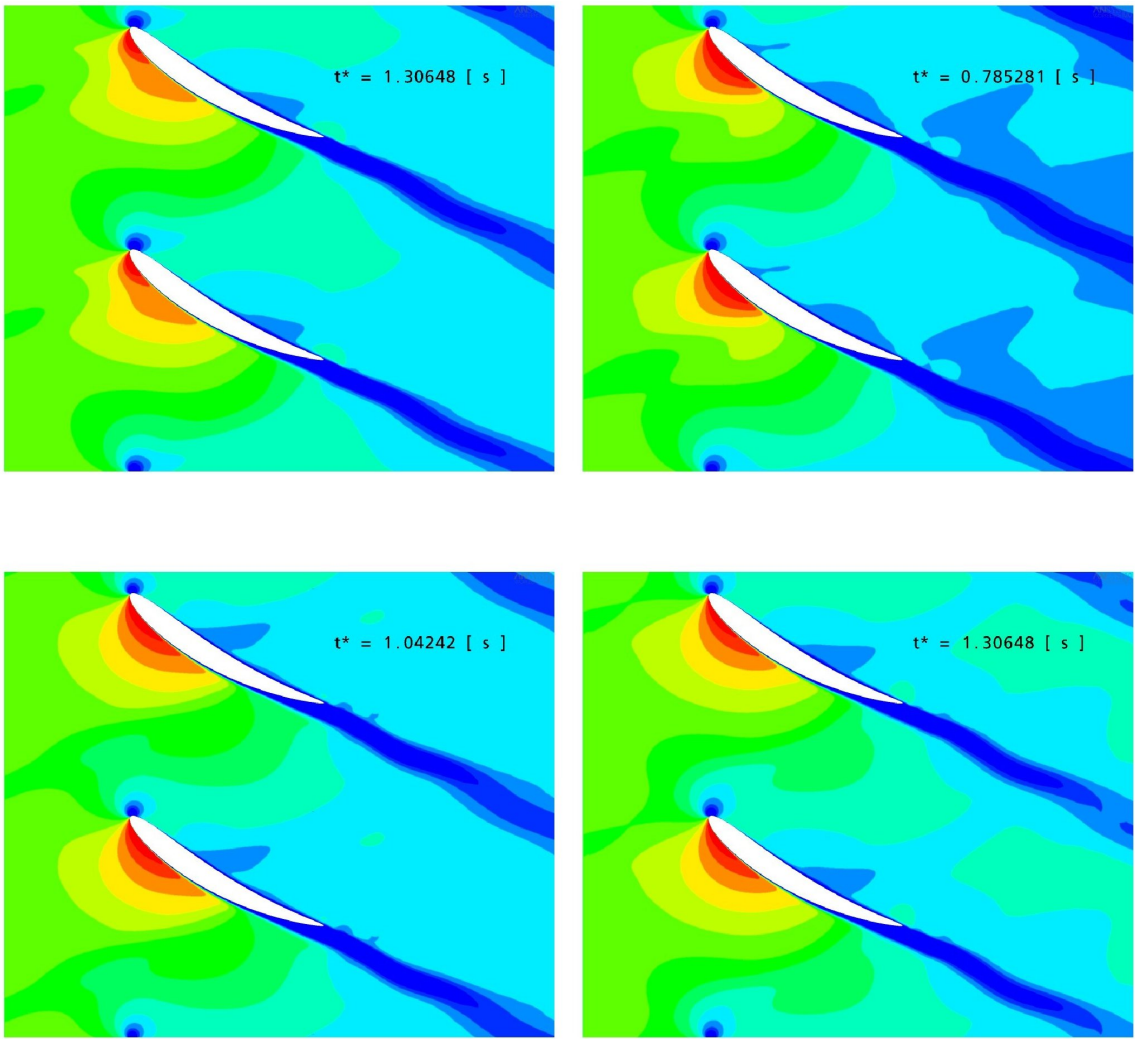

Figure A.20: CFD results for Run 2 - Velocity through passage at varying rotor passing time

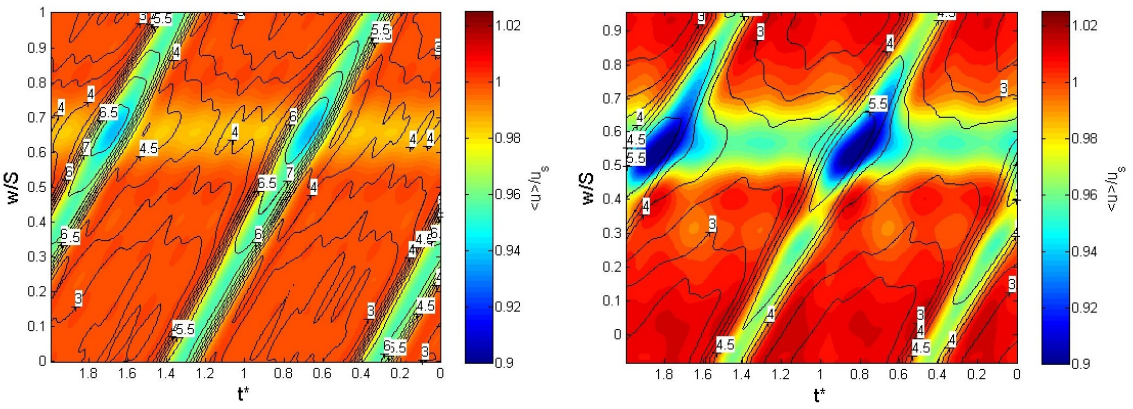

a) Normalised velocity (shading) & Tu (line) at Inlet

b) Normalised velocity (shading) & Tu (line) at 42.7%c upstream of stator leading edge

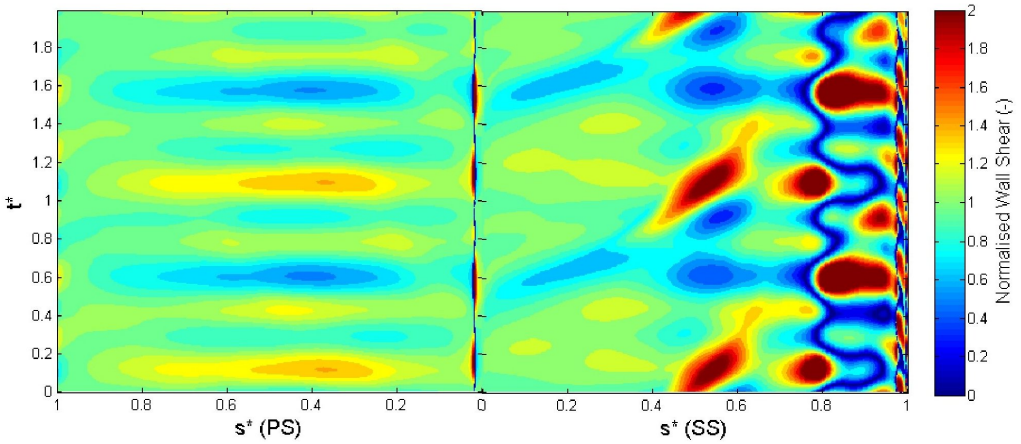

c) Normalised wall shear stress on blade surface

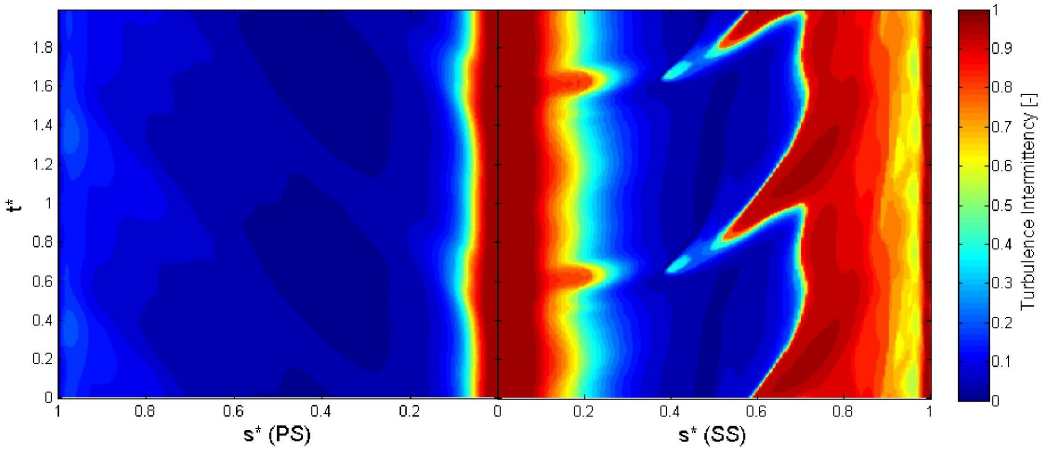

d) Turbulence intermittency at 0.2 mm from blade surface

Figure A.21: CFD results for Run 3

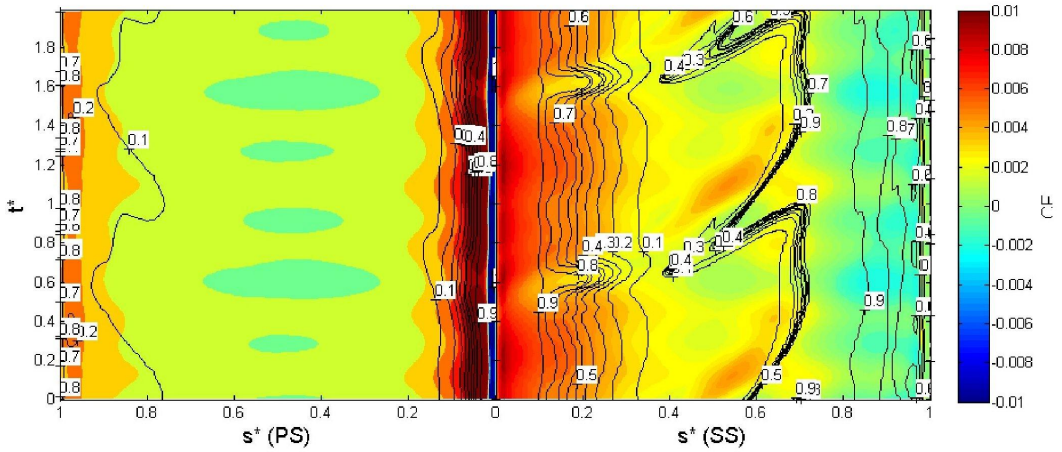

a) Local skin friction (shading) and turbulence intermittency (line) on blade surface

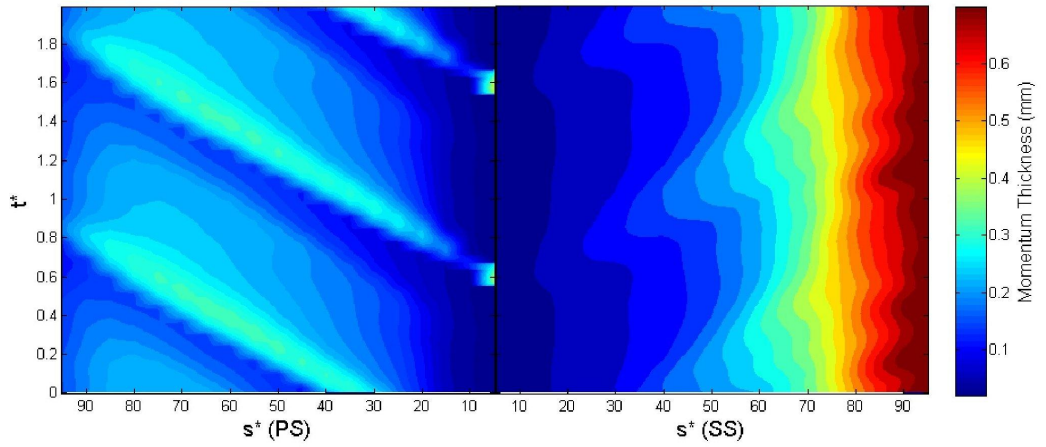

b) Momentum thickness on blade surface

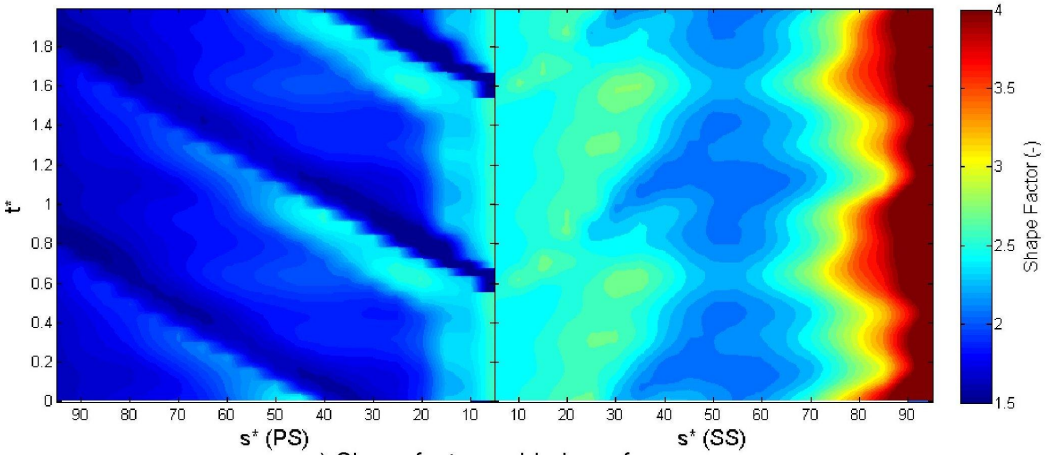

c) Shape factor on blade surface

Figure A.22: CFD results for Run 3

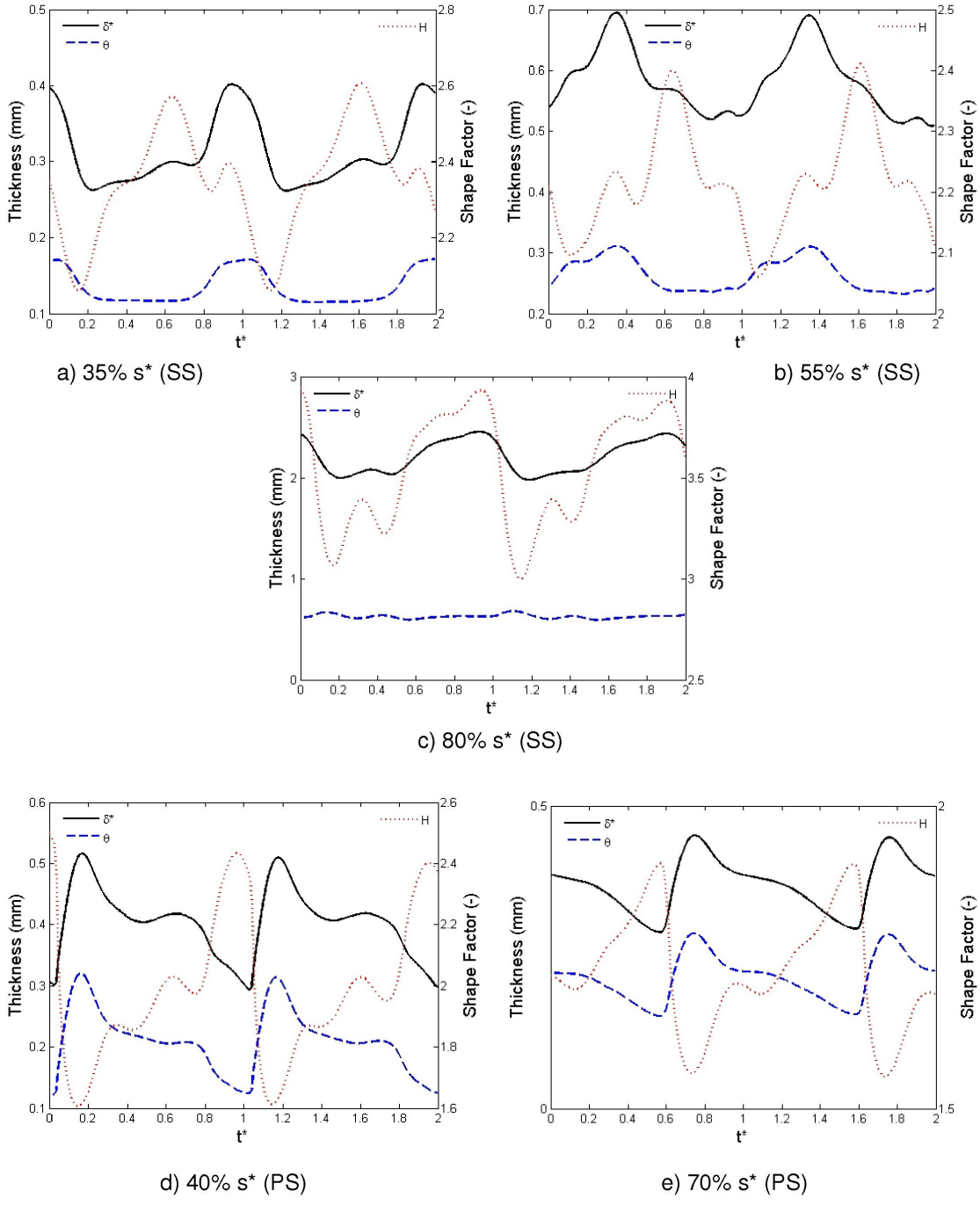

Figure A.23: CFD results for Run 3 - Integral parameters at various distances along suction (SS) and pressure (PS) surfaces

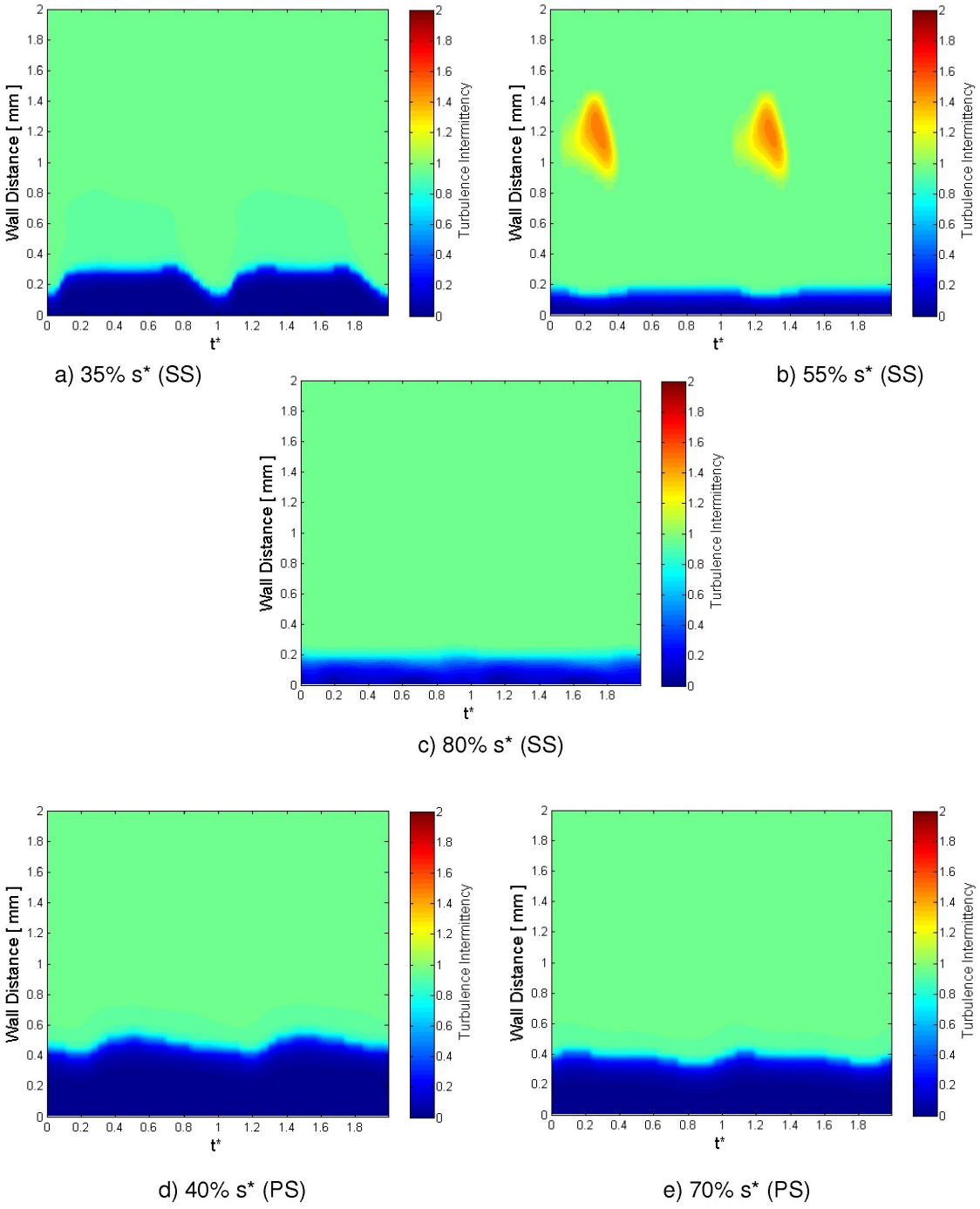

Figure A.24: CFD results for Run 3 - Intermittency at various distances along suction (SS) and pressure (PS) surfaces

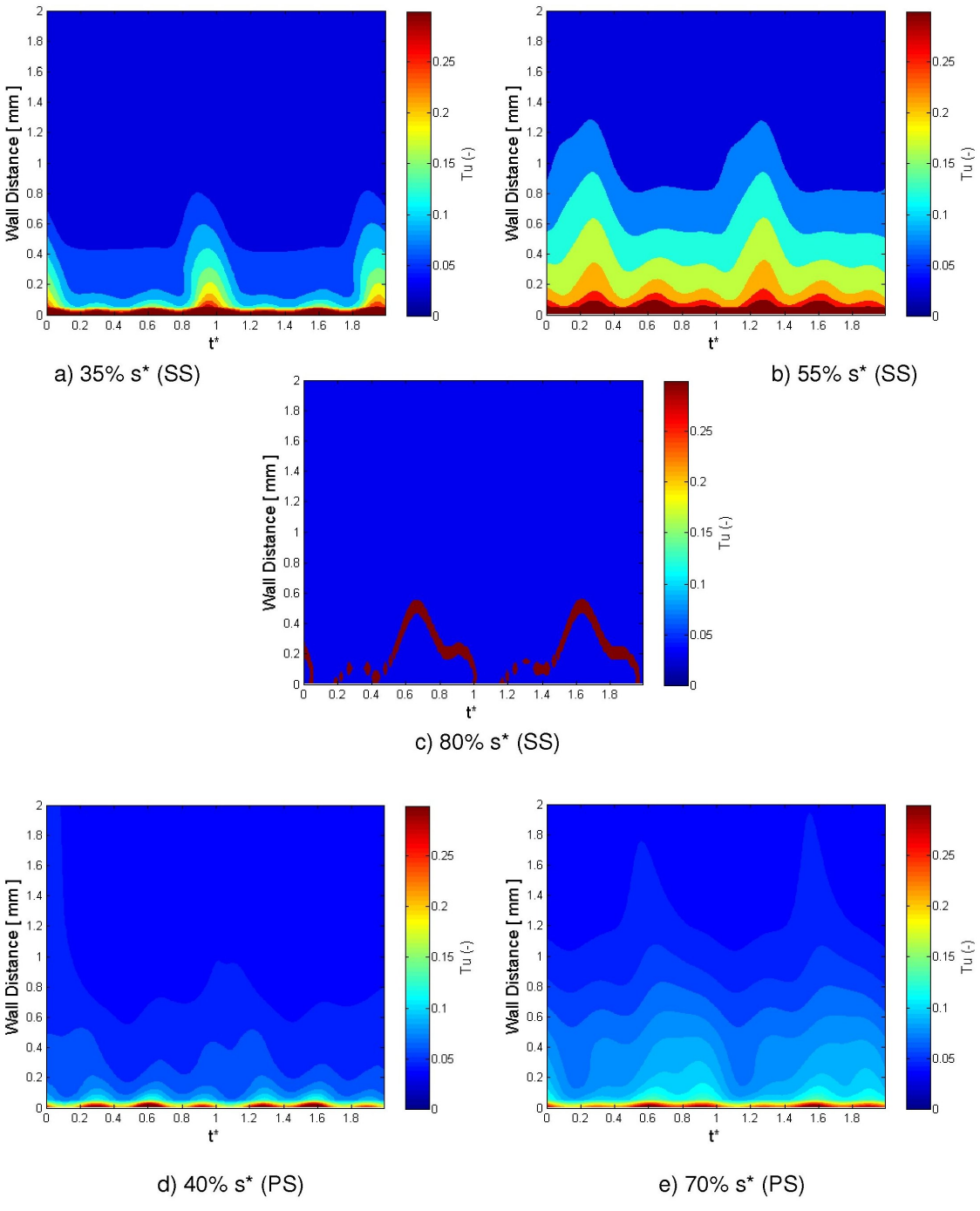

Figure A.25: CFD results for Run 3 - Turbulence intensity at various distances along suction (SS) and pressure (PS) surfaces

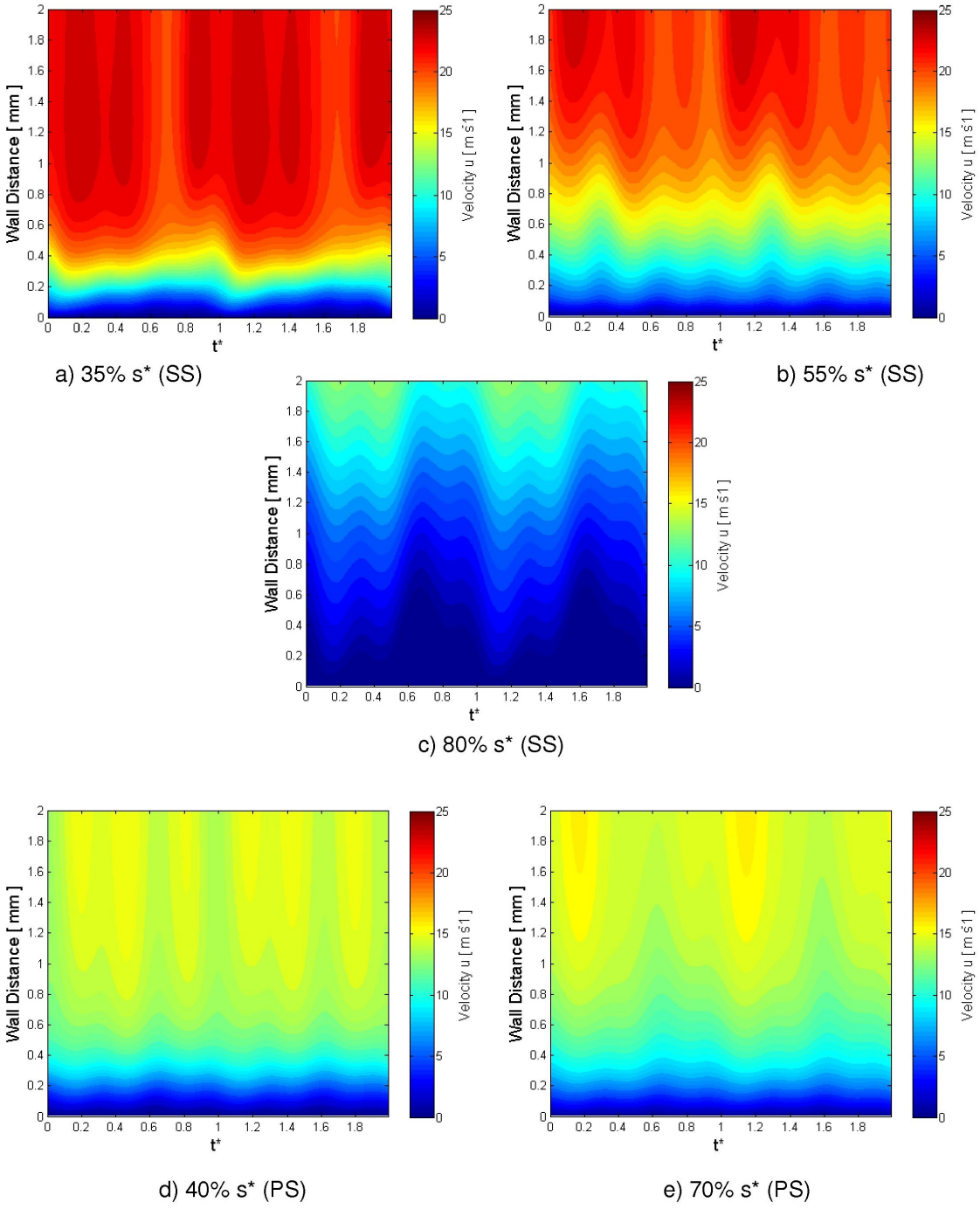

Figure A.26: CFD results for Run 3 - Tangential velocity at various distances along suction (SS) and pressure (PS) surfaces

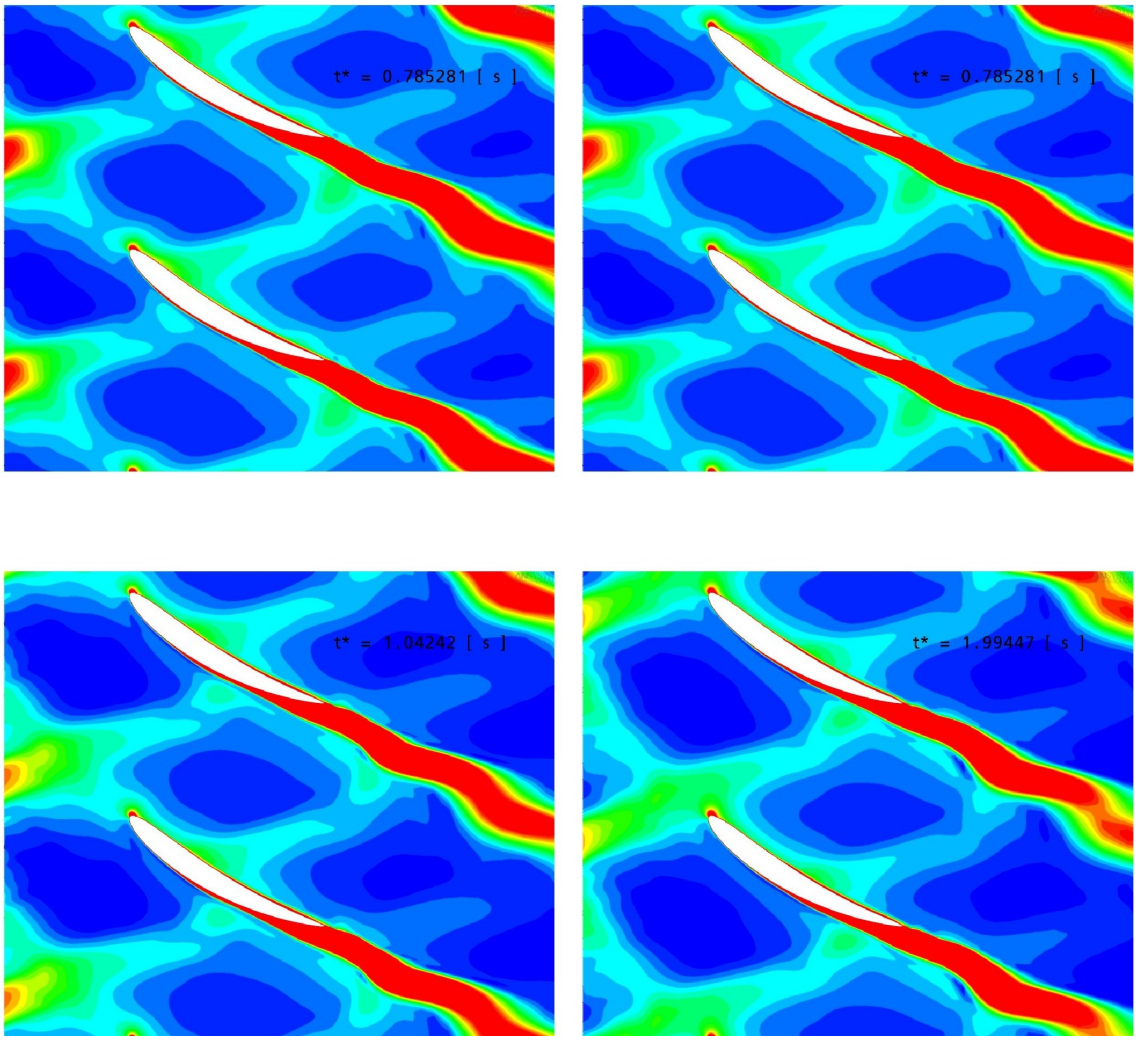

Figure A.27: CFD results for Run 3 - Wake turbulence transport through the domain at varying rotor passing time

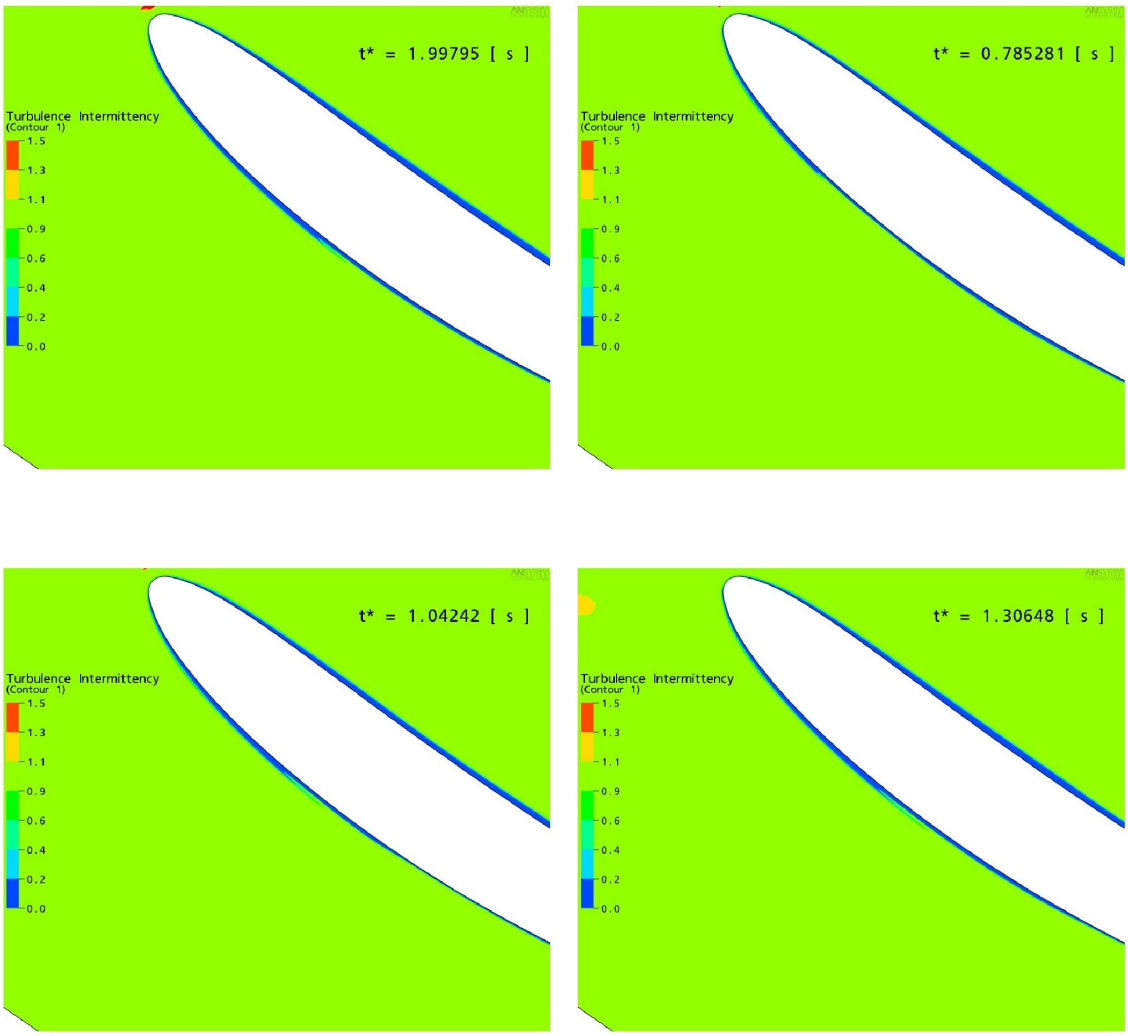

Figure A.28: CFD results for Run 3 - Intermittency in the boundary layer at varying rotor passing time

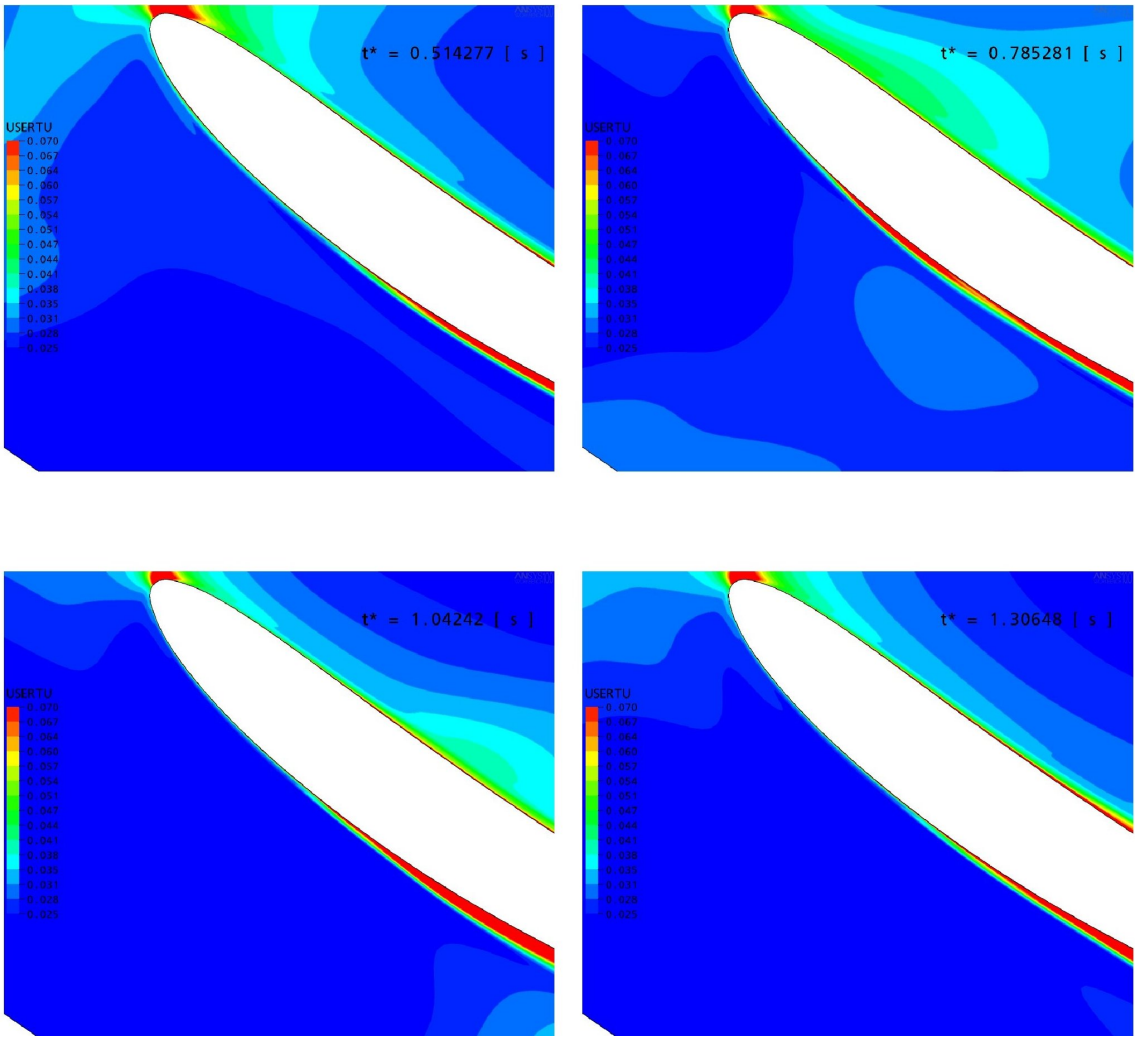

Figure A.29: CFD results for Run 3 - Wake turbulence transport effects on the stator boundary layer at varying rotor passing time

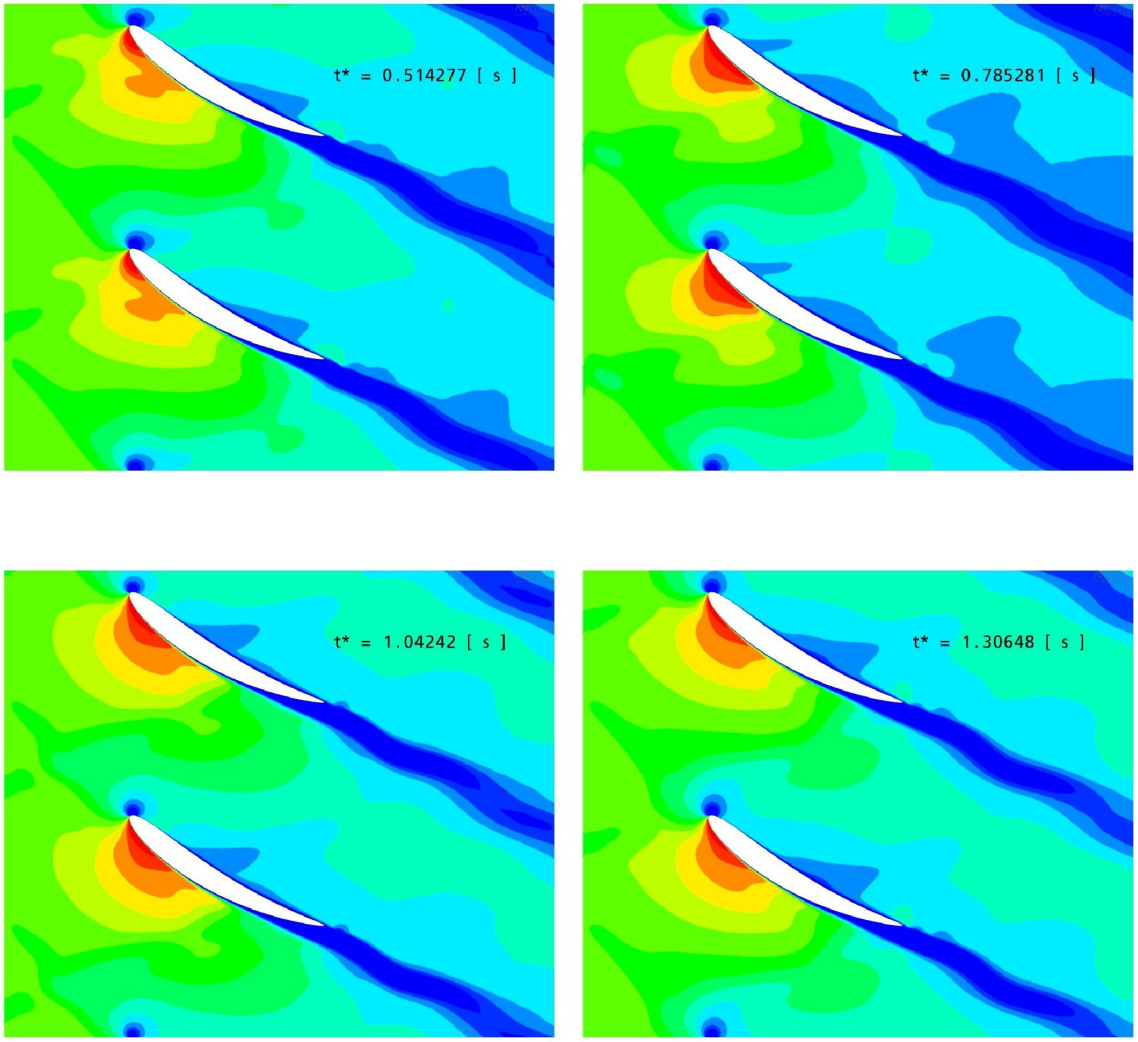

Figure A.30: CFD results for Run 3 - Velocity through passage at varying rotor passing time

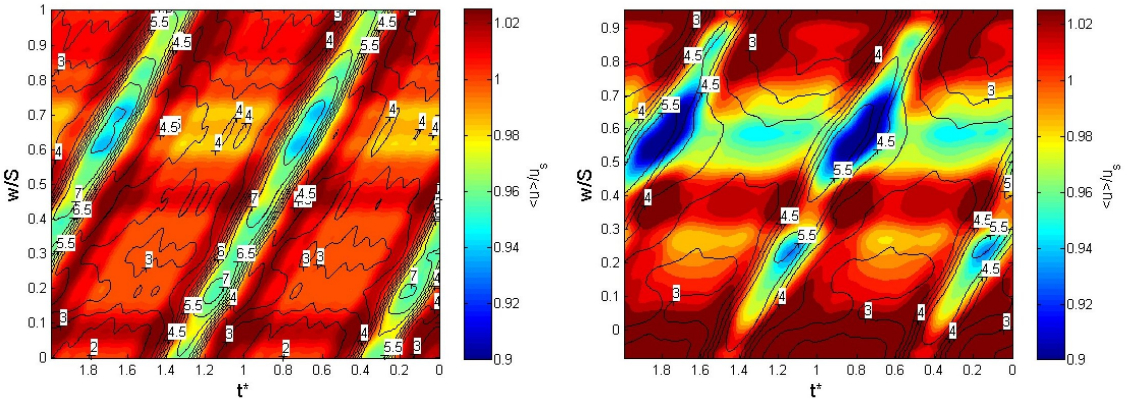

a) Normalised velocity (shading) & Tu (line) at Inlet

b) Normalised velocity (shading) & Tu (line) at 42.7%c upstream of stator leading edge

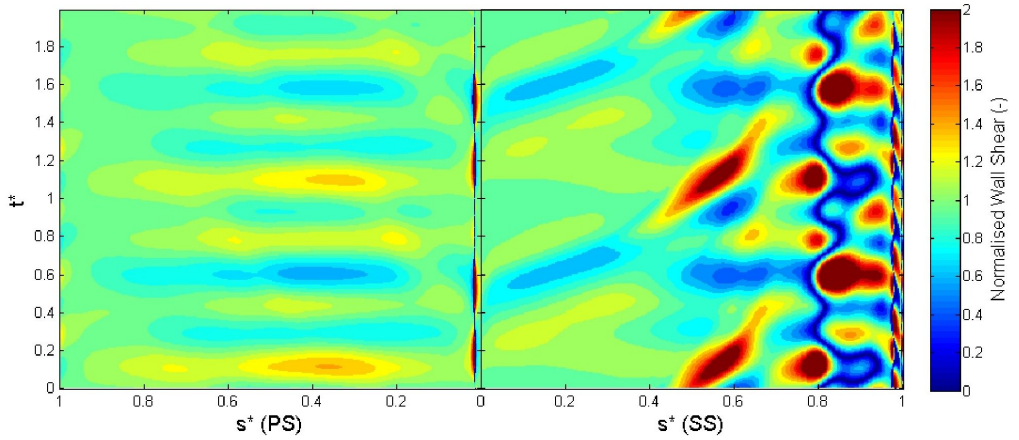

c) Normalised wall shear stress on blade surface

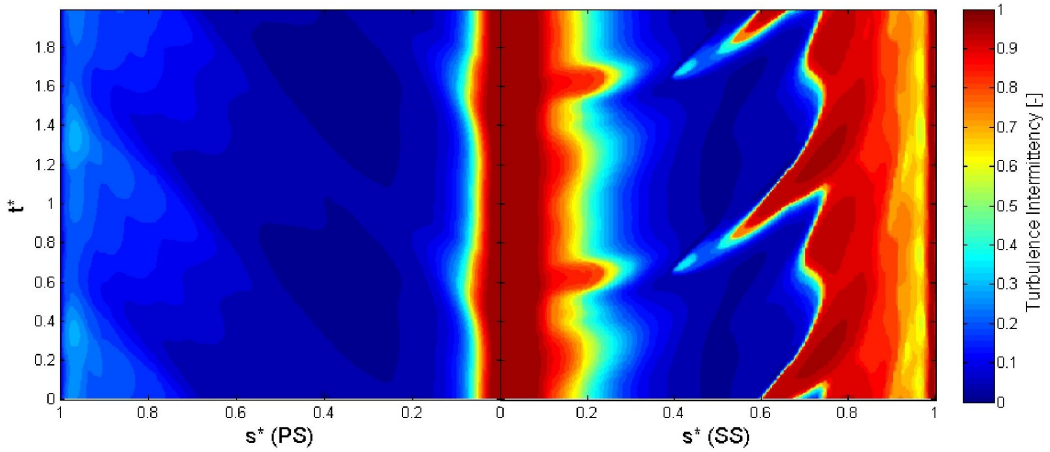

d) Turbulence intermittency at 0.2 mm from blade surface

Figure A.31: CFD results for Run 4

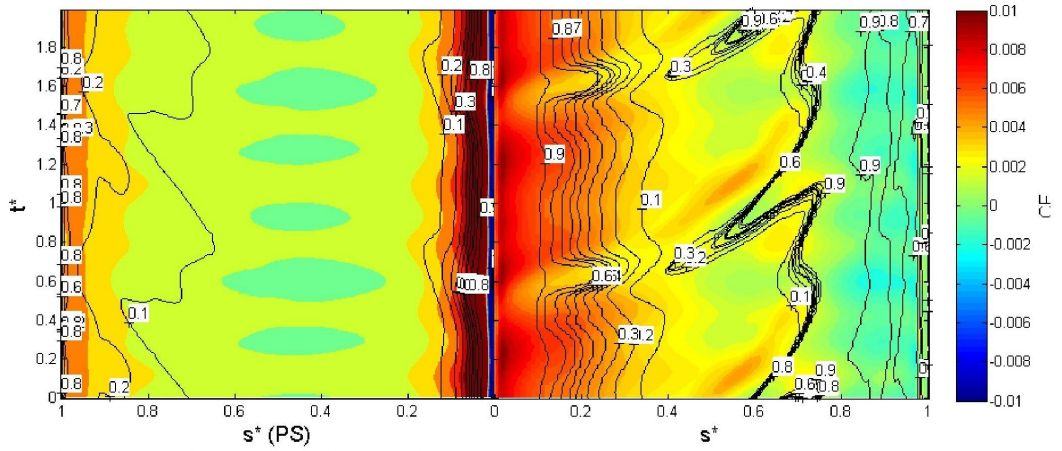

a) Local skin friction (shading) and turbulence intermittency (line) on blade surface

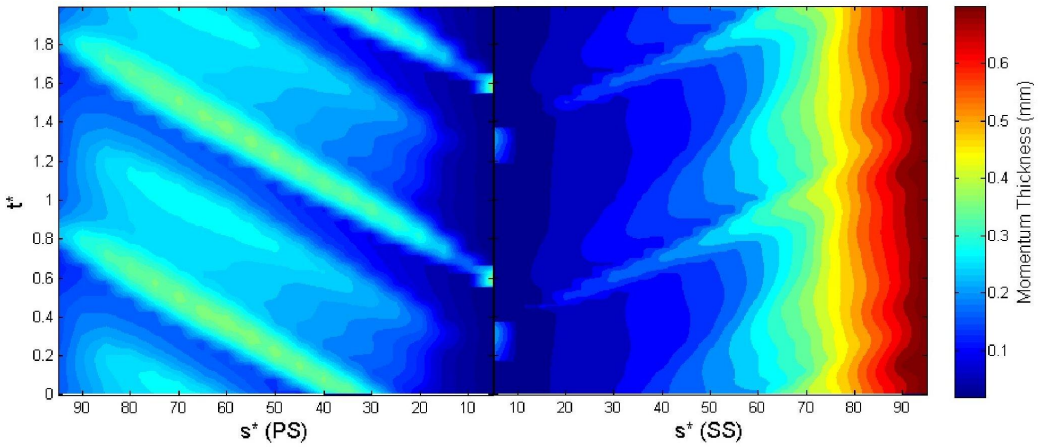

b) Momentum thickness on blade surface

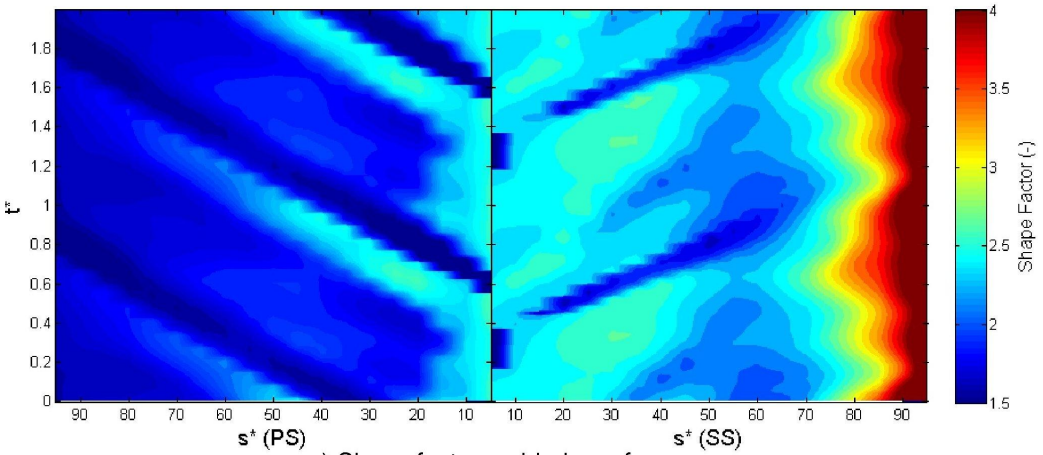

c) Shape factor on blade surface

Figure A.32: CFD results for Run 4

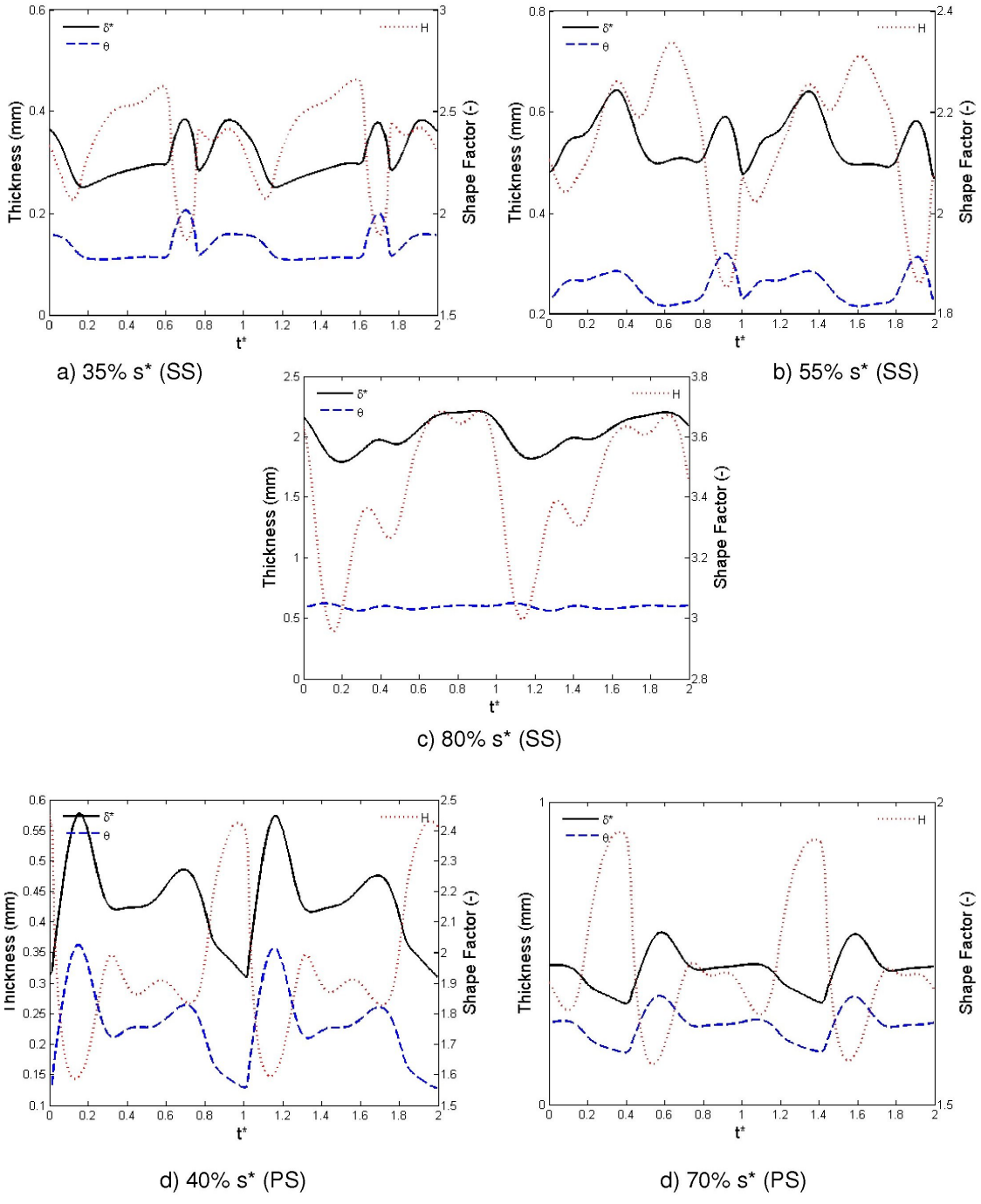

Figure A.33: CFD results for Run 4 - Integral parameters at various distances along suction (SS) and pressure (PS) surfaces

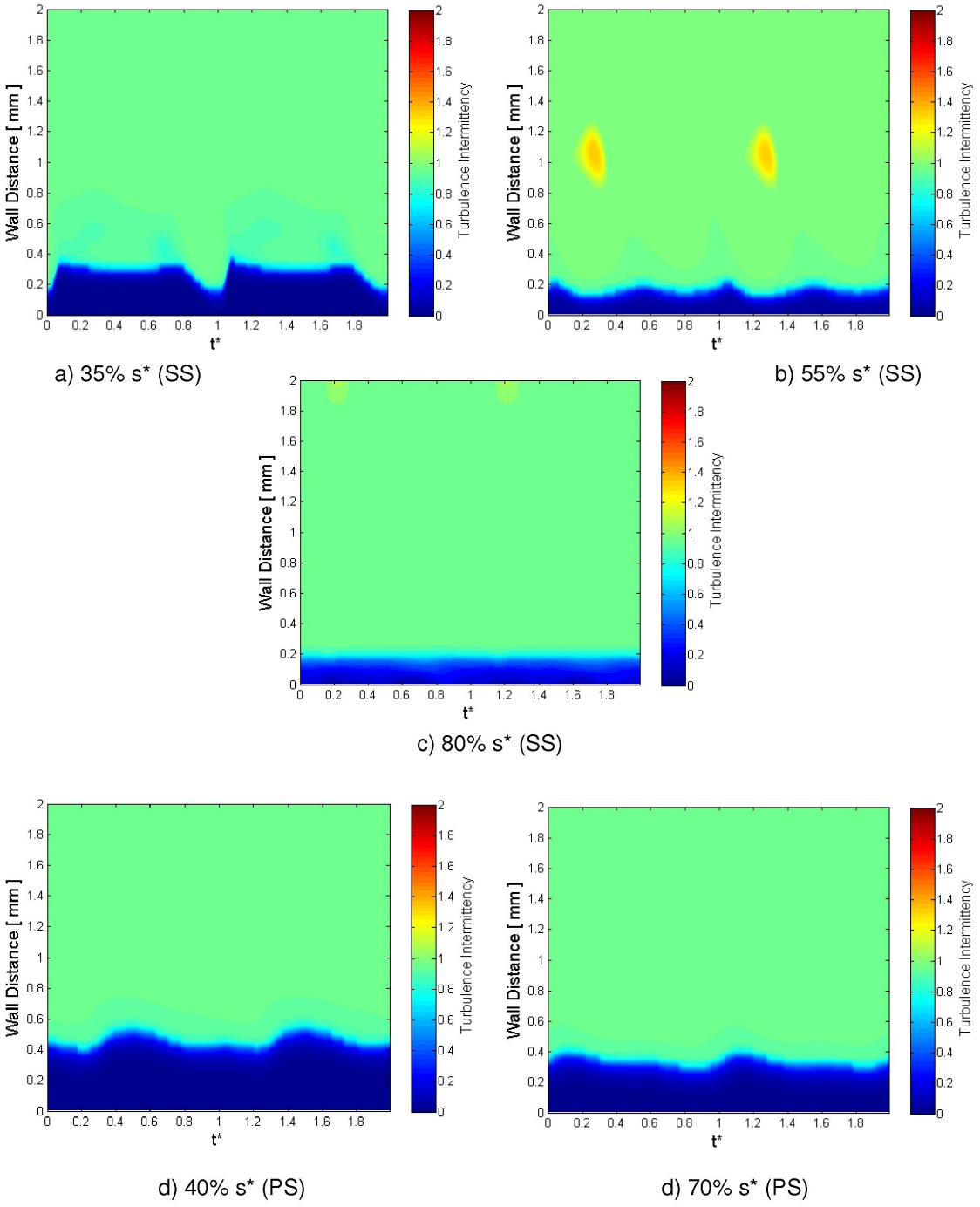

Figure A.34: CFD results for Run 4 - Intermittency at various distances along suction (SS) and pressure (PS) surfaces

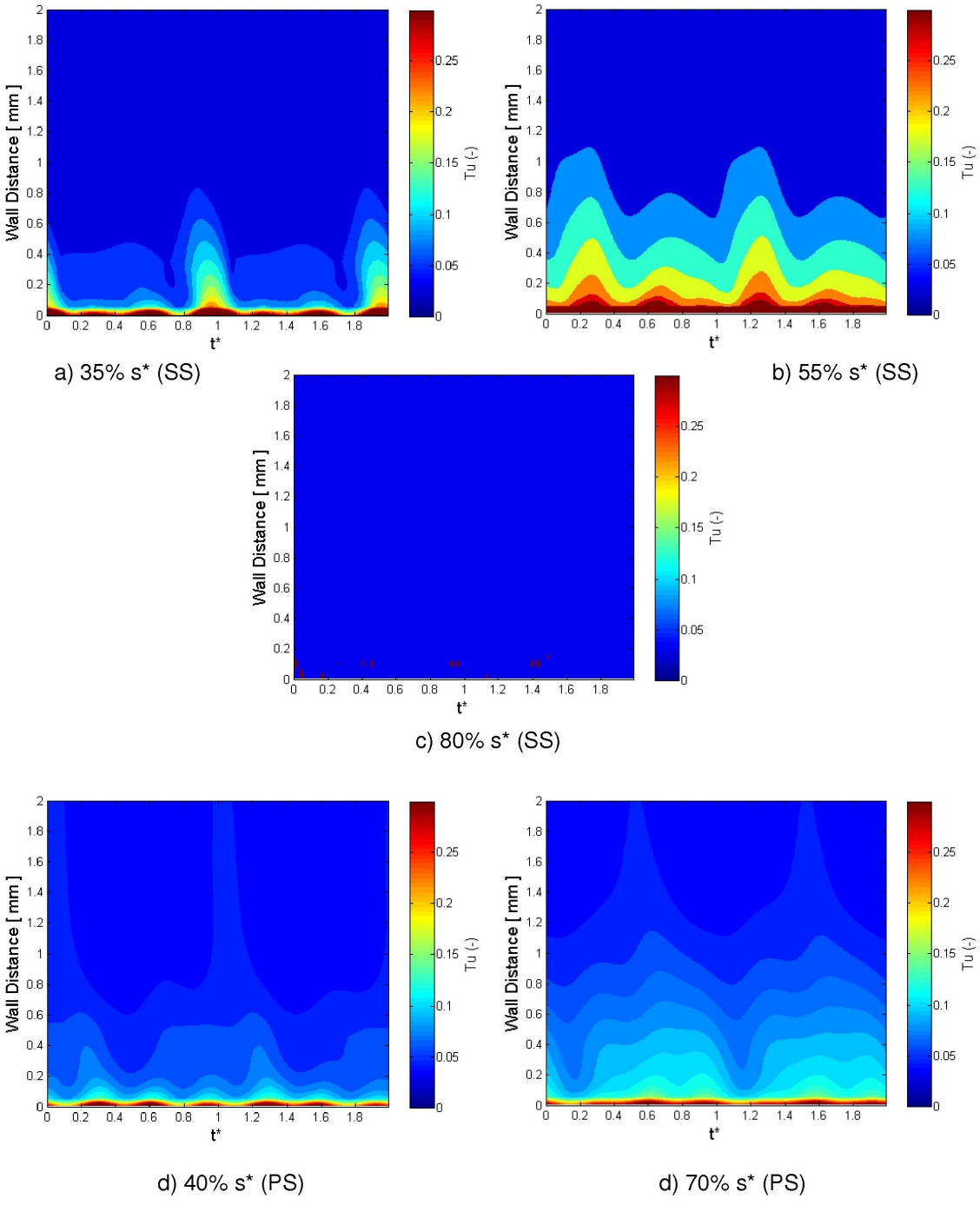

Figure A.35: CFD results for Run 4 - Turbulence intensity at various distances along suction (SS) and pressure (PS) surfaces

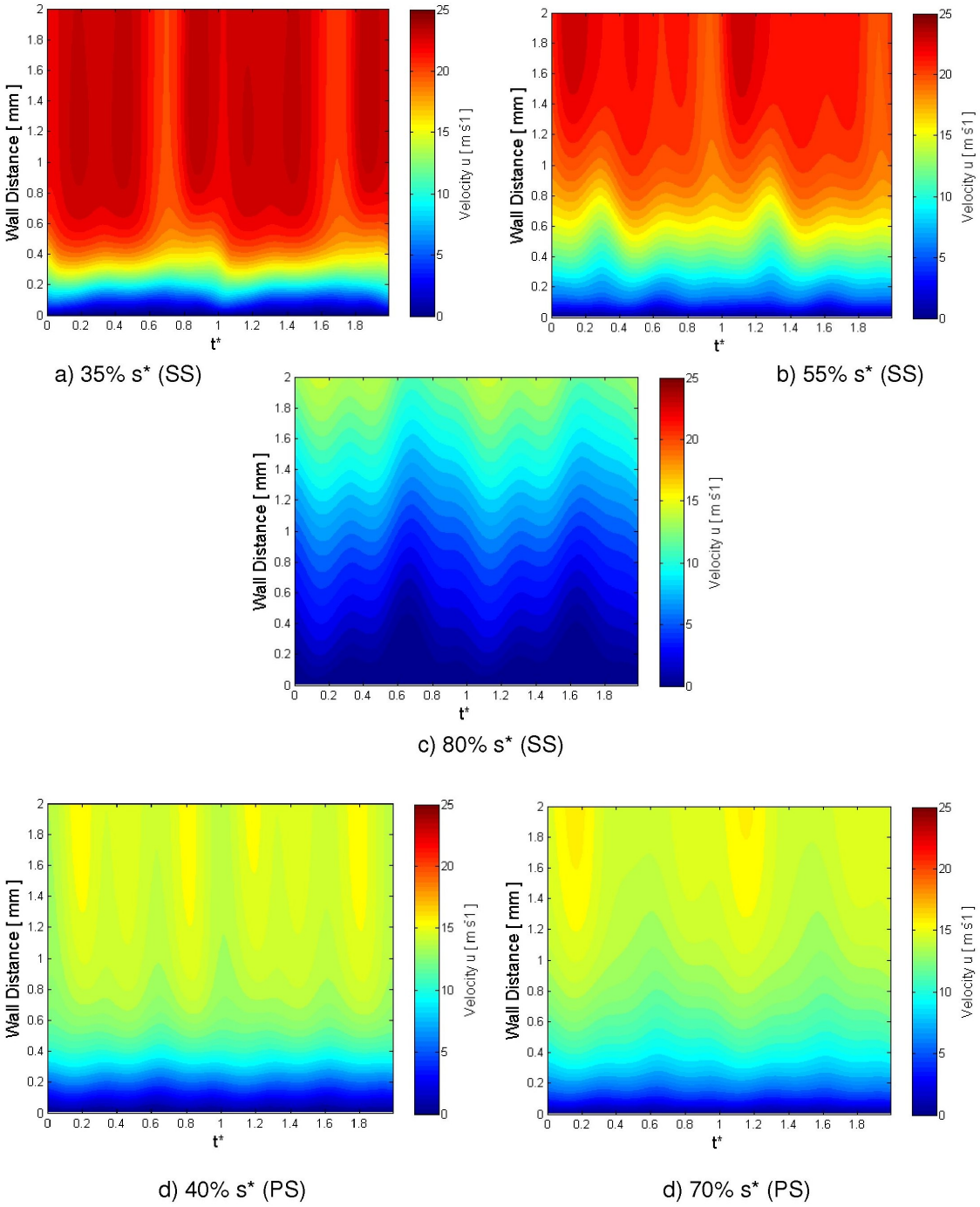

Figure A.36: CFD results for Run 4 - Tangential velocity at various distances along suction (SS) and pressure (PS) surfaces

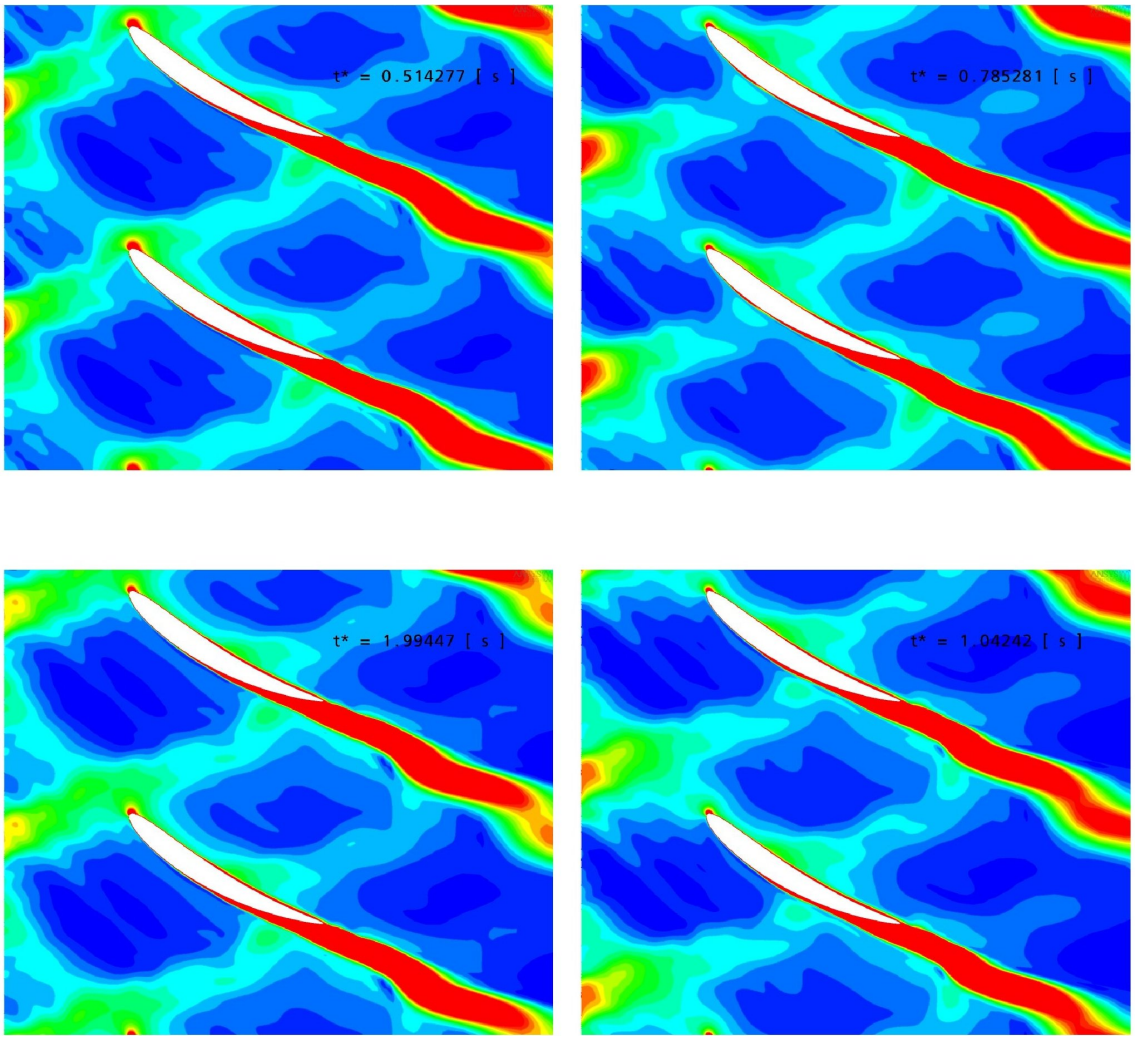

Figure A.37: CFD results for Run 4 - Wake turbulence transport through the domain at varying rotor passing time

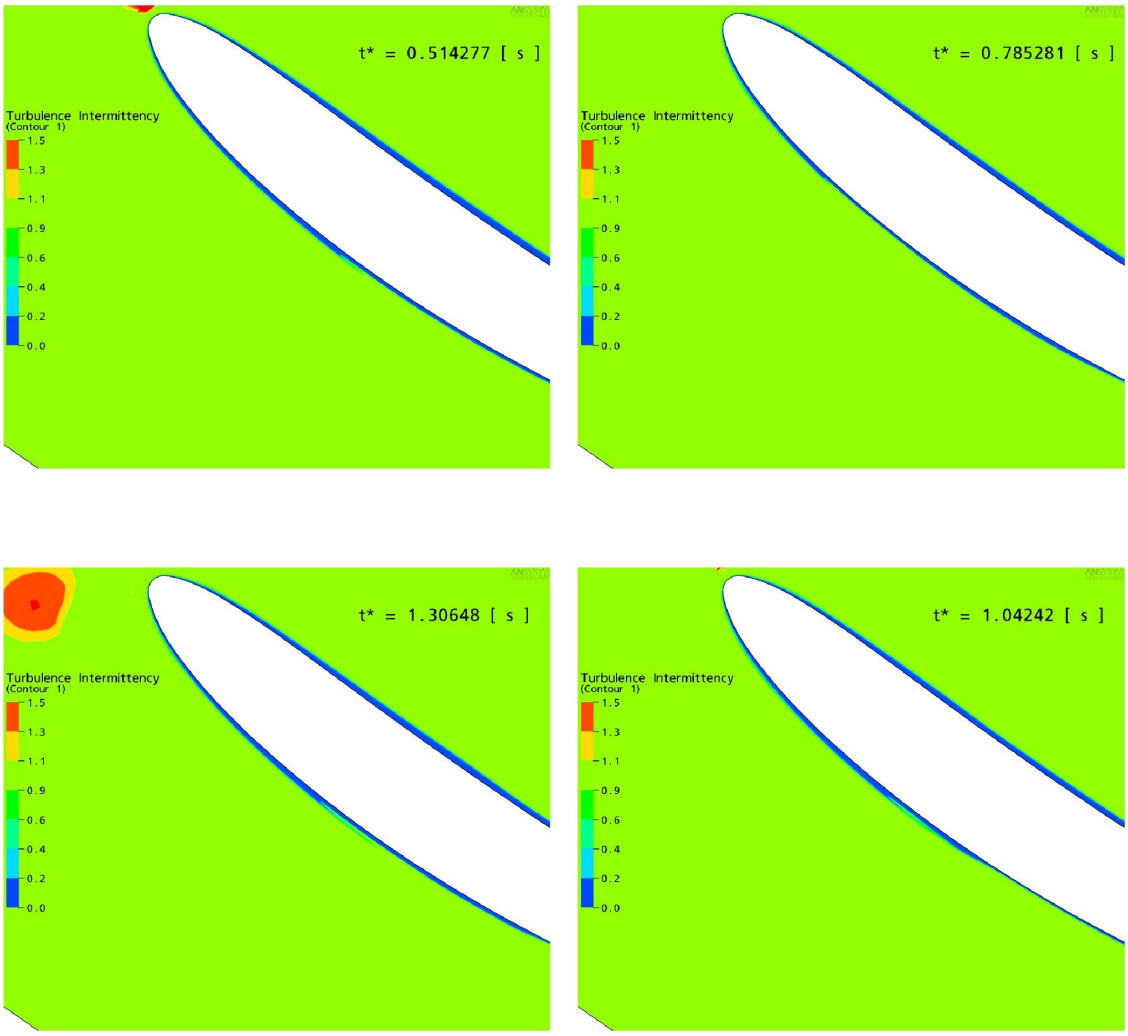

Figure A.38: CFD results for Run 4 - Intermittency in the boundary layer at varying rotor passing time

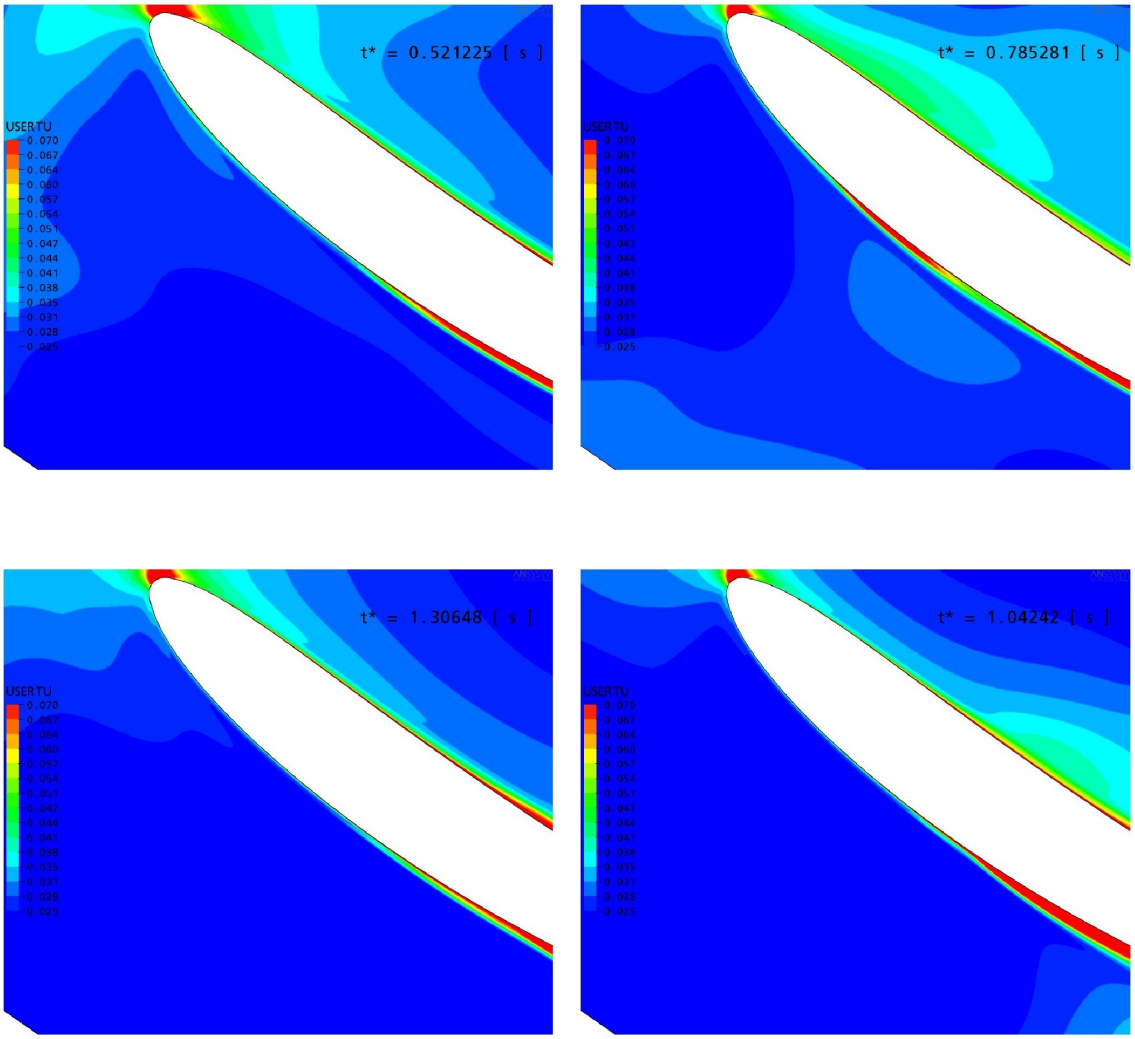

Figure A.39: CFD results for Run 4 - Wake turbulence transport effects on the stator boundary layer at varying rotor passing time

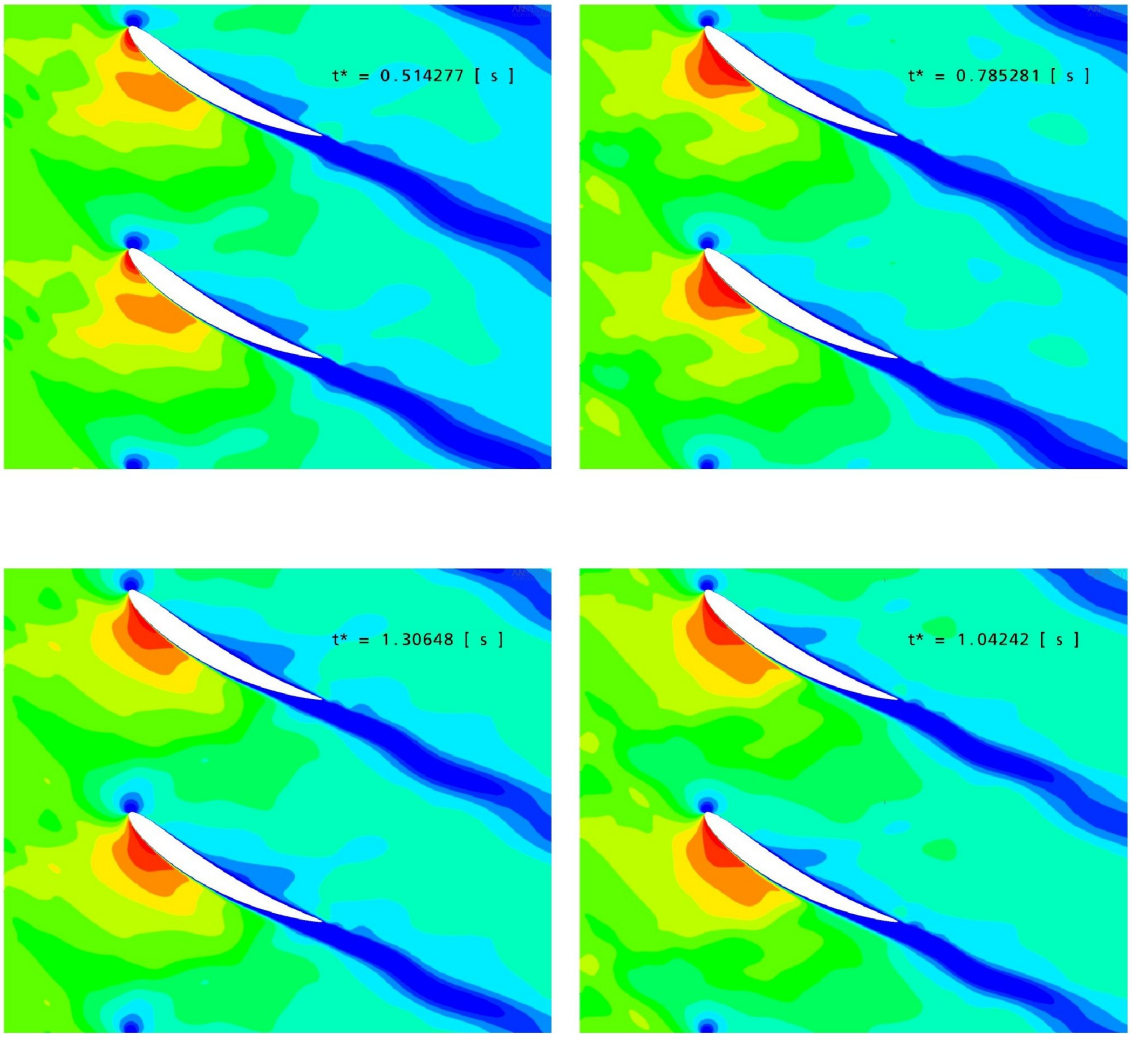

Figure A.40: CFD results for Run 4 - Velocity through passage at varying rotor passing time

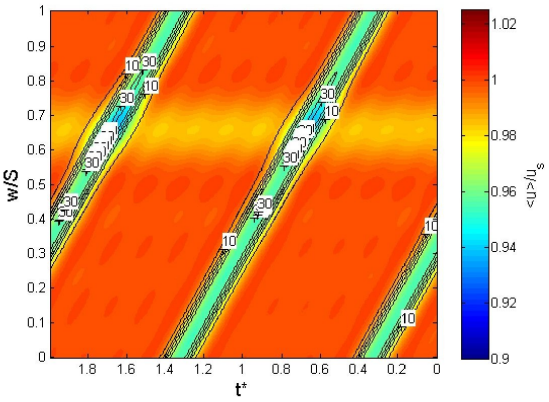

a) Normalised velocity (shading) & Tu (line) at Inlet

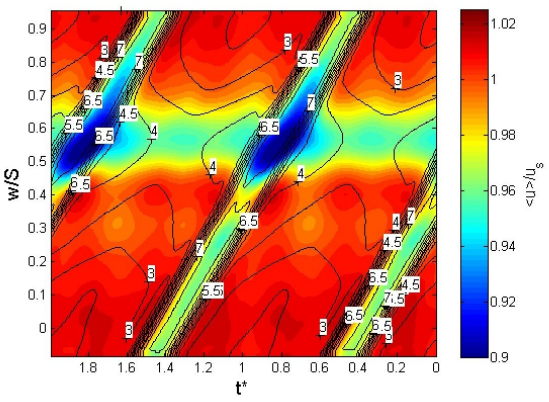

b) Normalised velocity (shading) & Tu (line) at 42.7%c upstream of stator leading edge

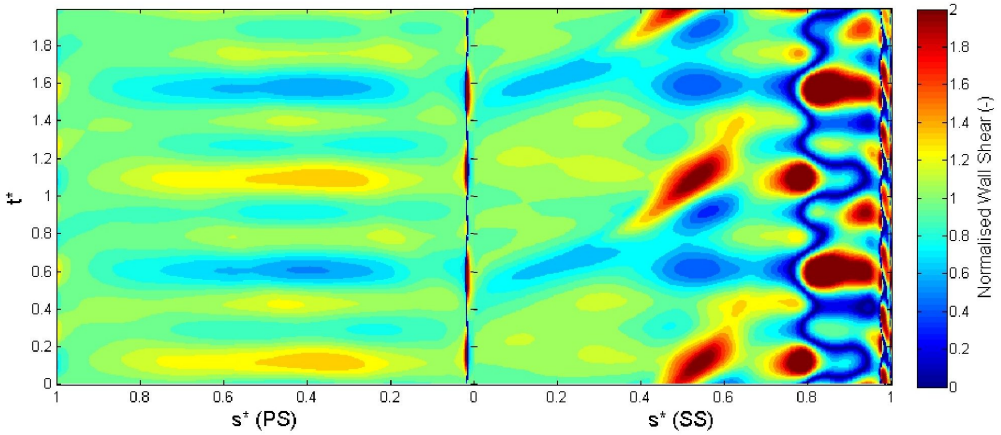

c) Normalised wall shear stress on blade surface

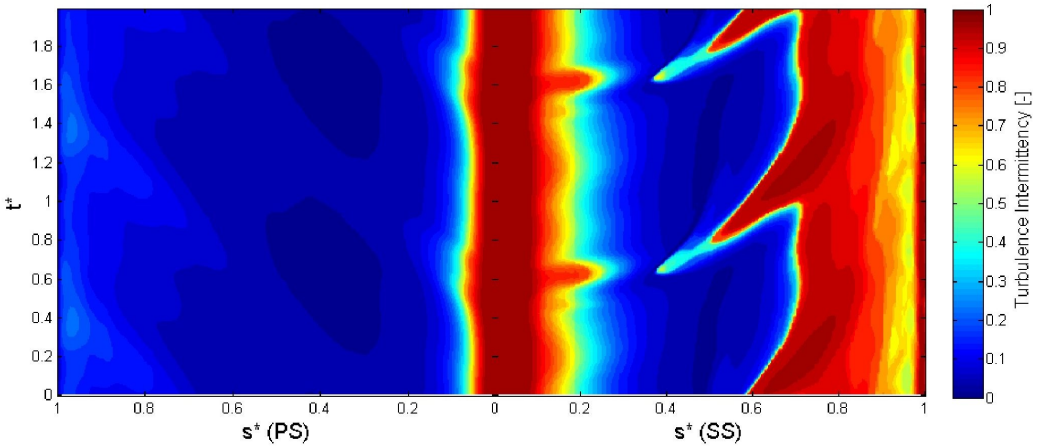

d) Turbulence intermittency at 0.2 mm from blade surface

Figure A.41: CFD results for Run 5

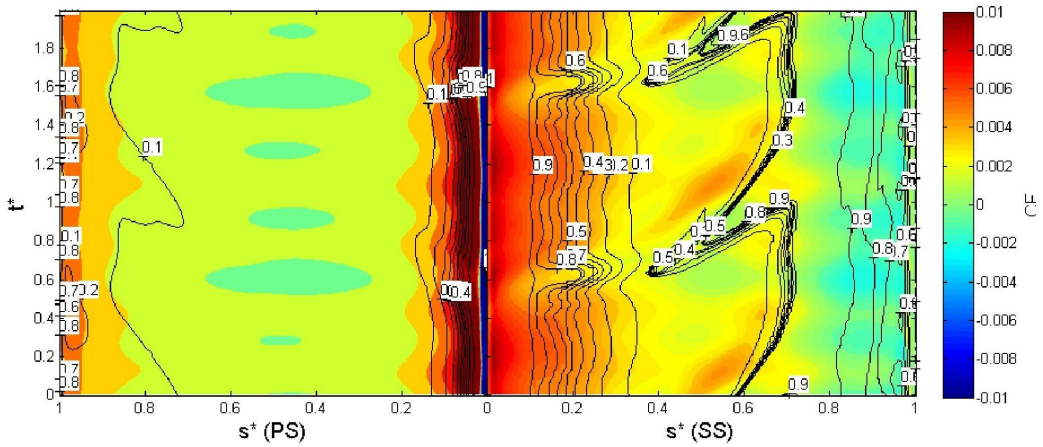

a) Local skin friction (shading) and turbulence intermittency (line) on blade surface

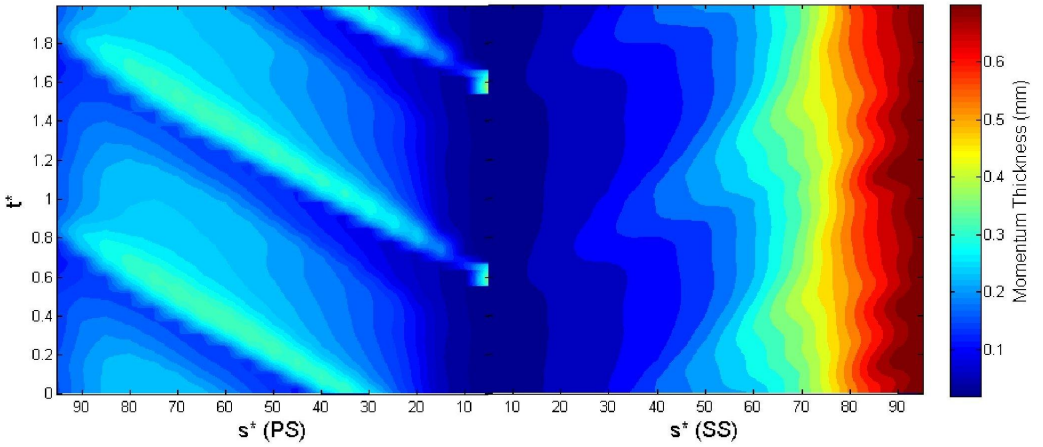

b) Momentum thickness on blade surface

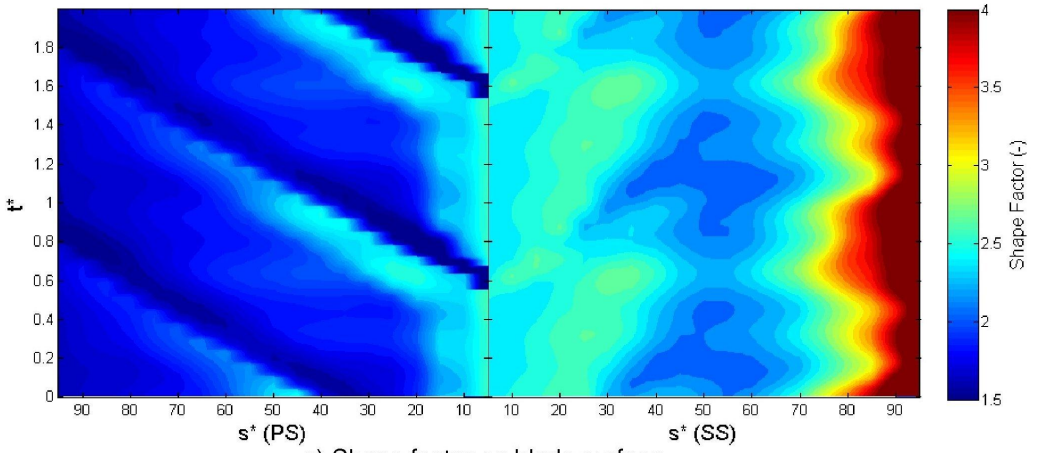

c) Shape factor on blade surface

Figure A.42: CFD results for Run 5

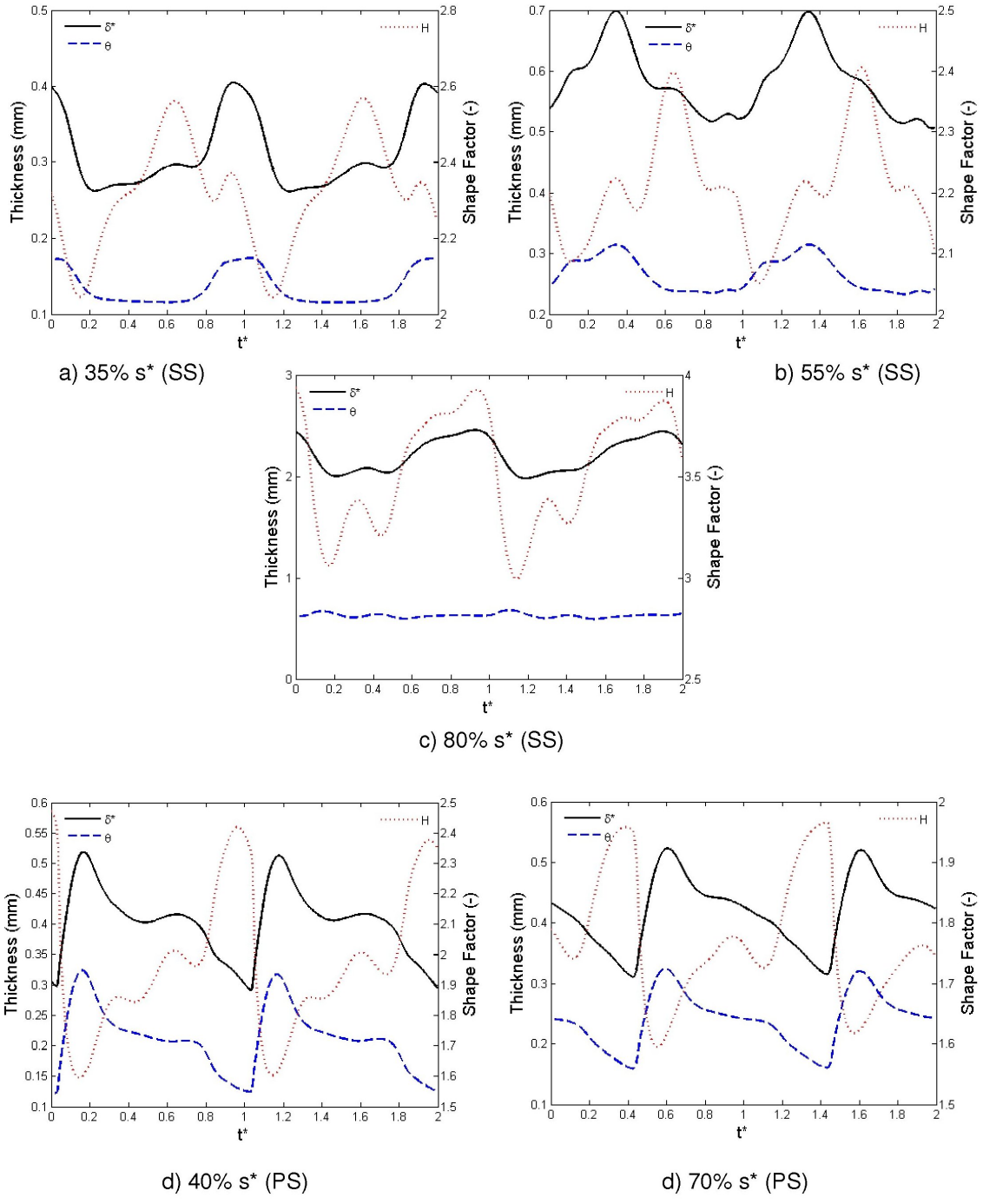

Figure A.43: CFD results for Run 5 - Integral parameters at various distances along suction (SS) and pressure (PS) surfaces

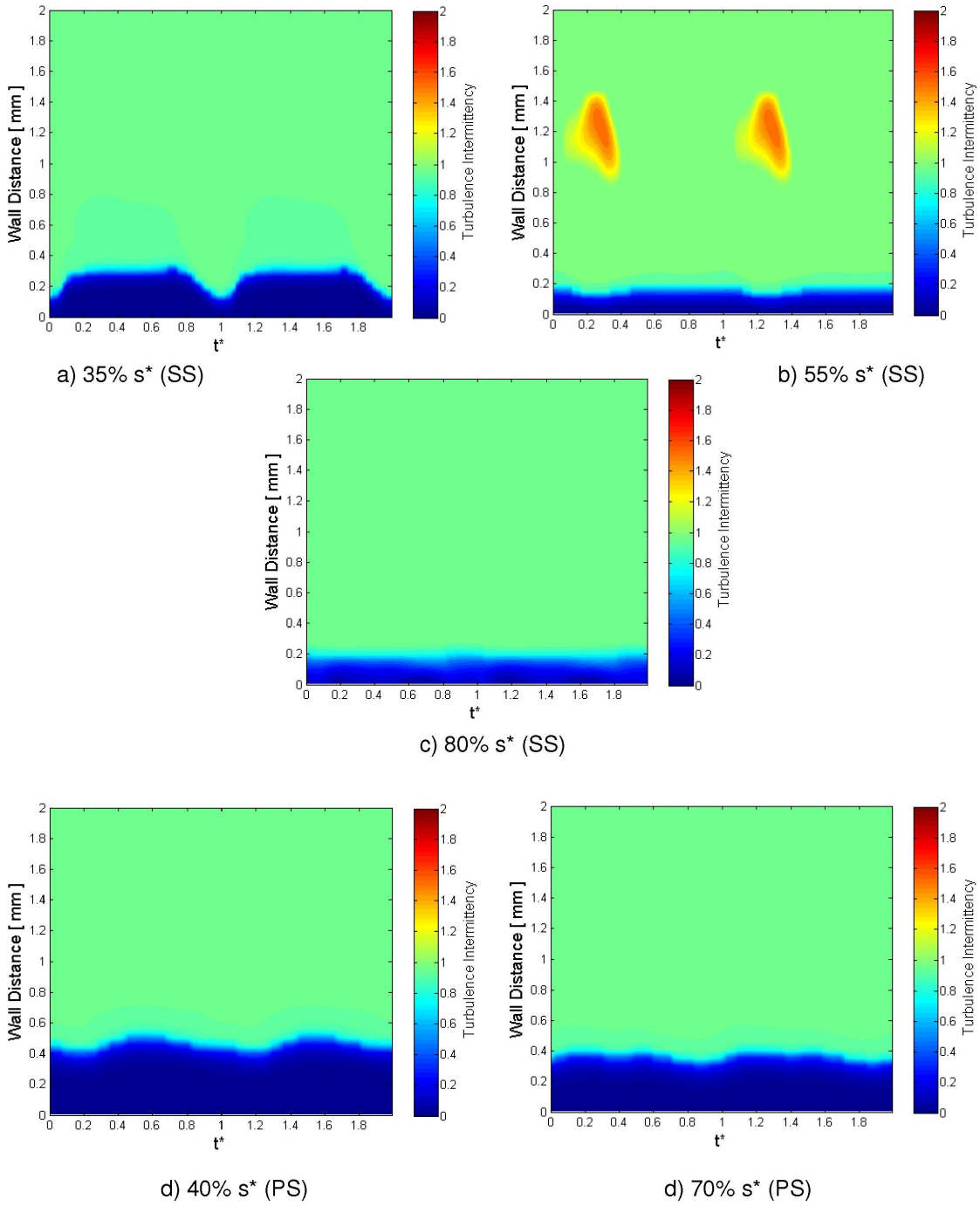

Figure A.44: CFD results for Run 5 - Intermittency at various distances along suction (SS) and pressure (PS) surfaces

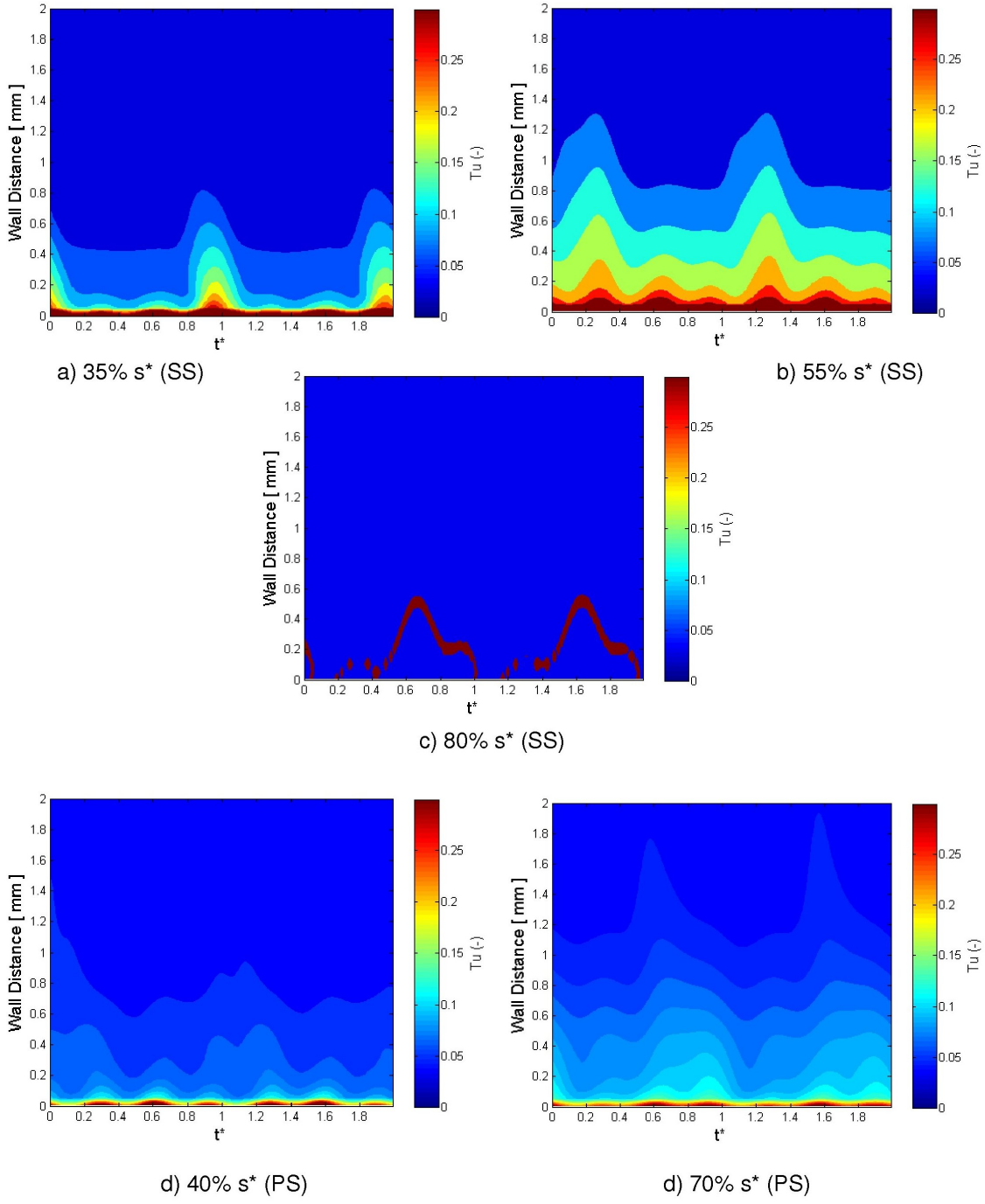

Figure A.45: CFD results for Run 5 - Turbulence intensity at various distances along suction (SS) and pressure (PS) surfaces

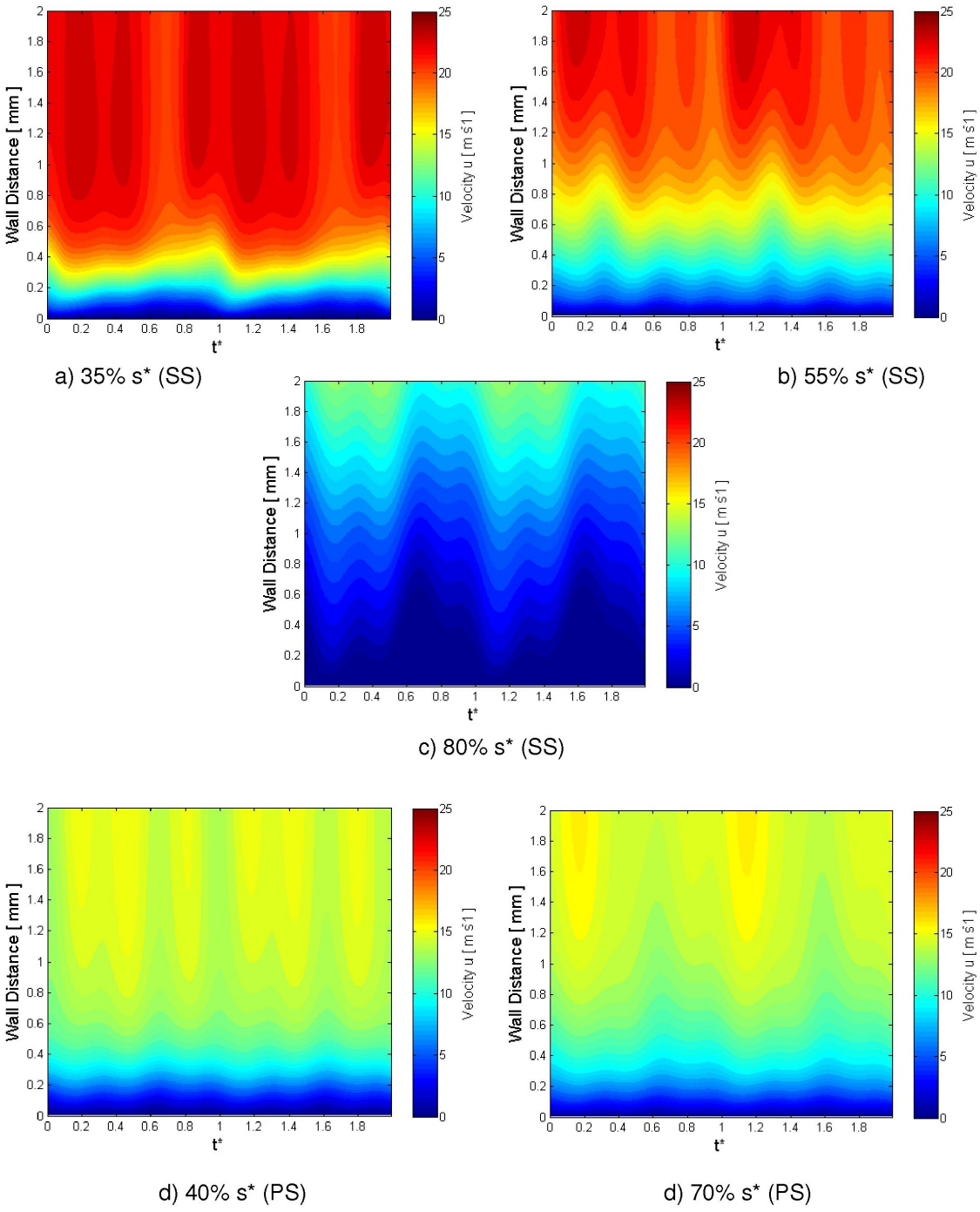

Figure A.46: CFD results for Run 5 - Tangential velocity at various distances along suction (SS) and pressure (PS) surfaces

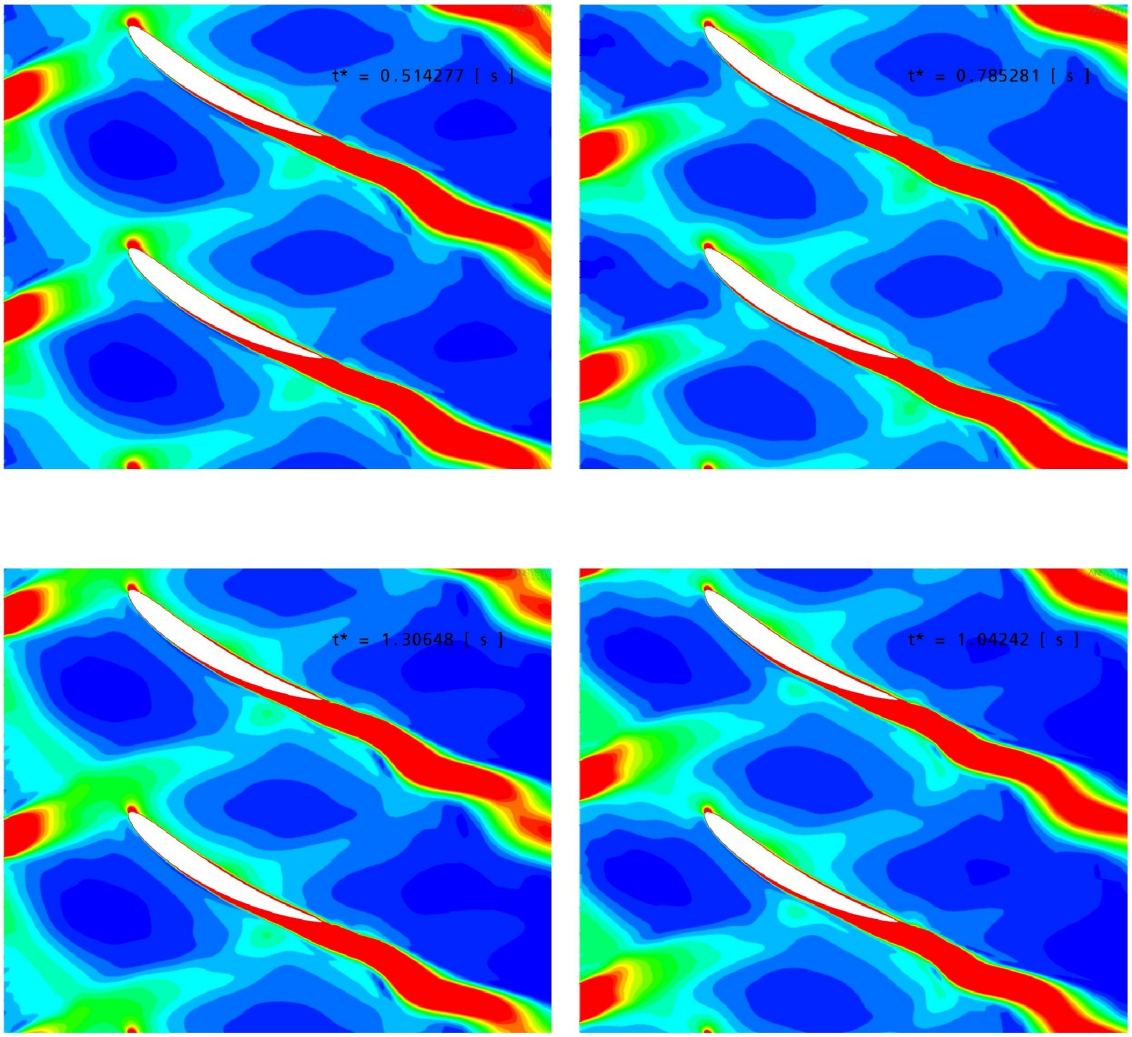

Figure A.47: CFD results for Run 5 - Wake turbulence transport through the domain at varying rotor passing time

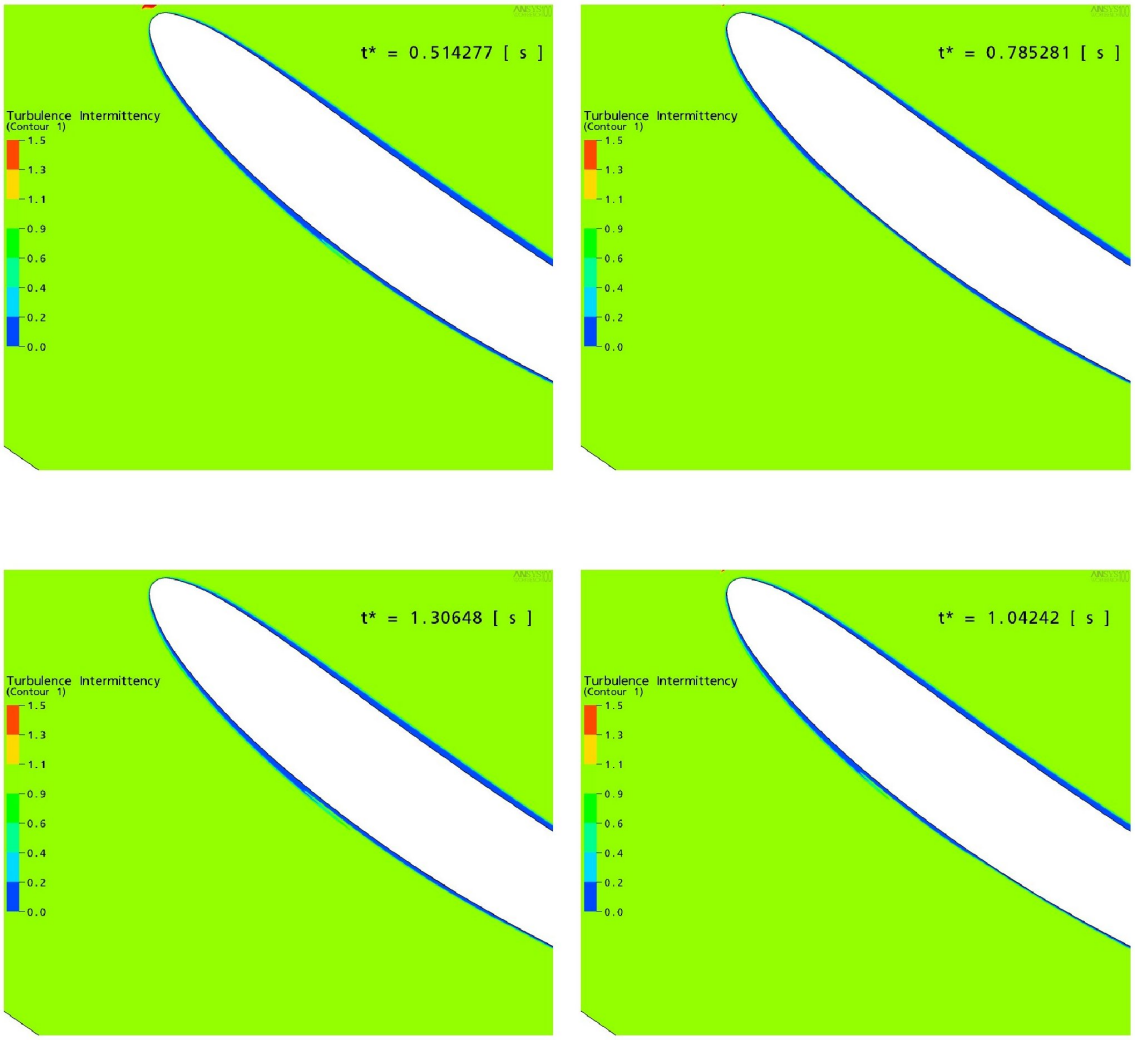

Figure A.48: CFD results for Run 5 - Intermittency in the boundary layer at varying rotor passing time

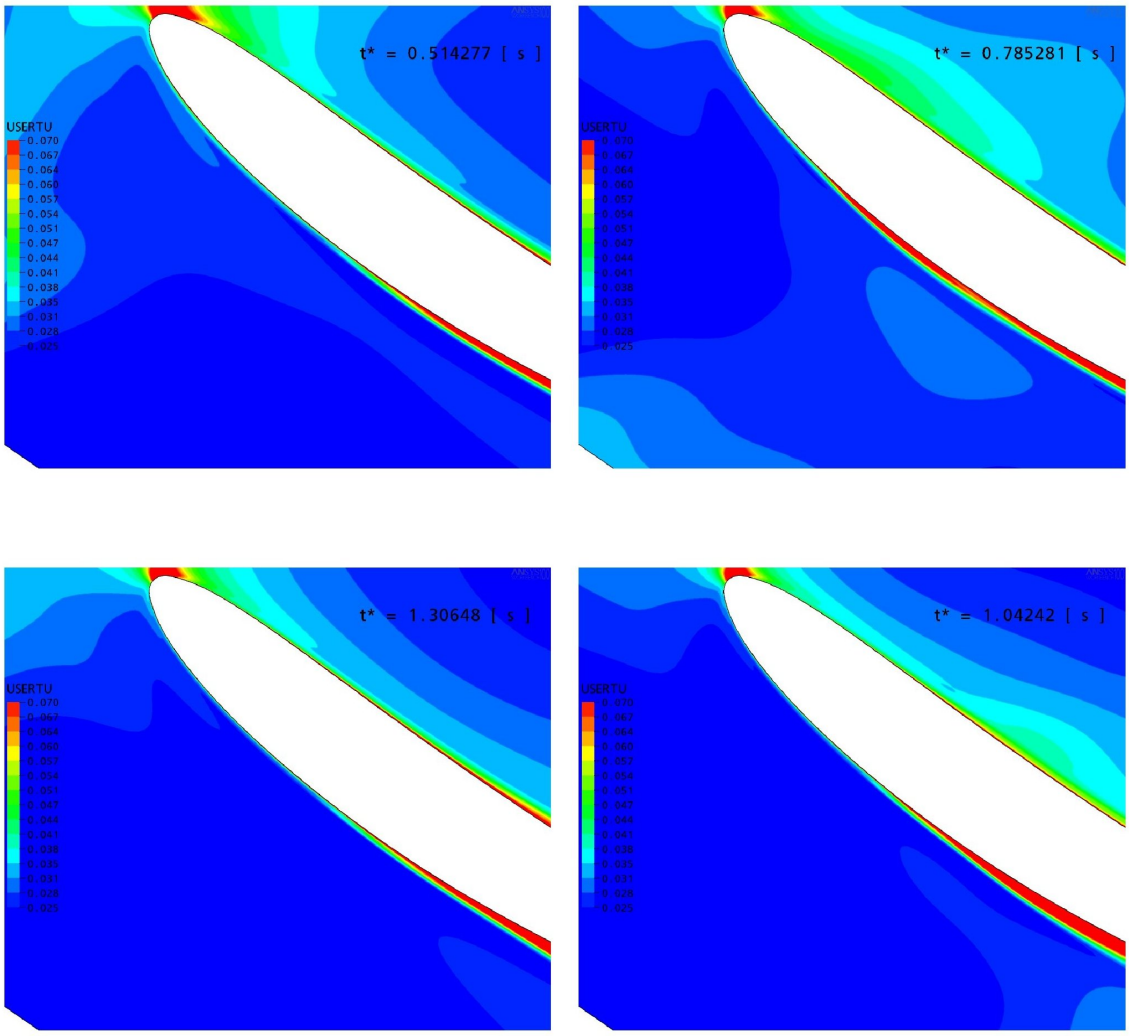

Figure A.49: CFD results for Run 5 - Wake turbulence transport effects on the stator boundary layer at varying rotor passing time

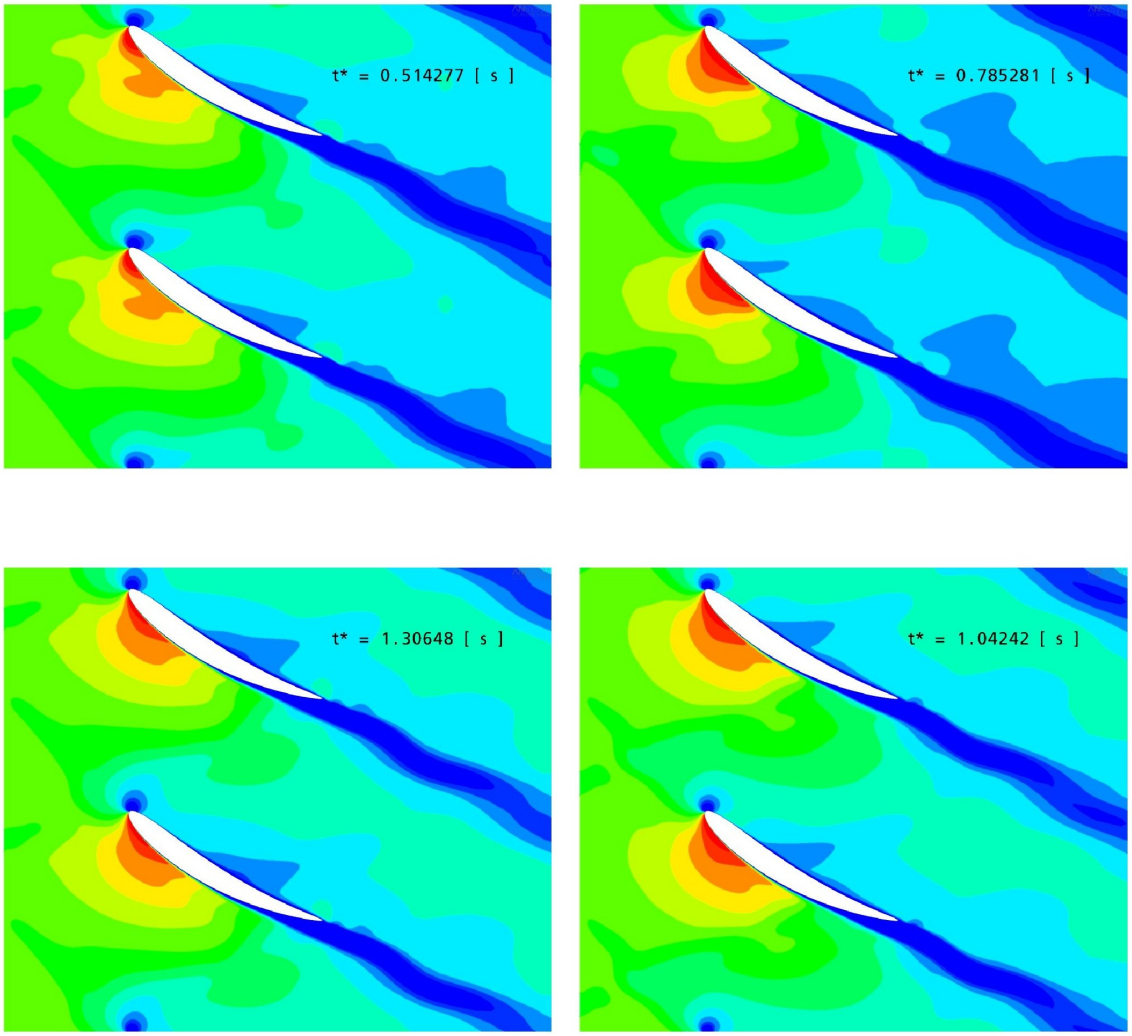

Figure A.50: CFD results for Run 5 - Velocity through passage at varying rotor passing time

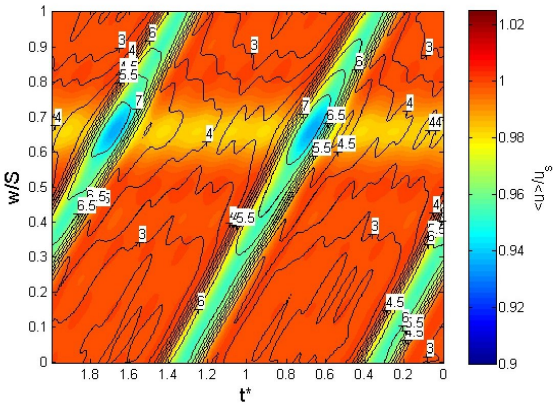

a) Normalised velocity (shading) & Tu (line) at Inlet

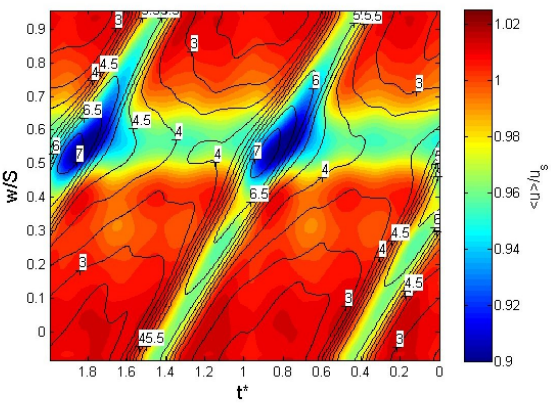

b) Normalised velocity (shading) & Tu (line) at 42.7%c upstream of stator leading edge

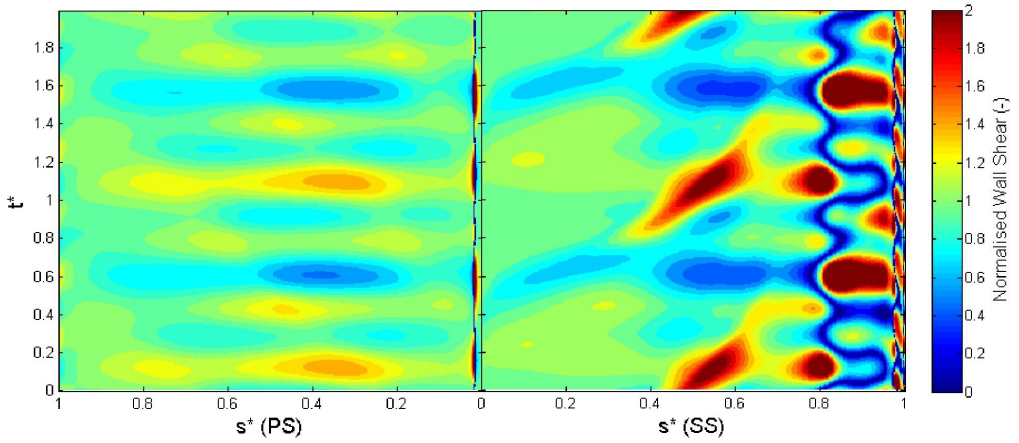

c) Normalised wall shear stress on blade surface

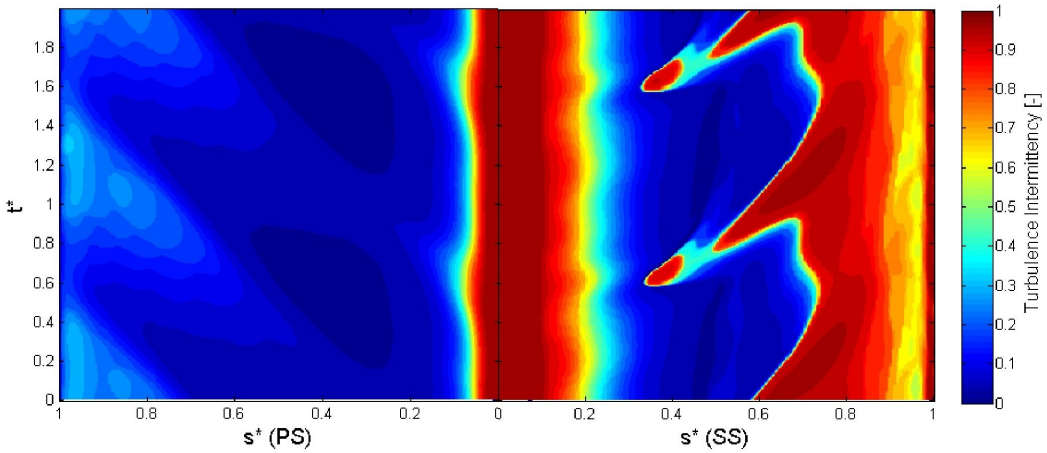

d) Turbulence intermittency at 0.2 mm from blade surface

Figure A.51: CFD results for Run 6

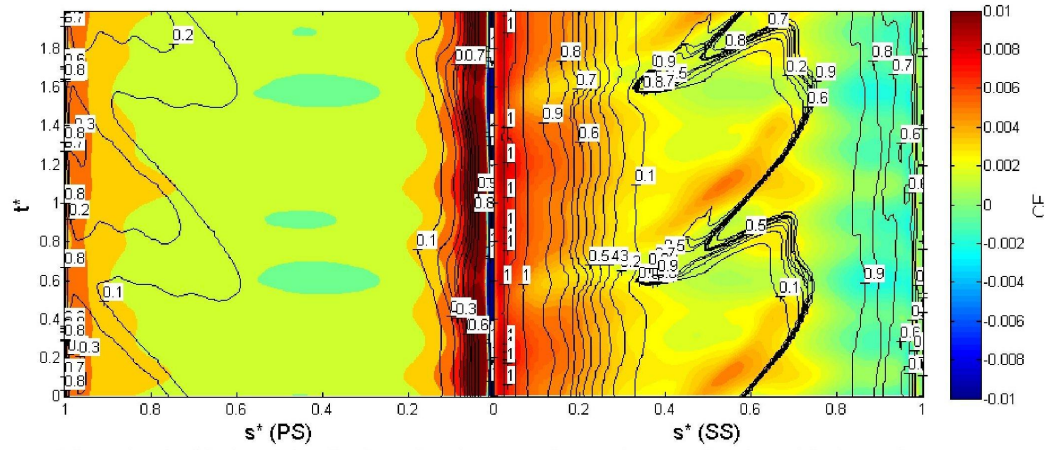

a) Local skin friction (shading) and turbulence intermittency (line) on blade surface

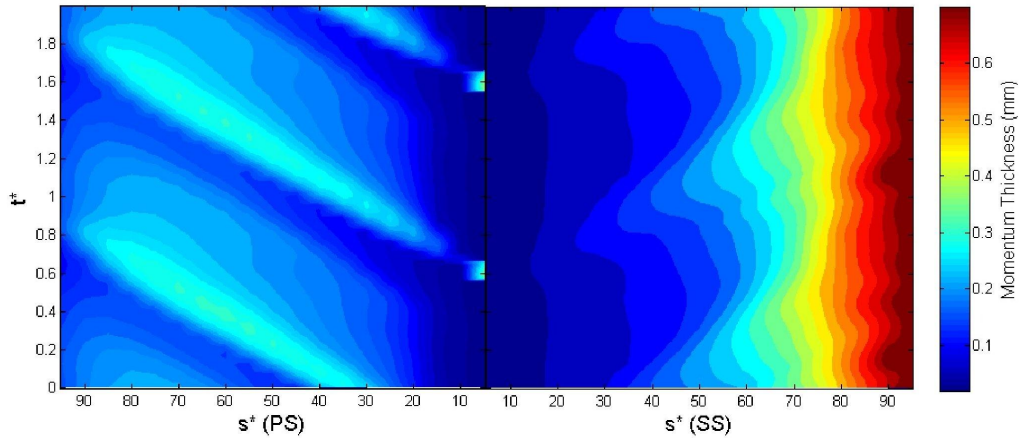

b) Momentum thickness on blade surface

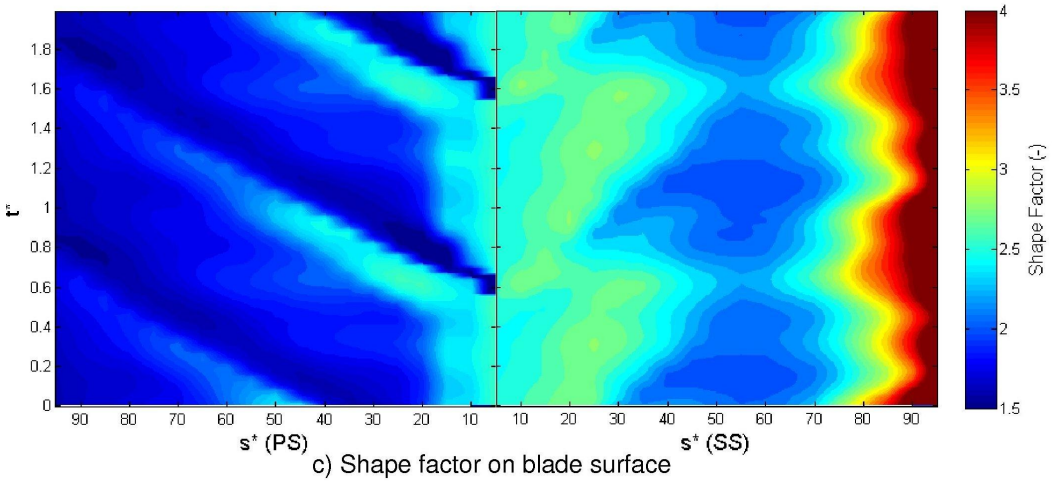

c) Shape factor on blade surface

Figure A.52: CFD results for Run 6

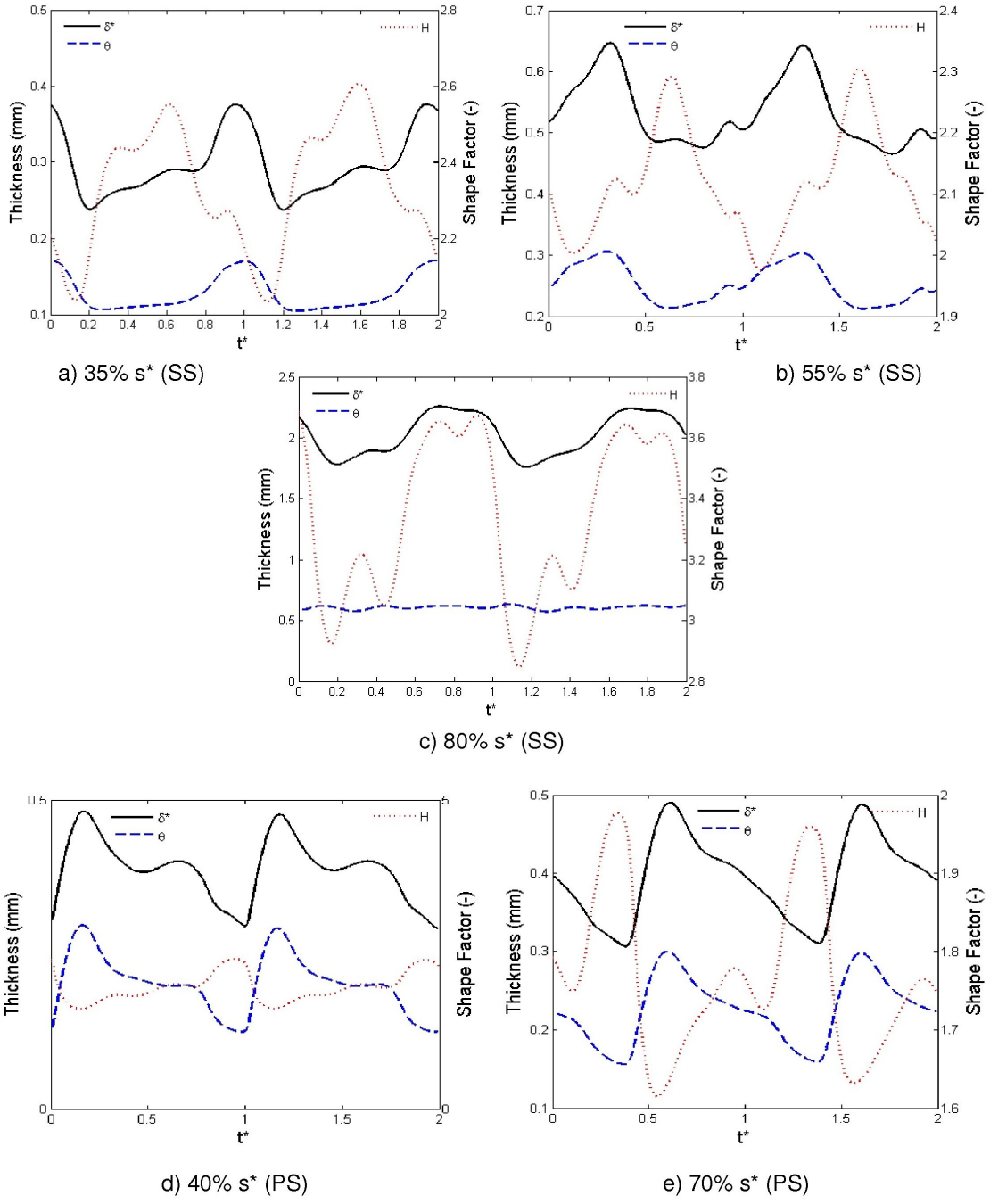

Figure A.53: CFD results for Run 6 - Integral parameters at various distances along suction (SS) and pressure (PS) surfaces

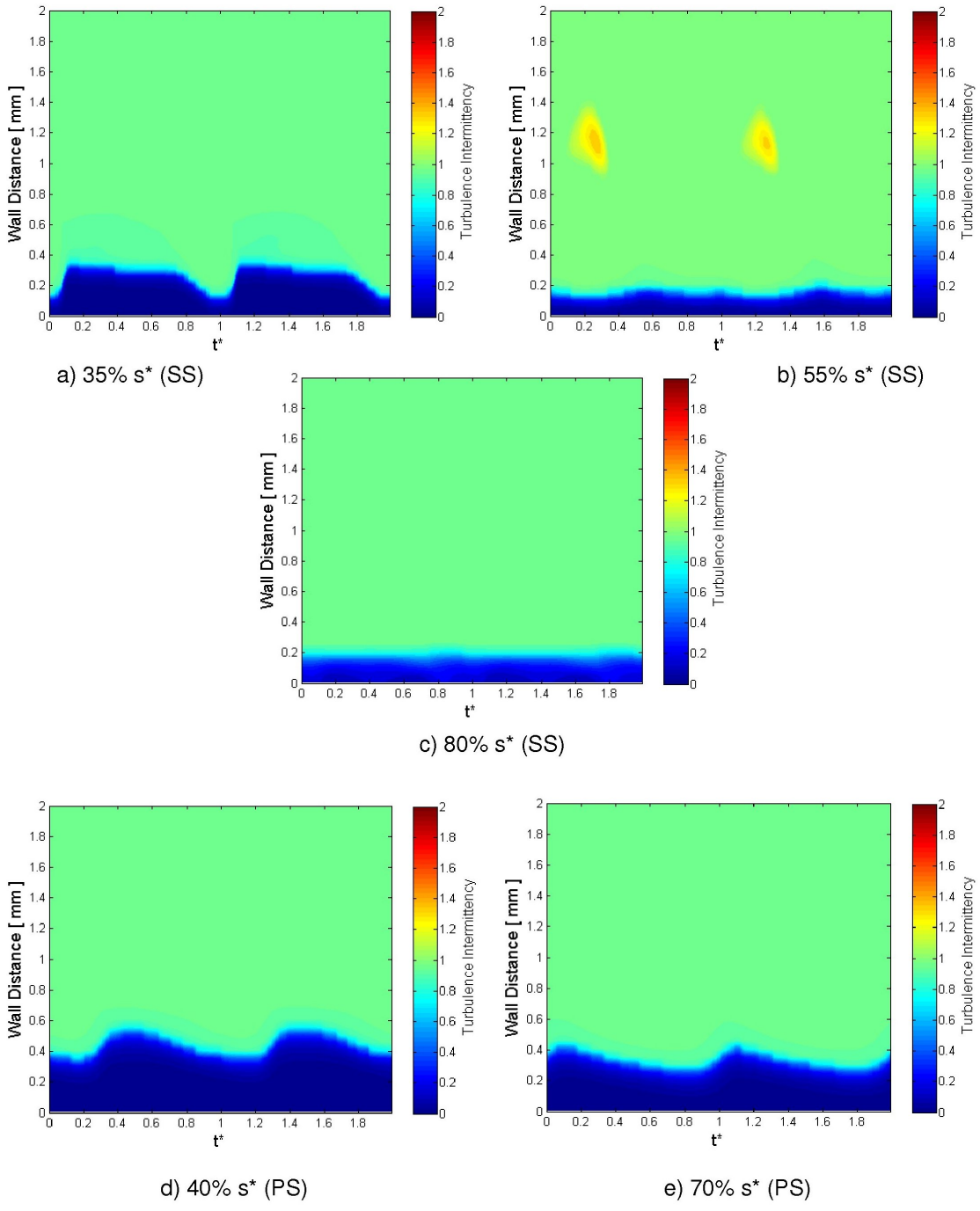

Figure A.54: CFD results for Run 6 - Intermittency at various distances along suction (SS) and pressure (PS) surfaces

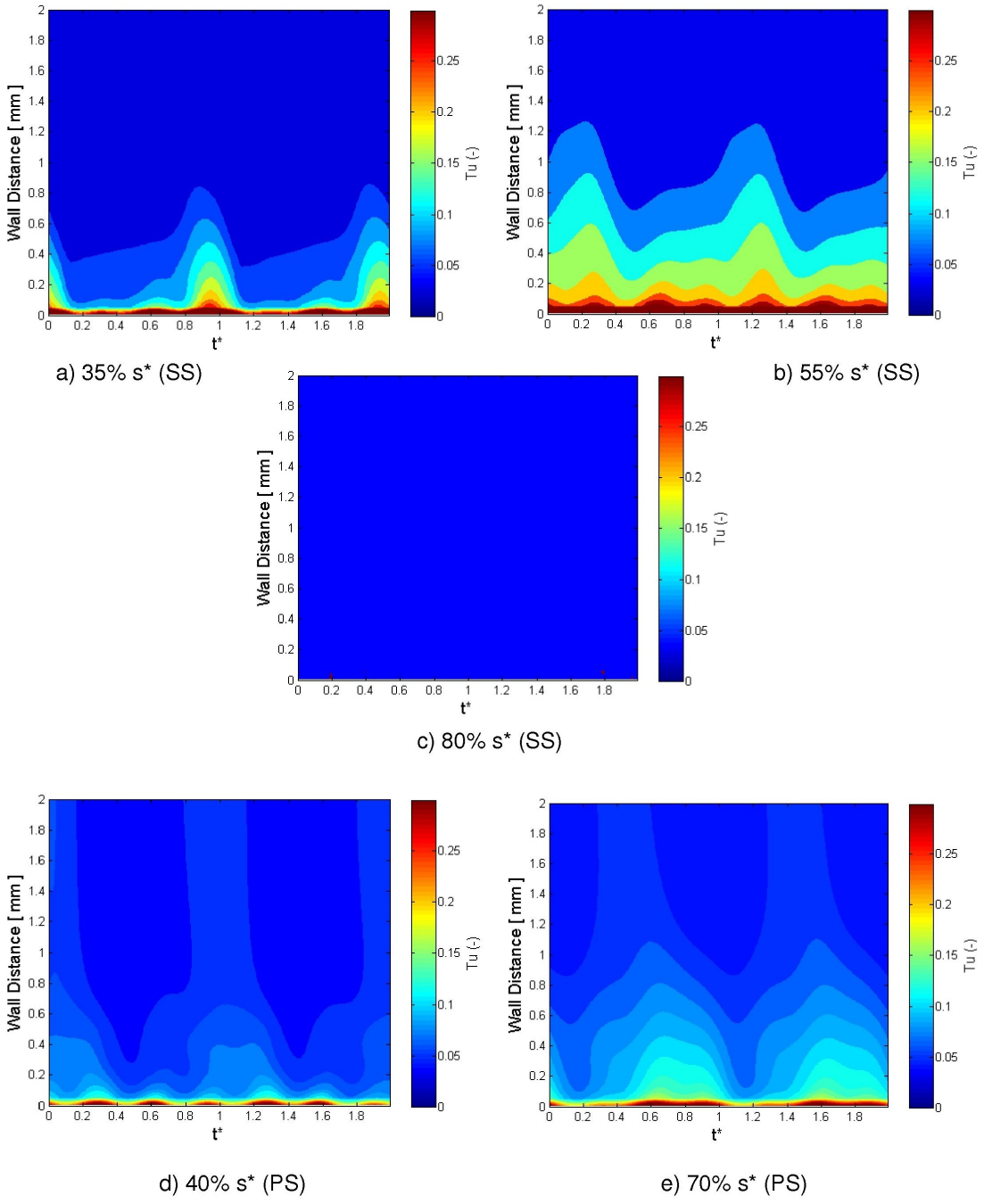

Figure A.55: CFD results for Run 6 - Turbulence intensity at various distances along suction (SS) and pressure (PS) surfaces

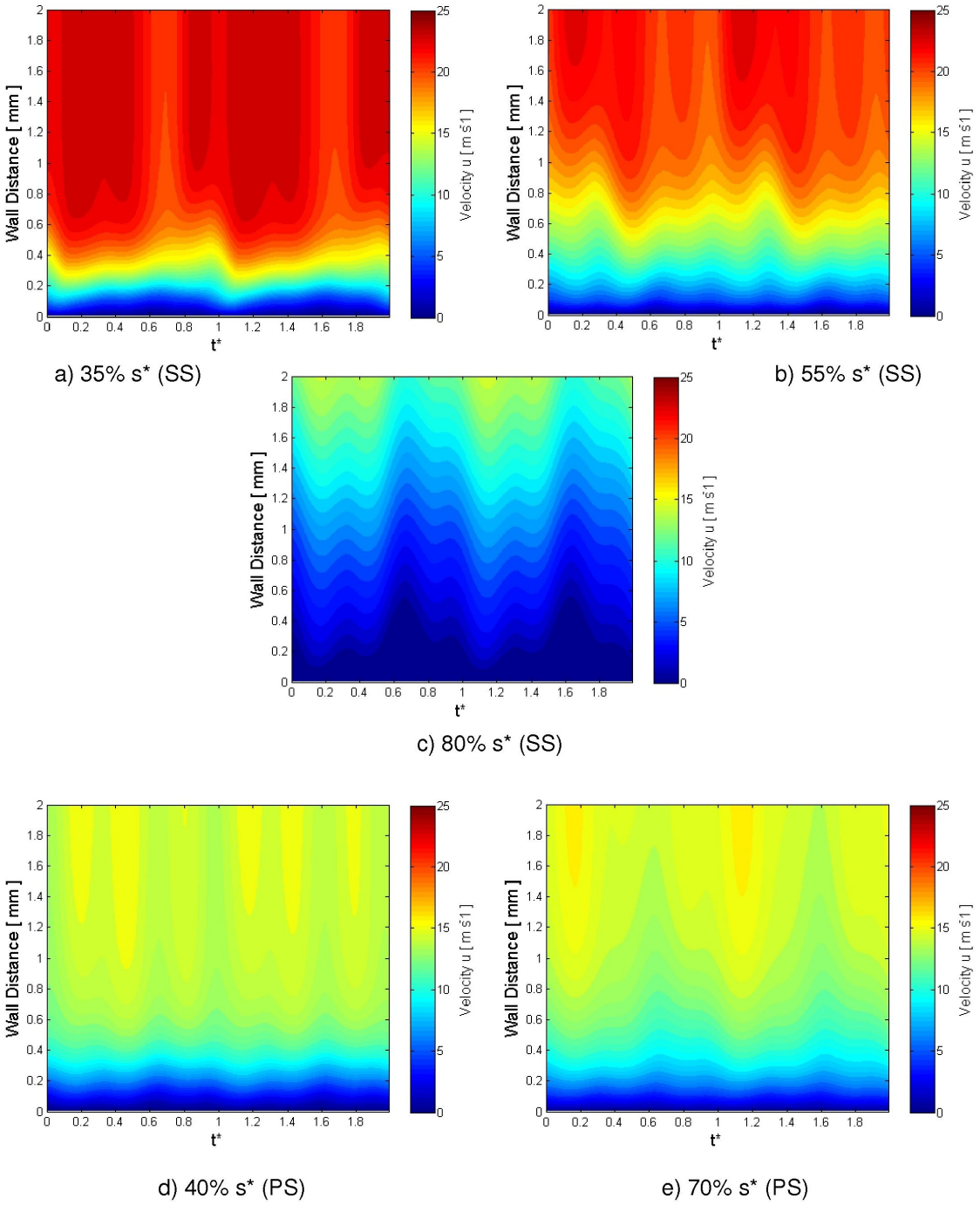

Figure A.56: CFD results for Run 6 - Tangential velocity at various distances along suction (SS) and pressure (PS) surfaces

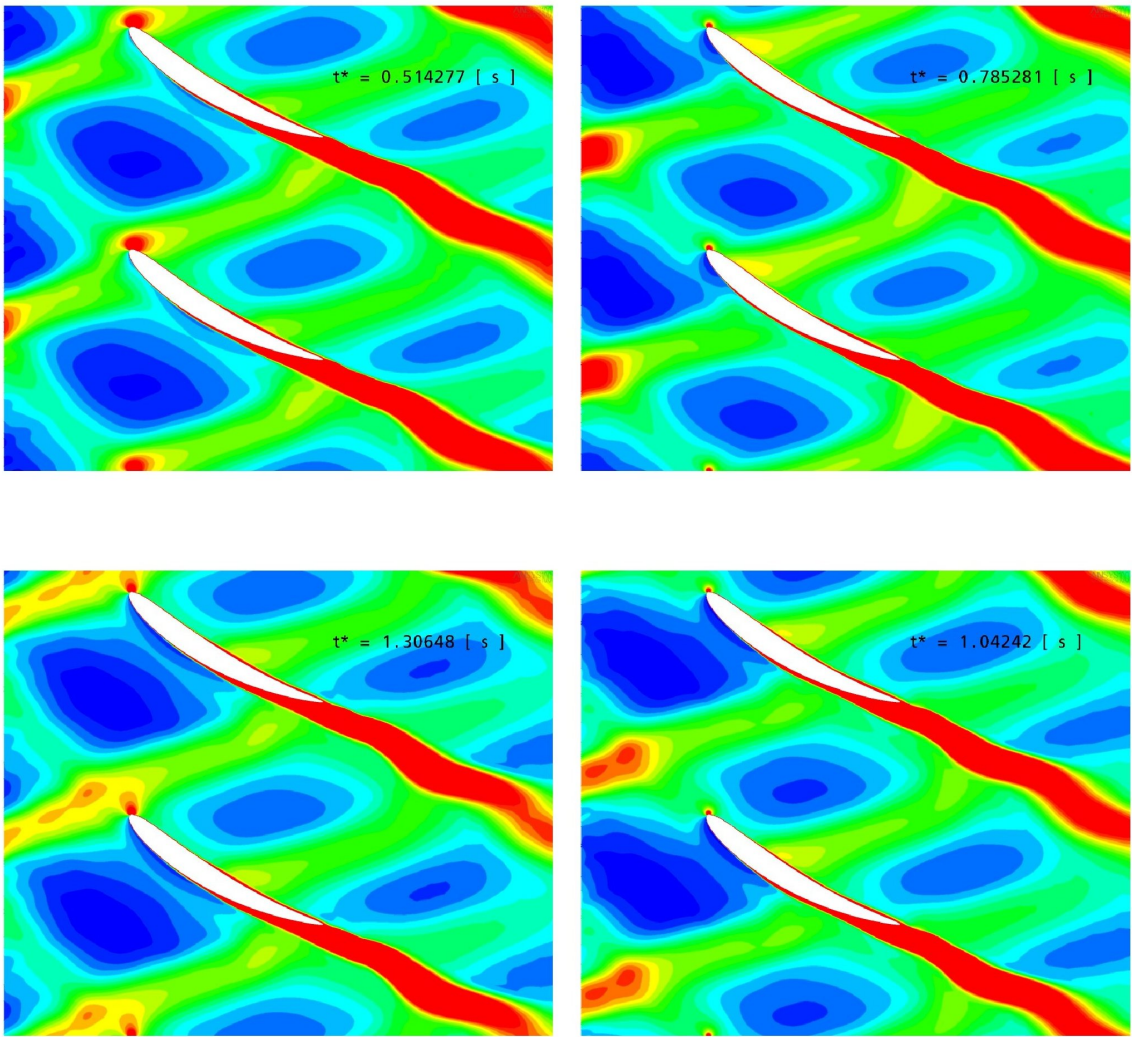

Figure A.57: CFD results for Run 6 - Wake turbulence transport through the domain at varying rotor passing time

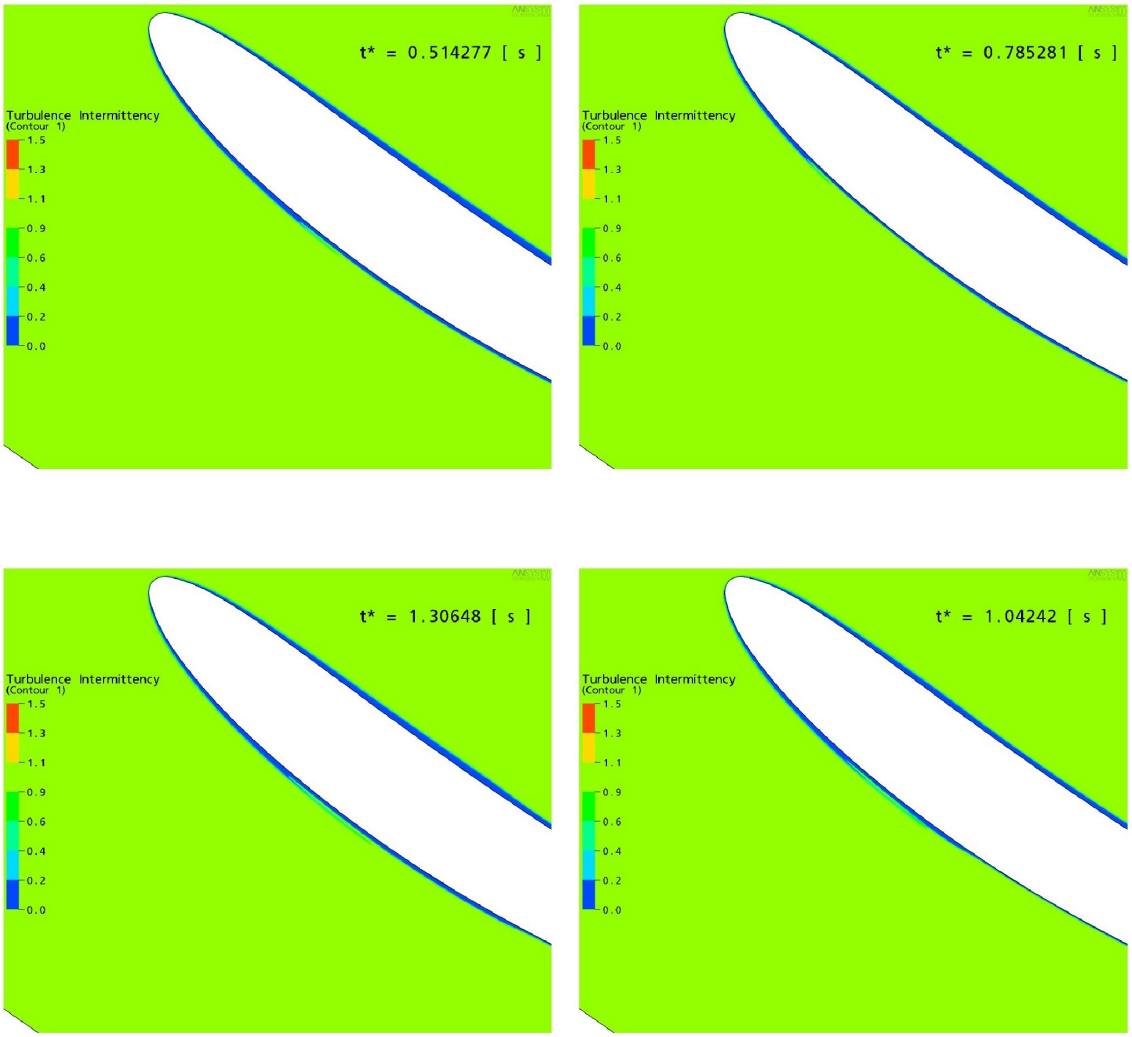

Figure A.58: CFD results for Run 6 - Intermittency in the boundary layer at varying rotor passing time

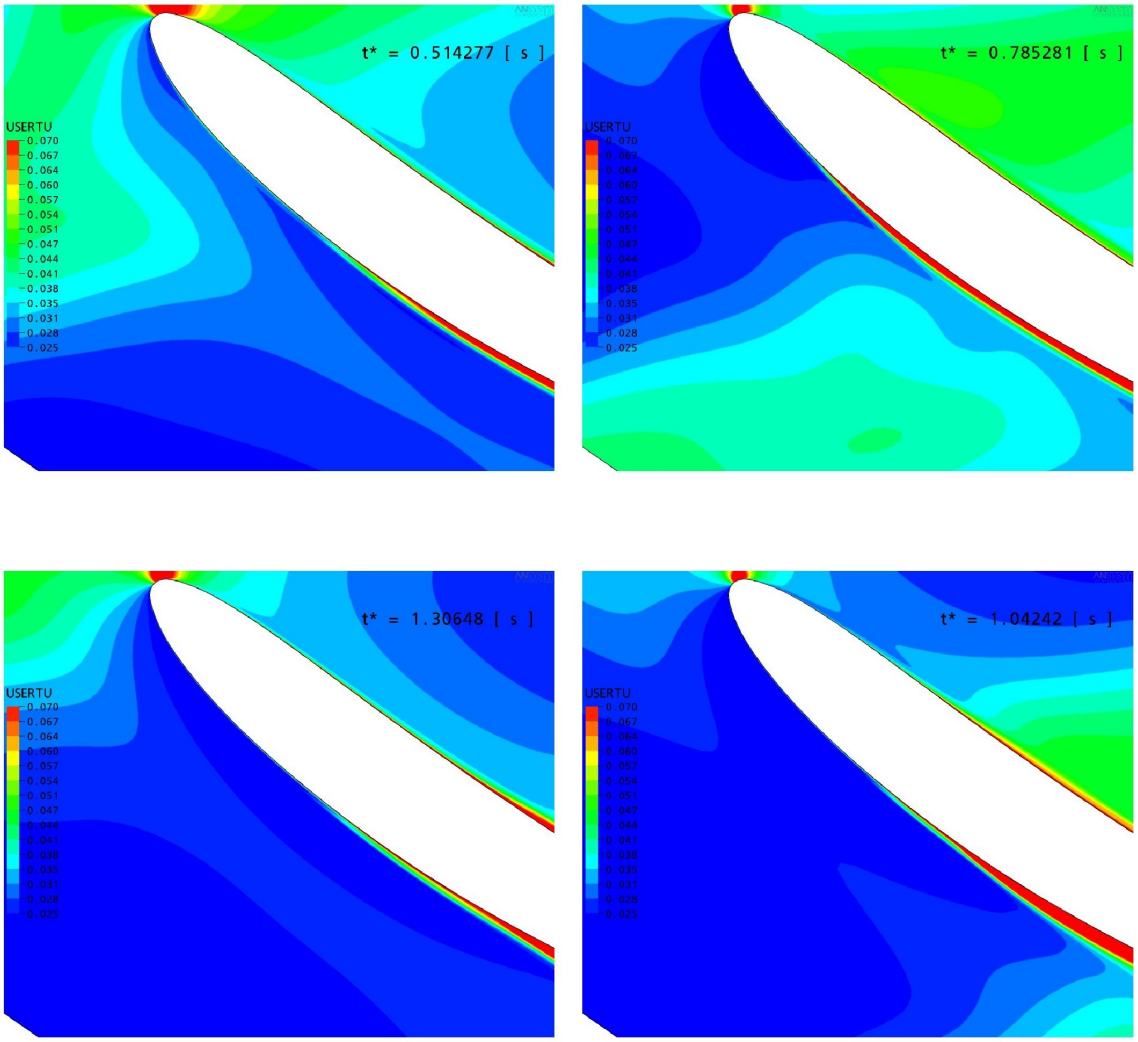

Figure A.59: CFD results for Run 6 - Wake turbulence transport effects on the stator boundary layer at varying rotor passing time

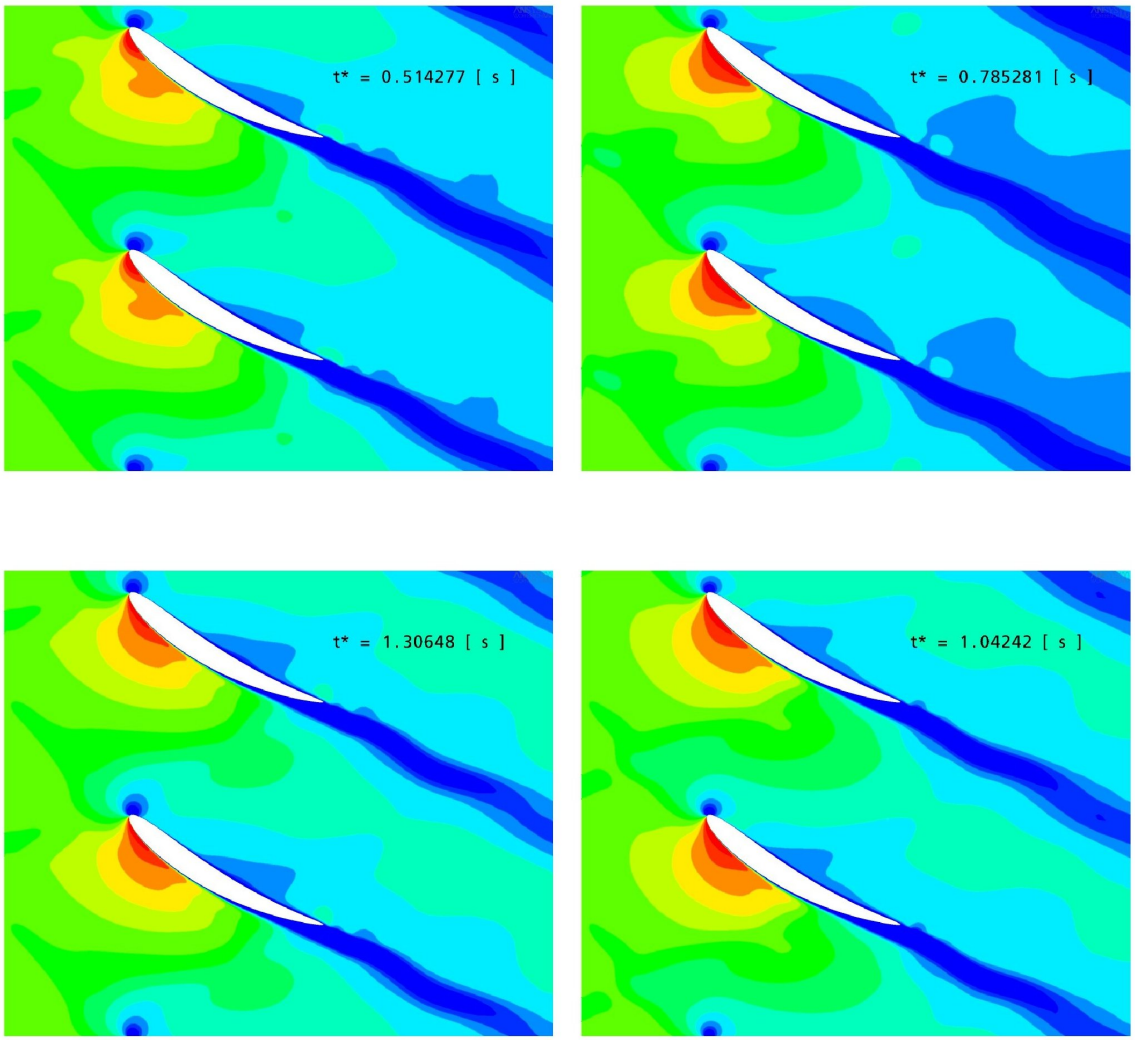

Figure A.60: CFD results for Run 6 - Velocity through passage at varying rotor passing time

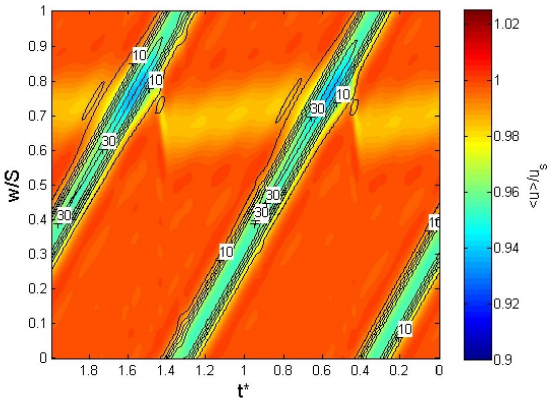

a) Normalised velocity (shading) & Tu (line) at Inlet

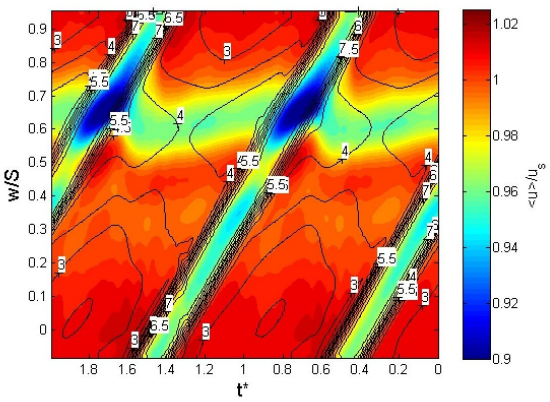

b) Normalised velocity (shading) & Tu (line) at 42.7%c upstream of stator leading edge

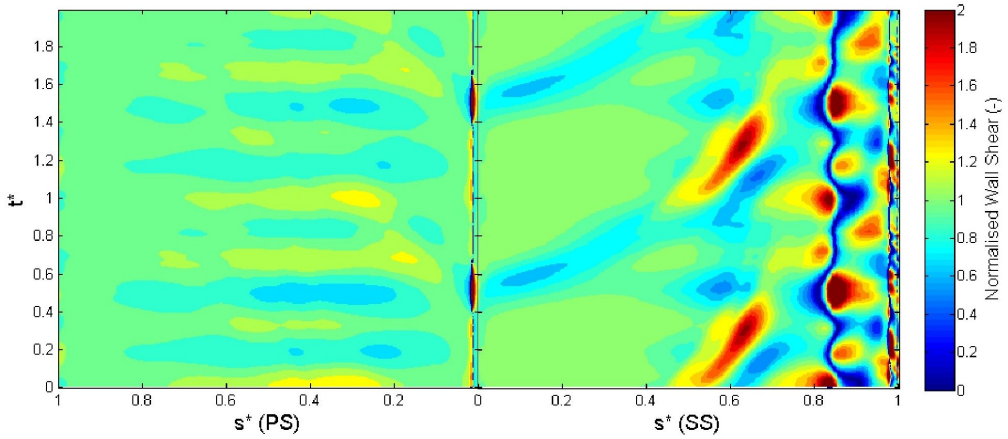

c) Normalised wall shear stress on blade surface

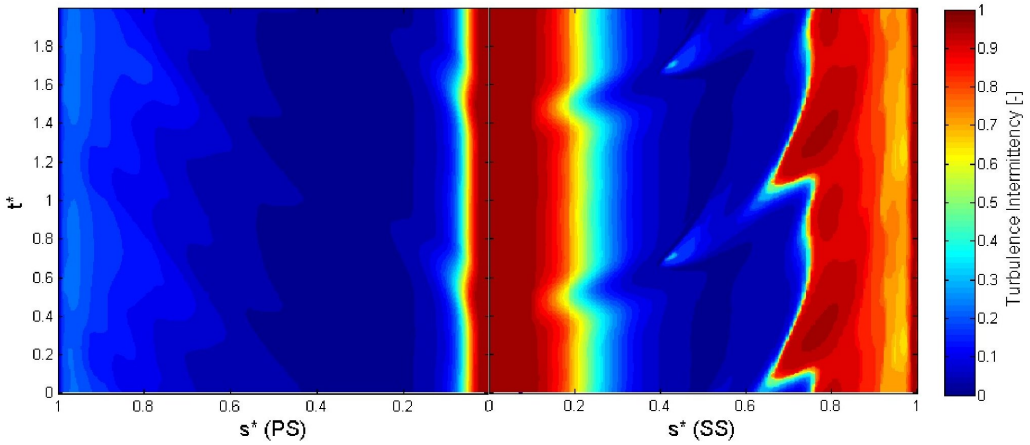

d) Turbulence intermittency at 0.2 mm from blade surface

Figure A.61: CFD results for Run 7

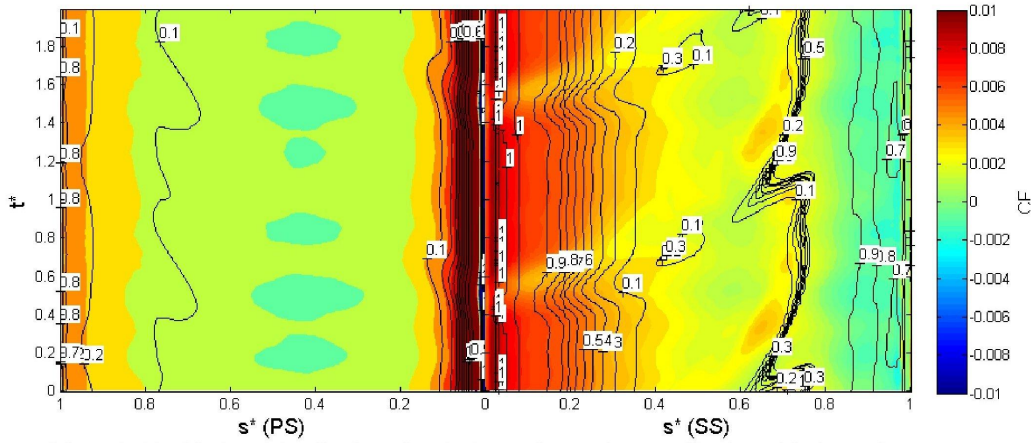

a) Local skin friction (shading) and turbulence intermittency (line) on blade surface

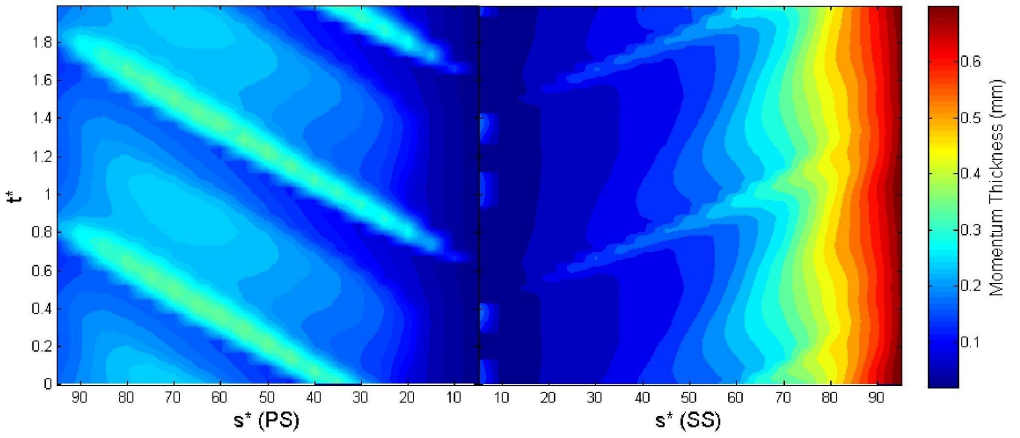

b) Momentum thickness on blade surface

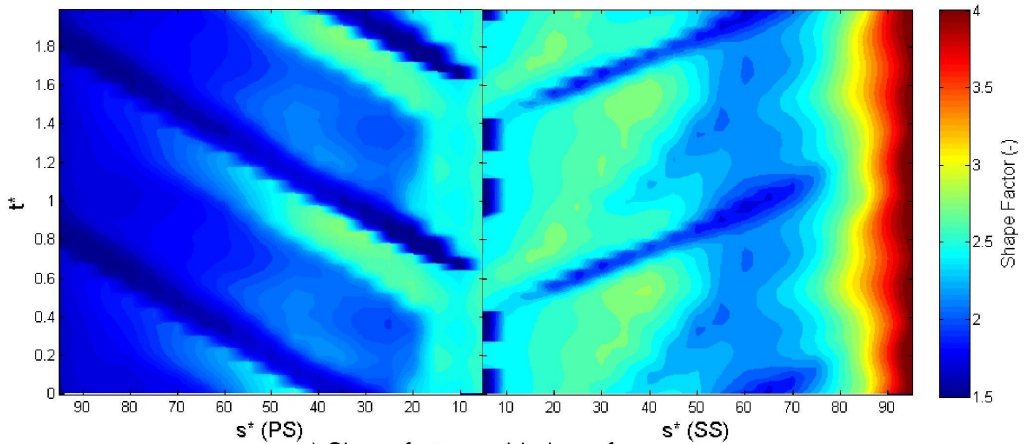

c) Shape factor on blade surface

Figure A.62: CFD results for Run 7

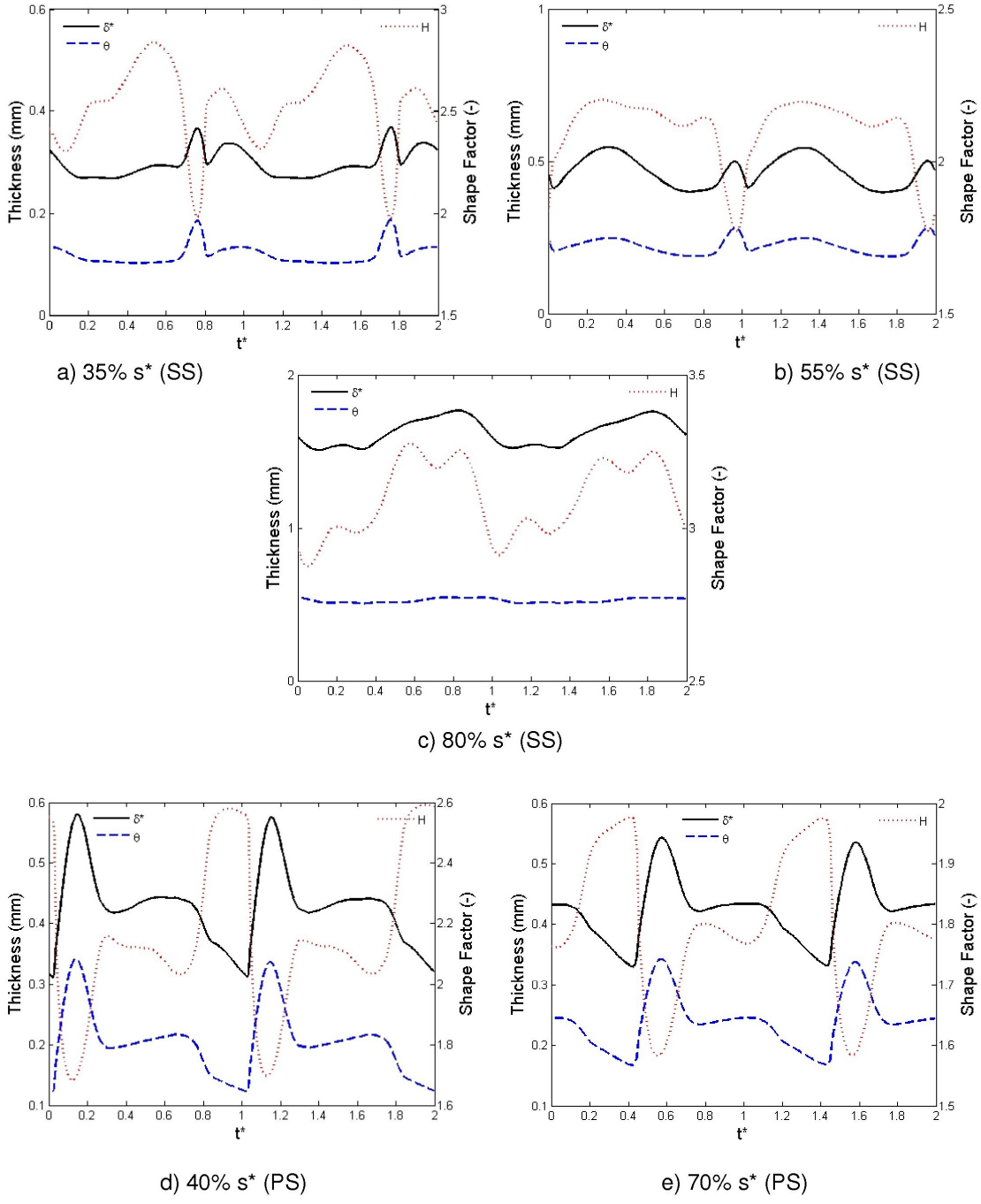

Figure A.63: CFD results for Run 7 - Integral parameters at various distances along suction (SS) and pressure (PS) surfaces

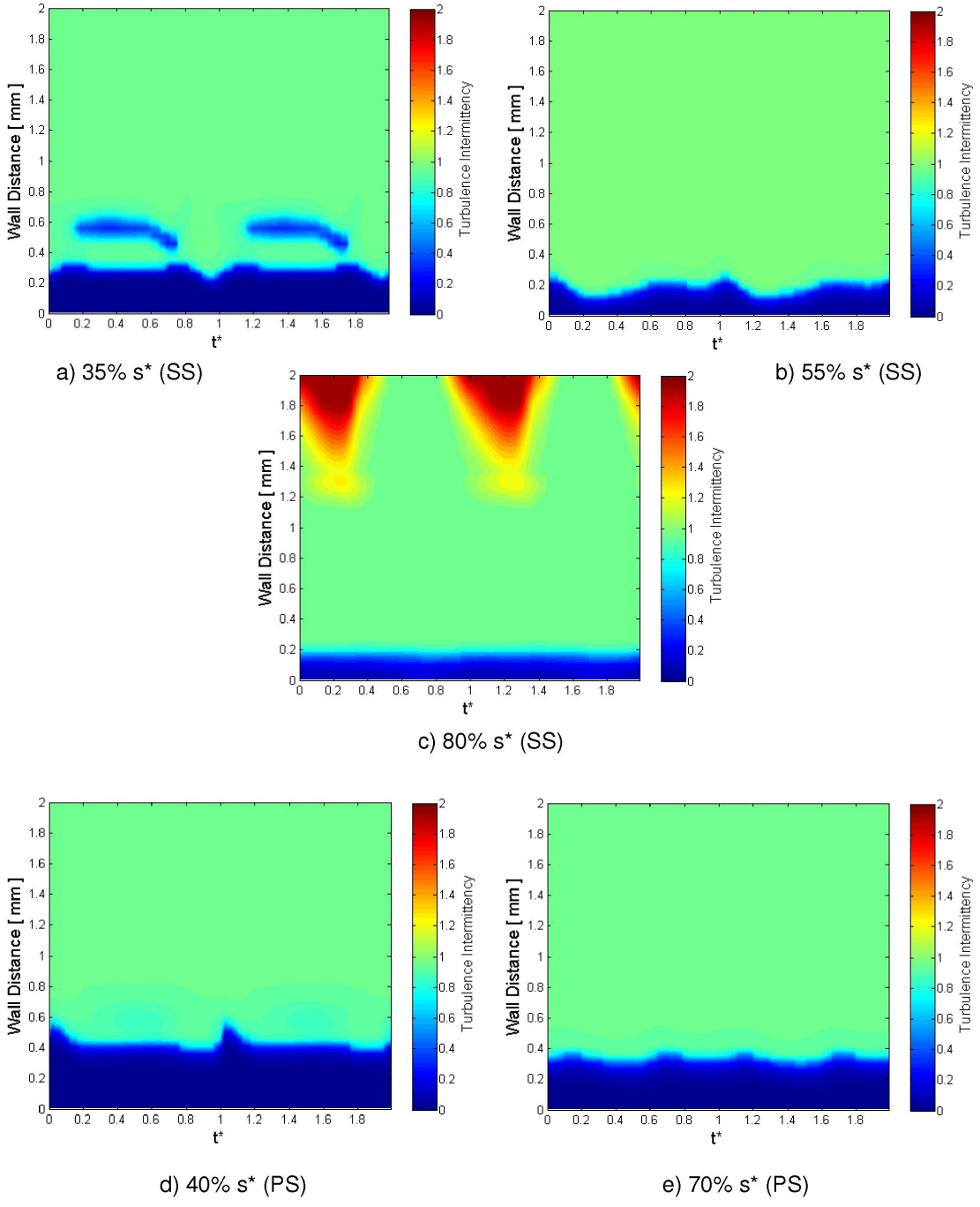

Figure A.64: CFD results for Run 7 - Intermittency at various distances along suction (SS) and pressure (PS) surfaces

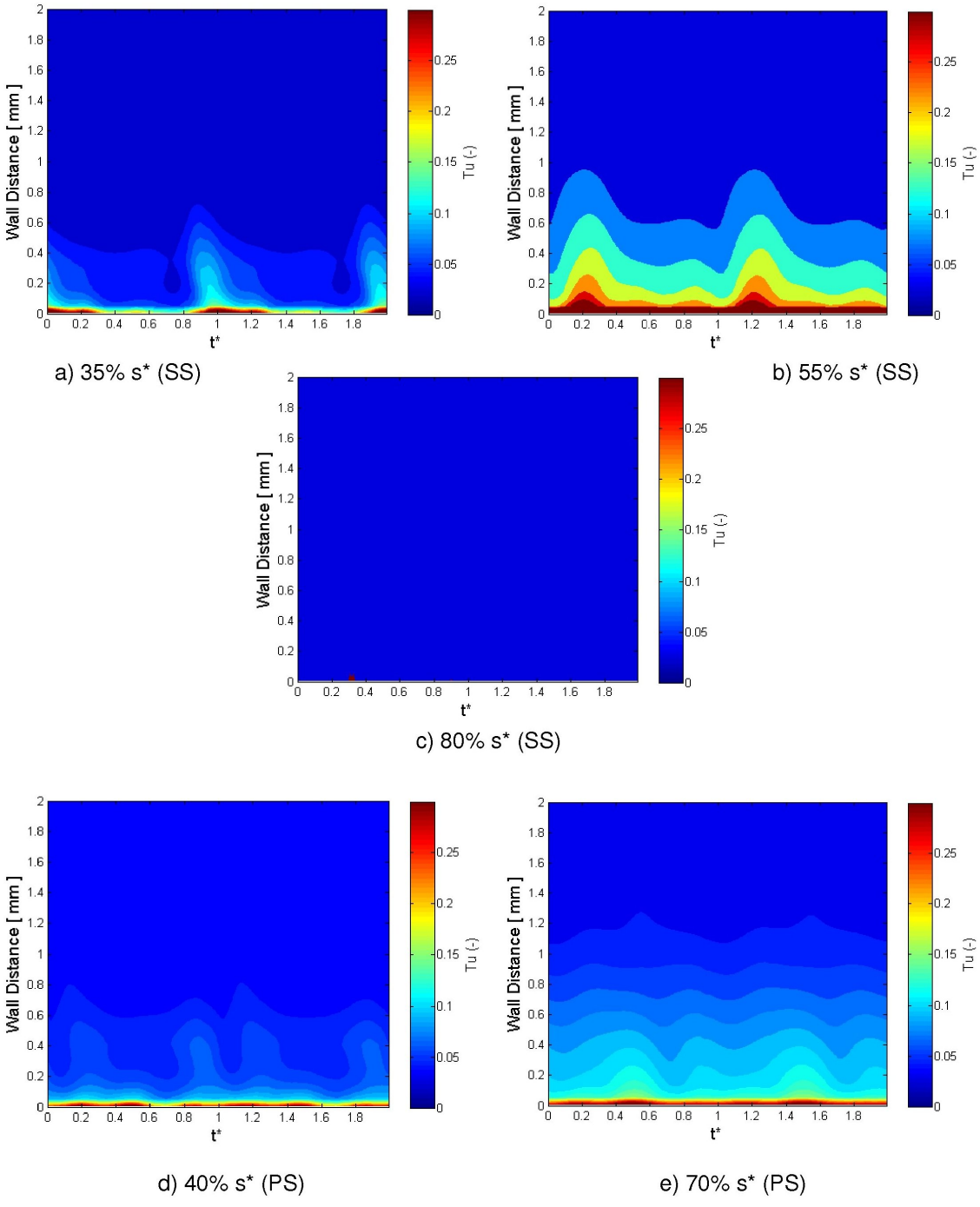

Figure A.65: CFD results for Run 7 - Turbulence intensity at various distances along suction (SS) and pressure (PS) surfaces

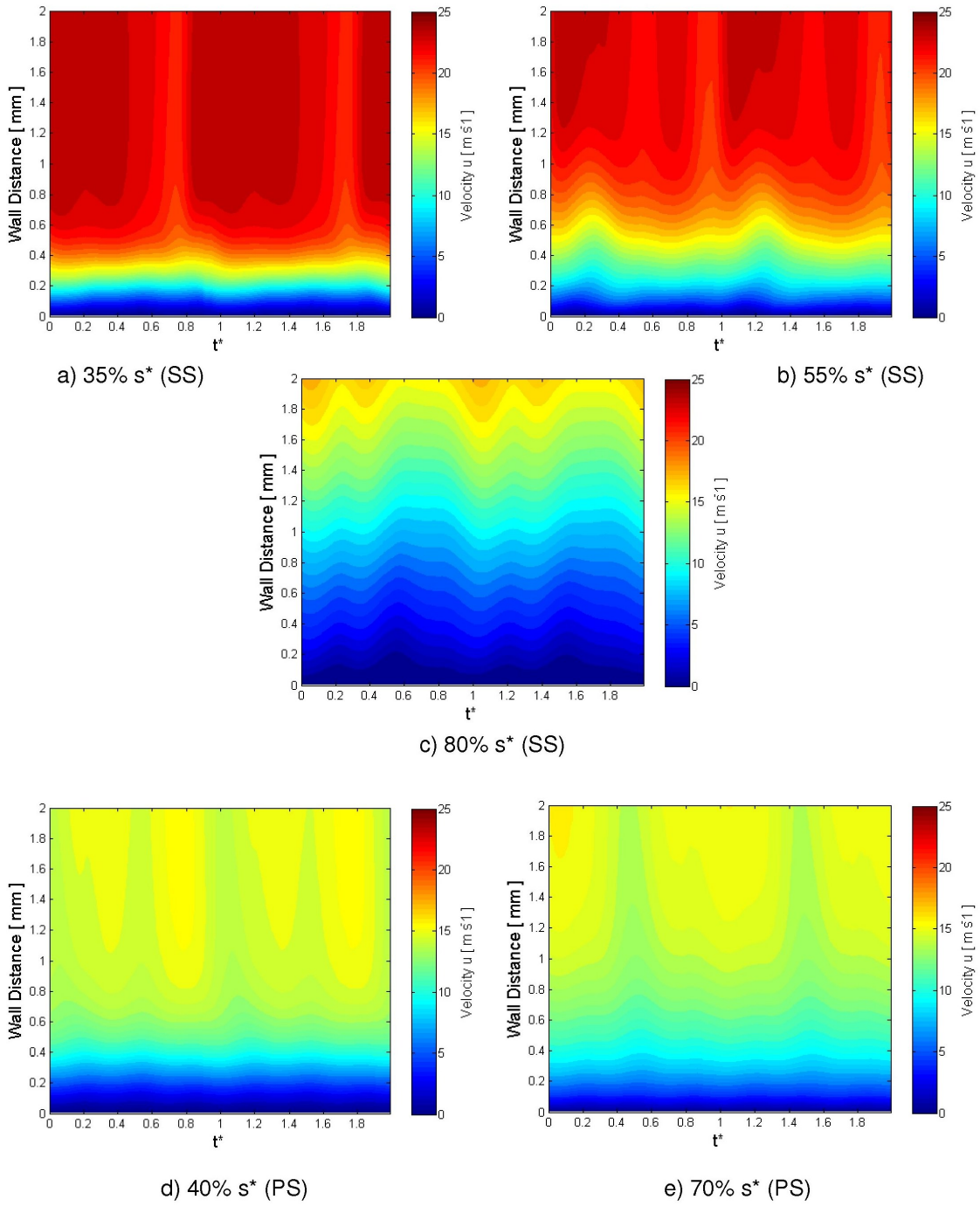

Figure A.66: CFD results for Run 7 - Tangential velocity at various distances along suction (SS) and pressure (PS) surfaces

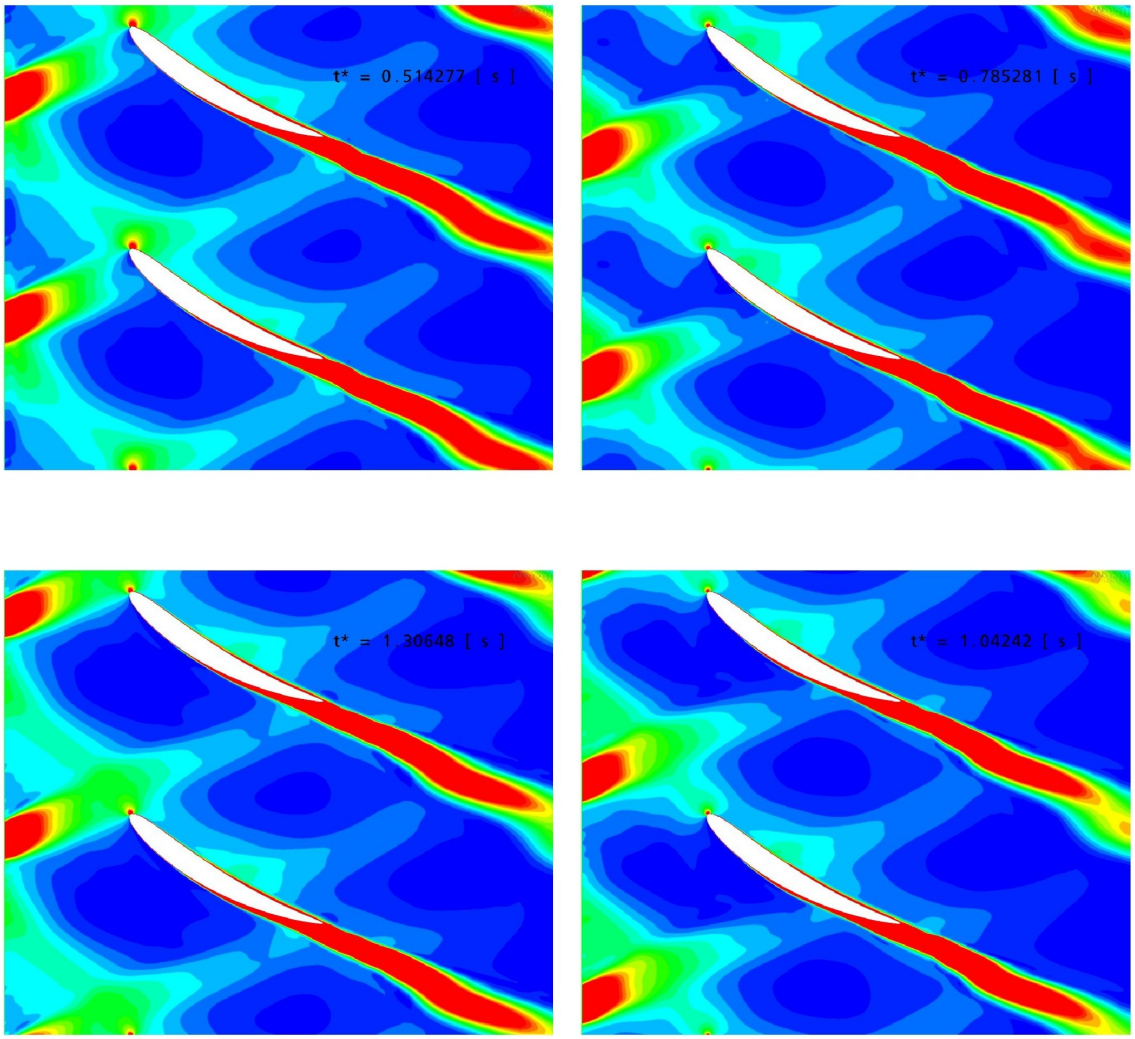

Figure A.67: CFD results for Run 7 - Wake turbulence transport through the domain at varying rotor passing time

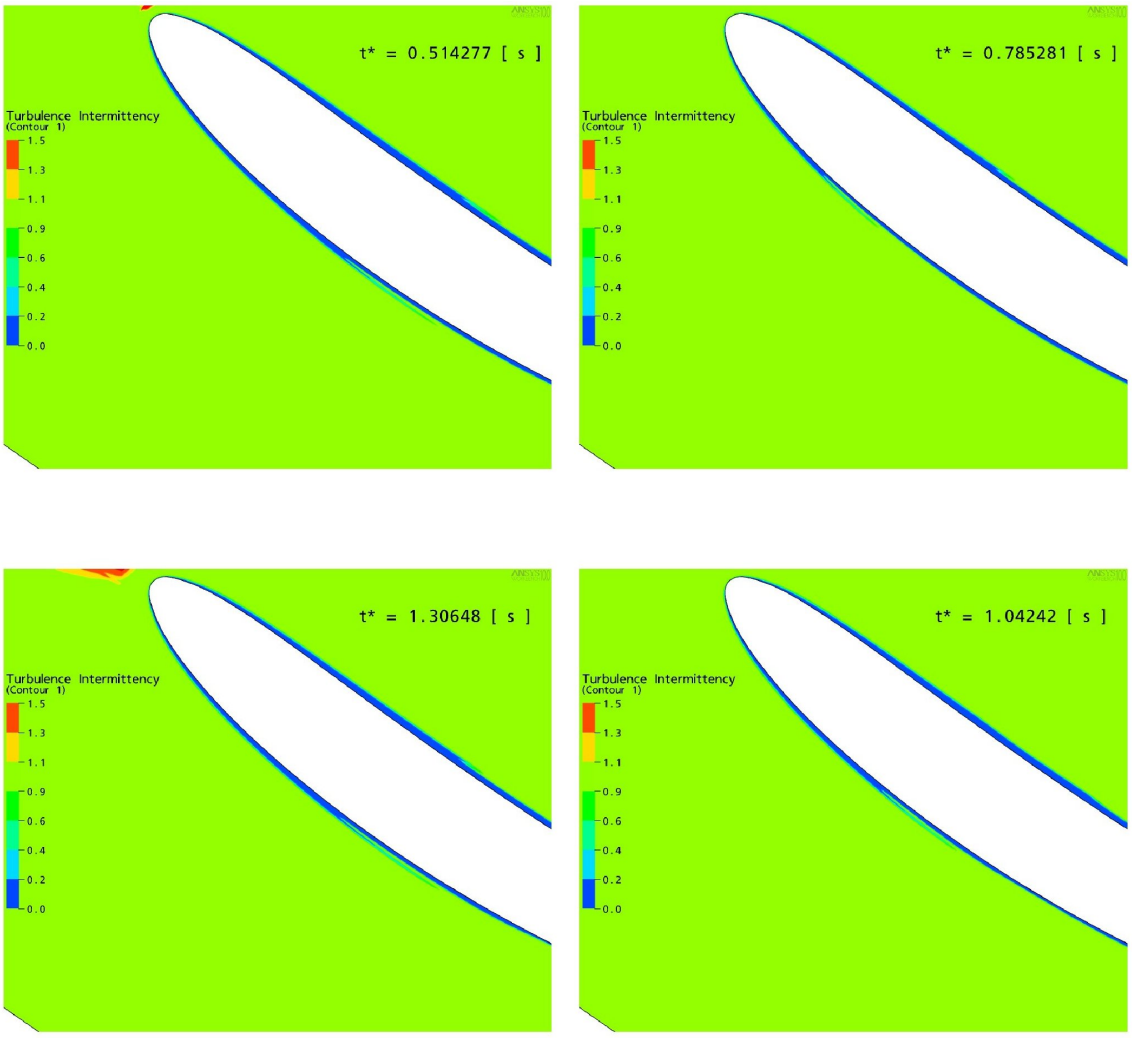

Figure A.68: CFD results for Run 7 - Intermittency in the boundary layer at varying rotor passing time

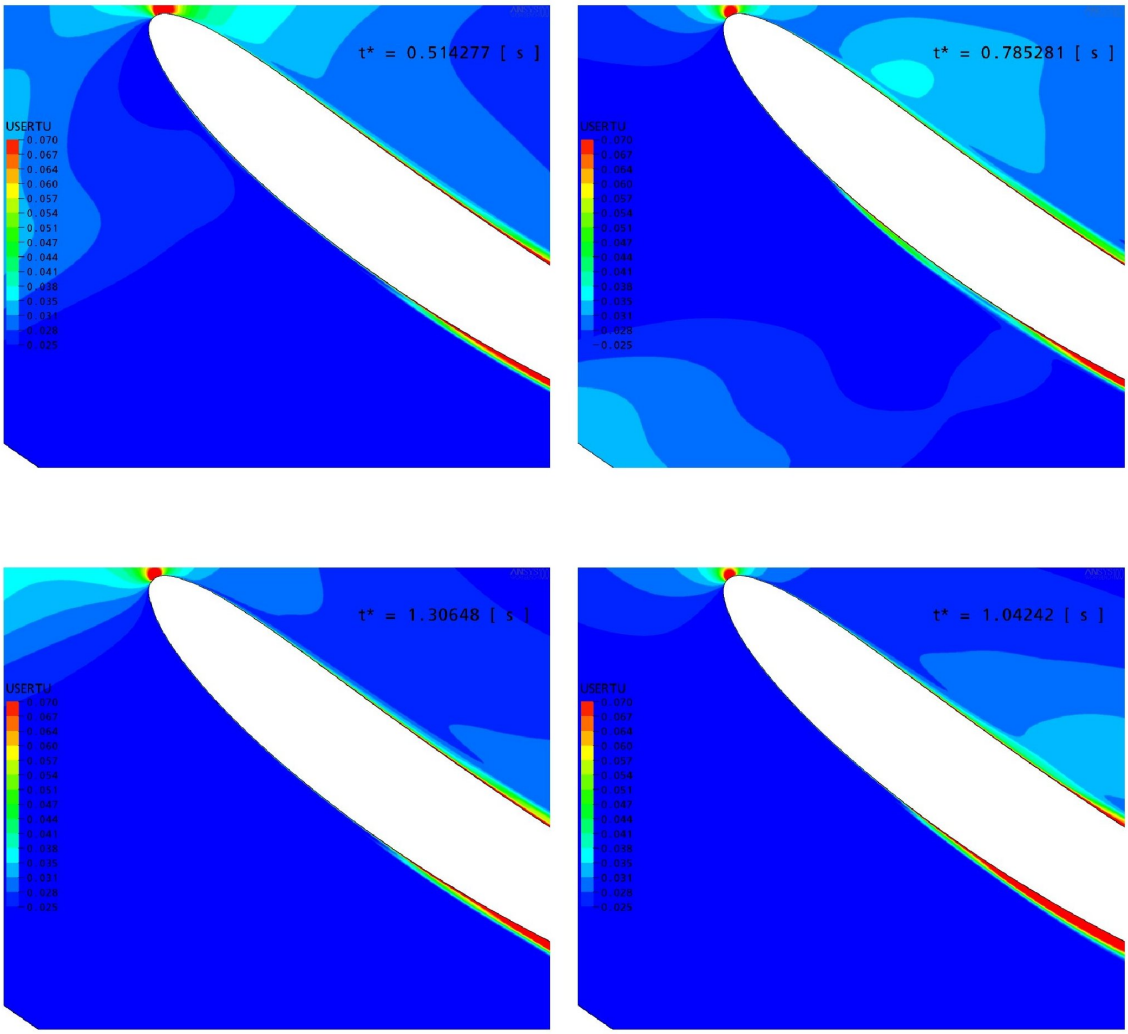

Figure A.69: CFD results for Run 7 - Wake turbulence transport effects on the stator boundary layer at varying rotor passing time

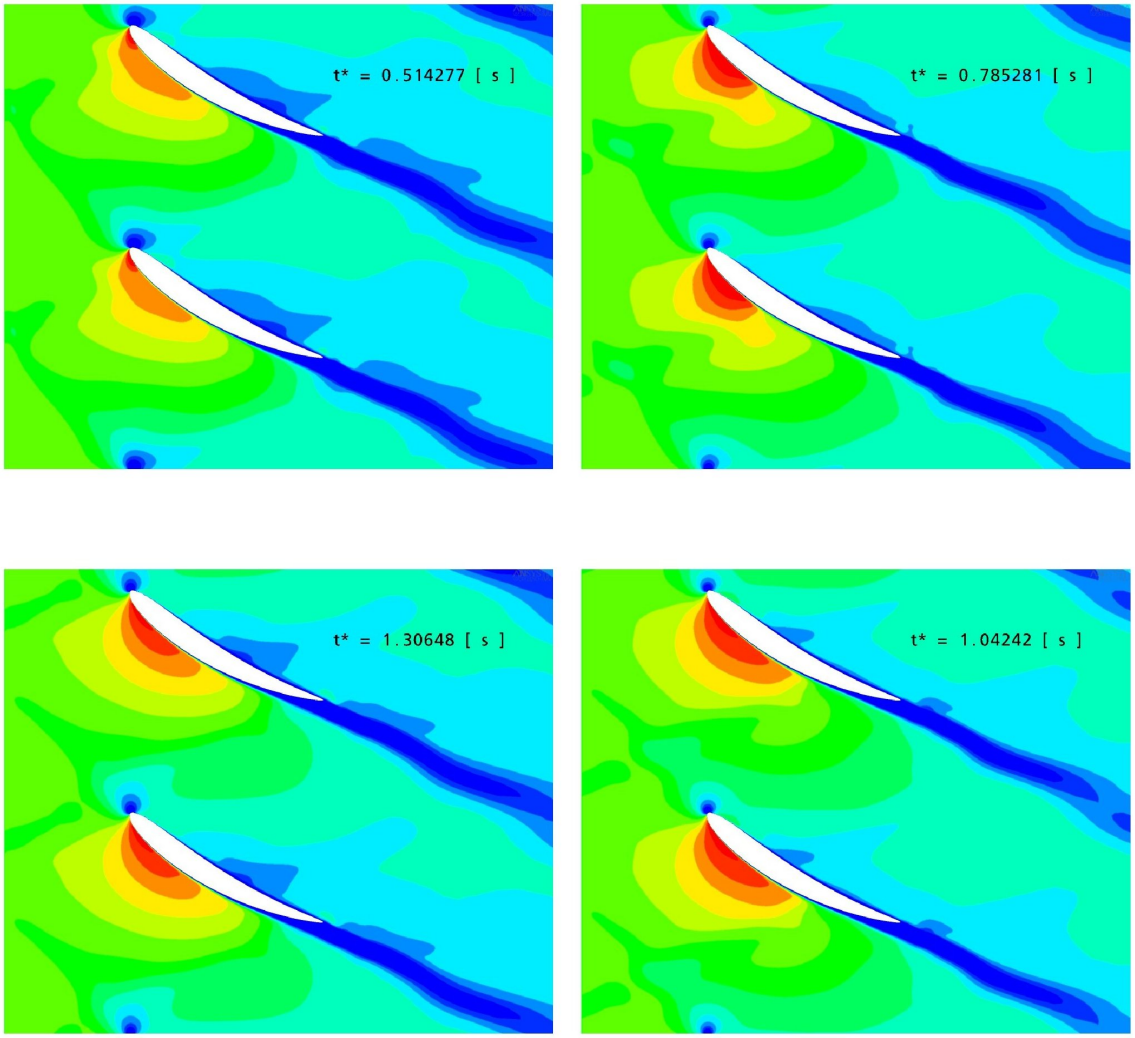

Figure A.70: CFD results for Run 7 - Velocity through passage at varying rotor passing time

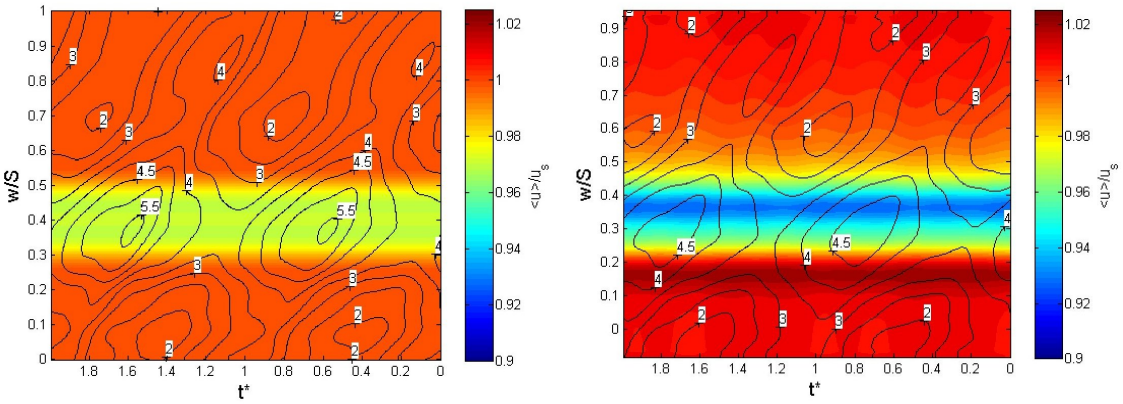

a) Normalised velocity (shading) & Tu (line) at Inlet

b) Normalised velocity (shading) & Tu (line) at 42.7%c upstream of stator leading edge

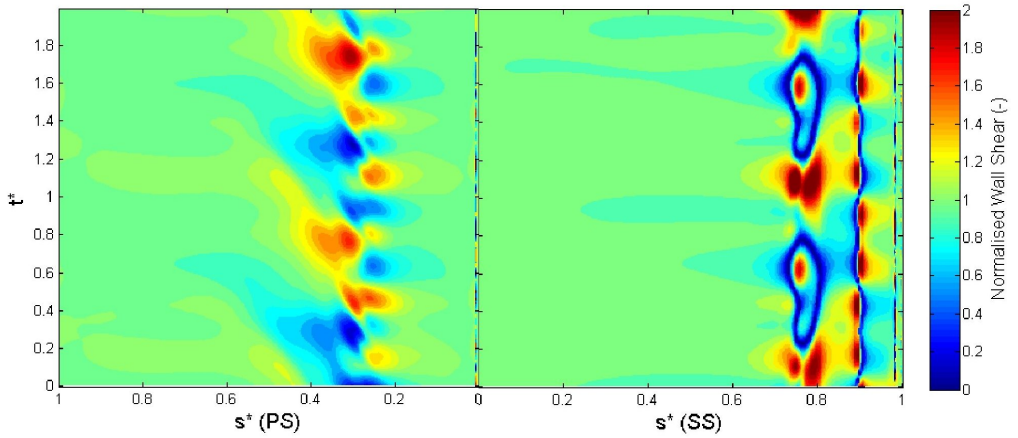

c) Normalised wall shear stress on blade surface

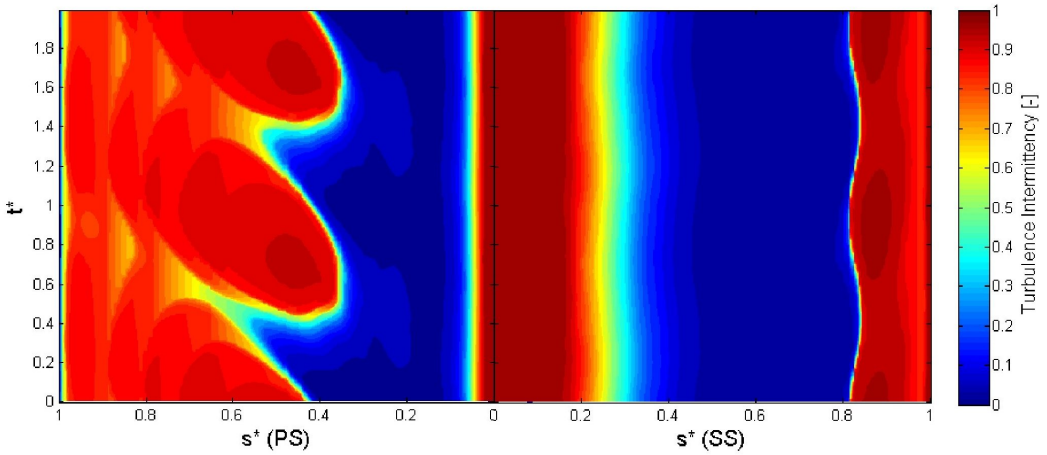

d) Turbulence intermittency at 0.2 mm from blade surface

Figure A.71: CFD results for low loading case

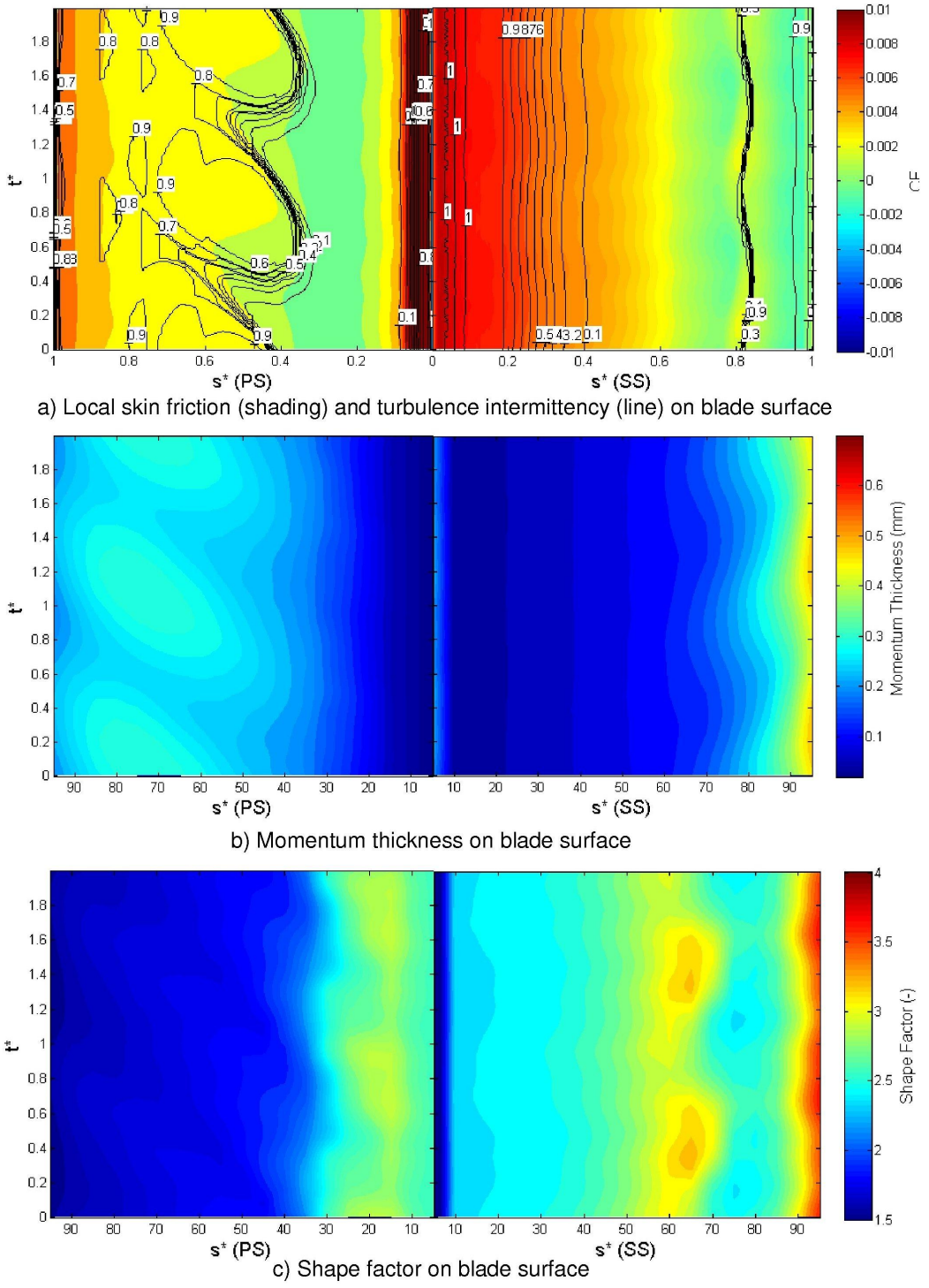

a) Local skin friction (shading) and turbulence intermittency (line) on blade surface

b) Momentum thickness on blade surface

c) Shape factor on blade surface

Figure A.72: CFD results for low loading case

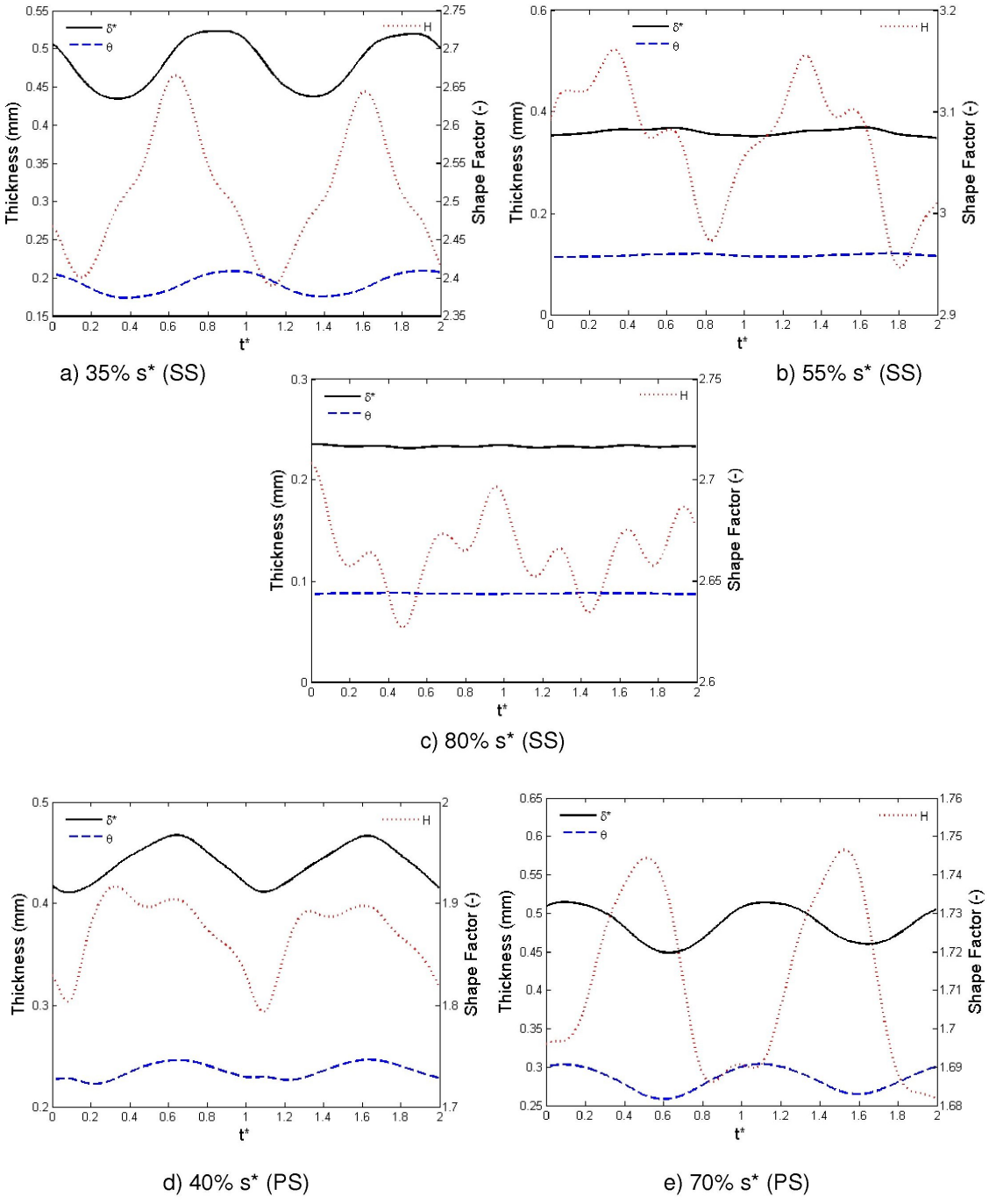

Figure A.73: CFD results for low loading case - Integral parameters at various distances along suction (SS) and pressure (PS) surfaces

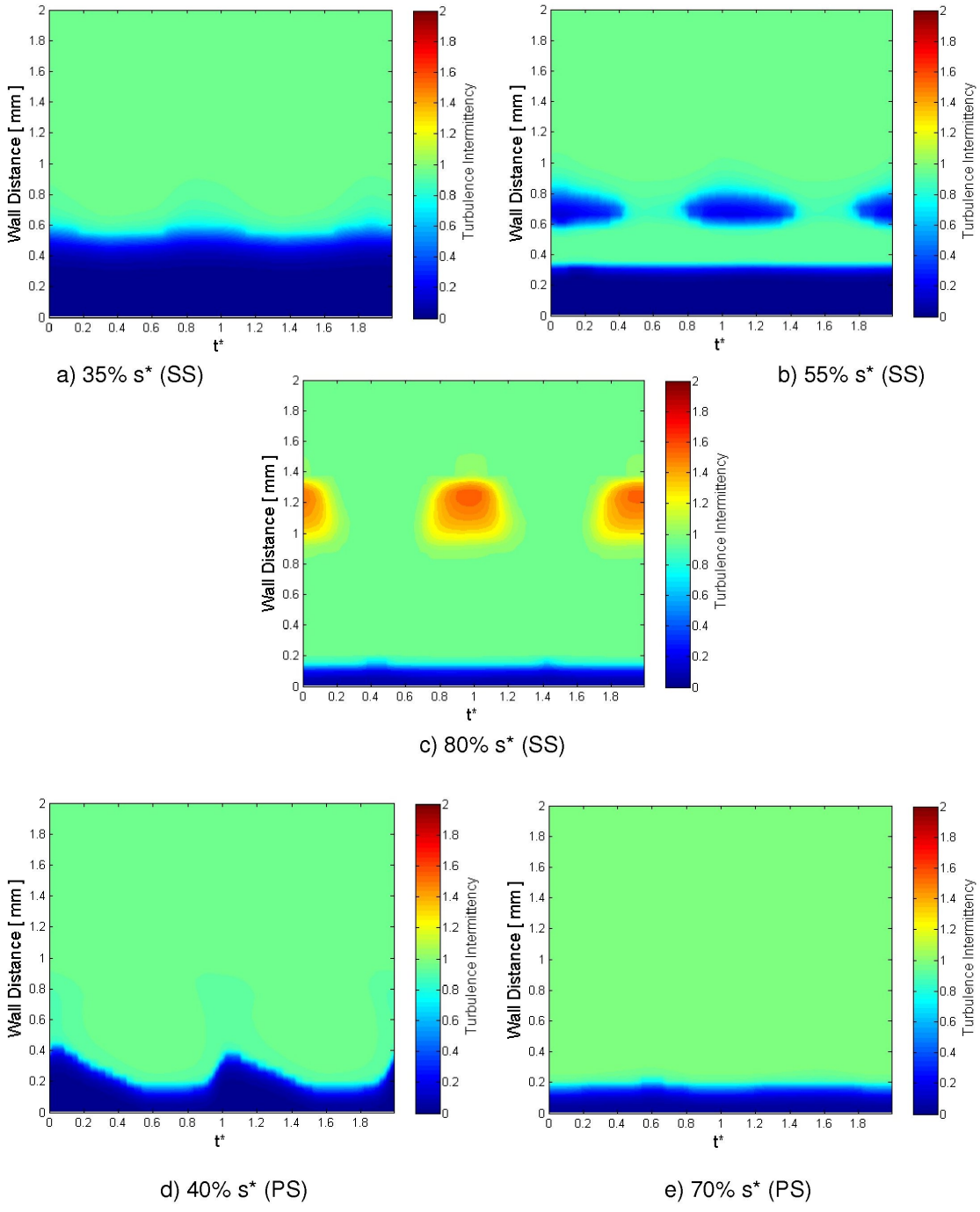

Figure A.74: CFD results for low loading case - Intermittency at various distances along suction (SS) and pressure (PS) surfaces

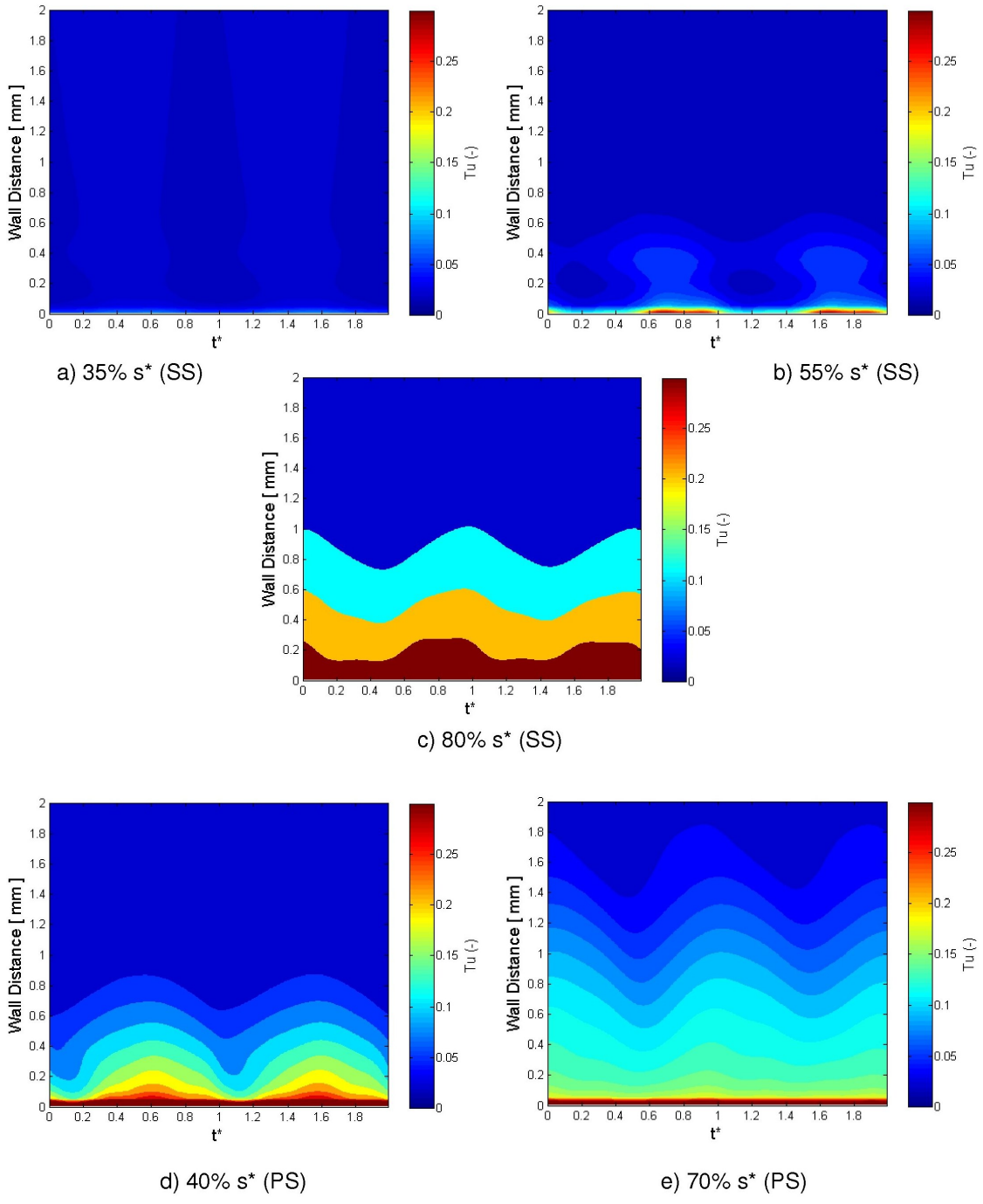

Figure A.75: CFD results for low loading case - Turbulence intensity at various distances along suction (SS) and pressure (PS) surfaces

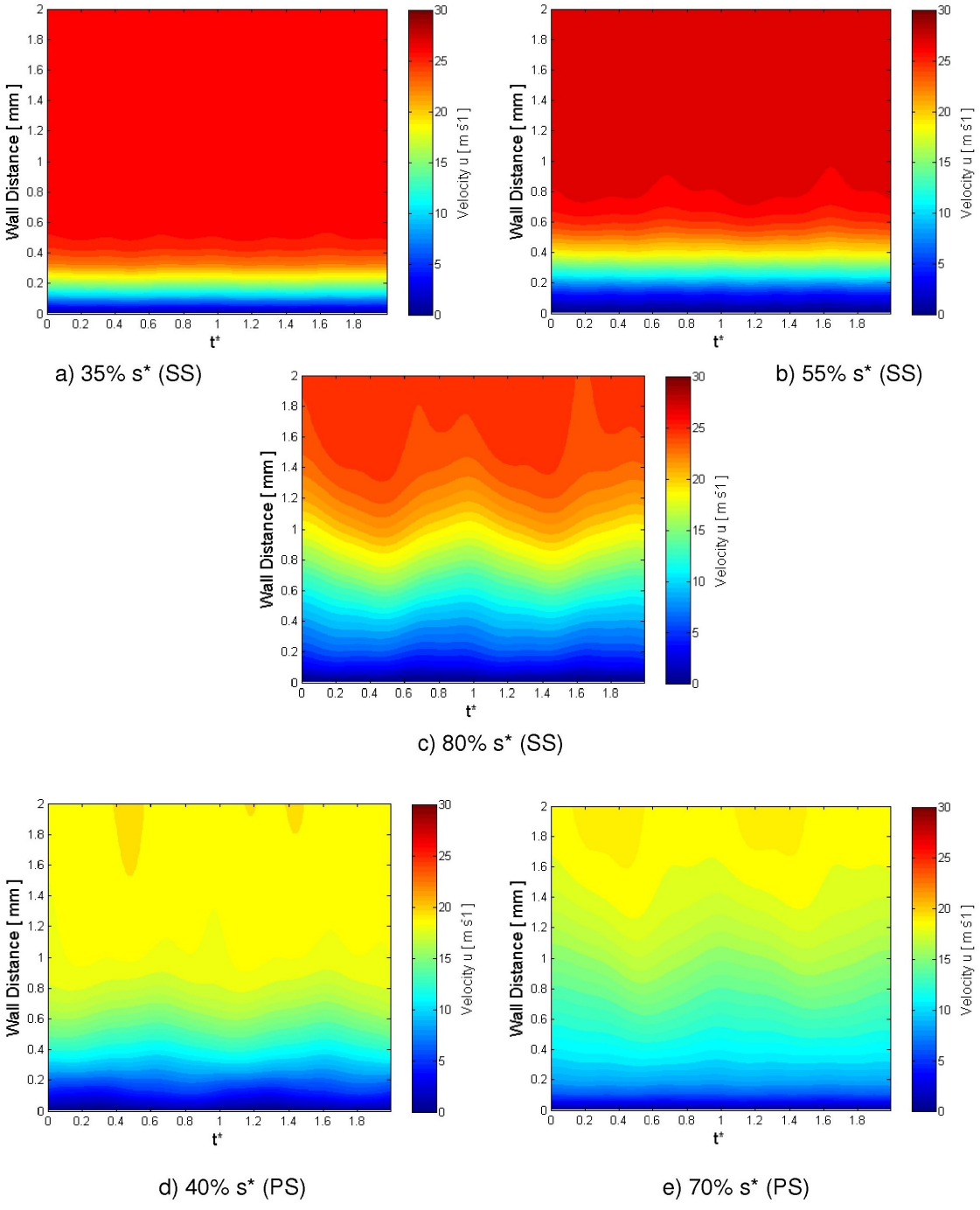

Figure A.76: CFD results for low loading case - Tangential velocity at various distances along suction (SS) and pressure (PS) surfaces

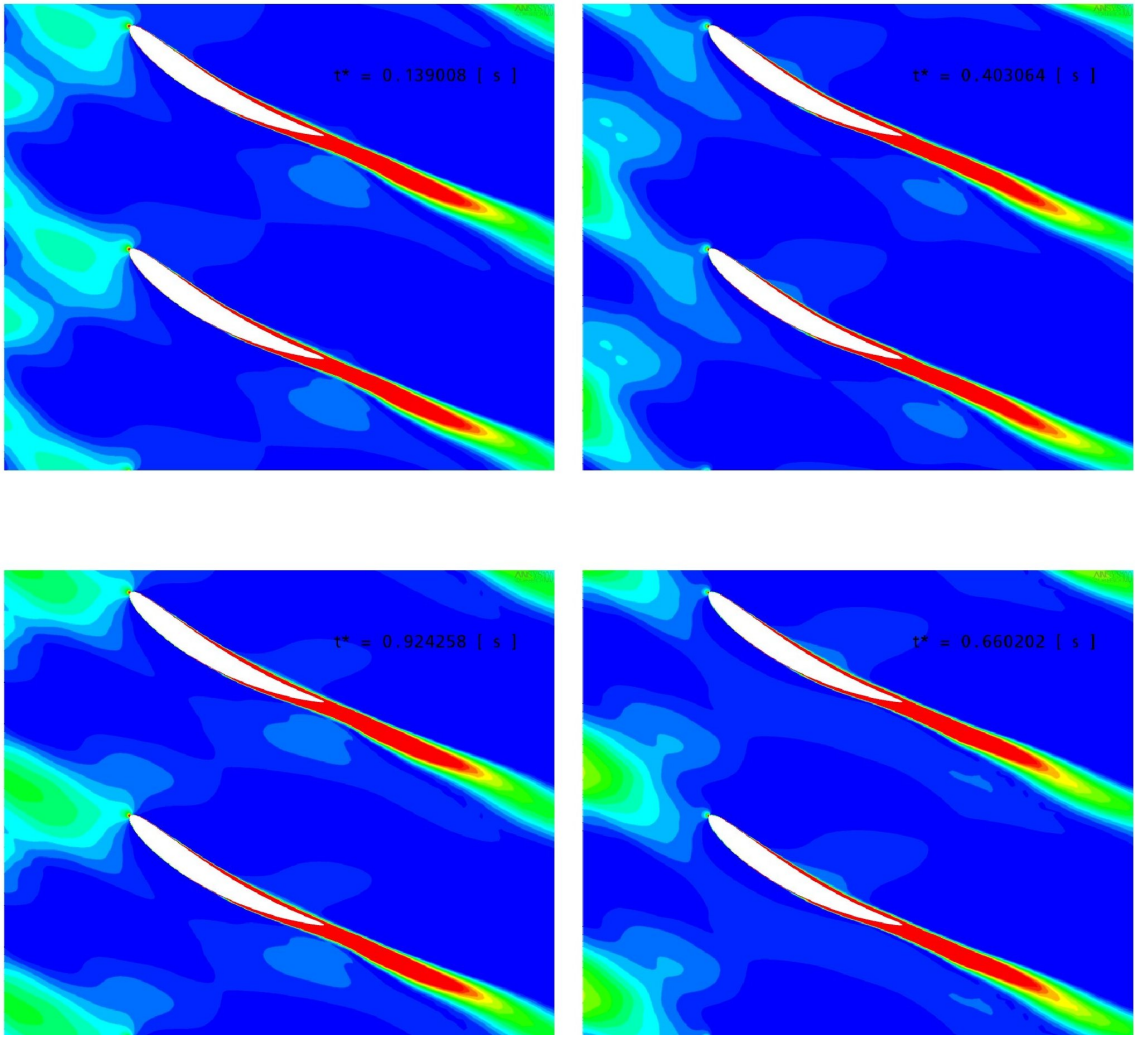

Figure A.77: CFD results for low loading case - Wake turbulence transport through the domain at varying rotor passing time

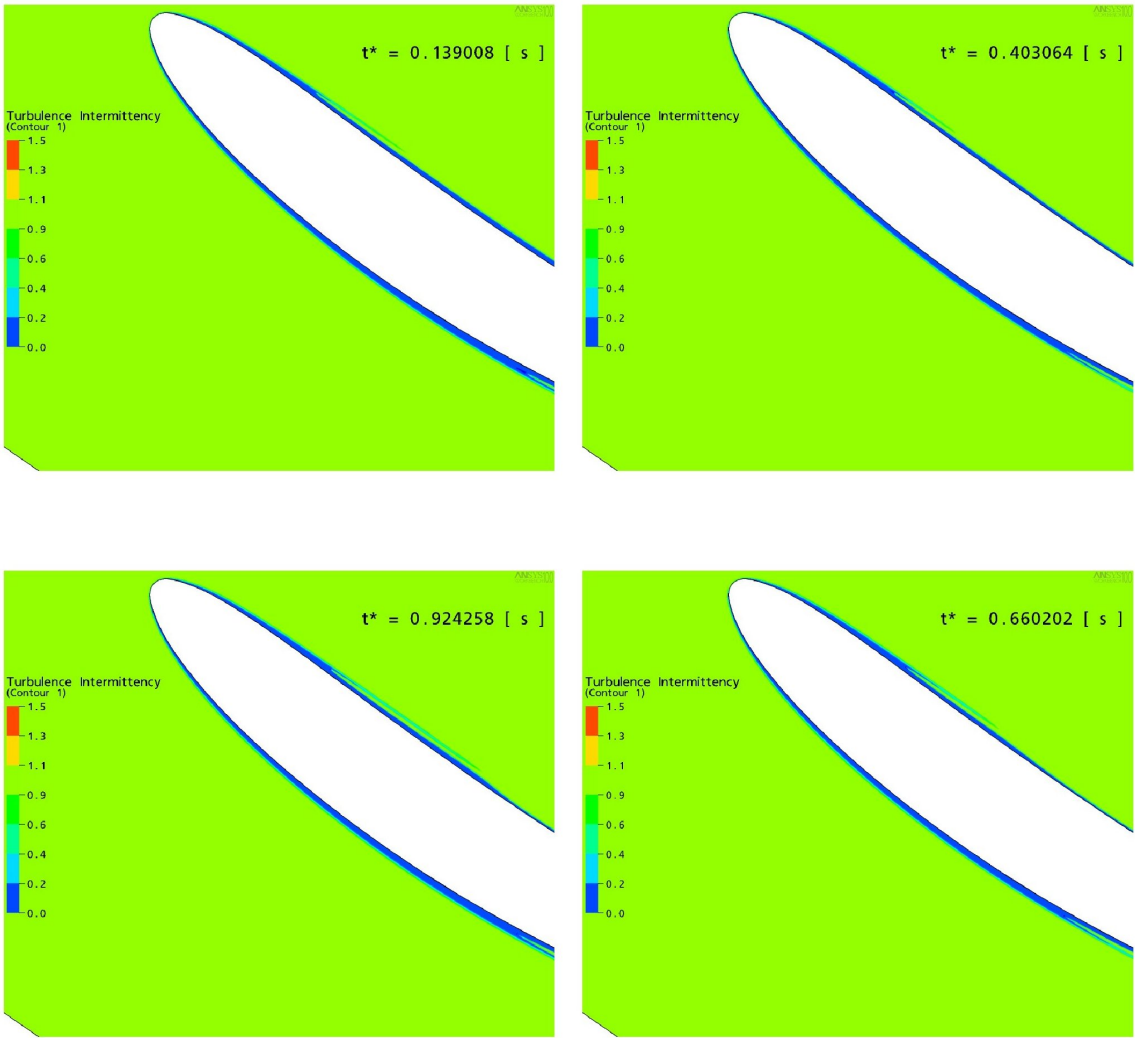

Figure A.78: CFD results for low loading case - Intermittency in the boundary layer at varying rotor passing time

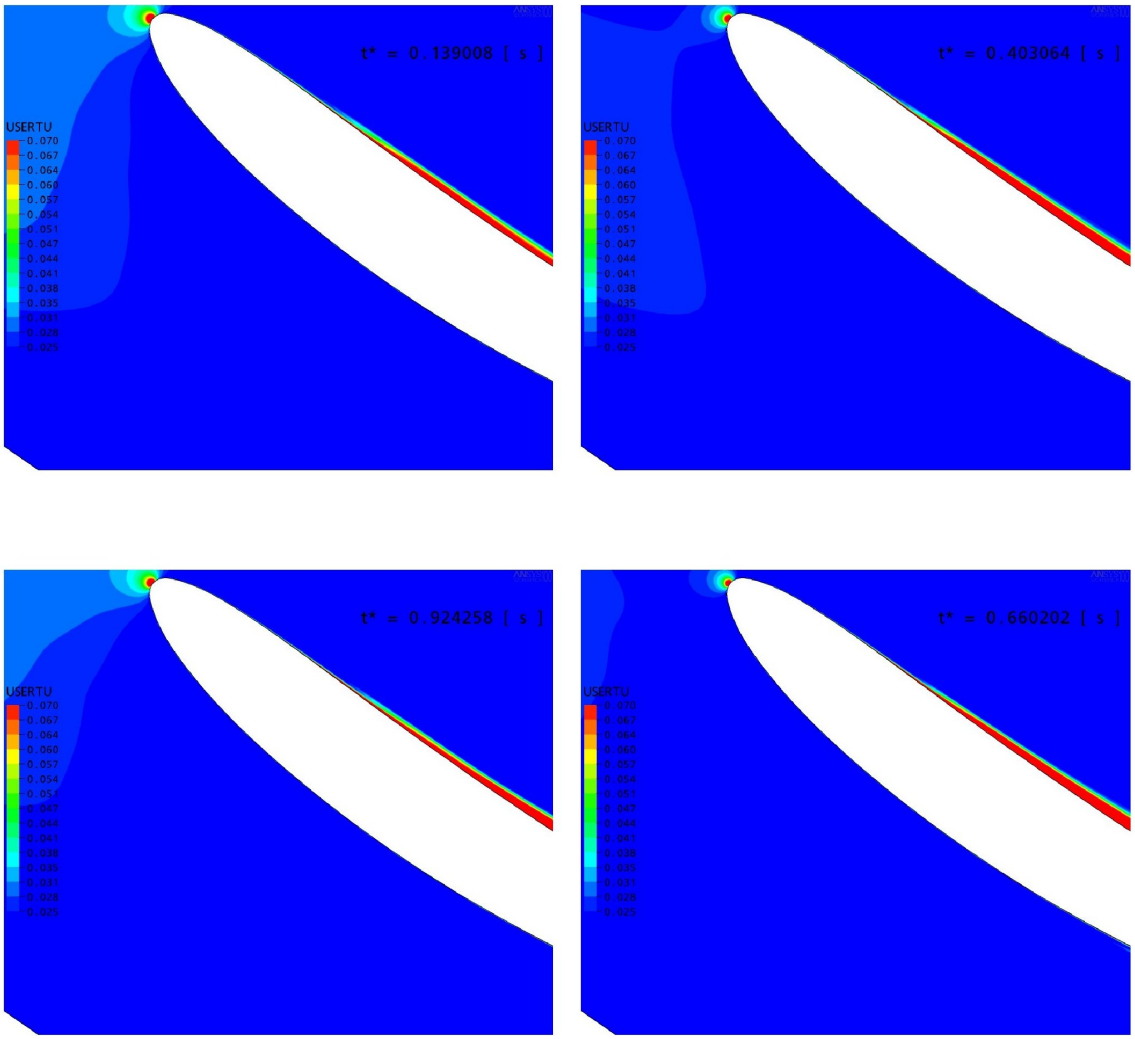

Figure A.79: CFD results for low loading case - Wake turbulence transport effects on the stator boundary layer at varying rotor passing time

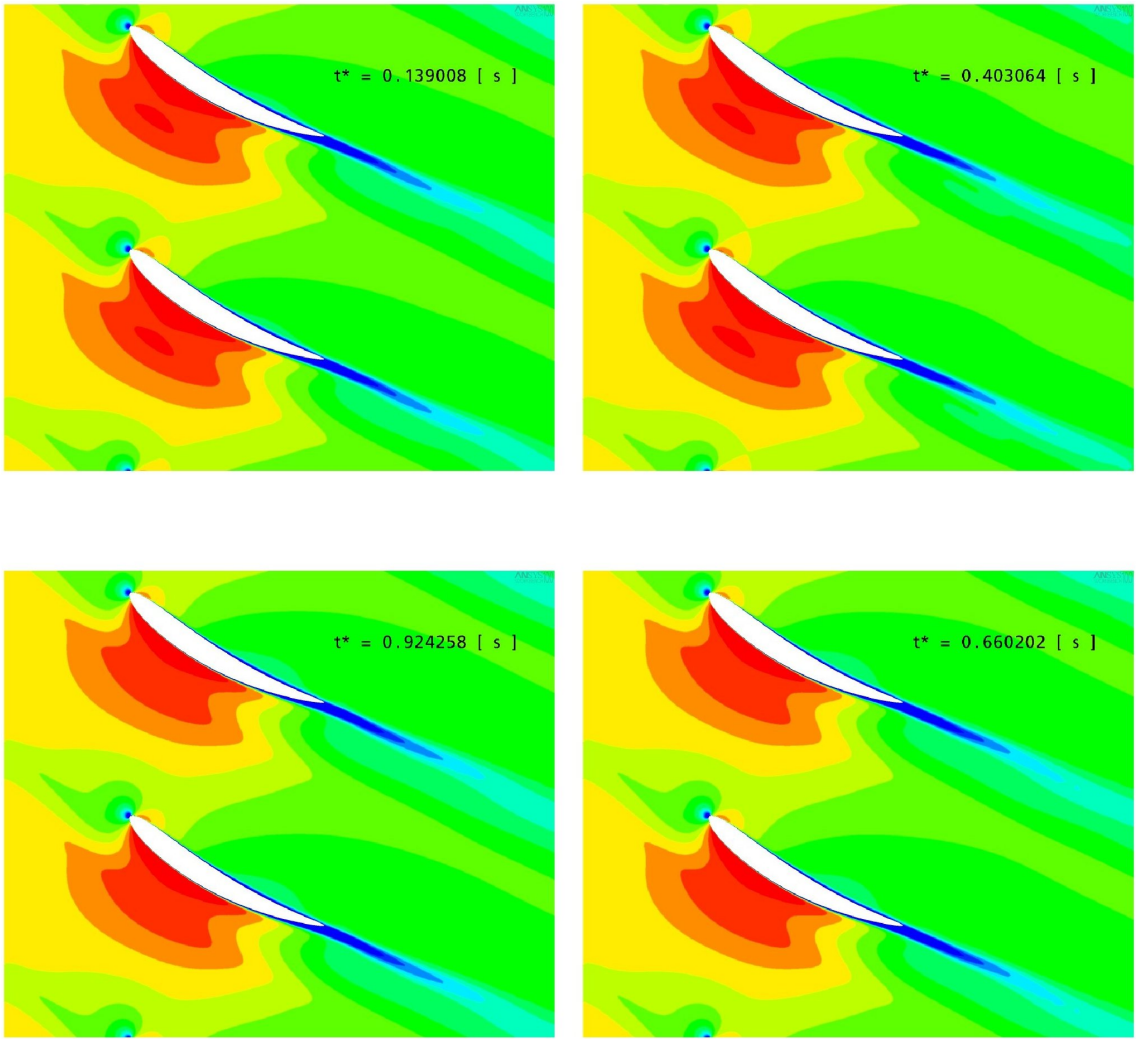

Figure A.80: CFD results for low loading case - Velocity through passage at varying rotor passing time

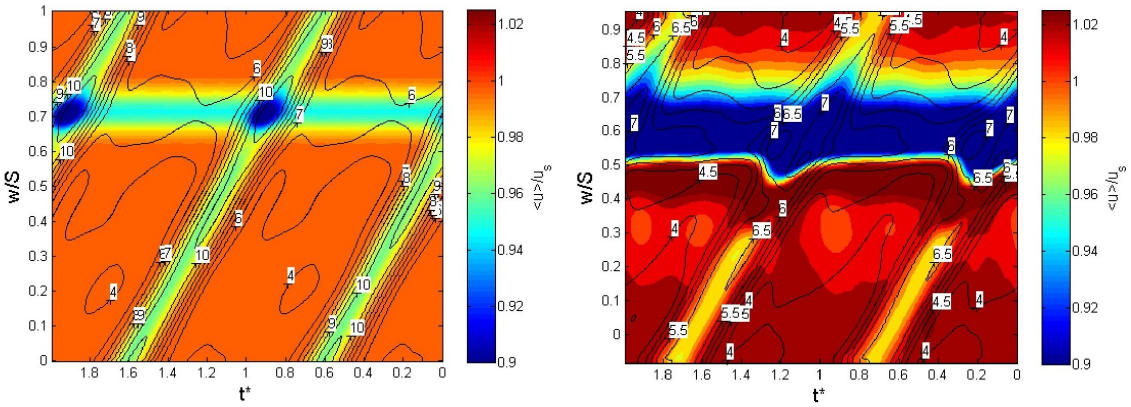

a) Normalised velocity (shading) & Tu (line) at Inlet

b) Normalised velocity (shading) & Tu (line) at 42.7%c upstream of stator leading edge

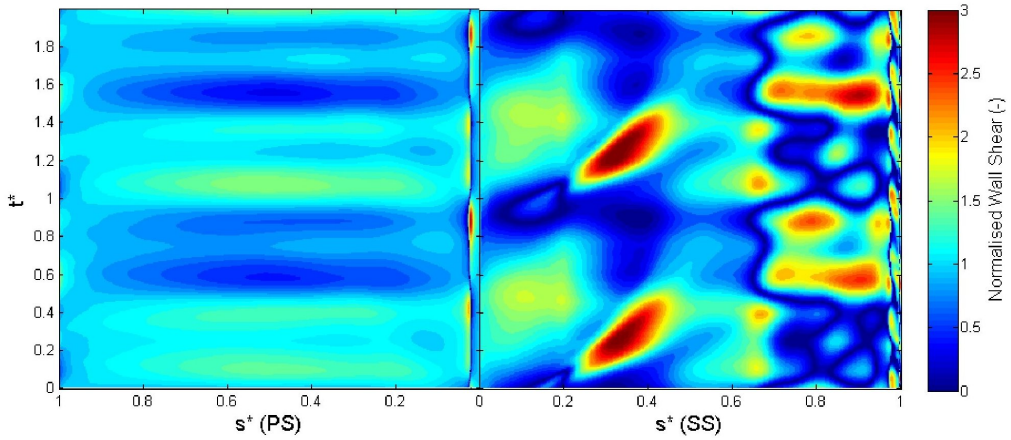

c) Normalised wall shear stress on blade surface

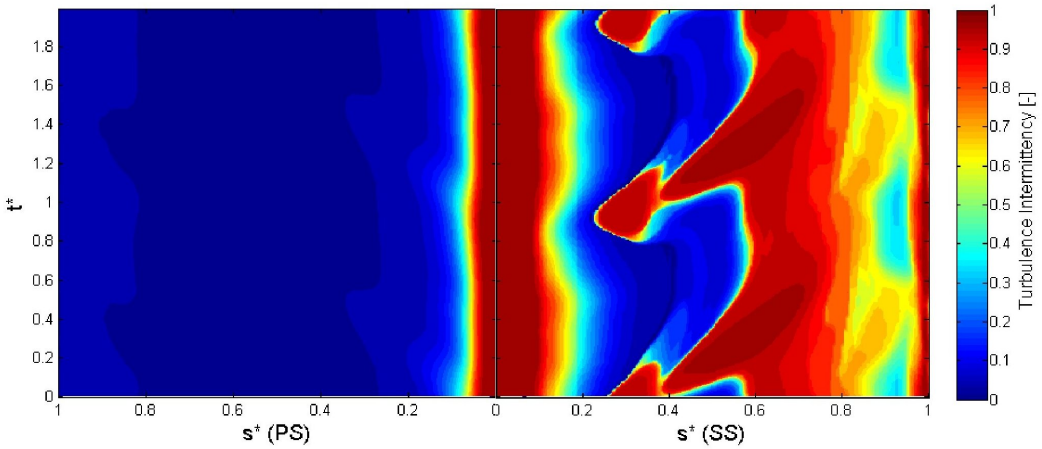

d) Turbulence intermittency at 0.2 mm from blade surface

Figure A.81: CFD results for high loading case

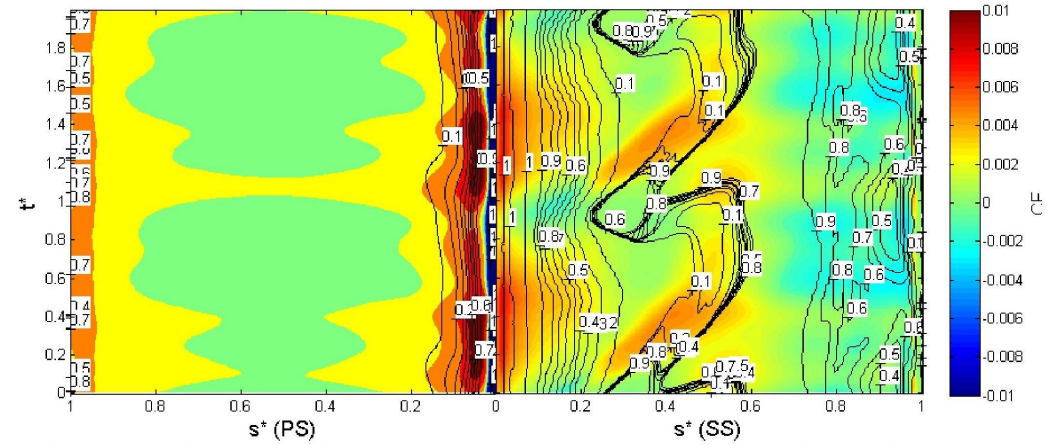

a) Local skin friction (shading) and turbulence intermittency (line) on blade surface

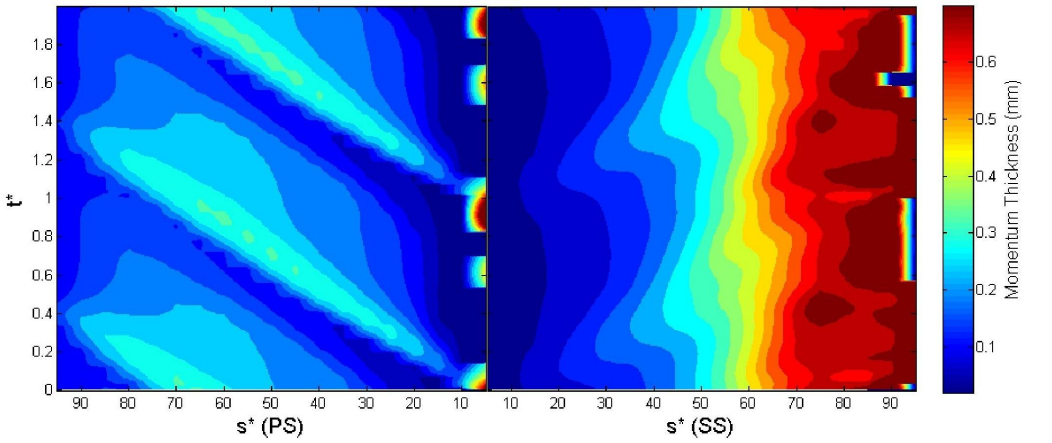

b) Momentum thickness on blade surface

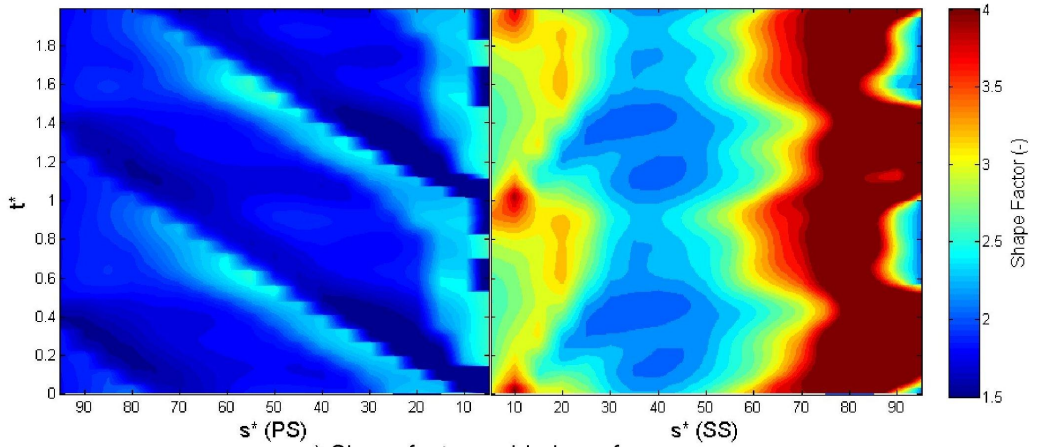

c) Shape factor on blade surface

Figure A.82: CFD results for high loading case

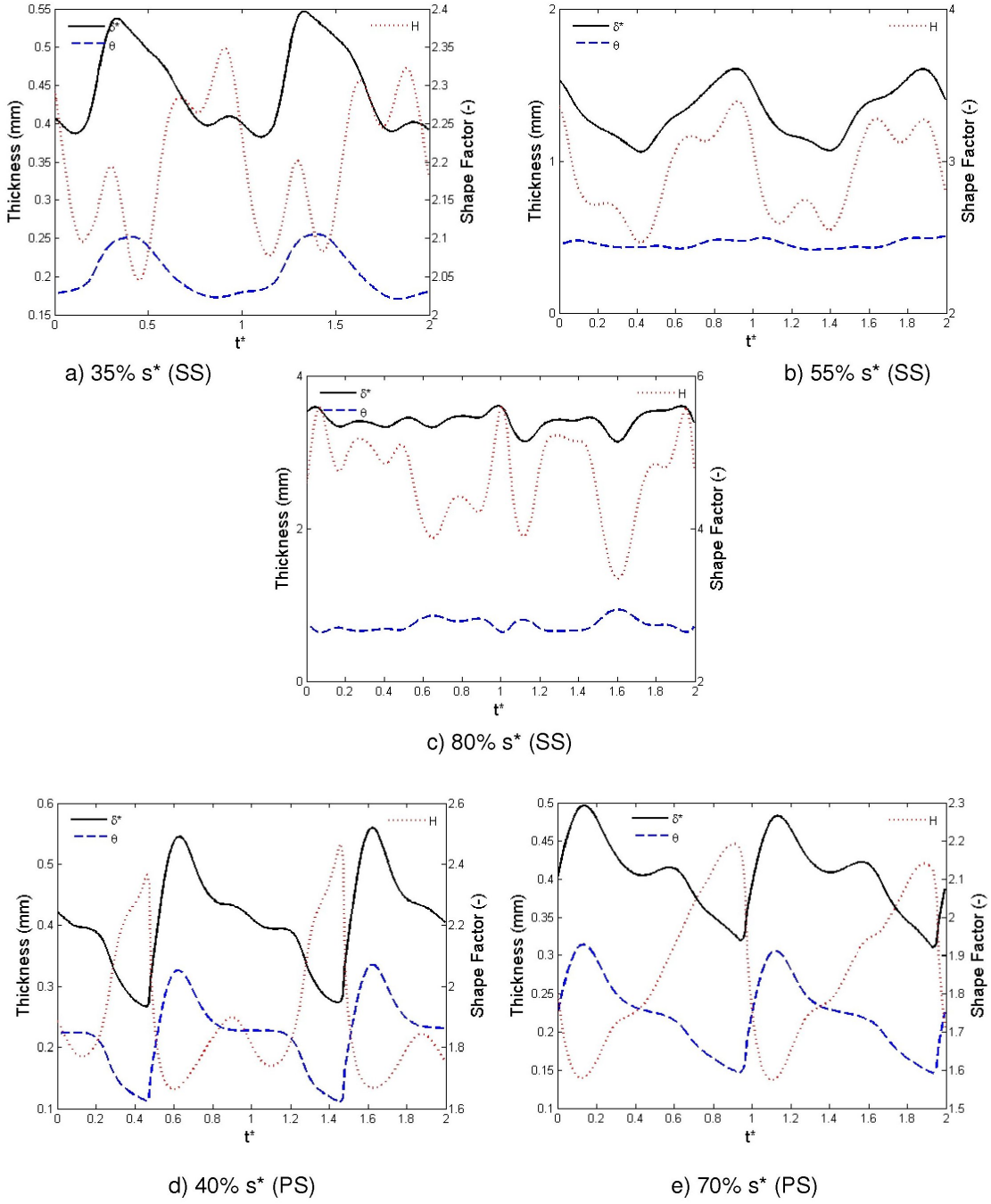

Figure A.83: CFD results for high loading case - Integral parameters at various distances along suction (SS) and pressure (PS) surfaces

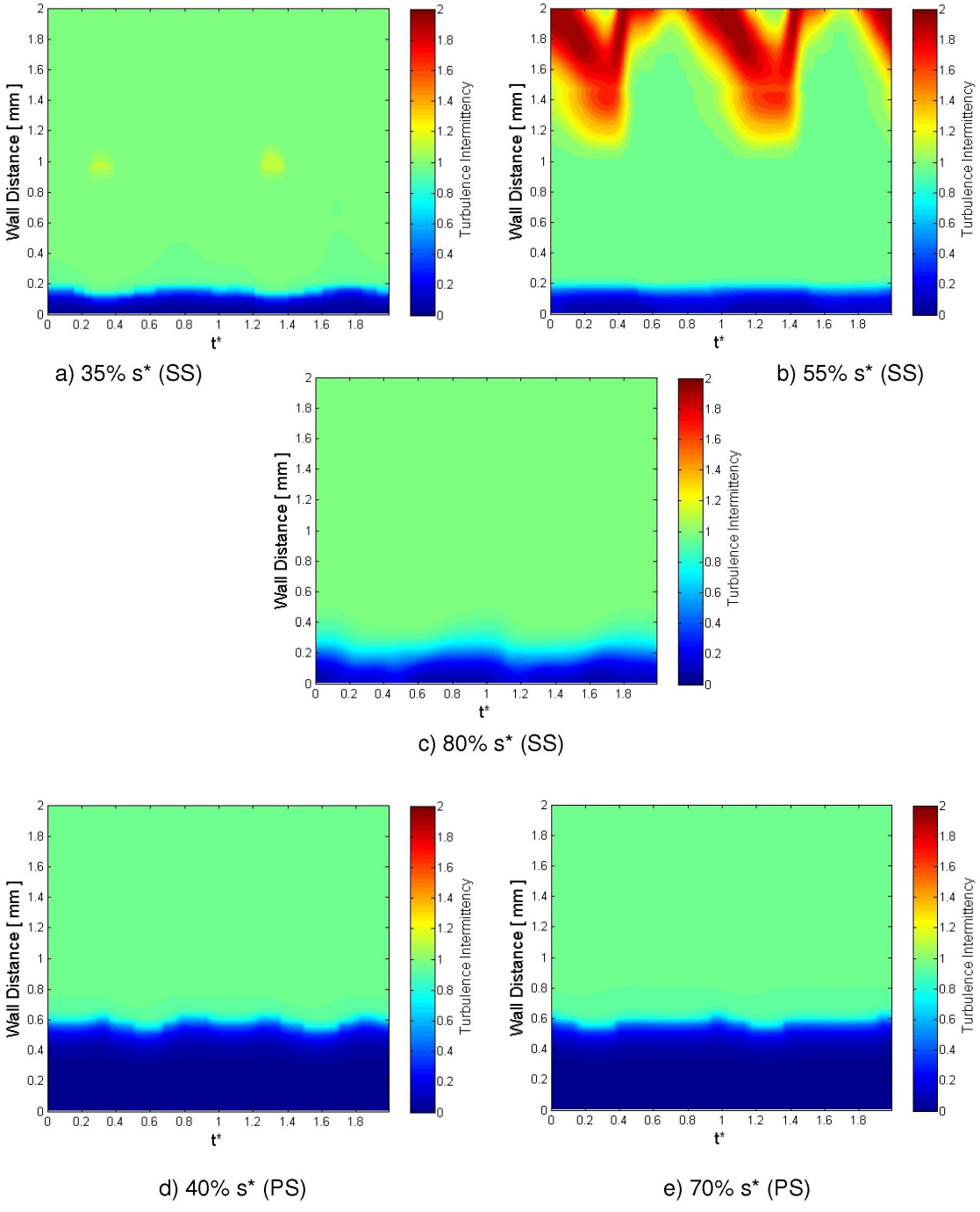

Figure A.84: CFD results for high loading case - Intermittency at various distances along suction (SS) and pressure (PS) surfaces

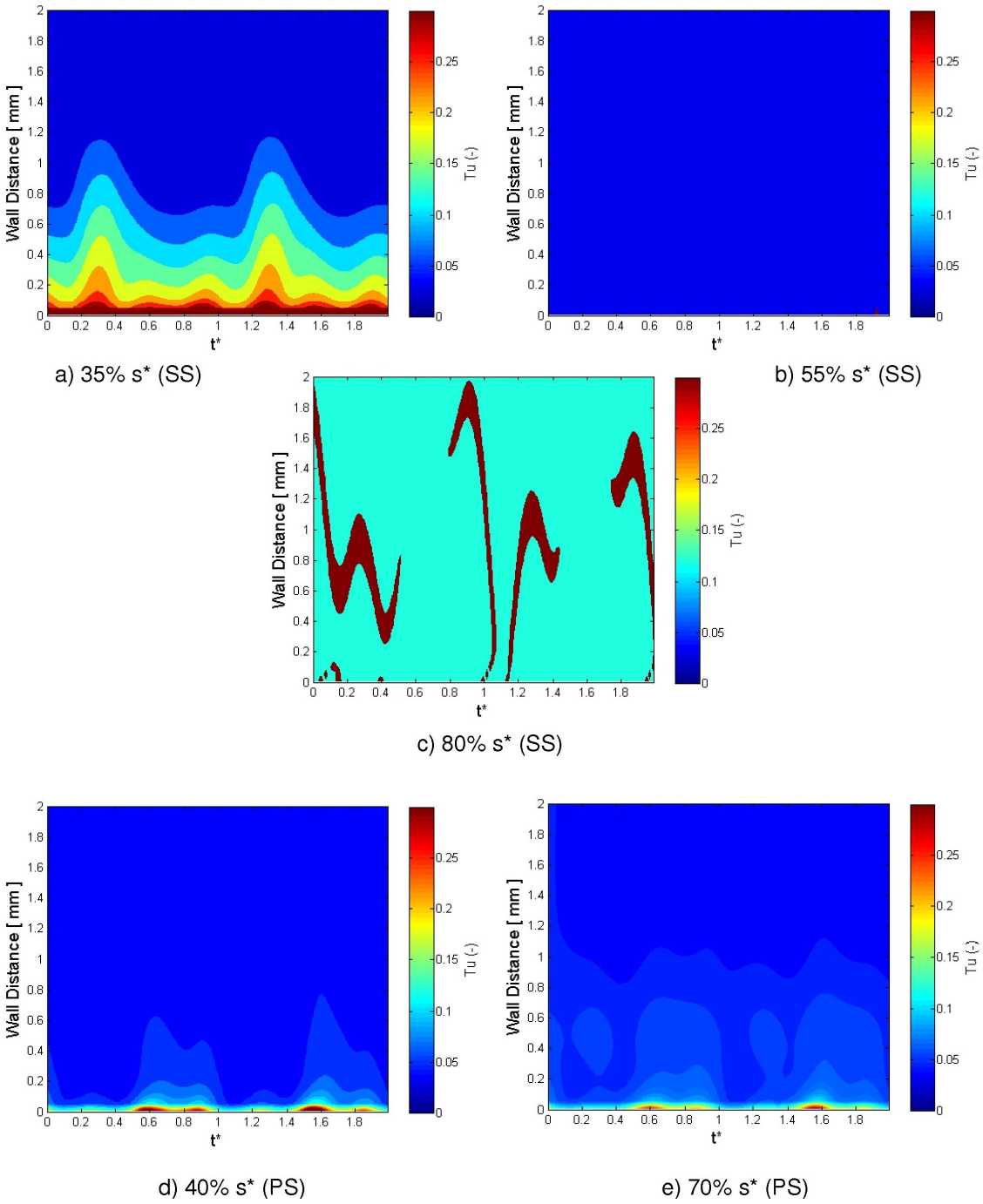

Figure A.85: CFD results for high loading case - Turbulence intensity at various distances along suction (SS) and pressure (PS) surfaces

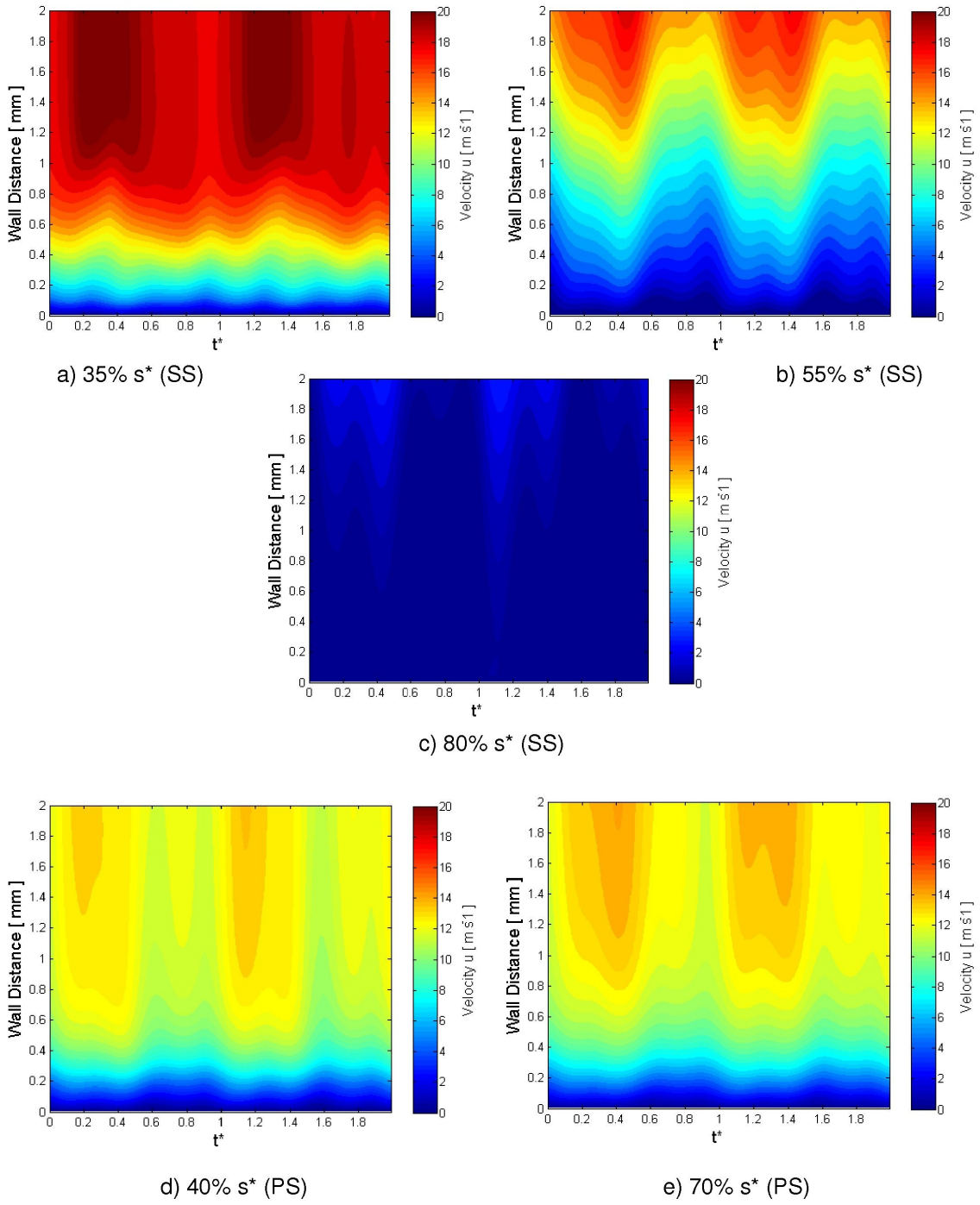

Figure A.86: CFD results for high loading case - Tangential velocity at various distances along suction (SS) and pressure (PS) surfaces

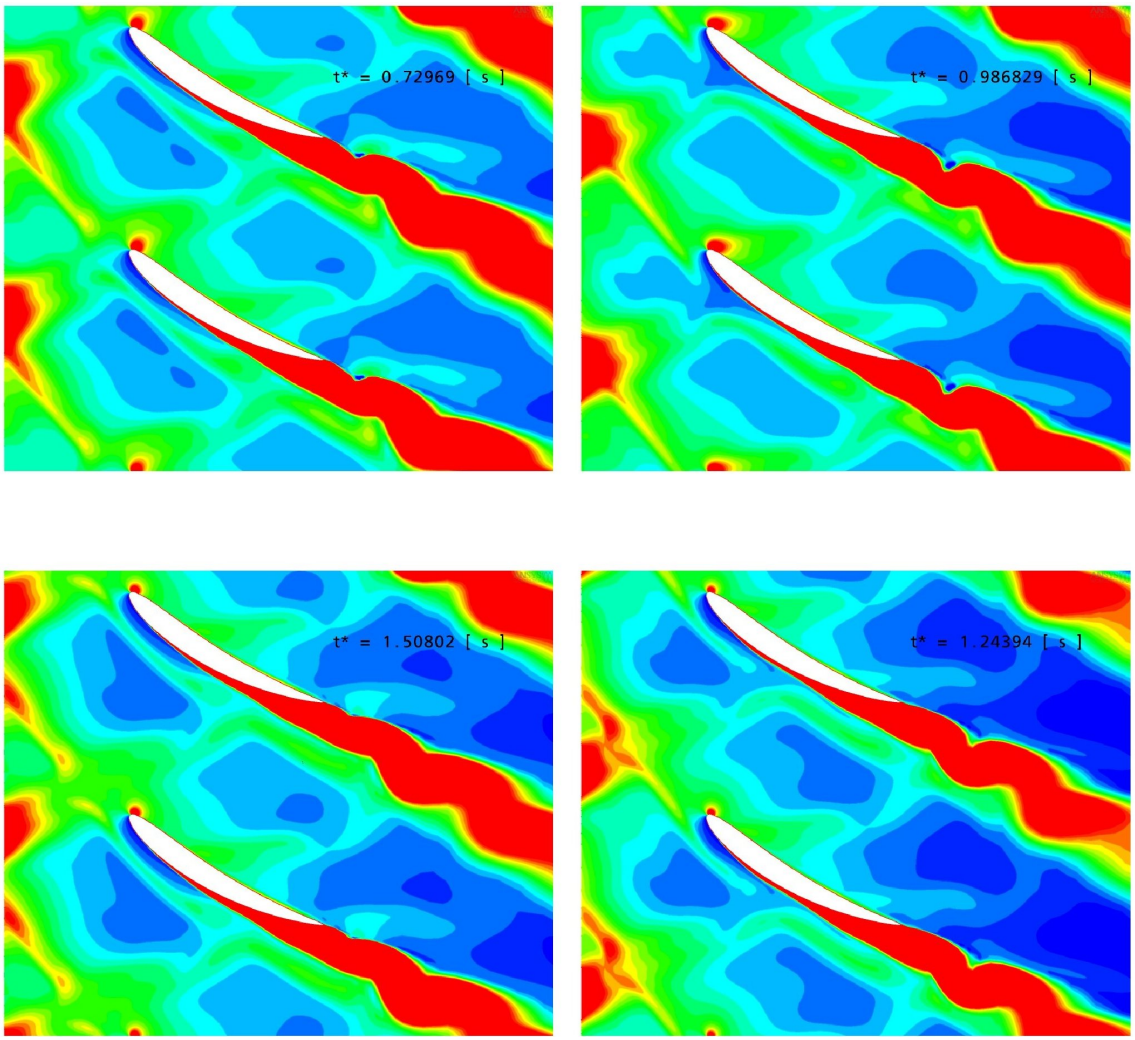

Figure A.87: CFD results for high loading case - Wake turbulence transport through the domain at varying rotor passing time

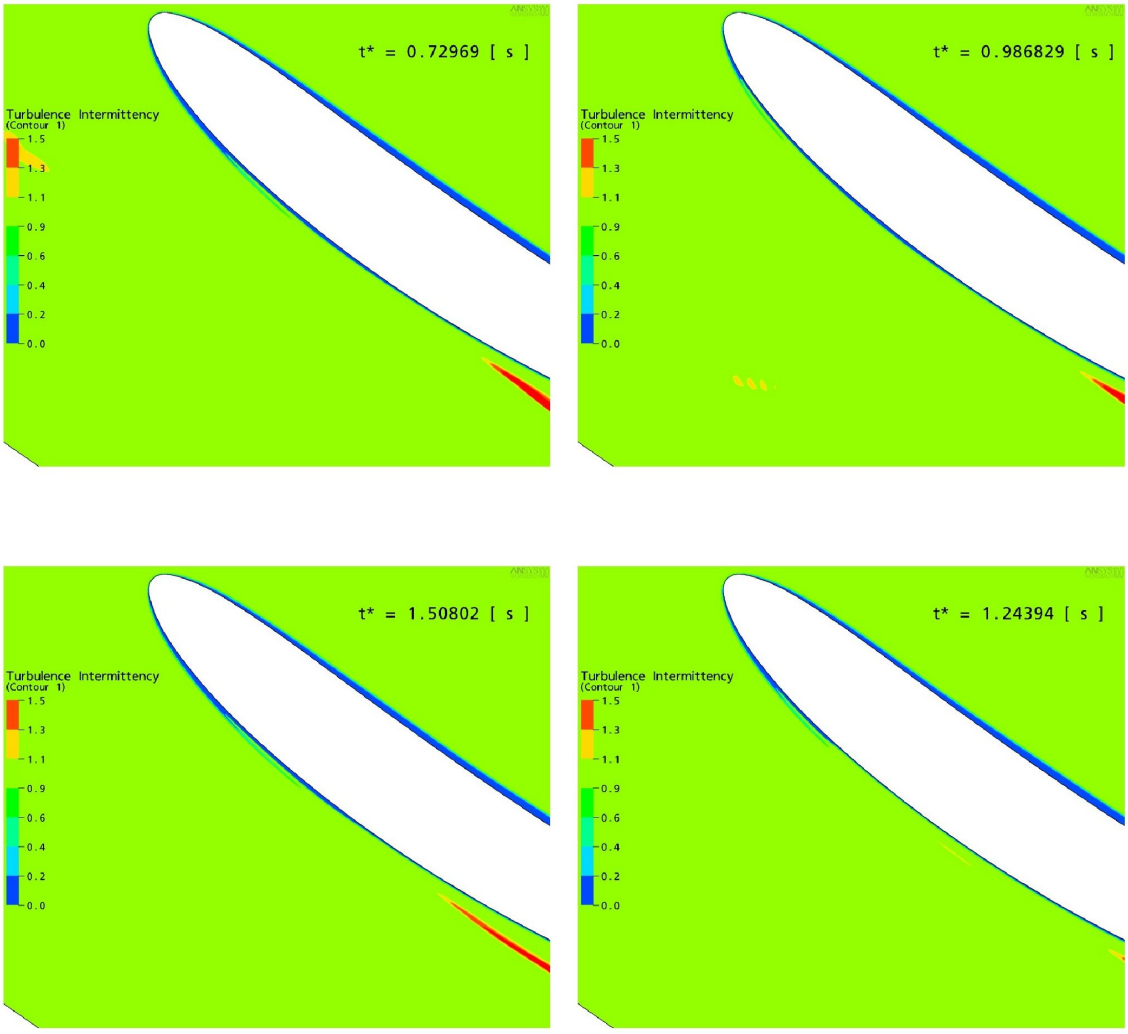

Figure A.88: CFD results for high loading case - Intermittency in the boundary layer at varying rotor passing time

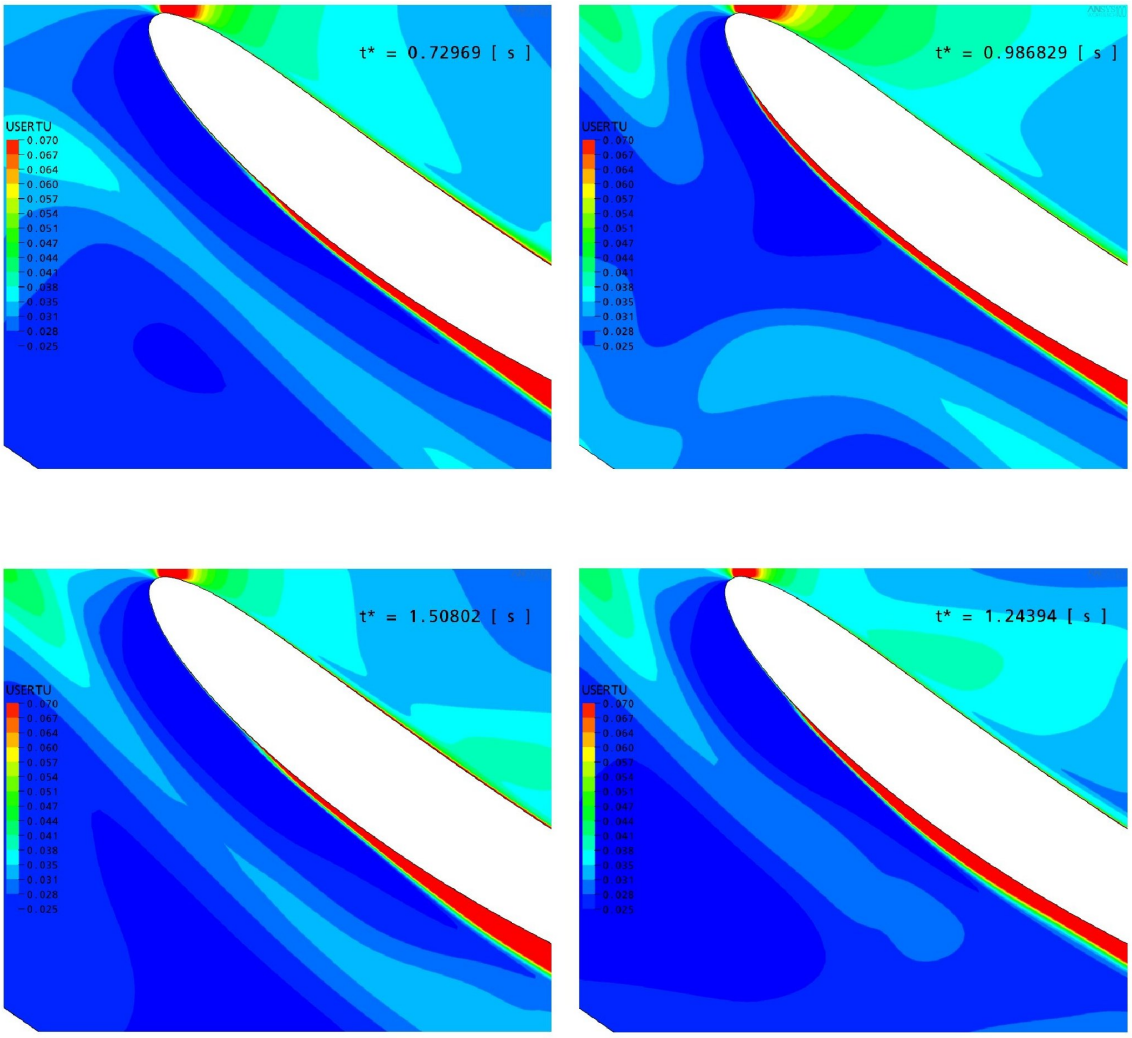

Figure A.89: CFD results for high loading case - Wake turbulence transport effects on the stator boundary layer at varying rotor passing time

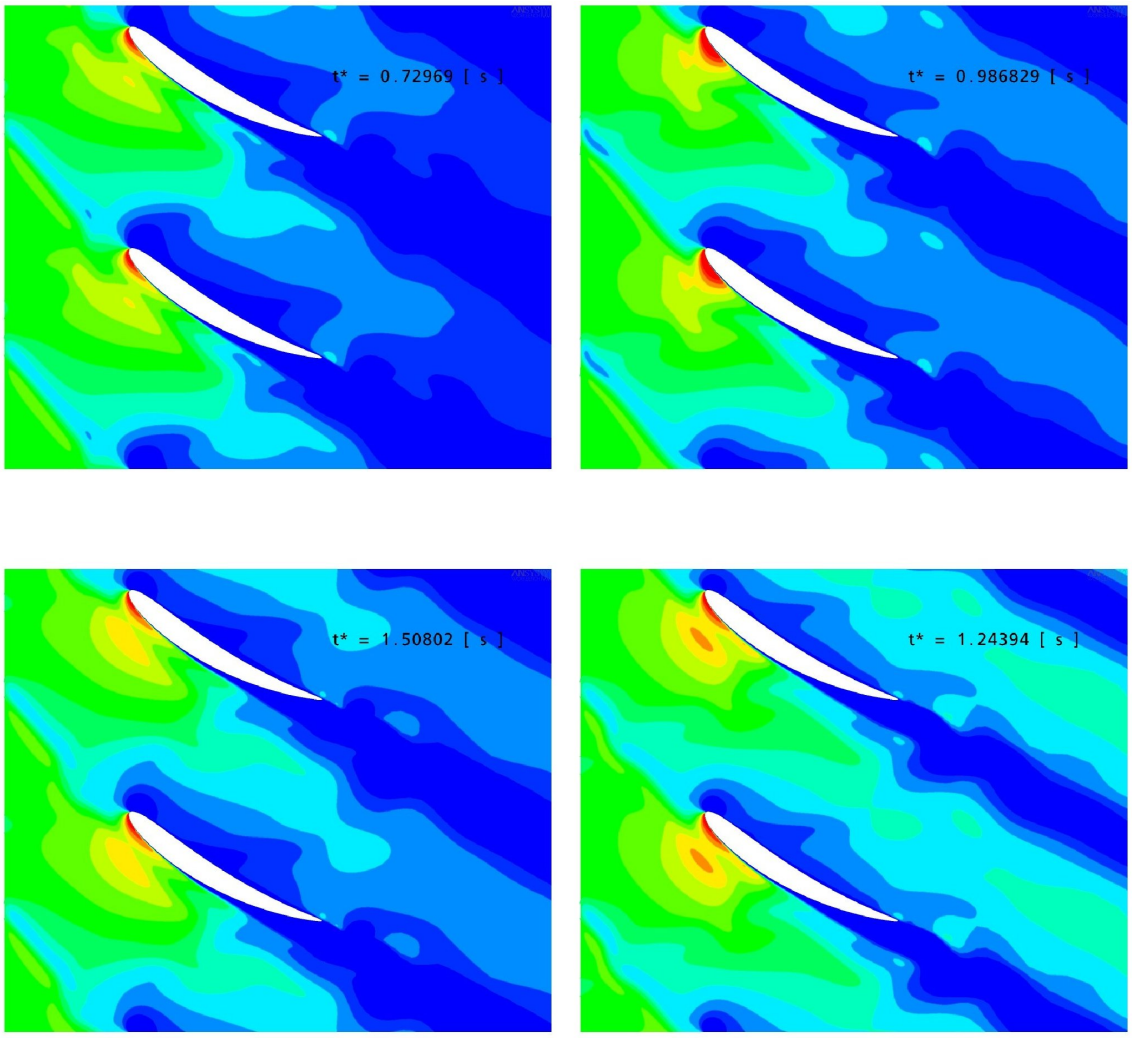

Figure A.90: CFD results for high loading case - Velocity through passage at varying rotor passing time

This page has been left intentionally blank.

Appendix B

3D Unsteady Results Figures

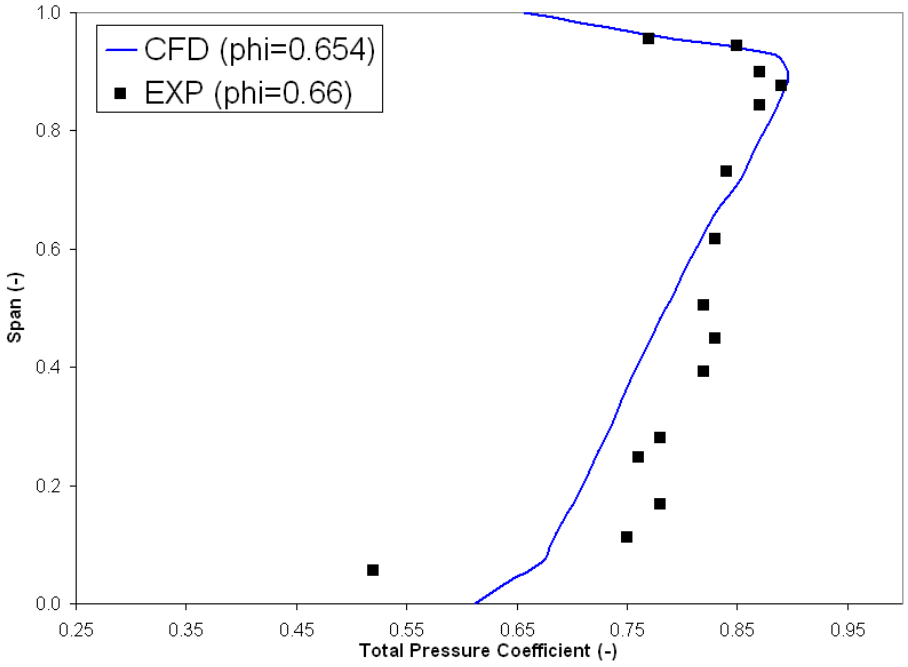

Figure B.1: Comparison of experimental and CFD results for rotor exit pressure coefficient

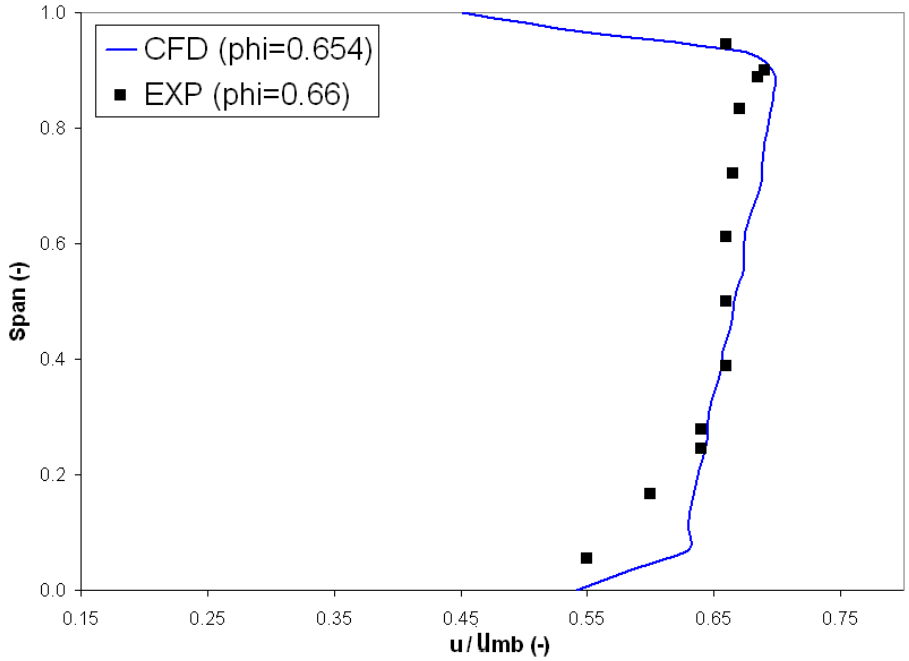

Figure B.2: Comparison of experimental and CFD results for rotor exit axial velocity coefficient

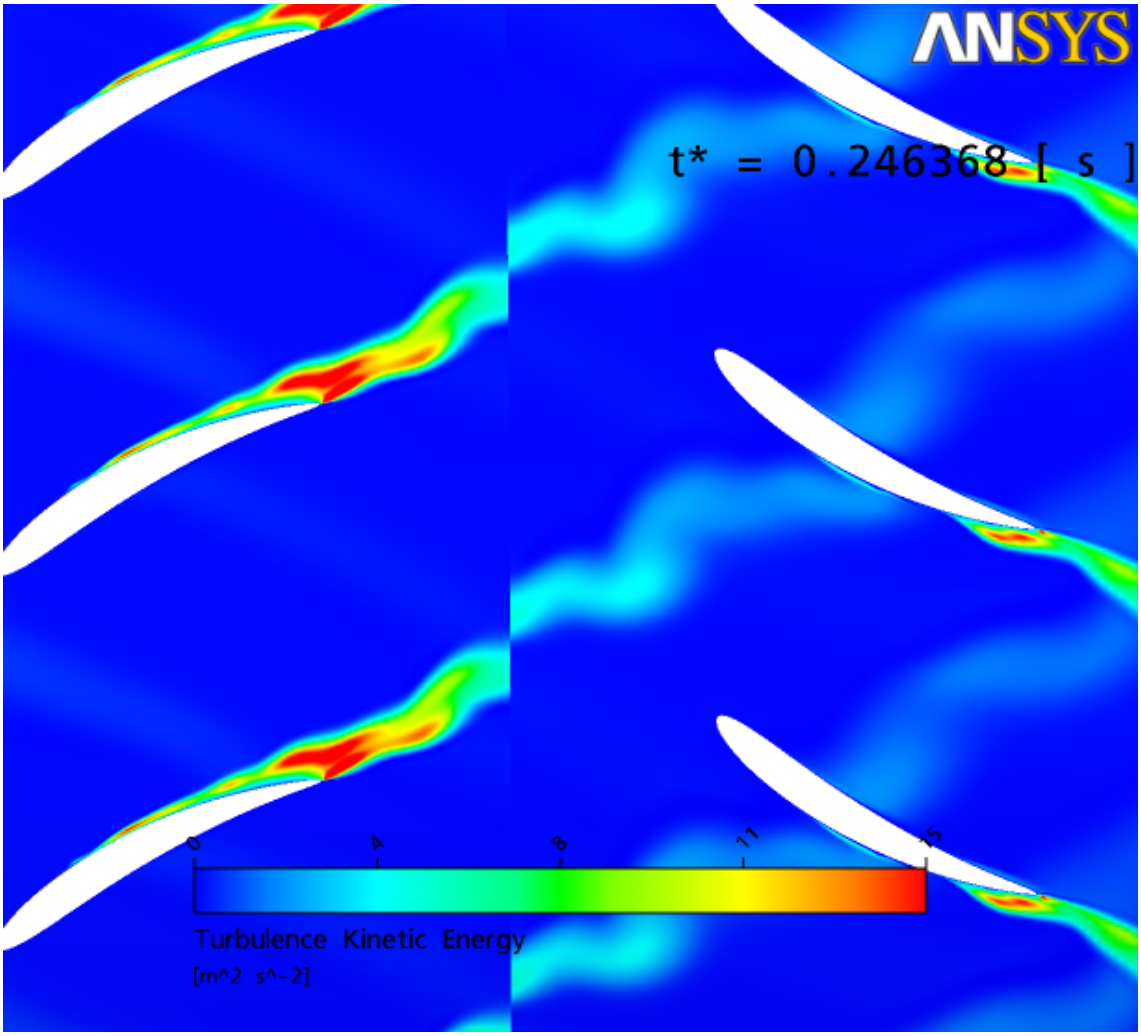

Figure B.3: CFD results for 3D case - Wake turbulent kinetic energy transport through the rotor and stator domains at t* = 0.246368

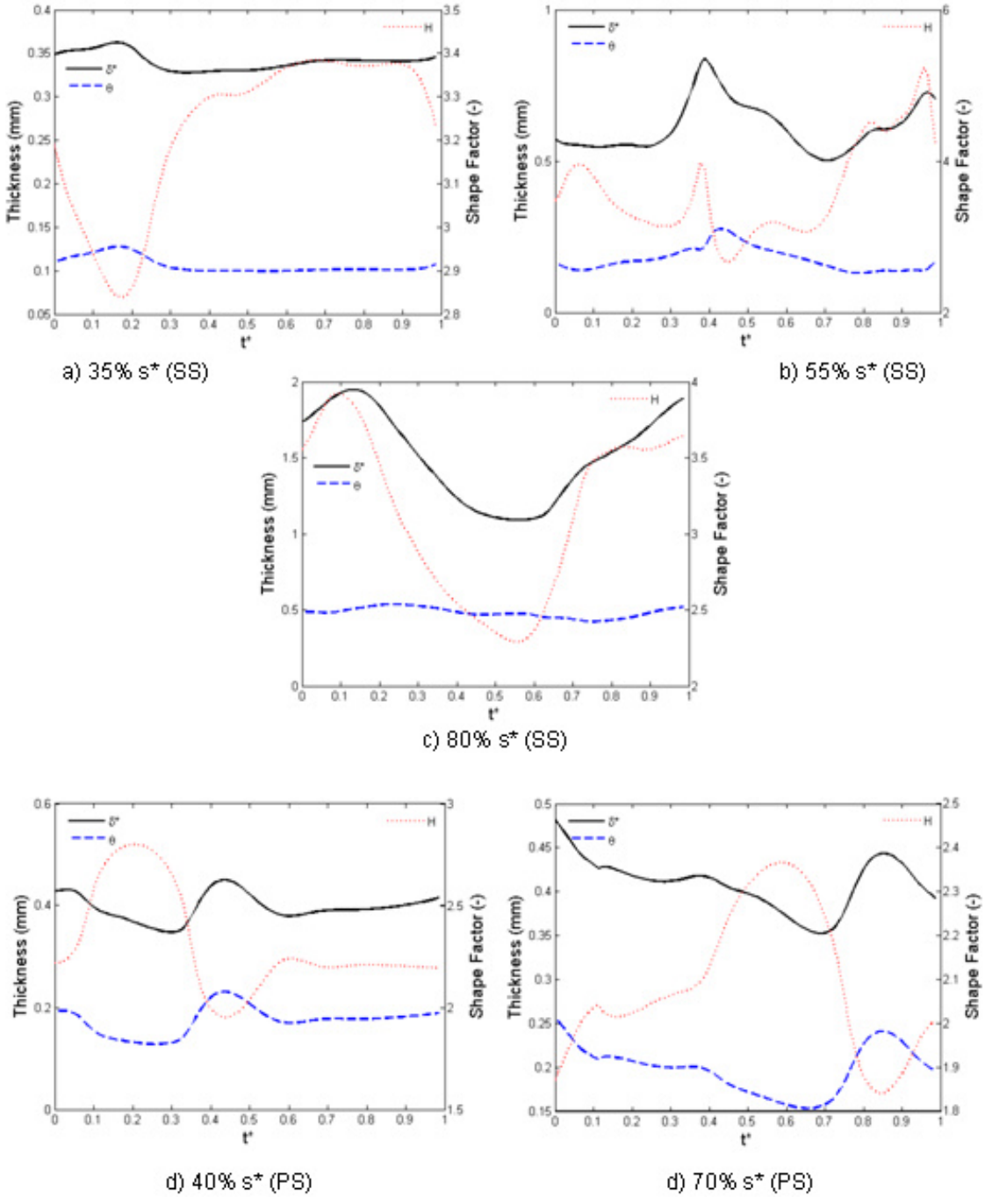

Figure B.4: CFD results for 3D case - Integral parameters at various distances along suction (SS) and pressure (PS) surfaces

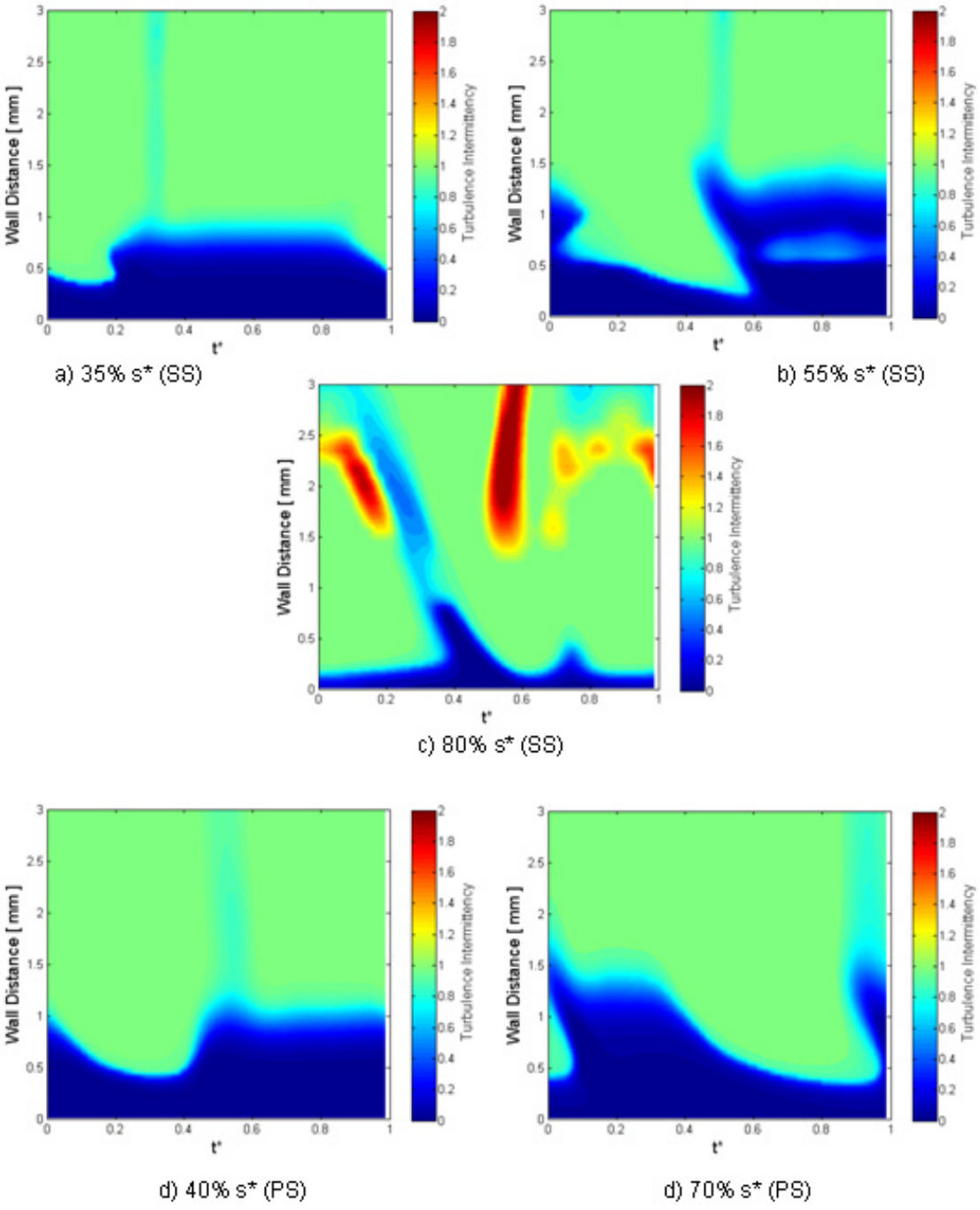

Figure B.5: CFD results for 3D case - Intermittency at various distances along suction (SS) and pressure (PS) surfaces

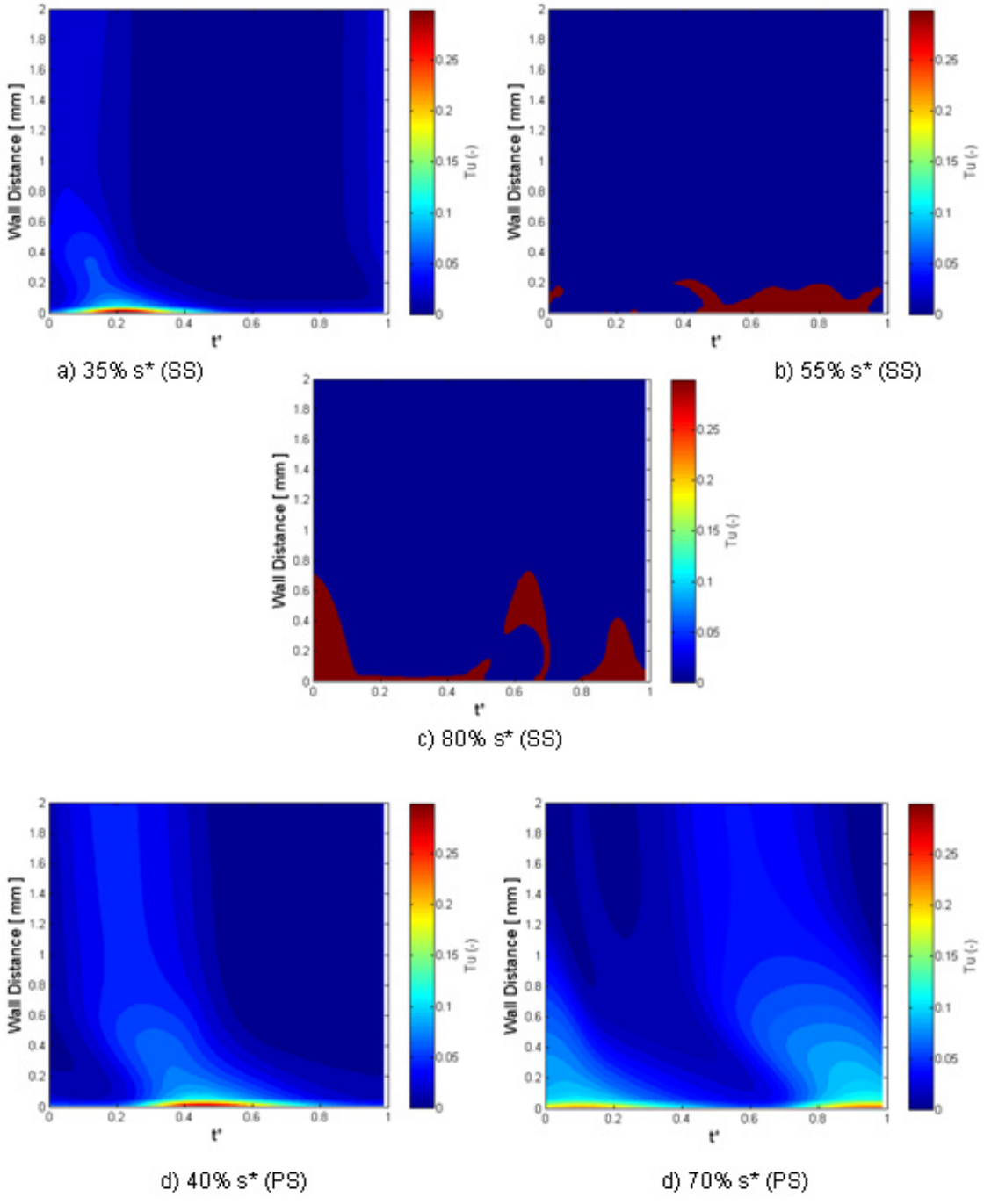

Figure B.6: CFD results for 3D case - Turbulence intensity at various distances along suction (SS) and pressure (PS) surfaces

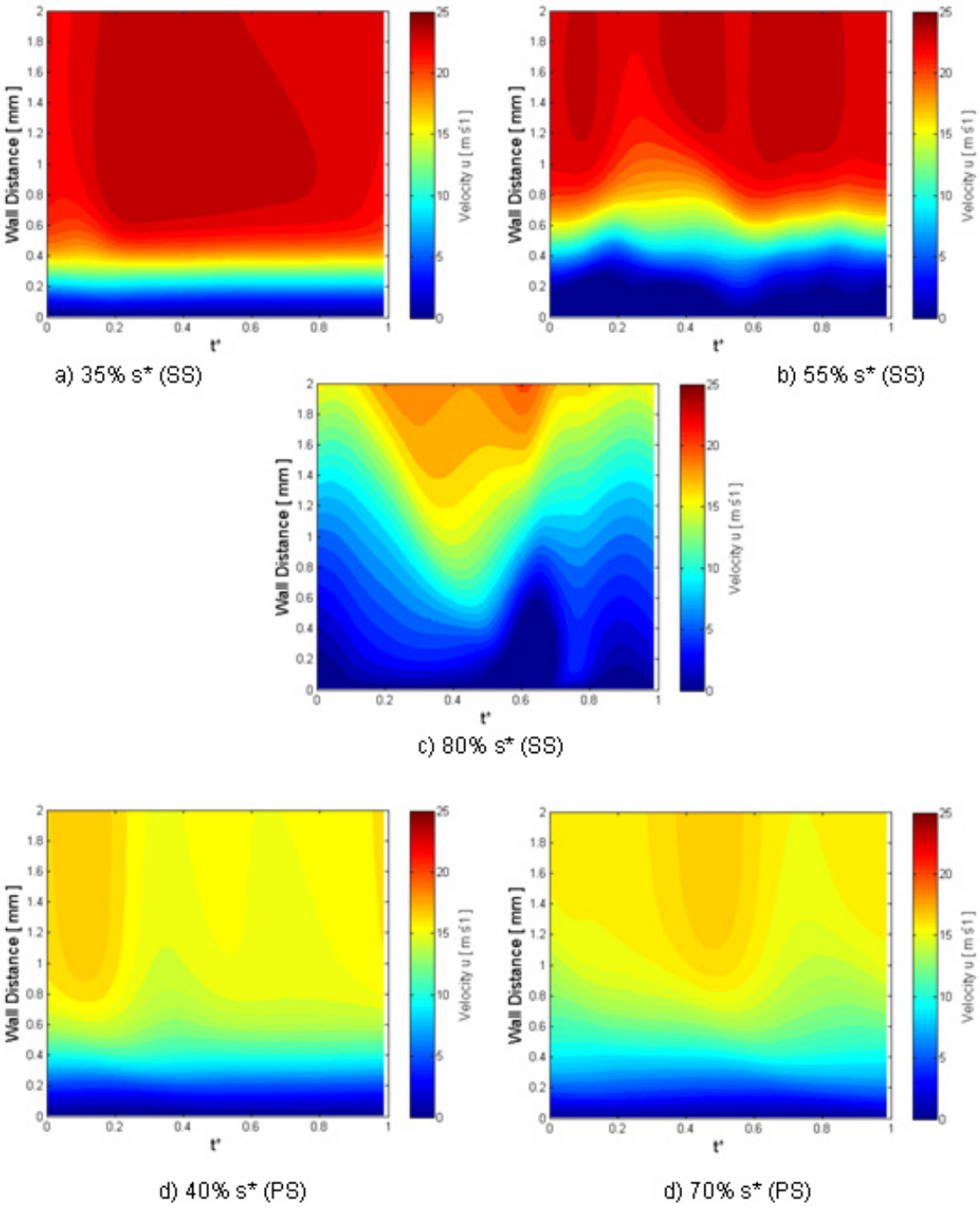

Figure B.7: CFD results for 3D case - Tangential velocity at various distances along suction (SS) and pressure (PS) surfaces